Nonlinear Control of Unmanned Aerial Vehicles

Systems With an Attitude

MARCUS GREIFF
DEPARTMENT OF AUTOMATIC CONTROL | LUND UNIVERSITY

Nonlinear Control of Unmanned Aerial Vehicles: Systems With an Attitude

Marcus Greiff

LUND
UNIVERSITY

Department of Automatic Control

Ph.D. Thesis TFRT-1131
ISBN 978-91-8039-047-7 (print)
ISBN 978-91-8039-048-4 (web)
ISSN 0280–5316

Department of Automatic Control
Lund University
Box 118
SE-221 00 LUND
Sweden

Printed in Sweden by MediaTryck.
Lund 2021

Abstract

This thesis deals with the general problem of controlling rigid-body systems through space, with a special focus on unmanned aerial vehicles (UAVs). Several promising UAV control algorithms have been developed over the past decades, enabling truly astounding feats of agility when combined with modern sensing technologies. However, these control algorithms typically come without global stability guarantees when implemented with estimation algorithms. Such control systems work well most of the time, but when introducing the UAVs more widely in society, it becomes paramount to prove that stability is ensured regardless of how the control system is initialized.

The main motivation of the research lies in providing such (almost) global stability guarantees for an entire UAV control system. We develop algorithms that are implementable in practice and for which (almost) all initial errors result in perfect tracking of a reference trajectory. In doing so, both the tracking and the estimation errors are shown to be bounded in time along (almost) all solutions of the closed-loop system. In other words, if the initialization is sound and the initial errors are small, they will remain small and decrease in time, and even if the initial errors are large, they will not increase with time.

As the field of UAV control is mature, this thesis starts by reviewing some of the most promising approaches to date in Part I. The ambition is to clarify how various controllers are related, provide intuition, and demonstrate how they work in practice. These ideas subsequently form the foundation on which a new result is derived, referred to as a nonlinear *filtered output feedback*. This represents a diametrically different approach to the control system synthesis. Instead of a disjoint controller/estimator design, the proposed method is comprised of two controller/estimator pairs, which when combined through a special interconnection term yields a system with favorable stability properties.

While the first part of the thesis deals with theoretical controller design, Part II concerns application examples, demonstrating how the theory can solve challenging problems in modern society. In particular, we consider the problem of circumnavigation for search and rescue missions and show how UAVs can gather data from radioactive sites to estimate radiation intensity.

Acknowledgments

I am extremely grateful for my years at the Department of Automatic Control in Lund, and for the support that I have received from all of its past and present members throughout my studies. I first got interested in control theory after several inspiring conversations with Karl Johan Åström. However, it was a combination of meetings with Anders Rantzer and Richard Murray, along with a project course supervised by Martina Maggio and Fredrik Bagge Carlson that truly sealed my fate as a control theorist.

Firstly, I would like to thank my advisor Anders Robertsson, for the unyielding encouragement in all things professional and private. Your curiosity is infectious, and you have always been supportive of my endeavors, introducing me to nonlinear control as well as to Erjen Lefeber. I am grateful to you both for guidance, patience, and help in addressing the various problems in this thesis. I can say without hesitation that few of the developments made in this thesis would have been possible without Erjen's incredible intuition and mathematical ability. I have learned much from you.

Secondly, I would like to thank my co-supervisors Zhiyong Sun and Bo Bernhardsson. Your excellent technical skill sets have improved both my problem-solving and scientific writing. I am especially grateful to Zhiyong for our many fruitful collaborations, to Bo for guidance and for inspiring me to pursue doctoral studies, and to both of you for proof reading the thesis.

I would like to thank the past and present members of the SSF-project "Semantic mapping and visual navigation for smart robots", especially Kalle Åström and Patrik Persson. Without you, some of the most interesting experiments presented in this thesis would not have been possible.

Thank you Arnaud Taffanel, Tobias Antonsson, Marcus Eliasson, and Kristoffer Richardsson at Bitcraze AB, for your support and encouragement in my early experiments with the Crazyflie. I learned valuable lessons from you during our debugging sessions in the Malmö basement, and our amazing late-night demo-preparations in various Belgian hotel rooms.

I would like to thank several graduates of the department. Karl Berntorp, thank you for introducing me to filtering and estimation theory. While much

of our joint work falls well beyond the scope of this thesis, I count it as some of my most interesting results to date. Björn Olofsson, thank you for help in proof reading many early drafts over the years. You have been incredibly generous with your time. Mattias Fält, thank you for your guidance throughout my time at the department, and for our memorable travels through France. Fredrik Bagge Carlson, thank you for introducing me to Julia and for inspiring me to pursue a doctoral degree.

In addition, I would like to thank all of my friends at the department for their encouragement over the years, but especially Richard Pates, Martina Maggio, Claudio Mandioli, Johan Ruuskanen, Albin Heimersson, Marcus Thelander Andreen, Gautham Nayak Seetanadi, Olof Troeng, Nils Vreman, Pauline Kergus, Kaoru Yamamoto, Martin Karlsson, Martin Heyden, Emil Vladu, and Frida Heskebeck. I would also thank my dear friends outside of academia, especially Henrik Omling, Malte Arnold, Oliver Walsh, and Björn Nilsson, your company has been truly invaluable over the past years.

Finally, I would like to express my sincere thanks to Flora, Lennart, Malin, Emma, and Jacob. You are my greatest inspiration. Thank you for your unwavering support and (occasional) appreciation of incomprehensible plots.

Financial Support

I am grateful for the generous financial support of the projects that I have been working on. Specifically, this thesis was funded by two main sources:

- The SSF-project "Semantic mapping and visual navigation for smart robots" (RIT15-0038).
- The ELLIIT-project "Autonomous Radiation Mapping and Isotope Composition Identification by Mobile Gamma Spectroscopy".

Contents

1

Introduction

1.1 Background and Motivation

The field of control theory concerns the computation of a control signal that is used to actuate a system based on (partial) information of its state. The state is a concise representation of the system at any given time, and its composition and evolution in time can be modeled in various ways depending on the context in which the system is analyzed. For unmanned aerial vehicles (UAVs), which are the main subject of this thesis, the state is often defined as the configurations of the UAV (position and rotation) and their velocities. These states evolve in time by nonlinear dynamics, as governed by the laws of classical mechanics. The UAVs are actuated through external forces and torques generated by a set of rotors. While the exact configurations of the rotors vary both in number and relative location, it is common to use a configuration of four rotors with aligned rotational axes for reasons related to the mathematical concept of controllability. This form of UAV is commonly referred to as a quadrotor. While the control systems in this thesis are developed specifically for quadrotor UAVs, they may also be used for other UAVs, such as satellites, or form the basic building blocks in robotic manipulation applications. A flying quadrotor is illustrated in Figure 1.1.

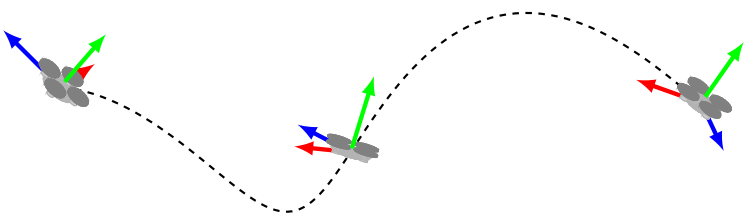

Figure 1.1 Three configurations of a quadrotor UAV in motion.

For all of these systems, a common control objective is to achieve stabilization about some stationary configuration of interest. In the case of the UAV, this could be to drive the system to a stable hovering position. More generally, the control objective could be to track a feasible time-varying reference trajectory. Throughout this thesis, we focus on the latter tracking problem to enable flights along time-varying trajectories as depicted in Figure 1.1. In either case, secondary objectives are often considered, such as to minimize a cost expressed in the errors and control signals over time, or to ensure robustness of the closed-loop system to certain classes of disturbances.

Depending on the context and specifications, many approaches can be taken to solving the same control problem. In this thesis, we primarily distinguish between four different problems. The first is the computation of the control signal (forces and torques), from a given state (configurations and their velocities), which is commonly referred to as a *full state feedback* (FSF) problem. However, in order to implement such a controller, the state needs to be known in time. For this purpose, the system is equipped with sensors which generate information on the states, and the inference of the state conditioned on such measurements is commonly known as a *full state estimation* (FSE) problem. Alternatively, a feedback law can be constructed directly from the measurements, also known as an *output feedback* (OF) control problem. Finally, one may consider co-designing controller and estimator with the constraint that the control signal should be computed from the estimates without explicitly using the measurements in the feedback law, which is referred to as a *filtered output feedback* (FOF) problem (see Figure 1.2).

It may seem that combining a solution to (A), the full state feedback problem, and (B), the estimation problem, makes it uninteresting to consider the notion of a filtered output feedback (provided that an estimate of the state, $\boldsymbol{x}$, is represented in the filter memory, $\boldsymbol{\zeta}$). However, the estimator in (B) introduces additional dynamics, which may cause the combined system to become unstable in the nonlinear setting. This is somewhat counter-intuitive, as one may expect that a cascade of two nonlinear systems whose errors independently decay to zero will itself result in a stable system. However, the separation principle does not apply generally in nonlinear systems (see the discussion on the peaking phenomenon in Sec. 2.5), unless stringent conditions are met by both (A) and (B). These conditions will be made more precise in Chapter 2, but do not hold for many of the popular approaches to (A) and (B). Generally, the problem becomes difficult to analyze beyond local approximations of the error dynamics when combining (A) and (B).

In contrast, problems (C) and (D) may be solved to guarantee global or almost global stability properties - that is, regardless of how large the initial estimation and control errors are, the system will always reach a state of stability or perfect tracking. What's more, with the powerful tools of Lyapunov theory used throughout this thesis (see Sec. 2.4), one may

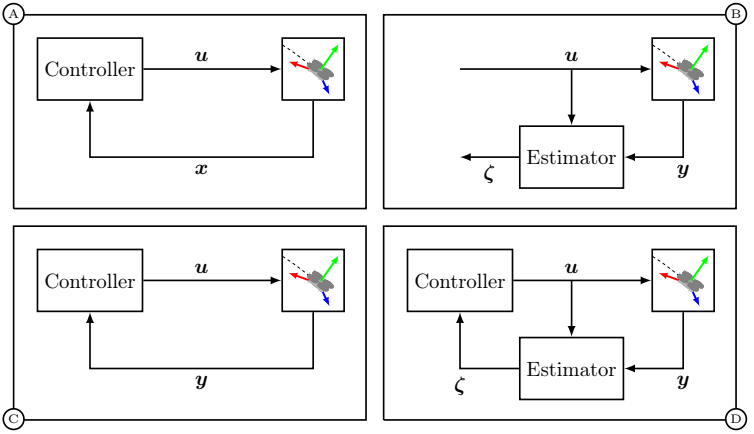

Figure 1.2 Block diagrams of various UAV control systems where the state is denoted $\boldsymbol{x}$, the measurements by $\boldsymbol{y}$, the control signals by $\boldsymbol{u}$, and the estimator memory by $\boldsymbol{\zeta}$. Sketches of (A) a full state feedback, (B) a full state estimator, (C) an output feedback, and (D) a filtered output feedback.

express a positive definite function in the errors and show that the errors are bounded and decaying in time. Still, the FOF solution in (D) enjoys two important advantages over the OF solution in (C). The first is that it can be designed to yield estimates of the true system states which represent physically important signals, which can be used by an operator or higher-level control systems. For instance, with an OF solution, we would know the memory of the controller and the resulting control signal, but might not be able to infer the configurations and velocities of the system. The second advantage of the FOF solution is that the measurements are not used directly in the feedback law. Instead, the measurements are filtered, and the filter memory is used in the filtered output feedback. Consequently, the measurement noise does not appear directly in the control signal, but is first filtered through a nonlinear system. Thus, apart from ensuring general stability properties of the closed-loop system, a solution in (D) can be expected to have a smoother control signal when compared to a solution in (C). This will prove to be important when considering the cascade analysis of the control system in (D).

1.1.1 Part I - Theoretical Developments

Due to the great practical utility of the UAV and the intricacies of its mathematical description, the associated control and estimation problems have attracted significant attention in the research community over the past decades. As a consequence, the literature is mature, and there exist many important and useful solutions to the FSF stabilization and tracking problems.

However, it is not always clear when one solution should be preferred over another. As such, a topic of the thesis is to clarify how a representative subset of these controllers are related, and use these insights to propose extensions ensuring robustness to relevant disturbances, and to explore various tuning strategies. To this end, the problem of designing FSF controllers corresponding to control system (A) in Figure 1.2 is discussed in Chapters 3 and 4.

As mentioned in the introduction, the separation principle that is often invoked in linear control system design to analyze combinations of full state feedback controllers in (A) and estimators in (B), does not apply in the general nonlinear setting. As such, if uniform (almost) global stability properties are to be shown for the closed-loop system, such arguments need to be made for specific controller and observer pairs, or by considering the (filtered) output feedback problem directly. Consequently, a topic of the thesis is to construct such a (filtered) output feedback controller in a deterministic framework for the pure attitude dynamics as well as the full UAV dynamics given the directional, gyroscopic and positional measurements that are ubiquitous in modern UAVs. The problem of designing FOF solutions corresponding to (D) in Figure 1.2 is discussed in Chapters 5 and 6.

While it is of great interest to know which of these solutions to use and when, it is equally important that they actually get used in practice. However, implementing low-level controllers on UAVs is a highly nontrivial task, as small errors in implementation or tuning can have disastrous consequences in practice. Therefore, many of the theoretical results of this thesis, along with several prior results, have been implemented in C such that the they may be simulated exactly as they are presented. This facilitates the testing and evaluation of code that can be run directly on the micro-controller of an intended application, or wrapped in any given programming language. Many commercial platforms do not permit a complete replacement of the firmware, but the hope is that making the software available in this form will serve to disseminate the ideas both within academia and the industry.

1.1.2 Part II - Application Examples

The low-level tracking controllers and estimators derived in Part I of this thesis are essential in solving many important problems in modern society. When considering applications such as navigating through the aisles of a supermarket for inventorying, or flying in close proximity to a radioactive surface in a nuclear surveying task, it is of great importance to abstract away the lower-level control system and consider a simplified system. For instance, with some of the controllers presented in Part I, if a sufficiently smooth reference trajectory for the closed-loop control system is generated, then there exist guarantees that it will be followed down to some known upper bound in the tracking errors. Consequently, the UAV applications are

simplified greatly, as we can consider a point moving around in the aisles and plan its movement such that its distance to the shelves is greater than the bounds on the tracking errors at all times. Thus ensuring that its movement will be safe provided that the reference trajectory is sufficiently smooth.

As a complement to the simulations and experiments in Part I, we consider two separate application examples, each with important theoretical contributions in addition to demonstrating the utility of good closed-loop control. These applications are: circumnavigation and target tracking in Chapter 8 and radiation estimation by mobile gamma spectroscopy in Chapter 9.

1.2 Co-author Affiliations

The co-authors of the included papers are listed below in no particular order.

Dr. Anders Robertsson,
Department of Automatic Control,
Lund University,
Lund, Sweden,
anders.robertsson@control.lth.se

Dr. Rolf Johansson,
Department of Automatic Control,
Lund University,
Lund, Sweden,
rolf.johansson@control.lth.se

Dr. Zhiyong Sun,
Department of Electrical Engineering,
Eindhoven Institute of Technology,
Eindhoven, The Netherlands,
z.sun@tue.nl

Dr. Erjen Lefeber,
Department of Mechanical Engineering,
Eindhoven Institute of Technology,
Eindhoven, The Netherlands,
a.a.j.lefeber@tue.nl

Dr. Mohammad Deghat,
Faculty of Engineering,
University of New South Wales,
Sydney, Australia,
m.deghat@unsw.edu.au

Dr. Karl Berntorp,
Control for Autonomy Group,
Mitsubishi Electric Research Laboratories,
Cambridge, Massachusetts, USA,
berntorp@merl.com

Dr. Emil Rofors,
Department of Nuclear Physics,
Lund University,
Lund, Sweden,
emil.rofors@nuclear.lu.se

Mr. Rikard Tyllström,
School of Aviation,
Lund University,
Lund, Sweden,
rikard.tyllstrom@tfhs.lu.se

Dr. Kalle Åström,
Center for Mathematical Sciences,
Lund University,
Lund, Sweden,
karl.astrom@math.lth.se

Mr. Patrik Persson,
Center for Mathematical Sciences,
Lund University,
Lund, Sweden,
patrik.persson@math.lth.se

1.3 Included Publications

In this section, the papers that are included in the thesis are stated in the order of appearance, along with explanations of the contributions made by each author. These are divided into three categories; those related to Part I (primarily theoretical), those related to Part II (application oriented), and those excluded entirely from the thesis in order to improve its cohesion.

1.3.1 Part I

The following publications are included in Part I of the thesis:

[P1] M. Greiff, Z. Sun, and A. Robertsson (2021f). "Attitude control on SU(2): stability, robustness, and similarities". *IEEE Control Systems Letters* **6**, pp. 73–78. DOI: 10.1109/LCSYS.2021.3049440

[P2] M. Greiff, Z. Sun, and A. Robertsson (2021e). "Tuning and analysis of geometric tracking controllers on SO(3)". In: *2021 American Control Conference (ACC)*. IEEE, pp. 1674–1680. DOI: 10.23919/ACC50511.2021.9482745

[P3] M. Greiff and A. Robertsson (2018). "Incremental reference generation for nonsingular control on SE(3)". In: *2018 IEEE Conference on Control Technology and Applications (CCTA)*, pp. 132–137. DOI: 10.1109/CCTA.2018.8511419

These publications were based on the ideas of M. Greiff, who also derived the theoretical results, conducted the supporting simulations and wrote the `AerialVehicleControl.jl` module published at CodeOcean [Greiff, 2020]. Z. Sun and A. Robertsson participated in the proof reading of the results, and helped structuring the papers and the ideas therein for increased clarity.

[P4] E. Lefeber, M. Greiff, and A. Robertsson (2020). "Filtered output feedback tracking control of a quadrotor UAV". *IFAC-PapersOnLine* **53**:2, pp. 5764–5770. DOI: 10.1016/j.ifacol.2020.12.1609

The ideas for this paper came during a visit of E. Lefeber to Lund University. They were initiated by E. Lefeber and derived collaboratively with M. Greiff during this visit. The results were subsequently implemented by M. Greiff, who was responsible for the numerical simulation studies. E. Lefeber and M. Greiff participated equally in the writing of the paper, and all of the authors helped structuring the paper to aid the clarity of its presentation. Parts of this paper were implemented by M. Greiff in the `AerialVehicleControl.jl` module and published for reproducibility at CodeOcean [Greiff, 2020].

1.3.2 Part II

The following publications are included in Part II of the thesis:

[P5] M. Greiff, M. Deghat, Z. Sun, and A. Robertsson (2021b). "Target localization and circumnavigation with integral action in R^2". *IEEE Control Systems Letters* **6**, pp. 1250–1255. DOI: 10.1109/LCSYS.2021.3091633

The main ideas were developed by M. Greiff from discussions with M. Deghat and Z. Sun. All authors contributed to the writing process, and M. Greiff was responsible for the implementation and generation of the numerical results. The experiments were conducted by M. Greiff, and the code used in the simulations and experiments is available at CodeOcean for transparency and reproducibility [Greiff, 2021].

[P6] M. Greiff, E. Rofors, A. Robertsson, R. Johansson, and R. Tyllström (2021d). "Gamma-ray imaging with spatially continuous intensity statistics". In: *2021 International Conference on Intelligent Robots and Systems (IROS)*. Article in press. IEEE

The main ideas were developed by M. Greiff, who also implemented the algorithms and conducted the numerical experiments. The data was acquired in experiments at the former nuclear power plant in Barsebäck, where the UAV was operated by R. Tyllström and the gamma detector was operated by E. Rofors. The paper was largely written by M. Greiff, with E. Rofors, A. Robertsson, R. Johansson, and R. Tyllström helping in structuring the paper.

1.3.3 Excluded papers

Several other papers were not included in the thesis. This was mainly done to improve the cohesion and clarity of its presentation, but also due to some of the work being related to US patents and ongoing projects at Mitsubishi Electric Research Laboratories. These are listed as follows:

M. Greiff and A. Robertsson (2017). "Optimisation-based motion planning with obstacles and priorities". *IFAC-PapersOnLine* **50**:1, pp. 11670–11676. DOI: 10.1016/j.ifacol.2017.08.1677

M. Greiff (2018). "A time-warping transformation for time-optimal movement in differentially flat systems". In: *2018 Annual American Control Conference (ACC)*. IEEE, pp. 6723–6730. DOI: 10.23919/ACC.2018.8431230

M. Greiff and K. Berntorp (2018). "Evaluation of the discrete time feedback particle filter for IMU-driven systems configured on SE(2)". In: *2018 Annual American Control Conference (ACC)*. IEEE, pp. 5683–5689. DOI: 10.23919/ACC.2018.8431134

M. Greiff, A. Robertsson, and K. Berntorp (2019a). "Performance bounds in positioning with the VIVE lighthouse system". In: *2019 22th International*

Conference on Information Fusion (FUSION). IEEE, pp. 1–8. ISBN: 978-1-7281-1840-6

Z. Sun, M. Greiff, A. Robertsson, and R. Johansson (2019). "Feasible coordination of multiple homogeneous or heterogeneous mobile vehicles with various constraints". In: *2019 International Conference on Robotics and Automation (ICRA)*. IEEE, pp. 1008–1013. DOI: 10.1109/ICRA.2019.8793834

M. Greiff, Z. Sun, A. Robertsson, and R. Johansson (2019b). "Temporal viability regulation for control affine systems with applications to mobile vehicle coordination under time-varying motion constraints". In: *2019 18th European Control Conference (ECC)*. IEEE, pp. 3571–3576. DOI: 10.23919/ECC.2019.8796018

M. Greiff, Z. Sun, and A. Robertsson (2020c). "Coordination control of double-integrator systems with time-varying weighted inputs". *IFAC-PapersOnLine* **53**:2, pp. 2489–2494. DOI: 10.1016/j.ifacol.2020.12.202

M. Greiff and K. Berntorp (2020). "Optimal measurement projections with adaptive mixture Kalman filtering for GNSS positioning". In: *2020 American Control Conference (ACC)*. IEEE, pp. 4435–4441. DOI: 10.23919/ACC45564.2020.9147675

M. Greiff, A. Robertsson, and K. Berntorp (2020a). "Exploiting linear substructure in linear regression Kalman filters". In: *2020 59th IEEE Conference on Decision and Control (CDC)*. IEEE, pp. 2942–2948. DOI: 10.1109/CDC42340.2020.9304191

M. Greiff, A. Robertsson, and K. Berntorp (2020b). "MSE-optimal measurement dimension reduction in Gaussian filtering". In: *2020 IEEE Conference on Control Technology and Applications (CCTA)*. IEEE, pp. 126–133. DOI: 10.1109/CCTA41146.2020.9206162

M. Greiff, K. Berntorp, S. Di Cairano, and K. Kim (Aug. 2021a). "Mixed-integer linear regression Kalman filters for GNSS positioning". In: *IEEE Conference on Control Technology and Applications (CCTA)*. Article in press. San Diego, CA, USA

In addition to these papers, journal extensions of [Greiff et al., 2019b; Sun et al., 2019] on temporal viability; the mixed-integer estimators in [Greiff et al., 2021a]; and the radiation inference method in [Greiff et al., 2021d] are being prepared or have been submitted. Additionally, a paper pertaining to quadrotor control on $\mathrm{SU}(2) \times \mathbb{R}^3$ has been submitted to the American Control Conference, and an extended version is available on arXiv as a pre-print.

M. Greiff, P. Persson, Z. Sun, A. Robertsson, and K. Åström (2021c). "Quadrotor control on SU(2) x R3 with SLAM integration". Version 1. arXiv: 2110.01099 [eess.SY]. URL: arxiv.org/abs/2110.01099

1.4 Contributions

The main contributions of this thesis are, in order of appearance:

- The introduction of a distance on SU(2) and subsequent derivation of continuous, discontinuous, and robust attitude controllers using this metric, with quantification of decay rates and the domains of attraction.
- A comparison of the aforementioned controllers with the analogous results on SO(3), and a clarification of how these relate to other methods used in the design of various controllers and estimators on SO(3).
- A method of tuning the controllers on SU(2) and SO(3) by solving a bilinear matrix inequality program, facilitating performance comparisons when optimally tuned with respect to certain closed-loop properties.
- The open-source implementation of these and prior results on attitude control in C for direct use on the micro-controllers of a target application, with the options for tuning and external simulation in Julia.
- The extension of the results in SU(2) to the control of UAV dynamics configured on $\mathrm{SU}(2) \times \mathbb{R}^3$, with validation in simulation and real-time examples demonstrating aggressive trajectory tracking maneuvers.
- The derivation of a filtered output feedback on SO(3), guaranteeing closed-loop stability for the tracking problem when assuming measurements from a nine degrees of freedom (9-DOF) inertial measurement unit (IMU), without these appearing directly in the control signal.
- A filtered output feedback controller on $\mathrm{SO}(3) \times \mathbb{R}^3$ for trajectory tracking, with saturated controls, assuming positional information and a 9-DOF IMU, and ensuring uniform almost global asymptotic stability.
- An extension of the circumnavigation and target tracking result in [Deghat et al., 2010] with integral action, facilitating rejection of disturbances caused by actuator errors, with experimental verification.
- An extension of the additive point-source localization (APSL) algorithm for radiation intensity inference in [Hellfeld et al., 2019] with Gaussian kernels, with subsequent experimental validation of the presented algorithm using a spectrometer mounted on a large UAV.

The notation SO(3), SU(2), and $\mathbb{R}$ will be explained in Chapter 2.

Table 1.1 Overview of the contents, separating Part I and Part II.

Chapter	Description	Overview
Chapter 2	Mathematical preliminaries for Part I of the thesis defining the dynamics and main theoretical tools.	Not given
Chapter 3	A collection of results on full state feedback for the attitude dynamics of a UAV, related to (A) in Figure 1.2.	Table 3.1
Chapter 4	A collection of results on geometric full state feedback for the UAV dynamics, related to (A) in Figure 1.2.	Table 4.1
Chapter 5	A collection of results on filtered output feedback for the attitude dynamics of a UAV, related to (D) in Figure 1.2.	Table 5.1
Chapter 6	A collection of results on filtered output feedback for the UAV dynamics, related to (D) in Figure 1.2.	Table 6.1
Chapter 7	Summary of Part I of the thesis	Not given
Chapter 8	The generalization of a result on circumnavigation and target tracking, with verification in simulation and examples in practice.	Sec. 8.1.2
Chapter 9	The generalization of an algorithm for radiation estimation with verification in simulation and examples in practice.	Sec. 9.1.2
Chapter 10	Summary of Part II of the thesis	Not given

1.5 Outline and Structure

This thesis is comprised of several chapters, each including (i) a mathematical problem formulation, with (ii) a brief motivation describing why it is considered, followed by (iii) an overview with of the results and examples of the chapter. The purpose of this is to give an overview what the chapters contain, and to clearly indicate what should be considered prior and original work, respectively. For an overview of the developments, Table 1.1 gives a description of each chapter, and a reference to secondary tables outlining their results and examples. These chapters are divided into two parts, and while both contain simulations as well as real-time examples, the first is focused on the theory of UAV control, while the latter concerns application examples.

Part I The first part concerns theoretical results related to control and estimation for systems with rotational degrees of freedom. In Part I, the mathematical preliminaries are given in Chapter 2, followed by the results on full state feedback (FSF) attitude control in Chapter 3, with results pertaining to the full UAV dynamics given in Chapter 4. The filtered output feedback (FOF) results are then derived separately for attitude dynamics and the full UAV dynamics. This is done in Chapters 5 and 6, respectively.

Part II The second part of the thesis concerns two very different applications which seek to demonstrate how the theoretical results can be applied practice. The first is an application to circumnavigation control in Chapter 8, where an output feedback controller is derived using some of the techniques in Chapter 6, incorporating smooth saturation functions to give sufficient conditions for collision avoidance. The second application in Chapter 9 pertains

Table 1.2 Overview of the explanatory videos with links to YouTube.

Name and Link	Description
chapter-3-simulations.mp4	Simulation examples in Chapter 3
chapter-4-simulations.mp4	Simulation examples in Chapter 4
chapter-4-spiraling.mp4	Real-time example of the spiraling maneuver in Chapter 4
chapter-4-inventorying.mp4	Real-time example of the inventorying task in Chapter 4
chapter-5-simulations.mp4	Simulation examples in Chapter 5
chapter-6-simulations.mp4	Simulation examples in Chapter 6
chapter-8-circumnav.mp4	Real-time example of the UGV control in Chapter 8
chapter-9-radiation.mp4	Real-time example of the radiation experiments in Chapter 9

to radiation estimation by mobile spectrometers mounted on UAVs, where spherical-radial cubature rules common to nonlinear Gaussian filtering are used infer the moments of an intensity function over a known surface.

Videos As this thesis concerns the control of moving and rotating bodies in space, the results are best explored in videos depicting the time-evolution of the signals and the system configurations. To provide intuition, a vast majority of the simulations and real-time experiments come with associated videos. These are uploaded in the Lund University Research Portal:

`http://portal.research.lu.se/portal/`

They are also available through the author's YouTube channel:

`http://www.youtube.com/channel/UCMn1bUgdQcIJ7MP-4N58Zgw`

The videos are referenced explicitly from the relevant figure captions, but a list of all of the video contributions is given in Table 1.2 for easier access.

Part I

Theoretical Developments

2

Preliminaries

Throughout the thesis, a wide range of topics are covered. In this chapter, definitions and concepts that appear in the chapters on full state feedback (Chapters 3 and 4) and filtered output feedback control (Chapters 5 and 6) are introduced, with mathematical intuition provided when possible.

2.1 Nomenclature and Definitions

Bold font is used to denote vectors, $\boldsymbol{x}$, with the element at an index i denoted x_i. Similarly, matrices are denoted capital bold font letters, $\boldsymbol{A}$, with an element at a row i and column j denoted $[\boldsymbol{A}]_{i,j}$. The real numbers are denoted $\mathbb{R}$, the complex numbers by $\mathbb{C}$ (with an imaginary unit i), and the integers are denoted by $\mathbb{Z}$. All positive real numbers are denoted $\mathbb{R}_{>0}$, or $\mathbb{R}_{\geq 0}$ if including the zero, and the complex numbers with a negative real part are denoted $\mathbb{C}_{<0}$. A concatenation of two vectors $\boldsymbol{x} \in \mathbb{C}^m$ and $\boldsymbol{y} \in \mathbb{C}^n$ is denoted by $(\boldsymbol{x};\ \boldsymbol{y}) = (\boldsymbol{x}^\top, \boldsymbol{y}^\top)^\top \in \mathbb{C}^{m+n}$. An ordered collection of objects $\boldsymbol{x} \in A$ and $\boldsymbol{y} \in B$ is denoted $(\boldsymbol{x}, \boldsymbol{y}) \in A \times B$, where the notation $(\boldsymbol{x}, \boldsymbol{y}) = (\boldsymbol{a}, \boldsymbol{b})$ implies that $\boldsymbol{x} = \boldsymbol{a} \in A$ and $\boldsymbol{y} = \boldsymbol{b} \in B$. The notation $\boldsymbol{I}$ refers to an identity matrix, and if it is necessary to clarify its dimensions, this is done by $\boldsymbol{I}_N \in \mathbb{R}^{N \times N}$. The zero matrix is denoted $\boldsymbol{0}$, and if necessary, its dimensions are written out as $\boldsymbol{0}_{M \times N} \in \mathbb{R}^{M \times N}$. The standard Kronecker product is denoted by $\otimes$ in the usual convention, such that for any $\boldsymbol{A} \in \mathbb{R}^{m \times n}$ and $\boldsymbol{B} \in \mathbb{R}^{k \times l}$,

$$\boldsymbol{A} \otimes \boldsymbol{B} = \begin{bmatrix} [\boldsymbol{A}]_{1,1}\boldsymbol{B} & \cdots & [\boldsymbol{A}]_{1,n}\boldsymbol{B} \\ \vdots & \ddots & \vdots \\ [\boldsymbol{A}]_{m,1}\boldsymbol{B} & \cdots & [\boldsymbol{A}]_{m,n}\boldsymbol{B} \end{bmatrix} \in \mathbb{R}^{mk \times nl}. \tag{2.1}$$

The eigenvalue with largest real part of a matrix $\boldsymbol{A}$ is denoted $\lambda_M(\boldsymbol{A})$, and the eigenvalue with the smallest real part is denoted $\lambda_m(\boldsymbol{A})$. The spectrum of a matrix is denoted $\text{spec}(\boldsymbol{A}) = \{\lambda_m(\boldsymbol{A}), ..., \lambda_M(\boldsymbol{A})\}$. The determinant and trace of a matrix $\boldsymbol{A}$ are written $\det(\boldsymbol{A})$ and $\text{Tr}(\boldsymbol{A})$, respectively. Throughout the

thesis, we work with the classical Lie groups $\mathrm{SO}(n)$ and $\mathrm{SU}(n)$, which will be defined shortly. These groups are equipped with a unique translation invariant probability measure (a Haar measure), hence, we can without ambiguity let $\mathcal{U}(G)$ denote a uniform distribution over any of these groups (see e.g., [Meckes, 2019, Lemma 2.1]). Similarly, a uniform distribution over a compact interval $I \subset \mathbb{R}^n$ is denoted $\mathcal{U}(I)$. The first time-derivative of a signal $\boldsymbol{x}(t)$ is denoted $(\mathrm{d}/\mathrm{d}t)\boldsymbol{x} = \dot{\boldsymbol{x}}$, often omitting the time-argument, the second time-derivative is written $(\mathrm{d}^2/\mathrm{d}t^2)\boldsymbol{x} = \ddot{\boldsymbol{x}}$, and its nth derivative is denoted $(\mathrm{d}^n/\mathrm{d}t^n)\boldsymbol{x} = \boldsymbol{x}^{(n)}$.

Definition 2.1—Vector Norm
A vector norm is denoted $\|\boldsymbol{x}\|$, and satisfies

(i) $\|\boldsymbol{x}+\boldsymbol{y}\| < \|\boldsymbol{x}\| + \|\boldsymbol{y}\|$ for all $\boldsymbol{x}, \boldsymbol{y} \in \mathbb{R}^m$,

(ii) $\|\alpha\boldsymbol{x}\| = |\alpha|\|\boldsymbol{x}\|$ for all $\boldsymbol{x} \in \mathbb{R}^m, \alpha \in \mathbb{R}$,

(iii) $\|\boldsymbol{x}\| > 0$ for all $\boldsymbol{x} \in \mathbb{R}^m \backslash \{\boldsymbol{0}\}$, and $\|\boldsymbol{x}\| = 0$ if and only if $\boldsymbol{x} = \boldsymbol{0}$. □

While $\|\cdot\|$ may refer to any vector norm, we will, for any $\boldsymbol{u} \in \mathbb{R}^m$, let $\|\boldsymbol{u}\| = (u_1^2 + \cdots + u_m^2)^{1/2}$ denote the usual two-norm unless stated otherwise. For matrices, we let $\|\cdot\|$ denote the induced two-norm, which in case of square matrices is the spectral norm. That is, if $\boldsymbol{A} \in \mathbb{C}^{n\times n}$, $\|\boldsymbol{A}\| = (\lambda_M(\boldsymbol{A}^*\boldsymbol{A}))^{1/2}$.

Definition 2.2—Continuity
Let function $f : \mathbb{R}^m \mapsto \mathbb{R}^n$ and $\boldsymbol{x}, \boldsymbol{y} \in \mathbb{R}^m$. The function f is said to be continuous at a point $\boldsymbol{x}$ if for all constants $\epsilon > 0$ there exists $\delta > 0$ such that

$$\|\boldsymbol{x}-\boldsymbol{y}\| < \delta \Rightarrow \|f(\boldsymbol{x}) - f(\boldsymbol{y})\| < \epsilon. \tag{2.2}$$

□

Definition 2.3—Piecewise Continuity
A function $f : \mathbb{R}^m \mapsto \mathbb{R}^n$ is said to be piecewise continuous on a set $D \subset \mathbb{R}^m$ if it is continuous at all points $\boldsymbol{x} \in D$ except for a finite number of points. □

Definition 2.4—Uniform Continuity
A function $f : \mathbb{R}^m \mapsto \mathbb{R}^n$ is said to be uniformly continuous on a set $D \subset \mathbb{R}^m$, if, for any $\epsilon > 0$, there exists a $\delta > 0$ such that (2.2) holds for all $\boldsymbol{x}, \boldsymbol{y} \in D$. □

Definition 2.5—Lipschitz Continuity
A function $f : \mathbb{R}^m \mapsto \mathbb{R}^n$ is said to be Lipschitz continuous on a set $D \subset \mathbb{R}^m$, with a Lipschitz constant $L > 0$, if $\|f(\boldsymbol{x}) - f(\boldsymbol{y})\| < L\|\boldsymbol{x}-\boldsymbol{y}\|$ for all $\boldsymbol{x}, \boldsymbol{y} \in D$. □

Definition 2.6—Function Smoothness
A function $f : \mathbb{R}^m \mapsto \mathbb{R}^n$, whose first N derivatives are continuous on the set $D \subset \mathbb{R}^m$ is said to belong to the function class $C^N(D)$. □

Generally, when discussing smoothness with respect to time, the domain of the function argument is omitted. When stating that a function or signal is C^N, then this implies a smoothness of degree N with respect to time.

To talk about proximity of points to the origin, a ball is defined as follows.

Definition 2.7
A ball of radius $r > 0$ is defined as $\mathcal{B}_r = \{\boldsymbol{x} \in \mathbb{R}^n | \|\boldsymbol{x}\| < r\}$. □

We also make frequent use of cross-products defined with a screw operator.

Definition 2.8—Screw operator
Let $\boldsymbol{S} : \mathbb{R}^3 \mapsto \mathbb{R}^{3\times3}$ such that for any $\boldsymbol{a}, \boldsymbol{b} \in \mathbb{R}^3$, $\boldsymbol{S}(\boldsymbol{a})\boldsymbol{b} = \boldsymbol{a} \times \boldsymbol{b}$, where then

$$\boldsymbol{S}(\boldsymbol{a}) = \begin{bmatrix} 0 & -a_3 & a_2 \\ a_3 & 0 & -a_1 \\ -a_2 & a_1 & 0 \end{bmatrix}. \tag{2.3}$$

□

The thesis deals with various attitude representations relating to specific matrix Lie groups, which will be defined next. The notation will follow [Hall, 2015], and the relevant details are summarized in Appendix A.1.

Definition 2.9—The Special Orthogonal Group SO(3)
Let $\mathrm{SO}(3) = \{\boldsymbol{R} \in \mathbb{R}^{3\times3} \mid \boldsymbol{R}^\top\boldsymbol{R} = \boldsymbol{I},\ \det(\boldsymbol{R}) = 1\}$, with an associated Lie algebra $\mathfrak{so}(3) = \{\boldsymbol{L}_1\omega_1 + \boldsymbol{L}_2\omega_2 + \boldsymbol{L}_3\omega_3 \in \mathbb{R}^{3\times3} \mid \boldsymbol{\omega} \in \mathbb{R}^3\}$ spanned by a basis

$$\boldsymbol{L}_1 = \begin{bmatrix} 0 & 0 & 0 \\ 0 & 0 & -1 \\ 0 & 1 & 0 \end{bmatrix}, \quad \boldsymbol{L}_2 = \begin{bmatrix} 0 & 0 & 1 \\ 0 & 0 & 0 \\ -1 & 0 & 0 \end{bmatrix}, \quad \boldsymbol{L}_3 = \begin{bmatrix} 0 & -1 & 0 \\ 1 & 0 & 0 \\ 0 & 0 & 0 \end{bmatrix}. \qquad \square$$

Definition 2.10—The Special Unitary Group SU(2)
Let $\mathrm{SU}(2) = \{\boldsymbol{X} \in \mathbb{C}^{2\times2} \mid \boldsymbol{X}^*\boldsymbol{X} = \boldsymbol{I},\ \det(\boldsymbol{X}) = 1\}$, with an associated Lie algebra $\mathfrak{su}(2) = \{\boldsymbol{L}_1\omega_1 + \boldsymbol{L}_2\omega_2 + \boldsymbol{L}_3\omega_3 \in \mathbb{C}^{2\times2} \mid \boldsymbol{\omega} \in \mathbb{R}^3\}$ spanned by a basis

$$\boldsymbol{L}_1 = \begin{bmatrix} 0 & i \\ i & 0 \end{bmatrix}, \quad \boldsymbol{L}_2 = \begin{bmatrix} 0 & -1 \\ 1 & 0 \end{bmatrix}, \quad \boldsymbol{L}_3 = \begin{bmatrix} i & 0 \\ 0 & -i \end{bmatrix}. \qquad \square$$

Let G be either SU(2) or SO(3) with associated algebra $\mathfrak{g}$ defined as above.

Definition 2.11
Let $[\cdot]_G^\wedge : \mathbb{R}^3 \mapsto \mathfrak{g}$, take $[\cdot]_G^\vee : \mathfrak{g} \mapsto \mathbb{R}^3$, and denote the associated exponential and logarithmic maps by $\mathrm{Exp}_G : \mathfrak{g} \mapsto G$ and $\mathrm{Log}_G : G \mapsto \mathfrak{g}$, respectively. □

We will not be working directly with the adjoint representations of G, but its exponential and logarithmic maps will be used in the subsequent chapters and are presented in Appendix A.1. Due their frequent use, the aptly named *vee* and *hat* maps in Definition 2.11 are written out below.

Definition 2.12—Hat and vee maps of SO(3)
From Definitions 2.9 and 2.11, it follows that if $\boldsymbol{K} = [\boldsymbol{\omega}]^{\wedge}_{\mathrm{SO}(3)} \in \mathfrak{so}(3)$, then

$$[\boldsymbol{\omega}]^{\wedge}_{\mathrm{SO}(3)} = \boldsymbol{S}(\boldsymbol{\omega}), \qquad [\boldsymbol{K}]^{\vee}_{\mathrm{SO}(3)} = \begin{bmatrix} [\boldsymbol{K}]_{3,2} \\ [\boldsymbol{K}]_{1,3} \\ [\boldsymbol{K}]_{2,1} \end{bmatrix}. \qquad \square$$

Definition 2.13—Hat and vee maps of SU(2)
From Definitions 2.10 and 2.11, it follows that if $\boldsymbol{K} = [\boldsymbol{\omega}]^{\wedge}_{\mathrm{SU}(2)} \in \mathfrak{su}(2)$, then

$$[\boldsymbol{\omega}]^{\wedge}_{\mathrm{SU}(2)} = \begin{bmatrix} i\omega_3 & -\omega_2 + i\omega_1 \\ \omega_2 + i\omega_1 & -i\omega_3 \end{bmatrix}, \quad [\boldsymbol{K}]^{\vee}_{\mathrm{SU}(2)} = \frac{1}{2} \begin{bmatrix} \Im([\boldsymbol{K}]_{1,2} + [\boldsymbol{K}]_{2,1}) \\ \Re([\boldsymbol{K}]_{2,1} - [\boldsymbol{K}]_{1,2}) \\ \Im([\boldsymbol{K}]_{1,1} - [\boldsymbol{K}]_{2,2}) \end{bmatrix}. \qquad \square$$

In the following, we also make use of the quaternion representation.

Definition 2.14—The Quaternion Space
The quaternion is a four-dimensional complex number, here defined in a Hamilton construction as in [Sola, 2017], with imaginary units $\{i, j, k\}$. Let

$$\tilde{\mathbb{H}} = \{a + ib + jc + kd \mid a, b, c, d \in \mathbb{R}, i^2 = j^2 = k^2 = ijk = -1\}. \qquad \square$$

Throughout this thesis, the conventional vector representation of the quaternion will be used, with $\boldsymbol{q} = (a, b, c, d)^{\top} \in \tilde{\mathbb{H}}$, with a real and imaginary part $\Re(\boldsymbol{q}) = a$ and $\Im(\boldsymbol{q}) = (b, c, d)^{\top}$, respectively.

From Definition 2.14, many interesting and relevant algebraic properties follow. In the convenient vector notation, these can be summarized as follows.

Definition 2.15—Quaternion Operations
The conjugate of a quaternion $\boldsymbol{q} \in \tilde{\mathbb{H}}$ is denoted $\boldsymbol{q}^*$, satisfying $\Re(\boldsymbol{q}) = \Re(\boldsymbol{q}^*)$ and $\Im(\boldsymbol{q}) = -\Im(\boldsymbol{q}^*)$. Furthermore, the multiplication of $\boldsymbol{p}, \boldsymbol{q} \in \tilde{\mathbb{H}}$ is denoted

$$\boldsymbol{p} \odot \boldsymbol{q} = [\boldsymbol{p}]_L \boldsymbol{q} = [\boldsymbol{q}]_R \boldsymbol{p} \in \tilde{\mathbb{H}}.$$

with the maps $[\cdot]_L : \tilde{\mathbb{H}} \mapsto \mathbb{R}^{4\times4}$ and $[\cdot]_R : \tilde{\mathbb{H}} \mapsto \mathbb{R}^{4\times4}$ stated in Appendix A.1.6. With this operation, the norm of a quaternion is defined as $\|\boldsymbol{q}\| = \boldsymbol{q} \odot \boldsymbol{q}^*$. The identity quaternion is defined as $\boldsymbol{q}_{\boldsymbol{I}} = (1, 0, 0, 0)^{\top} \in \tilde{\mathbb{H}}$, and with it, an inverse quaternion $\boldsymbol{q}^{-1} \in \tilde{\mathbb{H}}$ is defined as satisfying $\boldsymbol{q} \odot \boldsymbol{q}^{-1} = \boldsymbol{q}_{\boldsymbol{I}}$. $\square$

When considering rotations in a quaternion representation, it becomes relevant to define the space of unit quaternions. While the quaternion operations apply to quaternions more generally, we will at all times work with quaternions in a normalized space, defined using these operations as follows.

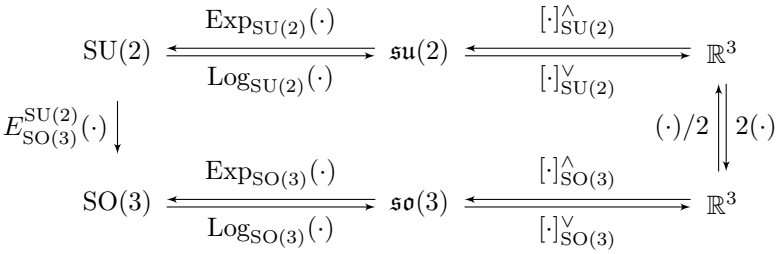

Figure 2.1 Relationships between SU(2) and SO(3) given Definition 2.17. Here $(\cdot)/2$ and $2(\cdot)$ denote a division and multiplication by 2, respectively.

Definition 2.16—The Unit Quaternion Space
The space of unit quaternions is defined as

$$\mathbb{H} = \{\boldsymbol{q} \in \tilde{\mathbb{H}} \mid \|\boldsymbol{q}\| = 1\}. \qquad \square$$

By this definition of the unit quaternion it can be seen that $\mathrm{SU}(2) \cong \mathbb{H}$, and for future reference, we embed the quaternion into elements of SU(2) by

$$\boldsymbol{q} = a + ib + jc + kd \in \mathbb{H} \quad \Leftrightarrow \quad \boldsymbol{X} = \begin{pmatrix} a+id & -c+ib \\ c+ib & a-id \end{pmatrix} \in \mathrm{SU}(2). \quad (2.4)$$

The mapping of SU(2) to SO(3) is a 2-to-1 homomorphism, and if $\boldsymbol{X} \in \mathrm{SU}(2)$, then both $\boldsymbol{X}$ and $-\boldsymbol{X}$ map to the same element on SO(3). In this thesis, we parameterize the rotation matrix in the unit quaternions as follows

$$\boldsymbol{R} = \begin{bmatrix} a^2+b^2-c^2-d^2 & 2(bc-ad) & 2(bd+ac) \\ 2(bc+ad) & a^2-b^2+c^2-d^2 & 2(cd-ab) \\ 2(bd-ac) & 2(cd+ab) & a^2-b^2-c^2+d^2 \end{bmatrix} \in \mathrm{SO}(3). \quad (2.5)$$

Definition 2.17—Attitude embedding
The embedding of a group G into group H is defined as $E^G_H : G \mapsto H$, and $E^{\mathbb{H}}_{\mathrm{SU}(2)}$, $E^{\mathrm{SU}(2)}_{\mathbb{H}}$, $E^{\mathrm{SU}(2)}_{\mathrm{SO}(3)}$, $E^{\mathbb{H}}_{\mathrm{SO}(3)}$ are given by (2.4) and (2.5), respectively. The relationships between the considered groups are illustrated in Figure 2.1. $\square$

Remark 2.1
Here, we note that if $\boldsymbol{X} \in \mathrm{SU}(2)$, $\boldsymbol{q} \in \mathbb{H}$ and $\boldsymbol{R} \in \mathrm{SO}(3)$ all represent the same attitude, using the embedding in Definition 2.17, then, for any $\boldsymbol{\omega} \in \mathbb{R}^3$,

$$\boldsymbol{R}\mathrm{Exp}_{\mathrm{SO}(3)}([2\boldsymbol{\omega}]^{\wedge}_{\mathrm{SO}(3)}), \quad \boldsymbol{X}\mathrm{Exp}_{\mathrm{SU}(2)}([\boldsymbol{\omega}]^{\wedge}_{\mathrm{SU}(2)}), \quad \boldsymbol{q} \odot \begin{bmatrix} \cos(\|\boldsymbol{\omega}\|) \\ \mathrm{sinc}(\|\boldsymbol{\omega}\|)\boldsymbol{\omega} \end{bmatrix},$$

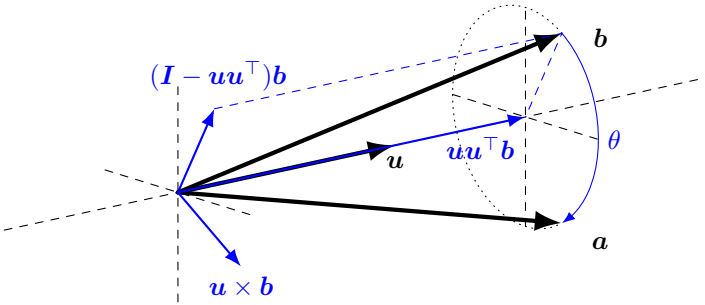

Figure 2.2 Illustration of the vector-rotation formula in Equation (2.7).

.

represent the same attitude on SO(3), where $\operatorname{sinc}(x) = \sin(x)x^{-1}$ (which should be interpreted in the limit as the argument approaches zero). Furthermore, for any $\boldsymbol{a}, \boldsymbol{b} \in \mathbb{R}^3$ with $\|\boldsymbol{a}\| = \|\boldsymbol{b}\|$, the following are equivalent

$$\boldsymbol{a} = \boldsymbol{R}\boldsymbol{b}, \qquad \boldsymbol{a} = [\boldsymbol{X}[\boldsymbol{b}]^\wedge_{\mathrm{SU}(2)}\boldsymbol{X}^*]^\vee_{\mathrm{SU}(2)}, \qquad \boldsymbol{a} = \Im\Big(\boldsymbol{q} \odot \begin{bmatrix} 0 \\ \boldsymbol{b} \end{bmatrix} \odot \boldsymbol{q}^*\Big). \tag{2.6}$$

□

Remark 2.2
From a mathematical point of view, having the element $\boldsymbol{X} \in \mathrm{SU}(2)$ multiplied with an element of the Lie algebra may seem odd. However, we note that $\boldsymbol{X}[\boldsymbol{b}]^\wedge_{\mathrm{SU}(2)}\boldsymbol{X}^* \in \mathfrak{su}(2)$. Furthermore, if $\boldsymbol{X} = \mathrm{Exp}_{\mathrm{SU}(2)}([\theta\boldsymbol{u}/2]^\wedge_{\mathrm{SU}(2)})$, with an angle $\theta \in \mathbb{R}$ and a unit vector $\boldsymbol{u} \in \mathbb{R}^3$, it can be shown that

$$[\boldsymbol{X}[\boldsymbol{b}]^\wedge_{\mathrm{SU}(2)}\boldsymbol{X}^*]^\vee_{\mathrm{SU}(2)} = (\boldsymbol{I} - \boldsymbol{u}\boldsymbol{u}^\top)\boldsymbol{b}\cos(\theta) + (\boldsymbol{u} \times \boldsymbol{b})\sin(\theta) + \boldsymbol{u}\boldsymbol{u}^\top\boldsymbol{b}, \tag{2.7}$$

which is recognized as the vector-rotation formula (see, e.g., [Sola, 2017]). As such, the rotation action described in (2.6) has a clear geometric interpretation (see Figure 2.2), representing a rotation of $\boldsymbol{b}$ about $\boldsymbol{u}$ by an angle θ. □

Since the map from SO(3) to SU(2) and $\mathbb{H}$ is non-unique, we will avoid it if possible. This ambiguity is one of the major reasons for designing estimators on SU(2) or $\mathbb{H}$, as any controller with an attitude representation in SU(2), $\mathbb{H}$ or SO(3) may then be used. If instead an estimator is designed on SO(3), then a controller operating with an attitude representation in SU(2) or $\mathbb{H}$ may give rise to the so-called dynamical unwinding phenomenon described in [Mayhew et al., 2011a] unless special care is taken in the controller implementation. To compare elements on SO(3) and SU(2) (and $\mathbb{H}$), we define two closely related distances as follows.

Definition 2.18—Distance on SO(3)
A distance on SO(3) is defined as $\Psi : \mathrm{SO}(3)^2 \mapsto [0, 2]$, where

$$\Psi(\boldsymbol{R}_1, \boldsymbol{R}_2) = \frac{1}{2}\mathrm{Tr}(\boldsymbol{I} - \boldsymbol{R}_1^\top \boldsymbol{R}_2). \qquad \square$$

For completeness and later use, a similar distance is defined on SU(2).

Definition 2.19—Distance on SU(2)
A distance on SU(2) is defined as $\Gamma : \mathrm{SU}(2)^2 \mapsto [0, 2]$, where

$$\Gamma(\boldsymbol{X}_1, \boldsymbol{X}_2) = \frac{1}{2}\mathrm{Tr}(\boldsymbol{I} - \boldsymbol{X}_1^* \boldsymbol{X}_2). \qquad \square$$

In the UAV literature, it is common to consider other distances and attitude parameterizations. While we generally opt to work directly with elements of SO(3), SU(2), and $\mathbb{H}$, using the distances in Definitions 2.18 and 2.19, we will also reference Euler or Tait-Bryan angles, defined as follows.

Definition 2.20—Rotation angles
Let ϕ be a pitch angle, θ a roll angle, and ψ a yaw angle. Let these angles parameterize an element $\boldsymbol{R}(\phi, \theta, \psi) \in \mathrm{SO}(3)$ in the ZYX-convention by,

$$\boldsymbol{R}(\phi,\theta,\psi) = \begin{bmatrix} \cos(\psi) & -\sin(\psi) & 0 \\ \sin(\psi) & \cos(\psi) & 0 \\ 0 & 0 & 1 \end{bmatrix} \begin{bmatrix} \cos(\theta) & 0 & \sin(\theta) \\ 0 & 1 & 0 \\ -\sin(\theta) & 0 & \cos(\theta) \end{bmatrix} \begin{bmatrix} 1 & 0 & 0 \\ 0 & \cos(\phi) & -\sin(\phi) \\ 0 & \sin(\phi) & \cos(\phi) \end{bmatrix}. \tag{2.8}$$

$\square$

To get a sense of how these rotation angles relate to the previously defined distances, it is simple to verify that for small rotational angles (in the sense that they are close to the origin), we have that $\|(\phi;\theta;\psi)\|^2 \approx 2\Psi(\boldsymbol{R}, \boldsymbol{I}) \approx 8\Gamma(\boldsymbol{X}, \boldsymbol{I})$. As such, when studying the forthcoming plots of attitude errors in the distances Ψ and Γ, this proportionality should be taken into consideration.

Remark 2.3
An appealing property of the distances in Definitions 2.18 and 2.19 is that they relate special elements of their associated manifolds. Specifically, every

$$\{\boldsymbol{R}_1^\top \boldsymbol{R}_2 \in \mathrm{SO}(3) | \mathrm{Tr}(\boldsymbol{R}_1^\top \boldsymbol{R}_2) = -1\} = \{\boldsymbol{R}_1^\top \boldsymbol{R}_2 \in \mathrm{SO}(3) | \Psi(\boldsymbol{R}_1, \boldsymbol{R}_2) = 2\}, \tag{2.9}$$

maps to elements of SU(2) in the set

$$\{\boldsymbol{X}_1^* \boldsymbol{X}_2 \in \mathrm{SU}(2) | \mathrm{Tr}(\boldsymbol{X}_1^* \boldsymbol{X}_2) = 0\} = \{\boldsymbol{X}_1^* \boldsymbol{X}_2 \in \mathrm{SU}(2) | \Gamma(\boldsymbol{X}_1, \boldsymbol{X}_2) = 1\}, \tag{2.10}$$

and vice versa. $\square$

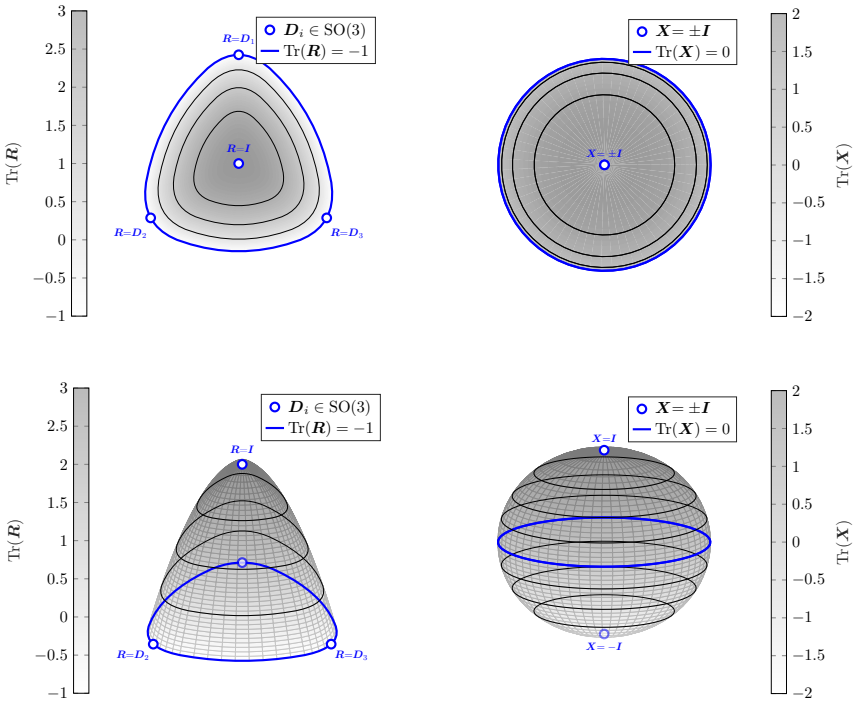

Figure 2.3 Illustration of the SO(3)-manifold as a surface in $\mathbb{R}^3$-space (left) and SU(2)-manifold as a surface in $\mathbb{R}^3$-space (right), with a darker color indicating an increasing trace of the elements of the manifold.

The set in (2.9) is of particular interest when designing controllers on SO(3). Typically, the error dynamics will give rise to one or more unstable equilibrium points with an attitude error in this set. Here we note that the set corresponding to $\Gamma(\boldsymbol{X}_1, \boldsymbol{X}_2) = 2$, namely $\{\boldsymbol{X}_1^* \boldsymbol{X}_2 \in \mathrm{SU}(2) \mid \Gamma(\boldsymbol{X}_1, \boldsymbol{X}_2) = 2\} = \{-\boldsymbol{I}\}$, is a set of measure zero while the set characterized by $\Psi(\boldsymbol{R}_1, \boldsymbol{R}_2) = 2$ is not. Therefore, when working with SO(3), it is common to consider three important diagonal elements of SO(3), which are defined as follows.

Definition 2.21
Let $\{\boldsymbol{D}_1, \boldsymbol{D}_2, \boldsymbol{D}_3\} \subset \{\boldsymbol{R} \in \mathrm{SO}(3) \mid \mathrm{Tr}(\boldsymbol{R}) = -1\}$, where

$$\boldsymbol{D}_1 = \mathrm{diag}(1, -1, -1), \ \boldsymbol{D}_2 = \mathrm{diag}(-1, 1, -1), \ \boldsymbol{D}_3 = \mathrm{diag}(-1, -1, 1). \quad \square$$

To illustrate the relation between SO(3) and SU(2), consider Figure 2.3. Here, the subsets of SO(3) and SU(2) defined in (2.9) and (2.10) are shown (in blue), along with the special diagonal elements in Definition 2.21.

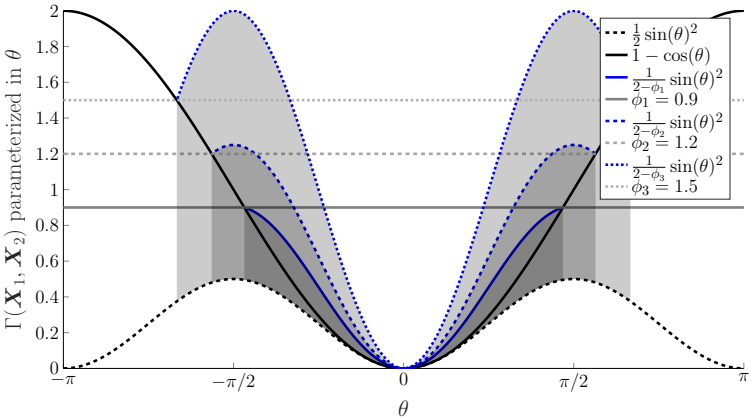

Figure 2.4 The distance $\Gamma(\boldsymbol{X}_1, \boldsymbol{X}_2)$ with the element $\boldsymbol{X}_1^* \boldsymbol{X}_2$ parameterized in a quaternion representing a rotation of 2θ about an arbitrary axis. The figure illustrates the bounds in (2.11) for three $\phi \in \{0.9, 1.2, 1.5\}$.

Here, we emphasize that every element on the blue line on SO(3) (left) maps to elements on the blue line on SU(2) (right) through Definition 2.17. Consequently, if a controller is designed to minimize a distance in Γ, and this causes the error trajectory on SU(2) to cross the blue line while converging to the identity element, we implicitly attain the theoretical maximum distance in Ψ on SO(3) at least once in the transient. This is related to the concept of dynamical unwinding, which will be discussed further in Chapter 3.

Yet another reason for introducing the Γ-distance in Definition 2.19, is that it facilitates a derivation of bounds in quantities that relate to an intuitive attitude error. This is shown in the following remark, which will be used frequently in the forthcoming controller derivations and stability proofs.

Remark 2.4
Define $\boldsymbol{q}_1 = E_{\mathbb{H}}^{\mathrm{SU}(2)}(\boldsymbol{X}_1)$ and $\boldsymbol{q}_2 = E_{\mathbb{H}}^{\mathrm{SU}(2)}(\boldsymbol{X}_2)$, then $\Gamma(\boldsymbol{X}_1, \boldsymbol{X}_2) = 1 - \Re(\boldsymbol{q}_1^* \odot \boldsymbol{q}_2)$. Let $\boldsymbol{q}_e = \boldsymbol{q}_1^* \odot \boldsymbol{q}_2$ and parameterize this quaternion by $\theta \in [-\pi, \pi]$ and a unit vector $\boldsymbol{u} \in \mathbb{R}^3$, such that $\Re(\boldsymbol{q}_e) = \cos(\theta)$ and $\Im(\boldsymbol{q}_e) = \sin(\theta)\boldsymbol{u}$, then,

$$\frac{1}{2}\sin^2(\theta) \leq \Gamma(\boldsymbol{X}_1, \boldsymbol{X}_2) \leq \frac{1}{2-\phi}\sin^2(\theta), \quad \forall \Gamma(\boldsymbol{X}_1, \boldsymbol{X}_2) \leq \phi < 2. \tag{2.11}$$

These inequalities are illustrated in Figure 2.1, and an important consequence is that if a controller can be expressed in an error that is a positive definite function in $\sin(\theta)$, then the Γ-distance may be upper and lower bounded in the errors. Consequently, it may be possible to construct Lyapunov function candidates that include explicit terms in this Γ-distance. □

2.2 Mechanics, Actuation and Reference Generation

This section introduces the relevant rigid-body dynamics defining the motions of the systems that are to be controlled. Specifically, various coordinate frames are defined in Sec. 2.2.1, with which the dynamics of a rotational body configured on SO(3) is presented in Sec. 2.2.2, and the equations of motion for the UAV configured on $\mathrm{SO}(3) \times \mathbb{R}^3$ are defined in Sec. 2.2.3. This is followed by a discussion on actuators in Sec. 2.2.4, before concluding with an example on reference generation and the concept of differential flatness in Sec. 2.2.5.

2.2.1 Coordinate Frames

In the following, we consider a body-fixed frame $\{\mathcal{B}\}$ which relates to an inertial frame $\{\mathcal{I}\}$ by a rotation, and this inertial frame relates to a global frame $\{\mathcal{G}\}$ through a translation. An attitude, represented by $\boldsymbol{R} \in \mathrm{SO}(3)$, $\boldsymbol{X} \in \mathrm{SU}(2)$, or $\boldsymbol{q} \in \mathbb{H}$, defines a rotation of a vector in the body frame $\{\mathcal{B}\}$ to the inertial frame $\{\mathcal{I}\}$. If necessary, the reference frame in which a vector $\boldsymbol{v} \in \mathbb{R}^3$ is considered is clarified with a sub-index, such that $\boldsymbol{v}_{\mathcal{B}}$ is defined in the body frame and $\boldsymbol{v}_{\mathcal{G}}$ is defined in the global frame. The basis vectors of the global frame is defined by $\boldsymbol{e}_i$, with the ith element set to 1, and the basis vectors of the body frame are defined by $\boldsymbol{b}_i \in \mathbb{R}^3$ with $i \in \{1, 2, 3\}$, such that

$$\boldsymbol{I}_3 = \begin{bmatrix} \boldsymbol{e}_1 & \boldsymbol{e}_2 & \boldsymbol{e}_3 \end{bmatrix} = \boldsymbol{R}^\top \begin{bmatrix} \boldsymbol{b}_1 & \boldsymbol{b}_2 & \boldsymbol{b}_3 \end{bmatrix}. \tag{2.12}$$

2.2.2 Attitude Dynamics

The dynamics of a mechanical system with a configuration, $\boldsymbol{Q}$, can be derived for first principles by formulating a Lagrangian in the kinetic energy, $T(\boldsymbol{Q}, \dot{\boldsymbol{Q}})$, and the potential energy, $U(\boldsymbol{Q})$, as $\mathcal{L}(\boldsymbol{Q}, \dot{\boldsymbol{Q}}) = T(\boldsymbol{Q}, \dot{\boldsymbol{Q}}) - U(\boldsymbol{Q})$. An action integral can then be expressed in the Lagrangian over a time $t \in [t_\circ, t_f]$, as

$$\mathfrak{G} = \int_{t_\circ}^{t_f} \mathcal{L}(\boldsymbol{Q}, \dot{\boldsymbol{Q}}) \mathrm{d}t. \tag{2.13}$$

From Hamilton's principle, the variation of the action integral is zero in time, implying a conservation of energy. The trajectories $(\boldsymbol{Q}(t), \dot{\boldsymbol{Q}}(t))$ satisfying this property are found in the solution to the Euler-Lagrange equation

$$\frac{\mathrm{d}}{\mathrm{d}t} \frac{\partial \mathcal{L}}{\partial \dot{\boldsymbol{Q}}} - \frac{\partial \mathcal{L}}{\partial \boldsymbol{Q}} = \boldsymbol{M}, \tag{2.14}$$

with $\boldsymbol{M}$ denoting a set of exogenous generalized forces, here forces and torques. Solving (2.14) becomes involved when considering systems configured on the Lie groups defined in Sec. 2.1, and is easiest done using a variational approach. A review of solutions for systems configured on Lie groups is found in [Lee,

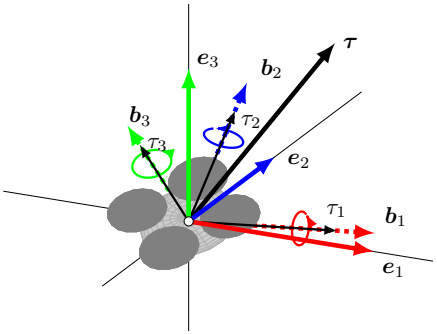

Figure 2.5 Illustration of a quadrotor UAV when only considering its attitude dynamics, with a configuration $\boldsymbol{Q} = \boldsymbol{R}$ driven by a set of torques, $\boldsymbol{\tau} = (\tau_1;\ \tau_2;\ \tau_3)$, defined in the body-fixed frame, $\{\mathcal{B}\}$ (dashed, red, blue, green), sharing the same origin as $\{\mathcal{G}\}$ (full, red, blue, green).

2008; Lee et al., 2017], and relevant results for the attitude dynamics of a UAV driven by external torques (see Figure 2.5) are summarized as follows.

Let $\boldsymbol{\rho}$ denote a vector from the center of the body fixed frame to a mass element, dm, and let $\boldsymbol{\omega}$ denote the body frame rate with respect to the inertial frame, with $\boldsymbol{\omega}$ defined in the body fixed frame. This mass element has a velocity of $\boldsymbol{\omega} \times \boldsymbol{\rho}$, and the kinetic energy of the system can be expressed

$$T(\boldsymbol{\omega}) = \frac{1}{2}\int_{\mathcal{B}} \|\boldsymbol{\omega} \times \boldsymbol{\rho}\|^2 dm(\boldsymbol{\rho}) = \frac{1}{2}\int_{\mathcal{B}} \boldsymbol{\omega}^\top \boldsymbol{S}(\boldsymbol{\rho})^\top \boldsymbol{S}(\boldsymbol{\rho})\boldsymbol{\omega} dm(\boldsymbol{\rho}) = \frac{1}{2}\boldsymbol{\omega}^\top \boldsymbol{J}\boldsymbol{\omega},$$

referring to an integration over the UAV mass in $\{\mathcal{B}\}$, where then

$$\boldsymbol{J} = \int_{\mathcal{B}} \boldsymbol{S}(\boldsymbol{\rho})^\top \boldsymbol{S}(\boldsymbol{\rho}) dm(\boldsymbol{\rho}), \tag{2.15}$$

denotes the standard inertia matrix. With $\boldsymbol{Q} = \boldsymbol{R}$, $\dot{\boldsymbol{Q}} = \boldsymbol{\omega}$ and absence of any potential energy, $\mathcal{L}(\boldsymbol{R}, \boldsymbol{\omega}) = T(\boldsymbol{\omega})$, following [Lee, 2008, Chapter 2.3.2] we arrive at the solution to (2.14) using intermediary variations on SO(3) as

$$\dot{\boldsymbol{R}} = \boldsymbol{R}\boldsymbol{S}(\boldsymbol{\omega}), \tag{2.16a}$$

$$\boldsymbol{J}\dot{\boldsymbol{\omega}} = \boldsymbol{S}(\boldsymbol{J}\boldsymbol{\omega})\boldsymbol{\omega} + \boldsymbol{\tau}, \tag{2.16b}$$

with $\boldsymbol{\tau}$ denoting generalized forces (here torques) defined in the body fixed frame (see Figure 2.5). Performing the same set of computations for attitudes configured on SU(2) instead of SO(3) only changes the attitude kinematics in (2.16a). Specifically, for $\boldsymbol{X} \in \mathrm{SU}(2)$ or $\boldsymbol{q} \in \mathbb{H}$, we instead obtain

$$\dot{\boldsymbol{X}} = \boldsymbol{X}[\boldsymbol{\omega}/2]^\wedge_{\mathrm{SU}(2)}, \tag{2.16c}$$

$$\dot{\boldsymbol{q}} = \frac{1}{2}\boldsymbol{q} \odot \begin{bmatrix} 0 \\ \boldsymbol{\omega} \end{bmatrix}, \tag{2.16d}$$

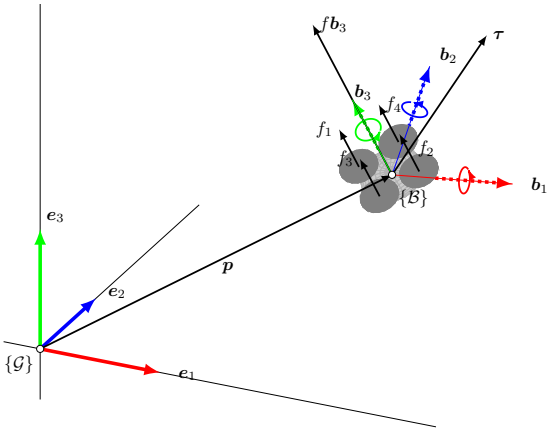

Figure 2.6 Illustration of a UAV defined by a configuration $\boldsymbol{Q} = (\boldsymbol{p}, \boldsymbol{R})$ defined with respect to the frames $\{\mathcal{G}\}$ and $\{\mathcal{B}\}$, driven by a set of torques, $\boldsymbol{\tau}$, and a force $f\boldsymbol{b}_3$, as the sum of the thrusts f_i generated by each rotor.

respectively. Regardless of the attitude parmeterization, we note that

$$\frac{\mathrm{d}}{\mathrm{d}t}\mathcal{L}(\boldsymbol{R}, \boldsymbol{\omega}) = \boldsymbol{\omega}^\top \boldsymbol{J}\dot{\boldsymbol{\omega}} = \boldsymbol{\omega}^\top (\boldsymbol{S}(\boldsymbol{J}\boldsymbol{\omega})\boldsymbol{\omega} + \boldsymbol{\tau}) = \boldsymbol{\omega}^\top \boldsymbol{\tau} = \boldsymbol{0}, \tag{2.17}$$

if $\boldsymbol{\tau} = \boldsymbol{0}$, implying (i) conservation of energy in the absence of external torques, (ii) an increase in rotational energy when the torque is aligned with $\boldsymbol{\omega}$, and (iii) a decrease in energy when they are pointing in the opposite directions.

2.2.3 UAV Dynamics

When instead considering the full UAV dynamics, the system's configuration is taken as a translation, $\boldsymbol{p}$, of the inertial frame relative to the global frame, and a rotation, $\boldsymbol{R}$, relating the body frame to the inertial frame, with a translation velocity, $\boldsymbol{v}$, in the body-fixed frame, and an attitude rate, $\boldsymbol{\omega}$, also expressed in the body-fixed frame $\{\mathcal{B}\}$. The geometry is illustrated in Figure 2.6, with external forces and torques generated by positive rotor thrusts, $f_i > 0$.

The configuration of the system is $\boldsymbol{Q} = (\boldsymbol{p}, \boldsymbol{R})$, and its kinetic energy is

$$T(\boldsymbol{v}, \boldsymbol{\omega}) = \frac{1}{2}\int_{\mathcal{B}} \|\boldsymbol{\omega} \times \boldsymbol{\rho}\|^2 dm(\boldsymbol{\rho}) + \frac{1}{2}\int_{\mathcal{B}} \|\boldsymbol{v}\|^2 dm(\boldsymbol{\rho}) = \frac{1}{2}\boldsymbol{\omega}^\top \boldsymbol{J}\boldsymbol{\omega} + \frac{m}{2}\boldsymbol{v}^\top \boldsymbol{v}.$$

The potential energy of the system can be expressed as a function of the elevation of the UAV in the gravitational field, increasing with its height, as

$$U(\boldsymbol{p}) = mg\boldsymbol{e}_3 \cdot \boldsymbol{p}, \tag{2.18}$$

and the Lagrangian is $\mathcal{L}(\boldsymbol{p}, \boldsymbol{R}, \boldsymbol{v}, \boldsymbol{\omega}) = T(\boldsymbol{v}, \boldsymbol{\omega}) - U(\boldsymbol{p})$. Following [Lee, 2008, Chapter 2.3.5] with $-(\partial/\partial \boldsymbol{p})U(\boldsymbol{p}) = -mg\boldsymbol{R}^\top \boldsymbol{e}_3$, the solution to (2.14) is

$$\dot{\boldsymbol{p}} = \boldsymbol{R}\boldsymbol{v}, \tag{2.19a}$$
$$m\dot{\boldsymbol{v}} = -m\boldsymbol{S}(\boldsymbol{\omega})\boldsymbol{v} - mg\boldsymbol{R}^\top \boldsymbol{e}_3 + f\boldsymbol{e}_3, \tag{2.19b}$$
$$\dot{\boldsymbol{R}} = \boldsymbol{R}\boldsymbol{S}(\boldsymbol{\omega}), \tag{2.19c}$$
$$\boldsymbol{J}\dot{\boldsymbol{\omega}} = \boldsymbol{S}(\boldsymbol{J}\boldsymbol{\omega})\boldsymbol{\omega} + \boldsymbol{\tau}, \tag{2.19d}$$

where f denotes an external force and $\boldsymbol{\tau}$ denotes external torques, both generated by the actuators. The use of body-frame accelerations is common when implementing estimators, but reference generation and development of UAV control systems are often done with the velocities defined in the global frame, in which case the subsystems in (2.19a) and (2.19f) are replaced by

$$\dot{\boldsymbol{p}} = \boldsymbol{v}_{\mathcal{G}}, \tag{2.19e}$$
$$m\dot{\boldsymbol{v}}_{\mathcal{G}} = -mg\boldsymbol{e}_3 + f\boldsymbol{R}\boldsymbol{e}_3. \tag{2.19f}$$

Similar to the attitude dynamics, here using that $\boldsymbol{v}_{\mathcal{G}} = \boldsymbol{R}\boldsymbol{v}_{\mathcal{B}}$, we note that

$$\frac{\mathrm{d}}{\mathrm{d}t}\mathcal{L}(\boldsymbol{p}, \boldsymbol{R}, \boldsymbol{v}_{\mathcal{G}}, \boldsymbol{\omega}) = \frac{\mathrm{d}}{\mathrm{d}t}\mathcal{L}(\boldsymbol{p}, \boldsymbol{R}, \boldsymbol{v}_{\mathcal{B}}, \boldsymbol{\omega}) = f(\boldsymbol{v}_{\mathcal{B}} \cdot \boldsymbol{e}_3) + \boldsymbol{\omega} \cdot \boldsymbol{\tau} = \boldsymbol{0},$$

in the absence of external forces and torques, implying conservation of energy. Similarly, if the system is moving in the $\boldsymbol{b}_3$-direction, then a positive force implies an increase in energy. As the attitude dynamics can be expressed in various representations, the same holds true for (2.19), and we are free to exchange the attitude representation in (2.19c) with either (2.16c) or (2.16d), provided the vectors $\boldsymbol{e}_3$ and $\boldsymbol{v}$ in Equations (2.19b), (2.19b), and (2.19f), are rotated in accordance with Remark 2.1. The various permutations are not written out for brevity. The different representations of the attitude dynamics will be considered in Chapter 3, the global velocity model (Equations (2.19e) and (2.19f)) will be used in Chapter 4, and the body fixed-frame velocity model (Equations (2.19a) and (2.19b)) will be used in Chapter 6, here mainly with attitudes configured on SO(3).

2.2.4 Actuation

From blade element theory, the force generated by the ith rotor when running at a speed of Ω_i [rad/s] is approximately proportional to the rotor speed squared when the UAV is in a hovering state (see, e.g., [Bangura et al., 2016]). In the following, we therefore let $f_i \approx k\Omega_i^2$ and $\tau_{M_i} \approx b\Omega_i^2$ denote the force and torque induced about the rotor axis which is parallel with the body $\boldsymbol{b}_3$ direction and located in the $\boldsymbol{b}_1\boldsymbol{b}_2$-plane at a distance l [m] from the center of mass. Such quadratic approximations are common when modeling the

forces of multi-rotor UAVs, and have been used to perform impressive looping maneuvers in practice (see, e.g., [Mellinger et al., 2012]). These approximations are studied experimentally in [Greiff, 2017], and are a standard assumption in more theoretical UAV works [Lee et al., 2010; Lee et al., 2013]. Part of the appeal of this approximation is that the forces and torques can be related to the rotor speeds. When collected in a vector $\boldsymbol{\Omega} = (\Omega_1;\ \Omega_2;\ \Omega_3;\ \Omega_4) \in \mathbb{R}^4$,

$$(f;\ \boldsymbol{\tau}) \approx \boldsymbol{A}^+(\boldsymbol{\Omega}) = \begin{pmatrix} k \sum_{i=1}^{4} \Omega_i^2 \\ kl(\Omega_4^2 - \Omega_3^2) \\ kl(\Omega_1^2 - \Omega_2^2) \\ b(\Omega_1^2 + \Omega_2^2 - \Omega_3^2 - \Omega_4^2) \end{pmatrix}, \tag{2.20}$$

with the rotor setup depicted in Figure 2.6. Other rotor configurations are also possible, but should be devised such that the map $\boldsymbol{A}^+$ is surjective if $\Omega_i > 0$. In doing so, the problem of rotor control can be abstracted away in its entirety, and this is the reason why many UAV control problems are formulated with the forces and torques $(f;\ \boldsymbol{\tau})$ as control signals. However, any errors in these approximations will result in disturbances on the control inputs, which should be addressed when constructing the control systems.

2.2.5 Differential Flatness and Reference Generation

When considering UAV applications beyond simple stabilization, it becomes necessary to generate reference trajectories for the controlled system to follow. This problem of motion planning is not considered in the thesis, but to demonstrate the proposed controllers, we still require methods of generating feasible reference trajectories. For this purpose, we make use of the property of differential flatness described in [Fliess et al., 1995; Fliess et al., 1999].

Definition 2.22
A system, $\Sigma : \dot{\boldsymbol{x}} = \boldsymbol{f}(\boldsymbol{x}, \boldsymbol{u})$, with a state $\boldsymbol{x} \in \mathbb{R}^n$, $\boldsymbol{u} \in \mathbb{R}^m$, where $\boldsymbol{f}$ is a smooth vector field, is called differentially flat if there exist outputs $\boldsymbol{\gamma} \in \mathbb{R}^m$,

$$\boldsymbol{\gamma} = \boldsymbol{h}(\boldsymbol{x}, \boldsymbol{u}, \dot{\boldsymbol{u}}, \cdots, \boldsymbol{u}^{(r)}), \tag{2.21}$$

such that

$$\boldsymbol{x} = \boldsymbol{\phi}(\boldsymbol{\gamma}, \dot{\boldsymbol{\gamma}}, \cdots, \boldsymbol{\gamma}^{(q)}), \tag{2.22a}$$

$$\boldsymbol{u} = \boldsymbol{\beta}(\boldsymbol{\gamma}, \dot{\boldsymbol{\gamma}}, \cdots, \boldsymbol{\gamma}^{(q)}), \tag{2.22b}$$

where $\{\mathbf{h}, \boldsymbol{\phi}, \boldsymbol{\beta}\}$ are smooth functions. □

Here, we let $\mathbb{F}_\Sigma$ denote a flat output space associated with a system Σ such that $\boldsymbol{\gamma} \in \mathbb{F}_\Sigma$. By this definition, for any differentially flat system Σ, given a sufficiently smooth trajectory $\boldsymbol{\gamma}(t) \in \mathbb{F}_\Sigma$, the states and control signals of the system can be evaluated at any time without integration. In other words, the flat system can be transformed into a trivial system without dynamics. While sometimes difficult to show, several mechanical rigid-body systems exhibit the property of differential flatness (see, e.g., [Nieuwstadt et al., 1994; Lewis and Murray, 1997; Rathinam and Murray, 1998]). The UAV dynamics in (2.19) are considered in [Mellinger et al., 2012], and the relevant maps used in this thesis are detailed in [Greiff, 2017, Chapter 3]. As such, it should come as no surprise that the attitude subsystem in (2.16) is differentially flat.

Example 2.1
Regardless of parameterization, the attitude dynamics in (2.16) has three inputs, and we therefore seek a flat output trajectory $\boldsymbol{\gamma}(t) \in \mathbb{R}^3$. Here, we drop the time argument and parameterize the attitude in a set of quaternions,

$$\boldsymbol{q}(\boldsymbol{\gamma}) = \begin{bmatrix} \cos(\gamma_3/2) \\ 0 \\ 0 \\ \sin(\gamma_3/2) \end{bmatrix} \odot \begin{bmatrix} \cos(\gamma_2/2) \\ 0 \\ \sin(\gamma_2/2) \\ 0 \end{bmatrix} \odot \begin{bmatrix} \cos(\gamma_1/2) \\ \sin(\gamma_1/2) \\ 0 \\ 0 \end{bmatrix}. \tag{2.23a}$$

By this particular parameterization, the rotational angles in Definition 2.20 constitute a flat output with $\boldsymbol{\gamma} = (\phi;\ \theta;\ \psi)$, with $E^{\mathbb{H}}_{\mathrm{SO}(3)}(\boldsymbol{q}(\boldsymbol{\gamma}))$ resulting a rotation matrix parameterized as in (2.8). Given (2.23a), the first and second time-derivative of the quaternion in (2.23a) can be expressed in the flat outputs by the chain rule, as $\dot{\boldsymbol{q}}(\boldsymbol{\gamma}, \dot{\boldsymbol{\gamma}})$ and $\ddot{\boldsymbol{q}}(\boldsymbol{\gamma}, \dot{\boldsymbol{\gamma}}, \ddot{\boldsymbol{\gamma}})$. The states and control signals of (2.16) can then be written in the signals $(\boldsymbol{\gamma}, \dot{\boldsymbol{\gamma}}, \ddot{\boldsymbol{\gamma}})$, as

$$\boldsymbol{\omega}(\boldsymbol{\gamma}, \dot{\boldsymbol{\gamma}}) = 2\Im\{\boldsymbol{q}(\boldsymbol{\gamma})^* \odot \dot{\boldsymbol{q}}(\boldsymbol{\gamma}, \dot{\boldsymbol{\gamma}})\}, \tag{2.23b}$$

$$\dot{\boldsymbol{\omega}}(\boldsymbol{\gamma}, \dot{\boldsymbol{\gamma}}, \ddot{\boldsymbol{\gamma}}) = 2\Im\{\dot{\boldsymbol{q}}(\boldsymbol{\gamma}, \dot{\boldsymbol{\gamma}})^* \odot \dot{\boldsymbol{q}}(\boldsymbol{\gamma}) + \boldsymbol{q}(\boldsymbol{\gamma})^* \odot \ddot{\boldsymbol{q}}(\boldsymbol{\gamma}, \dot{\boldsymbol{\gamma}}, \ddot{\boldsymbol{\gamma}})\}, \tag{2.23c}$$

$$\boldsymbol{\tau}(\boldsymbol{\gamma}, \dot{\boldsymbol{\gamma}}, \ddot{\boldsymbol{\gamma}}) = \boldsymbol{J}\dot{\boldsymbol{\omega}}(\boldsymbol{\gamma}, \dot{\boldsymbol{\gamma}}, \ddot{\boldsymbol{\gamma}}) - \boldsymbol{S}(\boldsymbol{J}\boldsymbol{\omega}(\boldsymbol{\gamma}, \dot{\boldsymbol{\gamma}}))\boldsymbol{\omega}(\boldsymbol{\gamma}, \dot{\boldsymbol{\gamma}}). \tag{2.23d}$$

Here, $\boldsymbol{\phi}$ is defined by (2.23a) and (2.23b), and $\boldsymbol{\beta}$ is defined by (2.23d). We also note that it is possible to define $\boldsymbol{h}$ with $\boldsymbol{\gamma}$ as a function of $\boldsymbol{q}$ through (2.23a), but this map will not be unique unless constraints are imposed on $\boldsymbol{\gamma}$. □

This abstraction greatly simplifies the implementation of the control systems, as the only requirement on $\boldsymbol{\gamma} : \mathbb{R}_{\geq 0} \mapsto \mathbb{R}^3$ is sufficient smoothness, specifically that $\boldsymbol{\gamma}$ is C^2. Similar equations can be expressed for the full UAV dynamics, where trajectories $\boldsymbol{\gamma} : \mathbb{R}_{\geq 0} \mapsto \mathbb{R}^4$ that are C^4 can be expanded into the states and control signals of (2.19) (see, e.g., [Greiff, 2017, Chapter 3]).

EXAMPLE 2.2
Consider an implementation where a joystick is used to control a differentially flat system, and let $\boldsymbol{\gamma}_c(t)$ denote commands in the flat outputs. The commands may be discontinuous, and to generate feasible trajectory, define a vector $\boldsymbol{X}_f = (\boldsymbol{\gamma};\ \boldsymbol{\gamma}^{(1)};\ \cdots;\boldsymbol{\gamma}^{(q)}) \in \mathbb{R}^{m(q+1)}$, and construct a system with a pole of multiplicity $m(q+1)$ in $-c<0$, with a characteristic polynomial

$$p(\lambda) = ((\lambda + c)^{q+1})^m = (\lambda^{q+1} + a_q\lambda^q + \cdots + a_1\lambda + a_0)^m, \tag{2.24}$$

realized with unit static gain,

$$\Sigma_f:\quad \dot{\boldsymbol{X}}_f(t) = \begin{bmatrix} \boldsymbol{0} & \boldsymbol{I} & \cdots & \boldsymbol{0} & \boldsymbol{0} \\ \boldsymbol{0} & \boldsymbol{0} & \cdots & \boldsymbol{0} & \boldsymbol{0} \\ \vdots & \vdots & \ddots & \vdots & \vdots \\ \boldsymbol{0} & \boldsymbol{0} & \cdots & \boldsymbol{0} & \boldsymbol{I} \\ -a_0\boldsymbol{I} & -a_1\boldsymbol{I} & \cdots & -a_{q-1}\boldsymbol{I} & -a_q\boldsymbol{I} \end{bmatrix} \boldsymbol{X}_f(t) + \begin{bmatrix} \boldsymbol{0} \\ \boldsymbol{0} \\ \vdots \\ \boldsymbol{0} \\ a_0\boldsymbol{I} \end{bmatrix} \boldsymbol{\gamma}_c(t). \tag{2.25}$$

Filtering the input commands in this manner yields a smooth trajectory $\boldsymbol{\gamma}(t) \in \mathbb{R}^m$ that is (at least) C^q, with the qth derivatives known in $\boldsymbol{X}_f$.

This approach to reference generation is demonstrated with the UAV attitude dynamics in (2.16) with (2.16d). Consider computing a trajectory $(\boldsymbol{q}_r, \boldsymbol{\omega}_r, \boldsymbol{\tau}_r)$ using the flatness equations in Example 2.1 from $\boldsymbol{X}_f$ in (2.25) when injecting discontinuous step commands in $\boldsymbol{\gamma}_c$. Simulating the dynamics (2.16) in open loop with the computed torques $\boldsymbol{\tau}_r$, the state trajectory $(\boldsymbol{q}, \boldsymbol{\omega})$ is identical to the trajectory $(\boldsymbol{q}_r, \boldsymbol{\omega}_r)$, as shown in Figure 2.7. □

Example 2.2 demonstrates that it is generally simple to construct a state trajectory $(\boldsymbol{x}, \boldsymbol{u})$ for a differentially flat system $\Sigma : \dot{\boldsymbol{x}} = \boldsymbol{f}(\boldsymbol{x}, \boldsymbol{u})$. Therefore, we abstract away the problem of motion planning. Instead of considering specific methods for reference generation, we represent all such methods by a system $\Sigma_r : \dot{\boldsymbol{x}}_r = \boldsymbol{f}(\boldsymbol{x}_r, \boldsymbol{u}_r)$, whose states and control signals are expanded from an analytical trajectory $\boldsymbol{\gamma}(t)$. This is done in all of the forthcoming simulations and real-time experiments (see Figure 2.8). To facilitate implementations, the method of pre-filtering input commands as well as the flatness maps associated with (2.16) and (2.19) are available in C in [Greiff, 2020].

REMARK 2.5
When considering differential flatness in the context of any variant of the attitude dynamics in Sec. 2.2.2, here referred to as Σ^a, the flat output space is defined as $\boldsymbol{\gamma} = (\phi;\ \theta;\ \psi) \in \mathbb{F}_{\Sigma^a}$ with the rotational angles in Definition 2.20, parameterizing elements of SU(2) and SO(3) through Definition 2.17.

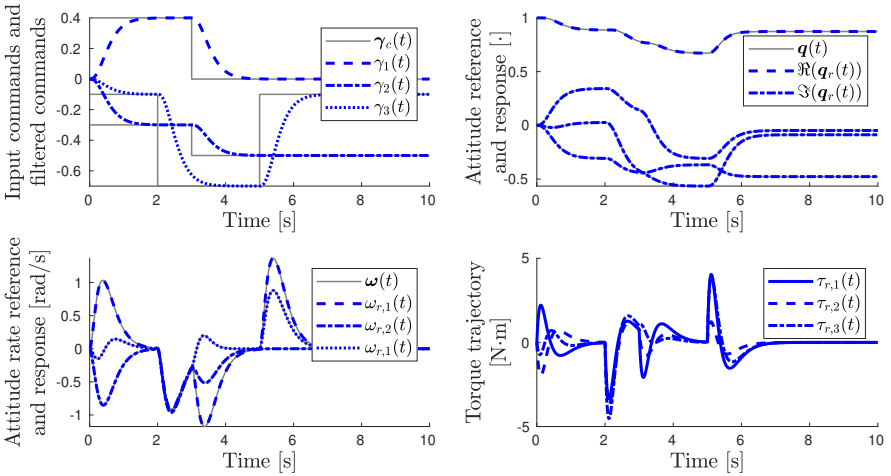

Figure 2.7 Example of the filtered reference generation using the property of differential flatness. *Top, left:* Input commands $\boldsymbol{\gamma}_c$ (gray), and smooth flat output trajectory $\boldsymbol{\gamma}$ (blue). *Top, right:* Quaternion reference trajectory (blue) and response (gray). *Bottom, left:* Attitude rate reference trajectory (blue) and response (gray). *Bottom, right:* Torque reference trajectory.

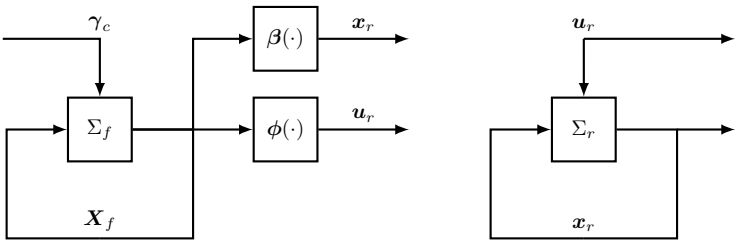

Figure 2.8 *Left:* Reference generation for a differentially flat system from input commands by smoothing through a system Σ_f in the form of (2.25). *Right:* Representation of the reference generation used in the thesis.

Remark 2.6
When instead considering differential flatness in the context of the UAV dynamics in 2.2.3, here referred to as a system Σ, the flat output space is defined with $\boldsymbol{\gamma} = (p_1;\ p_2;\ p_3;\ \psi) \in \mathbb{F}_\Sigma$. These flatness equations are generally defined with velocities in the global frame, with $(\boldsymbol{p}_\mathcal{G}, \boldsymbol{v}_\mathcal{G}, \boldsymbol{R}, \boldsymbol{\omega}) = \boldsymbol{\phi}(\boldsymbol{\gamma}, \cdots, \boldsymbol{\gamma}^{(4)})$ and $(f, \boldsymbol{\tau}) = \boldsymbol{\beta}(\boldsymbol{\gamma}, \cdots, \boldsymbol{\gamma}^{(4)})$ (see [Greiff, 2017]). However, the

trajectory can easily be converted to velocities and accelerations in $\{\mathcal{B}\}$ by

$$\boldsymbol{v}_{\mathcal{B}} = \boldsymbol{R}^{\top}\boldsymbol{v}_{\mathcal{G}}, \tag{2.26a}$$

$$\dot{\boldsymbol{v}}_{\mathcal{B}} = -\boldsymbol{S}(\boldsymbol{\omega})\boldsymbol{R}^{\top}\boldsymbol{v}_{\mathcal{G}} - g\boldsymbol{R}^{\top}\boldsymbol{e}_3 + (f/m)\boldsymbol{e}_3, \tag{2.26b}$$

As such, regardless of the UAV dynamics being defined with velocities in the global or the body frame, and regardless of the choice of attitude parameterization, a flat output trajectory in $\mathbb{F}_{\Sigma}$ can be expanded into a full state and control signal trajectory of the UAV dynamics in (2.19). □

In summary, two systems are of primary interest in this thesis: the UAV attitude dynamics in Sec. 2.2.2 and the full UAV dynamics as described in Sec. 2.2.3. These systems are actuated using a set of rotors that generate torques and forces using the rotor approximation in (2.20) (see Sec. 2.2.4). In the remainder of the thesis, the coordinates will be defined in an east-north-up fashion, such that the gravitational acceleration is negative along $\boldsymbol{e}_3$ in $\{\mathcal{G}\}$, and the actuating force generated by the rotors is defined as being positive along $\boldsymbol{b}_3$ in $\{\mathcal{B}\}$. As such, various results defined differently in other papers will be restated in this notation to avoid any confusion. All future plots will follow the same color coding of basis vectors as used in Figure 2.5 and Figure 2.6, with $\boldsymbol{b}_1$, $\boldsymbol{b}_2$, and $\boldsymbol{b}_3$ visualized red, blue and green, respectively. Finally, the differential flatness discussed in Sec. 2.2.5 will only be referred to in specific examples. Due to the relative ease with which complete state trajectories can be computed for these differentially flat systems, we will abstract away the problem of motion planning. Instead of considering specific methods of reference generation, as shown in the left-most diagram in Figure 2.8, we assume the existence of a reference system that obeys the same dynamics as the system that is to be controlled.

2.3 Numerical Analysis and Integration Theory

When studying continuous nonlinear and non-autonomous systems, any numerical verification of the theoretical results require explicit numerical computation of the system trajectories at discrete points in time. For this purpose, we make use of the classical Runge-Kutta methods in all subsequent simulations, see e.g., [Atkinson, 1988]. This wide class of algorithms are concerned with the integration of nonlinear and non-autonomous systems in the form

$$\dot{\boldsymbol{x}} = f(t, \boldsymbol{x}), \qquad t \in [t_\circ, t_f], \qquad \boldsymbol{x}(t) \in \mathbb{R}^n, \tag{2.27}$$

where, if the system state is known at a time t_k as $\boldsymbol{x}(t_k) = \boldsymbol{x}_k$, with a local time step $h_k = t_{k+1} - t_k$, the state at $\boldsymbol{x}_{k+1} \triangleq \boldsymbol{x}(t_{k+1})$ is computed as

$$\boldsymbol{x}_k^{(i)} = \boldsymbol{x}_k + h_k \sum_{j=1}^{i-1} a_{ij} \boldsymbol{k}^{(j)}, \tag{2.28a}$$

$$\boldsymbol{k}_k^{(i)} = f(t_k + c_i h_k, \boldsymbol{x}_k^{(i)}), \tag{2.28b}$$

$$\boldsymbol{x}_{k+1} = \boldsymbol{x}_k + h_k \sum_{j=1}^{s} b_j \boldsymbol{k}^{(j)}. \tag{2.28c}$$

The coefficients $\{a_{ij}\}_{1 \leq i \leq j < s}$, $\{b_i\}_{1 \leq i < s}$, and $\{c_i\}_{1 \leq i < s}$ are chosen according to a Butcher tableau [Butcher, 2016] to yield a method of desired accuracy. In this thesis, a fixed-step explicit 4-stage RK method (RK4) is used, with the coefficients chosen by a Butcher tableau in Appendix A.2. The local truncation error is then of order $O(h_k^5)$, such that systems simulated at time-steps in the order of $h_k = 10^{-3}$ for all k result in a local truncation error approaching machine precision. Historically, the classical RK methods have been used for the simulation of ordinary differential equations with $\boldsymbol{x}(t) \in \mathbb{R}^n$, but the systems considered in this thesis will typically be configured on special manifolds, such as the Lie-groups SO(3) and SU(2). In the literature pertaining to UAV control, it is common to perform the integration in $\mathbb{R}^n$, and then project the state back to its manifold on each time-step, which in the case of SO(3) and SU(2) would imply an orthogonalization, and for the quaternion kinematics implies a normalization. These are defined in Appendix A.1.3, as

$$\text{Proj}_{\text{SO}(3)} : \mathbb{R}^{3\times 3} \mapsto \text{SO}(3), \qquad \text{Proj}_{\text{SU}(2)} : \mathbb{C}^{2\times 2} \mapsto \text{SU}(2). \tag{2.29}$$

However, in [Crouch and Grossman, 1993], an elegant solution is developed for systems configured on Lie groups, commonly refereed to as the Crouch-Grossman Lie group methods (CG). The general idea is to use the exponential maps associated with the Lie groups to keep the state in its configuration manifold over all stages in multi-step algorithms such as the RK methods.

The butcher-tableau for a subset of these methods are given in [Jackiewicz et al., 2000], and are also summarized in Appendix A.2. The exact adaption of these methods to the context of quaternions has been discussed in [Andrle and Crassidis, 2013; Sveier et al., 2019]. Due to the implications of Definition 2.17, it is sufficient to develop methods for SU(2), as such algorithms also permit the simulation of systems partly evolving on SO(3).

Starting from [Crouch and Grossman, 1993], we consider a GC where subsets of the state are configured on Lie groups G_l of dimension 3. Consider N distinct elements $\boldsymbol{Y}^l \in G_l$ for $l = 1, \cdots, N$. Let $\boldsymbol{z} \in \mathbb{R}^n$, and take the full state of the system in (2.27) to have an internal representation as

$$\boldsymbol{x}(t) \in G_1 \times \cdots \times G_N \times \mathbb{R}^n = D_x, \qquad t \in [t_\circ, t_f] = D_t.$$

To facilitate the CG algorithm, we decompose the state into two distinct parts. The first concerns the dynamics of $\boldsymbol{z}$, with a function $f_0 : D_t \times D_x \mapsto \mathbb{R}^n$, and the second describes the kinematics of each $\boldsymbol{Y}^l$ as a function of the state $\boldsymbol{x}$, with N functions $f_l : D_t \times D_x \mapsto \mathbb{R}^3$, as

$$\dot{\boldsymbol{z}} = f_0(t, \boldsymbol{x}), \tag{2.30a}$$

$$\dot{\boldsymbol{Y}}^l = \boldsymbol{Y}^l [f_l(t, \boldsymbol{x})]^\wedge_{G_l}, \qquad \forall l = 1, \cdots, N. \tag{2.30b}$$

The s-stage CG algorithm in [Andrle and Crassidis, 2013], when stated in the context of SU(2), SO(3), $\mathbb{H}$, for the left-invariant case, can be written

$$\boldsymbol{x}_k^{(1)} = \boldsymbol{x}_k, \tag{2.31a}$$

$$\boldsymbol{k}_k^{(i)} = f_0(t_k + c_i h_k, \boldsymbol{x}_k^{(i)}), \tag{2.31b}$$

$$\boldsymbol{K}_k^{l,(i)} = h_k [f_l(t_k + c_i h_k, \boldsymbol{x}_k^{(i)})]^\wedge_{G_l}, \qquad \forall l = 1, ..., N \tag{2.31c}$$

$$\boldsymbol{z}_k^{(i)} = \boldsymbol{z}_k + h_k \sum_{j=1}^{i-1} a_{ij} \boldsymbol{k}^{(j)}, \tag{2.31d}$$

$$\boldsymbol{Y}_k^{l,(i)} = \boldsymbol{Y}_k^l \prod_{j=1}^{i-1} \mathrm{Exp}_{G_l}(a_{ij} \boldsymbol{K}_k^{l,(j)}), \qquad \forall l = 1, ..., N \tag{2.31e}$$

$$\boldsymbol{z}_{k+1} = \boldsymbol{z}_k + h_k \sum_{j=1}^{s} b_j \boldsymbol{k}^{(j)}, \tag{2.31f}$$

$$\boldsymbol{Y}_{k+1}^l = \boldsymbol{Y}_k^l \prod_{j=1}^{s} \mathrm{Exp}_{G_l}(b_j \boldsymbol{K}_k^{l,(j)}), \qquad \forall l = 1, ..., N \tag{2.31g}$$

Note that if the attitude is represented as a set of N complex-valued 2×2 matrices or quaternions, the associated rotation matrices can be evaluated at any point in time by Definition 2.17. Consequently, while not being restricted

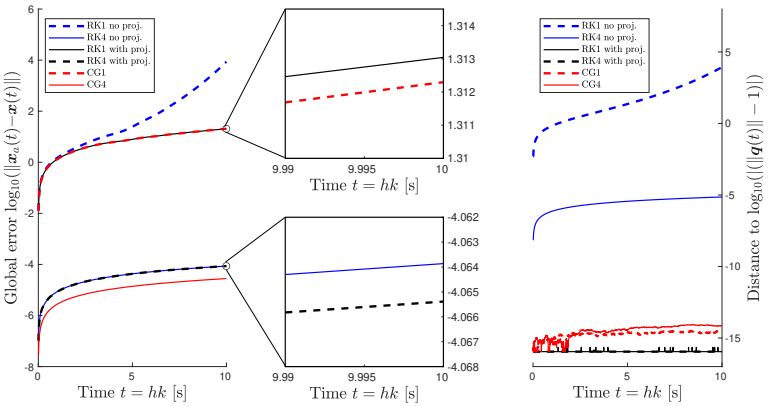

Figure 2.9 *Left:* Global error in time between the true analytical solution and solution computed by numerical integration when using the RK-methods (with and without projection) and the CG methods. *Center:* Zoom on the global errors at around $t = 10$. *Right:* Distance between the numerically integrated quaternion and $\mathbb{H}$ in time, as measured by $|\|\boldsymbol{q}(t)\| - 1|$.

to quaternions, the CG-method is implemented with an internal quaternion representation. To illustrate these methods, an example of the algorithms in (2.29) and (2.31) is given by simulating the attitude dynamics in (3.1).

Example 2.3
Consider the attitude dynamics in (3.1) with $\boldsymbol{\tau}(t) = \mathbf{0}$ for all $t \geq t_\circ$, and let $\boldsymbol{J} = \text{diag}(J_T, J_T, J_3) \succ \mathbf{0}$ with the initial conditions $\boldsymbol{q}(t_\circ) = \boldsymbol{q}_\circ$ and $\boldsymbol{\omega}(t_\circ) = \boldsymbol{\omega}_\circ$ at $t_\circ = 0$. Interestingly, the solution to this ODE is known analytically from [Andrle and Crassidis, 2013]. This analytical solution, here denoted $\boldsymbol{x}_a(t) \in \mathbb{H} \times \mathbb{R}^3$, is stated in the notation of the thesis in Appendix A.2.2. As such, we can evaluate the global integration errors of the numerical integration schemes. For this example, we start by writing the system on the CG form. For instance, if $\boldsymbol{x} \in \text{SU}(2) \times \mathbb{R}^3$, with $\boldsymbol{z} = \boldsymbol{\omega} \in \mathbb{R}^3$, $\boldsymbol{Y}^1 \in \text{SU}(2)$, then

$$f_0(t, \boldsymbol{x}) = \boldsymbol{J}^{-1}\boldsymbol{S}(\boldsymbol{J}\boldsymbol{\omega})\boldsymbol{\omega}, \quad f_1(t, \boldsymbol{x}) = (1/2)\boldsymbol{\omega}. \tag{2.32}$$

The resulting truncation errors are shown in Figure 2.9, when running the $s = \{1, 4\}$ stage RK algorithm (with and without projection), as well as the $s = \{1, 4\}$ stage CG algorithm, both with an internal attitude representation on $\mathbb{H}$. Here, the system is initialized with $\boldsymbol{q}_\circ = \boldsymbol{q}_{\boldsymbol{I}}$, a random $\boldsymbol{\omega}_\circ$ with $\|\boldsymbol{\omega}_\circ\| = 20$, with the parameters $J_T = 0.7$, $J_3 = 0.5$ and $h_k = 10^{-2}$ for all k. From this example, we can draw several conclusions that will determine how the systems of the thesis are simulated and implemented in real-time. The main takeaways are summarized in Remarks 2.7, 2.8, 2.9, and 2.10. □

Remark 2.7
In some software, such as the Julia package `DifferentialEquations.jl`, one has great freedom in manipulating the solver memory, permitting projections on each time-step. However, when using tools such as Simulink, one might see severe errors in time as the global integration errors build up in the internal memory of the solver, despite an external projection back to the configuration manifold (as this does not change the internal solver memory in Simulink). If the system is not too stiff, and the time-step chosen sufficiently small, then simulations can be done without resetting the internal memory of the solver, as the comparison of the RK4 method with and without the projection to $\mathbb{H}$ clearly demonstrates. We emphasize that if investigating errors that should go to zero down to machine precision for relatively stiff system using tools such as Simulink, then it is imperative to monitor the distance of the numerically integrated quaternions to $\mathbb{H}$ to assess the accumulated integration errors. □

Remark 2.8
In this thesis, we avoid direct integration on SO(3), and instead integrate all attitudes on $\mathbb{H}$. While the CG-methods tend to be superior to an RK with projection for relatively stiff systems (as demonstrated in Figure 2.9 and discussed in [Andrle and Crassidis, 2013]), we use RK methods of order ≥ 4 with the time-step set to $h = 10^{-3}$ in the simulations, as the local truncation error in both methods then approaches machine precision $O(10^{-15})$. The main reason for this is to simplify the implementation and to avoid that artifacts of the discretization appear in the studied signals. The simulation examples in the forthcoming chapters are all implemented in Simulink. □

Remark 2.9
While the projection is less important in high-order methods, it becomes very important as order of the method decreases. For the explicit first-order methods in Figure 2.9, which will be used when discretizing and implementing the controllers, we note that a first-order CG-algorithm performs very similar to the first-order RK method with projection. However, when removing the projection, the errors quickly increase in time. While either may be used, we will consider the first order CG-method when discretizing any dynamic continuous controller or estimator with dynamics in the applications. This is the method of discretization used in the implementations in [Greiff, 2020].□

Remark 2.10
When considering the C-code in [Greiff, 2020], any output feedback controller implementation with a dynamic estimator (to be defined later) needs to be simulated using a single step-method from Julia using `DifferentialEquations.jl`. Presently, each time the controller is called, its internal memory is updated, rendering multi-step methods infeasible to use.□

2.4 Lyapunov Stability Theory

Lyapunov stability theory is an umbrella term for a set of powerful tools that can be employed to analyze the properties of dynamical systems, first published in the monograph of Lyapunov [Lyapunov, 1892] (with an English translation of the original in [Lyapunov, 1992]). The theory sets out a generic framework for studying the solutions of ordinary differential equations without explicit computation of their solutions. These tools are frequently used in the controller design for UAVs, and will also be applied in this thesis. In this section, we give the relevant definitions, following the notation in the seminal work of [Khalil, 2002], and proceed by detailing relevant results for linear autonomous, linear non-autonomous, and nonlinear non-autonomous systems.

2.4.1 Definitions

In this thesis, we are primarily concerned with trajectory tracking for nonlinear non-autonomous systems. In the most general case, we seek to represent the tracking or estimate error dynamics of a controlled system in the form

$$\dot{\boldsymbol{x}} = f(t, \boldsymbol{x}), \qquad t \in [t_\circ, \infty) = D_t \subseteq \mathbb{R}_{\geq 0}, \qquad \boldsymbol{x} \in D_{\boldsymbol{x}} \subseteq \mathbb{R}^n, \tag{2.33}$$

where $f : D_t \times D_{\boldsymbol{x}} \mapsto \mathbb{R}^n$ is piece-wise continuous in t and locally Lipschitz continuous in $\boldsymbol{x}$ on $D_{\boldsymbol{x}}$, where $D_{\boldsymbol{x}}$ is a compact domain that contains $\boldsymbol{x} = \mathbf{0}$ in its interior. This point is said to be an equilibrium point of (2.33) if

$$f(t, \boldsymbol{x}) = \mathbf{0}, \quad \forall t \geq t_\circ. \tag{2.34}$$

Using Lyapunov theory, the stability properties of the origin $\boldsymbol{x} = \mathbf{0}$ of the non-autonomous system in (2.33) can be characterized in ways that, in modern control theory, succeed the stability concepts in the thesis of Lyapunov. To talk about these concepts, we first introduce a set of comparison functions.

Definition 2.23—Class $\mathcal{K}$ function [Khalil, 2002, Definition 4.2] A function $\alpha : [0, a) \mapsto [0, \infty)$ is said to belong to class $\mathcal{K}$ if it is (i) continuous in its argument, (ii) strictly increasing, and (iii) $\alpha(0) = 0$. □

Definition 2.24—Class $\mathcal{KL}$ function [Khalil, 2002, Definition 4.3] A function $\beta : [0, a) \times [0, \infty) \mapsto [0, \infty)$ is said to belong to class $\mathcal{KL}$ if (i) it is continuous in its arguments, (ii) for each fixed s, the mapping $\beta(r, s)$ belongs to class $\mathcal{K}$ with respect to each fixed r, (iii) for each fixed r, the mapping $\beta(r, s)$ is decreasing with respect to s, and (iv) $\beta(r, s) \to 0$ as $s \to \infty$. □

With these comparison functions, several forms of stability can be defined.

Definition 2.25
The origin $\boldsymbol{x} = \mathbf{0}$ of the non-autonomous system in (2.33) is said to be

- Stable, if there exists an $\alpha \in \mathcal{K}$ and a constant $r > 0$, such that

$$\|\boldsymbol{x}(t)\| \leq \alpha(\|\boldsymbol{x}(t_\circ)\|), \quad \forall t \geq t_\circ \geq 0, \quad \forall \boldsymbol{x}(t_\circ) \in \mathcal{B}_r \subseteq D_{\boldsymbol{x}}. \tag{2.35}$$

- Globally Stable, if (2.35) holds for all initial conditions $\boldsymbol{x}(t_\circ)$.
- Unstable, if it is not stable.
- Asymptotically Stable (AS), if there is a $\beta \in \mathcal{KL}$ and $r > 0$, such that

$$\|\boldsymbol{x}(t)\| \leq \beta(\|\boldsymbol{x}(t_\circ)\|, t - t_\circ), \quad \forall t \geq t_\circ \geq 0, \quad \forall \boldsymbol{x}(t_\circ) \in \mathcal{B}_r. \tag{2.36}$$

- Globally Asymptotically Stable (GAS), if (2.36) holds for all $\boldsymbol{x}(t_\circ)$.
- Exponentially Stable (ES), if it is AS, and (2.36) is satisfied with

$$\beta(r, s) = kre^{-\gamma s}, \qquad k > 0, \ \gamma > 0. \tag{2.37}$$

- Globally Exponentially Stable (GES), if the system is GAS for a class-$\mathcal{KL}$ function on the form given in (2.37).
- Almost Globally Asymptotically Stable (AGAS), if the origin is GAS except for a set of unstable equilibrium points, $\mathcal{E}$, of measure zero.
- Asymptotically attractive, if for each $r > 0$ and each $\sigma > 0$, there exist a time $T > 0$ such that

$$\boldsymbol{x}(t_\circ) \in \mathcal{B}_r \Rightarrow \boldsymbol{x}(t) \in \mathcal{B}_\sigma, \quad \forall t \geq T + t_\circ. \qquad \square$$

Remark 2.11
These definitions of stability are quite simple and appealing, essentially following [Khalil, 2002, Definition 4.4] but written in terms of $\mathcal{K}$ and $\mathcal{KL}$-functions, made possible [Khalil, 2002, Lemma 4.5]. The notion of *almost global* asymptotic stability is not found among these more common stability definitions. It was coined in the field of attitude control, and this definition has been used for several decades (see, e.g., [Tsiotras, 1998; Sanyal and Chaturvedi, 2008]). It should be understood as the region of asymptotic attraction being global, except for a negligible set of initial conditions. An AGAS system is stable in the same sense that a damped two-dimensional pendulum is stable about its configuration with least potential energy. The condition of asymptotic attractiveness is defined as in [Loria et al., 2005]. $\square$

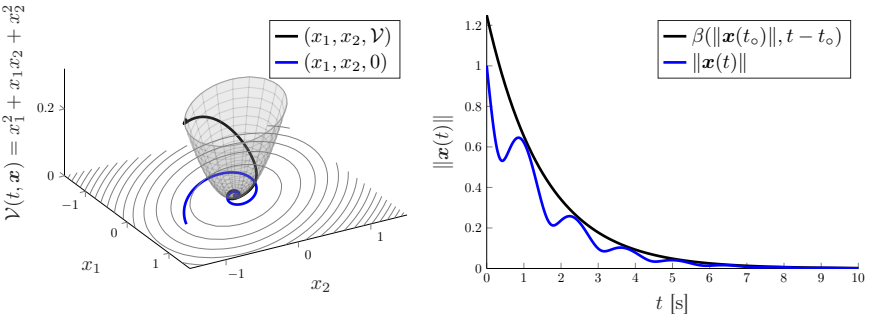

Figure 2.10 *Left:* Illustration of a Lyapunov function over the phase plane for a system in $D_{\boldsymbol{x}} = \mathbb{R}^2$ and its level sets, with the state trajectory and in the phase plane (blue), and the Lyapunov function evaluated along this trajectory (black) converging to the origin in time. *Right:* The norm of the state trajectories, bounded by an exponential class $\mathcal{KL}$-function in (2.37).

Here, the different notions of stability are more or less interesting depending on the considered application. For instance, if (2.33) is linear in $\boldsymbol{x}$ and autonomous, then asymptotic and exponential stability becomes a distinction without a difference. However, in the more general case where (2.33) is non-linear and non-autonomous, the form of the stability has significant implications for the robustness of the system to disturbances. As we shall see later, it is possible to construct systems which are GAS that have unbounded trajectories for arbitrarily small bounded disturbances. In order to guarantee certain robustness properties, we therefore require the even stronger notions of *uniform* stability, which implies an independence of the initial time $t_\circ$.

Definition 2.26
If any of the conditions in Definition 2.25 hold independently of the initial time $t_\circ$, then the convergence of the errors is uniform (U), here abbreviated as US, UGS, UAS, UGAS, UAGAS, UES, and UGES, respectively. Here, UAGAS should be understood as uniform convergence to the set $\mathcal{E}$ in Definition 2.25.□

In general, the idea of Lyapunov theory is to prove certain stability properties in Definition 2.25 by constructing a positive definite function in $\boldsymbol{x}$, here denoted $\mathcal{V}(t, \boldsymbol{x})$, whose convergence or divergence in time can be studied along all possible trajectories of (2.33) on some domain. The main idea is illustrated in Figure 2.10, here for an exponentially stable system, where the states decay according to the $\mathcal{KL}$-function in (2.37). In the remainder of this chapter, various stability theorems will be presented for the cases where the system in (2.33) is linear and nonlinear in $\boldsymbol{x}$, respectively. All of these theorems will follow the basic idea and intuition depicted in Figure 2.10.

2.4.2 Linear Systems

Throughout the thesis, we consider the local stability properties of specific equilibrium points, in which case the system's error dynamics will often be locally linear and possibly non-autonomous. Consequently, we begin by summarizing relevant results for the stability analysis of systems in the form

$$\dot{\boldsymbol{x}} = \boldsymbol{A}(t)\boldsymbol{x}, \qquad \boldsymbol{x}_\circ = \boldsymbol{x}(t_\circ). \tag{2.38}$$

For such systems, the existence of a quadratic Lyapunov function is related to the solution of an associated Lyapunov equation, summarized as follows.

THEOREM 2.1—[KHALIL, 2002, THEOREM 4.10]
Consider the system in (2.38) and assume that $\boldsymbol{A}(t)$ is continuous and bounded. Assume that for a continuous $\boldsymbol{Q}(t) = \boldsymbol{Q}(t)^\top$, there exists a continuously differentiable solution $\boldsymbol{P}(t) = \boldsymbol{P}(t)^\top$ to matrix differential equation,

$$\boldsymbol{A}(t)^\top \boldsymbol{P}(t) + \boldsymbol{P}(t)\boldsymbol{A}(t) + \dot{\boldsymbol{P}}(t) + \boldsymbol{Q}(t) = \boldsymbol{0}, \tag{2.39a}$$

referred to as the Lyapunov equation, and there exist $c_i \in \mathbb{R}_{\geq 0}$, such that

$$c_1\boldsymbol{I} \preccurlyeq \boldsymbol{P}(t) \preccurlyeq c_2\boldsymbol{I}, \qquad\qquad c_3\boldsymbol{I} \preccurlyeq \boldsymbol{Q}(t). \tag{2.39b}$$

If for all $t \geq t_\circ$, $c_2 \geq c_1 > 0$, and

- $c_3 > 0$, the system is UES.
- $c_3 = 0$, the system is US. □

For such systems, the stability proof follows by constructing an associated function $\mathcal{V}(t, \boldsymbol{x}) = \boldsymbol{x}(t)^\top \boldsymbol{P}(t)\boldsymbol{x}(t)$. This is a special version of Lyapunov's second method, which comes with a more general result in the nonlinear system setting. It facilitates proofs that all solutions of the system in (2.38) converge to the origin or remain bounded, independent of the initial conditions. We also note that in this linear setting, UAS is equivalent to UES.

THEOREM 2.2—[ANTSAKLIS AND MICHEL, 2006, THEOREM 5.4, CHAP. 6]
If $\|\boldsymbol{A}(t)\|$ is bounded for all $t \geq t_\circ$, (2.38) is UAS if and only if it is UES. □

These theorems provide a good starting point for analyzing systems with special structure in $\boldsymbol{A}(t)$. To see this, we first give the following definition.

DEFINITION 2.27
Let $(\boldsymbol{P}, \boldsymbol{Q})$ be a solution to (2.39) where $\boldsymbol{P} = \boldsymbol{P}^\top \succ \boldsymbol{0}$ and $\boldsymbol{Q} = \boldsymbol{Q}^\top \succeq \boldsymbol{0}$. □

This thesis deals with mechanical systems with rotational degrees of freedom, which have several particular properties, such as skew-symmetric structure in the dynamics. As such, we will at times use the following lemma.

Lemma 2.1
If $\boldsymbol{A}(t) = \boldsymbol{M}_1^{-1}(\boldsymbol{S}(t) - \boldsymbol{M}_2(t))$ where $\boldsymbol{S}(t)$ is a bounded, real-valued, skew-symmetric matrix, and $\boldsymbol{M}_1 = \boldsymbol{M}_1^\top \succ \boldsymbol{0}$, and $\boldsymbol{M}_2(t) = \boldsymbol{M}_2(t)^\top \succ \boldsymbol{0}$ is positive definite, continuous and bounded, then $(\boldsymbol{M}_1, 2\boldsymbol{M}_2(t))$ solves (2.39). □

Proof. The proof is verified by inserting the proposed solution. Some special cases of related systems were studied in e.g., [Barnett and Storey, 1967]. □

More complicated structures can be considered, and a result that will be used frequently in the forthcoming proofs can be summarized as follows.

Lemma 2.2
If $\bar{\boldsymbol{A}}(t) = \boldsymbol{F} \otimes \boldsymbol{I}_m + \boldsymbol{I}_n \otimes \boldsymbol{S}(t)$ where $\boldsymbol{F} \in \mathbb{R}^{n\times n}$ solves (2.39) with $(\boldsymbol{P}, \boldsymbol{Q})$ and $\boldsymbol{S}(t) \in \mathbb{R}^{m\times m}$ is bounded, real-valued skew-symmetric, then $\bar{\boldsymbol{A}}(t)$ solves the Lyapunov equation in (2.39) with $(\bar{\boldsymbol{P}}, \bar{\boldsymbol{Q}}) = (\boldsymbol{P} \otimes \boldsymbol{I}_m, \boldsymbol{Q} \otimes \boldsymbol{I}_m)$. □

Proof. The proof follows form (2.1), and is summarized in Appendix A.3.□

This is appealing, as it simplifies to problem of analyzing stability for a non-autonomous system characterized by $\bar{\boldsymbol{A}}(t) \in \mathbb{R}^{nm\times nm}$ to the analysis of a smaller autonomous system characterized by a system matrix $\boldsymbol{F} \in \mathbb{R}^{n\times n}$. Other structures can be analyzed in a similar manner, such as the second-order systems discussed in [Chetaev et al., 1961; Müller and Schiehlen, 1977; Bernstein and Bhat, 1995], which will be used in the thesis. However, it is not always easy to apply such results directly. As hinted before, we can take various orthogonal or symmetric similarity transforms to massage $\boldsymbol{A}(t)$ into a more suitable form for analysis. We also consider time-varying orthogonal transformations with $\boldsymbol{R}(t) \in \mathrm{SO}(3)$, where following lemma applies.

Lemma 2.3
Consider the system in (2.38), and take any orthogonal transform $\boldsymbol{R}(t) \in \mathrm{SO}(3)$ evolving in time with a set of bounded velocities $\boldsymbol{\omega}(t)$, such that $\dot{\boldsymbol{R}}(t) = \boldsymbol{R}(t)[\boldsymbol{\omega}(t)]^\wedge_{\mathrm{SO}(3)}$. By a change of coordinates $\boldsymbol{z}(t) = \boldsymbol{R}(t)\boldsymbol{x}(t)$,

$$\dot{\boldsymbol{z}} = (\boldsymbol{R}(t)\boldsymbol{A}(t)\boldsymbol{R}(t)^\top + [\boldsymbol{R}(t)\boldsymbol{\omega}(t)]^\wedge_{\mathrm{SO}(3)})\boldsymbol{z}(t) = \bar{\boldsymbol{A}}(t) + \boldsymbol{S}(t), \tag{2.40}$$

where $\bar{\boldsymbol{A}}(t) = \boldsymbol{R}(t)\boldsymbol{A}(t)\boldsymbol{R}(t)^\top$ and $\boldsymbol{S}(t)$ is skew-symmetric. □

Proof. The proof is given in Appendix A.3. □

By applying such a time-varying transform, we obtain a similar term as when using a stationary orthogonal transformation, plus a skew-symmetric term (which vanishes when the rates driving the rotation $\boldsymbol{\omega}(t) \equiv 0$). However, as we have already seen in Lemma 2.1, adding a skew-symmetric time-varying matrix to the system matrix can potentially be dealt with, if it results in a structure that admits analysis using, for instance, Lemma 2.1.

Lemma 2.4
Consider a system

$$\boldsymbol{E}\dot{\boldsymbol{x}} = \boldsymbol{A}(t)\boldsymbol{x}, \tag{2.41}$$

with $\boldsymbol{E} = \boldsymbol{E}^\top \succ \boldsymbol{0}$. Assume that the system

$$\dot{\boldsymbol{x}} = \boldsymbol{A}(t)\boldsymbol{x}, \tag{2.42}$$

is uniformly exponentially stable or uniformly stable by Theorem 2.1 with $(\boldsymbol{P}, \boldsymbol{Q}(t))$. If $\boldsymbol{P}$ is time-invariant and commutes with $\boldsymbol{E}$, then (2.41) is:

- UES if (2.42) is UES,
- US if (2.42) is US. □

Proof. The proof is given in Appendix A.3. □

2.4.3 Nonlinear Systems

In Sec. 2.4.2, if the system is autonomous, the Lyapunov equation (2.39) can be solved to synthesize a quadratic Lyapunov function. In the nonlinear setting, finding a suitable Lyapunov function is often the most challenging part of a stability proof. However, once found, theorems analogous to Theorem 2.1 can be used to analyze the stability of the system.

Theorem 2.3—[Khalil, 2002, Theorem 4.8]
Let $\boldsymbol{x} = \boldsymbol{0}$ be an equilibrium point of the system (2.33) and $D_{\boldsymbol{x}} \subseteq \mathbb{R}^n$ be a domain containing $\boldsymbol{x} = \boldsymbol{0}$. Let $\mathcal{V} : D_t \times D_{\boldsymbol{x}} \mapsto \mathbb{R}_{\geq 0}$ be a continuously differentiable function such that

$$W_1(\boldsymbol{x}) \leq \mathcal{V}(t, \boldsymbol{x}) \leq W_2(\boldsymbol{x}), \tag{2.43a}$$

$$\frac{\partial \mathcal{V}}{\partial t} + \frac{\partial \mathcal{V}}{\partial \boldsymbol{x}} f(t, \boldsymbol{x}) \leq 0, \tag{2.43b}$$

for all $t \in D_t$ and $\boldsymbol{x} \in D_{\boldsymbol{x}}$, where $W_1(\boldsymbol{x})$ and $W_2(\boldsymbol{x})$ are continuous positive definite functions on $D_{\boldsymbol{x}}$. Then, $\boldsymbol{x} = \boldsymbol{0}$ is US. □

A useful extension of Theorem 2.3 can be made if imposing a more strict condition on (2.43b), allowing UAS and UGAS to be concluded.

Theorem 2.4—[Khalil, 2002, Theorem 4.9]
If the second assumption of Theorem 2.3 in (2.43b) is strengthened to

$$\frac{\partial \mathcal{V}}{\partial t} + \frac{\partial \mathcal{V}}{\partial \boldsymbol{x}} f(t, \boldsymbol{x}) \leq -W_3(\boldsymbol{x}), \tag{2.44}$$

for all $t \in D_t$ and $\boldsymbol{x} \in D_{\boldsymbol{x}}$, where $W_3(\boldsymbol{x})$ is a continuous positive definite function, then $\boldsymbol{x} = \boldsymbol{0}$ is UAS. Finally, if $W_1(\boldsymbol{x})$ is radially unbounded, then $\boldsymbol{x} = \boldsymbol{0}$ is UGAS. □

THEOREM 2.5—[KHALIL, 2002, THEOREM 4.10]
If the positive definite functions W_1, W_2, W_3 in Theorem 2.4 can be expressed as $W_i(\boldsymbol{x}) = c_i\|\boldsymbol{x}\|^a$ for some positive $c_i > 0$ and $a > 0$, then the origin $\boldsymbol{x} = \mathbf{0}$ is UES on $D_{\boldsymbol{x}}$. If the assumptions hold globally, then $\boldsymbol{x} = \mathbf{0}$ is UGES.

There are tools available by which asymptotic stability properties may be shown even in the case where the time-derivative of $\mathcal{V}(t, \boldsymbol{x})$ is negative semi-definite. In this thesis, we will primarily use a result attributed to Barbălat, originally presented in [Barbălat, 1959]. This is commonly referred to as the Lemma of Barbălat, and can be used to show asymptotic (but not uniform) stability properties of systems using Lyapunov-like functions.

LEMMA 2.5—LEMMA OF BARBĂLAT [BARBĂLAT, 1959]
Let $\phi : \mathbb{R}_{\geq 0} \mapsto \mathbb{R}$ be a uniformly continuous function on its domain. Suppose that $\lim_{t\to\infty} \int_0^t \phi(\tau)d\tau$ exists and is finite. Then $\phi(t) \to 0$ as $t \to \infty$. □

REMARK 2.12
A concise proof is given by contradiction in [Khalil, 2002, Lemma 8.2], and the result is very useful for showing asymptotic stability properties. The most common is to find a positive definite function $\mathcal{V}(t, \boldsymbol{x})$ in $\boldsymbol{x}$, with a negative (semi-)definite time-derivative, and let $\phi(t) \triangleq (\mathrm{d}/\mathrm{d}t)\mathcal{V}(t, \boldsymbol{x})$. If it is possible to show uniform continuity of $\phi(t)$, which in practice can be done by showing that $(\mathrm{d}^2/\mathrm{d}t^2)\mathcal{V}(t, \boldsymbol{x})$ is bounded for all times, then Lemma 2.5 can be invoked to conclude convergence of $\boldsymbol{x}(t)$ to an invariant set. □

Lemma 2.5 has also been extended and reformulated in various ways to simplify its use. A relevant extended version was given in [Micaelli, 1993].

LEMMA 2.6—MICHAELLI'S EXTENSION [MICAELLI, 1993, LEMMA 1, PP 34]
Let $f : \mathbb{R}_{\geq 0} \mapsto \mathbb{R}$ and $g : \mathbb{R}_{\geq 0} \mapsto \mathbb{R}$, where f is differentiable and g is uniformly continuous on their respective domains. If $\lim_{t\to\infty} f(t) = l$ and $\lim_{t\to\infty}(\dot{f}(t) - g(t)) = 0$, then $\lim_{t\to\infty} \dot{f}(t) = \lim_{t\to\infty} g(t) = 0$. □

This result was rewritten on an instructive form in the thesis of Lefeber in [Lefeber, 2000], which will be used in the forthcoming developments.

LEMMA 2.7—LEFEBER'S FORM [LEFEBER, 2000, LEMMA 2.2.12]
Let $f : \mathbb{R}_{\geq 0} \mapsto \mathbb{R}$ be any differentiable function. If $f(t)$ converges to zero as $t \to \infty$ and its derivative satisfies

$$\dot{f}(t) = f_0(t) + \eta(t), \qquad \forall t \geq 0, \tag{2.45}$$

where $f_0 : \mathbb{R}_{\geq 0} \mapsto \mathbb{R}$ is uniformly continuous and $\eta : \mathbb{R}_{\geq 0} \mapsto \mathbb{R}$. If $\eta(t)$ tends to zero as $t \to \infty$, then $\dot{f}(t)$ and $f_0(t)$ tend to zero as $t \to \infty$. □

These lemmas are very useful in concluding asymptotic convergence to an invariant set, which will typically contain multiple equilibrium points. As the Barbashin-Krasovskii-LaSalle theorems do not generally apply in the non-autonomous setting, we will use other tools to analyze such invariant sets further. To show local instability, we use local linearizations of the error dynamics, or a useful instability result by Chetaev in [Chetaev et al., 1961].

THEOREM 2.6—[HAHN, 1967, THEOREM 42.6]
Assume that (2.33) has an equilibrium point in the origin, and that there exists a function $\mathcal{C}(t, \boldsymbol{x})$ satisfying $\mathcal{C}(t, \mathbf{0}) = \mathbf{0}$ for all $t \geq t_\circ$, such that:

- There exists a non-empty domain $\mathcal{G} = \{(t, \boldsymbol{x}) \in D_t \times D_{\boldsymbol{x}} \mid \mathcal{C}(t, \boldsymbol{x}) < 0\}$
- At least one component $\mathcal{G}_i \subset \mathcal{G}$ is contiguous with $\boldsymbol{x} = \mathbf{0}$ for all $t \in D_t$, and on this component $\mathcal{C}(t, \boldsymbol{x})$ is bounded from below for all $t \in D_t$.
- There exist a neighborhood of the origin, $\mathcal{U} = \{(t, \boldsymbol{x}) \in D_t \times \mathcal{B}_r\}$ for some arbitrarily small $r > 0$ such that $\dot{\mathcal{C}}(t, \boldsymbol{x}) < 0$, $\forall (t, \boldsymbol{x}) \in (D_t \times \mathcal{B}_r) \cap \mathcal{G}_i$.

Then, the equilibrium point $\boldsymbol{x} = \mathbf{0}$ is locally unstable. □

REMARK 2.13
This slight restatement of the last point of the theorem is possible due to the discussion on [Hahn, 1967, Page 202]. When working with the Lemmas of Barbălat in 2.5, 2.6, and 2.7 to characterize an invariant set $\mathcal{E} \subset D_{\boldsymbol{x}}$, this Chetaev instability theorem often proves useful. By construction, the associated Lyapunov-like function $\mathcal{V}(t, \boldsymbol{x}) \geq 0$ will typically satisfy $\dot{\mathcal{V}}(t, \boldsymbol{x}) < 0$ for all $\boldsymbol{x} \in D_{\boldsymbol{x}} \backslash \mathcal{E}$. Assume that for some $\tilde{\boldsymbol{x}} \in \mathcal{E}$, it holds that $\mathcal{V}(t, \tilde{\boldsymbol{x}}) = c > 0$. Then, it may be possible to construct a function $\mathcal{C}(t, \boldsymbol{x}) = \mathcal{V}(t, \boldsymbol{x} + \tilde{\boldsymbol{x}}) - c$. If we can find any direction in which $\mathcal{G}$ is non-empty, instability follows. □

A drawback of using Lemmas 2.5, 2.6, and 2.7, followed by Theorem 2.6, is that they (unlike Theorem 2.4) only can be used to conclude asymptotic stability properties in the non-autonomous nonlinear setting, and not uniform convergence properties. However, there are alternative routes toward showing uniform stability even with so-called weak Lyapunov functions. Specifically, the ideas of Matrosov, dating back to the work in [Matrosov, 1962]. The basic idea is to find an auxiliary function that is uniformly bounded, and show that its time-derivative is negative on the domain where the time-derivative of the weak Lyapunov function vanishes. The ideas of Matrosov were notably extended in [Loria et al., 2005], presenting a result with multiple auxiliary ordered functions whose derivative bounds satisfy nested properties. This is illustrated in Figure 2.4.3. In this thesis, we will use a variant of this specific nested Matrosov Theorem, as presented below. It will be used in conjunction with the various Lemmas of Barbălat, to show uniform stability properties when the error dynamics are nonlinear and non-autonomous.

THEOREM 2.7—[LEFEBER ET AL., 2017, THEOREM 2]
Consider the system in (2.33), but with $f : \mathbb{R}_{\geq 0} \times \mathbb{R}^n \mapsto \mathbb{R}^n$, where f is locally bounded, continuous, and locally uniformly continuous in t. If there exist j differentiable functions $\mathcal{V}_i : \mathbb{R}_{\geq 0} \times \mathbb{R}^n \mapsto \mathbb{R}$, bounded in t, and continuous functions $\mathcal{Y}_i : \mathbb{R}^n \mapsto \mathbb{R}$ for $i \in \{1, 2, \dots j\}$ such that

(i) $\mathcal{V}_1$ shows that the origin is UGS,

(ii) $\dot{\mathcal{V}}_i(t, \boldsymbol{x}) \leq \mathcal{Y}_i(\boldsymbol{x})$, for all $i \in \{1, 2, \dots, j\}$,

(iii) $\mathcal{Y}_i(\boldsymbol{x}) = 0$ for $i \in \{1, 2, \dots, k-1\} \Rightarrow \mathcal{Y}_k(\boldsymbol{x}) \leq 0$ for all $k \in \{1, 2, \dots, j\}$,

(iv) $\mathcal{Y}_i(\boldsymbol{x}) = 0$ for all $i \in \{1, 2, \dots, j\} \Rightarrow \boldsymbol{x} = \boldsymbol{0}$,

then the origin of (2.33) is UGAS. □

This is a slightly simpler way of stating the theorem in [Loria et al., 2005, Theorem 1], and it should be noted that the assumption (i) can be replaced when global stability cannot be shown, as discussed in [Loria et al., 2005].

THEOREM 2.8—[LORIA ET AL., 2005, THEOREM 2]
If assumption (i) in Theorem 2.7 is replaced by

(i.1) $\mathcal{V}_1$ shows that the origin is US;

(i.2) for each $\boldsymbol{x}(t_\circ)$, there is an $M_\circ > 0$ such that $\|\boldsymbol{x}(t)\| \leq M_\circ$, $\forall t_\circ$ and $t \geq t_\circ$;

(i.3) the map $\boldsymbol{x} \mapsto f(t, \boldsymbol{x})$ is locally Lipschitz continuous uniformly in t;

then the origin of (2.33) is UGAS. □

These theorems can be used with the Lemmas of Barbălat to show UGAS properties, and will be employed frequently in Chapter 5 and Chapter 6.

2.5 Cascade Theory

When considering non-linear and non-autonomous systems, certain structure in the dynamics may simplify the analysis significantly, much like in the linear setting. For mechanical systems, it is sometimes possible to write the dynamics as a cascade of two smaller subsystems. If so, several powerful stability results may be applied. In this section, we consider a system

$$\Sigma_1 : \ \dot{\boldsymbol{x}}_1 = f_1(t, \boldsymbol{x}_1) + g(t, \boldsymbol{x}_1, \boldsymbol{x}_2)\boldsymbol{x}_2 \tag{2.46a}$$
$$\Sigma_2 : \ \dot{\boldsymbol{x}}_2 = f_2(t, \boldsymbol{x}_2), \tag{2.46b}$$

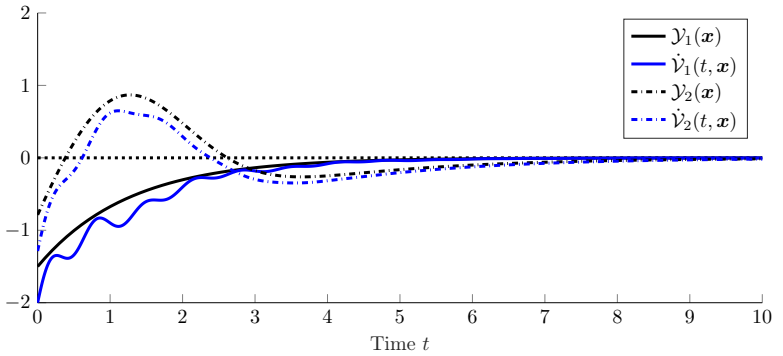

Figure 2.11 Illustration of the main idea of the nested Matrosov theorem. Assume that $\dot{\mathcal{V}}_1$ is negative semi-definite in $\boldsymbol{x}$, and $\mathcal{V}_1(t,\boldsymbol{x})$ can be used to show US of $\boldsymbol{x}=\mathbf{0}$. If there exists a differentiable function $\dot{\mathcal{V}}_2(t,\boldsymbol{x})$, whose time-derivative is upper bounded by a continuous function $\mathcal{Y}_2(\boldsymbol{x})$, such that $\mathcal{Y}_2(\boldsymbol{x}) \leq 0$ if $\mathcal{Y}_1(\boldsymbol{x})=\mathbf{0}$, and $\mathcal{Y}_1(\boldsymbol{x})=\mathcal{Y}_2(\boldsymbol{x})=\mathbf{0} \Rightarrow \boldsymbol{x}=\mathbf{0}$, then the origin is UGAS. Transiently, both $\dot{\mathcal{V}}_2(t,\boldsymbol{x})$ and $\mathcal{Y}_2(\boldsymbol{x})$ might be greater than zero.

where $f_1(t,\boldsymbol{x}_1)$ is continuously differentiable in its arguments, and $f_2(t,\boldsymbol{x}_2)$ and $g(t,\boldsymbol{x}_1,\boldsymbol{x}_2)$ are both continuous in their arguments and locally Lipschitz in $\boldsymbol{x}$. If we consider the unperturbed system $g(t,\boldsymbol{x}_1,\boldsymbol{x}_2)\equiv\mathbf{0}$, here written as

$$\Sigma_1' : \ \dot{\boldsymbol{x}}_1 = f_1(t,\boldsymbol{x}_1), \tag{2.47a}$$

one may expect that certain stability properties for the simpler system $\{\Sigma_1',\Sigma_2\}$ could be used to analyze the stability of the cascade $\{\Sigma_1,\Sigma_2\}$. However, it is not sufficient to just consider the stability of $\{\Sigma_1',\Sigma_2\}$, as certain properties of the interconnection $g(t,\boldsymbol{x}_1,\boldsymbol{x}_2)\boldsymbol{x}_2$ may result in a *peaking* phenomena and lead to instability. This is demonstrated in the example below.

Example 2.4
Consider a simple autonomous cascaded system in the form

$$\Sigma_1 : \ \dot{x}_1 = -(1-x_2)x_1^3 \qquad x_1(t_\circ)=x_{1\circ}, \tag{2.48}$$
$$\Sigma_2 : \ \dot{x}_2 = -x_2 \qquad x_2(t_\circ)=x_{2\circ}, \tag{2.49}$$

with $t_\circ=0$. Then, $\Sigma_1' : \ \dot{x}_1=-x_1^3$ and the interconnection term becomes $g(t,x_1,x_2)x_2=x_1^3x_2$. If removing the interconnection term, Σ_1' is GAS and Σ_2 is GES. However, when connecting the two, the solution is given by

$$x_1(t)=\operatorname{sign}(x_{1\circ})(x_{1\circ}^{-2}+2x_{2\circ}(e^{-t}-1)+2t)^{-1/2}, \quad x_2(t)=x_{2\circ}e^{-t}. \tag{2.50}$$

Clearly, it is possible to find initial conditions for which the denominator in $x_1(t)$ approaches zero for a finite escape time $t_{esc}>0$. Despite the two

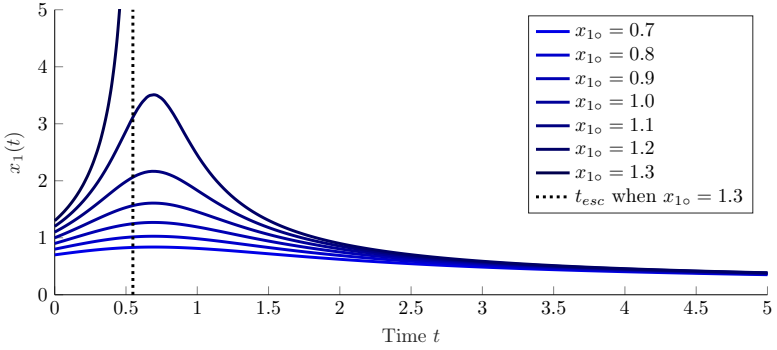

Figure 2.12 Illustration of the peaking phenomenon in Example 2.4.

subsystems being GES and GAS, the closed-loop is unstable and may diverge at a finite escape time, $t_{esc}(x_{1\circ}, x_{2\circ})$, here a function of the initial conditions. This is illustrated in Figure 2.5 for $x_{2\circ} = 2$ and varying $x_{1\circ} \in \{0.6, ..., 1.3\}$. □

Despite this pathological example, it is possible to show uniform global asymptotic stability properties of a cascade on the form in (2.46), if one poses special conditions on for instance the growth rate of the interconnection term. Such cascades have been studied in [Panteley and Loria, 1998; Loria et al., 2000], and relevant sufficient conditions are proposed to ensure uniform stability of the cascade in (2.46), as summarized in the following theorem.

Theorem 2.9—[Panteley and Loria, 1998, Theorem 1]
If the assumptions (A1)-(A3) are satisfied, the cascade in (2.46) is UGS.

(A1) The system $\Sigma_1' : \dot{x}_1 = f_1(t, \boldsymbol{x}_1)$ is UGS with a Lyapunov function $\mathcal{V}(t, \boldsymbol{x}_1)$ that is positive definite and proper, which satisfies

$$\left\| \frac{\partial \mathcal{V}}{\partial \boldsymbol{x}_1} \right\| \|\boldsymbol{x}_1\| \leq c_1 \mathcal{V}(t, \boldsymbol{x}_1), \quad \forall \|\boldsymbol{x}_1\| \geq \eta, \tag{2.51}$$

where $c_1 > 0$ and $\eta > 0$. Assume that $(\partial \mathcal{V}/\partial \boldsymbol{x}_1)(t, \boldsymbol{x}_1)$ is bounded uniformly in t for all $\|\boldsymbol{x}_1\| \leq \eta$. That is, there exists a constant $c_2 > 0$ such that for all $t \geq t_\circ \geq 0$

$$\left\| \frac{\partial \mathcal{V}}{\partial \boldsymbol{x}_1} \right\| \leq c_2, \quad \forall \|\boldsymbol{x}_1\| \leq \eta. \tag{2.52}$$

(A2) The function $g(t, \boldsymbol{x}_1, \boldsymbol{x}_2)$ satisfies

$$\|g(t, \boldsymbol{x}_1, \boldsymbol{x}_2)\| \leq \theta_1(\|\boldsymbol{x}_2\|) + \theta_1(\|\boldsymbol{x}_2\|)\|\boldsymbol{x}_1\|, \tag{2.53}$$

where $\theta_1, \theta_2 : \mathbb{R}_{\geq 0} \mapsto \mathbb{R}_{\geq 0}$ are continuous.

(A3) The system $\Sigma_2 : \dot{\boldsymbol{x}}_2 = f_2(t, \boldsymbol{x}_2)$ is UGAS and for all $t_\circ > 0$,

$$\int_{t_\circ}^{\infty} \|\boldsymbol{x}_2(t; t_\circ, \boldsymbol{x}_2(t_\circ))\| \mathrm{d}t \leq \phi(\|\boldsymbol{x}_2(t_\circ)\|), \tag{2.54}$$

where ϕ is a class-$\mathcal{K}$ function. □

Example 2.5
For the system studied in Example 2.4, let $\mathcal{V}(t, x_1) = \frac{1}{2}x_1^2$ be a Lyapunov function associated with Σ_1'. Take $c_1 = 2$ and $c_2 = \eta$ for any $\eta > 0$. Then,

$$\left\| \frac{\partial \mathcal{V}}{\partial x_1} \right\| \|x_1\| = \|x_1\| \|x_1\| = \|x_1\|^2 \leq c_1 \mathcal{V}(t, x_1), \qquad \forall \|x_1\| \geq \eta, \tag{2.55}$$

□

and $\|(\partial \mathcal{V})/(\partial x_1)\| = \|x_1\| \leq c_2$ for all $\|x_1\| \leq \eta$. As the system Σ_1' is UGS, (A1) is satisfied. Clearly, by the solution in $x_2(t)$ in (2.50), we have that (A3) is also satisfied with $\phi(s) = s$. However, as $g(t, x_1, x_2) = x_1^3$, Assumption (A2) is violated, and we cannot conclude UGS for the cascade, as expected.

Here, the condition (A1) can be strengthened to show UGAS in the entire cascade, as also pointed out in [Panteley and Loria, 1998].

Theorem 2.10—[Panteley and Loria, 1998, Theorem 2]
Assume that Σ_1' in (2.47) is UGAS. If the associated Lyapunov function satisfies (2.51) and Assumptions (A2)-(A3) hold, then (2.46) is UGAS. □

A number of alternative conditions can be expressed. For a review of such assumptions, refer to, e.g., [Lefeber, 2000] or [Loria and Panteley, 2005]. The main point of these assumptions is to guarantee uniform boundedness of solutions, as by virtue of converse Lyapunov theory, if Σ_1' in (2.47) is UGAS, and Σ_2 in (2.46b) is UGAS, and solutions remain uniformly globally bounded (UGB), the cascade in $\{\Sigma_1, \Sigma_2\}$ in (2.46) is UGAS (see, e.g., [Loria and Panteley, 2005, Lemma 2.1] for a proof of necessity and sufficiency).

In this thesis, we will work with a distilled form of the above theory as presented in [Lefeber et al., 2017, Theorem 5], utilizing the result in [Loria and Panteley, 2005, Proposition 2.3] and summarized as follows.

Theorem 2.11—[Lefeber et al., 2017, Theorem 5]
Assume that $f_1(t, \boldsymbol{x}_1)$ is continuously differentiable in $(t, \boldsymbol{x}_1)$; and that $f_2(t, \boldsymbol{x}_2)$ and $g(t, \boldsymbol{x}_1, \boldsymbol{x}_2)$ are continuous in their arguments, and locally Lipschitz in $\boldsymbol{x}_2$ and $(\boldsymbol{x}_1, \boldsymbol{x}_2)$, respectively. If (i) the origins of the systems Σ_1' in (2.47) and Σ_2 in (2.46b) are UGAS, and (ii) the solutions to the cascaded system $\{\Sigma_1, \Sigma_2\}$ in (2.46) are uniformly bounded, then the origin of the system $\{\Sigma_1, \Sigma_2\}$ in (2.46) is UGAS. Furthermore, if the origins of Σ_1' in (2.47) and Σ_2 in (2.46b) are ULES, the origin of $\{\Sigma_1, \Sigma_2\}$ in (2.46) is ULES.

2.6 Robustness Concepts

When discussing robustness, we consider perturbed systems in the form

$$\dot{\boldsymbol{x}} = f(t, \boldsymbol{x}) + \boldsymbol{\Delta}(t, \boldsymbol{x}), \tag{2.56}$$

where f is defined as in (2.33), and an additive disturbance $\boldsymbol{\Delta}(t, \boldsymbol{x})$ which is continuous in its arguments and bounded in $\|\boldsymbol{\Delta}(t, \boldsymbol{x})\| \leq L$. If f had been linear and autonomous, there exist many ways to characterize the system's robustness. One could be to compute a system norm, such as the $\mathcal{H}_\infty$-norm, which for any asymptotically stable system characterizes the worst-case effects of an input disturbance to an output. In such a linear setting, AS implies ES, and for any such system $\dot{\boldsymbol{x}}(t) = \boldsymbol{A}\boldsymbol{x}(t) + \boldsymbol{\Delta}(t, \boldsymbol{x})$ with a Hurwitz $\boldsymbol{A}$, all solutions $\|\boldsymbol{x}(t)\|$ remain bounded if $\|\boldsymbol{\Delta}(t, \boldsymbol{x})\|$ is bounded. For non-linear and non-autonomous systems, one may therefore think that a LES and GAS system would yield similar properties, but as shown in [Panteley et al., 1999; Loria and Panteley, 2005], it is possible to construct pathological examples which yield unbounded state trajectories for arbitrarily small disturbances.

Example 2.6
Consider a system defined by $a(t) = (t+1)^{-1}$, with

$$\dot{x} = f(x, t) = \begin{cases} -a(t)\text{sign}(x) & \text{if } |x| > a(t) \\ -x & \text{if } |x| \leq a(t) \end{cases}. \tag{2.57}$$

Here, f is locally Lipschitz uniformly in t, and the system is GAS and LES. However, when adding any perturbation $\Delta(t) = L \neq 0$, solutions grow unbounded as $t \to \infty$. In fact, one can show that $\lim_{t\to\infty} |x(t)/t| = |L|$. □

This curious result is obtained due to the lack of uniform asymptotic stability, as the gains in the $\mathcal{KL}$-function depend on the initial error $\|x(t_\circ)\|$ as well as the initial time $t_\circ$. Hence, if the system in (2.57) would have been UGAS or ULES, such examples would be eliminated. In general, one can show generic robustness results for small disturbances Δ if the stability is uniform.

Theorem 2.12—[Khalil, 1996, Theorem 3.14 with Lemma 5.3]
Let $\boldsymbol{x} = \boldsymbol{0}$ be an UAS equilibrium point on $\mathcal{B}_r$ for the system in (2.33) where $f : D_t \times \mathcal{B}_r \mapsto \mathbb{R}^n$ is continuously differentiable, and the Jacobian $[\partial f/\partial \boldsymbol{x}]$ is bounded on $\mathcal{B}_r$, uniformly in t. Then, for the perturbed system in (2.56), for any $\boldsymbol{x}(t_\circ) \in \mathcal{B}_R$ and any sufficiently small $\|\boldsymbol{\Delta}(\boldsymbol{x}, t)\| \leq L \leq \bar{L}(R)$,

$$\|\boldsymbol{x}(t)\| \leq \beta(\|\boldsymbol{x}(t_\circ)\|, t - t_\circ) \qquad \forall t \in [t_\circ, t_\circ + T], \tag{2.58a}$$

$$\|\boldsymbol{x}(t)\| \leq \rho(L) \qquad \forall t \geq t_\circ + T, \tag{2.58b}$$

where $\beta \in \mathcal{KL}$ and R satisfies $\beta(R, 0) < r$, with a finite time T, and $\rho \in \mathcal{K}$.□

Consequently, a system in (2.33), with relatively mild assumptions on f (specifically continuous differentiability and a locally bounded Jacobian in $\boldsymbol{x}$), the properties of ULAS, and implicitly UGAS, UAGAS, ULES, and UGES yield quantifiable local robustness properties to bounded input disturbances. This is why we put significant emphasis on concluding uniform stability properties for the controllers that result in non-autonomous error dynamics.

Remark 2.14
While mild, the assumption of continuous differentiability may be violated when using special controllers that switch between different feedback laws. This assumption is, for instance, violated by the system in Example 2.6 at any time where the state traverses the line $\pm a(t)$, and will require special consideration when deriving discontinuous feedback laws. □

Below, we summarize a useful theorem which migrates the assumption of continuous differentiability to a Lyapunov function. This theorem will be used to conclude ultimate boundedness of solutions and give explicit estimates of this bound when considering controller robustness.

Theorem 2.13—[Khalil, 2002, Theorem 4.18]
Consider the system in (2.33) with $D_{\boldsymbol{x}} \subset \mathbb{R}^n$ containing the origin, and let $\mathcal{V} : D_t \times D_{\boldsymbol{x}} \mapsto \mathbb{R}_{\geq 0}$ be a continuously differentiable function such that

$$\alpha_1(\|\boldsymbol{x}\|) \leq \mathcal{V}(t, \boldsymbol{x}) \leq \alpha_2(\|\boldsymbol{x}\|), \tag{2.59a}$$

$$\frac{\partial \mathcal{V}}{\partial t} + \frac{\partial \mathcal{V}}{\partial \boldsymbol{x}} f(t, \boldsymbol{x}) \leq -W_3(\boldsymbol{x}), \quad \forall \|\boldsymbol{x}\| \geq \mu > 0, \tag{2.59b}$$

for all $(t, \boldsymbol{x}) \in D_t \times D_{\boldsymbol{x}}$, where $\alpha_1, \alpha_2 \in \mathcal{K}$, and $W_3(\boldsymbol{x})$ is a continuous positive definite function on $D_{\boldsymbol{x}}$. Take $r > 0$ such that $\mathcal{B}_r \subset D_{\boldsymbol{x}}$, and suppose that

$$\mu < (\alpha_2^{-1} \circ \alpha_1)(r). \tag{2.60}$$

Then, there exists a class $\mathcal{KL}$ function β for every initial state $\boldsymbol{x}(t_\circ)$ satisfying $\|\boldsymbol{x}(t_\circ)\| \leq (\alpha_2^{-1} \circ \alpha_1)(r)$, and a $T \geq 0$ (dependent on $\boldsymbol{x}(t_\circ)$ and μ) such that

$$\|\boldsymbol{x}(t)\| \leq \beta(\|\boldsymbol{x}(t_\circ)\|, t - t_\circ), \qquad \forall t \in [t_\circ, t_\circ + T], \tag{2.61a}$$

$$\|\boldsymbol{x}(t)\| \leq (\alpha_1^{-1} \circ \alpha_2)(\mu), \qquad \forall t \geq t_\circ + T. \tag{2.61b}$$

□

3

Full State Feedback: Attitude Dynamics

3.1 Introduction

In this chapter, the problem of controller design for the attitude dynamics of the UAV is studied. To recapitulate, the system is configured on either SO(3) or SU(2), with the sub-index $(\cdot)_r$ denoting a reference. The states evolve by

$$\dot{\boldsymbol{R}} = \boldsymbol{R}\boldsymbol{S}(\boldsymbol{\omega}), \qquad \dot{\boldsymbol{R}}_r = \boldsymbol{R}_r\boldsymbol{S}(\boldsymbol{\omega}_r), \tag{3.1a}$$

$$\dot{\boldsymbol{X}} = \boldsymbol{X}[\boldsymbol{\omega}/2]^{\wedge}_{\mathrm{SU}(2)}, \qquad \dot{\boldsymbol{X}}_r = \boldsymbol{X}_r[\boldsymbol{\omega}_r/2]^{\wedge}_{\mathrm{SU}(2)}, \tag{3.1b}$$

$$\boldsymbol{J}\dot{\boldsymbol{\omega}} = \boldsymbol{S}(\boldsymbol{J}\boldsymbol{\omega})\boldsymbol{\omega} + \boldsymbol{\tau}, \qquad \boldsymbol{J}\dot{\boldsymbol{\omega}}_r = \boldsymbol{S}(\boldsymbol{J}\boldsymbol{\omega}_r)\boldsymbol{\omega}_r + \boldsymbol{\tau}_r, \tag{3.1c}$$

respectively, with an inertia matrix $\boldsymbol{J} = \boldsymbol{J}^{\top} \succ \boldsymbol{0}$. Here, $\boldsymbol{R} \in \mathrm{SO}(3)$ and $\boldsymbol{X} \in \mathrm{SU}(2)$ denote attitudes, with $\boldsymbol{\omega} \in \mathbb{R}^3$ and $\boldsymbol{\tau} \in \mathbb{R}^3$ denoting the attitude rate and controlled torque, respectively, both defined in body-fixed frame $\{\mathcal{B}\}$ (see Sec. 2.2.1). The initial conditions at a time $t_\circ \in \mathbb{R}$ are defined on

$$\boldsymbol{R}(t_\circ) \in \mathrm{SO}(3), \qquad \boldsymbol{R}_r(t_\circ) \in \mathrm{SO}(3), \tag{3.2a}$$

$$\boldsymbol{X}(t_\circ) \in \mathrm{SU}(2), \qquad \boldsymbol{X}_r(t_\circ) \in \mathrm{SU}(2), \tag{3.2b}$$

$$\boldsymbol{\omega}(t_\circ) \in \mathbb{R}^3, \qquad \boldsymbol{\omega}_r(t_\circ) \in \mathbb{R}^3. \tag{3.2c}$$

By virtue of the embedding in Definition 2.17, we have that if $\boldsymbol{R}(t_\circ) = E^{\mathrm{SU}(2)}_{\mathrm{SO}(3)}(\boldsymbol{X}(t_\circ)) \in \mathrm{SO}(3)$ and $\boldsymbol{R}_r(t_\circ) = E^{\mathrm{SU}(2)}_{\mathrm{SO}(3)}(\boldsymbol{X}_r(t_\circ)) \in \mathrm{SO}(3)$, then $\boldsymbol{R}(t) = E^{\mathrm{SU}(2)}_{\mathrm{SO}(3)}(\boldsymbol{X}(t)) \in \mathrm{SO}(3)$ and $\boldsymbol{R}_r(t) = E^{\mathrm{SU}(2)}_{\mathrm{SO}(3)}(\boldsymbol{X}_r(t)) \in \mathrm{SO}(3)$ for all $t \geq t_\circ$. Consequently, we can design controllers using either (3.1a) or (3.1b). The properties of the attitude controllers depend on the choice of attitude representation and the distances associated with their configuration manifolds. In one of its more general forms, the deterministic attitude tracking control problem treated in this chapter can be stated concisely as follows.

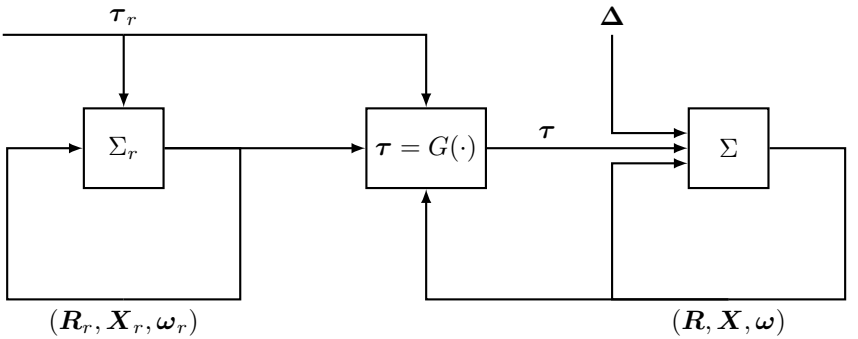

Figure 3.1 A full state feedback attitude controller, with a reference system, Σ_r, a controlled system, Σ, and an exogenous disturbance $\boldsymbol{\Delta}$.

Problem 3.1
Consider a system with a state $\boldsymbol{x} = (\boldsymbol{R}, \boldsymbol{\omega}) \in \mathrm{SO}(3) \times \mathbb{R}^3$, with an associated reference trajectory $\boldsymbol{x}_r = (\boldsymbol{R}_r, \boldsymbol{\omega}_r) \in \mathrm{SO}(3) \times \mathbb{R}^3$, driven by torques $\boldsymbol{\tau} \in \mathbb{R}^3$ and $\boldsymbol{\tau}_r \in \mathbb{R}^3$ respectively. Let $\boldsymbol{R} = E^{\mathrm{SU}(2)}_{\mathrm{SO}(3)}(\boldsymbol{X}) \in \mathrm{SO}(3)$ and $\boldsymbol{R}_r = E^{\mathrm{SU}(2)}_{\mathrm{SO}(3)}(\boldsymbol{X}_r) \in \mathrm{SO}(3)$ by Definition 2.17, satisfying the dynamics in (3.1) with initial conditions in (3.2). Find a feedback law using full state information,

$$\boldsymbol{\tau} = G(\boldsymbol{X}, \boldsymbol{\omega}, \boldsymbol{X}_r, \boldsymbol{\omega}_r, \boldsymbol{\tau}_r), \tag{3.3}$$

such that $\boldsymbol{x}(t) \to \boldsymbol{x}_r(t)$ as $(t - t_\circ) \to \infty$, and characterize the equilibria. □

Ideally, the feedback law, G, should result in UGAS or UGES error dynamics, to ensure certain robustness properties through Theorem 2.12 and facilitate the cascade analysis in forthcoming chapters using Theorem 2.11. However, we know from the Poincaré-Brouwer Theorem [Brouwer, 1909] that this requires discontinuous feedback laws. Consequently, we can at best hope to find almost globally stabilizing controllers with continuous feedback laws.

When discussing robustness, we primarily study the case of disturbances, $\boldsymbol{\Delta}(t) \in \mathbb{R}^3$, that are continuous, bounded in the two-norm, $\|\boldsymbol{\Delta}(t)\| \leq L$, and enter additively on the control signal torques. Specifically, we replace the controlled attitude rate subsystem in (3.1c) by a perturbed system defined as

$$\boldsymbol{J}\dot{\boldsymbol{\omega}} = \boldsymbol{S}(\boldsymbol{J}\boldsymbol{\omega})\boldsymbol{\omega} + \boldsymbol{\tau} + \boldsymbol{\Delta}. \tag{3.4}$$

Such disturbances are of special interest, as they arise in real-rime applications due to modeling errors in the inertia (see 2.2.3) and the quadratic rotor approximations (see Sec. 2.2.4), to name but two. An overview with the reference system, controlled system, and disturbance, is given in Figure 3.1.

3.1.1 Chapter Motivation

Problem 3.1 has been solved in many ways in the literature. The most basic forms of controllers parameterize the rotation in terms of Euler angles, and map errors in these angles and their derivatives to the controlled torque, such as the work of [Luukkonen, 2011; Garcia et al., 2012]. These controllers at best yield local stability properties, but are nonetheless frequently used in practical applications, such as the Crazyflie and the PixHawk PX4 flight controllers [Bitcraze, 2021a; PixHawk, 2021]. Slightly more advanced model-based methods perform a single or successive linearizations of the error dynamics, and employ tools from linear systems theory to compute stabilizing controllers. This includes the linear quadratic regulators (LQR) approach in [Bouabdallah et al., 2004], and closely related model predictive control approaches (MPC) in [Manikonda et al., 1999; Slegers et al., 2006; Abdolhosseini et al., 2013]. Here the stability results are also local, as the controllers depend on local linearizations to convexify the constraints, or nonlinear optimization methods with which feasibility and constraint satisfaction generally cannot be guaranteed. In addition, most MPC solutions involve explicitly solving a numerical optimization problem on each time step, which drastically increases the computational burden of the controller. The closely related explicit MPC (EMPC) approach, applied to attitude control in [Hegrenæs et al., 2005], amounts to a gain scheduled piece-wise linear feedback law derived with respect to an LQR-like cost function. The resulting closed-loop system needs to be analyzed with a set of linear matrix inequalities (LMIs) to show stability by a common Lyapunov function [Johansson and Rantzer, 1997; Ferrari-Trecate et al., 2001].

3.1.2 Contributions

In this chapter, we do not focus on optimal control with linear feedback laws. Instead, we study nonlinear controllers for which uniform global or almost global stability properties can be proven, in order to facilitate the analysis in later chapters. To this end, a technical assumption in the explicit vector control law in [Chaturvedi et al., 2011] is examined, whereby the geometric controller on SO(3) in [Lee et al., 2010] is shown to be a subset of the controllers parameterized in this generalized explicit vector feedback law. Consequently, alternative proofs of asymptotic stability are given for the controller in [Lee et al., 2010], permitting a characterization of its behavior outside of the associated domain of exponential attraction. We also provide an estimate of the ultimate bound of the errors when subjected to a common class of load disturbances, quantifying the magnitude of permissible disturbances for which the controllers are provably stable. However, apart from studying how these prior works relate, the novelties of the chapter include a set of three controllers on SU(2) derived using the Γ-distance in Definition 2.19, published in [Greiff et al., 2021f]. These results relate to prior work in the

quaternion formalism, but a slightly unconventional approach is taken in the stability proof. This facilitates the derivation of [Greiff et al., 2021f, Proposition 3], which is of particular relevance to real-time applications, as this controller will be shown to yield superior robustness properties for the disturbances considered in Figure 3.1. To facilitate real-time experiments, a C-implementation of the various controllers can be found as open source code in [Greiff, 2020], and this should also be considered a contribution of this chapter. Finally, we present a method of tuning the controllers through a set of bilinear matrix inequalities in [Greiff et al., 2021e].

3.1.3 Overview

We begin by considering an explicit vector-control law in Sec. 3.2 for the case where the controller gains are uniform. Next, we present the geometric controller on SO(3) in [Lee et al., 2010], there derived with respect to the distance $\Psi : \mathrm{SO}(3)^2 \mapsto [0, 2]$. This is done in Sec. 3.3, where the latter controller is shown to be parameterized by the generalized explicit vector controllers. We emphasize that this controller yields asymptotic stability properties for small controller gains, and proceed to derive the ultimate bounds for time-varying load disturbances, entering as in (3.4), and also review a related robust controller in Sec. 3.4. Using similar differential geometric tools as in [Lee et al., 2010], we subsequently derive a geometric attitude controller on SU(2) in Sec. 3.5 based on the distance $\Gamma : \mathrm{SU}(2)^2 \mapsto [0, 2]$, relating it to classical results with imaginary quaternion errors, and also characterizing its ultimate bounds. We next present a globally exponentially stable discontinuous controller on SU(2) in Sec. 3.6. Finally, a robust version of the controller on SU(2) is given in Sec. 3.7. For these controllers, a tuning problem is posed in Sec. 3.8 as a set of bilinear matrix inequalities (BMIs), here solved using an alternating semi-definite programming (ASDP) approach. This results in a convenient tuning method of the aforementioned feedback laws over the set of provably feasible controllers and bounded load disturbances. Using this method, a comparison of the controllers is given in Sec. 3.9, with recommendations for attitude controller implementations in Sec. 3.10. To give a holistic view, the results and examples are summarized in Table 3.1.

3.2 Continuous Explicit Vector Control on SO(3)

A relatively common approach to the attitude tracking control problem is to consider correction terms defined by cross-products of rotated vectors. We refer to this family of methods as *explicit vector control*. It is with such ideas that the stabilizing controller in [Sanyal and Chaturvedi, 2008; Chaturvedi et al., 2011] and explicit complementary filters in [Mahony et al., 2008; Euston et al., 2008; Mahony et al., 2012] are all derived. In this subsection, we

Table 3.1 Overview of the results and examples of Chapter 3. Here, [1] indicates work of others, proofs given elsewhere; [2] indicates work tangential with others, but with independent proofs given; and [3] indicates new work.

Reference	Description
Thm. 3.1 [2]	Slight generalization of [Chaturvedi et al., 2011, Thm. 2]
Thm. 3.2 [1]	Continuous control of [Lee et al., 2010, Prop. 1]
Prop. 3.1 [3]	Ultimate boundedness result related to Thm. 3.2
Thm. 3.3 [1]	Robust control on SO(3) of [Lee et al., 2013, Prop. 2]
Thm. 3.4 [2]	Continuous control on SU(2) [Greiff et al., 2021f, Prop. 1]
Prop. 3.2 [3]	Ultimate boundedness result related to Thm. 3.4
Thm. 3.5 [2]	Discontinuous control on SU(2)[Greiff et al., 2021f, Prop. 2]
Thm. 3.6 [3]	Robust control on SU(2) [Greiff et al., 2021f, Prop. 3]
Example 3.1	Simulation with Thm. 3.1 and Thm. 3.2
Example 3.2	Simulation with Thm. 3.3, demonstrating robustness properties
Example 3.3	Simulation with Thm. 3.4, with two different initializations
Example 3.4	Simulation with Thm. 3.5, with two different initializations
Example 3.5	Simulation with Thm. 3.6, demonstrating robustness properties
Example 3.5	Simulation with Thm. 3.6, demonstrating ultimate bound in ϵ_X
Example 3.7	Simulation with Thm. 3.6, demonstrating effects of noise
Example 3.8	Computation of an optimal tuning for Thm. 3.3 and Thm. 3.6

present such a controller in the context of Problem 3.1, removing the need for using orthogonal vectors in [Chaturvedi et al., 2011], and investigating the consequences of lifting a technical assumption of the distinctness of controller gains in [Mahony et al., 2008]. For this discussion, we consider an attitude error $\boldsymbol{R}_e = \boldsymbol{R}_r^\top \boldsymbol{R}$, but refrain from using the distance $\Psi(\boldsymbol{R}_r, \boldsymbol{R})$, in favor of considering errors defined by cross products. Assume knowledge of a set of linearly independent directions $\{\boldsymbol{v}_1, ..., \boldsymbol{v}_N \in \mathbb{R}^3 | \|\boldsymbol{v}_i \times \boldsymbol{v}_j\| \neq 0 \; \forall \; i \neq j\}$, then, we can approach the attitude control problem by trying to minimize the angle between $\boldsymbol{y}_{ri}(t) = \boldsymbol{R}_r(t)^\top \boldsymbol{v}_i$ and $\boldsymbol{y}_i(t) = \boldsymbol{R}(t)^\top \boldsymbol{v}_i$, by rotating the attitude about the axis $\boldsymbol{y}_{ri}(t) \times \boldsymbol{y}_i(t)$ where then $\boldsymbol{R}(t) = \boldsymbol{R}_r(t)$ implies that $\boldsymbol{y}_{ri}(t) \times \boldsymbol{y}_i(t) = \boldsymbol{0}$. As a thought experiment, consider the simplified setting in Figure 3.2 with a single direction $\boldsymbol{v}_i$ in the $\boldsymbol{e}_1\boldsymbol{e}_2$-plane such that $(\boldsymbol{y}_{ri}(t) \times \boldsymbol{y}_i(t)) \| \boldsymbol{e}_3$. To drive $\boldsymbol{y}_i$ to $\boldsymbol{y}_{ri}$, we could construct a feedback law $\dot{\omega}_e = -\theta_e - \omega_e$, or study the related feedback law $\boldsymbol{e}_3 \dot{\omega}_e = \boldsymbol{y}_i(t) \times \boldsymbol{y}_{ri}(t) - \boldsymbol{e}_3 \omega_e$. This intuition is at the heart of the explicit vector feedback laws, where multiple weighted cross-product errors are summed. A slight generalization of the stabilization result in [Chaturvedi et al., 2011] is then given as follows.

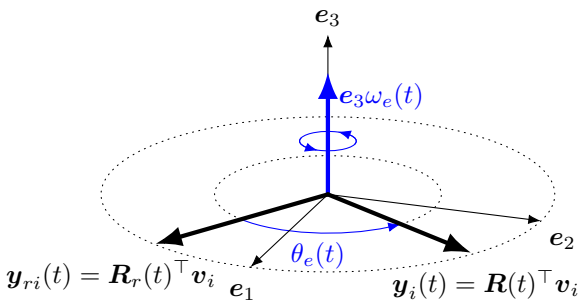

Figure 3.2 Sketch of the intuition behind the explicit vector controller.

THEOREM 3.1—GENERALIZED EXPLICIT VECTOR-CONTROL ON SO(3) Consider the control errors $\boldsymbol{R}_e = \boldsymbol{R}_r^\top \boldsymbol{R}$ and $\boldsymbol{e}_\omega = \boldsymbol{\omega} - \boldsymbol{R}_e^\top \boldsymbol{\omega}_r$. Take $\boldsymbol{K}_\omega = \boldsymbol{K}_\omega^\top \succ 0$, $N > 2$ gains $k_i > 0$ and linearly independent $\boldsymbol{v}_i \in \mathbb{R}^3$, such that

$$\sum_{i=1}^{N} k_i \boldsymbol{v}_i \boldsymbol{v}_i^\top \triangleq \boldsymbol{M} = \boldsymbol{U}\boldsymbol{\Lambda}\boldsymbol{U}^\top \succ \boldsymbol{0}, \tag{3.5}$$

with a diagonal $\boldsymbol{\Lambda}$ and orthogonal $\boldsymbol{U}$. The system in (3.1), in feedback with

$$\boldsymbol{\tau} = \sum_{i=1}^{N} k_i \boldsymbol{S}(\boldsymbol{v}_i)\boldsymbol{R}_e^\top \boldsymbol{v}_i - \boldsymbol{K}_\omega \boldsymbol{e}_\omega - \boldsymbol{S}(\boldsymbol{J}\boldsymbol{\omega})\boldsymbol{\omega} - \boldsymbol{J}(\boldsymbol{S}(\boldsymbol{\omega})\boldsymbol{R}_e^\top \boldsymbol{\omega}_r - \boldsymbol{R}_e^\top \dot{\boldsymbol{\omega}}_r), \tag{3.6}$$

renders the equilibrium point $(\boldsymbol{R}_e, \boldsymbol{e}_\omega) = (\boldsymbol{I}, \boldsymbol{0})$ ULES and UAGAS if the eigenvalues of $\boldsymbol{M}$ are distinct. In this case, three additional unstable equilibrium points are located at $(\boldsymbol{R}_e, \boldsymbol{e}_\omega) \in \{(\boldsymbol{U}\boldsymbol{D}_i\boldsymbol{U}^\top, \boldsymbol{0})\}_{i=1}^3$. If the eigenvalues of $\boldsymbol{M}$ are uniform, the equilibrium point $(\boldsymbol{R}_e, \boldsymbol{e}_\omega) = (\boldsymbol{I}, \boldsymbol{0})$ is ULES and UAS, with all solutions converging to a point in $\mathcal{E} = \{(\boldsymbol{R}_e, \boldsymbol{e}_\omega) \in \mathrm{SO}(3) \times \mathbb{R}^3 \mid \mathrm{Tr}(\boldsymbol{R}_e) \in \{-1, 3\}, \boldsymbol{e}_\omega = \boldsymbol{0}\}$, and every point in $\mathcal{E} \backslash \{(\boldsymbol{I}, \boldsymbol{0}) \in \mathrm{SO}(3) \times \mathbb{R}^3\}$ is unstable. □

Proof. The proof is stated in its entirety in Appendix B.1, and follows by expressing the error dynamics of the closed-loop system and the construction of a Lyapunov function candidate in the errors as

$$\mathcal{V} = \sum_{i=1}^{N} \frac{k_i}{2} \|\boldsymbol{R}_e \boldsymbol{v}_i - \boldsymbol{v}_i\|^2 + \frac{1}{2} \boldsymbol{e}_\omega^\top \boldsymbol{J} \boldsymbol{e}_\omega. \tag{3.7}$$

Along the solution of the error dynamics, it is shown that $(\mathrm{d}/\mathrm{d}t)\mathcal{V} \leq 0$ and uniformly continuous. A characterization of an invariant set is found by Lemma 2.5 (Barbălat) and subsequent signal chasing with Lemma 2.7. The proof is then concluded with a linearization about the equilibrium points. □

With the natural choice of attitude rate tracking error, which essentially represents a comparison of the rotation time-derivatives $\dot{\boldsymbol{R}}$ and $\dot{\boldsymbol{R}}_r$ in the tangent space $\mathrm{T}_{\boldsymbol{R}}\mathrm{SO}(3)$, the control law stated in a slightly more general form than in [Chaturvedi et al., 2011]. Importantly, the proof here also shows of ULES and UAS for the case of uniform gains. However, as the proof is finalized with Lemma 2.5 (Barbălat) and local linearizations of the resulting equilibrium points, it is difficult to characterize the nature of the exponential decay of the errors on larger subsets of SO(3) containing $\boldsymbol{R}_e = \boldsymbol{I}$. This will be necessary for a discussion on robustness and controller tuning. However, a natural way of studying the transient behavior of the error dynamics becomes apparent when treating the problem in a differential geometric setting.

3.3 Continuous Geometric Control on SO(3)

Consider next the geometric attitude controller in [Lee et al., 2010]. Here, the controller is derived for the full UAV dynamics, but the ideas pertaining to the attitude control are illuminating. The developments are done with an attitude error element $\boldsymbol{R}_e = \boldsymbol{R}_r^\top \boldsymbol{R} \in \mathrm{SO}(3)$, using the distance $\Psi(\boldsymbol{R}_r, \boldsymbol{R})$ in Definition 2.18 to construct a Lyapunov function candidate with which uniform exponential stability is shown for a large subset of $(\boldsymbol{R}_e, \boldsymbol{\omega}_e) \in \mathrm{SO}(3) \times \mathbb{R}^3$. The result is briefly summarized in the notation of this thesis as follows.

Theorem 3.2—Continuous Geometric Control on SO(3)
Let $\boldsymbol{R}_e = \boldsymbol{R}_r^\top \boldsymbol{R} \in \mathrm{SO}(3)$, and consider the control errors

$$\boldsymbol{e}_{\boldsymbol{R}} = \frac{1}{2}[\boldsymbol{R}_e - \boldsymbol{R}_e^\top]^\vee_{\mathrm{SO}(3)} \in \mathbb{R}^3, \tag{3.8a}$$

$$\boldsymbol{e}_{\boldsymbol{\omega}} = \boldsymbol{\omega} - \boldsymbol{R}_e^\top \boldsymbol{\omega}_r \in \mathbb{R}^3, \tag{3.8b}$$

$$\boldsymbol{z} = (\|\boldsymbol{e}_{\boldsymbol{R}}\|, \|\boldsymbol{e}_{\boldsymbol{\omega}}\|)^\top \in \mathbb{R}^2_{\geq 0}. \tag{3.8c}$$

Take any set of gains $(k_R, k_\omega, k_c) \in \mathbb{R}^3_{>0}$ such that the matrices

$$\boldsymbol{W} = \begin{bmatrix} \frac{k_c k_R}{\lambda_M(\boldsymbol{J})} & -\frac{k_c k_w}{2\lambda_m(\boldsymbol{J})} \\ -\frac{k_c k_w}{2\lambda_m(\boldsymbol{J})} & k_\omega - k_c \end{bmatrix}, \quad \boldsymbol{M}_1 = \frac{1}{2}\begin{bmatrix} k_R & -k_c \\ -k_c & \lambda_m(\boldsymbol{J}) \end{bmatrix}, \quad \boldsymbol{M}_2 = \frac{1}{2}\begin{bmatrix} \frac{2k_R}{2-\phi} & k_c \\ k_c & \lambda_M(\boldsymbol{J}) \end{bmatrix}, \tag{3.9}$$

are all positive definite. With initial errors on the domain

$$D = \left\{ \begin{bmatrix} \boldsymbol{e}_{\boldsymbol{R}}(t_\circ) \\ \boldsymbol{e}_{\boldsymbol{\omega}}(t_\circ) \end{bmatrix} \in \mathbb{R}^6 \;\middle|\; \begin{matrix} \Psi(\boldsymbol{R}_r(t_\circ), \boldsymbol{R}(t_\circ)) \leq \phi < 2, \\ \boldsymbol{z}(t_\circ)^\top \boldsymbol{M}_2 \boldsymbol{z}(t_\circ) \leq k_R \phi \end{matrix} \right\}, \tag{3.10}$$

the system (3.1) driven with a full state feedback

$$\boldsymbol{\tau} = -k_R \boldsymbol{e}_{\boldsymbol{R}} - k_\omega \boldsymbol{e}_{\boldsymbol{\omega}} - \boldsymbol{S}(\boldsymbol{J}\boldsymbol{\omega})\boldsymbol{\omega} - \boldsymbol{J}(\boldsymbol{S}(\boldsymbol{\omega})\boldsymbol{R}_e^\top \boldsymbol{\omega}_r - \boldsymbol{R}_e^\top \dot{\boldsymbol{\omega}}_r), \tag{3.11}$$

yields a single equilibrium point in $(\boldsymbol{e}_R, \boldsymbol{e}_{\boldsymbol{\omega}}) = (\mathbf{0}, \mathbf{0})$, which is UES on a domain $D \subset \mathbb{R}^6$ in (3.10). In addition, this point is UAS for all initial errors on a much larger domain than D, as all solutions converge to a point in $\mathcal{E} = \{(\boldsymbol{R}_e, \boldsymbol{e}_{\boldsymbol{\omega}}) \in \mathrm{SO}(3) \times \mathbb{R}^3 \mid \Psi(\boldsymbol{R}_r, \boldsymbol{R}) \in \{0, 2\}, \boldsymbol{e}_{\boldsymbol{\omega}} = \mathbf{0}\}$, with every equilibrium point in $\mathcal{E} \backslash \{(\boldsymbol{I}, \mathbf{0})\}$ being unstable. □

Proof of Theorem 3.2. The first part of the proof is given in [Lee et al., 2011, Appendix B], and follows by analysis of a Lyapunov function candidate

$$\mathcal{V} = k_R \Psi(\boldsymbol{R}_r, \boldsymbol{R}) + k_c \boldsymbol{e}_{\boldsymbol{\omega}} \cdot \boldsymbol{e}_{\boldsymbol{R}} + \frac{1}{2} \boldsymbol{e}_{\boldsymbol{\omega}} \cdot \boldsymbol{J} \boldsymbol{e}_{\boldsymbol{\omega}}, \tag{3.12}$$

where it is shown that all closed-loop trajectories remain within D, on which

$$\boldsymbol{z}^\top \boldsymbol{M}_1 \boldsymbol{z} \leq \mathcal{V} \leq \boldsymbol{z}^\top \boldsymbol{M}_2 \boldsymbol{z}, \qquad \dot{\mathcal{V}} \leq -\boldsymbol{z}^\top \boldsymbol{W} \boldsymbol{z}, \tag{3.13}$$

whereby the equilibrium point $\boldsymbol{z} = \mathbf{0} \Leftrightarrow (\boldsymbol{e}_{\boldsymbol{R}}, \boldsymbol{e}_{\boldsymbol{\omega}}) = (\mathbf{0}, \mathbf{0})$ is uniformly exponentially stable for all initial errors on $D \subset \mathbb{R}^6$ by Theorem 2.4. The last claim follows directly from Remark 3.1 below. □

Remark 3.1
The geometric tracking control on SO(3) in Theorem 3.2 is equivalent to the controller in Theorem 3.1, provided the latter is tuned with $\boldsymbol{K}_\omega = k_\omega \boldsymbol{I}$, $N = 3$ and $k_i = k_R/2$ for all $i \in \{1, 2, 3\}$, with the directions $(\boldsymbol{v}_1, \boldsymbol{v}_2, \boldsymbol{v}_3) = \boldsymbol{I}$. □

Proof of Remark 3.1. This is shown algebraically in Appendix B.2. □

As such, there is an equivalence between the two controllers in Theorem 3.1 and Theorem 3.2, which permits discussions of robustness in the former, and statements about transient behavior outside of D in the latter. To illustrate their closed-loop properties, the decay of the Lyapunov function in (3.12) and the associated bounds in (3.13), a simulation example is given in Example 3.1.

Example 3.1
In this example, the continuous geometric controller on SO(3) in Theorem 3.2 is demonstrated for a system with a randomized dense inertia matrix satisfying $\lambda_m(\boldsymbol{J}) = 0.5$ and $\lambda_M(\boldsymbol{J}) = 1$. The initial conditions at $t_\circ = 0$ are randomized on $\boldsymbol{X}(t_\circ), \boldsymbol{X}_r(t_\circ) \sim \mathcal{U}(\mathrm{SU}(2))$ with $\boldsymbol{\omega}(t_\circ) \sim \mathcal{U}([-1, 1]^3)$ and $\boldsymbol{\omega}_r(t_\circ) = \mathbf{0}$, and the reference dynamics are driven by a torque trajectory

$$\boldsymbol{\tau}_r(t) = (\sin(2\pi t + 1);\ 2\sin(2\pi t + 2);\ \tfrac{1}{2}\sin(2\pi t + \tfrac{1}{2})) \in \mathbb{R}^3. \tag{3.14}$$

The resulting tracking performance when tuned with $k_R = 4$ and $k_\omega = 2$ is shown in Figure 3.3, with the attitude trajectories, the Lyapunov function with bounds (bottom, left), and the Lyapunov function time-derivative with its upper bound (bottom, right). Despite the highly volatile reference trajectory (top, right), the tracking errors decrease monotonically to machine precision, and excellent tracking is achieved in a matter of seconds. □

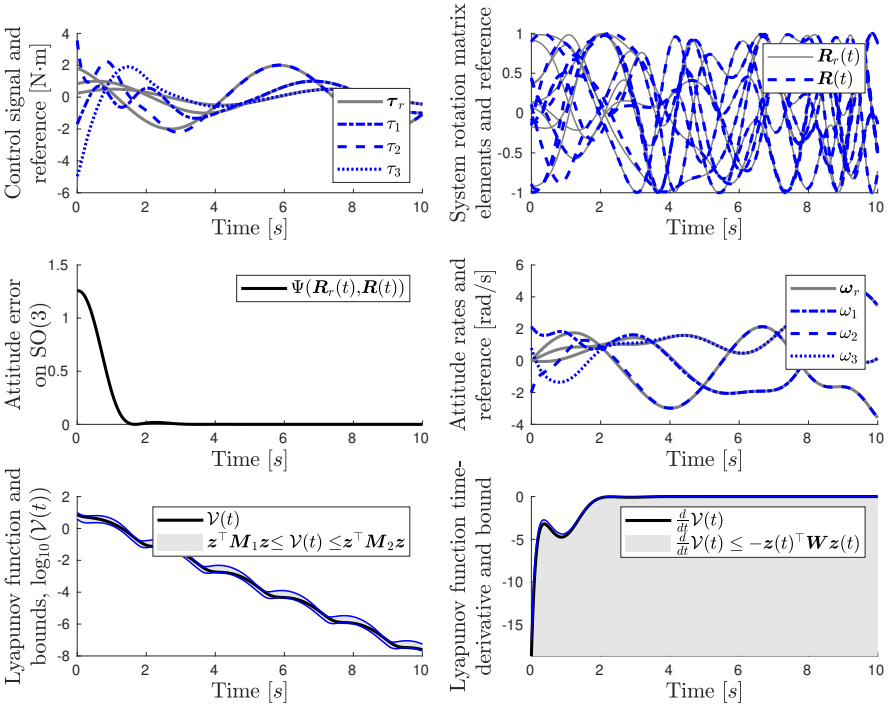

Figure 3.3 Example of the continuous geometric attitude control on SO(3) in Theorem 3.2. *Top left:* Torques driving the reference system $\boldsymbol{\tau}_r$ (gray), and controlled torque $\boldsymbol{\tau}$ (blue). *Top right:* Elements of the reference rotation $\boldsymbol{R}_r$ (gray), and controlled rotation $\boldsymbol{R}$ (blue). *Center left:* Attitude error on SO(3). *Center right:* Attitude rate reference $\boldsymbol{\omega}_r$ (gray) and system response $\boldsymbol{\omega}$ (blue). *Bottom left:* Lyapunov function in (3.12), depicted in the 10-logarithm and the bounds (3.13) expressed in $\boldsymbol{z}$. *Bottom right:* Lyapunov function time-derivative and upper bound in (3.13). The simulated system response is shown in the video chapter-3-simulations.mp4.

Remark 3.2
The only requirement for (3.13) to hold is that $\Psi(\boldsymbol{R}_r(t), \boldsymbol{R}(t)) \leq \phi,\ \forall\, t \geq t_\circ$, and a sufficient condition for this can be stated in terms of the Lyapunov function $\mathcal{V}$ in (3.12). For $k_c = 0$ it is seen that $(\mathrm{d}/\mathrm{d}t)\mathcal{V} \leq 0$, whereby

$$k_R \Psi(\boldsymbol{R}_r(t), \boldsymbol{R}(t)) \leq \mathcal{V}(t)|_{k_c=0} \leq \mathcal{V}(t_\circ)|_{k_c=0} < k_R \phi,\ \ \forall\, t \geq t_\circ. \tag{3.15}$$

Consequently,

$$\mathcal{V}(t_\circ)|_{k_c=0} < k_R \phi \Rightarrow \Psi(\boldsymbol{R}_r(t), \boldsymbol{R}(t)) < \phi,\ \ \forall\, t \geq t_\circ.$$

However, it is clear that this greatly restricts the initial attitude rate errors that can be used. If $\Psi(\boldsymbol{R}_r(t_\circ), \boldsymbol{R}(t_\circ)) = \phi_\circ < \phi < 2$, then the inequalities

in (3.15) hold only if $\boldsymbol{e}_{\boldsymbol{\omega}}(t_\circ)^\top \boldsymbol{J}\boldsymbol{e}_{\boldsymbol{\omega}}(t_\circ) < 2k_R(\phi - \phi_\circ)$. Consequently, making $\phi_\circ$ large implies that $\phi - \phi_\circ$ is small, which in turn requires large k_R and small $\|\boldsymbol{e}_{\boldsymbol{\omega}}(t_\circ)\|$ for the system to be initialized within the domain D in (3.10). □

As the volume of D becomes small for large $\phi_\circ$ and finite k_R, it is of great importance to know how the closed loop system behaves when initialized outside of D. This is why the observation in Remark 3.1 is important. For practically any initialization where $\Psi(\boldsymbol{R}_r(t_\circ), \boldsymbol{R}(t_\circ)) < 2$ or $\boldsymbol{e}_{\boldsymbol{\omega}}(t_\circ) \neq \boldsymbol{0}$, the error trajectories asymptotically converge to the domain D, and within this domain, the worst-case exponential decay rates can be quantified by the quadratic forms in (3.13). However, in contrast to the explicit vector-control in Theorem 3.1, which technically parameterizes a larger family of controllers, the geometric controller is exponentially stable on a region characterized by D in (3.10). As such, it is possible to give uniform boundedness results when the closed-loop system is perturbed with additive bounded load disturbances.

Proposition 3.1
Consider the perturbed system

$$\dot{\boldsymbol{R}} = \boldsymbol{R}\boldsymbol{S}(\boldsymbol{\omega}) \tag{3.16a}$$

$$\boldsymbol{J}\dot{\boldsymbol{\omega}} = \boldsymbol{S}(\boldsymbol{J}\boldsymbol{\omega})\boldsymbol{\omega} + \boldsymbol{\tau} + \boldsymbol{\Delta}, \tag{3.16b}$$

where $\boldsymbol{\Delta}(t) \in \mathbb{R}^3$ is continuous in time and $\|\boldsymbol{\Delta}\| \leq L$ for all $t \geq t_\circ$. Let (3.16) be controlled by a feedback (3.11) in Theorem 3.2, with $(k_R, k_\omega, k_c) \in \mathbb{R}^3_{>0}$ resulting in a set of positive definite matrices $\boldsymbol{M}_1, \boldsymbol{M}_2, \boldsymbol{W}$ in (3.9). For any

$$L < \frac{\theta\sqrt{\phi k_R}\lambda_m(\boldsymbol{W})\lambda_m(\boldsymbol{M}_1)}{\delta\lambda_M(\boldsymbol{M}_2)}, \tag{3.17}$$

with

$$\delta \triangleq \sqrt{1 + k_c^2\lambda_M(\boldsymbol{J}^{-1})^2}, \quad \theta \in (0,1), \tag{3.18}$$

the errors are ultimately bounded when

$$\|\boldsymbol{z}(t_\circ)\| \leq \frac{\sqrt{\phi k_R}\lambda_m(\boldsymbol{M}_1)}{\lambda_M(\boldsymbol{M}_2)}. \tag{3.19}$$

That is, there exist a class-$\mathcal{KL}$ function, β, and time, $T \geq t_\circ$ for which

$$\|\boldsymbol{z}(t)\| \leq \beta(\|\boldsymbol{z}(t_\circ)\|, t - t_\circ), \qquad \forall t \in [t_\circ, t_\circ + T], \tag{3.20a}$$

$$\|\boldsymbol{z}(t)\| < r = \sqrt{\phi k_R\lambda_m(\boldsymbol{M}_1)}/\lambda_M(\boldsymbol{M}_2), \qquad \forall t \geq t_\circ + T. \tag{3.20b}$$

Furthermore, on the interval $t_\circ \leq t \leq t_\circ + T$, the error decay is bounded by

$$\dot{\mathcal{V}} \leq -\frac{\lambda_m(\boldsymbol{W})}{\lambda_M(\boldsymbol{M}_2)}(1-\theta)\mathcal{V}, \tag{3.21}$$

where $\mathcal{V}$ is the Lyapunov function defined in (3.12). □

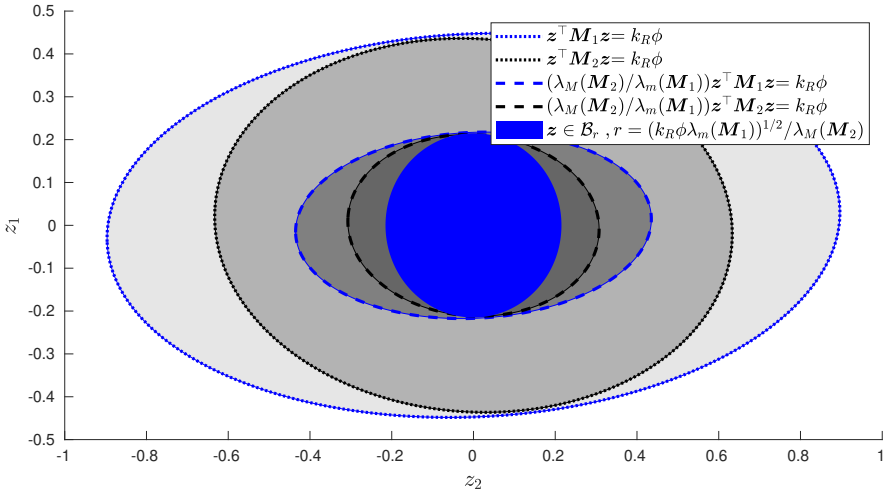

Figure 3.4 Sets in $\boldsymbol{z}$ containing $\mathcal{B}_r$ used in the proof of Proposition 3.1, evaluated numerically for a feasible tuning and the $\boldsymbol{J}$ and ϕ in Example 3.1.

Proof. To show this, the main idea is to use the Lyapunov function in (3.12) with its associated bounds in $\boldsymbol{M}_1, \boldsymbol{M}_2, \boldsymbol{W}$, and factorize the Lyapunov time-derivative along the perturbed error dynamics to a form $\dot{\mathcal{V}} = -(1-\theta)\boldsymbol{z}^\top \boldsymbol{W}\boldsymbol{z} - \|\boldsymbol{z}\|(\lambda_m(\boldsymbol{W})\theta\|\boldsymbol{z}\| - \delta L)$. One then has to present a sufficient condition for $\Psi(\boldsymbol{R}_r, \boldsymbol{R}) < \phi$ for all $t \geq t_\circ$, which can be found in the largest ball $\boldsymbol{z}(t_\circ) \in \mathcal{B}_r$ guaranteeing that $\mathcal{V}(t_\circ) \leq k_R\phi$. Here, the ideas in (3.15) cannot be used, and we instead need to consider the sets depicted in Figure 3.4. Application of Theorem 2.13 yields the result, with the full proof in Appendix B.3. □

From this proposition, it is evident that tuning the controller is a nontrivial task. Here, $\lambda_M(\boldsymbol{M}_2)$ will dominate $\lambda_m(\boldsymbol{M}_1)$ for any feasible controller tuning. Consequently, if we maximize the decay rate, that is, to decrease $\lambda_M(\boldsymbol{M}_2)$ and increase $\lambda_m(\boldsymbol{W})$, the permissible disturbance bound L will increase, and the ultimate bound in (3.41) will also be affected non-trivially in the tuning parameters. If we both aim to increase the decay rate and decrease the ultimate bound, we not only have to select k_R and k_ω in a clever way based on $\boldsymbol{J}$ and ϕ, but also pick a suitable k_c. While it may be difficult to find a good tuning, it is simple to find a feasible tuning, as shown in Remark 3.3.

Remark 3.3—[Lee et al., 2011, Appendix B]
For $k_R > 0, k_\omega > 0$, the matrices $\boldsymbol{W}, \boldsymbol{M}_1, \boldsymbol{M}_2$ in (3.9) are positive definite if

$$0 < k_c < \min\left\{k_\omega, \frac{4k_\omega k_R \lambda_m(\boldsymbol{J})^2}{k_\omega^2 \lambda_M(\boldsymbol{J}) + 4k_R\lambda_m(\boldsymbol{J})^2}, \sqrt{k_R\lambda_m(\boldsymbol{J})}\right\}. \tag{3.22}$$

□

To explore the influence of ϕ on the decay rates and ultimate bounds, we will pose and solve a BMI in Sec. 3.8 to find an optimal controller tuning with respect to a cost expressed in an ultimate bound and worst-case error decay rates. However, other modifications of the controller can be done to achieve significantly smaller ultimate bounds. An appealing approach is to introduce an additional term in the feedback law, by which the ultimate bound can be pushed down further. This is referred to as a robust version of the continuous geometric controller, and will be presented next.

3.4 Robust Geometric Control on SO(3)

The robust geometric controller was first published in [Lee et al., 2013, Proposition 2], and seeks to extend the previous feedback law in Theorem 3.2 with an additive term to handle load disturbances, $\boldsymbol{\Delta}$, of arbitrary magnitude, $\|\boldsymbol{\Delta}\| \leq L$. This is made possible by including L explicitly in the feedback law, and implementing a term which dominates those arising in $\dot{\mathcal{V}}$ by virtue of $\boldsymbol{\Delta}$.

Theorem 3.3—Robust geometric attitude control on SO(3) Consider the system

$$\dot{\boldsymbol{R}} = \boldsymbol{R}\boldsymbol{S}(\boldsymbol{\omega}) \tag{3.23a}$$

$$\boldsymbol{J}\dot{\boldsymbol{\omega}} = \boldsymbol{S}(\boldsymbol{J}\boldsymbol{\omega})\boldsymbol{\omega} + \boldsymbol{\tau} + \boldsymbol{\Delta}, \tag{3.23b}$$

where $\boldsymbol{\Delta}(t) \in \mathbb{R}^3$ is continuous in time and $\|\boldsymbol{\Delta}\| \leq L$ for all $t \geq t_\circ$. Take any tuning $\boldsymbol{k} = (k_R, k_\omega, k_c) \in \mathbb{R}^3_{>0}$ resulting in a set of positive definite matrices $\boldsymbol{M}_1, \boldsymbol{M}_2, \boldsymbol{W}$ in (3.9), and define the errors as in (3.8a). Take the perturbed system in (3.23) to be in closed-loop feedback with the control law

$$\boldsymbol{\tau} = -k_R\boldsymbol{e}_R - k_\omega\boldsymbol{e}_{\boldsymbol{\omega}} - \boldsymbol{\mu}_{\boldsymbol{R}} \tag{3.24a}$$

$$- \boldsymbol{S}(\boldsymbol{J}\boldsymbol{\omega})\boldsymbol{\omega} - \boldsymbol{J}(\boldsymbol{S}(\boldsymbol{\omega})\boldsymbol{R}^\top\boldsymbol{R}_r\boldsymbol{\omega}_r - \boldsymbol{R}^\top\boldsymbol{R}_r\dot{\boldsymbol{\omega}}_r), \tag{3.24b}$$

$$\boldsymbol{\mu}_{\boldsymbol{R}} = \frac{L^2\boldsymbol{e}_A}{L\|\boldsymbol{e}_A\| + \epsilon_R}, \tag{3.24c}$$

$$\boldsymbol{e}_A = \boldsymbol{e}_{\boldsymbol{\omega}} + k_c\boldsymbol{J}^{-1}\boldsymbol{e}_{\boldsymbol{R}}. \tag{3.24d}$$

For any choice of parameter ϵ_R satisfying

$$0 < \epsilon_R < \frac{\lambda_m(\boldsymbol{M}_1(\boldsymbol{k}))\lambda_m(\boldsymbol{W}(\boldsymbol{k}))}{\lambda_M(\boldsymbol{M}_2(\boldsymbol{k}))}\phi(2-\phi), \tag{3.25}$$

the errors are ultimately bounded in ϵ_R, as

$$\lim_{t-t_\circ\to\infty} \|\boldsymbol{z}\|^2 \leq \gamma(L;\boldsymbol{k}) \triangleq \frac{\lambda_M(\boldsymbol{M}_2(\boldsymbol{k}))}{\lambda_m(\boldsymbol{M}_1(\boldsymbol{k}))\lambda_m(\boldsymbol{W}(\boldsymbol{k}))}\epsilon_R. \tag{3.26}$$

□

Proof. Refer to the original proof in [Lee et al., 2013, Proof of Proposition 2 in Appendix 8.2]. The key insight is that with the proposed feedback law, we get an upper bound on the Lyapunov function time-derivative as $\dot{\mathcal{V}} \leq -\boldsymbol{z}^\top \boldsymbol{W}\boldsymbol{z} + \epsilon_R$, facilitating the rest of the proof. □

Remark 3.4
This feedback law significantly attenuates the effects of large load disturbances at the cost of making the control signal volatile for large L and small ϵ_R and increasing sensitivity to measurement noise.

To demonstrate this result, we again consider a closed-loop simulation example, but this time with the perturbed attitude dynamics in (3.23), and with a significant additive load disturbance, as defined in Example 3.2.

Example 3.2
Here, we use the same simulation setup as in Example 3.1, but with load disturbances that are realized such that $\|\boldsymbol{\Delta}\| = L = 1$ for all $t \geq t_\circ = 0$, with

$$\boldsymbol{\Delta}(t) \triangleq L\frac{\bar{\boldsymbol{\Delta}}(t)}{\|\boldsymbol{\Delta}(t)\|}, \quad \bar{\boldsymbol{\Delta}}(t) \triangleq (\sin(t);\ \sin(4t + \tfrac{\pi}{2});\ \sin(8t + \tfrac{\pi}{4})) \in \mathbb{R}^3. \quad (3.27)$$

Just as before, we get an initial attitude error of approximately $\phi \approx 1.25$, which, in this particular case, means that we may pick any ϵ_R on the interval

$$0 < \epsilon_R < \bar{\epsilon}_R \triangleq \frac{\lambda_m(\boldsymbol{M}_1(\boldsymbol{k}))\lambda_m(\boldsymbol{W}(\boldsymbol{k}))}{\lambda_M(\boldsymbol{M}_2(\boldsymbol{k}))}\phi(2-\phi) \approx 0.0315, \quad (3.28)$$

and for this example, we let $\epsilon_R = 0.01\bar{\epsilon}_R = 3.15 \cdot 10^{-4}$, which in turn implies that all trajectories converge to an error within the ultimate bound

$$\gamma(L; \boldsymbol{k}) \approx 0.0093. \quad (3.29)$$

The resulting system response is shown in Figure 3.5, depicting the control signals, the disturbance in (3.28), the attitude error and attitude rate trajectories, the Lyapunov function with bounds, and the Lyapunov function time-derivative with its upper bound. The errors in $\boldsymbol{z}$ are also shown in the two-norm, along with the ultimate bound γ in the bottom-most subplot.

This can be compared with the robustness result for the continuous geometric controller in Theorem 3.2. By Proposition 3.1, the maximal permitted load disturbances for (with $\theta \to 1$) is $L = 0.0591$, which is significantly smaller than the magnitude of the disturbance used in this example. Furthermore, even if the result would hold for such a large disturbance, we have that the corresponding ultimate bound is $\gamma(L; \boldsymbol{k}) \approx 0.0393$ when computed for Theorem 3.2 using Proposition 3.1, which is significantly larger than the corresponding bound computed for the robust controller in (3.29). Additionally, as the ultimate bound with the robust controller is proportional to ϵ_R, we can reduce it even further by picking a smaller tuning parameter ϵ_R. □

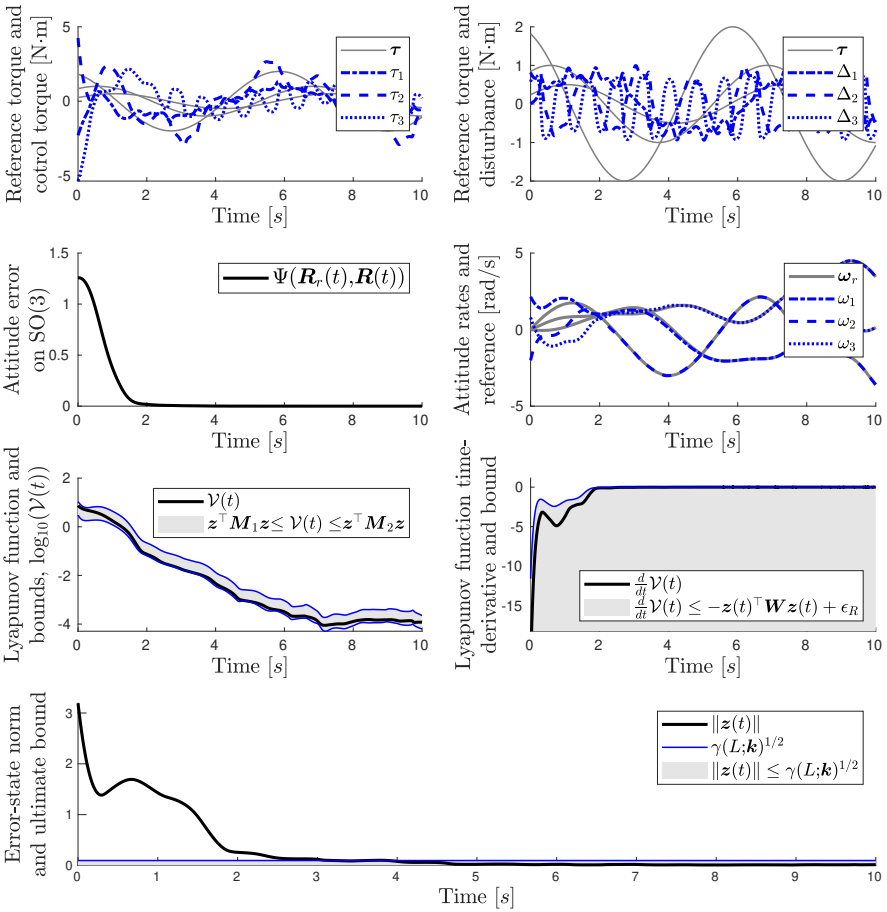

Figure 3.5 Example of the continuous geometric attitude control on SO(3) in Theorem 3.3. *Top left:* Torques driving the reference system $\boldsymbol{\tau}_r$ (gray), and controlled torque $\boldsymbol{\tau}$ (blue). *Top right:* Torques driving the reference system $\boldsymbol{\tau}_r$ (gray), and disturbance $\boldsymbol{\Delta}$ (blue). *Top center, left:* Attitude error in the SO(3)-distance. *Top center, right:* Attitude rate reference (gray) and system response (blue, dashed). *Bottom center, left:* Lyapunov function in the 10-logarithm and the upper and lower bounds expressed in $\boldsymbol{z}$. *Bottom center, right:* Lyapunov function time-derivative and upper bound. *Bottom:* Errors $\|\boldsymbol{z}\|$ converging a value smaller than the ultimate bound estimate. The simulated system response is shown in the video chapter-3-simulations.mp4.

The results in Theorems 3.1, 3.2, and 3.3, are considered the state of the art for attitude tracking control on SO(3). This is due to their relative simplicity, computational efficiency, and robustness to commonly arising disturbances. In the preceding sections we have highlighted some equivalences between these controllers, and provided an conservative estimate of the ultimate bound when using the popular feedback law in Theorem 3.2. In the remainder of this chapter, we derive analogous feedback laws on SU(2), and show how these relate to the literature of control based on imaginary quaternion errors.

3.5 Continuous Geometric Control on SU(2)

Next, we derive a set of closely related controllers on SU(2), which will later enable a proof of exponential stability for all attitude errors configured on SO(3), with a controller corresponding to $\phi = 1$. For this discussion, we let the elements $\boldsymbol{X}_r, \boldsymbol{X} \in \mathrm{SU}(2)$ denote the reference attitude and controlled attitude, respectively. We now make use of the distance $\Gamma(\boldsymbol{X}_r, \boldsymbol{X})$ in Definition 2.19, and to simplify the notation, we here let $[\cdot]^\vee = [\cdot]^\vee_{\mathrm{SU}(2)}$ and $[\cdot]^\wedge = [\cdot]^\wedge_{\mathrm{SU}(2)}$.

Theorem 3.4—Continuous geometric attitude control on SU(2) Let $\boldsymbol{X}_e = \boldsymbol{X}_r^* \boldsymbol{X} \in \mathrm{SU}(2)$, and consider the control errors

$$\boldsymbol{e}_{\boldsymbol{X}} = \frac{1}{2}[\boldsymbol{X}_e - \mathrm{Tr}(\boldsymbol{X}_e)\boldsymbol{I}/2]^\vee \quad \in \mathbb{R}^3, \tag{3.30a}$$

$$\boldsymbol{e}_{\boldsymbol{\omega}} = \boldsymbol{\omega} - [(\boldsymbol{X}_e)^*[\boldsymbol{\omega}_r]^\wedge(\boldsymbol{X}_e)]^\vee \in \mathbb{R}^3, \tag{3.30b}$$

$$\boldsymbol{z} = (\|\boldsymbol{e}_{\boldsymbol{X}}\|, \|\boldsymbol{e}_{\boldsymbol{\omega}}\|)^\top \quad \in \mathbb{R}^2_{\geq 0}. \tag{3.30c}$$

Take any set of gains $(k_X, k_\omega, k_c) \in \mathbb{R}^3_{>0}$ such that the matrices

$$\boldsymbol{W} = \begin{bmatrix} \frac{k_c k_X}{\lambda_M(\boldsymbol{J})} & -\frac{k_c k_w}{2\lambda_m(\boldsymbol{J})} \\ -\frac{k_c k_w}{2\lambda_m(\boldsymbol{J})} & k_\omega - \frac{k_c}{4} \end{bmatrix}, \quad \boldsymbol{M}_1 = \frac{1}{2}\begin{bmatrix} 4k_X & -k_c \\ -k_c & \lambda_m(\boldsymbol{J}) \end{bmatrix}, \quad \boldsymbol{M}_2 = \frac{1}{2}\begin{bmatrix} \frac{8k_X}{2-\phi} & k_c \\ k_c & \lambda_M(\boldsymbol{J}) \end{bmatrix}, \tag{3.31}$$

are positive definite. Then, for any initial error on the domain

$$D = \left\{ \begin{bmatrix} \boldsymbol{e}_{\boldsymbol{X}}(t_\circ) \\ \boldsymbol{e}_{\boldsymbol{\omega}}(t_\circ) \end{bmatrix} \in \mathbb{R}^6 \;\middle|\; \begin{matrix} \Gamma(\boldsymbol{X}_r(t_\circ), \boldsymbol{X}(t_\circ)) \leq \phi < 2, \\ \boldsymbol{z}(t_\circ)^\top \boldsymbol{M}_2 \boldsymbol{z}(t_\circ) \leq k_X \phi \end{matrix} \right\}, \tag{3.32}$$

driving the system (3.1) with a full state feedback

$$\begin{aligned} \boldsymbol{\tau} = &- k_X \boldsymbol{e}_{\boldsymbol{X}} - k_\omega \boldsymbol{e}_{\boldsymbol{\omega}} - \boldsymbol{S}(\boldsymbol{J}\boldsymbol{\omega})\boldsymbol{\omega} \\ &+ \boldsymbol{J}[-[\boldsymbol{e}_{\boldsymbol{\omega}}/2]^\wedge \boldsymbol{X}_e^*[\boldsymbol{\omega}_r]^\wedge \boldsymbol{X}_e + \boldsymbol{X}_e^*[\dot{\boldsymbol{\omega}}_r]^\wedge \boldsymbol{X}_e + \boldsymbol{X}_e^*[\boldsymbol{\omega}_r]^\wedge \boldsymbol{X}_e[\boldsymbol{e}_{\boldsymbol{\omega}}/2]^\wedge]^\vee, \end{aligned} \tag{3.33}$$

yields an equilibrium $(\boldsymbol{e}_{\boldsymbol{X}}, \boldsymbol{e}_{\boldsymbol{\omega}}) = (\boldsymbol{0}, \boldsymbol{0})$, which is ULES on D, corresponding to $(\boldsymbol{X}_e, \boldsymbol{e}_{\boldsymbol{\omega}}) = (\boldsymbol{I}, \boldsymbol{0})$. In addition, this equilibrium point is UAGAS, with the only other equilibrium $(\boldsymbol{X}_e, \boldsymbol{e}_{\boldsymbol{\omega}}) = (-\boldsymbol{I}, \boldsymbol{0}) \in \mathrm{SU}(2) \times \mathbb{R}^3$ being unstable. □

Proof. The proof uses techniques and ideas similar to the proof of Theorem 3.2, and follows by proposing a Lyapunov function candidate

$$\mathcal{V} = k_X \Gamma(\boldsymbol{X}_r, \boldsymbol{X}) + k_c \boldsymbol{e}_{\boldsymbol{\omega}} \cdot \boldsymbol{e}_{\boldsymbol{X}} + \frac{1}{2} \boldsymbol{e}_{\boldsymbol{\omega}} \cdot \boldsymbol{J} \boldsymbol{e}_{\boldsymbol{\omega}}. \tag{3.34}$$

It is shown that all closed-loop trajectories remain within D, where then

$$\boldsymbol{z}^\top \boldsymbol{M}_1 \boldsymbol{z} \leq \mathcal{V} \leq \boldsymbol{z}^\top \boldsymbol{M}_2 \boldsymbol{z}, \qquad \dot{\mathcal{V}} \leq -\boldsymbol{z}^\top \boldsymbol{W} \boldsymbol{z}, \tag{3.35}$$

whereby the equilibrium $\boldsymbol{z} = \boldsymbol{0} \Leftrightarrow (\boldsymbol{e}_{\boldsymbol{X}}, \boldsymbol{e}_{\boldsymbol{\omega}}) = (\boldsymbol{0}, \boldsymbol{0}) \Leftrightarrow (\boldsymbol{X}_e, \boldsymbol{e}_{\boldsymbol{\omega}}) = (\boldsymbol{I}, \boldsymbol{0})$ is uniformly exponentially stable for all initial errors on $D \subset \mathbb{R}^6$. The proof of UAGAS follows by application of the Lemma of Barbălat to the Lyapunov function with $k_c = 0$, and subsequent linearization about the two resulting equilibrium points. The proof is given in its entirety in Appendix B.4. □

This is, seemingly, a very similar result to the geometric controller on SO(3) in Theorem 3.2. We arrive at a slightly different set of matrices defining the set of feasible controllers, and in contrast to the controller in Theorem 3.2, the resulting stable closed-loop equilibrium point UAGAS for finite controller gains. Consequently, the matrices in (3.31) permit studies of worst-case decay rates on the domain D in (3.32), but as the point $(\boldsymbol{X}_e, \boldsymbol{e}_{\boldsymbol{\omega}}) = (\boldsymbol{I}, \boldsymbol{0})$ is UAGAS, almost all error trajectories converge to D. As such, the controller derived in Theorem 3.4 is UAGAS (just as Theorem 3.1) and ULES with an associated with a domain of exponential attraction (just as Theorem 3.2), but this comes at a potential cost of dynamical unwinding, a curious phenomenon that can be treated in relation to the sketch in Figure 2.3 as follows.

Remark 3.5—Dynamical Unwinding
Let $\boldsymbol{R}_r = E^{\mathrm{SU}(2)}_{\mathrm{SO}(3)}(\boldsymbol{X}_r), \boldsymbol{R} = E^{\mathrm{SU}(2)}_{\mathrm{SO}(3)}(\boldsymbol{X})$. Any initial error on $\Gamma(\boldsymbol{X}_r, \boldsymbol{X}) \geq 1$ will necessarily transiently pass through the line $\Gamma(\boldsymbol{X}_r, \boldsymbol{X}) = 1 \Leftrightarrow \Psi(\boldsymbol{R}_r, \boldsymbol{R}) = 2$. Consequently, if the system is initialized with a large distance in $\Gamma(\boldsymbol{X}_r(t_\circ), \boldsymbol{X}(t_\circ))$, this will correspond to a small distance in $\Psi(\boldsymbol{R}_r(t_\circ), \boldsymbol{R}(t_\circ))$, but transient configurations will still necessarily attain a maximal distance $\Psi(\boldsymbol{R}_r(t), \boldsymbol{R}(t)) = 2$ as $\Gamma(\boldsymbol{X}_r(t), \boldsymbol{X}(t)) = 1$ at least once before asymptotically $\lim_{(t-t_\circ)\to 0} \Gamma(\boldsymbol{X}_r(t), \boldsymbol{X}(t)) = 0 \Rightarrow \lim_{(t-t_\circ)\to 0} \Psi(\boldsymbol{R}_r(t), \boldsymbol{R}(t)) = 0$. □

This is sometimes used to dismiss controllers which operate with quaternions. However, if the system state and the reference state are both configured on SU(2), then for any sufficiently small initial error on a domain D with $\phi < 1$, we have that $\Gamma(\boldsymbol{X}_r(t), \boldsymbol{X}(t)) < 1$ for all $t \geq t_\circ$. Consequently, for such small initial errors, closed-loop control with Theorem 3.4 will not give rise to the phenomenon of dynamical unwinding described in Remark 3.5. Even the case where the system state is configured on SO(3) can be handled using specialized lifting techniques [Mayhew et al., 2012] (see, e.g., Chapter 4).

Similar to the geometric controller on SO(3), Theorem 3.4 also characterizes a worst-case decay rate on a domain of exponential attraction. As such, an analogous estimate of an ultimate bound can be derived in the event of a continuous and bounded disturbance $\boldsymbol{\Delta}(t)$ acting on the control signals.

PROPOSITION 3.2
Consider the system

$$\dot{\boldsymbol{X}} = \boldsymbol{X}[\boldsymbol{\omega}/2]^{\wedge}_{\mathrm{SU}(2)}, \tag{3.36a}$$

$$\boldsymbol{J}\dot{\boldsymbol{\omega}} = \boldsymbol{S}(\boldsymbol{J}\boldsymbol{\omega})\boldsymbol{\omega} + \boldsymbol{\tau} + \boldsymbol{\Delta}, \tag{3.36b}$$

where $\boldsymbol{\Delta}(t) \in \mathbb{R}^3$ is continuous in time and $\|\boldsymbol{\Delta}\| \leq L$ for all $t \geq t_\circ$. Let (3.36) be controlled by a feedback (3.50) in Theorem 3.4, tuned with $(k_X, k_\omega, k_c) \in \mathbb{R}^3_{>0}$ resulting in positive definite matrices $\boldsymbol{M}_1, \boldsymbol{M}_2, \boldsymbol{W}$ in (3.31). For any

$$L < \frac{\theta\sqrt{\phi k_R}\lambda_m(\boldsymbol{W})\lambda_m(\boldsymbol{M}_1)}{\delta\lambda_M(\boldsymbol{M}_2)}, \tag{3.37}$$

with

$$\delta \triangleq \sqrt{1 + k_c^2\lambda_M(\boldsymbol{J}^{-1})^2}, \quad \theta \in (0,1), \tag{3.38}$$

the errors are ultimately bounded when

$$\|\boldsymbol{z}(t_\circ)\| \leq \frac{\sqrt{\phi k_R}\lambda_m(\boldsymbol{M}_1)}{\lambda_M(\boldsymbol{M}_2)}. \tag{3.39}$$

That is, there exist a class-$\mathcal{KL}$ function, β, and time, $T \geq t_\circ$ for which

$$\|\boldsymbol{z}(t)\| \leq \beta(\|\boldsymbol{z}(t_\circ)\|, t - t_\circ), \qquad \forall t \in [t_\circ, t_\circ + T], \tag{3.40}$$

$$\|\boldsymbol{z}(t)\| < r = \sqrt{\phi k_R \lambda_m(\boldsymbol{M}_1)}/\lambda_M(\boldsymbol{M}_2), \qquad \forall t \geq t_\circ + T. \tag{3.41}$$

Furthermore, on the interval $t_\circ \leq t \leq t_\circ + T$, the error decay is bounded by

$$\dot{\mathcal{V}} \leq -\frac{\lambda_m(\boldsymbol{W})}{\lambda_M(\boldsymbol{M}_2)}(1-\theta)\mathcal{V}, \tag{3.42}$$

where $\mathcal{V}$ is the Lyapunov function defined in (3.34). □

Proof. The proof is omitted for brevity and completely analogous to that of Proposition 3.1, but with the quadratic forms bounding (3.34) instead defined by the matrices in (3.31) and with the Γ-distance replacing that of Ψ. □

Much like the controller in Theorem 3.2, finding a feasible tuning is trivial, with a sufficient condition for positive definiteness of the matrices given below. However, to choose a good tuning, we need to choose (k_X, k_ω, k_c) with respect to the worst-case decay rates, the ultimate bound in Proposition 3.2, the maximal attitude error ϕ and the inertia $\boldsymbol{J}$, which is a far more difficult task.

Remark 3.6—[Greiff et al., 2021f]
For $(k_X, k_\omega) \in \mathbb{R}^2_{>0}$, the matrices $\boldsymbol{W}, \boldsymbol{M}_1, \boldsymbol{M}_2$ in (3.31) are positive definite if

$$0 < k_c < \min\left\{4k_\omega, \frac{4k_\omega k_X \lambda_m(\boldsymbol{J})^2}{\lambda_M(\boldsymbol{J})k_w^2 + \lambda_m(\boldsymbol{J})^2 k_X}, 2\sqrt{k_X \lambda_m(\boldsymbol{J})}\right\}. \tag{3.43}$$

□

Remark 3.7
With the continuous geometric control on SU(2) in Theorem 3.4, the attitude error $\boldsymbol{e_X}$ is proportional to the imaginary quaternion error $\Im(\boldsymbol{q}_r^* \odot \boldsymbol{q})$, which is frequently used to design PD-controllers. The earliest known results for the stabilizing control of the attitude dynamics using the imaginary quaternion errors were presented in [Mortensen, 1968], subsequently extended with three variant control laws in [Wie and Barba, 1985]. Here, under the assumption of a diagonal inertia matrix and $\boldsymbol{\omega}_r = \boldsymbol{0}$, "Control law 1" in [Wie and Barba, 1985] is analogous to Theorem 3.4. Related stabilization results were comprehensively reviewed in [Tsiotras, 1995] and extended in [Tayebi and McGilvray, 2006], in which the stabilization problem was solved in the quaternion representation showing almost global asymptotic convergence of an error on $\mathbb{H} \times \mathbb{R}^3$, and local exponential convergence. Consequently, similar ideas are frequently used to design heuristic tracking controllers for the attitude dynamics, see [Cutler and How, 2012; Fresk and Nikolakopoulos, 2013]. However, we remark that many of the heuristic PD controller omit the dynamic feed-forward terms in Theorem 3.4 that arise from the time-variance of $\boldsymbol{X}_r$, which are required in order to show exponential stability and enable a discussion on robustness in the tracking case. The analysis in Proposition 3.2 indicates why these controllers are frequently implemented in practice, as the dynamic feed-forward terms, if ignored, enter as load disturbances. These perturbations, if small, yield ultimately bounded errors, explaining the tracking behavior reported as a "phase lag" in [Fresk and Nikolakopoulos, 2013]. □

To show that the behavior described in Remark 3.7 is eliminated by the introduction of the dynamic feed-forward terms, to demonstrate the dynamical unwinding described in Remark 3.5, and to validate the proposed theory, a closed-loop example is given using Theorem 3.4. This example mirrors that in Example 3.1 for the geometric controller on SO(3).

Example 3.3
In this example, the continuous geometric feedback controller on SU(2) in Theorem 3.4 is run with a simulation setup identical to that in Example 3.1. The resulting tracking performance with a tuning $k_X = 8, k_c = 1, k_\omega = 2$, for a $\phi = 1.61$, is shown in Figure 3.6. Here we note that as the Lyapunov function in (3.34) is defined with the distance $\Gamma(\boldsymbol{X}_r, \boldsymbol{X})$ on SU(2), it converges to an attitude error at the identity element of SU(2), and implicitly the

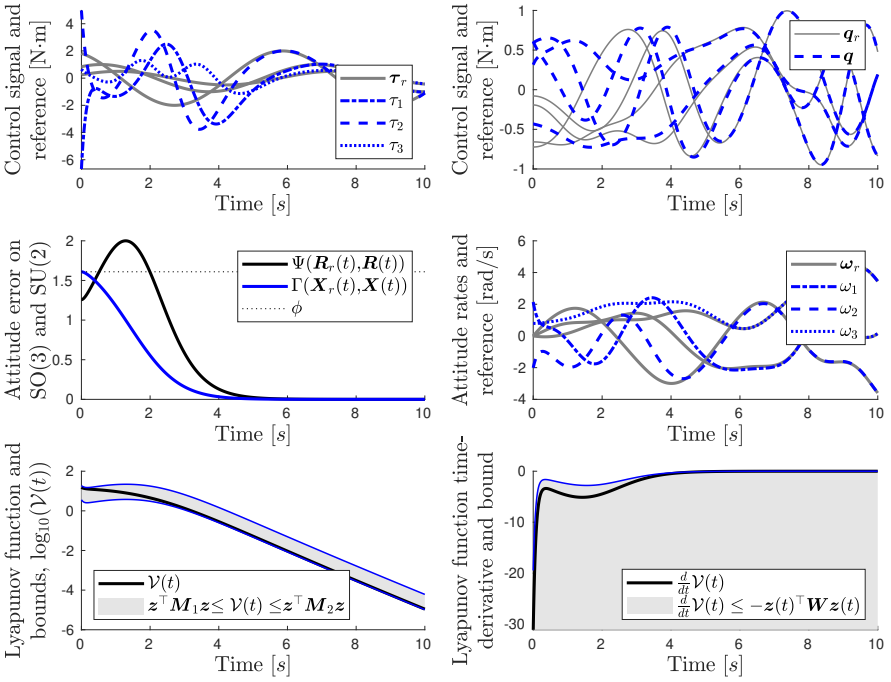

Figure 3.6 Example of the continuous geometric attitude control on SU(2) in Theorem 3.4 for small attitude rate errors. *Top left:* Reference torques $\boldsymbol{\tau}_r$ (gray), and controlled torque $\boldsymbol{\tau}$ (blue). *Top right:* Attitude visualized as quaternions, $\boldsymbol{q}_r$ (gray), and attitude $\boldsymbol{q}$ (blue). *Center left:* Attitude error on SO(3) (black) and SU(2) (blue). *Center right:* Attitude rate reference $\boldsymbol{\omega}_r$ (gray) and system response $\boldsymbol{\omega}$ (blue). *Bottom left:* Lyapunov function in (3.34), depicted in the 10-logarithm and the bounds (3.35). *Bottom right:* Lyapunov function time-derivative and bound in (3.35). The simulated system response is shown in the video chapter-3-simulations.mp4.

identity element on SO(3). Note that the attitude error transiently attains the maximum possible distance on SU(2) of $\Psi(\boldsymbol{R}_r, \boldsymbol{R}) = 2$ at around $t = 1.5$ [s]. This an example of the dynamical unwinding phenomenon described in Remark 3.5, here induced by initializing an attitude error $\Gamma(\boldsymbol{X}_r, \boldsymbol{X}) > 1$. Due to the large initial error on SU(2), significantly more control effort is required this initial transient (c.f. the torques in Figure 3.3 and Figure 3.6).

The simulation in Figure 3.6 is representative of the tracking behavior of a UAV with large initial attitude errors. In this case, the system is not initialized on D, but convergence to D and subsequent exponential convergence to $(\boldsymbol{X}_e, \boldsymbol{e}_{\boldsymbol{\omega}}) = (\boldsymbol{I}, \boldsymbol{0})$ is guaranteed for almost all initial errors, as this point is UAGAS by Theorem 3.4. The reason that the bounds on $\mathcal{V}$ and $\dot{\mathcal{V}}$ hold

during the initial transient is that the attitude error $\Gamma(\boldsymbol{X}_r, \boldsymbol{X})$ (blue) never exceeds $\phi = 1.61$ for which the bounds in (3.35) are evaluated. Recall, the condition for $\Gamma(\boldsymbol{X}_r, \boldsymbol{X}) \leq \phi$ given in (3.32) is sufficient but not necessary. The upper bound on $\dot{\mathcal{V}}$ is visibly less tight in particular example, explained by the behavior of the upper bound on Γ illustrated in Figure 2.1 for larger ϕ.

To further emphasize the importance of the UAGAS, we instead initialize the system with an attitude error $\boldsymbol{\omega}(t_\circ) \sim \mathcal{U}([-10, 10]^3)$ and consider a less aggressive tuning with $k_X = 2, k_c = 0.1, k_\omega = 1$, the rest of the simulation parameters are kept the same. The result is depicted in Figure 3.7, and once again the bounds are not guaranteed to hold when $\mathcal{V}(t) > \phi$, but the system converges to a zero tracking error, approaching the domain D to never again escape after $t_D \approx 2.4$ [s]. The bounds with which exponential convergence is shown do not necessarily hold for $t_\circ \leq t < t_D$, but in this particular case they do nonetheless, as the attitude error does not exceed ϕ in the initial transient.

As convergence to D is ensured by the UAGAS property shown in Theorem 3.4, and worst-case decay rates and robustness properties can be guaranteed on this domain, we can choose to view ϕ as a locality parameter in the tuning process. It is noteworthy that even for an initialization far outside of D, we may still have $\Gamma(\boldsymbol{X}_r(t), \boldsymbol{X}(t)) < \phi$ on $t_\circ \leq t < t_D$ (see Figure 3.7). It is also worth noting that as SU(2) is a two-to-one covering of SO(3), we can represent any $\boldsymbol{R}_e \in \mathrm{SO}(3)$ with an element in the set $\{\boldsymbol{X}_e \in \mathrm{SU}(2) \mid \mathrm{Tr}(\boldsymbol{X}_e) \geq 0\}$. Consequently, it is possible to generalize the continuous controller result in a discontinuous setting and show global stability properties. Such modifications will be considered in the next subsection.

3.6 Discontinuous Geometric Control on SU(2)

By virtue of the embedding in Definition 2.17, we have that $\boldsymbol{R} = E^{\mathrm{SU}(2)}_{\mathrm{SO}(3)}(\boldsymbol{X}) = E^{\mathrm{SU}(2)}_{\mathrm{SO}(3)}(-\boldsymbol{X})$. Consequently, $\boldsymbol{X} \to \pm\boldsymbol{I}$ implies that $\boldsymbol{R} \to \boldsymbol{I}$, and we could therefore partition the attitude error into two distinct domains along $\Gamma(\boldsymbol{X}_r, \boldsymbol{X}) = 1$,

$$\mathrm{SU}(2)^+ = \{\boldsymbol{X}_r^* \boldsymbol{X} \in \mathrm{SU}(2) | \Gamma(\boldsymbol{X}_r, \boldsymbol{X}) \leq 1\}, \tag{3.44a}$$

$$\mathrm{SU}(2)^- = \{\boldsymbol{X}_r^* \boldsymbol{X} \in \mathrm{SU}(2) | \Gamma(\boldsymbol{X}_r, \boldsymbol{X}) > 1\}, \tag{3.44b}$$

and design two different feedback laws on these two subsets of SU(2). This idea is not uncommon in the field of attitude control when using the quaternion representation, see, e.g., [Salcudean, 1991; Fragopoulos and Innocenti, 2004; Mayhew et al., 2011a; Mayhew et al., 2011b; Brescianini et al., 2013; Brescianini and D'Andrea, 2018], among many other similar works.

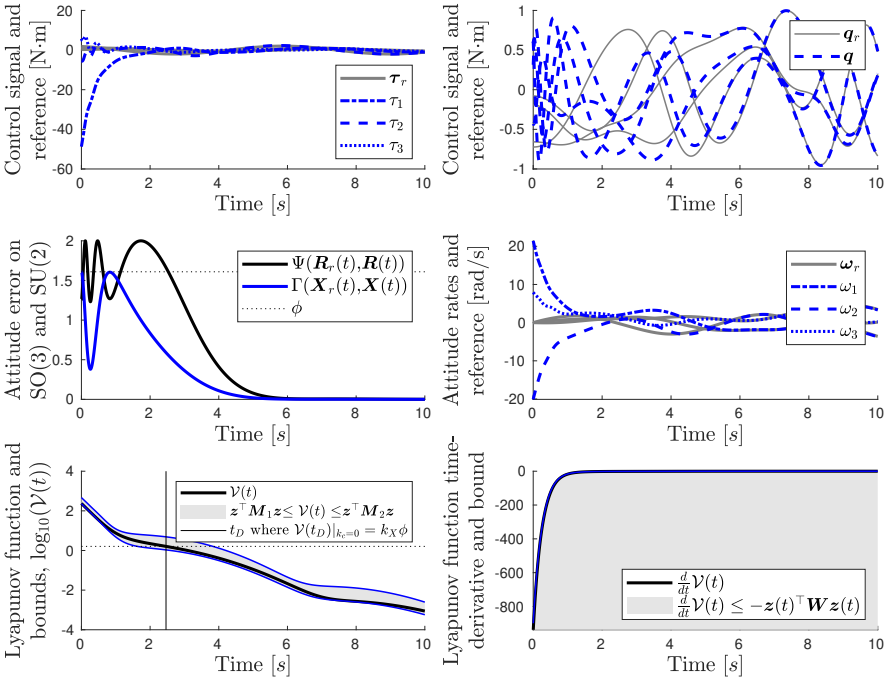

Figure 3.7 Example of the continuous geometric attitude control on SU(2) in Theorem 3.4 for large attitude rate errors. *Top left:* Reference torques $\boldsymbol{\tau}_r$ (gray), and controlled torque $\boldsymbol{\tau}$ (blue). *Top right:* Attitude visualized as quaternions, $\boldsymbol{q}_r$ (gray), and attitude $\boldsymbol{q}$ (blue). *Center left:* Attitude error on SO(3) (black) and SU(2) (blue). *Center right:* Attitude rate reference $\boldsymbol{\omega}_r$ (gray) and system response $\boldsymbol{\omega}$ (blue). *Bottom left:* Lyapunov function in (3.34), depicted in the 10-logarithm and the bounds (3.35). *Bottom right:* Lyapunov function time-derivative and upper bound in (3.35). The simulated system response is shown in the video chapter-3-simulations.mp4.

By the proposed partition in (3.44a), $\mathrm{SU}(2)^+ \cup \mathrm{SU}(2)^- = \mathrm{SU}(2)$, and for each element $\boldsymbol{X}_r^* \boldsymbol{X} \in \mathrm{SU}(2)^-$, there exists an element $-\boldsymbol{X}_r^* \boldsymbol{X} \in \mathrm{SU}(2)^+$. As such, a controller can be constructed to ensure convergence to a point $\boldsymbol{X}_r^* \boldsymbol{X} \to \boldsymbol{I}$ if $\boldsymbol{X}_r^* \boldsymbol{X} \in \mathrm{SU}(2)^+$ and $\boldsymbol{X}_r^* \boldsymbol{X} \to -\boldsymbol{I}$ if $\boldsymbol{X}_r^* \boldsymbol{X} \in \mathrm{SU}(2)^-$. Conceptually, this can be viewed as gain-scheduled controller, permitting every $\boldsymbol{X}_e \in \mathrm{SU}(2)$ to be covered by a set of two controllers, both tuned for $\phi = 1$, but with opposite signs in the P-gain. For this discussion, we define an inverse distance on SU(2) as follows.

Definition 3.1
Let $\bar{\Gamma} : \mathrm{SU}(2) \times \mathrm{SU}(2) \mapsto [0, 2]$, be defined by

$$\bar{\Gamma}(\boldsymbol{X}_1, \boldsymbol{X}_2) = 2 - \Gamma(\boldsymbol{X}_1, \boldsymbol{X}_2) = \frac{1}{2}\mathrm{Tr}(\boldsymbol{X}_1^* \boldsymbol{X}_2 - \boldsymbol{I}). \tag{3.45}$$

□

Given this definition, we can make an observation analogous to Remark 2.4.

Remark 3.8
Let $\boldsymbol{q}_1 = E_{\mathbb{H}}^{\mathrm{SU}(2)}(\boldsymbol{X}_1)$ and $\boldsymbol{q}_2 = E_{\mathbb{H}}^{\mathrm{SU}(2)}(\boldsymbol{X}_2)$, then it can be seen that

$$\Gamma(\boldsymbol{X}_1, \boldsymbol{X}_2) = 1 - \Re(\boldsymbol{q}_1^* \odot \boldsymbol{q}_2), \qquad \bar{\Gamma}(\boldsymbol{X}_1, \boldsymbol{X}_2) = \Re(\boldsymbol{q}_1^* \odot \boldsymbol{q}_2) - 1. \tag{3.46}$$

Consequently, if we let $\boldsymbol{q}_e = \boldsymbol{q}_1^* \odot \boldsymbol{q}_2$ and take this quaternion by a double angle θ and a unit vector $\boldsymbol{u}$, such that $\Re(\boldsymbol{q}_e) = \cos(\theta)$ and $\Im(\boldsymbol{q}_e) = \sin(\theta)\boldsymbol{u}$,

$$\frac{1}{2}\|\Im(\boldsymbol{q}_e)\|^2 \leq \Gamma(\boldsymbol{X}_1, \boldsymbol{X}_2) \leq \|\Im(\boldsymbol{q}_e)\|^2, \quad \forall \Gamma(\boldsymbol{X}_1, \boldsymbol{X}_2) \leq 1, \tag{3.47a}$$

$$\frac{1}{2}\|\Im(\boldsymbol{q}_e)\|^2 \leq \bar{\Gamma}(\boldsymbol{X}_1, \boldsymbol{X}_2) \leq \|\Im(\boldsymbol{q}_e)\|^2, \quad \forall \bar{\Gamma}(\boldsymbol{X}_1, \boldsymbol{X}_2) \leq 1, \tag{3.47b}$$

as illustrated in Figure 3.6. These bounds will be used in the stability analysis of the discontinuous attitude controller on SU(2), presented below. □

Theorem 3.5—Discontinuous geometric attitude control on SU(2)
Let $\boldsymbol{X}_e = \boldsymbol{X}_r^* \boldsymbol{X} \in \mathrm{SU}(2)$, and consider the control errors

$$\boldsymbol{e}_{\boldsymbol{X}}^{\pm} = \begin{cases} +\frac{1}{2}[\boldsymbol{X}_e - \mathrm{Tr}(\boldsymbol{X}_e)\boldsymbol{I}/2]_{\mathrm{SU}(2)}^{\vee} \in \mathbb{R}^3 & \text{if} \quad \boldsymbol{X}_e \in \mathrm{SU}(2)^+ \\ -\frac{1}{2}[\boldsymbol{X}_e - \mathrm{Tr}(\boldsymbol{X}_e)\boldsymbol{I}/2]_{\mathrm{SU}(2)}^{\vee} \in \mathbb{R}^3 & \text{if} \quad \boldsymbol{X}_e \in \mathrm{SU}(2)^- \end{cases} \tag{3.48a}$$

$$\boldsymbol{e}_{\boldsymbol{\omega}} = \boldsymbol{\omega} - [(\boldsymbol{X}_e)^*[\boldsymbol{\omega}_r]_{\mathrm{SU}(2)}^{\wedge}(\boldsymbol{X}_e)]_{\mathrm{SU}(2)}^{\vee} \in \mathbb{R}^3, \tag{3.48b}$$

Take any set of gains $(k_X, k_\omega, k_c) \in \mathbb{R}^3_{>0}$ such that the matrices

$$\boldsymbol{W} = \begin{bmatrix} \frac{k_c k_X}{\lambda_M(\boldsymbol{J})} & -\frac{k_c k_w}{2\lambda_m(\boldsymbol{J})} \\ -\frac{k_c k_w}{2\lambda_m(\boldsymbol{J})} & k_\omega - \frac{k_c}{4} \end{bmatrix}, \; \boldsymbol{M}_1 = \frac{1}{2}\begin{bmatrix} 4k_X & -k_c \\ -k_c & \lambda_m(\boldsymbol{J}) \end{bmatrix}, \; \boldsymbol{M}_2 = \frac{1}{2}\begin{bmatrix} 8k_X & k_c \\ k_c & \lambda_M(\boldsymbol{J}) \end{bmatrix}, \tag{3.49}$$

are all positive definite. Driving the system in (3.1) with a feedback

$$\begin{aligned} \boldsymbol{\tau} = &- k_X \boldsymbol{e}_{\boldsymbol{X}}^{\pm} - k_\omega \boldsymbol{e}_{\boldsymbol{\omega}} - \boldsymbol{S}(\boldsymbol{J}\boldsymbol{\omega})\boldsymbol{\omega} \\ &+ \boldsymbol{J}[-[\boldsymbol{e}_{\boldsymbol{\omega}}/2]^{\wedge}\boldsymbol{X}_e^*[\boldsymbol{\omega}_r]^{\wedge}\boldsymbol{X}_e + \boldsymbol{X}_e^*[\dot{\boldsymbol{\omega}}_r]^{\wedge}\boldsymbol{X}_e + \boldsymbol{X}_e^*[\boldsymbol{\omega}_r]^{\wedge}\boldsymbol{X}_e[\boldsymbol{e}_{\boldsymbol{\omega}}/2]^{\wedge}]^{\vee}, \end{aligned} \tag{3.50}$$

yields an equilibrium point $(\boldsymbol{e}_{\boldsymbol{X}}^{\pm}, \boldsymbol{e}_{\boldsymbol{\omega}}) = (\boldsymbol{0}, \boldsymbol{0})$ which is globally exponentially stable. In addition, the resulting system is GES toward $(\boldsymbol{R}_e, \boldsymbol{e}_{\boldsymbol{\omega}}) = (\boldsymbol{I}, \boldsymbol{0}) \in \mathrm{SO}(3) \times \mathbb{R}^3$ for all initial $(\boldsymbol{X}_e(t_\circ), \boldsymbol{e}_{\boldsymbol{\omega}}(t_\circ)) \in \mathrm{SU}(2) \times \mathbb{R}^3$. □

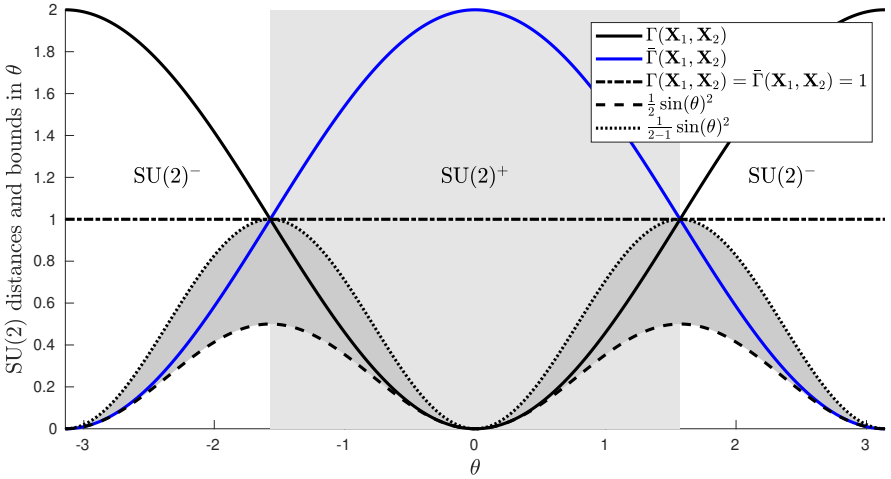

Figure 3.8 Illustration of the distance Γ with the element $\boldsymbol{X}_1, \boldsymbol{X}_2$ parameterized in a special quaternion, such that $\theta \in [-\pi, \pi]$ covers all of $\mathbb{H}$ and implicitly all of SU(2). The figure illustrates the two sets $\mathrm{SU}(2)^+$ and $\mathrm{SU}(2)^-$, and the bounds on the distances Γ and $\bar{\Gamma}$ expressed in the norm of the imaginary part of the attitude error.

Proof. The proof is similar to that of Theorem 3.4. It is sketched here and given in Appendix B.6. A hybrid Lyapunov function candidate is defined, as

$$\mathcal{V}^{\pm} \triangleq \begin{cases} \mathcal{V}^+ & \text{if} \quad \boldsymbol{X}_e \in \mathrm{SU}(2)^+, \\ \mathcal{V}^- & \text{if} \quad \boldsymbol{X}_e \in \mathrm{SU}(2)^-, \end{cases} \tag{3.51}$$

constructed similar to $\mathcal{V}$ in (3.34), with

$$\mathcal{V}^+ = k_X \Gamma(\boldsymbol{X}_r, \boldsymbol{X}) + k_c \boldsymbol{e}_{\boldsymbol{\omega}} \cdot \boldsymbol{e}_{\boldsymbol{X}}^{\pm} + \frac{1}{2} \boldsymbol{e}_{\boldsymbol{\omega}} \cdot \boldsymbol{J} \boldsymbol{e}_{\boldsymbol{\omega}}, \tag{3.52a}$$

$$\mathcal{V}^- = k_X \bar{\Gamma}(\boldsymbol{X}_r, \boldsymbol{X}) - k_c \boldsymbol{e}_{\boldsymbol{\omega}} \cdot \boldsymbol{e}_{\boldsymbol{X}}^{\pm} + \frac{1}{2} \boldsymbol{e}_{\boldsymbol{\omega}} \cdot \boldsymbol{J} \boldsymbol{e}_{\boldsymbol{\omega}}. \tag{3.52b}$$

It is then possible to show that $\mathcal{V}^{\pm}$ satisfies the bounds in (3.35) globally when defined with $\phi = 1$, and that $\mathcal{V}^{\pm}$ is continuous when traversing $\Gamma(\boldsymbol{X}_r, \boldsymbol{X}) = 1$. The result follows by application of the comparison lemma. □

Example 3.4
In this example, the discontinuous geometric controller on SU(2) in Theorem 3.5 is demonstrated with the same simulation setup as used in examples 3.1 and 3.3. The controller parameters from Example 3.3 are also reused, that

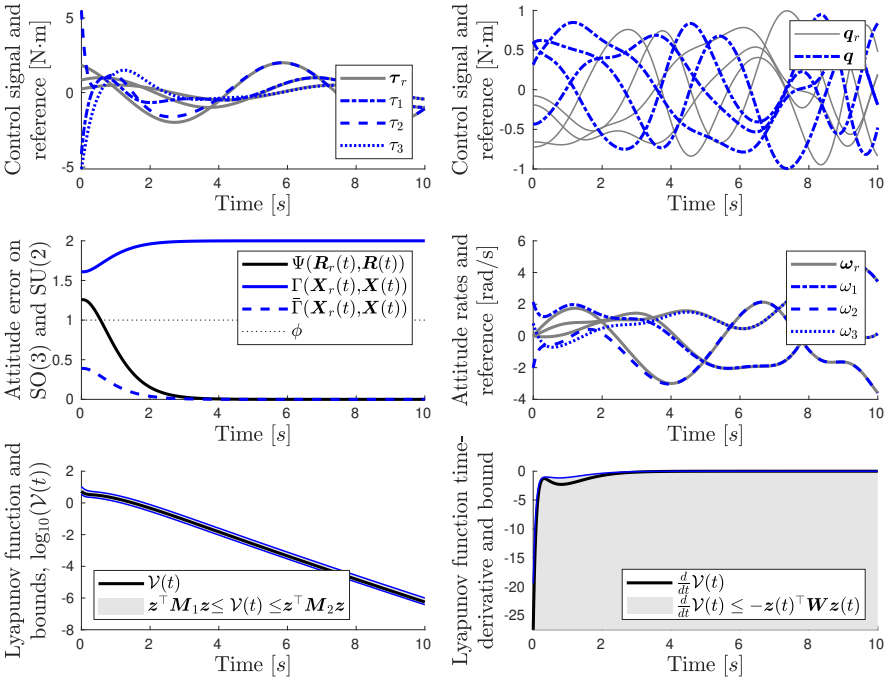

Figure 3.9 Example of the discontinuous geometric attitude control on SU(2) in Theorem 3.5 small attitude rate errors. *Top left:* Torques driving the reference system $\boldsymbol{\tau}_r$ (gray), and controlled torque $\boldsymbol{\tau}$ (blue). *Top right:* Attitude visualized as quaternions, $\boldsymbol{q}_r$ (gray), and attitude $\boldsymbol{q}$ (blue). *Center left:* Attitude error on SO(3) (black) and on SU(2) with the distance Γ (blue) and $\bar{\Gamma}$ (blue, dashed). *Center right:* Attitude rate reference $\boldsymbol{\omega}_r$ (gray) and system response $\boldsymbol{\omega}$ (blue). *Bottom left:* Lyapunov function in (3.51), depicted in the 10-logarithm and the bounds (3.35) (with $\phi = 1$). *Bottom right:* Lyapunov function time-derivative and bound in (3.35) (with $\phi = 1$). The simulated system response is shown in the video chapter-3-simulations.mp4.

is, $(k_X, k_c, k_\omega) = (8, 1, 2)$. The resulting trajectory tracking performance is shown in Figure 3.9, and we note that the controller converges to an attitude error $\bar{\Gamma}(\boldsymbol{X}_r, \boldsymbol{X}) = 0$ with $\boldsymbol{X}_e \in \mathrm{SU}(2)^-$, which implies a zero error on SO(3) in $\Psi(\boldsymbol{R}_r, \boldsymbol{R}) = 0$. However, the distance in which the continuous controller on SU(2) was expressed goes to $\Gamma(\boldsymbol{X}_r, \boldsymbol{X}) = 2$. Consequently, we have achieved a tracking control on SU(2), which corresponds to the continuous tracking control on SU(2) if $\boldsymbol{X}_e \in \mathrm{SU}(2)^+$, but converging to $\boldsymbol{X}_e = -\boldsymbol{I}$ on $\mathrm{SU}(2)^-$.

The bounds on the Lyapunov function $\mathcal{V}^\pm$ and $(\mathrm{d}/\mathrm{d}t)\mathcal{V}^\pm$ shown in Figure 3.9 are clearly tighter than the corresponding bounds in the case of the continuous controller with the same tuning in Figure 3.6, as here, the

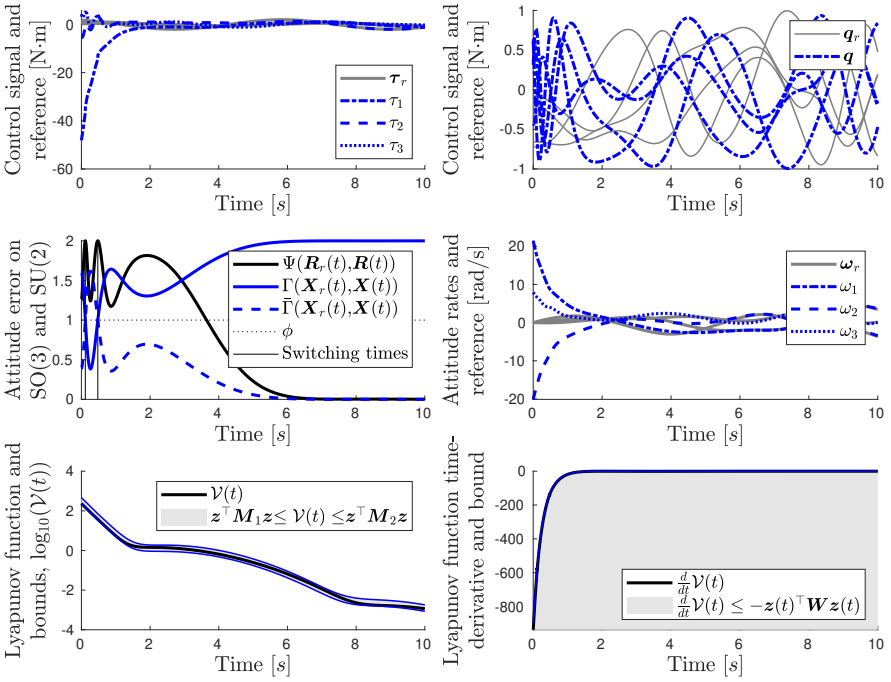

Figure 3.10 Example of the discontinuous geometric attitude control on SU(2) in Theorem 3.5 for large attitude rate errors. *Top left:* Torques driving the reference system $\boldsymbol{\tau}_r$ (gray), and controlled torque $\boldsymbol{\tau}$ (blue). *Top right:* Attitude visualized as quaternions, $\boldsymbol{q}_r$ (gray), and attitude $\boldsymbol{q}$ (blue). *Center left:* Attitude error on SO(3) (black) and on SU(2) with the distance Γ (blue) and $\bar{\Gamma}$ (blue, dashed). *Center right:* Attitude rate reference $\boldsymbol{\omega}_r$ (gray) and system response $\boldsymbol{\omega}$ (blue). *Bottom left:* Lyapunov function in (3.51), depicted in the 10-logarithm and the bounds (3.35) (with $\phi = 1$). *Bottom right:* Lyapunov function time-derivative and bound in (3.35) (with $\phi = 1$). The simulated system response is shown in the video chapter-3-simulations.mp4.

bounds are defined with the same tuning but a smaller ϕ. Furthermore, the bounds defined with $\phi = 1$ hold globally, and we do not need to worry about convergence to some domain of exponential attraction when the errors are large. To illustrate this, we again consider a modified simulation where $k_X = 2, k_c = 0.1, k_\omega = 1$ and let $\boldsymbol{\omega}(t_\circ) \sim \mathcal{U}([-10, 10]^3)$. The result is shown in Figure 3.10, where we see that the system is initialized on $\boldsymbol{X}_e \in \mathrm{SU}(2)^-$, transitions across the line $\mathrm{Tr}(\boldsymbol{X}_e) = 0$ to $\mathrm{SU}(2)^+$ at $t_1 \approx 0.1$ [s] before traversing this line once again at $t_2 \approx 0.4$ [s] and converging to $\boldsymbol{X}_e \to -\boldsymbol{I} \in \mathrm{SU}(2)^-$. The Lyapunov function $\mathcal{V}^\pm$ is continuous at the switching times; but its time-derivative $\dot{\mathcal{V}}^\pm$ is not continuous at $t \in \{t_1, t_2\}$.

As such, $\mathcal{V}^{\pm}$ is not generally continuously differentiable, as a transition between the two partitions on SU(2) at a time t_s implies a jump in $(\mathrm{d}/\mathrm{d}t)\mathcal{V}^{\pm}(t_s)$ if $\boldsymbol{e}_{\boldsymbol{X}}^{\pm}(t_s) \cdot \boldsymbol{e}_{\boldsymbol{\omega}}(t_s) \neq \boldsymbol{0}$. This is common to discontinuous feedback laws with quaternion representations (see, e.g., [Mayhew et al., 2011b, Section 3]). When initializing the system close to $\Gamma(\boldsymbol{X}_r(t_\circ), \boldsymbol{X}(t_\circ)) = 1$, an arbitrarily small disturbance can be artificially constructed to prevent the global convergence of the errors to one of the two equilibrium points. This lack of continuous differentiability is the reason for developing a robust controller on SU(2) from the continuous feedback. However, it should be noted that similar results can be derived for the discontinuous case, provided that the errors are sufficiently small and the references computed such that switching is eliminated.

3.7 Robust Geometric Control on SU(2)

In this section, we give an analogue to the robust controller on SO(3) in Theorem 3.3 by extending the continuous feedback law on SU(2) in Theorem 3.4.

Theorem 3.6—Robust geometric attitude control on SU(2) Consider the attitude system in (3.1) with the perturbed dynamics in (3.4), where $\boldsymbol{\Delta}(t) \in \mathbb{R}^3$ is continuous in time and $\|\boldsymbol{\Delta}\| \leq L$ for all $t \geq t_\circ$. Take any tuning $\boldsymbol{k} = (k_X, k_\omega, k_c)$ resulting in a set of positive definite matrices $\boldsymbol{M}_1, \boldsymbol{M}_2, \boldsymbol{W}$ in (3.31), and define the errors $\boldsymbol{e}_{\boldsymbol{X}}$ and $\boldsymbol{e}_{\boldsymbol{\omega}}$ as in (3.30). Take the perturbed system in (3.4) to be in closed-loop feedback with

$$\begin{aligned}\boldsymbol{\tau} = &- k_X \boldsymbol{e}_{\boldsymbol{X}} - k_\omega \boldsymbol{e}_{\boldsymbol{\omega}} - \boldsymbol{\mu}_{\boldsymbol{X}} - \boldsymbol{S}(\boldsymbol{J}\boldsymbol{\omega})\boldsymbol{\omega} \qquad (3.53a)\\ &+ \boldsymbol{J}[-[\boldsymbol{e}_{\boldsymbol{\omega}}/2]^{\wedge}\boldsymbol{X}_e^*[\boldsymbol{\omega}_r]^{\wedge}\boldsymbol{X}_e + \boldsymbol{X}_e^*[\dot{\boldsymbol{\omega}}_r]^{\wedge}\boldsymbol{X}_e + \boldsymbol{X}_e^*[\boldsymbol{\omega}_r]^{\wedge}\boldsymbol{X}_e[\boldsymbol{e}_{\boldsymbol{\omega}}/2]^{\wedge}]^{\vee}\\ \boldsymbol{\mu}_{\boldsymbol{X}} = &\frac{L^2 \boldsymbol{e}_A}{L\|\boldsymbol{e}_A\| + \epsilon_X}, \qquad (3.53b)\\ \boldsymbol{e}_A = &\boldsymbol{e}_{\boldsymbol{\omega}} + k_c \boldsymbol{J}^{-1}\boldsymbol{e}_{\boldsymbol{X}}. \qquad (3.53c)\end{aligned}$$

For any choice of parameter ϵ_X satisfying

$$0 < \epsilon_X < \frac{\lambda_m(\boldsymbol{M}_1(\boldsymbol{k}))\lambda_m(\boldsymbol{W}(\boldsymbol{k}))}{\lambda_M(\boldsymbol{M}_2(\boldsymbol{k}))}\phi(2-\phi), \qquad (3.54)$$

the errors are ultimately bounded in ϵ_X, as

$$\lim_{t-t_\circ\to\infty} \|\boldsymbol{z}\|^2 \leq \gamma(L;\boldsymbol{k}) = \frac{\lambda_M(\boldsymbol{M}_2(\boldsymbol{k}))}{\lambda_m(\boldsymbol{M}_1(\boldsymbol{k}))\lambda_m(\boldsymbol{W}(\boldsymbol{k}))}\epsilon_X. \qquad (3.55)$$

□

Proof. Similar to the proof in [Lee et al., 2013], we get an upper bound on the Lyapunov function time-derivative as $\dot{\mathcal{V}} \leq -\boldsymbol{z}^{\top}\boldsymbol{W}\boldsymbol{z} + \epsilon_X$, facilitating the rest of the proof, which is stated in its entirety in Appendix B.7. □

Instead of characterizing the effects of a bounded and continuous load disturbance $\|\boldsymbol{\Delta}(t)\| \leq L$ on the errors in the control system, as done in Proposition 3.2, we now proactively include L in the feedback law and introduce a tuning parameter ϵ_X. Similar to the result in Theorem 3.3, this generally results in a much smaller ultimate bound, which depends on the parameters $\boldsymbol{k} = (k_X, k_c, k_\omega)$. However, this bound now becomes proportional to ϵ_X, permitting the system to perform well even in the event of large load disturbances, at a cost of increased volatility in the control signal for small errors, and an increased sensitivity to measurement noise.

Example 3.5
In this example, we consider a simulation setup similar to Example 3.3, but now with robust controller in Theorem 3.6 controlling a system with a randomized dense inertia matrix satisfying $\lambda_m(\boldsymbol{J}) = 0.5$ and $\lambda_M(\boldsymbol{J}) = 1$. The initial conditions at $t_\circ = 0$ are sampled from $\boldsymbol{X}(t_\circ), \boldsymbol{X}_r(t_\circ) \sim \mathcal{U}(\mathrm{SU}(2))$ with $\boldsymbol{\omega}(t_\circ) \sim \mathcal{U}([-1,1]^3)$ and $\boldsymbol{\omega}_r(t_\circ) = \boldsymbol{0}$. The reference dynamics are driven by the sinusoidal torque trajectories in (3.14). We also inject a synthetic disturbance $\boldsymbol{\Delta}(t)$, which is continuous and of a slightly smaller magnitude than $\boldsymbol{\tau}_r(t)$, satisfying $\|\boldsymbol{\Delta}(t)\| = L = 1$ for all $t \geq t_\circ$. The disturbance is realized as

$$\boldsymbol{\Delta}(t) \triangleq L\frac{\bar{\boldsymbol{\Delta}}(t)}{\|\boldsymbol{\Delta}(t)\|}, \quad \bar{\boldsymbol{\Delta}}(t) \triangleq (\sin(t);\ \sin(4t + \tfrac{\pi}{2});\ \sin(8t + \tfrac{\pi}{4})) \in \mathbb{R}^3, \quad (3.56)$$

and the controller is tuned with $k_X = 12, k_c = 2, k_\omega = 3$. The response is shown in terms of in the familiar torque, disturbance, attitude, attitude rate, Lyapunov function and Lyapunov function time derivative plots in Figure 3.11.

Despite the large and volatile load disturbance, the closed-loop system behaves similar to the continuous geometric controller on SU(2) when the tracking errors are large (c.f., Figure 3.6). However, as these errors become small, the Lyapunov function no longer decays monotonically, as $\mathcal{V} \leq -\boldsymbol{z}^\top \boldsymbol{W}\boldsymbol{z} + \epsilon_X$. It is clear that for the chosen ϵ_X, this will result in a small ultimate bound, with the disturbance being nearly invisible in the attitude tracking error and the attitude rate plots (see Figure 3.11). □

Remark 3.9
In practice, the maximally allowed ϵ_X in (3.54) may be very small if ϕ is large. However, similar to how the Lyapunov function bounds hold for initial errors violating the sufficient conditions for the error trajectories to remain in D, it may be useful to include even larger terms in ϵ_X in practice. □

To (i) illustrate the utility of setting larger ϵ_X; (ii) show the proportionality of the asymptotic errors to ϵ_X; and (iii) give a sense of how the continuous attitude controller behaves for the same disturbance, consider Example 3.6.

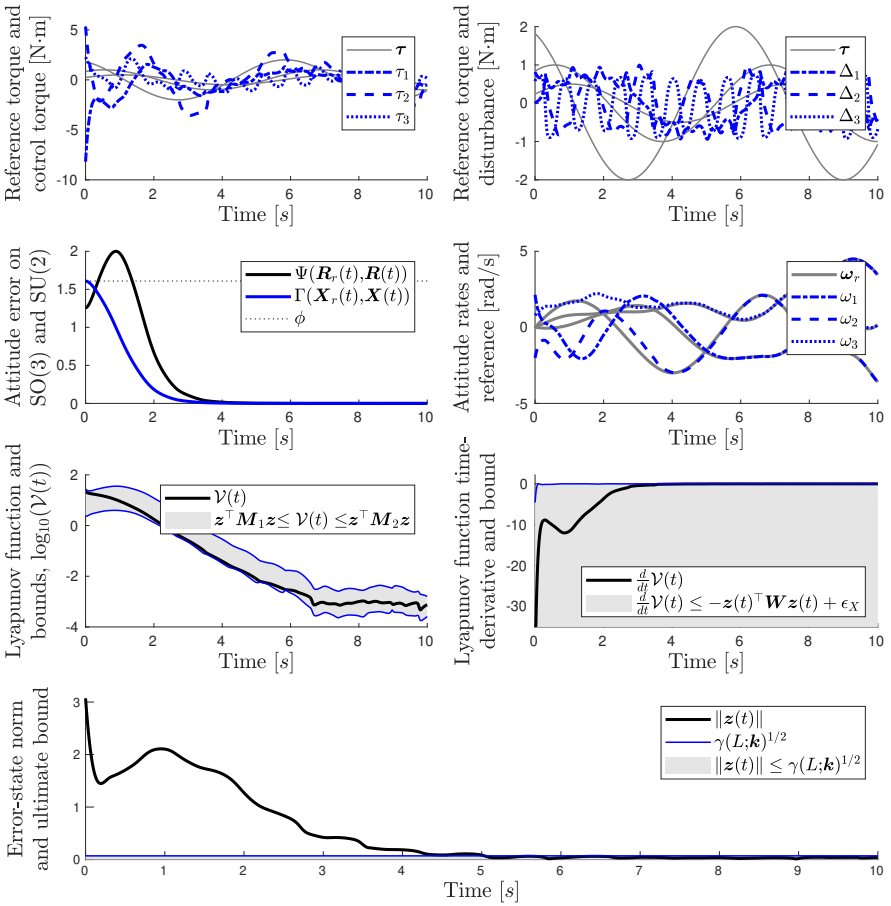

Figure 3.11 Example of the robust geometric attitude control on SO(3) in Theorem 3.6. *Top left:* Torques driving the reference system $\boldsymbol{\tau}_r$ (gray), and controlled torque $\boldsymbol{\tau}$ (blue). *Top right:* Torques driving the reference system $\boldsymbol{\tau}_r$ (gray), and disturbance $\boldsymbol{\Delta}$ (blue). *Top center, left:* Attitude error in the SO(3)-distance (black) and in the SU(2)-distance (blue). *Top center, right:* Attitude rate reference (gray) and system response (blue, dashed). *Bottom center, left:* Lyapunov function in the 10-logarithm and the upper and lower bounds expressed in $\boldsymbol{z}$. *Bottom center, right:* Lyapunov function time-derivative and upper bound. *Bottom:* Errors $\|\boldsymbol{z}\|$ converging a value smaller than the ultimate bound estimate. The simulated system response is shown in the video chapter-3-simulations.mp4.

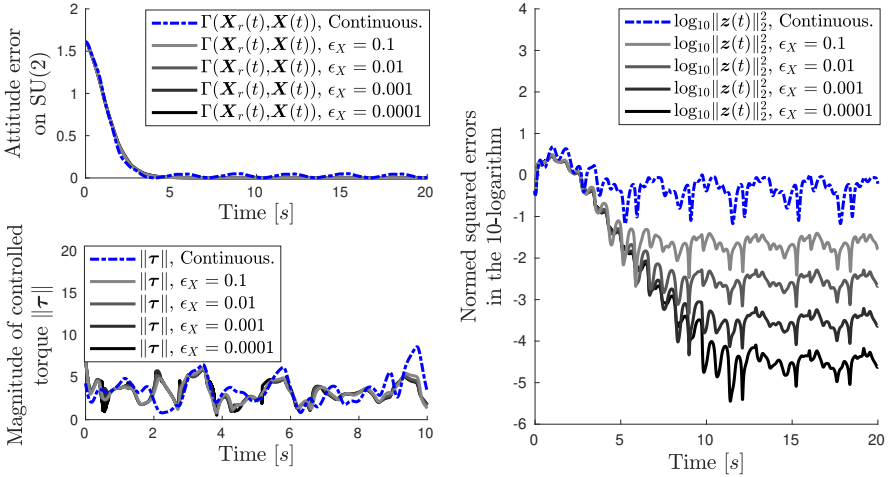

Figure 3.12 Example comparing controllers on SU(2) *without measurement noise*, specifically the geometric controller in Theorem 3.4 (blue) and its robust counterpart in Theorem 3.6 (gray) when tuned with decreasing ϵ_X (darker). *Top left:* Attitude errors on SU(2). *Bottom, left:* Norm of the control signal torques. *Right:* Squared control errors in the 10-logarithm. The simulated system response is shown in the video chapter-3-simulations.mp4.

Example 3.6

Here, we use the same simulation setup as in Example 3.5 with the exact same controller tuning, the only exception being that the disturbance is now characterized by $L = 3$. This permits a comparison of the continuous geometric controller in Theorem 3.4 to the robust version of the controller in Theorem 3.6 for different values of $\epsilon_X \in \{0.1, 0.01, 0.001, 0.0001\}$. Given the relatively large ϕ, only $e_X = \{0.001, 0.0001\}$ satisfy the sufficient conditions for $\Gamma(\boldsymbol{X}_r(t)), \boldsymbol{X}(t) < \phi$ for all $t \geq t_\circ$ in (3.54). However, in the system response depicted in Figure 3.12, it can be seen that larger ϵ_X can yield significant performance increases in the asymptotic trajectory tracking.

In the attitude tracking errors (top left in Figure 3.12), the load disturbance is clearly visible when using with Theorem 3.4 (blue), but still very well attenuated given the relatively large load disturbance. This is a reflection of the inherent robustness properties of the continuous geometric controller from Theorem 2.12, as highlighted in Proposition 3.2. However, the effect of the load disturbance is nearly invisible in the same subplot when studying the robust version of the controller, implemented with any of the considered ϵ_X (black/gray). The difference in tuning is immediately clear from the error subplot of Figure 3.12 (right in Figure 3.12), where a decreasing ϵ_X (darker) yields a smaller bound, and the proportionality of the ultimate bound to ϵ_X

is clearly seen. Finally, we note that the magnitudes of the control signals are very similar in the continuous controller in Theorem 3.4 and the robust controllers Theorem 3.6 (bottom, left). When $\epsilon_X = 0.1$, the control signal is smooth in the two-norm, but as ϵ_X becomes smaller, we observe more rapid changes in $\boldsymbol{\mu}_{\boldsymbol{X}}$ and implicitly $\boldsymbol{\tau}$ whenever $\boldsymbol{e}_A$ in (3.53c) becomes small. This happens around $t = 3$ and $t = 5.2$, where the torque changes rapidly. □

Remark 3.10
Despite the temptation of pushing down the ultimate bound through ϵ_X, it is often not desirable to make this parameter very small in practice. The reason being that a smaller ϵ_X makes the system increasingly stiff and sensitive to measurement noise close to the stable equilibrium point $\boldsymbol{e}_{\boldsymbol{X}} = \boldsymbol{e}_{\boldsymbol{\omega}} = \mathbf{0}$. □

To demonstrate this, a final simulation example is given below.

Example 3.7
Consider the same simulation setup as in Examples 3.5 and 3.6, with the exact same controller tuning, but a disturbance characterized by $L = 3$. However, in this simulation we consider gyroscopic measurement noise. Specifically, we take this noise to be Gaussian, which at a time-step k is realized as $\boldsymbol{\omega}_k^n \sim \mathcal{N}(\mathbf{0}, \sigma_\omega^2 \boldsymbol{I})$, entering additively on $\boldsymbol{\omega}$. Here we consider a noise density of 0.014 $[^\circ/\mathrm{s}/\sqrt{\mathrm{Hz}}]$ corresponding to a high-performance BMI088 gyroscope [Bosch Sensortec, 2020], which when sampled at a constant rate of 500 [Hz] corresponds to a standard deviation in the noise of $\sigma_\omega = 0.0039$. The system response with the additive gyroscopic noise is shown in Figure 3.13.

Here we observe a ringing effect in the control signals associated with the smaller ϵ_X. This is seen with ϵ_X as large as 0.01. However, the effect is barely visible in the case where $\epsilon_X = 0.1$, which still achieves asymptotic errors that are more than a magnitude lower than those achieved by Theorem 3.4. As such, if the volatility in the control signals becomes problematic, then ϵ_X can be increased, loosing the stability properties shown in Theorem 3.4, but yielding significant performance increases over its non-robust counterparts. □

The examples in this section illustrate the utility of the robust controller on SU(2), but also that it can become sensitive to measurement noise if ϵ_X is small. The exact same reasoning holds for the geometric controller on SO(3) in Theorem 3.2 and its robust counterpart in Theorem 3.3. As such, it becomes interesting to ask how small the ultimate bound can be made, and how large the worst-case error decay rates can be made for a given ϵ_X. This problem is addressed in the next section using optimization-based tuning methods.

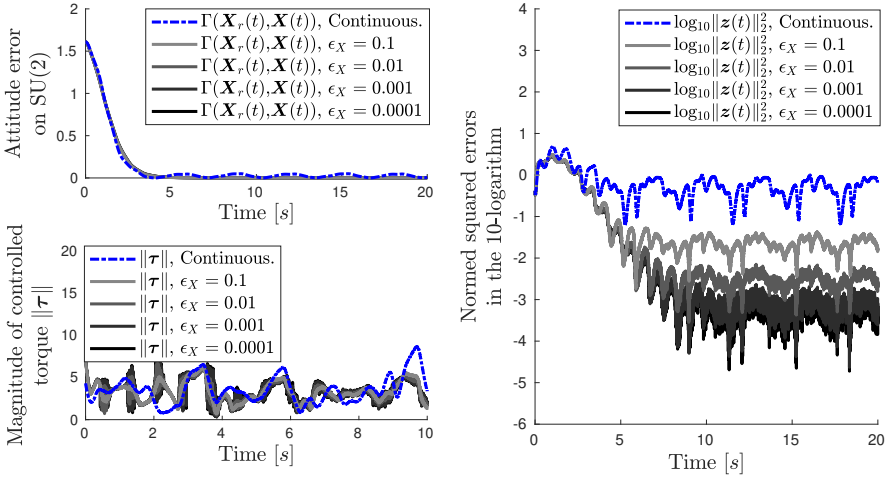

Figure 3.13 Example comparing controllers on SU(2) *with measurement noise*, specifically the geometric controller in Theorem 3.4 (blue) and its robust counterpart in Theorem 3.6 (gray) when tuned with decreasing ϵ_X (darker). *Top left:* Attitude errors on SU(2). *Bottom, left:* Norm of the control signal torques. *Right:* Squared control errors in the 10-logarithm.

3.8 Tuning by Bilinear Matrix Inequalities

The controllers presented in this chapter can be tuned in many ways, but here we envision a scenario where an engineer is aware of reasonable magnitudes of the initial attitude errors, permitting the definition of a domain D by ϕ on which performance is to be considered. All of the controllers will be stabilizing outside of this domain, but are here tuned specifically for trajectories on D. The task is to tune the controllers given ϕ, to minimize the ultimate bound and maximize the error decay rate on D. To this end, we note that all of the geometric controllers, both on SO(3) and SU(2), are defined by three controller parameters, here represented as $\boldsymbol{k} \in \mathbb{R}^3_{>0}$. For the controller in

- Theorem 3.2, let $\boldsymbol{k} = (k_R;\ k_c;\ k_\omega)$, with $\boldsymbol{W}, \boldsymbol{M}_1, \boldsymbol{M}_2$ in (3.9);
- Theorem 3.3, let $\boldsymbol{k} = (k_R;\ k_c;\ k_\omega)$, with $\boldsymbol{W}, \boldsymbol{M}_1, \boldsymbol{M}_2$ in (3.9);
- Theorem 3.4, let $\boldsymbol{k} = (k_X;\ k_c;\ k_\omega)$, with $\boldsymbol{W}, \boldsymbol{M}_1, \boldsymbol{M}_2$ in (3.31);
- Theorem 3.5, let $\boldsymbol{k} = (k_X;\ k_c;\ k_\omega)$, with $\boldsymbol{W}, \boldsymbol{M}_1, \boldsymbol{M}_2$ in (3.49);
- Theorem 3.6, let $\boldsymbol{k} = (k_X;\ k_c;\ k_\omega)$, with $\boldsymbol{W}, \boldsymbol{M}_1, \boldsymbol{M}_2$ in (3.31).

The decay rates can be expressed in $\boldsymbol{M}_2$ and $\boldsymbol{W}$ in all of the five controllers, but the ultimate bounds on the tracking errors will be quite different. In the

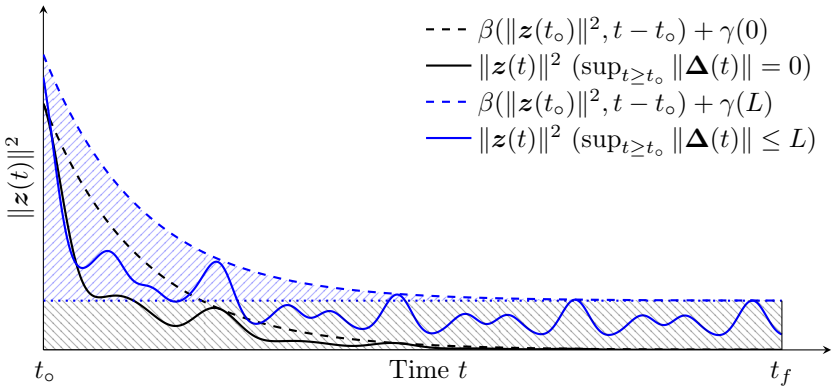

Figure 3.14 Bounds on the errors $\|\boldsymbol{z}\|^2$ when controlling the perturbed system with a robust feedback in Theorem 3.3 or 3.6.

case of the continuous geometric controllers on SO(3) and SU(2), the effect of small load disturbances on the tracking errors is given by Propositions 3.1 and Propositions 3.2 respectively, and in the case of the robust controllers, this bound is given in (3.26) and (3.55), respectively.

Remark 3.11
Note that for the considered controllers, $\boldsymbol{M}_1$ and $\boldsymbol{M}_2$ are linear in the controller parameters, but $\boldsymbol{W}$ is not, as it in all above cases includes a cross-term with a factor k_c. Thus, $\boldsymbol{W}$ is not linear, but rather bilinear in $\boldsymbol{k}$. For future reference, we let $\boldsymbol{k}_A = (k_R, k_\omega)$ in the context of Theorems 3.2 and 3.3, and let $\boldsymbol{k}_A = (k_X, k_\omega)$ in the context of Theorems 3.4, 3.5 and 3.6. Then, for fixed k_c, the matrix $\boldsymbol{W}$ is linear in $\boldsymbol{k}_A$, and for fixed $\boldsymbol{k}_A$, it is linear in k_c. □

In formulating the tuning problem, we consider Figure 3.14, and seek a controller that quickly drives the errors to an ultimate bound (minimizing the shaded blue area), and that this ultimate bound is small (minimizing the shaded black area). In [Greiff et al., 2021e], this was expressed as a cost in a negative weighted decay rate and a weighted ultimate bound with respect to Theorem 3.3 for specific ϵ_R. In this section, we consider a cost function which has a more natural interpretation, leading to a slight reformulation of the tuning problem, allowing it to be posed for all the aforementioned controllers.

Consider a generic cost in terms of the worst-case decay rates of the errors given a disturbance bounded in L, over a finite time $t \in [t_\circ, t_f]$, defined as

$$\bar{J}(\boldsymbol{k}) = \int_{t_\circ}^{t_f} \|\boldsymbol{z}(t)\|^2 \mathrm{d}t, \tag{3.57}$$

and consider solving a constrained optimization problem

$$\min_{\boldsymbol{k}\in\mathbb{R}_{\geq 0}} \max_{\|\boldsymbol{\Delta}\|\leq L} \bar{J}(\boldsymbol{k}), \qquad \boldsymbol{M}_1(\boldsymbol{k}) \succ 0, \qquad \boldsymbol{M}_2(\boldsymbol{k}) \succ 0, \qquad \boldsymbol{W}(\boldsymbol{k}) \succ 0. \tag{3.58}$$

Without loss of generality, let $t_\circ = 0$. Using the worst-case decay rates in $\|\boldsymbol{z}\|$,

$$\begin{aligned}\max_{\|\boldsymbol{\Delta}\|\leq L} \bar{J}(\boldsymbol{k}) &\leq \int_0^{t_f} \|\boldsymbol{z}(t_\circ)\|^2 e^{-d(\boldsymbol{k})t}\mathrm{d}t + \int_0^{t_f} \gamma(L;\boldsymbol{k})\mathrm{d}t \\ &= \|\boldsymbol{z}(t_\circ)\|^2 \frac{1-e^{-t_f d(\boldsymbol{k})}}{d(\boldsymbol{k})} + t_f\gamma(L;\boldsymbol{k}) \\ &\leq w_1 \frac{1}{d(\boldsymbol{k})} + w_2\gamma(L;\boldsymbol{k}) \triangleq J(\boldsymbol{k}),\end{aligned}$$

with the last inequality becomes tight as $t_f d(\boldsymbol{k})$ grows large, and with the weights given by $w_1 \triangleq \|\boldsymbol{z}(t_\circ)\|^2$ and $w_2 \triangleq t_f$. As such, the general optimization in (3.58) can be relaxed slightly and written as

$$\min_{\boldsymbol{k}\in\mathbb{R}_{\geq 0}} J(\boldsymbol{k}), \qquad \boldsymbol{M}_1(\boldsymbol{k}) \succ 0, \qquad \boldsymbol{M}_2(\boldsymbol{k}) \succ 0, \qquad \boldsymbol{W}(\boldsymbol{k}) \succ 0. \tag{3.59}$$

Remark 3.12
The cost $J(\boldsymbol{k})$ is closely related to that in [Greiff et al., 2021e], but introduces an inverse weighted decay rate instead of a negative decay rate, thus getting a clear interpretation of the cost which is minimized, as an upper bound to $\bar{J}(\boldsymbol{k})$ (3.57) for the worst possible disturbance $\|\boldsymbol{\Delta}\| \leq L$, on a finite interval $t \in [t_\circ, t_f]$, when the weights are chosen as $w_1 \triangleq \|\boldsymbol{z}(t_\circ)\|^2$ and $w_2 \triangleq t_f$. □

The problem in (3.59) can be solved directly by an interior point method, or by the alternating semi-definite programming (ASDP) approach in [Greiff et al., 2021e], which is shown to be numerically superior for a related set of problems. Such an algorithm can be formulated as follows. Define the vector $\boldsymbol{\epsilon} = (\epsilon_1, \epsilon_2, \epsilon_3)^\top \in \mathbb{R}^3_{>0}$ such that its elements bound the relevant eigenvalues of the matrices in (3.59), with

$$\epsilon_1 \leq \lambda_m(\boldsymbol{M}_1), \qquad \epsilon_2 \geq \lambda_M(\boldsymbol{M}_2), \qquad \epsilon_3 \leq \lambda_m(\boldsymbol{W}). \tag{3.60}$$

Then, the cost in (3.59) can be upper bounded in these variables as

$$J(\boldsymbol{k}) \leq w_1 \frac{\epsilon_2}{\epsilon_3} + w_2 \frac{\epsilon_2}{\epsilon_1\epsilon_3} \triangleq J(\boldsymbol{\epsilon}). \tag{3.61}$$

This bound can be linearized about a point $\boldsymbol{\epsilon}^*$, as

$$J(\boldsymbol{\epsilon};\boldsymbol{\epsilon}^*) \approx J(\boldsymbol{\epsilon}^*) + \nabla_{\boldsymbol{\epsilon}} J(\boldsymbol{\epsilon})|_{\boldsymbol{\epsilon}=\boldsymbol{\epsilon}^*}(\boldsymbol{\epsilon}-\boldsymbol{\epsilon}^*) + o(\|\boldsymbol{\epsilon}-\boldsymbol{\epsilon}^*\|^2). \tag{3.62}$$

where the gradient of the bound in $\boldsymbol{\epsilon}$ can be computed explicitly as

$$\nabla_{\boldsymbol{\epsilon}} J(\boldsymbol{\epsilon}) = \left[-\frac{w_2 \epsilon_2}{\epsilon_1^2 \epsilon_3}, \quad \frac{w_1}{\epsilon_3} + \frac{w_2}{\epsilon_1 \epsilon_3}, \quad -\frac{\epsilon_2 w_1}{\epsilon_3^2} - \frac{w_2 \epsilon_2}{\epsilon_1 \epsilon_3^2} \right]. \tag{3.63}$$

As noted in [Greiff et al., 2021e], the minimization of $J(\boldsymbol{\epsilon})$, close to a point $\boldsymbol{\epsilon}^*$ can then be written as a set of bilinear matrix inequalities with a locally linear cost, and solved efficiently by an alternating SDP heuristic. Here, we write a set of constraints which ensure controller feasibility, lower and upper bound the controller parameters in $\boldsymbol{k}_+$, also ensuring that (3.60) holds, as

$$F_1(\boldsymbol{k}_A, k_c, \boldsymbol{\epsilon}) = \boldsymbol{M}_1(\boldsymbol{k}) - \epsilon_1 \boldsymbol{I} \succ \boldsymbol{0}, \tag{3.64a}$$
$$F_2(\boldsymbol{k}_A, k_c, \boldsymbol{\epsilon}) = \epsilon_2 \boldsymbol{I} - \boldsymbol{M}_2(\boldsymbol{k}) \succ \boldsymbol{0}, \tag{3.64b}$$
$$F_3(\boldsymbol{k}_A, k_c, \boldsymbol{\epsilon}) = \boldsymbol{W}(\boldsymbol{k}) - \epsilon_3 \boldsymbol{I} \succ \boldsymbol{0}, \tag{3.64c}$$
$$F_4(\boldsymbol{k}_A, k_c, \boldsymbol{\epsilon}) = \text{diag}(\boldsymbol{k}, \boldsymbol{\epsilon}) \succ \boldsymbol{0}, \tag{3.64d}$$
$$F_5(\boldsymbol{k}_A, k_c, \boldsymbol{\epsilon}) = \text{diag}(\boldsymbol{k}_+) - \text{diag}(\boldsymbol{k}) \succ \boldsymbol{0}. \tag{3.64e}$$

The relaxed tuning problem in (3.59), can then be stated as

$$\min_{(\boldsymbol{k}, \boldsymbol{\epsilon}) \in \mathbb{R}^6} J(\boldsymbol{k}), \quad F_i(\boldsymbol{k}_A, k_c, \boldsymbol{\epsilon}) \succ \boldsymbol{0} \ \ \forall i \in 1, ..., 5. \tag{3.65}$$

Furthermore, when relaxing (3.65) by minimizing the upper bound $J(\boldsymbol{\epsilon})$ in (3.61) (which is tight when (3.60) is tight), then for any $\boldsymbol{\epsilon}$ close to $\boldsymbol{\epsilon}^*$ and fixing $k_c = k_c^*$, the problem is convex in $\boldsymbol{k}_A$ and $\boldsymbol{\epsilon}$, with

$$\min_{(\boldsymbol{k}_A, \boldsymbol{\epsilon}) \in \mathbb{R}^5} J(\boldsymbol{\epsilon}; \boldsymbol{\epsilon}^*), \quad F_i(\boldsymbol{k}_A, k_c^*, \boldsymbol{\epsilon}) \succ \boldsymbol{0} \ \ \forall i \in 1, ..., 5. \tag{3.66}$$

Similarly, linearizing $J(\boldsymbol{\epsilon})$ at $\boldsymbol{\epsilon}^*$ and fixing $\boldsymbol{k}_A = \boldsymbol{k}_A^*$, the problem is locally convex in k_c and $\boldsymbol{\epsilon}$, and can be written

$$\min_{(k_c, \boldsymbol{\epsilon}) \in \mathbb{R}^4} J(\boldsymbol{\epsilon}; \boldsymbol{\epsilon}^*), \quad F_i(\boldsymbol{k}_A^*, k_c, \boldsymbol{\epsilon}) \succ \boldsymbol{0} \ \ \forall i \in 1, ..., 5. \tag{3.67}$$

Consequently, the BMI-problem defined in (3.65), can be solved approximately by sequentially linearizing the upper bound of the objective function, and iterating (3.66) and (3.67). This is referred to as an ASDP heuristic, and outlined in Algorithm 1. These iterations are continued until a numerical tolerance γ_{tol} is reached, or the maximum number of iterations have transpired. To initialize the algorithm, the system inertia, $\boldsymbol{J}$, the upper bound on the attitude errors, ϕ, the tuning weights, w_1 and w_2, and an initial $\boldsymbol{k}_A$ are all required. The algorithm then computes a feasible k_c given by Remarks 3.3 and 3.6, then proceeds to initialize a feasible $\boldsymbol{\epsilon}$, before iterating (3.66) and (3.67) until convergence. Here, the algorithm is implemented with the SDPT3 solver [Toh et al., 1999] called through CVX [Grant and Boyd, 2014] using Matlab.

Receive $\boldsymbol{J}, \phi, w_1, w_2, \boldsymbol{k}_A^{(0)}, \gamma_{tol}, N_{max}$;
Compute feasible $k_c^{(0)}$;
Compute feasible $\boldsymbol{\epsilon}^{(0)}$;
for $i = 1, ..., N_{max}$ **do**
  Linearize the objective function $J(\boldsymbol{\epsilon}; \boldsymbol{\epsilon}^{(i-1)})$;
  Solve (3.66) for $\boldsymbol{k}_A^*, \boldsymbol{\epsilon}_A^*$ with fixed $k_c = k_c^{(i-1)}$;
  Linearize the objective function $J(\boldsymbol{\epsilon}; \boldsymbol{\epsilon}_A^*)$;
  Solve (3.67) for $k_c^*, \boldsymbol{\epsilon}_B^*$ with fixed $\boldsymbol{k}_A = \boldsymbol{k}_A^*$;
  Set $\boldsymbol{k}^{(i)} = (\boldsymbol{k}_A^*, k_c^*)^\top, \boldsymbol{\epsilon}^{(i)} = \boldsymbol{\epsilon}_B^*$;
  if $\|\nabla_{\boldsymbol{\epsilon}} J(\boldsymbol{\epsilon}^{(i)})\| \leq \gamma_{tol}$ **then**
    Return: $\boldsymbol{k}^{(i)}, \boldsymbol{\epsilon}^{(i)}$
  end
end

Algorithm 1: The ASDP algorithm for the robust tuning problem.

Example 3.8
To demonstrate this numerical approach to controller tuning, consider the tuning of the robust controllers in Theorem 3.3 and 3.6 by solving the optimization problem in (3.59) using the ASDP in Algorithm 1. In both cases, an optimal tuning is found with respect to the cost $J(\boldsymbol{k})$ when fixing the smallest eigenvalue of the inertia at $\lambda_m(\boldsymbol{J}) = 0.1$ while varying its largest eigenvalue $\lambda_M(\boldsymbol{J}) \in [0.1, 1]$ and the initial attitude error $\phi \in [0.1, 1.99]$.

The parameters are constrained by $\boldsymbol{k}_+ = (5;\ 5;\ 5)$ and the weights are chosen as $w_1 = 1$ and $w_2 = 0.6$, corresponding to a problem considered with an initial error of $\|\boldsymbol{z}(t_\circ)\| \leq 1$ over $t_f - t_\circ = 60$ [s] with a parameter $\epsilon_X = \epsilon_R = 0.01$. It is verified that the convergence criteria in Algorithm 1 is met (typically in five to eight ASDP iterations), with the inequalities in (3.60) being tight to the numerical tolerances. A total of 400 combinations of $\lambda_M(\boldsymbol{J})$ and ϕ are considered for each controller, and in all cases, the gains $\{k_R, k_X\}$ converge to the upper bound defined by $\boldsymbol{k}_+$. As such, only the results for k_c, k_ω, and cost $J(\boldsymbol{k})$ are shown in Figure 3.15.

From this numerical study, we note that the optimal controller gains $\boldsymbol{k}$ vary little in ϕ, but change significantly with the difference $\lambda_M(\boldsymbol{J}) - \lambda_m(\boldsymbol{J})$. In general, when tuning the robust controllers, one should attempt to maximize k_R, and choose a $k_\omega \approx k_R$ when $\lambda_M(\boldsymbol{J}) - \lambda_m(\boldsymbol{J}) = 0$, and decrease k_ω as $\lambda_M(\boldsymbol{J}) - \lambda_m(\boldsymbol{J})$ increases. The cross-term k_c should be chosen relatively small even as $\lambda_M(\boldsymbol{J}) \approx \lambda_m(\boldsymbol{J})$, and should also decrease slightly as $\lambda_M(\boldsymbol{J}) - \lambda_m(\boldsymbol{J})$ increases. For both controllers, it is advised to make k_R or k_X as large as the noise levels and actuators permit, and then choose k_ω smaller and k_c significantly smaller, both decreasing with $\lambda_M(\boldsymbol{J}) - \lambda_m(\boldsymbol{J})$ regardless of ϕ. □

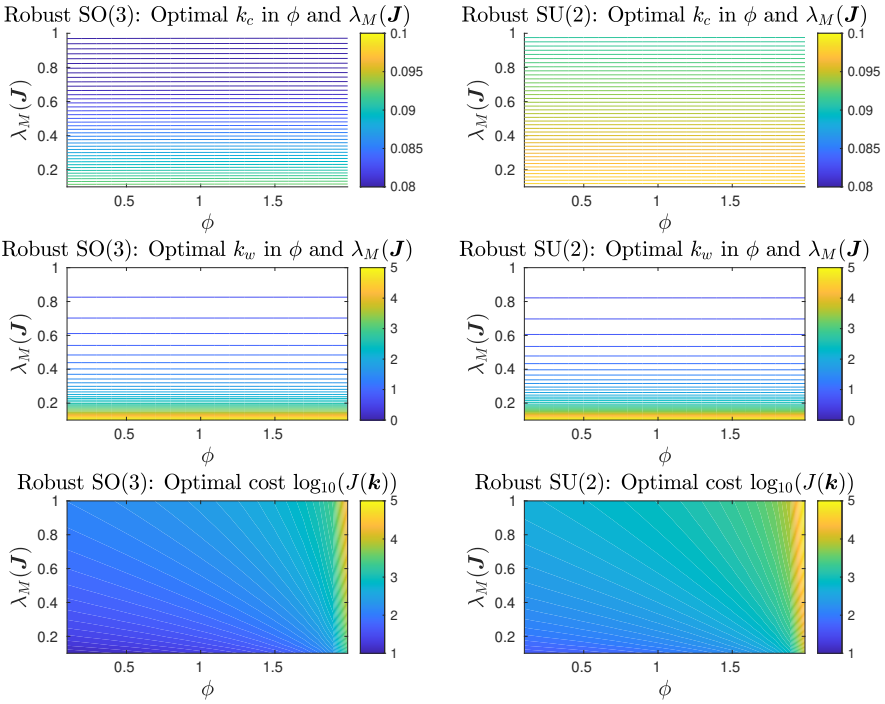

Figure 3.15 Example of an optimal tuning for the robust controllers in Theorem 3.3 (left) and in Theorem 3.6 (right). *Top:* Optimally tuned k_c as a function of $(\phi, \lambda_M(\boldsymbol{J}))$. *Center:* Optimally tuned k_ω as a function of $(\phi, \lambda_M(\boldsymbol{J}))$. *Bottom:* Optimal cost $J(\boldsymbol{k})$ as a function of $(\phi, \lambda_M(\boldsymbol{J}))$.

This example demonstrates that the optimal tuning of the robust controllers depends greatly on the inertia, and less on the initial attitude error. In contrast, the cost depends on both $\boldsymbol{J}$ and ϕ, exploding for both controllers as $\phi \to 2$ (as then the worst-case decay rate approaches zero), but also increasing significantly with $\lambda_M(\boldsymbol{J})$ for fixed $\lambda_m(\boldsymbol{J})$. Despite being similar, the generally higher cost for the controller on SU(2) indicates that a bound of $k_R \leq 5$ and $k_X \leq 5$ could might mean very different things. Indeed, a cost expressed in $\boldsymbol{z}$ defined with $\boldsymbol{e_R}$ on SO(3) is fundamentally different to a cost expressed in $\boldsymbol{z}$ defined with $\boldsymbol{e_X}$ on SU(2), making a direct comparison difficult. To clarify how the controllers are related and what might constitute a fair comparison, their similarities and differences are highlighted in Sec. 3.9.

3.9 Similarities and Differences

At this point, it is clear that there exist many good solutions to Problem 3.1, and several such controllers are presented and demonstrated in various numerical examples. It is also evident that many of the controllers on SU(2) are similar to those on SO(3); yet, their subtle differences have meaningful consequences when considering a real-time implementation.

Controllers on SO(3) To recapitulate, a slight generalization of the controllers in [Chaturvedi et al., 2011] is given in Theorem 3.1. Importantly, two cases are considered: one in which the matrix $\boldsymbol{M} = \sum_{i=1}^{N} k_i \boldsymbol{v}_i \boldsymbol{v}_i^\top$ has a distinct spectrum, and one in which all of its eigenvalues are equal. While the property of UAGAS (as defined in this thesis) is lost in the latter, this makes little practical difference. The former description becomes interesting when considering the design of (filtered) output feedback laws with directional measurements, as the controller can be realized by a set of measured rotated vectors instead of direct knowledge of $\boldsymbol{R}$. The controller in Theorem 3.1 is closely related to the popular geometric controllers in [Lee et al., 2011], derived with respect to the Ψ-distance, and summarized in Theorem 3.2. Indeed, Theorem 3.1 parameterizes controller in Theorem 3.2, as evident from Remark 3.1, but the latter comes with a very different stability proof permitting an extension to a robust controller in [Lee et al., 2013], here summarized in Theorem 3.3. In particular, this last controller should be considered in favor of the others when there is reason to suspect significant load disturbances.

Controllers on SU(2) A completely analogous set of controllers is derived on SU(2) in [Greiff et al., 2021f], here included to illustrate exactly how the controllers on SO(3) relate to those on SU(2). From the discussion in Remark 3.7, several PD-controllers based on imaginary quaternion errors can be interpreted as geometric controllers on SU(2) with respect to the distance Γ in Definition 2.19, but the proof provided here shows ULES and UAGAS. By the proofs construction, a partition of SU(2) can be made to construct a discontinuous feedback law, recovering the attitude controllers in [Mayhew et al., 2011a; Brescianini and D'Andrea, 2018] and showing GES. Importantly, due to the construction of the proof, a robustness result is made possible in Theorem 3.6, completely analogous to that in Theorem 3.3. All of these controllers can be used to great effect in a real-time implementation, but caution must be taken when implementing Theorem 3.4 and 3.6, as these may give rise to dynamical unwinding, as described in Remark 3.5, if the reference trajectory and estimated attitudes are not computed with care.

Local Behavior When considering the tuning and comparison of controllers on SO(3) and SU(2), it is relevant to ask if it is fair to bound the controller gains in the same way, given that the attitude errors are fun-

damentally different. To investigate this, consider a parameterization of all $\boldsymbol{q} \in \mathbb{H}$ by a double angle $\theta \in [-\pi, \pi]$ and a normal vector $\boldsymbol{u} \in \mathbb{R}^3$, such that $\Re(\boldsymbol{q}) = \cos(\theta)$ and $\Im(\boldsymbol{q}) = \sin(\theta)\boldsymbol{u}$. If $\boldsymbol{R}_r^\top \boldsymbol{R} = E^{\mathbb{H}}_{\mathrm{SO}(3)}(\boldsymbol{q})$ and $\boldsymbol{X}_r^* \boldsymbol{X} = E^{\mathbb{H}}_{\mathrm{SU}(2)}(\boldsymbol{q})$, For the attitude control error in Theorems 3.2 and 3.3, we then get $\boldsymbol{e}_{\boldsymbol{R}} = 2\cos(\theta)\sin(\theta)\boldsymbol{u} = \sin(2\theta)\boldsymbol{u}$. Similarly, for the attitude error in Theorems 3.4, 3.5, and 3.6, we obtain $\boldsymbol{e}_{\boldsymbol{X}} = (1/2)\sin(\theta)\boldsymbol{u}$. As such,

$$\sup_{\boldsymbol{R}_r \in \mathrm{SO}(3), \boldsymbol{R} \in \mathrm{SO}(3)} \|\boldsymbol{e}_{\boldsymbol{R}}\| = 1, \qquad \sup_{\boldsymbol{X}_r \in \mathrm{SU}(2), \boldsymbol{X} \in \mathrm{SU}(2)} \|\boldsymbol{e}_{\boldsymbol{X}}\| = \frac{1}{2}. \tag{3.68}$$

From this, we can make two important observations:

- if we wish to find a tuning for the controllers on SO(3) and SU(2) that gives the same maximal contribution to the control signal torque over all possible attitude errors, then we should find a tuning where $k_X = 2k_R$;
- however, if they are to yield similar local decay in the errors, we should instead compare the controllers when tuned such that $k_X = 4k_R$. This can be seen in that $k_R \boldsymbol{e}_{\boldsymbol{R}} \approx 2k_R\theta$ and $k_X \boldsymbol{e}_{\boldsymbol{X}} \approx (1/2)k_X\theta$ for small θ.

This last point is also evident from the local linearizations conducted about $(\boldsymbol{R}_e, \boldsymbol{e}_{\boldsymbol{\omega}}) = (\boldsymbol{I}, \boldsymbol{0})$ and $(\boldsymbol{X}_e, \boldsymbol{e}_{\boldsymbol{\omega}}) = (\boldsymbol{I}, \boldsymbol{0})$ in the proofs of Theorems 3.1 and 3.4, respectively. When writing out the same linearization for the geometric controller on SO(3), and using the equivalence in Remark 3.1, we obtain a second-order system in (B.19) and (B.68), with a damping term $\mathcal{K} = k_R \boldsymbol{I}$ for the geometric controllers on SO(3), whereas the geometric controllers on SU(2) yield a damping term of $\mathcal{K} = (k_X/4)\boldsymbol{I}$. A takeaway from this insight is that if considering similar magnitude of the attitude corrections in the SO(3) and SU(2) controllers, such that $k_X = 2k_R$, then the controllers on SO(3) yields a faster local decay of the errors and give a greater "bang for the buck".

Large Initial Errors One the other hand, if the initial attitude errors are expected to be large, we note that a complete covering of SU(2) can be achieved with a worst case decay rate characterized by $\phi = 1$ using Theorem 3.5. The corresponding geometric controllers in SO(3) are UAS, but the worst-case decay rate becomes arbitrarily small as $\phi \to 2$ for finite k_R. This becomes relevant in practical applications pertaining to UAV control. Here, the system is often initialized on a flat surface with the reference trajectory set to move it upward in a take-off maneuver, where then approximately $\boldsymbol{R}_r(t_\circ)\boldsymbol{e}_3 \| \boldsymbol{e}_3$, $\boldsymbol{R}(t_\circ)\boldsymbol{e}_3 \| \boldsymbol{e}_3$, and where typically $\boldsymbol{e}_{\boldsymbol{\omega}}(t_\circ)$ is small. In this case, a rotation of the reference system relative to the physical system of an angle π about $\boldsymbol{e}_3$ yields $\|\boldsymbol{e}_{\boldsymbol{R}}(t_\circ)\| \approx 0$, and potentially slow convergence of the tracking errors if implementing the geometric continuous or robust controllers on SO(3). On the other hand, for the controllers on SU(2), the same initial configuration yields

$\|\boldsymbol{e_X}(t_\circ)\| \approx 1/2$, attaining its theoretical maximum in this configuration, as described in (3.68). The takeaway is that for large initial attitude errors, it is generally favorable to implement the SU(2)-configured controllers.

The Robust Controllers It may seem like the robust controllers are favorable at all times. As Example 3.6 clearly demonstrates, this is certainly true if only considering a continuous deterministic load disturbance. However, when introducing measurement noise, these controllers may result in a volatile control signal that may exhibit a ringing behavior for small errors $\boldsymbol{e}_A$. This can be particularly problematic if the torques are generated by rotors, and can cause significant wear and tear on the hardware. In such scenarios, the tuning parameters $\{\epsilon_R, \epsilon_X\}$ can be increased, or the corresponding geometric controller on SO(3) or SU(2) should be considered instead. In Example 3.7, it was shown that the former can yield asymptotic errors which are orders of magnitude lower than the corresponding geometric controller. However, when increasing $\{\epsilon_R, \epsilon_X\}$, the sufficient condition for the distance $\{\Psi, \Gamma\}$ to remain small is violated. As these distances can be measured actively in the implementation, it is relatively simple to implement continuous geometric controllers in Theorem 3.2 and Theorem 3.4, that switch on the $\{\boldsymbol{\mu_R}, \boldsymbol{\mu_X}\}$-terms for a larger $\{\epsilon_R, \epsilon_X\}$ and monitors the associated distance $\{\Psi, \Gamma\}$, switching back in the unlikely event that the distances exceed a predefined ϕ.

3.10 Summary

In this chapter, the problem of attitude tracking control has been discussed extensively. The reason for giving such attention to Problem 3.1 is that its solutions are instrumental in designing control laws for the full UAV dynamics. These solution often form the inner-most controllers in cascaded controller approaches, and the presented results will be used in the remainder of Part I.

To summarize, various controllers on SO(3) were considered, starting with a slight generalization of [Chaturvedi et al., 2011, Theorem 2] as summarized in Theorem 3.1. The popular controller in [Lee et al., 2010, Proposition 1] was then reviewed, here summarized in Theorem 3.2. In doing so, it was shown that the latter represents a subset of the controllers parameterized by the former. However, the method of proof employed in Theorem 3.2 gave rise to bounds on the Lyapunov function that became highly informative for the tuning problem. These bounds were used to give an estimate of the ultimate bound in Proposition 3.1, and also facilitated the derivation of a robust controller in [Lee et al., 2013, Proposition 2], as summarized in Theorem 3.3.

Following this, a distance on SU(2) was introduced, where similar methods were used to find three analogous controllers in [Greiff et al., 2021f], including:

- A continuous controller with UAGAS and ULES properties and known decay rates for domains parameterized in ϕ (see Theorem 3.4);
- A discontinuous controller with GES properties (see Theorem 3.5);
- A robust feedback law on SU(2) with an estimate of a uniform ultimate bound for continuous and bounded load disturbances (see Theorem 3.6).

In doing so, several PD-like controllers in imaginary quaternion errors were recovered, both by the continuous and discontinuous controllers (see Remark 3.7). However, their stability proofs also facilitated a fruitful discussion on robustness to a realistic class of load disturbances, with the robust controller in Theorem 3.6, analogous to its counterpart on SO(3) in Theorem 3.3.

Additionally, a tuning method was presented based on relaxed BMIs [Greiff et al., 2021e], facilitating a theoretical comparison of the various controllers in Sec. 3.9, as well as tuning guidelines supported by these numerical results. The main takeaways from this discussion on controller tuning were that:

- Compared to the controllers on SU(2), the controllers on SO(3) give comparatively large corrections for small errors when constraining the controllers to yield an equal contribution to the torque control signal;
- There exist realistic physical initial error configurations in which the attitude errors on SO(3) are close zero, whereas the attitude errors on SU(2) are maximized;
- The robust versions of the controllers should be considered for tracking problems with bounded load disturbances, but the controller gains then need to be chosen with care in the presence of measurement noise.

In conclusion, we propose that the controller be chosen based on the shape of the set of possible initial attitude errors, specifically with reference to the magnitude of the initial errors characterized by ϕ. More generally, we suggest using the SU(2)-controllers when the attitude tracking errors are assumed to be large, and the SO(3)-controllers when they are assumed to be small, as the latter gives more "bang for the buck" when in close proximity to a zero tracking error. Furthermore, we suggest a tuning based on the intuition presented in Sec. 3.9, or a direct solution of the associated bilinear matrix inequality program, and that the controllers be compared and evaluated in simulation for the specific system to be controlled before conducting a real-time implementation. To facilitate this comparison, and to simplify their use in experiments, the controllers were coded in C and published open-source on CodeOcean and in the Julia package AerialVehicleControl.jl [Greiff, 2020].

4

Full State Feedback: UAV dynamics

4.1 Introduction

In this chapter, the previous results on trajectory tracking control for attitude dynamics are used to construct feedback laws for the full UAV dynamics. In the following, consider a description of the UAV dynamics with the translation velocities defined with respect to the global frame $\{\mathcal{G}\}$, as summarized in (2.19c)-(2.19f). The objective is to control this system, here restated as

$$\Sigma \; : \; \begin{cases} \Sigma^p \; : \; \begin{cases} \dot{\boldsymbol{p}} &= \boldsymbol{v} \\ m\dot{\boldsymbol{v}} &= -mg\boldsymbol{e}_3 + f\boldsymbol{R}\boldsymbol{e}_3 \end{cases} \\ \Sigma^a \; : \; \begin{cases} \dot{\boldsymbol{R}} &= \boldsymbol{R}\boldsymbol{S}(\boldsymbol{\omega}) \\ \boldsymbol{J}\dot{\boldsymbol{\omega}} &= \boldsymbol{S}(\boldsymbol{J}\boldsymbol{\omega})\boldsymbol{\omega} + \boldsymbol{\tau} \end{cases} \end{cases}, \tag{4.1}$$

along the trajectories of a reference system that obeys the same dynamics,

$$\Sigma_r \; : \; \begin{cases} \Sigma_r^p \; : \; \begin{cases} \dot{\boldsymbol{p}}_r &= \boldsymbol{v}_r \\ m\dot{\boldsymbol{v}}_r &= -mg\boldsymbol{e}_3 + f_r\boldsymbol{R}_r\boldsymbol{e}_3 \end{cases} \\ \Sigma_r^a \; : \; \begin{cases} \dot{\boldsymbol{R}}_r &= \boldsymbol{R}_r\boldsymbol{S}(\boldsymbol{\omega}_r) \\ \boldsymbol{J}\dot{\boldsymbol{\omega}}_r &= \boldsymbol{S}(\boldsymbol{J}\boldsymbol{\omega}_r)\boldsymbol{\omega}_r + \boldsymbol{\tau}_r \end{cases} \end{cases}, \tag{4.2}$$

when assuming full knowledge of the states $(\boldsymbol{x}, \boldsymbol{v}, \boldsymbol{R}, \boldsymbol{\omega}) \in \mathbb{R}^3 \times \mathbb{R}^3 \times \mathrm{SO}(3) \times \mathbb{R}^3$. It should be noted that this assumption of full state information is typically violated in real-time implementations, which generally require the estimation of the states in Σ from available measurements. In contrast to Chapter 3, we do not explicitly consider additive input disturbances in the problem formulation, instead opting to study the control system as sketched in Figure 4.1.

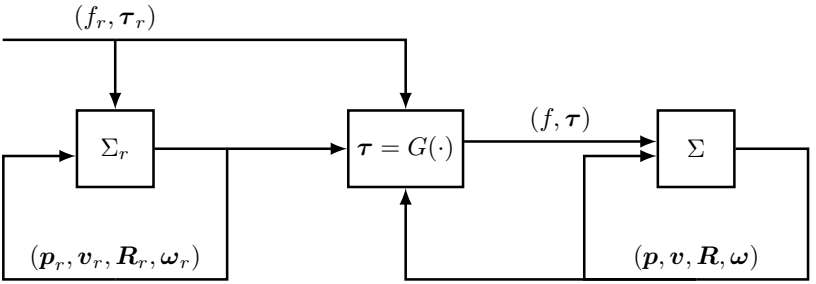

Figure 4.1 Sketch of a full state feedback, G, for the UAV dynamics, Σ, which is to follow a trajectory characterized by a reference system, Σ_r.

Given that the UAV translation dynamics in Σ^p behaves as a double integrator in $\mathbb{R}^3$, it is relatively easy to construct a stabilizing feedback law, with the exception of the input constraint that depends on $\boldsymbol{R}$. An example is a simple proportional-derivative (PD) feedback law in the translation dynamics, resulting in a desired force $\boldsymbol{f}_d \in \mathbb{R}^3$ defined in the global frame. To actuate Σ^p with this desired force, the UAV must be oriented in a specific manner. For the purpose of designing such controllers, we recall the results on attitude control derived in Chapter 3. Consider the computation of a so-called *desired attitude reference trajectory*, here sub-indexed $(\cdot)_d$. Noting that the attitude subsystem Σ^a can be actuated along any feasible reference trajectory satisfying the attitude dynamics, the controller can be constructed by computing a trajectory $(\boldsymbol{R}_d, \boldsymbol{\omega}_d, \dot{\boldsymbol{\omega}}_d) \in \mathrm{SO}(3) \times \mathbb{R}^3 \times \mathbb{R}^3$ satisfying the same dynamics as Σ^a_r, and that asymptotically converges to $(\boldsymbol{R}_r, \boldsymbol{\omega}_r, \dot{\boldsymbol{\omega}}_r) \in \mathrm{SO}(3) \times \mathbb{R}^3 \times \mathbb{R}^3$. This basic intuition will guide the forthcoming developments, and the problem of designing a full state feedback is formulated concisely as follows.

Problem 4.1
Consider a system with a state $\boldsymbol{x} = (\boldsymbol{p}, \boldsymbol{v}, \boldsymbol{R}, \boldsymbol{\omega}) \in \mathbb{R}^3 \times \mathbb{R}^3 \times \mathrm{SO}(3) \times \mathbb{R}^3$, with an associated reference trajectory $\boldsymbol{x}_r = (\boldsymbol{p}_r, \boldsymbol{v}_r, \boldsymbol{R}_r, \boldsymbol{\omega}_r) \in \mathbb{R}^3 \times \mathbb{R}^3 \times \mathrm{SO}(3) \times \mathbb{R}^3$, driven by $(f, \boldsymbol{\tau}) \in \mathbb{R}_{\geq 0} \times \mathbb{R}^3$ and $(f_r, \boldsymbol{\tau}_r) \in \mathbb{R}_{\geq 0} \times \mathbb{R}^3$, respectively, evolving by the UAV dynamics in (4.1) and (4.2), respectively. Assume that the state $\boldsymbol{x}$ is known and design a feedback law, G, such that $\boldsymbol{x} \to \boldsymbol{x}_r$ as $t \to \infty$, and characterize the stability properties of the closed-loop system. □

4.1.1 Chapter Motivation

Due to the wide interest in UAVs within the research community and the industry alike, a variety of tools from control theory have been used to construct full state feedback solutions to Problem 4.1. The very simplest solutions include proportional-integral-derivative (PID) controllers with errors expressed in positions and Euler angles (see, e.g., [Bouabdallah et al., 2004; Luukkonen,

2011; Garcia et al., 2012]). Such approaches can be analyzed and tuned with respect to a linearized system model, but they can also be implemented and tuned directly on the physical system. This explains the popularity of the PID controller in practical applications, such as the Crazyflie and the PixHawk PX4 flight controllers [Bitcraze, 2021a; PixHawk, 2021]. Slightly more advanced approaches that make direct use of the linearized system dynamics include the linear quadratic regulators (LQR) (see, e.g., [Antsaklis and Michel, 2006]), where a stabilizing linear feedback law is found to achieve linear quadratic performance objective. Such controllers were developed for UAVs in [Bouabdallah et al., 2004] and demonstrated in practice with UAVs in [How et al., 2008]. This family of controllers can be generalized to state-dependent LQR, where the system is re-linearized and the associated optimization problem is solved online. Recent results for UAVs demonstrating significant agility are found in [Foehn and Scaramuzza, 2018]. The closely related approach of model predictive control (MPC) involves solving an optimization problem online over a moving horizon (see,e.g., [Garcia et al., 1989]). Similar to the LQR approaches, the linear MPC has been applied to the problem of quadrotor tracking, with experimental results in [Bouffard et al., 2012], and extensions to nonlinear MPC-approaches in [Kaufmann et al., 2020], demonstrating impressive complex maneuvers. For a recent survey, see e.g. [Kim et al., 2019].

Due to the high rates at which the measurements are sampled, it is not uncommon to implement the UAV controllers at rates of 500-1000 [Hz]. Consequently, stabilizing or tracking controllers are often implemented directly on the processor of the UAV, which then comes with constraints on the available computational power. While the computationally light linear feedback laws can be implemented on smaller UAVs, they lack global stability properties. In contrast, the more advanced methods such as state-dependent LQR in [Foehn and Scaramuzza, 2018] and nonlinear MPC in [Kaufmann et al., 2020] require significant computational resources. For large angle maneuvers with controllers implemented directly on the processor of the UAV, it becomes interesting to study simple feedback laws derived using the tools of nonlinear control theory. Many such controllers are memory-less (unless integral action is introduced), require few computations, and come with rigorous stability guarantees. For UAVs, such methods include the dynamic feedback linearization in [Mokhtari and Benallegue, 2004], the back-stepping control approaches in [Das et al., 2009; Huang et al., 2010; Chen et al., 2016], and the sliding-mode control in [Merheb et al., 2015]. For a relevant survey, see, e.g., [Mo and Farid, 2019].

The above nonlinear control approaches come with certain drawbacks. For instance, control systems based on dynamic feedback linearization tend to be sensitive to modeling errors. While applied to control a quadrotor UAV in [Lee et al., 2009], such approaches are often found in combination with of linear robust controllers. For instance, the work of [Ryan and Kim, 2013] addresses this problem by a secondary $\mathcal{H}_\infty/\mathcal{H}_2$-performance objective

relating to errors in the feedback linearization. The sliding mode control approaches can give rise to chattering effects which may be prohibitive in real-time implementations, and the back-stepping methods tend to become extremely involved, making real-time implementations a challenging prospect. As an alternative, simple yet powerful nonlinear geometric feedback laws can be derived using the results in Chapter 3 and Lyapunov theory, leveraging algebraic properties of the configuration manifolds in the controller design.

To this latter category of controllers, we count the seminal work in [Lefeber et al., 2017], which shows UAGAS and ULES for the UAV system configured on $\mathrm{SO}(3) \times \mathbb{R}^3$ using Lyapunov theory and cascade theorems, starting from a variation of the attitude controller in Theorem 3.1. We also consider the geometric control approaches in [Lee et al., 2010; Mellinger et al., 2012; Goodarzi et al., 2013; Lee et al., 2013; Lee, 2015] for systems on $\mathrm{SO}(3) \times \mathbb{R}^3$, based on the controllers in Theorem 3.2 and 3.3. Similar controllers include those developed for $\mathbb{H} \times \mathbb{R}^3$ in [Brescianini et al., 2013; Brescianini and D'Andrea, 2018], based on variations of the attitude controllers in Theorem 3.4 and 3.5. These works present powerful controllers leveraging the solutions in Chapter 3, and directly address Problem 4.1. Their implementations are computationally light, and yield global or almost global closed-loop stability or attractiveness properties of the tracking errors in an idealized setting (without disturbances and noise). When combined with reference generation utilizing differential flatness, the tracking performance of such control systems rivals the state of the art nonlinear MPC approaches (see [Sun et al., 2021]).

Given this introduction to nonlinear UAV control, we stress that Problem 4.1 is solved when considered in the idealized setting with full state information. Consequently, we discuss how these controllers are related, highlighting considerations that need to be made when considering a real-time implementation, and demonstrate how they can be used to perform large-angle maneuvers in practice. We stress that all of the controllers presented in this chapter require full state information. When combined with an independently designed estimator, this introduces additional memory and dynamics which may lead to instability. Recall, the cascade of two stable systems, in this case the tracking error dynamics and the estimation error dynamics, need not be stable unless stringent conditions on the systems and their interconnection are satisfied (see Sec. 2.5). Despite this, the controllers in this chapter work exceptionally well in practice, as the forthcoming examples will demonstrate.

4.1.2 Contributions

In this chapter, we demonstrate how the attitude controllers from Chapter 3 can be leveraged to control the full UAV dynamics in the form stated in (4.1). In particular, we focus on the continuous geometric attitude controller on $\mathrm{SO}(3)$ and its counterpart on $\mathrm{SU}(2)$. These results and their extensions to the

UAV dynamics are considered the state of the art for nonlinear UAV control. A new stability proof for continuous and discontinuous controllers on $\mathrm{SU}(2) \times \mathbb{R}^3$ is given, following the same geometric ideas in [Lee et al., 2010]. This should be seen as a minor contribution, as tangential results have been given in different notations in [Brescianini et al., 2013; Brescianini and D'Andrea, 2018]. But it is worth noting that these last two works do not provide a complete stability proofs for the positional and attitude tracking errors, which are given in this chapter. While we seek to clarify how the controllers are related, the main contribution of this chapter lies in the discussion of the considerations that are required in a real-time implementation, and subsequent demonstration of the presented controllers both in simulation and in practice.

4.1.3 Overview

We start by presenting the geometric controller on $\mathrm{SO}(3) \times \mathbb{R}^3$ in [Lee et al., 2010]. This is done in Sec. 4.2, commenting on considerations than need to be made when implementing the controller in real-time. This is followed by the presentation of an analogous result on $\mathrm{SU}(2) \times \mathbb{R}^3$ in Sec. 4.3. Both controllers are demonstrated in simulation examples, followed by two real-time examples in Sec. 4.4. The summary in 4.5 concludes the chapter, highlighting the benefits and drawbacks of using the proposed controllers. To give an overview of the chapter, the results and examples are summarized in Table 4.1.

Table 4.1 Overview of the results and examples of Chapter 4. Here, [1] indicates work of others, proofs given elsewhere; [2] indicates work tangential with others, but with independent proofs given; and [3] indicates new work.

Reference	Description
Prop. 4.1 [1]	Continuous geometric control on $\mathrm{SO}(3) \times \mathbb{R}^3$, originally in [Lee et al., 2010, Prop. 3]
Prop. 4.2 [1]	Asymptotic attractiveness result associated with Prop. 4.1, given in [Lee et al., 2010, Prop. 4]
Prop. 4.3 [2]	Continuous and discontinuous geometric control on $\mathrm{SU}(2) \times \mathbb{R}^3$, not yet published elsewhere
Prop. 4.4 [2]	Asymptotic attractiveness result associated with Prop. 4.3, not yet published elsewhere
Example 4.1	Simulation example with Prop. 4.1, circular maneuver
Example 4.2	Simulation example with Prop. 4.3, looping on a torus
Sec. 4.4.1	Real-time example with Prop. 4.3, spiraling maneuver
Sec. 4.4.2	Real-time example with Prop. 4.3, supermarket inventorying

4.2 Geometric Control on $\mathbf{SO(3)} \times \mathbb{R}^3$

A rigorous solution to Problem 4.1 is given in [Lee et al., 2010] and with more detail in [Lee et al., 2011]. This controller is here stated for the UAV dynamics as defined in (4.1). The main difference is that the force, f, is positive along $\boldsymbol{b}_3$ (instead of being positive along $-\boldsymbol{b}_3$ as assumed in [Lee et al., 2010; Lee et al., 2011]). A set of translation control errors are defined in $\boldsymbol{e_p} = \boldsymbol{p} - \boldsymbol{p}_r \in \mathbb{R}^3$ and $\boldsymbol{e_v} = \boldsymbol{v} - \boldsymbol{v}_r \in \mathbb{R}^3$. Combined with the reference acceleration, these errors can be used to compute a desired force in $\{\mathcal{G}\}$, as

$$\boldsymbol{f}_d = -k_p \boldsymbol{e_p} - k_v \boldsymbol{e_v} + mg\boldsymbol{e}_3 + m\ddot{\boldsymbol{p}}_r. \tag{4.3}$$

As the considered system Σ in (4.1) is only capable of generating forces along the $\boldsymbol{b}_3$-direction, its attitude needs to be controlled to a desired attitude, $\boldsymbol{R}_d(t) \in \mathrm{SO}(3)$, which transiently may differ from $\boldsymbol{R}_r(t) \in \mathrm{SO}(3)$ when correcting for the errors in $\boldsymbol{e_p}$ and $\boldsymbol{e_v}$. Consider expressing this attitude in terms a set of desired body basis vectors $\boldsymbol{b}_{d,i} \in \mathbb{R}^3$, forming a desired body frame $\{\mathcal{B}_d\}$. It is clear that $\boldsymbol{b}_{d,3} = \boldsymbol{f}_d / \|\boldsymbol{f}_d\|$, but the final degree of freedom can be fixed in many ways. Three such examples are given below, where:

(i) the body basis vector $\boldsymbol{b}_{d,1}$ is provided explicitly;

(ii) the body basis vector $\boldsymbol{b}_{d,1}$ is computed from $\boldsymbol{R}_r$;

(iii) the body basis vector $\boldsymbol{b}_{d,1}$ is defined with respect to $\boldsymbol{b}_{d,3}$.

In the second case, (ii), the desired body direction can be computed through a sequence of projections as outlined in [Lee et al., 2010], where

$$\boldsymbol{b}_{d,1} = -\frac{1}{\|\boldsymbol{b}_{d,3} \times \boldsymbol{b}_{r,1}\|}(\boldsymbol{b}_{d,3} \times (\boldsymbol{b}_{d,3} \times \boldsymbol{b}_{r,1})). \tag{4.4}$$

This permits a construction of the desired rotation, desired attitude rate and desired attitude rate time-derivative for case (i) and case (ii), as

$$\boldsymbol{R}_d = \begin{bmatrix} \boldsymbol{b}_{d,1} & (\boldsymbol{b}_{d,3} \times \boldsymbol{b}_{d,1}) & \boldsymbol{b}_{d,3} \end{bmatrix} \in \mathrm{SO}(3), \tag{4.5a}$$

$$\boldsymbol{\omega}_d = [\boldsymbol{R}_d^\top \dot{\boldsymbol{R}}_d]^\vee_{\mathrm{SO}(3)} \in \mathbb{R}^3, \tag{4.5b}$$

$$\dot{\boldsymbol{\omega}}_d = [\dot{\boldsymbol{R}}_d^\top \dot{\boldsymbol{R}}_d + \boldsymbol{R}_d^\top \ddot{\boldsymbol{R}}_d]^\vee_{\mathrm{SO}(3)} \in \mathbb{R}^3. \tag{4.5c}$$

Alternatively, in the case (iii), the element $\boldsymbol{R}_A = \mathrm{Exp}_{\mathrm{SO}(3)}([\boldsymbol{a}]^\wedge_{\mathrm{SO}(3)}) \in \mathrm{SO}(3)$ that minimizes the rotational angle $\|\boldsymbol{a}\|$, and aligns $\boldsymbol{f}_d$ and $\boldsymbol{e}_3$ in the sense that $\boldsymbol{b}_{d3} \triangleq (b_1;\ b_2;\ b_3) = \boldsymbol{R}_A \boldsymbol{e}_3$, can be expressed in $\boldsymbol{b}_{d3}$ as

$$\boldsymbol{R}_A = \begin{bmatrix} 1 - \frac{b_1^2}{1+b_3} & -\frac{b_1 b_2}{1+b_3} & b_1 \\ -\frac{b_1 b_2}{1+b_3} & 1 - \frac{b_2^2}{1+b_3} & b_2 \\ -b_1 & -b_2 & b_3 \end{bmatrix} \in \mathrm{SO}(3), \tag{4.6}$$

which may subsequently be combined by a rotation

$$\boldsymbol{R}_B = \begin{bmatrix} \cos(\psi_r) & -\sin(\psi_r) & 0 \\ \sin(\psi_r) & \cos(\psi_r) & 0 \\ 0 & 0 & 1 \end{bmatrix} \in \mathrm{SO}(3). \tag{4.7}$$

The desired rotation can then be formed as $\boldsymbol{R}_d = \boldsymbol{R}_A \boldsymbol{R}_B \in \mathrm{SO}(3)$. This is the same idea as used in computing the desired quaternion in [Brescianini and D'Andrea, 2018], where an angle $\alpha = \mathrm{atan2}(\sqrt{f_{d1}^2 + f_{d2}^2}, f_{d3})$ defines

$$\boldsymbol{n} = \frac{1}{\sqrt{f_{d1}^2 + f_{d2}^2}} \begin{bmatrix} -f_{d2} \\ f_{d1} \\ 0 \end{bmatrix}, \quad \boldsymbol{q}_A = \begin{bmatrix} \cos(\frac{\alpha}{2}) \\ n_1 \sin(\frac{\alpha}{2}) \\ n_2 \sin(\frac{\alpha}{2}) \\ n_3 \sin(\frac{\alpha}{2}) \end{bmatrix}, \quad \boldsymbol{q}_B = \begin{bmatrix} \cos(\frac{\psi_r}{2}) \\ 0 \\ 0 \\ \sin(\frac{\psi_r}{2}) \end{bmatrix}, \tag{4.8}$$

forming the desired quaternion $\boldsymbol{q}_d = \boldsymbol{q}_A \odot \boldsymbol{q}_B$. Here, it is simple to verify that $\boldsymbol{R}_A \boldsymbol{R}_B = E^{\mathbb{H}}_{\mathrm{SO}(3)}(\boldsymbol{q}_A \odot \boldsymbol{q}_B)$ through the embedding in Definition 2.17, and it should be noted that $\boldsymbol{q}_A$ in (4.8) is undefined as $\boldsymbol{b}_{d3} \| \boldsymbol{e}_3$, unlike $\boldsymbol{R}_A$ in (4.6), which is only undefined as $\boldsymbol{b}_{d3} \cdot \boldsymbol{e}_3 = -1$.

Remark 4.1
While the approach to computing the reference rotation in (ii) is undefined when $\boldsymbol{b}_{d,3} \| \boldsymbol{b}_{r,1}$, the approach in (iii) is only undefined as $\boldsymbol{b}_{d,3} = -\boldsymbol{e}_3$. As such, both approaches contain singularities which need to be dealt with in an implementation, and the system may exhibit significant volatility close to these points. Apart from considering highly extreme maneuvers, this generally does not pose any problems in practice. However, if a trajectory is planned such that $\boldsymbol{b}_{d,3} \neq -\boldsymbol{e}_3$ and $\boldsymbol{b}_{d,3} \| \boldsymbol{b}_{r,1}$, then it may instead be favorable to compute the desired rotation by integration on SO(3). Instead of considering the alignment of $\boldsymbol{b}_{d,3}(t)$ and $\boldsymbol{e}_3$ at a time t, we can in the same way consider the alignment of $\boldsymbol{b}_{d,3}(t)$ and $\boldsymbol{b}_{d,3}(t-h)$ in an element $\delta\boldsymbol{R}(t)$ as pointed out in [Greiff and Robertsson, 2018], letting $\boldsymbol{R}_A(t) = \delta\boldsymbol{R}(t)\boldsymbol{R}_A(t-h)$, where then

$$\boldsymbol{b}_{d,3}(t) = \delta\boldsymbol{R}(t)\boldsymbol{b}_{d,3}(t-h) = \delta\boldsymbol{R}(t)\boldsymbol{R}_A(t-h)\boldsymbol{e}_3 = \boldsymbol{R}_A(t)\boldsymbol{e}_3. \tag{4.9}$$

As such, $\boldsymbol{R}_A(t)$ is well defined if $\{\delta\boldsymbol{R}(t-hk) \in \mathrm{SO}(3) | t_\circ \leq hk \leq t, k \in \mathbb{N}\}$ are well defined, facilitating non-singular reference generation for any given maneuver, provided that h is sufficiently small in relation to $(\mathrm{d}/\mathrm{d}t)\boldsymbol{R}_A$. □

With a desired reference trajectory $(\boldsymbol{R}_d, \boldsymbol{\omega}_d, \dot{\boldsymbol{\omega}}_d)$, computed using any of the methods (i), (ii) and (iii), the geometric tracking controller in [Lee et al., 2010, Proposition 3] can be expressed in the notation of the thesis as follows.

Proposition 4.1—Geometric Control on $\mathrm{SO}(3) \times \mathbb{R}^3$
Consider the dynamics (4.1) controlled by a feedback where:

- the torques, $\boldsymbol{\tau}$, are computed by the controller (3.11) in Theorem 3.2 implemented to track a desired attitude trajectory $(\boldsymbol{R}_d, \boldsymbol{\omega}_d, \dot{\boldsymbol{\omega}}_d)$;
- the desired attitude reference trajectory is formed by (4.5); and
- the actuating force is computed as $f = \boldsymbol{f}_d \cdot \boldsymbol{R}\boldsymbol{e}_3$, with the desired force $\boldsymbol{f}_d$ computed as described in (4.3).

Assume that:

(A1) the reference trajectory $(\boldsymbol{R}_d, \boldsymbol{\omega}_d, \dot{\boldsymbol{\omega}}_d)$ is well defined at all times;

(A2) there exists a bound $\|mg\boldsymbol{e}_3 + m\ddot{\boldsymbol{p}}_r\| \leq B_f$ for all $t \geq t_\circ$;

(A3) the initial attitude error satisfies $\Psi(\boldsymbol{R}_d(t_\circ), \boldsymbol{R}(t_\circ)) \leq \phi < 1$;

(A4) the initial positional error satisfies $\|\boldsymbol{e}_{\boldsymbol{p}}(t_\circ)\| < B_p$ for a fixed $B_p > 0$;

(A5) the controller parameters $(k_p, k_v, k_R, k_\omega, c_a, c_p) \in \mathbb{R}^6_{>0}$, are chosen such that for an $\alpha = \sqrt{\phi(2-\phi)} < 1$, the matrices

$$\boldsymbol{M}_1^{aa} \triangleq \frac{1}{2}\begin{bmatrix} k_R & -c_a \\ \star & \lambda_m(\boldsymbol{J}) \end{bmatrix}, \qquad \boldsymbol{M}_1^{pp} \triangleq \frac{1}{2}\begin{bmatrix} k_p & -c_p \\ \star & m \end{bmatrix}, \tag{4.10}$$

$$\boldsymbol{M}_2^{aa} \triangleq \frac{1}{2}\begin{bmatrix} \frac{2k_R}{2-\phi} & c_a \\ \star & \lambda_M(\boldsymbol{J}) \end{bmatrix}, \qquad \boldsymbol{M}_2^{pp} \triangleq \frac{1}{2}\begin{bmatrix} k_p & c_p \\ \star & m \end{bmatrix},$$

$$\boldsymbol{W}^{aa} = \begin{bmatrix} \frac{c_a k_R}{\lambda_M(\boldsymbol{J})} & -\frac{c_a k_w}{2\lambda_m(\boldsymbol{J})} \\ \star & k_\omega - c_a \end{bmatrix}, \quad \boldsymbol{W}^{pp} \triangleq \begin{bmatrix} \frac{c_p k_p}{m}(1-\alpha) & -\frac{c_p k_v}{2m}(1+\alpha) \\ \star & k_v(1-\alpha) - c_p \end{bmatrix},$$

are all positive definite, and there exist a matrix

$$\boldsymbol{W}^{pa} \triangleq \begin{bmatrix} \frac{B_f c_p}{m} & 0 \\ B_f + k_p B_p & 0 \end{bmatrix}, \tag{4.11}$$

such that $B_z = 4\lambda_m(\boldsymbol{W}^{aa})\lambda_m(\boldsymbol{W}^{pp}) - \|\boldsymbol{W}^{pa}\|^2 > 0$.

Let $\boldsymbol{z}_p = (\|\boldsymbol{e}_{\boldsymbol{p}}\|; \|\boldsymbol{e}_{\boldsymbol{v}}\|) \in \mathbb{R}^2_{\geq 0}$, $\boldsymbol{z}_a = (\|\boldsymbol{e}_{\boldsymbol{R}}\|; \|\boldsymbol{e}_{\boldsymbol{\omega}}\|) \in \mathbb{R}^2_{\geq 0}$, and define a domain

$$D = \left\{ \begin{bmatrix} \boldsymbol{e}_{\boldsymbol{p}}(t_\circ) \\ \boldsymbol{e}_{\boldsymbol{v}}(t_\circ) \\ \boldsymbol{e}_{\boldsymbol{R}}(t_\circ) \\ \boldsymbol{e}_{\boldsymbol{\omega}}(t_\circ) \end{bmatrix} \in \mathbb{R}^{12} \;\middle|\; \begin{array}{c} \Psi(\boldsymbol{R}_d(t_\circ), \boldsymbol{R}(t_\circ)) \leq \phi < 1, \\ \|\boldsymbol{e}_{\boldsymbol{\omega}}(t_\circ)\|^2 \leq \frac{2}{\lambda_M(\boldsymbol{J})} k_R(\phi - \Psi(\boldsymbol{R}_d(t_\circ), \boldsymbol{R}(t_\circ))), \\ \lambda_M(\boldsymbol{M}_2^{aa})\|\boldsymbol{z}_a(t_\circ)\|^2 + \lambda_M(\boldsymbol{M}_2^{pp})\|\boldsymbol{z}_p(t_\circ)\|^2 \leq \frac{1}{2}k_p B_p^2 \end{array} \right\}, \tag{4.12}$$

Given (A1)-(A5), the point $(\boldsymbol{e}_{\boldsymbol{p}}, \boldsymbol{e}_{\boldsymbol{v}}, \boldsymbol{e}_{\boldsymbol{R}}, \boldsymbol{e}_{\boldsymbol{\omega}}) = (\boldsymbol{0}, \boldsymbol{0}, \boldsymbol{0}, \boldsymbol{0})$ is UES on D.□

Proof. The proof is given in [Lee et al., 2011, Appendix B and D], and follows by the analysis of a Lyapunov function candidate

$$\bar{\mathcal{V}} = \frac{1}{2}k_p\|\boldsymbol{e_p}\|^2 + \frac{1}{2}m\|\boldsymbol{e_v}\|^2 + c_p\boldsymbol{e_p}\cdot\boldsymbol{e_v} + k_R\Psi(\boldsymbol{R}_d,\boldsymbol{R}) + c_a\boldsymbol{e_R}\cdot\boldsymbol{e_\omega} + \frac{1}{2}\boldsymbol{e_\omega}\cdot\boldsymbol{J}\boldsymbol{e_\omega}. \tag{4.13}$$

Given the assumptions (A1)-(A5), for sufficiently small $c_p > 0$ and $c_a > 0$, it is shown that there exist positive definite matrices $\bar{\boldsymbol{M}}_1, \bar{\boldsymbol{M}}_2, \bar{\boldsymbol{W}} \in \mathbb{R}^{4\times4}$, and a representation of the errors $\bar{\boldsymbol{z}} = (\|\boldsymbol{e_p}\|; \|\boldsymbol{e_v}\|; \boldsymbol{e_R}\|; \|\boldsymbol{e_\omega}\|) \in \mathbb{R}^4_{\geq 0}$, such that

$$\bar{\boldsymbol{z}}^\top\bar{\boldsymbol{M}}_1\bar{\boldsymbol{z}} \leq \bar{\mathcal{V}} \leq \bar{\boldsymbol{z}}^\top\bar{\boldsymbol{M}}_2\bar{\boldsymbol{z}}, \quad \dot{\bar{\mathcal{V}}} \leq -\bar{\boldsymbol{z}}^\top\bar{\boldsymbol{W}}\bar{\boldsymbol{z}}, \tag{4.14}$$

along the solutions of the error dynamics. The proof can subsequently be completed using a result such as Theorem 2.5 to show UES. □

The domain D may seem overly restrictive, and it is reasonable ask how the system behaves when initialized outside of this domain. Just as with the geometric attitude control in Theorem 3.2, the origin of the error dynamics can be shown to be asymptotically attractive for much larger errors, see [Lee et al., 2010, Proposition 4], but does not result in an almost global result as defined in this thesis. To highlight this result, it is stated below.

Proposition 4.2
Consider the system Σ in (4.1) in closed-loop feedback with Proposition 4.1, but instead of assumption (A3), assume that the initial errors satisfy

$$\Psi(\boldsymbol{R}_d(t_\circ),\boldsymbol{R}(t_\circ)) \leq \phi < 2, \tag{4.15a}$$

$$\|\boldsymbol{e_\omega}(t_\circ)\|^2 \leq \frac{2}{\lambda_M(\boldsymbol{J})}k_R(\phi - \Psi(\boldsymbol{R}_d(t_\circ),\boldsymbol{R}(t_\circ))). \tag{4.15b}$$

Then the origin $(\boldsymbol{e_p},\boldsymbol{e_v},\boldsymbol{e_R},\boldsymbol{e_\omega}) = (\boldsymbol{0},\boldsymbol{0},\boldsymbol{0},\boldsymbol{0})$ is asymptotically attractive. □

Proof. The proof is given in [Lee et al., 2010, Appendix E], and follows by showing boundedness of solutions before the errors approach D, as defined in (4.12), after which the errors decay exponentially to the origin. □

Remark 4.2
It is worth noting that due to the equivalence between Theorem 3.1 and Theorem 3.2, the condition in (4.15b) can generally be ignored in practice, as all solutions asymptotically to an element in the set $\boldsymbol{R}_e \in \{\boldsymbol{I}\} \cup \mathcal{E}$ with $\mathcal{E} = \{\boldsymbol{R}_e \in \mathrm{SO(3)} \mid \mathrm{Tr}(\boldsymbol{R}_e) = -1\}$ forming a line on SO(3), and every equilibrium point associated with an element of $\mathcal{E}$ is unstable by Theorem 3.1.□

Having presented this result, we will now discuss some of the assumptions and their consequences when implementing the controller in real-time.

REMARK 4.3
While the constant B_f in Assumption (A2) is known in the reference trajectory, Assumption (A1) cannot generally be guaranteed, as both $\boldsymbol{f}_d$ and $\boldsymbol{b}_{d,3}$ are defined in the controller errors $(\boldsymbol{e_p}, \boldsymbol{e_v})$. Consequently, when implementing the controller, special checks need to be made to catch the cases where the reference rotation approaches a point for which $\boldsymbol{R}_d$ is undefined. This can be avoided by carefully designing the reference trajectory and assuming small attitude errors, or resorting to the integration outlined in Remark 4.1, but generally only becomes a problem during extreme large-angle maneuvers. □

REMARK 4.4
The system exhibits asymptotic attractiveness properties when initialized far outside of the domain of exponential attraction, as pointed out in Proposition 4.2 and Remark 4.2. However, the force may be negative transiently if (A3) is violated and the system is initialized outside of D. This becomes a significant problem when actuating the UAV from large initial errors with rotors that only spin in a single direction (as the f has to be positive under the rotor model in Sec. 2.2.4). In practice it is uncommon to have $\boldsymbol{f}_d \cdot \boldsymbol{b}_3 < 0$, unless considering extreme maneuvers such as accelerating downward from a hovering state with an acceleration greater than the gravitational acceleration. As we shall see in later examples, it is rare to have negative forces even in extremely aggressive looping maneuvers from large initial errors. □

REMARK 4.5
A more serious drawback of the controller in Proposition 4.1 is the need for computing the first and second time-derivatives of $\boldsymbol{R}_d$ when evaluating the desired attitude reference trajectory in (4.5). It should be noted that $\boldsymbol{R}_d$ is a function of $\boldsymbol{e_p}$ and $\boldsymbol{e_v}$, both of which are formed directly by the true states $\boldsymbol{p}$ and $\boldsymbol{v}$, which typically contain noise when estimated in practice. As such, any evaluation of $(\boldsymbol{\omega}_d, \dot{\boldsymbol{\omega}}_d)$ requires the signals $(\dot{\boldsymbol{e}}_x, \ddot{\boldsymbol{e}}_x, \dot{\boldsymbol{e}}_{\boldsymbol{p}}, \ddot{\boldsymbol{e}}_{\boldsymbol{p}})$ to be known. Unless a dedicated estimator is constructed, these signals have to be evaluated using numerical differentiation, which generally becomes problematic. □

In real-time implementations, the states of the system Σ in (4.1) are often estimated from a set of measurements by a filter. If so, the signal $\dot{\boldsymbol{e}}_{\boldsymbol{v}} = \ddot{\boldsymbol{p}} - \ddot{\boldsymbol{p}}_r$ can be computed in the estimates through (2.19f), facilitating an evaluation $\boldsymbol{\omega}_d$ in the memory if assuming knowledge of $(\boldsymbol{p}_r, \dot{\boldsymbol{p}}_r, \ddot{\boldsymbol{p}}_r, \dddot{\boldsymbol{p}}_r, \boldsymbol{R}_r, \dot{\boldsymbol{R}}_r)$. However, the signal $\dot{\boldsymbol{\omega}}_d$ typically becomes very noisy in real-time implementations, and as such, it is often advantageous to simply assume small desired attitude accelerations and let $\dot{\boldsymbol{\omega}}_d = \boldsymbol{0}$. This naturally sacrifices tracking performance and stability guarantees, especially during volatile large-angle maneuvers, but still results in good tracking performance if $\boldsymbol{\omega}_d$ is small. Before showing this, we first consider the tracking performance of Proposition 4.1 in an idealized setting, using numerical differentiation to compute $(\boldsymbol{R}_d, \boldsymbol{\omega}_d, \dot{\boldsymbol{\omega}}_d)$.

Example 4.1
To demonstrate the properties of the controller in Proposition 4.1, consider a simulation where a UAV is actuated along a circular trajectory. This reference trajectory is defined in the flat output space of the UAV, as

$$\boldsymbol{\gamma}(t) = (3\sin(t);\ 3\cos(t);\ 0;\ -t) \in \mathbb{F}_\Sigma, \tag{4.16}$$

and subsequently expanded through the differential flatness equations to yield the signals $(\boldsymbol{p}_r, \dot{\boldsymbol{p}}_r, \ddot{\boldsymbol{p}}_r, \boldsymbol{R}_r)$. Instead of using the complete state trajectory, the direction $\boldsymbol{b}_{r,1}$ is computed from $\boldsymbol{R}_r$, and used to define $\boldsymbol{R}_d$ though (4.4) and (4.5), with the signals $\boldsymbol{\omega}_d$ and $\dot{\boldsymbol{\omega}}_d$ computed by numerical differentiation of $\boldsymbol{R}_d$. The UAV system is defined with random initial conditions sampled from $\boldsymbol{p}(t_\circ), \boldsymbol{v}(t_\circ) \sim \mathcal{U}([-1,1]^3)$, and with significant initial attitude rate $\boldsymbol{\omega}(t_\circ) \sim \mathcal{U}([-3,3]^3)$ and $\boldsymbol{R}(t_\circ) \sim \mathcal{U}(\mathrm{SO}(3))$, here realized as

$$\boldsymbol{R}(t_\circ) = \begin{bmatrix} 0.51 & -0.05 & -0.86 \\ -0.78 & 0.41 & -0.48 \\ 0.37 & 0.91 & 0.17 \end{bmatrix} \in \mathrm{SO}(3). \tag{4.17}$$

The system parameters are taken as $m = 0.1$ with $g = 10$, and the inertia is randomized such that $\lambda_m(\boldsymbol{J}) = 0.05$ and $\lambda_M(\boldsymbol{J}) = 0.1$, here realized as

$$\boldsymbol{J} = \begin{bmatrix} 0.08 & 0.01 & 0.02 \\ 0.01 & 0.07 & 0.00 \\ 0.02 & 0.00 & 0.07 \end{bmatrix}, \tag{4.18}$$

when rounded to two digits. The controller in Proposition 4.1 is used to actuate the UAV along this reference trajectory, here tuned with

$$k_R = 4, \qquad k_\omega = 1, \qquad k_p = 0.3, \qquad k_v = 0.09. \tag{4.19}$$

The resulting system response is depicted in Figure 4.2, and relevant signals of the controlled system are plotted as function of time in Figure 4.3. Here, the attitude rates and control signals associated with the reference trajectory $(\boldsymbol{\omega}_r, f_r, \boldsymbol{\tau}_r)$ show the convergence of the tracking errors, despite not being explicitly used in the control system when implemented in this manner.

In this example, we note that near-perfect tracking is achieved over the 10 seconds during which the system is simulated, despite the very large initial attitude errors. We also note that the distance $\Psi(\boldsymbol{R}_d, \boldsymbol{R})$ quickly decays, but the distance $\Psi(\boldsymbol{R}_r, \boldsymbol{R})$ increases slightly as the translation error dynamics converge to the intended reference trajectory. For this example, $B_p = 2.52$, and given the reference trajectory, we can chose $B_f = 1.2$. Given these bounds and the parameter tuning in (4.19), the system is initialized outside of the domain of exponential attraction D in (4.12), indeed it is initialized outside of the region defined in Proposition 4.2 as well. However, due to

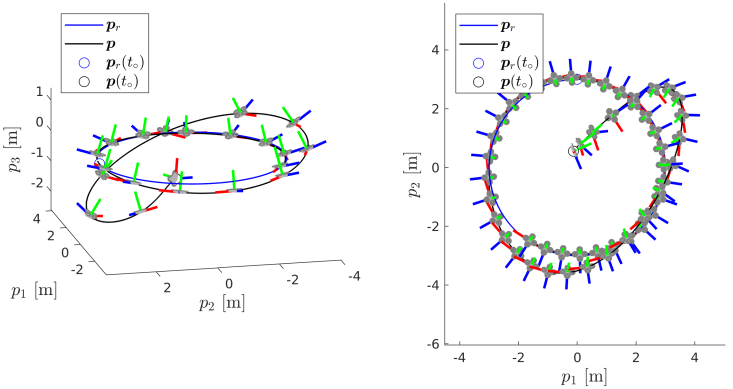

Figure 4.2 Simulated system response of Σ in (4.1) when controlled along Σ_r in (4.2) defined by the flat output trajectory in (4.16) using geometric controller in Proposition 4.1. Illustration of the system configurations, with the positional reference trajectory (blue), the positional trajectory (black), and the system attitude illustrated temporally equidistant over $t \in [0, 10]$ using the same color coding of the body basis vectors as used in Figure 2.5 and Figure 2.6. *Left:* Trajectory in three-dimensional space. *Right:* Projection onto the-$\boldsymbol{e}_1\boldsymbol{e}_2$ plane. The simulated system response is shown in the video chapter-4-simulations.mp4.

the asymptotic attractiveness properties of the controller, it converges to a small tracking error nonetheless. As the errors induced by the numerical differentiation in computing $(\boldsymbol{\omega}_d, \dot{\boldsymbol{\omega}}_d)$ using (4.5), the tracking errors do not decay to machine precision in this example (as expected). The bounds on $\bar{\mathcal{V}}$ and its time-derivative $\dot{\bar{\mathcal{V}}}$ are here satisfied at all times, with $\bar{\boldsymbol{M}}_1, \bar{\boldsymbol{M}}_2$, and $\bar{\boldsymbol{W}}$ constructed from (4.10) and (4.11) described in [Lee et al., 2011]. □

Remark 4.6
When the control system is implemented with numerical differentiation of $\boldsymbol{R}_d$ to compute $\boldsymbol{\omega}_d$ and $\dot{\boldsymbol{\omega}}_d$, the real-time implementation simplifies significantly, as the full flatness expansion is not needed. In this case, it is sufficient to know $(\boldsymbol{p}_r, \dot{\boldsymbol{p}}_r, \ddot{\boldsymbol{p}}_r, \boldsymbol{R}_r)$ to implement the controller. However, if taking this approach, measurement noise may severely corrupt the signal $\dot{\boldsymbol{R}}_d$ and even more so $\ddot{\boldsymbol{R}}_d$. As such, the controller implementation in Example 4.1 might not be well suited for real-time applications, depending on the noise levels.□

To summarize this section, the controller in Proposition 4.1 originally presented in [Lee et al., 2011, Propositions 3 and 4] is very powerful, yielding UES of an equilibrium point corresponding to a zero tracking error when initialized

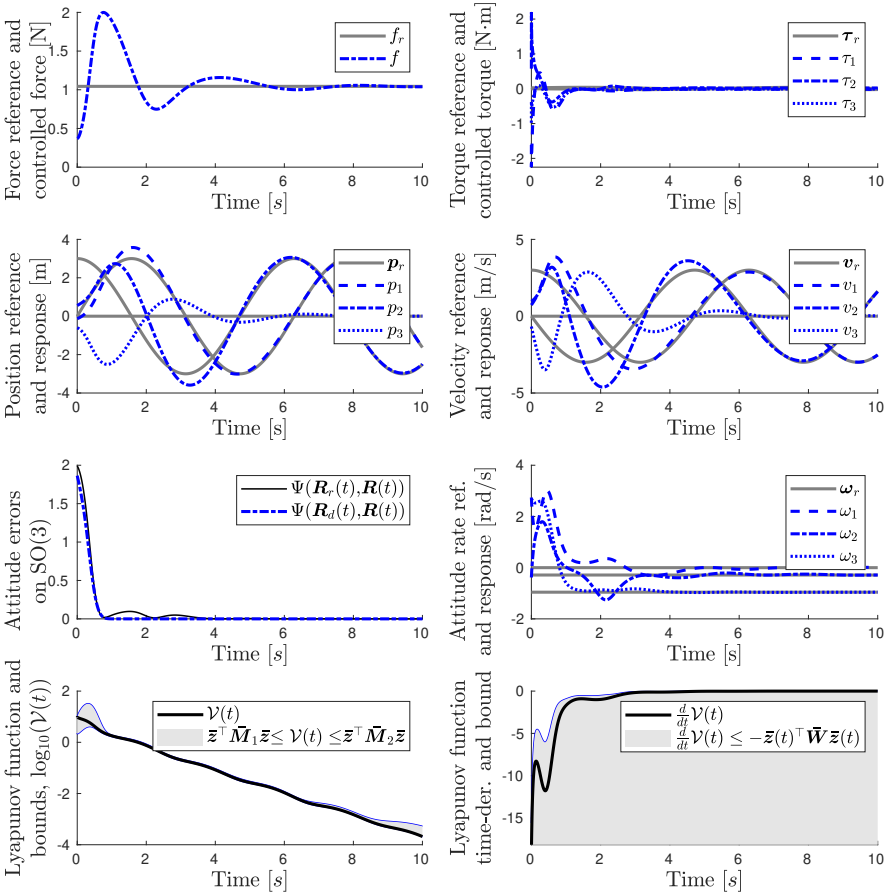

Figure 4.3 Simulated response of the UAV dynamics Σ in (4.1) when controlled along Σ_r in (4.2) by the full state feedback in Proposition 4.1. *Top, left:* The computed reference force f_r (gray) and control signal force f (blue). *Top, right:* The reference torques $\boldsymbol{\tau}_r$ (gray) and computed control signal torques $\boldsymbol{\tau}$ (blue). *Top center, left:* The positional reference $\boldsymbol{p}_r$ (gray) and response $\boldsymbol{p}$ (blue). *Top center, right:* The velocity reference $\boldsymbol{v}_r$ (gray) and response $\boldsymbol{v}$ (blue). *Bottom center, left:* The attitude error in the Ψ-distance on SO(3) with respect to the reference rotation $\boldsymbol{R}_r$ (black) and the desired rotation $\boldsymbol{R}_d$ (blue). *Bottom center, right:* The attitude rate reference $\boldsymbol{\omega}_r$ (gray) and response $\boldsymbol{\omega}$ (blue). *Bottom, left:* The Lyapunov function $\mathcal{V}$ in (4.13) in the 10-logarithm, and the associated quadratic bounds. *Bottom, left:* The Lyapunov function time-derivative, and its associated bound. The simulated system response is shown in the video chapter-4-simulations.mp4.

on the domain D in (4.12), and asymptotic attractiveness for large attitude errors as per Proposition 4.2. There are, however, some caveats to this control system, as highlighted in Remark 4.3 and 4.4 relating to the Assumption (A1) and (A3). But the most critical problem in the controller design is summarized in Remark 4.5 and relates to the computation of the desired reference trajectory $(\boldsymbol{R}_d, \boldsymbol{\omega}_d, \dot{\boldsymbol{\omega}}_d)$. When considering real-time implementations, we require either dedicated estimators, or numerical differentiation of potentially noisy control errors, or removal of parts of the dynamic feed-forward terms involving $\dot{\boldsymbol{\omega}}_d$ (then sacrificing the proven stability properties). Even so, we emphasize that this result is very powerful and incredibly useful in practice.

4.3 Geometric Control on $\mathbf{SU(2)} \times \mathbb{R}^3$

Given the strong similarities between the stability proofs of the attitude controllers on SO(3) and SU(2), it should come as no surprise that an very similar geometric controllers can be constructed for systems on $\mathrm{SU}(2) \times \mathbb{R}^3$. However, one significant different is that we now require an attitude reference $\boldsymbol{X}_d \in \mathrm{SU}(2)$. As discussed in Chapter 2, the conversion of an element $\boldsymbol{R} \in \mathrm{SO}(3)$ to $\boldsymbol{X} \in \mathrm{SU}(2)$ is not unique, as $\boldsymbol{R} = E_{\mathrm{SO}(3)}^{\mathrm{SU}(2)}(\pm\boldsymbol{X})$. When constructing the desired reference trajectory, an element $\boldsymbol{R}_d$ can be computed as described in Sec. 4.2, before choosing one of the possible elements $\pm\boldsymbol{X}_d \in \mathrm{SU}(2)$. If working with the discontinuous attitude controller, this choice does not affect the closed-loop system, as the errors decay regardless of the controller switching. However, if considering the continuous attitude controller, the desired attitude needs to be chosen with care such that $\boldsymbol{X}_d$ is continuous in time to avoid the phenomenon of dynamical unwinding (see Remark 3.5).

Remark 4.7
In a controller implementation running at a time-step of h [s], enforcing continuity in $\boldsymbol{X}_d(t)$ is rather simple. It can be done at a time t by computing one of the two elements $\bar{\boldsymbol{X}}_d(t) \in \mathrm{SU}(2)$ associated with $\boldsymbol{R}_d(t) \in \mathrm{SO}(3)$, taking

$$\boldsymbol{X}_d(t) = \begin{cases} +\bar{\boldsymbol{X}}_d(t), & \text{if } \Gamma(\bar{\boldsymbol{X}}_d(t), \boldsymbol{X}_d(t-h)) < \Gamma(-\bar{\boldsymbol{X}}_d(t), \boldsymbol{X}_d(t-h)) \\ -\bar{\boldsymbol{X}}_d(t), & \text{otherwise} \end{cases}.$$

The computation of $\bar{\boldsymbol{X}}_d$ from $\boldsymbol{R}_d$ can be done though Definition 2.17, or by other methods (e.g., using the ideas in [Bar-Itzhack, 2000]). □

It should be noted that the introduction of memory to ensure continuity of a quaternion was in fashion to Remark 4.7 was proposed in [Mayhew et al., 2012]. Assuming that a desired reference trajectory can be computed as described through Remark 4.7, a result analogous to Proposition 4.1 can be given for dynamics configured on $\mathrm{SU}(2) \times \mathbb{R}^3$ as follows.

PROPOSITION 4.3—GEOMETRIC CONTROL ON $\mathrm{SU}(2) \times \mathbb{R}^3$
Consider the dynamics (4.1) controlled by a feedback where:

- the torques, $\boldsymbol{\tau}$, are computed by the controller Theorem 3.4 implemented to track a desired attitude trajectory $(\boldsymbol{X}_d, \boldsymbol{\omega}_d, \dot{\boldsymbol{\omega}}_d)$;
- the desired attitude reference trajectory is formed by (4.5), expanding $\boldsymbol{R}_d$ or $\boldsymbol{q}_d$ into $\boldsymbol{X}_d \in \mathrm{SU}(2)$, and enforcing continuity by Remark 4.7;
- the actuating force is computed as $f = \boldsymbol{f}_d \cdot \boldsymbol{R}\boldsymbol{e}_3$, with the desired force $\boldsymbol{f}_d$ computed as described in (4.3).

Assume that:

(A1) the reference trajectory $(\boldsymbol{X}_d, \boldsymbol{\omega}_d, \dot{\boldsymbol{\omega}}_d)$ is well defined at all times;

(A2) there exists a bound $\|mg\boldsymbol{e}_3 + m\ddot{\boldsymbol{p}}_r\| \leq B_f$ for all $t \geq t_\circ$;

(A3) the initial attitude error satisfies $\Gamma(\boldsymbol{X}_d(t_\circ), \boldsymbol{X}(t_\circ)) \leq \phi < 2^{-3}$;

(A4) the initial positional error satisfies $\|\boldsymbol{e}_{\boldsymbol{p}}(t_\circ)\| < B_p$ for a fixed $B_p > 0$;

(A5) the controller parameters $(k_p, k_v, k_X, k_\omega, c_a, c_p) \in \mathbb{R}^6_{>0}$, are chosen such that for $\alpha = 2\sqrt{2\phi}$, the matrices

$$\boldsymbol{M}_1^{aa} \triangleq \frac{1}{2}\begin{bmatrix} 4k_X & -c_a \\ \star & \lambda_m(\boldsymbol{J}) \end{bmatrix}, \qquad \boldsymbol{M}_1^{pp} \triangleq \frac{1}{2}\begin{bmatrix} k_p & -c_p \\ \star & m \end{bmatrix}, \tag{4.20}$$

$$\boldsymbol{M}_2^{aa} \triangleq \frac{1}{2}\begin{bmatrix} \frac{8k_X}{2-\phi} & c_a \\ \star & \lambda_M(\boldsymbol{J}) \end{bmatrix}, \qquad \boldsymbol{M}_2^{pp} \triangleq \frac{1}{2}\begin{bmatrix} k_p & c_p \\ \star & m \end{bmatrix},$$

$$\boldsymbol{W}^{aa} = \begin{bmatrix} \frac{c_a k_X}{\lambda_M(\boldsymbol{J})} & -\frac{c_a k_w}{2\lambda_m(\boldsymbol{J})} \\ \star & k_\omega - \frac{c_a}{4} \end{bmatrix}, \quad \boldsymbol{W}^{pp} \triangleq \begin{bmatrix} \frac{c_p k_p}{m}(1-\alpha) & -\frac{c_p k_v}{2m}(1+\alpha) \\ \star & k_v(1-\alpha) - c_p \end{bmatrix},$$

are all positive definite, and there exist a matrix

$$\boldsymbol{W}^{pa} \triangleq 4\begin{bmatrix} \frac{B_f c_p}{m} & 0 \\ B_f + k_p B_p & 0 \end{bmatrix}, \tag{4.21}$$

such that $B_z = 4\lambda_m(\boldsymbol{W}^{aa})\lambda_m(\boldsymbol{W}^{pp}) - \|\boldsymbol{W}^{pa}\|^2 > 0$.

Let $\boldsymbol{z}_p = (\|\boldsymbol{e}_{\boldsymbol{p}}\|; \|\boldsymbol{e}_{\boldsymbol{v}}\|) \in \mathbb{R}^2_{\geq 0}$, $\boldsymbol{z}_a = (\|\boldsymbol{e}_{\boldsymbol{X}}\|; \|\boldsymbol{e}_{\boldsymbol{\omega}}\|) \in \mathbb{R}^2_{\geq 0}$, and define a domain

$$D = \left\{ \begin{bmatrix} \boldsymbol{e}_{\boldsymbol{p}}(t_\circ) \\ \boldsymbol{e}_{\boldsymbol{v}}(t_\circ) \\ \boldsymbol{e}_{\boldsymbol{X}}(t_\circ) \\ \boldsymbol{e}_{\boldsymbol{\omega}}(t_\circ) \end{bmatrix} \in \mathbb{R}^{12} \;\middle|\; \begin{array}{c} \Gamma(\boldsymbol{X}_d(t_\circ), \boldsymbol{X}(t_\circ)) \leq \phi < 2^{-3}, \\ \|\boldsymbol{e}_{\boldsymbol{\omega}}(t_\circ)\|^2 \leq \frac{2}{\lambda_M(\boldsymbol{J})} k_X(\phi - \Gamma(\boldsymbol{X}_d(t_\circ), \boldsymbol{X}(t_\circ))), \\ \lambda_M(\boldsymbol{M}_2^{aa})\|\boldsymbol{z}_a(t_\circ)\|^2 + \lambda_M(\boldsymbol{M}_2^{pp})\|\boldsymbol{z}_p(t_\circ)\|^2 \leq \frac{1}{2}k_p B_p^2 \end{array} \right\}, \tag{4.22}$$

Given (A1)-(A5), the point $(\boldsymbol{e}_{\boldsymbol{p}}, \boldsymbol{e}_{\boldsymbol{v}}, \boldsymbol{e}_{\boldsymbol{X}}, \boldsymbol{e}_{\boldsymbol{\omega}}) = (\boldsymbol{0}, \boldsymbol{0}, \boldsymbol{0}, \boldsymbol{0})$ is UES on D. □

Proof. The proof is given in Appendix B.8 and with more details in [Greiff et al., 2021c]. Similar to the proof of [Lee et al., 2010, Proposition 2], it follows by defining a Lyapunov function candidate

$$\bar{\mathcal{V}} = \frac{1}{2}k_p\|\boldsymbol{e_p}\|^2 + \frac{1}{2}m\|\boldsymbol{e_v}\|^2 + c_p\boldsymbol{e_p}\cdot\boldsymbol{e_v} + k_X\Gamma(\boldsymbol{X}_d, \boldsymbol{X}) + c_a\boldsymbol{e_X}\cdot\boldsymbol{e_\omega} + \frac{1}{2}\boldsymbol{e_\omega}\cdot\boldsymbol{J}\boldsymbol{e_\omega}. \tag{4.23}$$

Given the assumptions (A1)-(A5), it is shown all solutions initialized on D remain on this domain for all $t \geq t_\circ$. Furthermore, it is shown $\bar{\mathcal{V}}$ is continuously differentiable, and there exist a set of positive constants $c_1, c_2, c_3 > 0$ expressed in the eigenvalues of the matrices in (4.20) and the norm of (4.21), such that

$$c_1\|\bar{\boldsymbol{z}}\|^2 \leq \bar{\mathcal{V}} \leq c_2\|\bar{\boldsymbol{z}}\|^2, \quad (\mathrm{d}/\mathrm{d}t)\bar{\mathcal{V}} \leq -c_3\|\bar{\boldsymbol{z}}\|^2, \tag{4.24}$$

where $\bar{\boldsymbol{z}} = (\|\boldsymbol{e_p}\|; \|\boldsymbol{e_v}\|; \|\boldsymbol{e_X}\|; \|\boldsymbol{e_\omega}\|)$. This holds for all solutions of the error dynamics on D. Applying Theorem 2.5 shows UES of $\bar{\boldsymbol{z}} = \boldsymbol{0}$ on D. □

While powerful, it should be noted that the geometric controller on $\mathrm{SU}(2)\times\mathbb{R}^3$ in Proposition 4.3 suffers from the same problems as the geometric controller on $\mathrm{SO}(3)\times\mathbb{R}^3$ in Proposition 4.1, as outlined in Remarks 4.3, 4.4, and 4.5. It can encounter singularities in the computation of the desired reference attitude, it can result in negative actuation forces, and it too requires the numerical differentiation of the control errors to be implemented.

Remark 4.8
A completely analogous proof can be made with the discontinuous geometric controller on SU(2) in Theorem 3.5, then omitting the need for keeping the reference and system attitude continuous on SU(2). While such a controller can yield poor robustness properties for specific classes of disturbances, it does not require $\boldsymbol{X}_d(t)$ and $\boldsymbol{X}(t)$ to be continuous on SU(2), and the element selection in Remark 4.7 need not be used. In this case, the Lyapunov function is instead constructed using the function $\mathcal{V}^{\pm}$ in (3.51) associated with Theorem 3.5, as

$$\bar{\mathcal{V}}^{\pm} = \frac{1}{2}k_p\|\boldsymbol{e_p}\|^2 + \frac{1}{2}m\|\boldsymbol{e_v}\|^2 + c_1\boldsymbol{e_p}\cdot\boldsymbol{e_v} + \mathcal{V}^{\pm}. \tag{4.25}$$

The proof cannot be completed with Theorem 2.5, but has to be done using the comparison lemma (see, e.g., [Khalil, 1996, Lemma 2.5]). This yields exponential stability on a domain that can be expressed similar to (4.22). □

Just as asymptotic attractiveness of the origin can be shown for all initial errors satisfying $\Psi(\boldsymbol{R}_d(t_\circ), \boldsymbol{R}(t_\circ)) < 2$ for Proposition 4.1 in Proposition 4.2, a similar result can be derived for the geometric controller on $\mathrm{SU}(2)\times\mathbb{R}^3$.

Proposition 4.4
Consider the system Σ in (4.1) in closed-loop feedback with Proposition 4.3, but instead of assumption (A3), assume that the initial errors satisfy

$$\Gamma(\boldsymbol{X}_d(t_\circ), \boldsymbol{X}(t_\circ)) \leq \phi < 2, \tag{4.26a}$$

$$\|\boldsymbol{e}_{\boldsymbol{\omega}}(t_\circ)\|^2 \leq \frac{2}{\lambda_M(\boldsymbol{J})} k_X(\phi - \Gamma(\boldsymbol{X}_d(t_\circ), \boldsymbol{X}(t_\circ))). \tag{4.26b}$$

Then the origin $(\boldsymbol{e}_{\boldsymbol{p}}, \boldsymbol{e}_{\boldsymbol{v}}, \boldsymbol{e}_{\boldsymbol{X}}, \boldsymbol{e}_{\boldsymbol{\omega}}) = (\boldsymbol{0}, \boldsymbol{0}, \boldsymbol{0}, \boldsymbol{0})$ is asymptotically attractive. □

Proof. This becomes completely analogous to the proof in [Lee et al., 2010, Appendix E], therefore omitted for brevity. It follows by showing boundedness of solutions on $t \in [t_\circ, t^*]$, before the errors approach D as defined in (4.12) at a finite time t^*, after which the errors decay exponentially to the origin. □

A simulation example is given for an extremely aggressive maneuver, here with the desired attitude accelerations $\dot{\boldsymbol{\omega}}_d$ are removed as described in Remark 4.6 to show how such approximations affect the tracking performance.

Example 4.2
To demonstrate the controller in Proposition 4.3 for extremely aggressive trajectory tracking, consider a simulation where a UAV is actuated along a trajectory defined on the surface on a torus, defined parametrically in $\{\mathcal{G}\}$, as

$$\boldsymbol{T}(u, v) = (R + r\cos(u))\cos(v)\boldsymbol{e}_1 + (R + r\cos(u))\sin(v)\boldsymbol{e}_2 + r\sin(u)\boldsymbol{e}_3 \in \mathbb{R}^3,$$

where $u, v \in [0, 2\pi]$, $R > r > 0$. Take a flat output trajectory for a UAV, as

$$\boldsymbol{\gamma}(t) = (\boldsymbol{T}(\omega_u t, \omega_v t);\ \omega_v t) \in \mathbb{F}_\Sigma. \tag{4.27}$$

The velocity of the trajectory is given by $\omega_u = 1.2\pi$ and $\omega_v = 0.2\pi$, with the size of the torus determined by $R = 6$ and $r = 2$. This corresponds to a translation speed of $\|\boldsymbol{v}_r(t)\| = (\omega_v^2(r\cos(\omega_v t) + R)^2 + r^2\omega_u^2)^{1/2}$ such that $\|\boldsymbol{v}_r(t)\| \in [7.95, 9.06]$, and is too fast to be followed by a Crazyflie 2.0 UAV [Bitcraze, 2021c] that will be used in the forthcoming experiments (see Sec. 4.4). This example mainly serves to demonstrate the excellent trajectory tracking properties of the controller in Proposition 4.3.

The defined flat output trajectory is subsequently expanded through the differential flatness equations to yield the reference signals $(\boldsymbol{p}_r, \dot{\boldsymbol{p}}_r, \ddot{\boldsymbol{p}}_r, \boldsymbol{R}_r)$. Instead of using the complete state trajectory, the direction $\boldsymbol{b}_{r,1}$ is computed from $\boldsymbol{R}_r$, and used to define $\boldsymbol{R}_d$ though (4.4) and (4.5). The signal $\boldsymbol{\omega}_d$ is computed by numerical differentiation of $\boldsymbol{R}_d$, but we let $\dot{\boldsymbol{\omega}}_d = \boldsymbol{0}$ for all times. For this example, the geometric controller on SU(2) is implemented using the discontinuous controller in Theorem 3.5, and as such, we do not need to define a continuous reference trajectory $\boldsymbol{X}_d(t)$ by Remark 4.7. With this setup, the

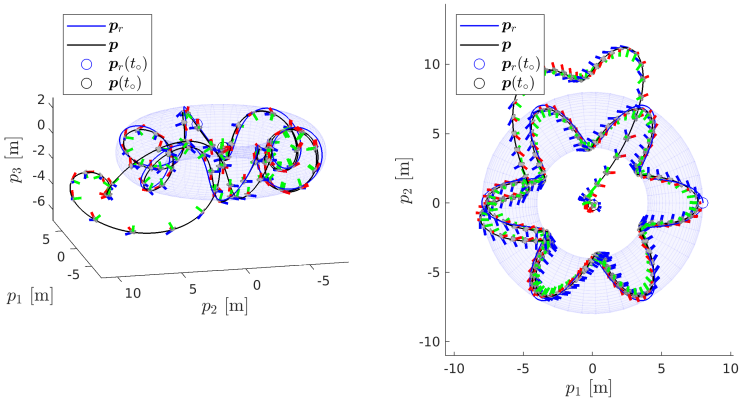

Figure 4.4 Simulated system response of the UAV dynamics Σ in (4.1) when controlled along Σ_r in (4.2) defined by the flat output trajectory in (4.27) when using the geometric controller in Proposition 4.3. Illustration of the system configurations, with the positional reference trajectory (blue), the positional trajectory (black), and the system attitude illustrated temporally equidistant over $t \in [0, 20]$ using the same color coding of the body basis vectors as used in Figure 2.5 and Figure 2.6. *Left:* Trajectory in three-dimensional space. *Right:* Projection onto the-$\boldsymbol{e}_1\boldsymbol{e}_2$ plane. The simulated system response is shown in the video chapter-4-simulations.mp4.

UAV is defined with initial conditions and parameters realized exactly the same as in Example 4.1, and the controller is tuned with

$$k_X = 8, \qquad k_\omega = 2, \qquad k_p = 0.2 \qquad k_v = 0.13. \tag{4.28}$$

The resulting system response is illustrated with its configurations in Figure 4.4 and relevant signals in time in Figure 4.5. In the latter, the attitude rates and control signals associated with the reference trajectory $(\boldsymbol{\omega}_r, f_r, \boldsymbol{\tau}_r)$ are also depicted, despite not being used explicitly in the control system.

As the state of the simulation evolves directly on $\mathrm{SU}(2)$, the trajectory $\boldsymbol{X}(t)$ is continuous in time, while the desired attitude $\boldsymbol{X}_d(t)$ may exhibit discontinuous jumps in time when Remark 4.7 is not implemented. As such, we observe expected periodic discontinuous jumps in the $\Gamma(\boldsymbol{X}_d, \boldsymbol{X})$. However, in all of these jumps, the Lyapunov function remains continuous. We note that the force f converges to a trajectory that is very similar to the force f_r computed in the flatness expansion, but there is a significant difference between the torques $\boldsymbol{\tau}_r$ and $\boldsymbol{\tau}$. This is due to the disturbances introduced by removing $\dot{\boldsymbol{\omega}}_d = \boldsymbol{0}$ in the feedback law. The induced disturbance gives rise to asymptotic errors that are visible in the Lyapunov function, clearly indicating the presence of small asymptotic errors. However, despite the

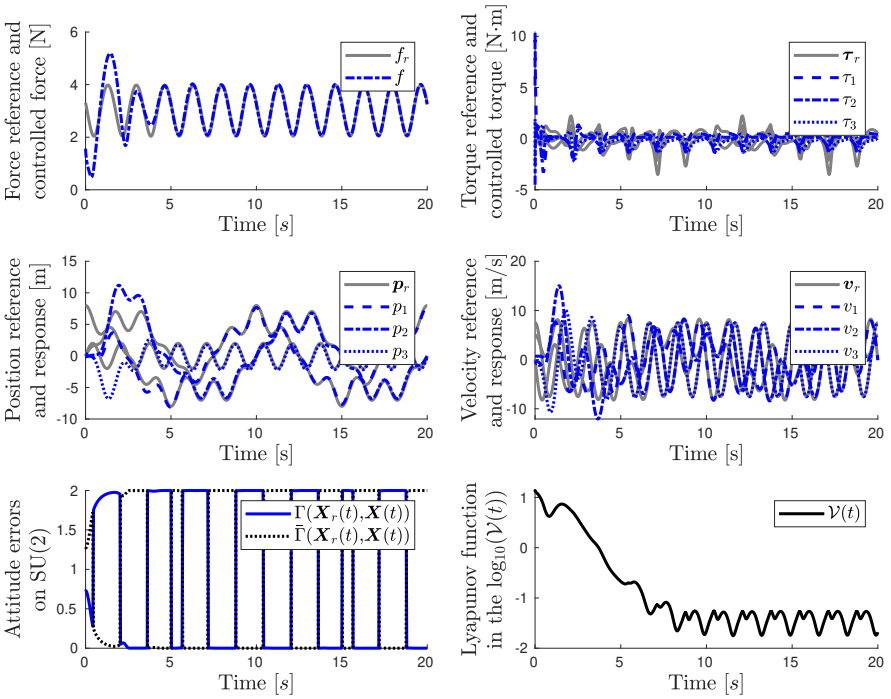

Figure 4.5 Simulated system response of the UAV dynamics Σ in (4.1) when controlled along Σ_r in (4.2) defined by the flat output trajectory in (4.27) with the full state feedback in Proposition 4.3 implemented with the discontinuous attitude controller in Theorem 3.5. *Top, left:* The reference force f_r (gray) and the computed control signal force f (blue). *Top, right:* The reference torque $\boldsymbol{\tau}_r$ (gray) and the computed control signal torques $\boldsymbol{\tau}$ (blue). *Center, left:* The positional reference $\boldsymbol{p}_r$ (gray) and the response $\boldsymbol{p}$ (blue). *Center, right:* The velocity reference $\boldsymbol{v}_r$ (gray) and the response $\boldsymbol{v}$ (blue). *Bottom, left:* The attitude error in the Γ-distance on SU(2) with respect to the reference rotation $\boldsymbol{X}_r$. *Bottom, right:* The Lyapunov function $\mathcal{V}$ in (4.25) in the 10-logarithm. The simulated system response is shown in the video chapter-4-simulations.mp4.

volatile trajectory, excellent tracking is still observed. If the noise levels in a real-time implementation makes it prohibitive to compute $\dot{\boldsymbol{\omega}}_d$ in the control errors, good tracking can typically be achieved when setting this term to zero. However, this will depend on the desired motion and the system's inertia. □

4.4 Real-Time Examples

In this section, the controller in Proposition 4.3 used in Example 4.2 is implemented on a small Crazyflie 2.0 UAV [Bitcraze, 2021c] and run in real-time. This is done for two separate scenarios. The first shows a spiraling maneuver using Ultra-Wideband measurements (see Sec. 4.4.1), and the second demonstrates how the controllers can be used for inventorying tasks using an on-board camera and simultaneous localization and mapping (see Sec. 4.4.2).

The control system in these examples consists of three components: (i) a reference generator, (ii) an estimator, and (iii) a controller. As such, it follows a conventional control system design with an independently developed estimator and controller, taking the estimates as input to a full state feedback solution to Problem 4.1. The components of the control system are described below in brevity to give a holistic view of the software implementation.

(i) The reference generator is implemented in the Crazyflie firmware as described in [Greiff, 2017], permitting independent planning of the flat outputs of the UAV, comprised of the global position, $\boldsymbol{p}$, and the system yaw, ψ. A trajectory is represented as a sequence of splines in each dimension, which can be comprised of polynomial curves, Bézier curves, sinusoidal curves, simple way-points, or any combination thereof. In the case of the way-points, these are smoothed to ensure a sufficient degree of continuity using the system, Σ_f, outlined in (2.25), with $m = 4$ and $q = 5$. Regardless of its parameterization, the flat output trajectory is expanded into a full state and control signal trajectory using the flatness equations associated with the UAV dynamics Σ in (2.19).

(ii) To estimate the states of the UAV, the multiplicative scalar-update extended Kalman filter in Bitcraze's stock firmware is used. For additional details on the filter implementation, refer to [Mueller et al., 2015; Mueller et al., 2016] or see the source code in [Bitcraze, 2021b].

(iii) In all of the examples, the controller is implemented as described in Proposition 4.3, using the discontinuous attitude controller on SU(2) in Theorem 3.5 implemented with $\dot{\boldsymbol{\omega}}_d = \mathbf{0}$, taking the approach in (4.8) to synthesize a desired attitude $\boldsymbol{q}_d \in \mathbb{H}$. Thus, the implementation corresponds closely to the controller used in the simulation of the torus looping maneuver in Example 4.2, but here executed at approximately 500 [Hz] instead of being run in continuous time.

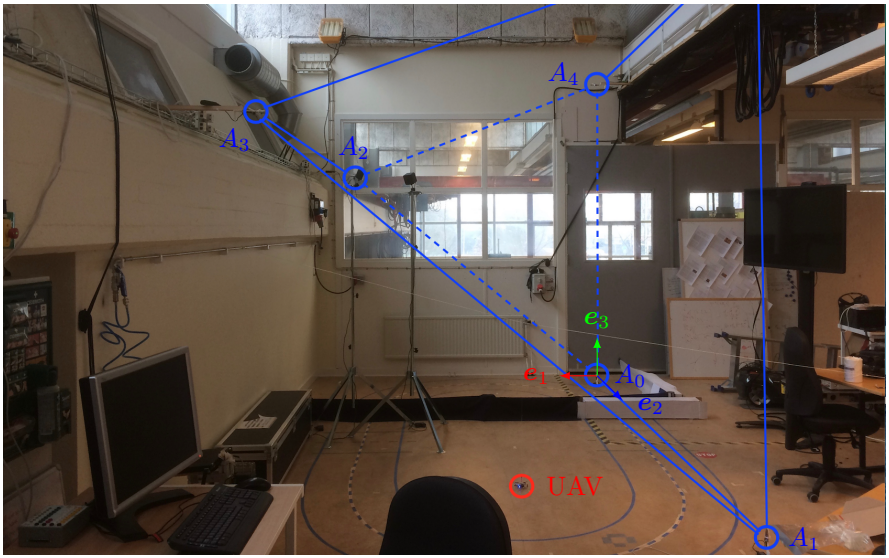

Figure 4.6 UWB anchor setup in the robotics laboratory, with the radio anchors and the convex hull of their positions highlighted in blue, and the Crazyflie UAV is marked in red. The global frame $\{\mathcal{G}\}$ is defined at the anchor A_0, and anchor A_5 is located outside of the picture above anchor A_1.

4.4.1 Aggressive Spiraling Maneuver

In this example, the Crazyflie is run with Bitcraze's Loco Positioning system [Bitcraze, 2021d], and set to takeoff and track a reference trajectory defined by a sequence of steps, followed by a rapid spiraling maneuver. The experimental setup is depicted in Figure 4.6, with the UWB anchors indicated in blue, and the convex hull of the anchors forming a triangular prism shape. In this example, the system is run in a two-way-ranging mode, and from the theory of UWB multilateration [Mueller et al., 2015], the flight-path is largely defined in the convex hull of the anchors to improve positioning performance.

Reference trajectory The reference trajectory is constructed by (i) a sequence of filtered steps in the $\boldsymbol{e}_2$- and $\boldsymbol{e}_3$-directions over 20 seconds. This is followed by (ii) a spiraling maneuver defined by a sinusoidal trajectory in the $\boldsymbol{e}_1\boldsymbol{e}_2$-plane, while ramping the elevation of the UAV linearly in time. This maneuver is conducted over 10 seconds, before (iii) steering the system to a point between anchor A_1 and A_5 with a single filtered step. Throughout the entire maneuver, the yaw angle is kept constant at zero, thus only exciting the positional dimensions of the flat outputs. The evaluation of the reference trajectory, filtering of the discontinuous step commands, and expansion of the flat outputs are all implemented in C, and done on the UAV processor.

Estimator To estimate the states of the UAV, the multiplicative EKF in Bitcraze's stock firmware is used. For additional details on the filter implementation, refer to [Mueller et al., 2015; Mueller et al., 2016] or see the source code in [Bitcraze, 2021b]. The 9-DOF IMU of the Crazyflie is used along with the UWB system run in a two-way ranging mode. For additional details on this mode of operation, refer to [Mueller et al., 2015; Greiff, 2017].

Controller The controller is implemented as described in Proposition 4.3, but using the discontinuous attitude controller on SU(2) in Theorem 3.5. Furthermore, the desired attitude accelerations are set to $\dot{\boldsymbol{\omega}}_d = \mathbf{0}$ in order to avoid computing the second time-derivative of the desired attitude numerically in the real-time implementation, as this was shown to work well (see Example 4.2). The desired attitude is computed using the third method (iii), and implemented directly on $\mathbb{H}$ using the quaternion form in (4.8).

Results and Discussion An example of an aggressive spiraling maneuver is depicted in Figure 4.7, in signals logged at approximately 20 [Hz] directly from the Crazyflie (including the expanded flat output trajectory), with all of the filtering and control algorithms run on the micro-controller of the Crazyflie. In this example, the element $\boldsymbol{X}_e \in \mathrm{SU}(2)$ was logged as a quaternion and later converted to a Γ-distance for visualization. The experiment setup and system response is shown in the video submission (see chapter-4-spiraling.mp4).

In this example, we start by noting that the Γ-distance takes a discontinuous jump as the controller activates at around $t_\circ = 3.2$ [s]. This is due to the control errors being computed in the control loop, which is not executing when the motors are turned off. During this time, a zero-vector is instead logged, resulting in a Γ-distance of 1. We note that the positional tracking is slightly worse than in the simulation examples, likely due to modeling errors and disturbances that were not present in the simulation. However, given that a low-cost UWB system is used for positioning, this tracking performance is deemed good. The experiment is repeatable, and here depicts one of many consecutive successful runs. We also note that attitude errors are induced when starting and exiting the sinusoidal maneuver, at $t - t_\circ = 20$ and $t - t_\circ = 40$, respectively. The reason for this is that the flat output trajectory is C^4 on $(t - t_\circ) \in \mathbb{R}_{>0} \backslash \{20, 40\}$, but it is not continuously differentiable at these two times. This results in a slight but visible increase in the attitude error, inducing a significant tracking error at these times. We emphasize that this is expected given how the reference trajectory is defined.

In summary, this example demonstrates that geometric attitude controller on SU(2) is well suited for use in practice. Despite letting $\dot{\boldsymbol{\omega}}_d = \mathbf{0}$ in the real-time implementation, the many additional disturbances present in practice, and the incorporation of estimates from an EKF with positional information governed by a low-cost UWB system, the implemented control system is clearly capable of perform aggressive large-angle maneuvers.

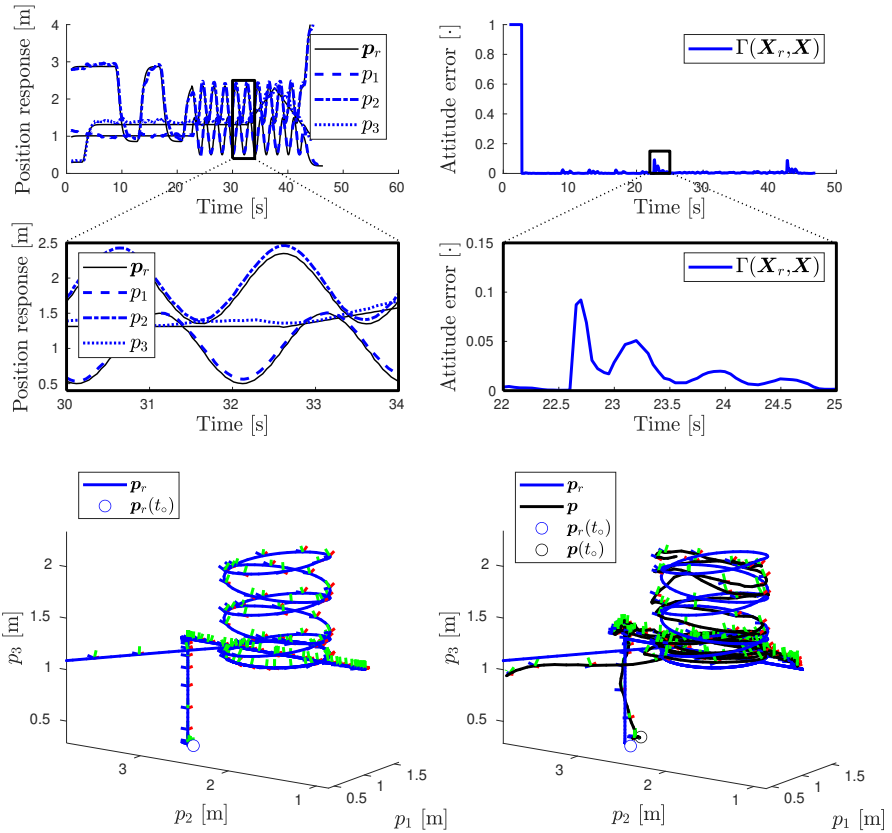

Figure 4.7 *System response* for *the spiraling scenario* in Sec. 4.4.1, as logged from a *real-time experiment*. *Top, left:* The positional reference $\boldsymbol{p}_r$ (black) and the response $\boldsymbol{p}$ (blue). *Top, right:* The tracking attitude error in the distance on SU(2), slightly increasing upon entering and exiting the spiraling maneuver. *Center, left:* Zoom on the positional response at the start of the spiraling maneuver. *Center, right:* Zoom on the attitude error when entering the spiraling maneuver. *Bottom, left:* Reference configurations trajectory in $\mathbb{R}^3$ in time. *Bottom, left:* System response in $\mathbb{R}^3$ in time, showing the reference trajectory, positional response, and measured rotation. The experiment setup and response is shown in the video chapter-4-spiraling.mp4.

Figure 4.8 Depiction of the setup in which the second example is run. A set of shelves with various drinks are to be scanned, with the camera facing the target shelf at all times. The origin of $\{\mathcal{G}\}$ is defined on a piece of paper.

4.4.2 Inventorying of Shelves

In this example, a small camera is mounted on the UAV, generating a video stream which is sent to a host computer via radio. On this computer, the simultaneous localization and mapping (SLAM) system developed from the work in [Persson, 2018], is run on the video stream in real-time. This facilitates a positioning without external motion capture system, and the positional estimate is subsequently streamed back to the UAV fused with the IMU-data in the onboard EKF. The experimental setup is depicted in Figure 4.8, and the objective of the example is for the UAV to scan the items on the shelves.

Reference trajectory In this example, we assume knowledge of the shelf location and geometry in the global frame $\{\mathcal{G}\}$, and plan a trajectory at a constant translation speed of 1 [m/s] along the shelves, scanning them in a predefined order. For this purpose, a set of linear splines are planned in the flat output space of the UAV with respect to the shelves, implementing a turn occurring after approximately 25 seconds in order to keep the shelf in the right-hand side in Figure 4.8 within the camera view. This can naturally be done using more advanced motion planning methods, lifting assumptions on the known geometry and free space, but such implementations are outside the scope of this example. It should be noted that the reference trajectory is C^0 and cannot be followed perfectly. When performing the flatness expansion, this will result in discontinuous signals. Note that all of the expanded reference

signals are discontinuous but still well defined when switching between the splines, and will induce tracking errors similar to the previous example.

Estimator To estimate the states of the UAV, the multiplicative EKF in Bitcraze's stock firmware is used once more. For additional details on the filter implementation, refer to [Mueller et al., 2015; Mueller et al., 2016; Bitcraze, 2021b]. The 9-DOF IMU of the Crazyflie is used along with positional information from the SLAM algorithm described in [Persson, 2018], using ORB-features in [Rublee et al., 2011] and the gyroscopic pre-integration method outlined in [Forster et al., 2017]. Additional details on the implementation of the SLAM system are given in [Greiff et al., 2021c]. The SLAM system is run on an external computer in real-time, communicating positional estimates to the Crazyflie which are queued in the EKF at a rate of approximately 50 [Hz]. Only the positional information in the SLAM system is fused in the onboard EKF. The estimated attitude from the SLAM system is stored separately.

Controller Once again, the controller is implemented as described in Proposition 4.3, with the discontinuous attitude controller on SU(2) in Theorem 3.5. The desired attitude accelerations are set to $\dot{\boldsymbol{\omega}}_d = \mathbf{0}$, and desired attitude is computed using the third method (iii), implemented directly on $\mathbb{H}$ by (4.8).

Results and Discussion The system response is shown in Figure 4.9, with references and estimates logged from the Crazyflie at approximately 20 [Hz], and estimates from the SLAM system at approximately 50 [Hz]. In addition, the initial configuration of the UAV at the start and the termination configuration are both´ depicted in Figure 4.10. The experiment setup and system response is shown in the video submission (see chapter-4-inventorying.mp4).

In this real-time example, the estimates from the SLAM system are logged separately and used to compute an attitude error with respect to the reference trajectory. As such, the attitude error in Figure 4.9 does not represent the attitude error on which the controller operates, but is the closest approximation to the true attitude error that can be computed. The reference attitude was sampled at the times where the SLAM system logged an attitude estimate, and this error is represented in the distance on SO(3). We note a slight lag in the positional trajectory tracking, and minor overshoots due to the rapidly changing velocity references (recall, these are discontinuous and cannot be followed perfectly). We also note that the turn is taken as intended, such that the UAV always faces the shelves, this is seen in the attitude error being small at all times, and also visible in the configuration response in the bottom-most subplots of Figure 4.9. We note that the attitude error increases as the system performs the turning maneuver, but that it remains small.

Finally, despite not having any external positioning system, and with the rapid 90° turn (which is a challenging maneuver for the SLAM system), the system remains stable and navigates back to the starting position down to a

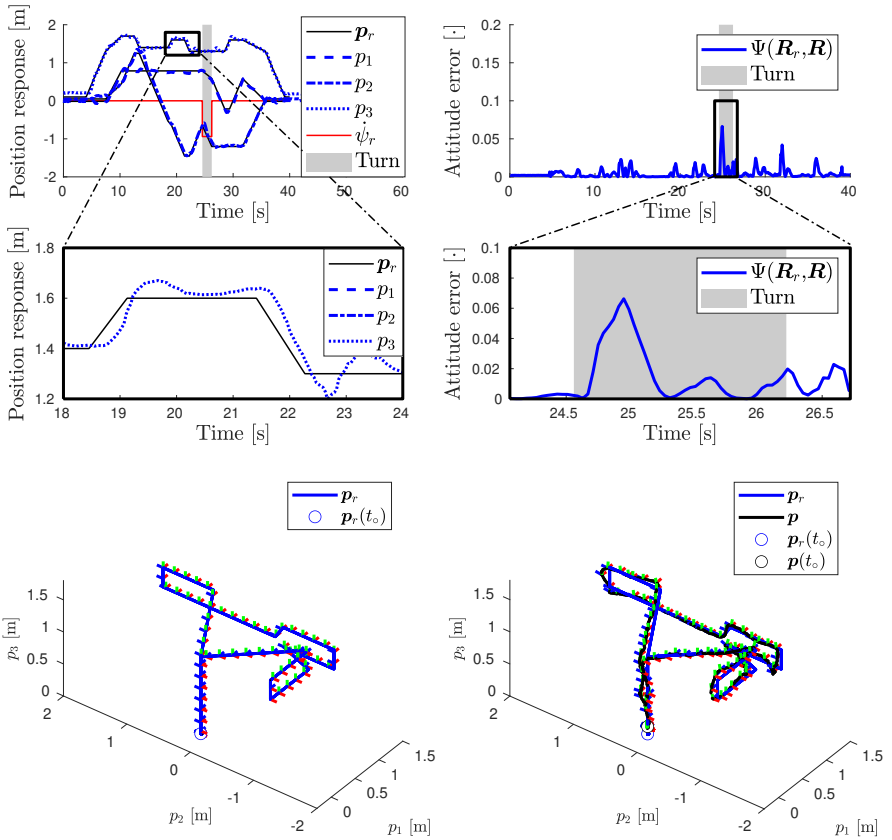

Figure 4.9 *System response* for *the inventorying scenario* in Sec. 4.4.2 as logged from a *real-time experiment*. *Top, left:* The positional reference $\boldsymbol{p}_r$ (black) and the response $\boldsymbol{p}$ (blue), along with the time-derivative of the yaw angle reference (red) indicating the time-interval during which the system is turning (gray). *Top, right:* The tracking attitude error in the distance on SO(3), slightly increasing during the turn, but otherwise small. *Center, left:* Zoom on the positional response in the elevation just before the turn, showing slight tracking errors and a small overshoot. *Center, right:* Zoom on the attitude error during the turn. *Bottom, left:* Reference configuration trajectory in $\mathbb{R}^3$. *Bottom, left:* System response in $\mathbb{R}^3$, showing the reference trajectory, positional response, and measured rotation. The experiment setup and system response is shown in the video chapter-4-inventorying.mp4.

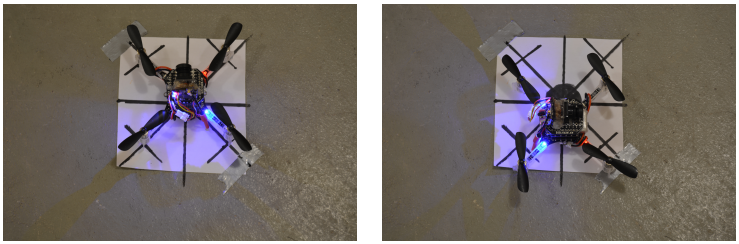

Figure 4.10 UAV configurations, $(\boldsymbol{p}, \boldsymbol{X})$, in the inventorying experiment. *Left*: Initial configuration at $t = t_\circ$. *Right*: Terminal configuration at $t = t_f$.

few centimeters (as illustrated in Figure 4.10). This is largely due to the high performance of the SLAM system in [Persson, 2018; Greiff et al., 2021c], but in no small part due to the sound control system implemented on the UAV.

The geometric attitude controller on $\mathrm{SU}(2) \times \mathbb{R}^3$ works well in practice, even when removing of the desired attitude accelerations in accordance with Example 4.2. It can automate tasks such as the inventorying of supermarkets, and remarkably, this real-time example was performed without any external motion capture system, but with additional computational power in the form of an external computer to host the SLAM algorithm.

4.5 Summary

In this chapter, the solutions to attitude tracking problem in Chapter 3 were leveraged to construct solutions to Problem 4.1. In particular, the continuous geometric controller on $\mathrm{SO}(3) \times \mathbb{R}^3$ in [Lee et al., 2010] was reviewed, and the exact same proof idea was used to derive a completely analogous set of controllers on $\mathrm{SU}(2) \times \mathbb{R}^3$, using the results in Theorems 3.4 and 3.5, respectively. When implemented with the discontinuous attitude controller in Theorem 3.5 and written out in the quaternion form, the controller in Proposition 4.3 becomes near-identical to the solution presented in the quaternion formalism in [Brescianini and D'Andrea, 2018] (disregarding control allocation). As such, the controllers in [Lee et al., 2010] and [Brescianini and D'Andrea, 2018] are closely related, as the latter can be interpreted as a geometric controller on $\mathrm{SU}(2) \times \mathbb{R}^3$ derived with respect to the distance Γ in Definition 2.19. In contrast to [Brescianini and D'Andrea, 2018], a different approach was taken to the stability proof, providing a joint Lyapunov function in the translation and attitude tracking errors and further motivating the use of this controller.

Both of the controllers work exceptionally well. This was demonstrated by the simulation examples in Examples 4.1 and 4.2, where aggressive maneuvers were followed down to expected numerical errors, rivaling the capabilities of complex nonlinear MPC approaches in [Foehn and Scaramuzza, 2018;

Kaufmann et al., 2020] with comparatively simple and memory-less feedback laws in Proposition 4.1 and 4.3. The latter controller was also demonstrated in two separate real-time examples: one including a complex spiraling maneuver, and the other involving a more realistic application to shelf inventorying.

While not undertaken in this chapter, it should be noted that the controller in Proposition 4.3 can be extended with integral action in the positional errors, completely analogously to the extensions of the work in [Lee et al., 2011] by [Goodarzi et al., 2013]. In addition, we note that the robust control approach on $\mathrm{SO}(3) \times \mathbb{R}^3$ in [Lee et al., 2013] starting from Theorem 3.3 can be replicated on $\mathrm{SU}(2) \times \mathbb{R}^3$ using Theorem 3.6 as a starting point. The reason for not doing this is that such extensions will retain some of the problems highlighted in this chapter, three of which can be summarized as follows:

- Firstly, the force f can attain negative values during extreme maneuvers, and there are points at which the desired attitude reference trajectory becomes ill defined. The latter can be dealt with, but there are no guarantees that the force is bounded away from zero in these controllers.
- Secondly, the computation of a desired trajectory $(\boldsymbol{R}_d, \boldsymbol{\omega}_d, \dot{\boldsymbol{\omega}}_d)$, necessarily requires a two-times differentiation of the translation control errors when using the proposed positional PD-feedback for the translation dynamics. In particular, the second time-derivative of $\boldsymbol{e}_v$ becomes problematic, as it involves a differentiation of the system's accelerations, resulting in very noisy signals. As a consequence, the impact of simply canceling this term was discussed, and as a fix, we let $\dot{\boldsymbol{\omega}}_d = \boldsymbol{0}$ in the experiments. This induces disturbances in the attitude control, but is a far more natural approach than to simply setting $\ddot{\boldsymbol{R}}_d$ to zero, and still permits excellent trajectory tracking as Example 4.2 demonstrates.
- Thirdly, even if the reference trajectory can be computed, the full state feedback solution is implemented based on filter estimates. This forms a triangular cascade on the form in (2.46), with the tracking errors constituting one subsystem and the estimation errors constituting the other. However, when considering their interconnection, need not be stable, as shown in the discussion of peaking in Sec. 2.5. Indeed, to show UAGAS in the entire closed-loop control system, we generally require stronger notions of stability than the asymptotic attractiveness.

The first problem was comprehensively addressed in the full state feedback solution presented in [Lefeber et al., 2017], in which the force is bound away from the origin. However, even for this controller, the second and third problems remain. This motivates the study of a related filtered output feedback problem in the forthcoming chapters, where stability of estimation and tracking errors are analyzed jointly, and the complete desired attitude reference trajectory can be evaluated without numerical differentiation.

5

Filtered Output Feedback: Attitude Dynamics

5.1 Introduction

In this chapter, we study the problem of finding a filtered output feedback (FOF) for the attitude dynamics of the UAV. That is, we seek to co-design an estimator and a controller and analyze the resulting closed loop system. Just as in Chapter 3, the system is configured on either SO(3) or SU(2), with the sub-index $(\cdot)_r$ denoting a reference, and the dynamics are given in (2.16). However, in this chapter we do not assume direct knowledge of the states. Instead, we assume knowledge of a set of measurements

$$\boldsymbol{y}_0(t) = \boldsymbol{\omega}(t) \in \mathbb{R}^3, \tag{5.1a}$$

$$\boldsymbol{y}_i(t) = \boldsymbol{R}(t)^\top \boldsymbol{v}_i \in \mathbb{R}^3, \quad i \in 1, ..., N, \tag{5.1b}$$

where $\boldsymbol{y}_0 \in \mathbb{R}^3$ are gyroscopic measurements registered by an IMU, and $\boldsymbol{y}_i \in \mathbb{R}^3$ with $i > 0$ are a set of N directions measured in the body frame, as rotated known directions in a global frame $\boldsymbol{v}_i \in \mathbb{R}^3$. The latter could for instance be measurements of the gravitational field as $\boldsymbol{v}_1$, measurements of a magnetic field as $\boldsymbol{v}_2$, or virtual measurements as the cross-product of the two directions, with $\boldsymbol{v}_3 = \boldsymbol{v}_1 \times \boldsymbol{v}_2$. Note that the measurements are taken to be deterministic, and that the filter design will be done in a deterministic framework along the lines of the estimators in [Mahony et al., 2008], ignoring any knowledge of measurement noise statistics. The noise is seen as an adversarial disturbance, with respect to which the controller should be robust.

Consequently, we seek a feedback law that does not use the measurements directly in the computation of the controls, in order to mitigate the influence of the measurement noise on the control signals and implicitly the states of the attitude dynamics. Furthermore, we seek controllers yielding uniform almost global and uniform local exponential stability properties.

5.1.1 The problem of Attitude Filtered Output Feedback

A controller that operates with the measurements in (5.1), and that does not include these measurements directly in the computation of the control signals is referred to as an attitude filtered output feedback (FOF). The problem formulation addressed in this chapter is summarized in Problem 5.1 as follows.

Problem 5.1
Consider a system with a state $\boldsymbol{x} = (\boldsymbol{R}, \boldsymbol{\omega}) \in \mathrm{SO}(3) \times \mathbb{R}^3$, with an associated reference trajectory $\boldsymbol{x}_r = (\boldsymbol{R}_r, \boldsymbol{\omega}_r) \in \mathrm{SO}(3) \times \mathbb{R}^3$, driven by $\boldsymbol{\tau} \in \mathbb{R}^3$ and $\boldsymbol{\tau}_r \in \mathbb{R}^3$, respectively. Let $\boldsymbol{R} = E^{\mathrm{SU}(2)}_{\mathrm{SO}(3)}(\boldsymbol{X}) \in \mathrm{SO}(3)$ and $\boldsymbol{R}_r = E^{\mathrm{SU}(2)}_{\mathrm{SO}(3)}(\boldsymbol{X}_r) \in \mathrm{SO}(3)$ by Definition 2.17, satisfying the dynamics in (2.16) and measurements in (5.1) with a known set of directions $\{\boldsymbol{v}_i\}_{i=1}^N$ in a global frame of reference. Define a filter memory, $\boldsymbol{\zeta}_a$, and an estimate update law in this memory, the measured signals, and reference trajectory, as

$$\frac{\mathrm{d}\boldsymbol{\zeta}_a}{\mathrm{d}t} = H_a(\boldsymbol{\zeta}_a, \{\boldsymbol{y}_i\}_{i=0}^N, \boldsymbol{X}_r, \boldsymbol{\omega}_r, \boldsymbol{\tau}_r, \boldsymbol{\tau}), \tag{5.2}$$

with an associated feedback law

$$\boldsymbol{\tau} = G_a(\boldsymbol{\zeta}_a, \boldsymbol{X}_r, \boldsymbol{\omega}_r, \boldsymbol{\tau}_r), \tag{5.3}$$

such that $\boldsymbol{x}(t) \to \boldsymbol{x}_r(t)$ as $t \to \infty$, and characterize the resulting equilibria.□

Just as in Chapter 3, we can at best hope to find almost globally stabilizing controllers if considering continuous feedback laws. In addition to finding such controllers, we seek to analyze them in terms of their resulting closed-loop stability properties. A schematic overview of the FOF attitude controller is given in Figure 5.1. In the controller implementations, the memory stored in the reference dynamics Σ_r^a and the attitude dynamics Σ^a will both be configured on SU(2). Similar to Chapter 3, a FOF controller on SU(2) or SO(3) refers to the configuration manifold on which the errors are considered, it does not refer to the complete memory of the controller.

5.1.2 Chapter Motivation

The somewhat exotic output feedback problem defined in Problem 5.1 is of great practical interest, as it deals with measurements that are ubiquitous in modern UAV applications and seeks to bound both the estimation and trajectory tracking errors over time. One of the first solutions to a related the tracking attitude filtered output feedback problem is presented in [Caccavale and Villani, 1999, Theorem 2], where two controllers are developed in the quaternion formalism. Local exponential stability is shown with a lead filter for the attitude rate estimation. While the controllers result in error dynamics with exponential stability properties, they rely on measuring the orientation

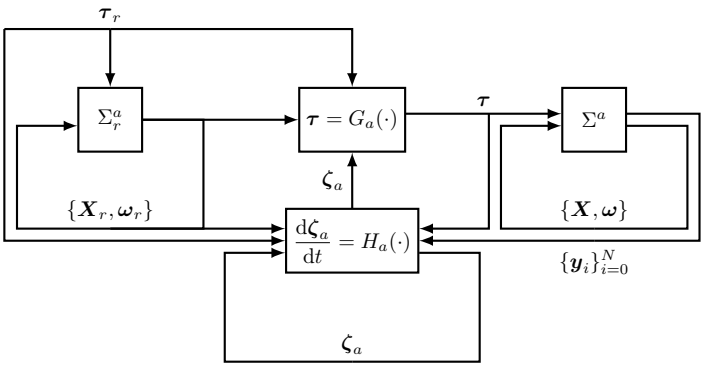

Figure 5.1 Sketch of the filtered output feedback attitude controller.

directly, and omit any measurement of the attitude rates, which are available in most modern UAV applications. A closely related solution, also in the quaternion representation and without attitude rate measurements, was presented by Tayebi in [Tayebi, 2008, Theorem 1]. Here, AGAS properties are shown of an equilibrium representing a zero tracking error, but in both of these works, the measurements and noise enter directly in the feedback law.

More recently, a solution to the attitude tracking filtered output feedback control problem is proposed in [Zou, 2016, Theorem 3], operating directly with elements of SO(3). Just as in [Caccavale and Villani, 1999] and [Tayebi, 2008], this work omits the gyroscopic measurements. In [Zou, 2016], the proposed solution has some caveats, namely that the control signal approaches $\boldsymbol{\tau}(t) \to \infty$ as $\Psi(\boldsymbol{R}_r, \boldsymbol{R}) \to 2$. Furthermore, the proof is finalized with Theorem 2.5, and concludes asymptotic stability. As such, little can be said about the robustness of the resulting closed-loop system. Other approaches, such as the work in [Shao et al., 2018], jointly consider tracking and observer errors for attitude dynamics when working with the full UAV dynamics. Here the problem of robustness is addressed by implementing an extended state observer, yielding a local ultimate boundedness result in [Shao et al., 2018, Theorem 1]. It is claimed to be an asymptotic stability result, but in the sense that the ultimate bound goes to zero as the observer bandwidth goes to infinity. It is not asymptotically stable as defined in this thesis, and the result is local, as per [Shao et al., 2018, Assumption 1]. A similar approach is taken in [Mishra et al., 2020] for a more general class of systems (but assuming full actuation). As the considered estimation and control errors are independently ULES and UAGAS, respectively, and the interconnection is shown to be LAS.

In the prior work on tracking filtered output feedback for attitude dynamics, the stability results tend to be local and lack the property of uniform convergence. Consequently, there is room for improvement by showing stronger

stability properties that implicitly guarantee a measure of robustness by Theorem 2.12. In addition, as it is possible to solve the problem locally without gyroscopic measurements, these are often excluded in more academic problem formulations. However, from a practical perspective, the inclusion of gyroscopic terms is more interesting, as these are typically available in practice. This information should therefore be leveraged in the problem formulation to improve the controller performance, further motivating Problem 5.1.

5.1.3 Contributions

The above considerations motivated the development of a solution to Problem 5.1 in [Lefeber, Greiff, and Robertsson, 2020, Proposition 2], which is the main theoretical contribution in this chapter. Contrary to the prior work on filtered output feedback solutions, the proposed control system:

(i) Assumes that the rotation is only known through directional measurements, similar to the formulation in the explicit nonlinear complementary filters in [Mahony et al., 2008] and explicit vector control in Theorem 3.1;

(ii) Assumes that the attitude rates are measured in the body frame;

(iii) Does not use any measurements directly in the computation of $\boldsymbol{\tau}$;

(iv) Results in a UAGAS and ULES solution to Problem 5.1.

This last point is of particular importance, as it facilitates extensions of the controller to the full UAV dynamics by cascade theorems. In addition, we provide rules of thumb for tuning, and several simulation examples to provide intuition and demonstrate the veracity of the theoretical results.

5.1.4 Overview

The output feedback result in [Tayebi, 2008] is reviewed in Sec. 5.2, highlighting its strengths, but also pointing out some potential problems in the approach. The solution in [Lefeber et al., 2020, Proposition 2], here referred to as explicit vector FOF, is then presented using the techniques employed in Chapter 3. This is done in Sec. 5.3, with a filter memory defined on $\mathrm{SO}(3) \times \mathbb{R}^3$. The proposed theory is illustrated by simulation examples, and insights for the tuning problem are given in Sec. 5.4, supported by simulations. To give an overview, the results and examples are summarized in Table 5.1.

Table 5.1 Overview of the results and examples of Chapter 5. Here, [1] indicates work of others, proofs given elsewhere; [2] indicates work tangential with others, but with independent proofs given; and [3] indicates new work.

Reference	Description
Thm. 5.1 [1]	Output feedback on $\mathbb{H}$, without gyroscopic measurements and with filter memory defined on $\mathbb{H}$ in [Tayebi, 2008, Thm. 2]
Thm. 5.2 [3]	Filtered output feedback on SO(3), with filter memory defined on $\mathrm{SO}(3) \times \mathbb{R}^3$ in [Lefeber, Greiff, and Robertsson, 2020, Prop. 2]
Example 5.1	Simulation example with the output feedback in Thm. 5.1
Example 5.2	Simulation example with the filtered output feedback in Thm. 5.2
Example 5.3	Simulation example with Thm. 5.2, demonstrating tuning ideas

5.2 Output Feedback Without Attitude Rates

Before giving the main result, we first summarize the related result in [Tayebi, 2008], which is an output feedback (or partial state feedback) that introduces an auxiliary system. It does not solve Problem 5.1, as the feedback (i) assumes that the rotation is known in a quaternion representation at all times; (ii) that the attitude rates are not measured; (iii) uses the measurements directly in the feedback; and (iv) yields AGAS. Nonetheless, the theorem is insightful, can be extended to the full UAV dynamics as done in [Abdessameud and Tayebi, 2010], can be summarized in the context of Problem 5.1 as follows.

THEOREM 5.1—[TAYEBI, 2008, THEOREM 1]
Define the filter memory by $\boldsymbol{\zeta} \triangleq \bar{\boldsymbol{q}} \in \mathbb{H}$ and consider the errors

$$\boldsymbol{q}_e = \boldsymbol{q}_r^{-1} \odot \boldsymbol{q}, \qquad \boldsymbol{R}_e = E^{\mathbb{H}}_{\mathrm{SO}(3)}(\boldsymbol{q}_e), \tag{5.4}$$

$$\tilde{\boldsymbol{q}} = \bar{\boldsymbol{q}}^{-1} \odot \boldsymbol{q}_e, \qquad \boldsymbol{\omega}_e = \boldsymbol{\omega} - \boldsymbol{R}_e^\top \boldsymbol{\omega}_r, \tag{5.5}$$

Consider the attitude dynamics in (2.16) with direct measurements of the quaternion attitude, $\boldsymbol{q} \in \mathbb{H}$. Define a feedback

$$\boldsymbol{\tau} = -k_1 \Im(\boldsymbol{q}_e) - k_2 \Im(\bar{\boldsymbol{q}}) + \boldsymbol{J}\boldsymbol{R}_e^\top \dot{\boldsymbol{\omega}}_r + \boldsymbol{S}(\boldsymbol{R}_e^\top \boldsymbol{\omega}_r)\boldsymbol{J}\boldsymbol{R}_e^\top \boldsymbol{\omega}_r, \tag{5.6a}$$

where the filter memory is updated by

$$\frac{\mathrm{d}\bar{\boldsymbol{q}}}{\mathrm{d}t} = \frac{1}{2}\bar{\boldsymbol{q}} \odot \begin{bmatrix} 0 \\ \boldsymbol{\delta}_{\boldsymbol{q}} \end{bmatrix}, \qquad \boldsymbol{\delta}_{\boldsymbol{q}} = \boldsymbol{K}_{\boldsymbol{q}} \Im(\tilde{\boldsymbol{q}}). \tag{5.6b}$$

For any controller gains $k_1 > 0, k_2 > 0$, and $\boldsymbol{K}_{\boldsymbol{q}} = \boldsymbol{K}_{\boldsymbol{q}}^\top \succ \boldsymbol{0}$, $\lim_{t\to\infty} \boldsymbol{q}_e = \pm \boldsymbol{q}_I$, $\lim_{t\to\infty} \tilde{\boldsymbol{q}} = \pm \boldsymbol{q}_I$, $\lim_{t\to\infty} \boldsymbol{\omega}_e = \boldsymbol{0} \Rightarrow \boldsymbol{R} \to \boldsymbol{R}_r$ and $\boldsymbol{\omega} \to \boldsymbol{\omega}_r$ as $t \to \infty$. □

Proof. The proof is given in [Tayebi, 2008, Theorem 1], here sketched in a different notation. It follows by analysis of the Lyapunov function candidate

$$\mathcal{V} = k_1\|\boldsymbol{q}_e - \boldsymbol{q}_I\|^2 + k_2\|\tilde{\boldsymbol{q}} - \boldsymbol{q}_I\|^2 + \frac{1}{2}\boldsymbol{\omega}_e^\top \boldsymbol{J}\boldsymbol{\omega}_e. \tag{5.7}$$

By plugging in the error dynamics, it is shown that $\dot{\mathcal{V}} = -k_2\Im(\tilde{\boldsymbol{q}})^\top \boldsymbol{K}_{\boldsymbol{q}}\Im(\tilde{\boldsymbol{q}}) \leq 0$ and also uniformly continuous along the solutions of the closed-loop system. As $\mathcal{V} \geq 0$, the proof follows directly by application of Lemma 2.5. □

While falling short of being a solution to Problem 5.1 (the feedback includes the measurements directly through $\boldsymbol{q}_e$ and $\boldsymbol{R}_e$, and does not use the directional measurements nor gyroscopic information, $\boldsymbol{\omega}$), the controller proposed by Tayebi is insightful. Remarkably, the tracking error $\boldsymbol{\omega}_e$ can be driven to zero without any gyroscopic information. The feedback is AGAS, which can be shown by further analyzing the Lyapunov function using, for instance, the instability result in Theorem 2.6.

Remark 5.1
The auxiliary system in (5.6b) is introduced to generate a passive map from the innovation term $\boldsymbol{\delta}_{\boldsymbol{q}}$ to $\Im(\tilde{\boldsymbol{q}})$, as is discussed in [Tayebi, 2008, Remark 3]. However, $\bar{\boldsymbol{q}}$ does not have a physical interpretation. This memory does not necessarily provide information that is useful outside of the controller. □

Remark 5.2
The controller requires knowledge of a quaternion attitude, but there exist no sensors capable of measuring such an attitude directly. Consequently, this attitude has to be reconstructed from the directional measurements in (5.1b), or some other sensory information. However, if this introduces dynamics in the attitude estimate, then the stability analysis needs to be reconsidered. □

In spite of Remarks 5.1 and 5.2, the controller in Theorem 5.1 has several uses. It is a partial-state feedback developed in the quaternion formalism, facilitated by the introduction of the auxiliary system in (5.6b). Additionally, some insights from its construction can be used to develop solutions to Problem 5.1. Before doing so, we first demonstrate the properties of the Tayebi's OF controller summarized in Theorem 5.1 with an example.

Example 5.1
In this example, the output feedback solution in Theorem 5.1 is simulated. The system is defined with randomized dense inertia matrix satisfying $\lambda_m(\boldsymbol{J}) = 0.5$ and $\lambda_M(\boldsymbol{J}) = 1$, analogous to the examples in Chapter 3, but with a different realization. Similarly, the initial conditions are randomized on $\boldsymbol{q}(t_\circ), \boldsymbol{q}_r(t_\circ), \bar{\boldsymbol{q}}(t_\circ) \sim \mathcal{U}(\mathbb{H})$ with $\boldsymbol{\omega}(t_\circ), \boldsymbol{\omega}_r(t_\circ) \sim \mathcal{N}(\boldsymbol{0}, \boldsymbol{I})$. From these initial conditions, the reference dynamics are driven by the torques

$$\boldsymbol{\tau}_r(t) = (\sin(2\pi t + 1);\ \sin(4\pi t + 2);\ \sin(6\pi t + 3)) \in \mathbb{R}^3. \tag{5.8}$$

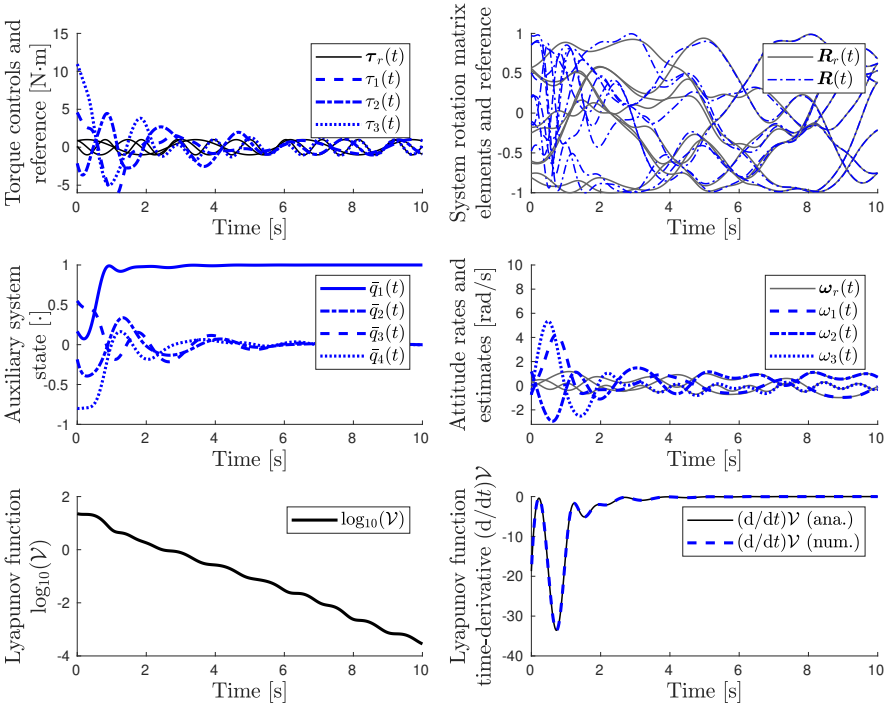

Figure 5.2 Closed-loop system response when in feedback with the filtered output feedback in Theorem 5.1. *Top, left:* Reference torque trajectory, $\boldsymbol{\tau}_r$, driving the reference dynamics, and computed control signals $\boldsymbol{\tau}$. *Top, right:* Elements of the reference attitude on $\boldsymbol{R}_r = E^{\mathbb{H}}_{\mathrm{SO}(3)}(\boldsymbol{q}_r) \in \mathrm{SO}(3)$ and the controlled attitude on $\boldsymbol{R} = E^{\mathbb{H}}_{\mathrm{SO}(3)}(\boldsymbol{q}) \in \mathrm{SO}(3)$. *Center, left:* The auxiliary quaternion $\bar{\boldsymbol{q}}$. *Center, right:* Attitude rates, and reference attitude rates. *Bottom, left:* Lyapunov function in the 10-logarithm. *Bottom, right:* Lyapunov function time-derivative, analytical (black) and numerical (blue). The simulated system response is shown in the video chapter-5-simulations.mp4.

The controller is tuned with $k_1 = k_2 = 10, \boldsymbol{K}_{\boldsymbol{q}} = 10\boldsymbol{I}_3$, and the simulation is run over $t \in [0, 10]$ [s], yielding the system response in Figure 5.2. To better study the signals $\mathcal{V}$ and $\dot{\mathcal{V}}$ for small errors, no measurement noise is added.

The figure shows a relatively large transient in the control signal torques, and how the auxiliary state $\bar{\boldsymbol{q}}$ converges to the identity element $\boldsymbol{q}_I$. Furthermore, when mapping the internal quaternion attitude representation to SO(3) and studying the top right and center right subplots, it is clear that the controller in Theorem 5.1 achieves the tracking properties specified in Problem 5.1. It is also worth noting the large transient in the attitude rates. These transients are often observed with the controller, as it does not include

any explicit measurements or estimates of the attitude rates. Finally, we note that the Lyapunov function candidate in (5.7) decays monotonically in time, and that its analytical time-derivative along the closed-loop solutions matches the numerically differentiated Lyapunov function, validating the implementation of Theorem 5.1 and the work in [Tayebi, 2008]. This result will serve as an inspiration for the FOF developments made in this chapter. □

5.3 Filtered Output Feedback With Attitude Rates

The key in constructing the FOF depicted in Figure 5.1 lies in the definition of the filter memory and the observer. From the discussions in Chapter 3, there are clear similarities between the generalized explicit vector control and the various geometric controllers on SU(2) and SO(3). However, the explicit vector control in Theorem 3.1 can be implemented based on cross-product errors in rotated vectors, making it an appealing starting point for the FOF controller derivation, considering the directional measurements in (5.1b). For this reason, and due to a slightly simpler algebra, we opt to work with SO(3). Consider an estimate of the rotation as $\hat{\boldsymbol{R}}(t) \in \mathrm{SO}(3)$, and an estimate of the attitude rate as $\hat{\boldsymbol{\omega}}(t) \in \mathbb{R}^3$, resulting in a filter memory $\boldsymbol{\zeta}_a \triangleq (\hat{\boldsymbol{R}}, \hat{\boldsymbol{\omega}})$ in Figure 5.1. These objects should be driven toward the states of the attitude dynamics, $\boldsymbol{x} = (\boldsymbol{R}, \boldsymbol{\omega})$. Inspired by the auxiliary system introduced in (5.6b), we seek two innovation terms $\boldsymbol{\delta}_{\boldsymbol{R}} \in \mathbb{R}^3$ and $\boldsymbol{\delta}_{\boldsymbol{\omega}} \in \mathbb{R}^3$, as functions of the measurements and the reference states. Naturally, the attitude innovation term, $\boldsymbol{\delta}_{\boldsymbol{R}}$, should enter multiplicatively as an element of $\mathfrak{so}(3)$ to keep the estimate $\hat{\boldsymbol{R}} \in \mathrm{SO}(3)$. With this intuition, we arrive at the following result.

Theorem 5.2—Explicit vector FOF on SO(3)
Define the filter memory $\boldsymbol{\zeta}_a = (\hat{\boldsymbol{R}}, \hat{\boldsymbol{\omega}}) \in \mathrm{SO}(3) \times \mathbb{R}^3$ and consider the errors

$$\boldsymbol{R}_e = \boldsymbol{R}_r \boldsymbol{R}^\top \in \mathrm{SO}(3), \qquad \tilde{\boldsymbol{R}} = \hat{\boldsymbol{R}} \boldsymbol{R}^\top \in \mathrm{SO}(3), \tag{5.9a}$$

$$\boldsymbol{\omega}_e = \boldsymbol{\omega}_r - \boldsymbol{\omega} \in \mathbb{R}^3, \qquad \tilde{\boldsymbol{\omega}} = \hat{\boldsymbol{\omega}} - \boldsymbol{\omega} \in \mathbb{R}^3, \tag{5.9b}$$

$$\hat{\boldsymbol{\omega}}_e = \boldsymbol{\omega}_r - \hat{\boldsymbol{\omega}} \in \mathbb{R}^3. \tag{5.9c}$$

The attitude dynamics in (2.16) with measurements in (5.1) in feedback with

$$\boldsymbol{\tau} = \boldsymbol{\tau}_r + \boldsymbol{S}(\boldsymbol{J}\hat{\boldsymbol{\omega}}_e)\boldsymbol{\omega}_r + \boldsymbol{K}_\omega \hat{\boldsymbol{\omega}}_e + \sum_{i=1}^{N} k_i \boldsymbol{S}(\boldsymbol{R}_r^\top \boldsymbol{v}_i)\hat{\boldsymbol{R}}^\top \boldsymbol{v}_i, \tag{5.10a}$$

where the estimates are computed by

$$\frac{\mathrm{d}\hat{\boldsymbol{R}}}{\mathrm{d}t} = \hat{\boldsymbol{R}}\boldsymbol{S}(\boldsymbol{\omega} + \boldsymbol{\delta}_{\boldsymbol{R}}) \tag{5.10b}$$

$$\frac{\mathrm{d}\boldsymbol{J}\hat{\boldsymbol{\omega}}}{\mathrm{d}t} = \boldsymbol{S}(\boldsymbol{J}\boldsymbol{\omega})\boldsymbol{\omega} + \boldsymbol{\tau} + \boldsymbol{\delta}_{\boldsymbol{\omega}}, \tag{5.10c}$$

with the innovation terms

$$\boldsymbol{\delta}_{\boldsymbol{R}} = -c_R \sum_{i=1}^{N} k_i \boldsymbol{S}(\hat{\boldsymbol{R}}^\top \boldsymbol{v}_i)(\boldsymbol{R}_r^\top \boldsymbol{v}_i + \boldsymbol{R}^\top \boldsymbol{v}_i) \tag{5.10d}$$

$$\boldsymbol{\delta}_{\boldsymbol{\omega}} = -\boldsymbol{J}\boldsymbol{S}(\boldsymbol{\omega}_r)\boldsymbol{\omega}_e - \boldsymbol{K}_{\boldsymbol{\omega}}\boldsymbol{\omega}_e - \boldsymbol{C}_{\boldsymbol{\omega}}\tilde{\boldsymbol{\omega}}, \tag{5.10e}$$

for any $\boldsymbol{K}_{\boldsymbol{\omega}} = \boldsymbol{K}_{\boldsymbol{\omega}}^\top \succ \boldsymbol{0}$, $\boldsymbol{C}_{\boldsymbol{\omega}} = \boldsymbol{C}_{\boldsymbol{\omega}}^\top \succ \boldsymbol{0}$, $c_R > 0$, and $k_i > 0$ such that $\boldsymbol{M} = \sum_{i=1}^{N} k_i \boldsymbol{v}_i \boldsymbol{v}_i^\top$ has distinct eigenvalues, renders the equilibrium point $(\boldsymbol{R}_e, \tilde{\boldsymbol{R}}, \boldsymbol{\omega}_e, \tilde{\boldsymbol{\omega}}) = (\boldsymbol{I}, \boldsymbol{I}, \boldsymbol{0}, \boldsymbol{0})$ UAGAS and ULES. There exists 15 other unique equilibrium points on $\mathrm{SO}(3)^2 \times \mathbb{R}^6$, all of which are locally unstable. □

Proof. The proof sketch was given in [Lefeber et al., 2020, Proposition 2] and is here summarized in brevity, with a rigorous and detailed proof given in Appendix C.1. First, the non-autonomous error dynamics in $\boldsymbol{R}_e, \tilde{\boldsymbol{R}}, \boldsymbol{\omega}_e, \tilde{\boldsymbol{\omega}}$ are derived. Secondly, a Lyapunov function candidate is proposed with

$$\mathcal{V}_1 = \sum_{i=1}^{N} \frac{k_i}{2} \|\boldsymbol{R}_e \tilde{\boldsymbol{R}}^\top \boldsymbol{v}_i - \boldsymbol{v}_i\|^2 + \frac{1}{2}\boldsymbol{\omega}_e^\top \boldsymbol{J}\boldsymbol{\omega}_e + \sum_{i=1}^{N} \frac{k_i}{2} \|\tilde{\boldsymbol{R}}\boldsymbol{v}_i - \boldsymbol{v}_i\|^2 + \frac{1}{2}\tilde{\boldsymbol{\omega}}^\top \boldsymbol{J}\tilde{\boldsymbol{\omega}}. \tag{5.11}$$

It is shown that the time derivative of this weak Lyapunov fuction candidate is negative semi-definite in the errors along the closed-loop solutions. Specifically,

$$\frac{\mathrm{d}\mathcal{V}_1}{\mathrm{d}t} = -c_R \left\| \sum_{i=1}^{N} k_i \boldsymbol{S}(\hat{\boldsymbol{R}}^\top \boldsymbol{v}_i)(\boldsymbol{R}_r^\top \boldsymbol{v}_i + \boldsymbol{R}^\top \boldsymbol{v}_i) \right\|^2 - \boldsymbol{\omega}_e^\top \boldsymbol{K}_{\boldsymbol{\omega}} \boldsymbol{\omega}_e - \tilde{\boldsymbol{\omega}}^\top C_{\boldsymbol{\omega}} \tilde{\boldsymbol{\omega}}. \tag{5.12}$$

Thirdly, by analysis with Lemma 2.5 and Lemma 2.7, it is shown that all trajectories of the error dynamics converge to an invariant set

$$\mathcal{S} = \left\{ (\boldsymbol{R}_e, \tilde{\boldsymbol{R}}, \boldsymbol{\omega}_e, \tilde{\boldsymbol{\omega}}) \in \mathrm{SO}(3)^2 \times \mathbb{R}^6 \middle| \begin{matrix} \sum_{i=1}^{N} k_i \boldsymbol{S}(\boldsymbol{R}_r^\top \boldsymbol{v}_i)\hat{\boldsymbol{R}}^\top \boldsymbol{v}_i = \boldsymbol{0}, & \boldsymbol{\omega}_e = \boldsymbol{0} \\ \sum_{i=1}^{N} k_i \boldsymbol{S}(\boldsymbol{R}^\top \boldsymbol{v}_i)\hat{\boldsymbol{R}}^\top \boldsymbol{v}_i = \boldsymbol{0}, & \tilde{\boldsymbol{\omega}} = \boldsymbol{0} \end{matrix} \right\}. \tag{5.13}$$

Furthermore, utilizing techniques similar to those used in proof of Theorem 3.1, specifically Lemma B.3 and the assumptions on $\boldsymbol{M}$, it is shown that all trajectories of the non-autonomous error dynamics converge to a set of 16 isolated equilibrium points $\mathcal{E} \subset \mathrm{SO}(3)^2 \times \mathbb{R}^6$. Fourthly, with $\mathcal{Y}_1 \triangleq \dot{\mathcal{V}}_1$ and

$$\mathcal{V}_2 = \boldsymbol{\omega}_e^\top \sum_{i=1}^{N} k_i \boldsymbol{S}(\boldsymbol{R}_r^\top \boldsymbol{v}_i)\hat{\boldsymbol{R}}^\top \boldsymbol{v}_i, \tag{5.14}$$

one can show that $(\mathrm{d}/\mathrm{d}t)\mathcal{V}_2 \leq \mathcal{Y}_2$, where $\mathcal{Y}_2$ is uniformly bounded in the initial errors, and negative as $\dot{\mathcal{V}}_1 = 0$. Thus, the nested Matrosov result in Theorem 2.7 is invoked to show uniform convergence to $\mathcal{E}$. To assess the local properties of the equilibrium points, Chetaev's instability result in Theorem 2.6 is used to show that $(\boldsymbol{R}_e, \tilde{\boldsymbol{R}}, \boldsymbol{\omega}_e, \tilde{\boldsymbol{\omega}}) = (\boldsymbol{I}, \boldsymbol{I}, \boldsymbol{0}, \boldsymbol{0})$ is the only locally stable point in $\mathcal{E}$. This is confirmed by a local linearization performed on $\mathrm{SO}(3)^2 \times \mathbb{R}^6$ about the point $(\boldsymbol{R}_e, \tilde{\boldsymbol{R}}, \boldsymbol{\omega}_e, \tilde{\boldsymbol{\omega}}) = (\boldsymbol{I}, \boldsymbol{I}, \boldsymbol{0}, \boldsymbol{0})$, a local representation of the errors, $\boldsymbol{X} \in \mathbb{R}^{12}$, evolve by a ULES non-autonomous descriptor system

$$\boldsymbol{E}\dot{\boldsymbol{X}} = \boldsymbol{A}(t)\boldsymbol{X}, \tag{5.15}$$

where $\boldsymbol{A}(t) \in \mathbb{R}^{12\times 12}$ and $\boldsymbol{0} \prec \boldsymbol{E} = \boldsymbol{E}^\top \in \mathbb{R}^{12\times 12}$. We stress that this is not shown by spectral conditions, but rather done using Lyapunov theory. Thus, $(\boldsymbol{R}_e, \tilde{\boldsymbol{R}}, \boldsymbol{\omega}_e, \tilde{\boldsymbol{\omega}}) = (\boldsymbol{I}, \boldsymbol{I}, \boldsymbol{0}, \boldsymbol{0})$ is ULES and UAGAS, concluding the proof. □

This is a powerful result, and a feasible solution to Problem 5.1. Furthermore, we note that the estimator is implementable given the available measurement information due to the availability of the gyroscopic rates. We emphasize that none of the taken measurements appear directly in the computation of the torques in (5.10a). Thus, all measurement noise passes through at least one integrator before appearing in the control signals. This is not the case with the full state feedback control laws in Chapter 3, where the noise in the gyroscopic measurements enter directly in the control signals, as $\boldsymbol{\omega}$ is a factor in $\boldsymbol{e}_{\boldsymbol{\omega}}$. Nor is it the case in the output feedback in Theorem 5.1, where the measurement noise in the attitude enters directly in the control signals.

Remark 5.3
A drawback of the proposed filtered output feedback attitude controller in Theorem 5.2 is that the proof is finalized with variants of Barbălat's Lemma, nested Matrosov theorems and local linearizations. Consequently, while all trajectories converge to the single stable equilibrium point, we cannot characterize the worst-case decay rates beyond a neighborhood of the stable equilibrium $(\boldsymbol{I}, \boldsymbol{I}, \boldsymbol{0}, \boldsymbol{0}) \in \mathcal{E}$. Similarly, while some robustness properties are afforded to non-autonomous systems with uniform stability properties (see Theorem 2.12), the resulting ultimate bounds become nontrivial to quantify in a sense that is informative for the tuning problem. This makes the tuning of the controller a nontrivial task, warranting its discussion in Sec. 5.4. □

To illustrate the properties of the resulting closed-loop system, we give a second simulation example (see Example 5.2). Here, the tracking performance of the controller and estimator is shown, along with their joint Lyapunov function in (5.11) and its associated time-derivative in (5.12) along the trajectories of the error dynamics. In addition, we show the proximity of the errors $\boldsymbol{R}_e(t)$ and $\tilde{\boldsymbol{R}}(t)$ to their associated equilibrium configurations $(\boldsymbol{R}_\circ, \tilde{\boldsymbol{R}}_\circ, \boldsymbol{0}, \boldsymbol{0}) \in \mathcal{E}$. This is visualized in the distances $\Psi(\boldsymbol{R}_e(t), \boldsymbol{R}_\circ)$ and $\Psi(\tilde{\boldsymbol{R}}(t), \tilde{\boldsymbol{R}}_\circ)$, respectively.

Example 5.2
In this example, the continuous FOF on SO(3) proposed in Theorem 5.2 is demonstrated. Consider a system with randomized dense inertia matrix satisfying $\lambda_m(\boldsymbol{J}) = 0.5$ and $\lambda_M(\boldsymbol{J}) = 1$, with the same realization as in Example 5.1. Similarly, the initial conditions are randomized on $\boldsymbol{R}(t_\circ), \boldsymbol{R}_r(t_\circ), \hat{\boldsymbol{R}}(t_\circ) \sim \mathcal{U}(\mathrm{SO}(3))$ with $\boldsymbol{\omega}(t_\circ), \boldsymbol{\omega}_r(t_\circ), \hat{\boldsymbol{\omega}}(t_\circ) \sim \mathcal{N}(\boldsymbol{0}, \boldsymbol{I})$. From these initial conditions, the reference dynamics is driven by $\boldsymbol{\tau}_r(t)$ in (5.8).

To define the measurement model of the 9-DOF IMU, we consider a first vector $\boldsymbol{v}_1 = (0, 0, -1)^\top$ corresponding to the gravitational field direction in the global east-north-up (ENU) coordinate frame. In addition, a second normal vector is randomized as $\boldsymbol{v}_2 = (-0.9754, -0.2086, -0.0713)^\top$, corresponding to the direction of the magnetic field in a global ENU frame. Finally, a virtual measurement direction is then constructed by $\boldsymbol{v}_3 = \boldsymbol{v}_1 \times \boldsymbol{v}_2$, such that for any $k_i > 0$, $\boldsymbol{M} \succ \boldsymbol{0}$. The estimator update law and controller are tuned with

$$k_1 = 2.0, \quad k_2 = 2.5, \quad k_3 = 3.0, \quad \boldsymbol{K}_{\boldsymbol{\omega}} = \boldsymbol{I}, \quad \boldsymbol{C}_{\boldsymbol{\omega}} = \boldsymbol{I}, \quad c_R = 2.$$

Given this tuning, we note that $\mathrm{spec}(\boldsymbol{M}) = \{1.95, 2.55, 2.98\}$. The estimates are driven from the random initial conditions with the update law in (5.10b), and the actuating torques are computed by the feedback in (5.10a). The resulting closed-loop system tracking performance is illustrated in Figure 5.3.

With this particular realization of the initial conditions, we get significant initial tracking and estimate attitude errors. Indeed at $t_\circ$, $\Psi(\boldsymbol{R}_r(t_\circ), \boldsymbol{R}(t_\circ)) \approx 1.99$ and $\Psi(\hat{\boldsymbol{R}}(t_\circ), \boldsymbol{R}(t_\circ)) \approx 1.95$. Despite this, we note a relatively fast convergence of the attitude estimate and tracking errors, and in less than 5 seconds, the system error trajectories reach a region close to the single stable equilibrium point $(\boldsymbol{I}, \boldsymbol{I}, \boldsymbol{0}, \boldsymbol{0}) \in \mathcal{E}$. To get a sense of the volatility of the rotation, the elements of the reference rotation, $\boldsymbol{R}_r(t)$, and the physical rotation, $\boldsymbol{R}(t)$, are plotted in the top left subplot, yielding visibly good tracking as $\Psi(\boldsymbol{R}_r, \boldsymbol{R}) \to 0$. We also note that the controlled torque signal satisfies $\boldsymbol{\tau} \to \boldsymbol{\tau}_r$, and that these signals are not excessively large transiently, despite the substantial initial attitude errors. The attitude rate estimate converges to the true attitude rate, with the true attitude rate subsequently driven to the reference trajectory. Finally, the Lyapunov function $\mathcal{V}_1$ proposed in (5.11) decays monotonically in the 10-logarithm, and its time-derivative is here strictly negative. Furthermore, the numerically differentiated Lyapunov function is plotted over the analytical expression in (5.12) when evaluated using the signals in system memory, coinciding perfectly, thus validating the derivations of the error dynamics and expression of the Lyapunov function time-derivative along solutions of the closed-loop system. □

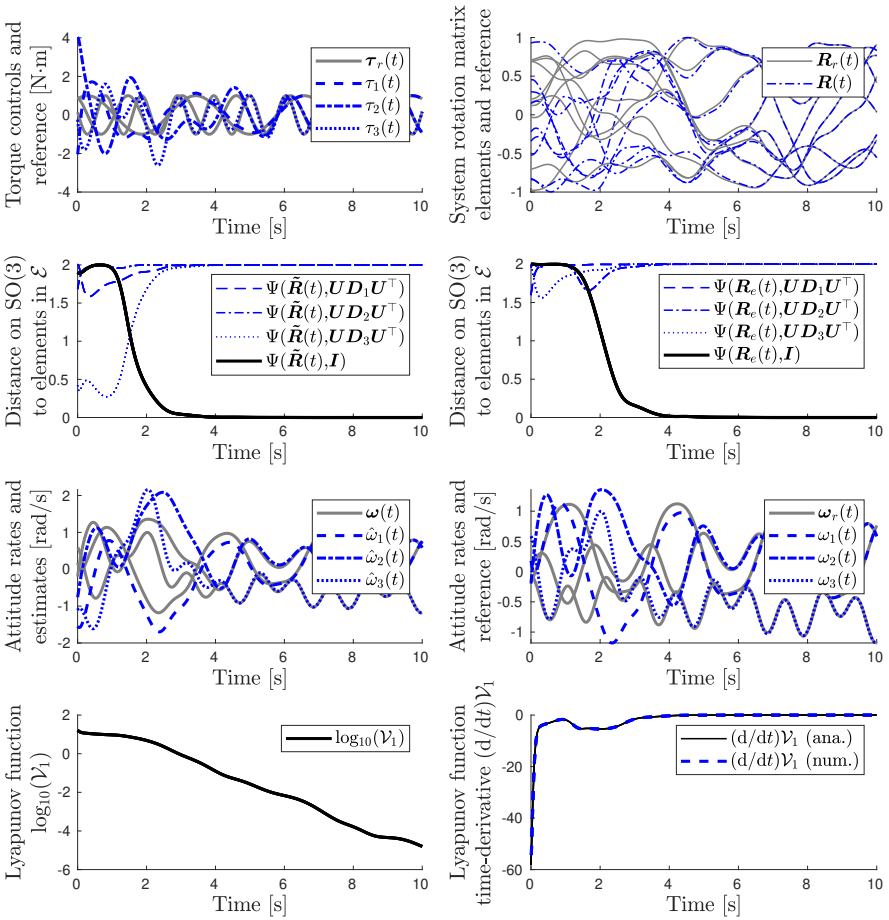

Figure 5.3 Closed-loop system response when in feedback with the filtered output feedback in Theorem 5.2. *Top, left:* Reference torque trajectory, $\boldsymbol{\tau}_r$, driving the reference dynamics, and computed control signals $\boldsymbol{\tau}$. *Top, right:* Elements of the reference attitude on $\boldsymbol{R}_r \in \mathrm{SO}(3)$ and the controlled attitude on $\boldsymbol{R} \in \mathrm{SO}(3)$. *Center top:* Distance to configurations in $\mathcal{E}$ on SO(3) for estimate and tracking errors, $\tilde{\boldsymbol{R}}$ and $\boldsymbol{R}_e$ respectively. *Center bottom:* Estimate attitude rates, attitude rates, and reference attitude rates. *Bottom, left:* Lyapunov function in the 10-logarithm. *Bottom, right:* Time-derivative of the Lyapunov function, analytically (black) and numerically (blue). The simulated system response is shown in the video chapter-5-simulations.mp4.

Remark 5.4
It should be noted that despite similar convergence rates in Example 5.1 and Example 5.2, the transient torque and attitude rates are much smaller in the latter simulation with Theorem 5.2. This is partly due to the use of the gyroscopic measurements in the latter (that appear directly in the Lyapunov function time-derivative). As such, this example indicates the importance of utilizing gyroscopic information if such measurements are available. However, a tuning-independent comparison of the controllers analogous to that made in Sec. 3.9 is not possible, as the error dynamics are fundamentally different.□

Remark 5.5
A great strength of the filtered output feedback solution in Theorem 5.2 is the joint Lyapunov function for controller and estimator, with associated uniform convergence properties, which can facilitate a productive cascade analysis for the full UAV dynamics. Such an analysis was undertaken in [Lefeber, Greiff, and Robertsson, 2020], and these results will be detailed in Chapter 6. □

Due to this joint Lyapunov function, if the tracking and estimate errors are initialized as small, they will never increase even if the trajectory becomes more volatile over time. Such guarantees are also possible to give with the output feedback in Theorem 5.1, but generally very difficult to show with the design approaches in Chapter 3 and 4, where the FSF solution needs to be combined with a full state estimator such as the EKF used in Sec. 4.4. However, a drawback with the FOF controller in Theorem 5.2 is that we do not know the worst case decay rates on subsets of $\mathrm{SO}(3)^2 \times \mathbb{R}^3$ containing the stable equilibrium point. Consequently, while tracking errors converge to a single stable equilibrium, we cannot quantify how fast it will decay in the initial transient. In practice this convergence tends to be fast, as Example 5.2 clearly demonstrates, but it complicates the problem of tuning the controller. This tuning problem is therefore addressed in the next section.

5.4 Asymptotic Behavior and Tuning

As the local properties of the error dynamics are known by the linearization in the proof of Theorem 5.2 (see Appendix C.1), some insights can be made about the rather difficult problem of tuning the proposed filtered output feedback controller. Judging by the Lyapunov function in (5.11), and its time derivative in (5.12), it may be tempting to chose a large c_R, as this seemingly increases the rate at which the errors decay. However, somewhat surprisingly, there are diminishing returns in increasing c_R. To see this, consider the matrix

$$\boldsymbol{D}(c_R, l_i) = \begin{bmatrix} 0 & 0 & 1 \\ c_R l_i & -2c_R l_i & 0 \\ -l_i & l_i & 0 \end{bmatrix}, \tag{5.16}$$

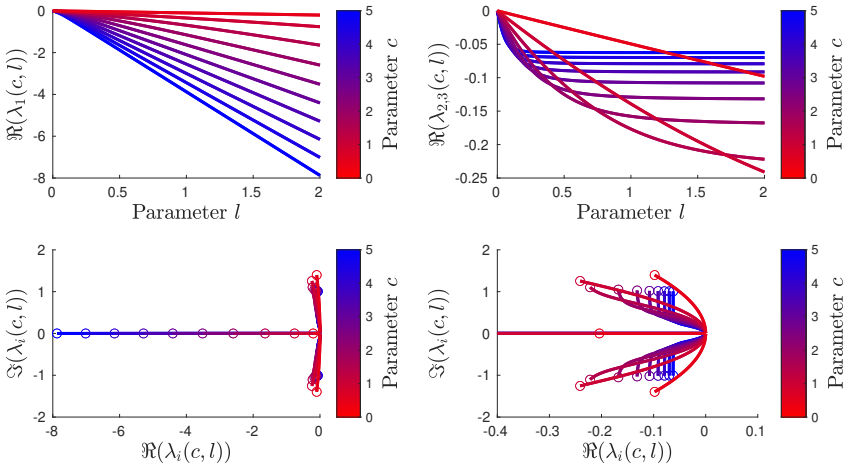

Figure 5.4 The spectrum of $\boldsymbol{D}(c,l)$ as a function of $l \in (0,2]$ for different values of $c \in (0,5]$ (black to blue). *Top, left:* Real part of the critically damped mode $\Re(\lambda_1(c,l))$. *Top, left:* Real part of the complex eigenvalue pair $\Re(\lambda_{2,3}(c,l))$. *Bottom, left:* Eigenvalues in the complex plane for increasing values of $l \in (0,2]$ with the marker o indicating the point where $l = 2$. *Bottom, right*: Zoom in on the origin of the eigenvalues of $\boldsymbol{D}(c,l)$.

which is shown to be Hurwitz in Lemma C.3 for all $c_R > 0, l_i > 0$. However, the real part of the complex-valued eigenvalue pair approaches zero from below with increasing c_R (for almost all values of l_i), while the strictly real eigenvalue is proportional to $-2c_R l_i$ for large c_R (see Figure 5.4).

This matrix in (5.16) becomes relevant when studying the asymptotic behavior of the system errors close to the exponentially stable equilibrium point $(\boldsymbol{R}_e, \tilde{\boldsymbol{R}}, \boldsymbol{\omega}_e, \tilde{\boldsymbol{\omega}}) = (\boldsymbol{I}, \boldsymbol{I}, \boldsymbol{0}, \boldsymbol{0})$. Consider small deviations from this point in the first two terms of the series expansion of the exponential map of SO(3),

$$\begin{aligned}\boldsymbol{R}_e(t) &= \mathrm{Exp}_{\mathrm{SO}(3)}([\boldsymbol{\epsilon}(t)]) = \boldsymbol{I} + [\boldsymbol{\epsilon}(t)]^{\wedge}_{\mathrm{SO}(3)} + o(\|\boldsymbol{\epsilon}\|^2) \approx \boldsymbol{I} + [\boldsymbol{\epsilon}(t)]^{\wedge}_{\mathrm{SO}(3)},\\ \tilde{\boldsymbol{R}}(t) &= \mathrm{Exp}_{\mathrm{SO}(3)}([\tilde{\boldsymbol{\epsilon}}(t)]) = \boldsymbol{I} + [\tilde{\boldsymbol{\epsilon}}(t)]^{\wedge}_{\mathrm{SO}(3)} + o(\|\tilde{\boldsymbol{\epsilon}}\|^2) \approx \boldsymbol{I} + [\tilde{\boldsymbol{\epsilon}}(t)]^{\wedge}_{\mathrm{SO}(3)}.\end{aligned} \tag{5.17}$$

In Appendix C.1, it is shown that when defining $\boldsymbol{X} \triangleq (\boldsymbol{\epsilon};\ \tilde{\boldsymbol{\epsilon}};\ \boldsymbol{\omega}_e;\ \tilde{\boldsymbol{\omega}})$, close to the point $\boldsymbol{X} = \boldsymbol{0}$, these errors evolve by a non-autonomous descriptor system,

$$\boldsymbol{E}\dot{\boldsymbol{X}} = \boldsymbol{A}(t)\boldsymbol{X}, \tag{5.18}$$

which is uniformly locally exponentially stable. We stress that this proof is done by means of Lyapunov theory without invoking spectrum conditions on $\boldsymbol{A}(t)$. However, the spectrum of $\boldsymbol{A}(t)$ can be used to gain some insight on the

system behavior, and it can be shown that at any given point in time $t \geq t_\circ$,

$$\operatorname{spec}(\boldsymbol{A}(t)) \in \{\boldsymbol{z}^* \bar{\boldsymbol{D}} \boldsymbol{z} - \boldsymbol{z}_3^* \bar{\boldsymbol{K}}_{\boldsymbol{\omega}}(t) \boldsymbol{z}_3 - \boldsymbol{z}_4^* \bar{\boldsymbol{C}}_{\boldsymbol{\omega}}(t) \boldsymbol{z}_4 | \bar{\boldsymbol{z}}^* \bar{\boldsymbol{z}} = 1\}, \tag{5.19}$$

where,

$$\operatorname{spec}(\bar{\boldsymbol{K}}_{\boldsymbol{\omega}}(t)) = \operatorname{spec}(\boldsymbol{K}_{\boldsymbol{\omega}}), \quad \operatorname{spec}(\bar{\boldsymbol{D}}) = \bigcup_{i=1}^{3} \operatorname{spec}(\boldsymbol{D}(c_R, l_i)), \tag{5.20a}$$

$$\operatorname{spec}(\bar{\boldsymbol{C}}_{\boldsymbol{\omega}}(t)) = \operatorname{spec}(\boldsymbol{C}_{\boldsymbol{\omega}}), \quad \{l_1, l_2, l_3\} = \operatorname{spec}\Big(\Big(\sum_{i=1}^{N} k_i\Big)\boldsymbol{I} - \boldsymbol{M}\Big), \tag{5.20b}$$

and $\boldsymbol{z} \triangleq (z_1^1; z_1^2; z_1^3; z_2^1; z_2^2; z_2^3; z_3^1; z_3^2; z_3^3) \in \mathbb{C}^9$, $\bar{\boldsymbol{z}} \triangleq (\boldsymbol{z}^1, \boldsymbol{z}^2, \boldsymbol{z}^3, \boldsymbol{z}^4) \in \mathbb{C}^{12}$, $\bar{\boldsymbol{K}}_{\boldsymbol{\omega}}$ and $\bar{\boldsymbol{C}}_{\boldsymbol{\omega}}$ are real and symmetric, and $\bar{\boldsymbol{D}} \in \mathbb{R}^{9\times 9}$ is real but not symmetric.

Consequently, it is very difficult to say exactly where the eigenvalues of $\boldsymbol{A}(t)$ will end up as a function of the tuning, without explicitly solving the associated eigenvalue problem along some time-varying reference trajectory. In addition, we cannot draw any conclusions of the stability of the system in (5.18) from $\operatorname{spec}(\boldsymbol{A}(t))$, as it is time-varying. But we can still use the general shape of this spectrum to guide our tuning. If the eigenvalues of any $\boldsymbol{D}(c_R, l_i)$ has a real-part close to zero, then we run the risk of having a small real-part in one or more of the eigenvalues in $\operatorname{spec}(\boldsymbol{A}(t))$. Consequently, a good rule of thumb is to pick c_R and l_i (implicitly k_i) so as to achieve a similar negative real part in $\lambda_i \in \operatorname{spec}(\boldsymbol{D}(c_R, l_i))$, with $\max \Re(\lambda_i) \approx \lambda_M(\boldsymbol{C}_\omega)$. As c_R is the same for each $\boldsymbol{D}(c_R, l_i)$, we should strive for similar l_i, however, they cannot be chosen identical, as $\boldsymbol{M}$ cannot have a uniform spectrum. To illustrate the effects of such a tuning, a numerical example is given below.

Example 5.3
For simplicity, let $\boldsymbol{J} = \boldsymbol{I}_3$ such that $\boldsymbol{E} = \boldsymbol{I}_{12}$ in (5.18). Take two different sets of parameters for the FOF controller in Theorem 5.2, as

(A) $\boldsymbol{C}_\omega = 0.5\boldsymbol{I},\ \boldsymbol{K}_\omega = 1.0\boldsymbol{I},\ c_R = 3.0,\ k_1 = 0.9,\ k_2 = 1.0,\ k_3 = 1.1,$

(B) $\boldsymbol{C}_\omega = 1.0\boldsymbol{I},\ \boldsymbol{K}_\omega = 0.5\boldsymbol{I},\ c_R = 0.1,\ k_1 = 7.2,\ k_2 = 8.0,\ k_3 = 8.8.$

The spectrum of the matrix in (5.20b) is then

(A) $\{l_1, l_2, l_3\} = \{\ 1.91,\ \ 1.97,\ \ 2.13\},$

(B) $\{l_1, l_2, l_3\} = \{15.24, 15.73, 17.07\},$

whereby we can compute the spectrum of $\boldsymbol{D}(c_R, l_1)$ as

(A) $\operatorname{spec}(\boldsymbol{D}(c_R, l_1)) = \{-0.04 - 1.00i, -0.04 + 1.00i, -11.92\},$

(B) $\operatorname{spec}(\boldsymbol{D}(c_R, l_1)) = \{-0.65 - 3.62i, -0.65 + 3.62i, -1.89\}.$

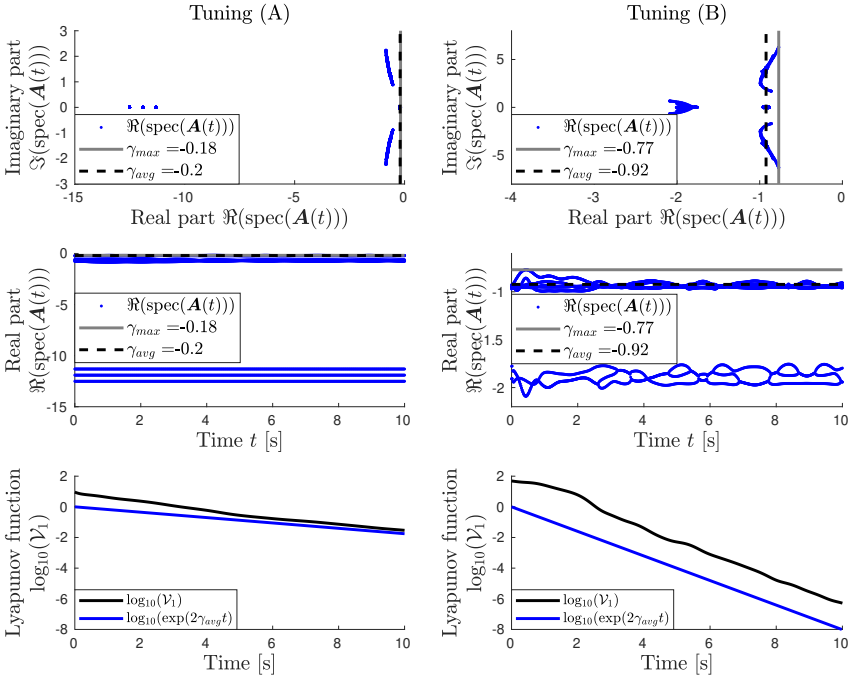

Figure 5.5 System response with the controller tuned with the parameters (A) to the left, and with the parameters (B) to the right. *Top:* The spectrum of $\boldsymbol{A}(t)$ in the complex plane (blue), with the maximum real part over all eigenvalues in time γ_{max} (gray) and the maximum average eigenvalue over $t \in [5, 10]$ as γ_{avg} (black, dashed). *Center:* The real-part of the spectrum of $\boldsymbol{A}(t)$ in time (blue), with the maximum real part over all eigenvalues in time γ_{max} (gray) and the maximum average eigenvalue over $t \in [5, 10]$ as γ_{avg} (black, dashed). *Bottom:* The decay of the Lyapunov function in (5.11) depicted in the 10 logarithm with tuning (A) left, and tuning (B) right.

with similar shapes of the spectra for $\boldsymbol{D}(c_R, l_2)$ and $\boldsymbol{D}(c_R, l_3)$ as well. In all cases, $\boldsymbol{D}(c_R, l_i)$ are Hurwitz, but we note a significant difference between the largest and smallest real parts of the eigenvalue associated with the tuning (A), whereas this difference is much smaller in tuning (B), where the largest real part of any eigenvalue is significantly further away from the origin than in tuning (A). This is in accordance with Figure 5.4. Therefore, with tuning (A) we might run into eigenvalues which are close to the origin, and significant variation in the eigenvalues of $\boldsymbol{A}(t)$ over the real axis. With tuning (B), the eigenvalues of $\boldsymbol{A}(t)$ are likely to be further away from the origin.

This is seen when plotting spectrum of $\boldsymbol{A}(t)$ in Figure 5.5 in time, here over $t \in [0, 10]$ using the same simulation setup as in Example 5.2 but with

$\boldsymbol{J} = \boldsymbol{I}$. The figure also shows the maximum real part of $\text{spec}(\boldsymbol{A}(t))$ in time, and the average asymptotic maximum real part of the $\text{spec}(\boldsymbol{A}(t))$, defined as

$$\gamma_{max} = \max_t \max_i (\Re(\lambda_i(t))) \qquad \lambda_i(t) \in \text{spec}(\boldsymbol{A}(t)) \quad t \in [0, 10], \tag{5.21a}$$

$$\gamma_{avg} = \frac{1}{5} \int_5^{10} \max_i (\Re(\lambda_i(t)))] \mathrm{d}t \quad \lambda_i(t) \in \text{spec}(\boldsymbol{A}(t)) \quad t \in [5, 10], \tag{5.21b}$$

respectively. The Lyapunov function $\mathcal{V}_1$ in (5.11) is also plotted along the solutions of the closed-loop system when using the associated controller. As the Lyapunov function is locally proportional to the system errors squared, we should expect its decay to be proportional to the decay of the slowest mode in the error dynamics when linearized at the stable equilibrium. That is, we should expect the slowest mode to decay roughly proportionally to $\exp(\gamma_{avg} t)$, with a squared error decay rate of approximately $\exp(2\gamma_{avg} t)$. This is seen in Figure 5.5, where the decay is shown alongside $\mathcal{V}_1$ in (5.11). □

From this example, it is clear that the choice of tuning parameters are highly consequential for the performance of a system controlled by Theorem 5.2, where the local errors decay a factor > 4.5 faster when using tuning (B) as compared to tuning (A). While it does not make sense to compare Lyapunov functions decay rates directly, we note that the local errors, $\boldsymbol{X} \in \mathbb{R}^{12}$, are defined the same way in both cases. It should be noted that all sets of parameters characterized by Theorem 5.2 are feasible and result in an UAGAS and ULES closed loop system, but the closed-loop tracking performance can vary significantly. In general, we propose the controller be tuned with $\{k_i\}_{i=1}^N$ for a given set $\{\boldsymbol{v}_i\}_{i=1}^N$ such that $\{l_i\}_{i=1}^3$ in (5.20b) are of a similar magnitude. We then propose to pick c_R based on Figure 5.4 such that $\text{spec}(\boldsymbol{D}(c_R, l_i))$ get similar negative real parts, and that this is approximately equal to $\lambda_M(\boldsymbol{C}_{\boldsymbol{\omega}})$. This rule of thumb is based on the shape of the possible spectra of $\boldsymbol{A}(t)$ characterized by (5.19), but the eigenvectors are time-varying and the local decay will depend on the time-varying signals in the error dynamics.

Remark 5.6
When considering the case $\boldsymbol{E} \neq \boldsymbol{I}$, we instead need to consider the eigenvalues of $\boldsymbol{E}^{-1}\boldsymbol{A}(t)$. This transformation changes the spectrum of $\boldsymbol{A}(t)$ in non-trivial ways, and it is advised to factor in the magnitude of $\boldsymbol{J}$ in $\boldsymbol{K}_{\boldsymbol{\omega}}$ and $\boldsymbol{C}_{\boldsymbol{\omega}}$ but to otherwise follow the above tuning advice aided by Figure 5.4. □

We emphasize that the spectrum of the system matrix of the descriptor system in (5.18) is not used to conclude stability of the local error dynamics, here specialized Lyapunov methods are required as the system is non-autonomous. However, this spectrum can nonetheless be used to gain some insight on the system characteristics. In the following chapters, we use the above ideas for tuning, aiming for a controller of type (B) rather than type (A).

5.5 Summary

In this chapter, the solutions in Chapter 3 were used as a starting point to solve Problem 5.1. In particular, the explicit vector controller in Theorem 3.1 was extended with an estimator, resulting in the FOF solution summarized in Theorem 5.2. Importantly, and in contrast to related approaches to full state feedback and output feedback control, this filtered output feedback result:

(i) Assumes that the rotation is known through directional measurements;

(ii) Assumes that the attitude rates are measured in the body frame;

(iii) Does not use any measurements directly in the computation of $\boldsymbol{\tau}$;

(iv) Results in a UAGAS and ULES closed-loop control system.

Theorem 5.2 facilitates important extensions to the full UAV dynamics, but is also a valuable result in its own right. By comparing the system response in Example 5.1 and Example 5.2, these numerical results suggest that the gyroscopic rates should be included in the controller if these signals are available in practice. Furthermore, the formulation with rotated directions is particularly appealing in that it does not require a reconstruction of attitude, an implicit weakness in much of the cited prior work, such as [Tayebi, 2008].

Just as in Theorem 3.1, the resulting control system poses very few restrictions on the controller gains. As such, it is relatively easy to find a feedback law that is stabilizing. However, the performance of the control system will vary greatly depending on the tuning. This was discussed in Sec. 5.4, where it was shown that the local decay rates depend both on the controller gains, but also on the reference trajectory $(\boldsymbol{R}_r, \boldsymbol{\omega}_r, \dot{\boldsymbol{\omega}}_r)$. Consequently, only general guidelines were given, highlighting some counter-intuitive relationships between the gains k_i and c_R with respect to the local decay rates. To assess the tuning in practice, it is recommended to implement the controller with the appropriate noise levels and explore various combinations of tuning parameters aided by the intuition provided in Sec. 5.4.

In this chapter, Problem 5.1 is solved to such an extent that the controller in Theorem 5.2 can be used to develop full UAV control systems (much like how the attitude control results in Chapter 3 facilitated the developments in Chapter 4). There are, however, certain aspects of the problem that may be studied further. Three conceivable directions can be summarized as follows:

- If the intended application is satellite positioning, with the attitude control being the sole goal, then integral action could be considered to attenuate load disturbances on the control inputs.

- The distance Ψ in Definition (2.18) could be used to upper-and lower bound the rotational term in the Lyapunov function (5.11), which could facilitate a characterization of the domain of exponential attraction.
- Finally, it may be interesting to explore similar controllers where the attitude rate errors are defined by rotated attitude rates similar to Theorem 5.1. It is quite possible that this can result in autonomous error dynamics and greatly simplify the stability analysis, but no such controllers have been found to date.

This last point is particularly interesting to consider in future work on filtered output feedback. However, the reason for defining the attitude rate errors of Theorem 5.2 as in (5.9) is highly intentional, which will become apparent when considering the cascade analysis for the full UAV dynamics.

6

Filtered Output Feedback: UAV dynamics

6.1 Introduction

As shown in the previous chapters, a common way to approach UAV control system design is to first consider (1) a full state feedback solution to control the attitude dynamics (see Chapter 3), which (2) is put into a cascade with a full state feedback translation controller (see Chapter 4), and finally (3) combined with a full state estimator. This approach is illustrated in Figure 6.1, and amounts to a separate design of estimator and controller. However, as dynamics are introduced in the estimator, it generally becomes difficult to make claims of stability for the entire closed-loop system.

Instead, we can leverage the filtered output feedback solution for the attitude dynamics in Chapter 5, and take a substantially different view of the control system, as illustrated with blue in Figure 6.1. Instead of considering a disjoint controller and estimator design, we now (i) find a filtered output feedback solution for the attitude dynamics, followed by (ii) the design a filtered output feedback controller for the translation dynamics, which permits an analysis of the entire control system through various cascade theorems.

In contrast to Chapter 4, where the problem of full state feedback was studied for the UAV dynamics, we now consider the equations of motion with the translation velocities defined in the body-frame. Furthermore, we do not assume knowledge of the system states, but rather assume measurements of the UAV position, and the measurements available through a 9-DOF IMU. Furthermore, unlike Chapter 5, we only consider the attitude as configured on SO(3), as its algebra is slightly easier to work with in the forthcoming derivations. Just as in previous chapters, the sub-index $(\cdot)_r$ denotes a reference,

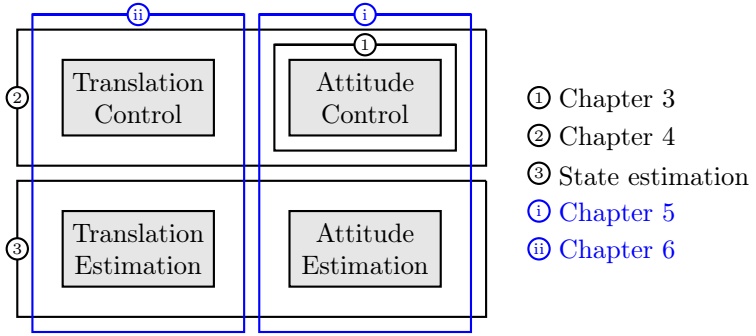

Figure 6.1 Abstraction of the UAV control system algorithms, with a conventional approach (black) and the approach taken in this chapter (blue).

and the objective is to drive the trajectories of a controlled system

$$\Sigma \; : \; \begin{cases} \Sigma^p \; : \; \begin{cases} \dot{\boldsymbol{p}} &= \boldsymbol{R}\boldsymbol{v} \\ \dot{\boldsymbol{v}} &= -\boldsymbol{S}(\boldsymbol{\omega})\boldsymbol{v} - g\boldsymbol{R}^\top \boldsymbol{e}_3 + (f/m)\boldsymbol{e}_3 \end{cases} \\ \Sigma^a \; : \; \begin{cases} \dot{\boldsymbol{R}} &= \boldsymbol{R}\boldsymbol{S}(\boldsymbol{\omega}) \\ \boldsymbol{J}\dot{\boldsymbol{\omega}} &= \boldsymbol{S}(\boldsymbol{J}\boldsymbol{\omega})\boldsymbol{\omega} + \boldsymbol{\tau} \end{cases} \end{cases}, \tag{6.1}$$

along the trajectories of a reference system

$$\Sigma_r \; : \; \begin{cases} \Sigma_r^p \; : \; \begin{cases} \dot{\boldsymbol{p}}_r &= \boldsymbol{R}_r\boldsymbol{v}_r \\ \dot{\boldsymbol{v}}_r &= -\boldsymbol{S}(\boldsymbol{\omega}_r)\boldsymbol{v}_r - g\boldsymbol{R}_r^\top \boldsymbol{e}_3 + (f_r/m)\boldsymbol{e}_3 \end{cases} \\ \Sigma_r^a \; : \; \begin{cases} \dot{\boldsymbol{R}}_r &= \boldsymbol{R}_r\boldsymbol{S}(\boldsymbol{\omega}_r) \\ \boldsymbol{J}\dot{\boldsymbol{\omega}}_r &= \boldsymbol{S}(\boldsymbol{J}\boldsymbol{\omega}_r)\boldsymbol{\omega}_r + \boldsymbol{\tau}_r \end{cases} \end{cases}, \tag{6.2}$$

knowing partial state information, defined in continuous time without noise

$$\boldsymbol{y}_{\boldsymbol{p}}(t) = \boldsymbol{p}(t), \tag{6.3a}$$
$$\boldsymbol{y}_{\boldsymbol{\omega}}(t) = \boldsymbol{\omega}(t), \tag{6.3b}$$
$$\boldsymbol{y}_i(t) = \boldsymbol{R}(t)^\top \boldsymbol{v}_i(t), \tag{6.3c}$$

collected in a measurement vector $\boldsymbol{y}(t) = (\boldsymbol{y}_{\boldsymbol{p}}(t);\ \boldsymbol{y}_{\boldsymbol{\omega}}(t);\ \boldsymbol{y}_1(t);\ \ldots;\ \boldsymbol{y}_N(t))$. Apart from these measurements, we assume that the reference trajectory is well defined, in the sense that the signals $(\boldsymbol{p}_r, \boldsymbol{v}_r, \boldsymbol{R}, \boldsymbol{\omega}_r, \dot{\boldsymbol{\omega}}_r, f_r, \dot{f}_r, \ddot{f}_r, \boldsymbol{\tau}_r)$ are bounded and $f_r > 0$ at all times. Note the difference between these conditions and Assumption (A1) in Propositions 4.1 and 4.3. Given these relatively mild conditions, the objective is to design a control system to drive Σ in (6.1) along the solutions of Σ_r in (6.2) given the measurements in (6.3), as illustrated in Figure 6.2.

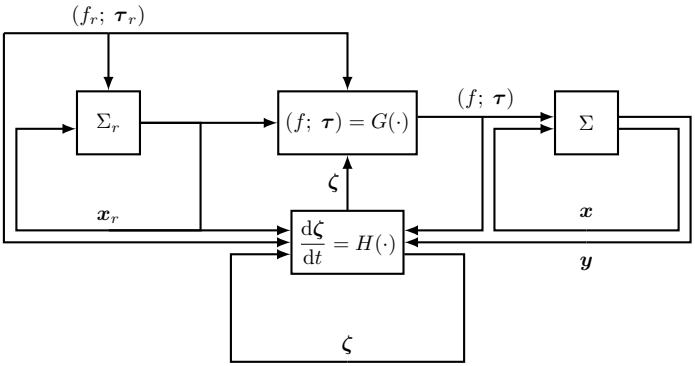

Figure 6.2 Sketch of the filtered output feedback controller.

From Theorem 5.2 in Chapter 5, it is clear that the subsystem Σ^a can be controlled along the solutions of any reference system Σ_r^a given the measurements in (6.3b) and (6.3c). Consequently, when devising the complete control system for the UAV dynamics, we start by considering the problem of controlling the subsystem Σ^p along the solutions of Σ_r^p given the measurements in (6.3a). We then present a method of interconnecting the two systems inspired by [Lefeber et al., 2017], by augmenting the reference dynamics Σ_r^a, to facilitate a stability analysis of the complete control system in Figure 6.2 using cascade theorems. As such, this chapter deals with two main problems. The first is to find a filtered output feedback for the positional dynamics when the velocities are unknown, and the second is to find a way of interconnecting the two subsystems. These problems are defined separately as follows.

6.1.1 The Problem of Positional Filtered Output Feedback

To simplify the analysis, the problem is considered with the translation velocities of the system in the body frame, unlike the dynamics considered in Chapter 4. Furthermore, two errors are defined as in [Lefeber et al., 2017],

$$\boldsymbol{p}_e = \boldsymbol{R}_r^\top(\boldsymbol{p}_r - \boldsymbol{p}), \qquad \boldsymbol{v}_e = \boldsymbol{v}_r - \boldsymbol{R}_r^\top \boldsymbol{R}\boldsymbol{v}. \tag{6.4}$$

In these signals, plugging in Σ^p and Σ_r^p, the error dynamics take the form

$$\dot{\boldsymbol{p}}_e = -\boldsymbol{S}(\boldsymbol{\omega}_r)\boldsymbol{p}_e + \boldsymbol{v}_e, \qquad \dot{\boldsymbol{v}}_e = -\boldsymbol{S}(\boldsymbol{\omega}_r)\boldsymbol{v}_e + \boldsymbol{u}, \tag{6.5}$$

where

$$\boldsymbol{u} = -(f/m)\boldsymbol{R}_r^\top \boldsymbol{R}\boldsymbol{e}_3 + (f_r/m)\boldsymbol{e}_3 \in \mathbb{R}^3, \tag{6.6}$$

is a virtual control input, which can be generated by controlling $\boldsymbol{R}$ and picking f with knowledge of $\boldsymbol{R}_r$ and f_r. Consequently, we can find a feedback law for the non-autonomous system in (6.5), with the idea of augmenting the reference system Σ_r^a such as to yield an equality in (6.6).

Remark 6.1
Another reason for this abstraction is to introduce a saturation of the virtual control input. This addresses the problem of negative thrusts highlighted in Chapter 4. By ensuring that $\boldsymbol{u}(t) \in \mathcal{B}_\gamma$, any $f(t)$ can be lower and upper bounded by imposing mild constraints on the reference trajectory. Assuming that $f_r^- \leq f_r(t) \leq f_r^+$ for finite constants $0 < f_r^- < f_r^+$, then $f_r^- - m\gamma \leq f(t) \leq f_r^+ + m\gamma$ for all $t \geq t_\circ$. This becomes important when considering actuator limitations, as rotors typically only spin in one direction (f cannot be negative) and generate a bounded maximum thrust (f is bounded). □

Remark 6.2
Note that the control input $\boldsymbol{u}$ differs slightly from that in [Lefeber et al., 2020], as we are consistently working with an east-north-up (ENU) coordinates in this thesis, as opposed to the north-east-down (NED) coordinates considered in [Lefeber et al., 2020]. With the consequence that the sign on the right-hand side of (6.6) is inverted. This results in subtle differences to [Lefeber et al., 2020] when later considering the interconnection of the two FOF controllers.□

With this introduction, the first problem of the chapter is to design a filtered output feedback controller for the system in (6.5), using only the positional measurements. This is done using a class of smooth saturation functions, which bound the virtual input $\boldsymbol{u}$ to a ball $\mathcal{B}_\gamma$ such that $\boldsymbol{u}$ retains a certain degree of smoothness. This problem is summarized as follows.

Problem 6.1
Consider a system with a state $\boldsymbol{x} = (\boldsymbol{p}, \boldsymbol{v}, \boldsymbol{R}, \boldsymbol{\omega}) \in \mathbb{R}^3 \times \mathbb{R}^3 \times \mathrm{SO}(3) \times \mathbb{R}^3$, with an associated reference trajectory $\boldsymbol{x}_r = (\boldsymbol{p}_r, \boldsymbol{v}_r, \boldsymbol{R}_r, \boldsymbol{\omega}_r) \in \mathbb{R}^3 \times \mathbb{R}^3 \times \mathrm{SO}(3) \times \mathbb{R}^3$, driven by $(f, \boldsymbol{\tau}) \in \mathbb{R}_{\geq 0} \times \mathbb{R}^3$ and $(f_r, \boldsymbol{\tau}_r) \in \mathbb{R}_{\geq 0} \times \mathbb{R}^3$, respectively, evolving by the UAV dynamics in (6.1) and (6.2), respectively. Consider a virtual control signal, $\boldsymbol{u}$, related to the signals $f, f_r, \boldsymbol{R}, \boldsymbol{R}_r$ as described in (6.6). Define a filter memory, $\boldsymbol{\zeta}_p$, and an update law in this memory, as

$$\frac{\mathrm{d}\boldsymbol{\zeta}_p}{\mathrm{d}t} = H_p(\boldsymbol{\zeta}_p, \boldsymbol{y}_p, \boldsymbol{x}_r, \boldsymbol{u}), \tag{6.7}$$

with an associated saturated feedback law

$$\boldsymbol{u} = G_p(\boldsymbol{\zeta}_p, \boldsymbol{x}_r) \in \mathcal{B}_\gamma, \tag{6.8}$$

for any saturation level $\gamma > 0$, such that the errors converge to $(\boldsymbol{p}_e, \boldsymbol{v}_e, \boldsymbol{\zeta}_p) \to (\boldsymbol{0}, \boldsymbol{0}, \boldsymbol{0})$ as $t \to \infty$, and that this equilibrium point is UGAS and ULES. □

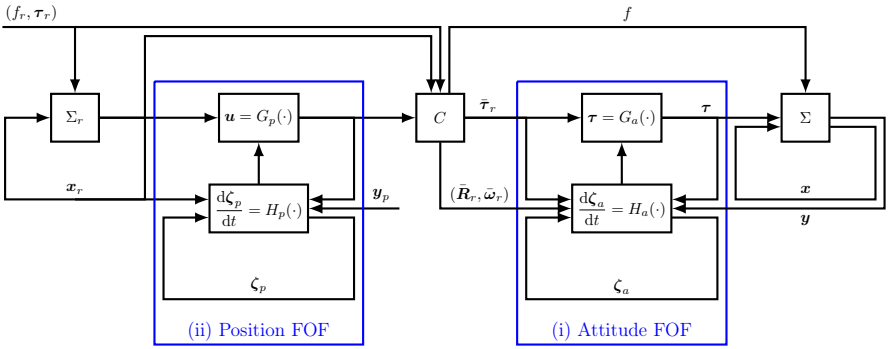

Figure 6.3 Sketch of the filtered output feedback controller, with the blue boxes directly relating to the control system abstraction in Figure 6.1.

6.1.2 The Problem of Full Filtered Output Feedback

If a solution to Problem 6.1 can be found, then we can consider steering the attitude subsystem Σ^a to an augmented reference trajectory, essentially combining the solution to Problem 5.1 and Problem 6.1. To this end, consider the slight expansion of Figure 6.2, as illustrated in Figure 6.3.

Here, the reference trajectory enters the positional FOF controller as well as the block denoted by C. The latter generates an augmented reference trajectory for the attitude FOF controller $(\bar{\boldsymbol{R}}_r, \bar{\boldsymbol{\omega}}_r, \bar{\boldsymbol{\tau}}_r)$ and computes f. In the field of UAV control, cascaded controller structures are common, where the positional controller defines a desired attitude for the attitude controller (see, e.g., Chapter 4). However, the abstraction in Figure 6.3 represents a notable departure from the standard controller paradigms. Instead of constructing a cascaded full state feedback for the UAV dynamics, and combining this with a full state estimator, we instead consider the stability of a pair of controller/observers independently, before combining them in a cascade. In doing so, the stability properties of the entire control system can be analyzed using cascade theorems. This second control problem is summarized as follows.

Problem 6.2
Consider a system with a state $\boldsymbol{x} = (\boldsymbol{p}, \boldsymbol{v}, \boldsymbol{R}, \boldsymbol{\omega}) \in \mathbb{R}^3 \times \mathbb{R}^3 \times \mathrm{SO}(3) \times \mathbb{R}^3$, with an associated reference trajectory $\boldsymbol{x}_r = (\boldsymbol{p}_r, \boldsymbol{v}_r, \boldsymbol{R}_r, \boldsymbol{\omega}_r) \in \mathbb{R}^3 \times \mathbb{R}^3 \times \mathrm{SO}(3) \times \mathbb{R}^3$, driven by $(f, \boldsymbol{\tau}) \in \mathbb{R}_{\geq 0} \times \mathbb{R}^3$ and $(f_r, \boldsymbol{\tau}_r) \in \mathbb{R}_{\geq 0} \times \mathbb{R}^3$, respectively, evolving by the UAV dynamics in (6.1) and (6.2), respectively. Define a filter memory, $\boldsymbol{\zeta}$, and an estimate update law in this memory, as

$$\frac{\mathrm{d}\boldsymbol{\zeta}}{\mathrm{d}t} = H(\boldsymbol{\zeta}, \boldsymbol{y}, \boldsymbol{x}_r, \boldsymbol{\tau}_r), \tag{6.9}$$

with an associated feedback law

$$(f;\ \boldsymbol{\tau}) = G(\boldsymbol{\zeta}, \boldsymbol{x}_r, f_r, \boldsymbol{\tau}_r), \tag{6.10}$$

such that $\boldsymbol{x}(t) \to \boldsymbol{x}_r(t)$ as $t \to \infty$, and characterize the stability properties of the resulting closed-loop system. □

6.1.3 Contributions

In this chapter, we present two key results from [Lefeber et al., 2020]. The first is a translational filtered output feedback solution to Problem 6.1, first published in [Lefeber et al., 2020, Proposition 1]. However, the main contribution of the chapter is the solution to Problem 6.2, originally published in [Lefeber et al., 2020, Proposition 3]. In doing so, we present all of the necessary details required for a real-time implementation of the control system, and provide additional details and simulation results to demonstrate the veracity of the proposed theory. With respect to prior work, the presented control system:

(i) Assumes the attitude to be measured through directional measurements;

(ii) Assumes that the attitude rates in the body frame are measured;

(iii) Assumes that the positions of the UAV are measured;

(iv) Does not use measurements directly in the computation of the controls;

(v) Confines the force, f, to a ball around the reference force, f_r;

(vi) Results in a UAGAS and ULES solution to Problem 6.2.

While there exist approaches to the problem of output feedback given the assumptions in (i)-(iii), such as the controller proposed in [Abdessameud and Tayebi, 2010, Theorem 1], the control system considered in this chapter is unique in that it (iv) does not use measurements directly in the computation of the control signals. This enables high-order derivatives of the positional errors to be expressed in the filter memory without requiring explicit numerical differentiation of the measurements. Furthermore, by (v), the actuating force, f, can be bounded away from the origin, complying with the physical constrains of UAVs that generally cannot produce negative thrusts (see Sec. 2.2.4). Finally, we emphasize that by (vi), the resulting control system comes with a joint stability proof of the trajectory tracking errors and estimation errors, making it a powerful solution for tracking UAV control applications when uniform almost global stability properties are deemed necessary.

6.1.4 Overview

We start by giving some supplementary mathematical preliminaries in Sec. 6.2, particularly concerning a class of vector-valued saturation functions that are key to finding a saturated feedback law. These results are used in Sec. 6.3, where a full state feedback solution is given for the sake of intuition before presenting the filtered output feedback analogue. The system interconnection is then presented in Sec. 6.4, followed by a cascade analysis in Sec. 6.5. A simulation example of the complete control system is then given in Sec. 6.6, and the summary in Sec. 6.7 concludes the chapter. To get an overview of the developments, the results and examples are summarized in Table 6.1.

Table 6.1 Overview of the results and examples of Chapter 6. Here, [1] indicates work of others, proofs given elsewhere; [2] indicates work tangential with others, but with independent proofs given; and [3] indicates new work.

Reference	Description
Prop. 6.1 [2]	Preliminary result on translation control analogous to [Lefeber et al., 2017], included to build intuition
Thm. 6.1 [3]	Translation filtered output feedback, with filter memory on $\mathbb{R}^9$ in [Lefeber, Greiff, and Robertsson, 2020, Prop. 1]
Thm. 6.2 [3]	Filtered output feedback for a UAV, with filter memory on $\mathrm{SO}(3) \times \mathbb{R}^{12}$ in [Lefeber, Greiff, and Robertsson, 2020, Prop. 3]
Example 6.1	Example on how the saturation functions can be constructed
Example 6.2	Simulation example with Thm. 6.1
Example 6.3	Simulation example with Thm. 6.1, showing saturated control
Example 6.4	Simulation example with Thm. 6.1, on control signal derivatives
Sec. 6.6.1	Simulation example with Thm. 6.2, stabilization, no noise
Sec. 6.6.2	Simulation example with Thm. 6.2, stabilization, with noise
Sec. 6.6.3	Simulation example with Thm. 6.2, tracking with noise

6.2 Preliminaries

Before presenting the filtered output feedback controllers, a general class of vector-valued saturation functions is defined. These functions will be instrumental in bounding the virtual control input $\boldsymbol{u}$ when solving Problem 6.1.

Definition 6.1
Let $\sigma : \mathbb{R}^n \mapsto \mathcal{B}_\gamma$ denote a vector-valued saturation function, with

$$\sigma(\boldsymbol{x}) = s(\|\boldsymbol{x}\|)\|\boldsymbol{x}\|^{-1}\boldsymbol{x}, \tag{6.11}$$

where $s : \mathbb{R}_{>0} \mapsto [0, \gamma]$ is a twice-continuous concave and increasing function for a $\gamma > 0$, and $s(0) = 0$, with $\lim_{y\to 0} s(y)y^{-1} = s'(0) > 0 \Rightarrow \sigma(\mathbf{0}) = \mathbf{0}$. □

This function bounds the input to a ball $\mathcal{B}_\gamma$, and importantly preserves the direction of the input, such that $\sigma(\boldsymbol{x})\|\boldsymbol{x}$. Equally important is that quadratic forms of the saturated output is bounded in quadratic forms of the input. As such, when designing saturated feedback laws, it is often productive to construct stability proofs with a Lyapunov-like function associated with saturated errors, which can be defined for any saturation function as follows.

Definition 6.2
Let $\mathcal{V}_\sigma : \mathbb{R}^n \mapsto \mathbb{R}_{\geq 0}$ denote a Lyapunov-like function associated with any saturation function σ in Definition 6.1, where

$$\mathcal{V}_\sigma(\boldsymbol{x}) = \int_0^{\|\boldsymbol{x}\|} s(y)dy, \tag{6.12}$$

which notably is positive definite in its argument and radially unbounded.□

Remark 6.3
A useful property of any $\mathcal{V}_\sigma(\boldsymbol{x})$ associated with a saturation function σ is that there exist positive constants $0 < c_1 \leq s'(0)^{-1}$ and $s'(0) \leq c_2$, such that

$$\frac{c_1}{2}\|\sigma(\boldsymbol{x})\|^2 \leq \mathcal{V}_\sigma(\boldsymbol{x}) \leq \frac{c_2}{2}\|\boldsymbol{x}\|^2. \tag{6.13}$$

□

Proof. The proof follows from Definition 6.2 and is given in Appendix C.2.□

As a consequence, we can express saturated signals of the errors in the closed-loop system, and construct stability proofs with Lyapunov function candidates that include terms in $\mathcal{V}_\sigma$. With these bounds, we can think of the functions $\mathcal{V}_\sigma$ as quadratic positive functions of their arguments, which will prove particularly useful in the forthcoming cascade analysis.

Remark 6.4
Another useful property of the saturation function σ is that the time-derivative of the function $\mathcal{V}_\sigma$ can be expressed in the time-derivative of its argument, as

$$\dot{\mathcal{V}}_\sigma(\boldsymbol{x}) = \dot{\boldsymbol{x}}^\top \sigma(\boldsymbol{x}), \quad \forall \boldsymbol{x} \in \mathbb{R}^n. \tag{6.14}$$

□

Proof. This follows from Definitions 6.1 and 6.2, see Appendix C.3. □

This fact can be used to find saturated feedback laws. If a control signal is constructed such that $\dot{\boldsymbol{x}} = -\sigma(\boldsymbol{x})$ in some error $\boldsymbol{x}$, then this typically results in a term in the Lyapunov function time-derivative which is negative in $\boldsymbol{x}$.

Example 6.1
An example of a function $s(y)$ that satisfies the conditions in Definition 6.1 is

$$s(y) = \gamma \tanh(\gamma^{-1} y), \tag{6.15}$$

resulting in $s(0) = 0$ and $s'(0) = 1\ \forall \gamma > 0$. In evaluating (6.12), the associated saturated Lyapunov-like function is $\mathcal{V}_\sigma(\boldsymbol{x}) = \gamma^2 \log(\cosh(\|\boldsymbol{x}\|\gamma^{-1}))$. While not restricted to this particular choice, we will use (6.15) as the nominal saturation function for future reference. Part of the reason for this particular choice is that $\sigma(\boldsymbol{x}) \approx \boldsymbol{x}$ for small $\boldsymbol{x}$ independently of γ, which becomes important when reasoning about the tuning of such saturated feedback laws. □

These saturation functions can be defined in many ways, and the abstraction of these functions along these lines has been done previously in the literature, notably in [Lefeber, 2000; Lefeber et al., 2017]. Here, we use a slightly different notation, opting to work with the two-norm instead of the squared two-norm, and to nominally use the hyperbolic tangent expression in (6.15). With these tools, a solution to Problem 6.1 is derived in Sec. 6.3.

6.3 Positional Saturated Filtered Output Feedback

To introduce the notion of a filtered output feedback with positional information, we first build some intuition by considering the problem of constructing a saturated full state feedback for the dynamics in (6.5). If assuming that both the positions and velocities are measured, a PD-like feedback law analogous to the translational controller presented in [Lefeber et al., 2017] can be constructed. Such a result is summarized in the above notation as follows.

Proposition 6.1
Assume that $\boldsymbol{\omega}_r$ is bounded, and take any $\sigma : \mathbb{R}^n \mapsto \mathcal{B}_\gamma$ by Definition 6.1. With the errors defined in (6.4) evolving by (6.5), in feedback with

$$\boldsymbol{u} = -\sigma(k_p \boldsymbol{p}_e + k_v \boldsymbol{v}_e) \in \mathcal{B}_\gamma, \tag{6.16}$$

where $k_p > 0$, $k_v > 0$, the point $(\boldsymbol{p}_e, \boldsymbol{v}_e) = (\boldsymbol{0}, \boldsymbol{0})$ is UGAS and ULES. □

Proof. The proof is given in Appendix C.4, and follows by the definition of a joint tracking error $\boldsymbol{e} \triangleq k_p \boldsymbol{p}_e + k_v \boldsymbol{v}_e$, and subsequent analysis of a Lyapunov function candidate using the associated $\mathcal{V}_\sigma$ in Definition 6.2, with

$$\mathcal{V}_1 = \frac{k_p}{2}\|\boldsymbol{v}_e\|^2 + \mathcal{V}_\sigma(\boldsymbol{e}). \tag{6.17}$$

It is shown that $\dot{\mathcal{V}}_1 \leq 0$ and uniformly continuous in time along the solutions of (6.5). Lemma 2.5 (Barbălat) is used with subsequent signal chasing by Lemma 2.7 to show GAS. Theorem 2.7 (Matrosov) shows UGAS, and ULES follows by linearization and application of Theorem 2.1 with Lemma 2.2. □

From this preliminary result, we note that when developing controllers for the error dynamics in (6.5), it is useful to jointly saturate the proportional and derivative parts of the feedback and construct a stability proof by including a quadratic term in the velocity tracking errors in the Lyapunov function. If combined with the function $\mathcal{V}_\sigma(\boldsymbol{e})$, the resulting Lyapunov function is positive definite in $\boldsymbol{e}$ and $\boldsymbol{v}_e$, facilitating a signal chasing through the error dynamics by which both of the tracking errors can be shown to converge to the origin.

With this intuition, we proceed to formulate a solution to Problem 6.1. The general idea is to construct a saturated feedback in a set of tracking error estimates $\hat{\boldsymbol{p}}_e \in \mathbb{R}^3$ and $\hat{\boldsymbol{v}}_e \in \mathbb{R}^3$. In doing so, the feedback will be saturated at all times, and the feedback G_p in Problem 6.1 will never include any of the measurements directly. However, just as with Tayebi's output feedback [Tayebi, 2008, Theorem 1] for the attitude dynamics summarized in Theorem 5.1, this can be simplified by the introduction of an auxiliary system. To this end, we define the memory of this system by $\boldsymbol{z} \in \mathbb{R}^3$, and the combined filter memory then takes the form $\boldsymbol{\zeta}_p \triangleq (\hat{\boldsymbol{p}}_e;\ \hat{\boldsymbol{v}}_e;\ \boldsymbol{z}) \in \mathbb{R}^9$. With this general intuition, a solution to Problem 6.1 is given as follows.

THEOREM 6.1—[LEFEBER ET AL., 2020, PROPOSITION 1]
Define a filter memory $\boldsymbol{\zeta} = (\hat{\boldsymbol{p}}_e;\ \hat{\boldsymbol{v}}_e;\ \boldsymbol{z}) \in \mathbb{R}^9$, and a set of errors in (6.4), as

$$\boldsymbol{p}_e = \boldsymbol{R}_r^\top(\boldsymbol{p}_r - \boldsymbol{p}), \qquad \boldsymbol{v}_e = \boldsymbol{v}_r - \boldsymbol{R}_r^\top \boldsymbol{R}\boldsymbol{v} \tag{6.18a}$$

$$\tilde{\boldsymbol{p}}_e = \boldsymbol{p}_e - \hat{\boldsymbol{p}}_e, \qquad \tilde{\boldsymbol{v}}_e = \boldsymbol{v}_e - \hat{\boldsymbol{v}}_e, \tag{6.18b}$$

$$\tilde{\boldsymbol{z}} = \boldsymbol{z} - \tilde{\boldsymbol{p}}_e. \tag{6.18c}$$

Assume that the positions are measured and that the signals $\boldsymbol{\omega}_r$ and $\dot{\boldsymbol{\omega}}_r$ are bounded. Consider the error dynamics in (6.5), in closed-loop feedback with

$$\boldsymbol{u} = -\sigma(k_p\hat{\boldsymbol{p}}_e + k_v\hat{\boldsymbol{v}}_e) \in \mathcal{B}_\gamma, \tag{6.19a}$$

where the filter memory is updated by

$$\dot{\hat{\boldsymbol{p}}}_e = -\boldsymbol{S}(\boldsymbol{\omega}_r)\hat{\boldsymbol{p}}_e + \hat{\boldsymbol{v}}_e + L_1\boldsymbol{z} \tag{6.19b}$$

$$\dot{\hat{\boldsymbol{v}}}_e = -\boldsymbol{S}(\boldsymbol{\omega}_r)\hat{\boldsymbol{v}}_e + \boldsymbol{u} + L_2\boldsymbol{z} \tag{6.19c}$$

$$\dot{\boldsymbol{z}} = -\boldsymbol{S}(\boldsymbol{\omega}_r)\boldsymbol{z} - (L_1 + L_3)\boldsymbol{z} + (L_1 + L_3)\tilde{\boldsymbol{p}}_e. \tag{6.19d}$$

For any controller gains $k_p > 0$, $k_v > 0$, saturation level $\gamma > 0$, and estimator gains $L_1 > 0$, $L_2 > 0$, and $L_3 > 2L_2/L_1$, the equilibrium point $(\boldsymbol{p}_e, \boldsymbol{v}_e, \tilde{\boldsymbol{p}}_e, \tilde{\boldsymbol{v}}_e, \tilde{\boldsymbol{z}}) = (\boldsymbol{0}, \boldsymbol{0}, \boldsymbol{0}, \boldsymbol{0}, \boldsymbol{0})$ is UGAS and ULES. □

Proof. The proof is given in Appendix C.5, and follows by the definition of a Lyapunov function candidate in the form

$$\mathcal{V}_1 = \mathcal{V}_\sigma(\hat{\boldsymbol{e}}) + \frac{1}{2}k_p \boldsymbol{v}_e^\top \boldsymbol{v}_e + \frac{a}{2}(\tilde{\boldsymbol{p}}_e - b\tilde{\boldsymbol{v}}_e)^\top(\tilde{\boldsymbol{p}}_e - b\tilde{\boldsymbol{v}}_e) + \frac{ac}{2}\tilde{\boldsymbol{v}}_e^\top \tilde{\boldsymbol{v}}_e + \frac{a}{6}\tilde{\boldsymbol{z}}^\top \tilde{\boldsymbol{z}}, \tag{6.20}$$

where $\hat{\boldsymbol{e}} \triangleq k_p \hat{\boldsymbol{p}}_e + k_v \hat{\boldsymbol{v}}_e$, with positive constants $a, b, c > 0$ expressed in the controller parameters. By defining a $\boldsymbol{X} = (\sigma(\hat{\boldsymbol{e}});\ \tilde{\boldsymbol{p}}_e;\ \tilde{\boldsymbol{v}}_e;\ \tilde{\boldsymbol{z}}) \in \mathbb{R}^{12}$, the time-derivative of $\mathcal{V}_1$ along the solutions of the error dynamics can be written

$$\dot{\mathcal{V}}_1 = -\boldsymbol{X}^\top \boldsymbol{M} \boldsymbol{X}. \tag{6.21}$$

If constraining the Lyapunov function candidate to the parameter values

$$b = \frac{2L_1}{3L_2}, \qquad\qquad c = \frac{2L_1^2}{9L_2^2} + \frac{1}{L_2}, \tag{6.22}$$

a sufficient condition for $\boldsymbol{M} \succ \boldsymbol{0}$ is found by taking L_3 and a sufficiently large,

$$L_3 > 2L_2/L_1, \quad a > \frac{(L_1 k_p + L_2 k_v)^2}{4k_v \min(\frac{L1}{3}, \frac{2L_1 - \sqrt{4L_1^2 - 4L_1 L_2 L_3 + L_2^2 L_3^2 + 16L_2^2} + L_2 L_3}{6L_2})}. \tag{6.23}$$

Given any such choice, $\dot{\mathcal{V}}_1 \leq 0$ along the solutions of the error dynamics, with $\mathcal{V}_1$ being positive definite in $\boldsymbol{X}$ and radially unbounded. Application of Lemma 2.5 (Barbălat) and subsequent signal chasing through Lemma 2.7 yields GAS. The Matrosov results in Theorem 2.7 yields UGAS, and a local linearization of the error dynamics shows ULES when invoking Lemma 2.2.□

This represents a feasible solution to Problem 6.1, as the controller is defined as a saturated nonlinear feedback in the estimated tracking errors $(\hat{\boldsymbol{p}}_e;\ \hat{\boldsymbol{v}}_e)$, which simultaneously confines the virtual control signal $\boldsymbol{u}$ to a ball $\mathcal{B}_\gamma$ for any desired $\gamma > 0$. Note that the estimator is implementable in the positional measurements, and that its implementation requires the reference trajectory $\boldsymbol{x}_r$ to be known. To illustrate the performance of the controller and its stability properties, a simulation example is given (see Example 6.2).

Example 6.2
In this example, the closed-loop behavior of the FOF controller in Theorem 6.1 is demonstrated in a simulation setup where the saturation level, defined by γ, can be varied. The system is initialized with $\boldsymbol{p}_e(t_\circ), \boldsymbol{v}_e(t_\circ), \hat{\boldsymbol{p}}_e(t_\circ), \hat{\boldsymbol{v}}_e(t_\circ), \boldsymbol{z}(t_\circ) \sim \mathcal{U}([-1,1]^3)$, with a reference $\boldsymbol{\omega}_r(t)$ as

$$\boldsymbol{\omega}_r(t) = (\sin(t+1);\ \sin(2t+2);\ \sin(3t+3)). \tag{6.24}$$

For the controller tuning, we let

$$k_p = 2\sqrt{k_v}, \qquad k_v = 5, \qquad L_1 = 4, \qquad L_2 = 4, \qquad L_3 = 4, \tag{6.25}$$

satisfying $L_3 > 2L_2/L_1$. To evaluate the Lyapunov function numerically, let

$$a = 1.129 \cdot 10^3, \qquad b = 2/3, \qquad c = 0.4722, \tag{6.26}$$

with b and c computed by (6.22) from (6.25), and a satisfying the condition in (6.23). We emphasize that any controller parameters satisfying $(k_p;\ k_v;\ L_1;\ L_2) \in \mathbb{R}^4_{>0}$ with an $L_3 > 2L_2/L_1$ represents a feasible controller tuning, rendering the origin UGAS and ULES. The explicit evaluation of the parameters (a, b, c) is only done to illustrate the decay of the Lyapunov function $\mathcal{V}_1$ in (6.20), and to demonstrate that the analytical expression derived in (6.21) holds numerically. Given a feasible choice of tuning parameters, we are free to pick any saturation level $\gamma > 0$ defining the ball $\mathcal{B}_\gamma$ to which $\boldsymbol{u}$ is constrained. For the purposes of this example, let the saturation function be defined by $s(y) = \gamma \tanh(y/\gamma)$ in accordance with Example 6.1, here with $\gamma = 2$. The resulting system response is illustrated in Figure 6.4.

In this simulation, we note that all of the errors $(\boldsymbol{p}_e, \boldsymbol{v}_e, \tilde{\boldsymbol{p}}_e, \tilde{\boldsymbol{v}}_e, \tilde{\boldsymbol{z}})$ converge to the origin, and that the virtual control input satisfies $\|\boldsymbol{u}\| \leq \gamma = 2$ for all $t > t_\circ$. The position and velocity tracking errors are correctly estimated, with $\tilde{\boldsymbol{p}}_e$ and $\tilde{\boldsymbol{v}}_e$ approaching the origin preceding the convergence of the tracking errors $\boldsymbol{p}_e$ and $\boldsymbol{v}_e$ to the origin. Furthermore, when evaluating the Lyapunov function $\mathcal{V}_1$ in (6.20) numerically, we note a linear decay in the 10-logarithm in time, illustrating the local exponential convergence properties. Finally, to ascertain that the analytical expression for the Lyapunov function time-derivative in (6.21) is correct, this expression is evaluated in the errors and plotted over the numerically differentiated Lyapunov function $\mathcal{V}_1$ in time. This demonstrates that the error dynamics have been correctly derived, and that $\mathcal{V}_1$ satisfies the differential relationship in (6.21) along its solutions. □

An interesting and important feature of the translation FOF in Theorem 6.1 is that the saturation level, γ, can be varied without affecting the stability properties of the system. Additionally, if constructing $\sigma(\boldsymbol{x})$ with a function $s(y)$ whose derivative in y at the origin does not depend on γ, then the local behavior of the system is unaffected by γ. This is the case for the saturation defined in Example 6.1. To illustrate this, the same exact simulation is repeated in a second example, where $\gamma \in \{1, 1.5, \cdots, 5.5, 6\}$ (see Example 6.3).

Example 6.3
In this example, the exact same simulation setup, parameters, and realization of the initial conditions and reference trajectory are used as in Example 6.2. A simulation of the translation error dynamics in closed-loop feedback with

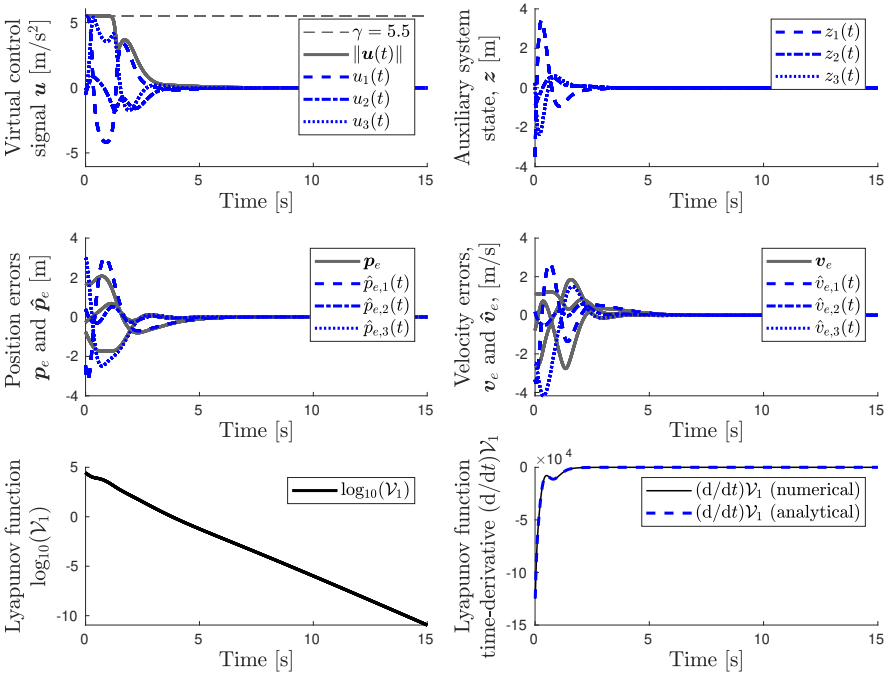

Figure 6.4 The system response when controlling the translation error dynamics in (6.5) through the virtual control input $\boldsymbol{u}$ using Theorem 6.1. *Top, left:* The control signal $\boldsymbol{u}(t) \in \mathcal{B}_\gamma$ and its norm $\|\boldsymbol{u}(t)\|$. *Top, right:* Trajectory of the auxiliary system state $\boldsymbol{z}(t)$. *Center, left:* The positional tracking error $\boldsymbol{p}_e(t)$ (black) and the estimated tracking error $\hat{\boldsymbol{p}}_e(t)$ (blue). *Center, right:* The velocity tracking error $\boldsymbol{v}_e(t)$ (black) and the estimated tracking error $\hat{\boldsymbol{v}}_e(t)$ (blue). *Bottom, left:* The Lyapunov function $\mathcal{V}_1$ in (6.20) decreasing in time, decaying exponentially for small errors. *Bottom, right:* The time-derivative $(\mathrm{d}/\mathrm{d}t)\mathcal{V}_1$ evaluated numerically from $\mathcal{V}_1$ (black) and analytically in the signals of the system using the expression in (6.21) (blue).

Theorem 6.1 is run for every saturation level in $\gamma \in \{1, 1.5, \cdots, 5.5, 6\}$, and the resulting trajectory of the Lyapunov function and the virtual control input is plotted in Figure 6.5, demonstrating that the bounds are saturated as expected, and that the associated Lyapunov function decays with the same rates after an initial transient which is longer for smaller saturation levels γ.

Based on this simulation, we note that virtual control input behaves as intended, and that it is confined to $\mathcal{B}_\gamma$ irrespective of the chosen $\gamma > 0$, as seen in the left-most subplot of Figure 6.5. By design, $\sigma(\hat{\boldsymbol{e}}) \approx \hat{\boldsymbol{e}}$ for small $\hat{\boldsymbol{e}}$ for all choices of γ. As such, the local convergence properties of the system is expected to be exponential and its decay is independent of the choice of γ,

which is seen in the right-most subplot of Figure 6.5. □

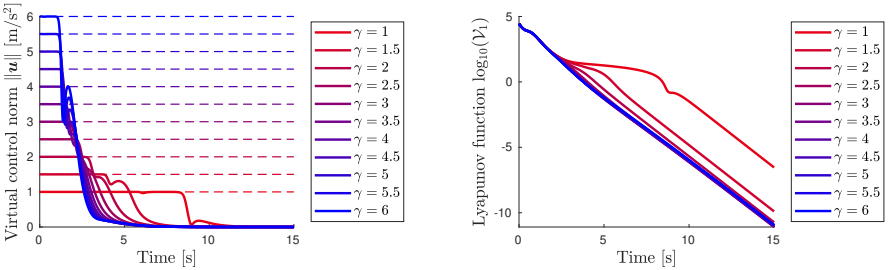

Figure 6.5 Virtual control signal norm when varying γ from $\gamma = 1$ (red) to $\gamma = 6$ (blue) in increments of 0.5. *Left:* Norm of the virtual control input $\|\boldsymbol{u}\|$ for an associated saturation level γ. *Right*: The Lyapunov function $\mathcal{V}_1$ in (6.20) depicted in the 10-logarithm, defined in the parameters in (6.26).

By the introduction of the filter memory, and knowledge of its time-derivatives, we can express not only $\boldsymbol{u}$, but also $\dot{\boldsymbol{u}}$ and $\ddot{\boldsymbol{u}}$ in the memory of the filter. This becomes important when designing the interconnection block in Figure 6.3. Specifically, consider any saturation function in Definition 6.1, letting $x \triangleq \|\hat{\boldsymbol{e}}\|$, and let $s'(x)$ and $s''(x)$ denote the first and second derivative of the function s with respect its argument. By the chain rule, we obtain

$$\begin{aligned}\frac{\mathrm{d}}{\mathrm{d}t}\sigma(\hat{\boldsymbol{e}}) =& \frac{s(x)}{x}\dot{\hat{\boldsymbol{e}}} + \Big(\frac{s'(x)}{x} - \frac{s(x)}{x^2}\Big)\dot{x}\hat{\boldsymbol{e}}, \qquad (6.27)\\ \frac{\mathrm{d}^2}{\mathrm{d}t^2}\sigma(\hat{\boldsymbol{e}}) =& \frac{s(x)}{x}\ddot{\hat{\boldsymbol{e}}} + \Big(\frac{s'(x)}{x} - \frac{s(x)}{x^2}\Big)(2\dot{x}\dot{\hat{\boldsymbol{e}}} + \ddot{x}\hat{\boldsymbol{e}}) + \Big(\frac{s''(x)}{x} - 2\frac{s'(x)}{x^2} + 2\frac{s(x)}{x^3}\Big)\dot{x}^2\hat{\boldsymbol{e}},\end{aligned}$$

where

$$\dot{x} = (\hat{\boldsymbol{e}}^\top\dot{\hat{\boldsymbol{e}}})\|\hat{\boldsymbol{e}}\|^{-1}, \qquad \ddot{x} = (\|\dot{\hat{\boldsymbol{e}}}\|^2 + \hat{\boldsymbol{e}}^\top\ddot{\hat{\boldsymbol{e}}})\|\hat{\boldsymbol{e}}\|^{-1} - (\hat{\boldsymbol{e}}^\top\dot{\hat{\boldsymbol{e}}})^2\|\hat{\boldsymbol{e}}\|^{-3}, \qquad (6.28a)$$

and

$$\begin{aligned}\hat{\boldsymbol{e}} =& k_p\hat{\boldsymbol{p}}_e + k_p\hat{\boldsymbol{p}}_e \qquad (6.29a)\\ \dot{\hat{\boldsymbol{e}}} =& -\boldsymbol{S}(\boldsymbol{\omega}_r)\hat{\boldsymbol{e}} + k_p\hat{\boldsymbol{v}}_e - k_v\sigma(\hat{\boldsymbol{e}}) + (k_pL_1 + k_vL_2)\boldsymbol{z} \qquad (6.29b)\\ \ddot{\hat{\boldsymbol{e}}} =& -\boldsymbol{S}(\dot{\boldsymbol{\omega}}_r)\hat{\boldsymbol{e}} - \boldsymbol{S}(\boldsymbol{\omega}_r)[-\boldsymbol{S}(\boldsymbol{\omega}_r)\hat{\boldsymbol{e}} + k_p\hat{\boldsymbol{v}}_e - k_v\sigma(\hat{\boldsymbol{e}}) + (k_pL_1 + k_vL_2)\boldsymbol{z}]\\ &+ k_p[-\boldsymbol{S}(\boldsymbol{\omega}_r)\hat{\boldsymbol{v}}_e - \sigma(\hat{\boldsymbol{e}}) + L_2\boldsymbol{z}] - k_v(\mathrm{d}/\mathrm{d}t)\sigma(\hat{\boldsymbol{e}})\\ &+ (k_pL_1 + k_vL_2)[-\boldsymbol{S}(\boldsymbol{\omega}_r)\boldsymbol{z} - (L_1 + L_3)\boldsymbol{z} + (L_1 + L_3)\tilde{\boldsymbol{p}}_e]. \qquad (6.29c)\end{aligned}$$

Note that these expressions should be interpreted in the limit as $x \to 0$. As highlighted in Chapter 4, one should be suspicious of seeing a second

time-derivative of the control signal appearing a practical application, as it tends to be very noisy if computed from measured signals in the system. This was one of the problems with the full state feedback approaches in Chapter 4. Here, these derivatives need not be computed by numerical differentiation, but can be evaluated directly from the filter memory. This is one of the major advantages in designing the *filtered output feedback*, and the main reason for G_p not including an argument in $\boldsymbol{y}_p$ in Problem 6.1.

If there is any measurement noise present, it only enters through $\tilde{\boldsymbol{p}}_e$ additively on $\ddot{\tilde{\boldsymbol{e}}}$ in (6.29c). Recall, this term can be expanded as $\tilde{\boldsymbol{p}}_e = \boldsymbol{R}_r^\top(\boldsymbol{p}_r - \boldsymbol{p}) - \hat{\boldsymbol{p}}_e$ by (6.18). As such, if the measured position $\boldsymbol{y}_p$ contains noise which is discontinuous, then we note that $\boldsymbol{u}$ is C^1, and if the noise is continuous, then $\boldsymbol{u}$ is C^2. To illustrate this, consider measurement noise that at a time $t > t_\circ$ is realized as additive zero-mean Gaussian noise $\boldsymbol{y}_p(t) = \boldsymbol{p}(t) + \boldsymbol{p}_n(t)$, with $\boldsymbol{p}_n(t) \sim \mathcal{N}(\boldsymbol{0}, \sigma_p^2 \boldsymbol{I})$, then it appears as an additive disturbance $k_n \boldsymbol{R}_r^\top \boldsymbol{p}_n(t)$ in (6.29c) with $k_n = -(k_p L_1 + k_v L_2)(L_1 + L_3)$. It does not enter directly in $\boldsymbol{u}$, or even $\dot{\boldsymbol{u}}$, and its effects on the control signal can be mitigated by decreasing the controller gains, at the cost of a larger initial transient in the tracking errors. To illustrate this, we once again make use of Example 6.2.

Example 6.4
Consider a simulation setup identical to that in Example 6.2. Take a slightly slower tuning, with $\gamma = 3, k_p = 1, k_v = 2, L_1 = 1, L_2 = 0.5, L_3 = 2$, such that $k_n = 6$. Take the hyperbolic tangent saturation function, then

$$s(y) = \gamma \tanh\left(\tfrac{y}{\gamma}\right), \quad s'(y) = \operatorname{sech}^2\left(\tfrac{y}{\gamma}\right), \quad s''(y) = -\tfrac{2}{\gamma}\tanh\left(\tfrac{y}{\gamma}\right)\operatorname{sech}^2\left(\tfrac{y}{\gamma}\right),$$

permitting an evaluation of both $\dot{\boldsymbol{u}}$ and $\ddot{\boldsymbol{u}}$ through (6.27), (6.28) and (6.29). When omitting the stochastic measurement noise, the analytically evaluated signals $(\dot{\boldsymbol{u}}, \ddot{\boldsymbol{u}})$ (black) are visualized over the numerically differentiated signals (blue) in Figure 6.6. When adding the positional measurement noise, here realized with $\sigma_p = 0.05$ and sampled at 100 [Hz], the resulting control signal derivatives are illustrated in Figure 6.7.

Firstly, we note the perfect overlap in the numerically evaluated control signal time-derivatives in Figure 6.6, when using the analytical evaluation through (6.27), (6.28) and (6.29). This illustrates that the estimator memory, $\boldsymbol{\zeta_p}$, can be leveraged in evaluating the control signal derivatives, and verifies that the provided expressions are correct, at least with respect to the hyperbolic saturation function. Secondly, when introducing the stochastic measurement noise in Figure 6.7, the disturbance is barely visible in the evaluation of $\dot{\boldsymbol{u}}$. As expected, it is clearly visible in the evaluation of $\ddot{\boldsymbol{u}}$, due to it appearing linearly in these signals. However, due to how it enters the dynamics of $\ddot{\tilde{\boldsymbol{e}}}$, its effects can be mitigated and controlled by tuning. □

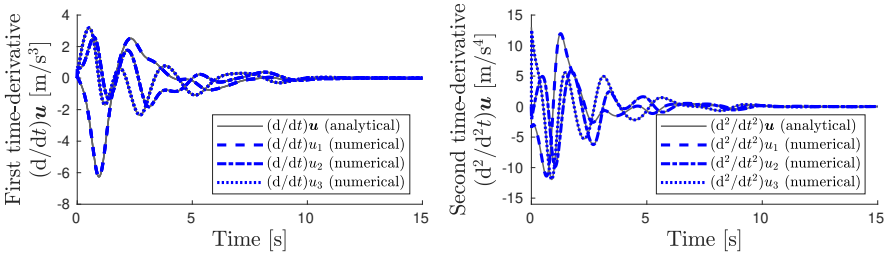

Figure 6.6 Evaluation of the control signal time-derivative in the case *without measurement noise*. The analytical expression evaluated in the solver memory (black) and the numerically differentiated signal computed from $\boldsymbol{u}$ (blue). *Left*: First time-derivative, $\dot{\boldsymbol{u}}$. *Right*: Second time-derivative, $\ddot{\boldsymbol{u}}$,

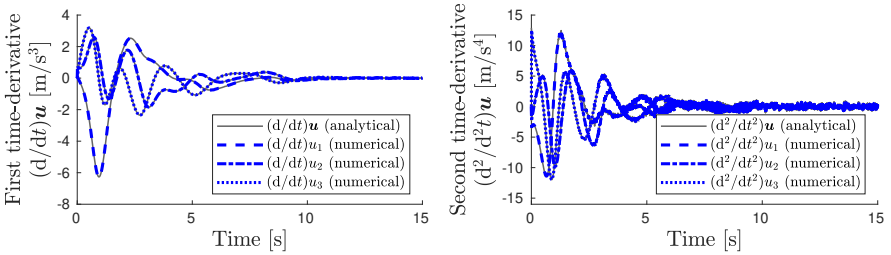

Figure 6.7 Evaluation of the control signal time-derivative in the case *with measurement noise*. The analytical expression evaluated in the solver memory (black) and the numerically differentiated signal computed from $\boldsymbol{u}$ (blue). *Left*: First time-derivative, $\dot{\boldsymbol{u}}$. *Right*: Second time-derivative, $\ddot{\boldsymbol{u}}$,

Remark 6.5
Just as with the attitude FOF in Theorem 5.2, knowledge of the behavior of the translational error dynamics when in closed-loop feedback with in Theorem 6.1 can be leveraged to gain some insight when tuning the controller. In Appendix C.5, it is shown that the local error dynamics are governed by a linear time-variant system in the form $\boldsymbol{A}(t) = \bar{\boldsymbol{F}} + \bar{\boldsymbol{S}}(t)$, where $\bar{\boldsymbol{F}} \in \mathbb{R}^{15\times 15}$ is Hurwitz and $\bar{\boldsymbol{S}}(t) \in \mathbb{R}^{15\times 15}$ is skew-symmetric and commutes with a class of structured solutions to the linear Lyapunov equation. As such, we can consider the spectrum of $\bar{\boldsymbol{F}}$ for the controller tuning, which can be expressed

$$p(\lambda) = (\lambda^2 + b_1\lambda + b_2)^3(\lambda^3 + a_1\lambda^2 + a_2\lambda + a_3)^3, \tag{6.30}$$

where the coefficients (b_1, b_2, a_1, a_3) are linear in the controller parameters $\boldsymbol{k} \triangleq (k_p, k_v, L_1, L_2, L_3)$, and a_2 is nonlinear in the parameters $\boldsymbol{k}$. As such, while direct pole-placement design is possible, a simpler approach is to formulate a constrained optimization problem which seeks to generate a desired pole

placement while enforcing the feasibility constraints on the parameters. For instance, if $\bar{\boldsymbol{\lambda}} \in \mathbb{C}^{15}$ denotes the solution to $p(\lambda) = 0$ as a function of $\boldsymbol{k}$, and we seek a critically damped tuning with a pole location $c < 0$, we can solve

$$\min_{\substack{\boldsymbol{k}\in\mathbb{R}_{>0} \\ L_3 > 2L_2/L_1}} \|c\mathbf{1}_{15} - \Re(\bar{\boldsymbol{\lambda}})\|^2 + \|\Im(\bar{\boldsymbol{\lambda}})\|^2. \tag{6.31}$$

Regardless of how the system is tuned, the solution to (6.30) should be investigated as it provides good intuition on the general local behavior of the system. However, much like Sec. 5.4, we emphasize that these error dynamics are non-autonomous, and that the tuning should be investigated in simulation as the local behavior will depend on the reference trajectory as well. □

To summarize, Theorem 6.1 represents a feasible solution to Problem 6.1. The feedback and estimator combination gives rise to an associated set of error dynamics in which the origin is UGAS and ULES. Furthermore, the solution permits the saturation of the virtual control input $\boldsymbol{u}$, and the first and second time-derivatives of this signal can be evaluated from the filter memory. This will be important for the developments in the next section, where a method of interconnecting the controllers in Theorem 5.2 and Theorem 6.1 is described.

6.4 Interconnection

To design the interconnection block, C, in Figure 6.2, we follow the approach taken in [Lefeber et al., 2017]. Given the definition of the virtual control in (6.6), it is clear that in order for this equality to hold, we require $f\boldsymbol{R}_r^\top \boldsymbol{R}\boldsymbol{e}_3$ to converge to $f_r\boldsymbol{e}_3 - m\boldsymbol{u}$. To this end, define the unit direction

$$\boldsymbol{f}_d = \begin{bmatrix} f_{d1} \\ f_{d2} \\ f_{d3} \end{bmatrix} = \frac{f_r\boldsymbol{e}_3 - m\boldsymbol{u}}{\|f_r\boldsymbol{e}_3 - m\boldsymbol{u}\|}. \tag{6.32}$$

From the previous discussion, we note that both $\dot{\boldsymbol{f}}_d$ and $\ddot{\boldsymbol{f}}_d$ are known in the memory of the filter, $\boldsymbol{\zeta}_p$. Furthermore, we can constrain the force such that $f_{d3} > 0$ for all times, provided that $\|\boldsymbol{u}\| \leq f_r^-/m$. To this end, we define a desired rotation as a rotation of $\theta = \arccos(\boldsymbol{e}_3 \cdot \boldsymbol{f}_d)$ about an axis of $\boldsymbol{n} = (\boldsymbol{e}_3 \times \boldsymbol{f}_d)\|(\boldsymbol{e}_3 \times \boldsymbol{f}_d)\|^{-1}$, which can be written compactly as

$$\boldsymbol{R}_d \triangleq \mathrm{Exp}_{\mathrm{SO}(3)}([\theta\boldsymbol{n}]^\wedge_{\mathrm{SO}(3)}) = \begin{bmatrix} 1 - \frac{f_{d1}^2}{1+f_{d3}} & -\frac{f_{d1}f_{d2}}{1+f_{d3}} & f_{d1} \\ -\frac{f_{d1}f_{d2}}{1+f_{d3}} & 1 - \frac{f_{d2}^2}{1+f_{d3}} & f_{d2} \\ -f_{d1} & -f_{d2} & f_{d3} \end{bmatrix} \in \mathrm{SO}(3). \tag{6.33}$$

This rotation satisfies $\boldsymbol{f}_d = \boldsymbol{R}_d \boldsymbol{e}_3$. Furthermore, we note that the time-derivative of the rotation matrix is known in $(\boldsymbol{f}_d, \dot{\boldsymbol{f}}_d)$, and as such

$$\boldsymbol{\omega}_d = [\boldsymbol{R}_d^\top \dot{\boldsymbol{R}}_d]^\vee. \tag{6.34}$$

Finally, as $\ddot{\boldsymbol{R}}_d$ is known in $(\boldsymbol{f}_d, \dot{\boldsymbol{f}}_d, \ddot{\boldsymbol{f}}_d)$, the attitude accelerations are simply

$$\dot{\boldsymbol{\omega}}_d = [\dot{\boldsymbol{R}}_d^\top \dot{\boldsymbol{R}}_d + \boldsymbol{R}_d^\top \ddot{\boldsymbol{R}}_d]^\vee. \tag{6.35}$$

Using the fact that $f = \|f_r \boldsymbol{e}_3 - m\boldsymbol{u}\|$ and the expression in (6.33), we can write $f_r \boldsymbol{e}_3 - m\boldsymbol{u} = f\boldsymbol{R}_d \boldsymbol{e}_3$, so the goal of choosing the torques $\boldsymbol{\tau}$ which make $f\boldsymbol{R}_r^\top \boldsymbol{R}\boldsymbol{e}_3$ converge to $f_r \boldsymbol{e}_3 - m\boldsymbol{u}$ can be replaced by the goal to determine $\boldsymbol{\tau}$ which makes $\boldsymbol{R}_r^\top \boldsymbol{R}$ converge to $\boldsymbol{R}_d$, or equivalently $\boldsymbol{R}$ to $\boldsymbol{R}_r \boldsymbol{R}_d$. Therefore, it is natural to consider an augmented reference rotation $\bar{\boldsymbol{R}}_r = \boldsymbol{R}_r \boldsymbol{R}_d$, where

$$\begin{aligned}
\dot{\bar{\boldsymbol{R}}}_r &= \dot{\boldsymbol{R}}_r \boldsymbol{R}_d + \boldsymbol{R}_r \dot{\boldsymbol{R}}_d && \text{(6.36a)}\\
&= \boldsymbol{R}_r \boldsymbol{S}(\boldsymbol{\omega}_r) \boldsymbol{R}_d + \boldsymbol{R}_r \boldsymbol{R}_d \boldsymbol{S}(\boldsymbol{\omega}_d) && \text{(6.36b)}\\
&= \boldsymbol{R}_r \boldsymbol{R}_d (\boldsymbol{S}(\boldsymbol{R}_d^\top \boldsymbol{\omega}_r) + \boldsymbol{S}(\boldsymbol{\omega}_d)) && \text{(6.36c)}\\
&= \bar{\boldsymbol{R}}_r \boldsymbol{S}(\bar{\boldsymbol{\omega}}_r), && \text{(6.36d)}
\end{aligned}$$

and $\bar{\boldsymbol{\omega}}_r \triangleq \boldsymbol{R}_d^\top \boldsymbol{\omega}_r + \boldsymbol{\omega}_d$. Finally, we note that the time-derivative of this signal,

$$\dot{\bar{\boldsymbol{\omega}}}_r = -\boldsymbol{S}(\boldsymbol{\omega}_d) \boldsymbol{R}_d^\top \boldsymbol{\omega}_r + \boldsymbol{R}_d^\top \dot{\boldsymbol{\omega}}_r + \dot{\boldsymbol{\omega}}_d, \tag{6.37}$$

can be expressed in (6.33), (6.34), and (6.35), whereby the augmented reference torques can be computed by inverting the attitude rate dynamics,

$$\boldsymbol{J}\dot{\bar{\boldsymbol{\omega}}}_r = \boldsymbol{S}(\boldsymbol{J}\bar{\boldsymbol{\omega}}_r)\bar{\boldsymbol{\omega}}_r + \bar{\boldsymbol{\tau}}_r \Rightarrow \bar{\boldsymbol{\tau}}_r = \boldsymbol{J}\dot{\bar{\boldsymbol{\omega}}}_r - \boldsymbol{S}(\boldsymbol{J}\bar{\boldsymbol{\omega}}_r)\bar{\boldsymbol{\omega}}_r. \tag{6.38}$$

To summarize, we have in this section defined a way of connecting the two subsystems by the construction of an augmented reference trajectory $(\bar{\boldsymbol{R}}_r, \bar{\boldsymbol{\omega}}_r, \bar{\boldsymbol{\tau}}_r)$ which satisfies the dynamics of the attitude subsystem and defines the interconnection block in Figure 6.3. This reference trajectory is computed from the virtual control input $(\boldsymbol{u}, \dot{\boldsymbol{u}}, \ddot{\boldsymbol{u}})$ which are available in the filter memory, $\boldsymbol{\zeta}_p$, and with this interconnection term, we can proceed to analyze the cascade of the entire closed-loop system, as will be done next.

6.5 Cascade Analysis

When closing the loop through the proposed interconnection, we no longer get the desired virtual control input to the system in (6.5), and the system is not perfectly actuated by the virtual control in (6.6), restated below,

$$\boldsymbol{u} = (f_r/m)\boldsymbol{e}_3 - (f/m)\boldsymbol{R}_r^\top \boldsymbol{R}\boldsymbol{e}_3 \in \mathbb{R}^3, \tag{6.39}$$

but it is rather actuated by a perturbed virtual control input,

$$\bar{\boldsymbol{u}} = (f_r/m)\boldsymbol{e}_3 - (f/m)\boldsymbol{R}_d\boldsymbol{e}_3 \in \mathbb{R}^3. \tag{6.40}$$

Note that $\bar{\boldsymbol{u}}$ can be expressed in $\boldsymbol{u}$, plus some additive perturbation, as

$$\begin{aligned}\bar{\boldsymbol{u}} &= \boldsymbol{u} - [(f_r/m)\boldsymbol{e}_3 - (f/m)\boldsymbol{R}_r^\top \boldsymbol{R}\boldsymbol{e}_3] + (f_r/m)\boldsymbol{e}_3 - (f/m)\boldsymbol{R}_d\boldsymbol{e}_3 && \text{(6.41a)}\\ &= \boldsymbol{u} - (f/m)\boldsymbol{R}_r^\top(\boldsymbol{R}_r\boldsymbol{R}_d\boldsymbol{R}^\top - \boldsymbol{I})\boldsymbol{R}\boldsymbol{e}_3 && \text{(6.41b)}\\ &= \boldsymbol{u} - \frac{\|f_r\boldsymbol{e}_3 - m\boldsymbol{u}\|}{m}\boldsymbol{R}_r^\top(\bar{\boldsymbol{R}}\boldsymbol{R}^\top - \boldsymbol{I})\boldsymbol{R}\boldsymbol{e}_3. && \text{(6.41c)}\end{aligned}$$

This perturbation vanishes as $\bar{\boldsymbol{R}}_r \to \boldsymbol{R}$, then resulting in $\bar{\boldsymbol{u}} \to \boldsymbol{u}$. Furthermore, the entire control system in Figure 6.3 can be written out in terms of this time-varying interconnection term and the error signals of the system.

Specifically, if the attitude control is done with the filtered output feedback solution in Theorem 5.2, implemented with respect to the augmented reference trajectory $(\bar{\boldsymbol{R}}_r, \bar{\boldsymbol{\omega}}_r, \bar{\boldsymbol{\tau}}_r)$, we can choose to represent its state on the form

$$\boldsymbol{X}_2 \triangleq \left(\sum_{i=1}^{N} k_i \boldsymbol{S}(\boldsymbol{v}_i)\boldsymbol{R}_e\boldsymbol{v}_i;\ \boldsymbol{\omega}_e;\ \sum_{i=1}^{N} k_i \boldsymbol{S}(\boldsymbol{v}_i)\tilde{\boldsymbol{R}}\boldsymbol{v}_i;\ \tilde{\boldsymbol{\omega}}\right) \in \mathbb{R}^{12}, \tag{6.42}$$

in the errors

$$\begin{aligned}\boldsymbol{R}_e &= \bar{\boldsymbol{R}}_r\boldsymbol{R}^\top \in \mathrm{SO}(3), & \tilde{\boldsymbol{R}} &= \hat{\boldsymbol{R}}\boldsymbol{R}^\top \in \mathrm{SO}(3), && \text{(6.43a)}\\ \boldsymbol{\omega}_e &= \bar{\boldsymbol{\omega}}_r - \boldsymbol{\omega} \in \mathbb{R}^3, & \tilde{\boldsymbol{\omega}} &= \hat{\boldsymbol{\omega}} - \boldsymbol{\omega} \in \mathbb{R}^3. && \text{(6.43b)}\end{aligned}$$

Furthermore, the dynamics of this system can then be written

$$\Sigma_2^a: \quad \dot{\boldsymbol{X}}_2 = \boldsymbol{f}_2(t, \boldsymbol{X}_2), \tag{6.44}$$

where the origin is UGAS and ULES by Theorem 5.2, as $(\bar{\boldsymbol{R}}_r, \bar{\boldsymbol{\omega}}_r, \bar{\boldsymbol{\tau}}_r)$ satisfies the attitude dynamics, the solutions converge uniformly globally asymptotically and locally uniformly exponentially to the invariant set $\mathcal{S}$ in (5.13).

Consider the errors of the translation subsystem in Theorem 6.1, and let

$$\boldsymbol{X}_1 \triangleq (\boldsymbol{p}_e;\ \boldsymbol{v}_e;\ \tilde{\boldsymbol{p}}_e;\ \tilde{\boldsymbol{v}}_e;\ \tilde{\boldsymbol{z}}) \in \mathbb{R}^{15}, \tag{6.45}$$

with

$$\Sigma_1^{p\prime}: \quad \dot{\boldsymbol{X}}_1 = \boldsymbol{f}_1(t, \boldsymbol{X}_1), \tag{6.46}$$

denoting the error dynamics of the closed-loop system when the interconnection term is omitted. When taking the interconnection into account, we can instead express the dynamics of the same errors as

$$\Sigma_1^{p}: \quad \dot{\boldsymbol{X}}_1 = \boldsymbol{f}_1(t, \boldsymbol{X}_1) + \boldsymbol{g}(t, \boldsymbol{X}_1, \boldsymbol{X}_2)\boldsymbol{X}_2, \tag{6.47}$$

where the interconnection term is defined as

$$\boldsymbol{g}(t, \boldsymbol{X}_1, \boldsymbol{X}_2)\boldsymbol{X}_2 = - \begin{bmatrix} \boldsymbol{0} \\ \boldsymbol{I} \\ \boldsymbol{0} \\ \boldsymbol{I} \\ \boldsymbol{0} \end{bmatrix} \frac{\|f_r \boldsymbol{e}_3 - m\boldsymbol{u}\|}{m} \boldsymbol{R}_r^\top (\boldsymbol{R}_e - \boldsymbol{I}) \boldsymbol{R} \boldsymbol{e}_3. \tag{6.48}$$

Finally, we have arrived at a description of the error dynamics as a triangular cascade structure, described by the systems $\{\Sigma_1^p, \Sigma_1^{p\prime}, \Sigma_2^a\}$ in the form (2.46), and its stability properties can be analyzed though the interconnection term, $\boldsymbol{g}$, using Theorem 2.9, or by showing uniform boundedness of solutions and applying Theorem 2.11. Taking the latter approach, the main result of this chapter can then be summarized in the notation of this thesis as follows.

THEOREM 6.2—[LEFEBER ET AL., 2020, PROPOSITION 3]
Consider the dynamics (6.2) in closed-loop feedback where:

- The torques, $\boldsymbol{\tau}$, are computed by the controller (5.10a) in Theorem 5.2 with respect to the augmented reference trajectory $(\bar{\boldsymbol{R}}_r, \bar{\boldsymbol{\omega}}_r, \bar{\boldsymbol{\tau}}_r)$,
- The augmented reference is formed through by $\boldsymbol{R}_d, \boldsymbol{\omega}_d$ and $\dot{\boldsymbol{\omega}}_d$ given by (6.33), (6.34) and, (6.35), as described in Sec. 6.4.
- The force $f = \|f_r \boldsymbol{e}_3 - m\boldsymbol{u}\|$, is computed from the saturated virtual control signal in $\boldsymbol{u}$ which in turn is computed by (6.19a) in Theorem 6.1.

Assume that

- A saturation function is chosen by Definition 6.1, with a saturation level γ such that $m\gamma < f_r^- \leq f_r(t) \leq f_r^+$ for all $t \geq t_\circ$.
- The reference trajectory is well defined, in the sense that the signals $(\boldsymbol{p}_r, \boldsymbol{v}_r, \boldsymbol{R}, \boldsymbol{\omega}_r, \dot{\boldsymbol{\omega}}_r, f_r, \dot{f}_r, \ddot{f}_r, \boldsymbol{\tau}_r)$ are bounded, with $f_r > 0$ for all $t \geq t_\circ$.
- Feasible controller gains are chosen as $k_p > 0$, $k_v > 0$, $L_1 > 0$, $L_2 > 0$, $L_3 > 2L_2/L_1$, $\boldsymbol{K}_\omega = \boldsymbol{K}_\omega^\top \succ \boldsymbol{0}$, $\boldsymbol{C}_\omega = \boldsymbol{C}_\omega^\top \succ \boldsymbol{0}$, $c_R > 0$, with N directions $\boldsymbol{v}_i \in \mathbb{R}^3$ with associated gains $k_i > 0$ such that $\boldsymbol{M} = \sum_{i=1}^N k_i \boldsymbol{v}_i \boldsymbol{v}_i^\top$ has distinct eigenvalues.

The equilibrium point $(\boldsymbol{p}_e, \boldsymbol{v}_e, \tilde{\boldsymbol{p}}_e, \tilde{\boldsymbol{v}}_e, \tilde{\boldsymbol{z}}, \boldsymbol{R}_e, \boldsymbol{\omega}_e, \tilde{\boldsymbol{R}}, \tilde{\boldsymbol{\omega}}) = (\boldsymbol{0}, \boldsymbol{0}, \boldsymbol{0}, \boldsymbol{0}, \boldsymbol{0}, \boldsymbol{I}, \boldsymbol{0}, \boldsymbol{I}, \boldsymbol{0})$ is UAGAS and ULES. The equilibrium points characterized by $\boldsymbol{R}_e \neq \boldsymbol{I}$ or $\tilde{\boldsymbol{R}} \neq \boldsymbol{I}$ are all locally unstable, and the set of initial conditions converging to these equilibrium points form a lower dimensional manifold. □

Proof. The proof of this theorem is given in [Lefeber et al., 2020] and follows the idea in [Lefeber et al., 2017], here stated with more details in the Appendix C.6. The main idea is to show that the solutions of the interconnected system remain bounded. By differentiating the Lyapunov function $\mathcal{V}_1^p$ in (6.20) along the solutions of the perturbed system Σ_1^p in (6.47), we obtain

$$\dot{\mathcal{V}}_1^p \leq \delta_1 \sqrt{\mathcal{V}_1^p} \|\boldsymbol{R}_e - \boldsymbol{I}\|. \tag{6.49}$$

Utilizing the fact that the subsystem Σ_2^a is UAGAS and ULES and considering the stability analysis on the almost global region of attraction of Σ_2^a, it can be shown that there exists a finite time $T \geq t_\circ$, after which the term $\|\boldsymbol{R}_e - \boldsymbol{I}\|$ decays exponentially to zero, and that $\|\boldsymbol{R}_e - \boldsymbol{I}\| \leq 2$ for all $t \in [t_\circ, T]$. As such, an upper bound for the Lyapunov function time-derivative is given by

$$\dot{\mathcal{V}}_1^p \leq \begin{cases} 2\delta_1 \sqrt{\mathcal{V}_1^p}, & \forall\, t \in [t_\circ, T] \\ 2\delta_1 \sqrt{\mathcal{V}_1^p} e^{-\delta_2 (t-T)}, & \forall\, t \geq T \end{cases}. \tag{6.50}$$

By the comparison lemma, a conservative upper bound on $\mathcal{V}_1^p$ can then be expressed in terms of two solutions, $\phi_A(t; t_\circ, x_\circ)$ and $\phi_B(t; t_\circ, x_\circ)$ associated with the differential equations in (6.50), stated explicitly in Appendix C.6. These solutions can be used to derive a finite upper bound of the Lyapunov function $\mathcal{V}_1^p$ along the solutions of Σ_1^p (also given in Appendix C.6), where

$$\sup_{t \geq t_\circ} \mathcal{V}_1^p(t) \leq \bar{B}(\mathcal{V}_1^p(t_\circ), T, \delta_1, \delta_2). \tag{6.51}$$

This bound is uniform in $t_\circ$ and illustrated in Figure 6.8. When considered on the domain of almost global asymptotic attraction of Σ_2^a, the solutions of the interconnected system Σ_1^p and Σ_2^a are uniformly bounded, UGAS and ULES of $\boldsymbol{X}_1 = \boldsymbol{0}$ and $\boldsymbol{X}_2 = \boldsymbol{0}$ in the cascade follow by Theorem 2.11. As such, the resulting cascade is ULES and UAGAS, with its almost global region of attraction characterized by the almost global region of attraction of Σ_2^a. □

The general shape of the bound of the Lyapunov function when considered along the solutions of Σ_1^p indicates that we might see a peak, which relates back to the *peaking phenomenon* outlined in Chapter 2, but as the solutions remain bounded due to Σ_2^a being ULES, both $\boldsymbol{X}_1$ and $\boldsymbol{X}_2$ converge to the origin. We note that this peak is rarely observed in practice, as the bound is very conservative and derived by upper-bounding negative semi-definite part of the Lyapunov function time-derivative to zero. We emphasize that this result is a joint stability proof for the tracking and estimation errors in the case of trajectory tracking UAV control based on positional measurements, directional measurements of the attitude, and gyroscopic measurements. Therefore, it solves Problem 6.2, as highlighted below.

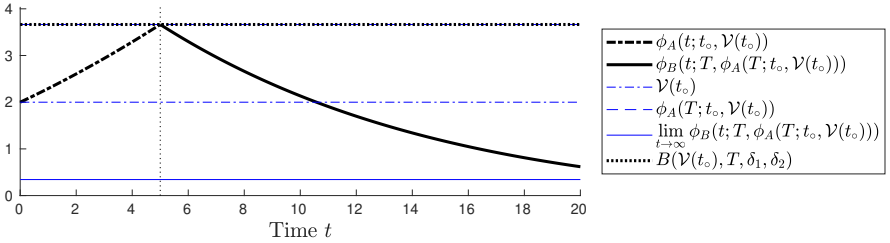

Figure 6.8 A conservative upper bound on $\mathcal{V}_1$ associated with the translation subsystem when interconnected with the attitude subsystem, here for a random δ with $T = 5$, showing boundedness of the solutions of Σ_1^p.

Remark 6.6
The controller in Theorem 6.2 solves Problem 6.2, as $\boldsymbol{p}_e \to \mathbf{0}$ implies $\boldsymbol{p} \to \boldsymbol{p}_r$, $\boldsymbol{R}_e \to \boldsymbol{I}$ implies both that $\boldsymbol{g}(t, \boldsymbol{X}_1, \boldsymbol{X}_2)\boldsymbol{X}_2 \to \mathbf{0}$ and that $\boldsymbol{R} \to \boldsymbol{R}_r$. Together with $\boldsymbol{v}_e \to \mathbf{0}$ and $\boldsymbol{\omega}_e \to \mathbf{0}$, this results in $\boldsymbol{v} \to \boldsymbol{v}_r$ and $\boldsymbol{\omega} \to \boldsymbol{\omega}_r$. □

6.6 Simulation Examples

To demonstrate the theoretical developments, a set of simulation examples are conducted. The first simulation in Sec. 6.6.1 demonstrates simple stabilization at stationary hovering configuration from extremely large initial errors. This simulation is conducted without noise to illustrate the potential peaking of the solutions in the translation subsystem, and to show the asymptotic convergence properties of the associated Lyapunov functions. This example is reexamined in Sec. 6.6.2, where the effects of measurement noise and modeling errors are studied in a stabilization example. Finally, a third example is given in Sec. 6.6.3 where the differential flatness discussed in Sec. 2.2.5 is employed to compute a reference trajectory corresponding to an aggressive trajectory-tracking maneuver. For simplicity, we refer to the Lyapunov function in (5.11) associated with the attitude subsystem Σ_2^a with the notation $\mathcal{V}_1^a$, and the Lyapunov function in (6.20) associated with $\Sigma_1^{p\prime}$ with the notation $\mathcal{V}_1^p$.

6.6.1 Stabilization With Large Initial Errors

In the first simulation example, the cascaded FOF control system in Theorem 6.2 is initialized with substantial errors. The reference trajectory is taken as a stationary hovering position, defined by a configuration $\boldsymbol{p}_r(t) = \mathbf{0}$ and $\boldsymbol{R}_r(t) = \mathrm{Exp}_{\mathrm{SO}(3)}([(\pi/2)\boldsymbol{e}_3]^\wedge_{\mathrm{SO}(3)})$ for all $t \geq t_\circ$, which then implies $(\boldsymbol{v}_r, \boldsymbol{\omega}_r, f_r, \dot{f}_r, \ddot{f}_r, \boldsymbol{\tau}_r) = (\mathbf{0}, \mathbf{0}, mg, 0, 0, \mathbf{0})$. The system is initialized with substantial errors, taking $\boldsymbol{p}(t_\circ) = (6;\ 8;\ 10)$ and letting $\boldsymbol{\omega}(t_\circ), \boldsymbol{v}(t_\circ), \hat{\boldsymbol{v}}_e(t_\circ), \hat{\boldsymbol{p}}_e(t_\circ), \boldsymbol{z}(t_\circ), \hat{\boldsymbol{\omega}}(t_\circ) \sim \mathcal{U}([-1,1]^3)$ with $\boldsymbol{R}(t_\circ), \hat{\boldsymbol{R}}(t_\circ) \sim$

$\mathcal{U}(\mathrm{SO}(3))$. The parameters are defined by a random dense inertia matrix $\boldsymbol{J} = \boldsymbol{J}^\top \succ \boldsymbol{0}$ satisfying $\lambda_m(\boldsymbol{J}) = 0.05$ and $\lambda_M(\boldsymbol{J}) = 0.1$, the gravitational acceleration is taken to be $g = 10$ [m/s^2], and the UAV mass is defined as $m = 0.1$ [kg]. The simulation is run from $t_\circ = 0$ over 15 [s]. In the considered realization, the inertia matrix is dense (here rounded to three digits), as

$$\boldsymbol{J} = 0.01 \cdot \begin{bmatrix} 6.7 & 1.2 & 1.5 \\ 1.2 & 6.4 & 1.9 \\ 1.5 & 1.9 & 7.6 \end{bmatrix}. \tag{6.52}$$

The initial attitudes on SO(3) (here rounded to two digits), are

$$\boldsymbol{R}(t_\circ) = \begin{bmatrix} -1.00 & 0.03 & 0.03 \\ 0.03 & -0.01 & 1.00 \\ 0.03 & 1.00 & 0.01 \end{bmatrix}, \quad \hat{\boldsymbol{R}}(t_\circ) = \begin{bmatrix} 0.03 & 0.36 & 0.93 \\ 0.36 & -0.87 & 0.33 \\ 0.93 & 0.33 & -0.16 \end{bmatrix},$$

resulting in substantial initial attitude errors, with

$$\Psi(\boldsymbol{R}_r(t_\circ), \boldsymbol{R}(t_\circ)) = 1.4960, \tag{6.53a}$$

$$\Psi(\boldsymbol{R}_r(t_\circ), \hat{\boldsymbol{R}}(t_\circ)) = 1.5817, \tag{6.53b}$$

$$\Psi(\boldsymbol{R}(t_\circ), \hat{\boldsymbol{R}}(t_\circ)) = 1.1506. \tag{6.53c}$$

The attitude controller is tuned with $(k_1, k_2, k_3, c_R, \boldsymbol{C}_\omega, \boldsymbol{K}_\omega) = (2, 2.5, 3, 2, \boldsymbol{I}, \boldsymbol{I})$, and the translation controller is tuned with the parameters $(k_p, k_v, L_1, L_2, L_3, \gamma) = (1, 2, 2.05, 2.0, 1.95, 8)$. Here, the tuning for the attitude subsystem was found using the ideas in Sec. 5.4. By similar reasoning, the parameters for the translation subsystem were obtained by placing the poles of the time-invariant part error dynamics when considered close to the stable equilibrium, by solving the optimization problem similar to that posed in Remark 6.5. The poles of the modes associated of the local tracking errors were placed in -1 in the complex plane, and the poles associated with the local estimation errors and auxiliary system dynamics were made slightly faster, in approximately -1.5 in the complex plane. The simulation results are depicted in signals mirroring Example 5.2 (in which only the attitude FOF was considered), but now following the augmented reference $(\bar{\boldsymbol{R}}_r, \bar{\boldsymbol{\omega}}_r, \bar{\boldsymbol{\tau}}_r)$, computed as described in Sec. 6.4. These signals are depicted in Figure 6.9. Similarly, the signals associated with the translation subsystem are plotted as in Example 6.2 are shown in Figure 6.10. Finally, to get a sense of the maneuver in space, the configurations of the UAV are depicted in Figure 6.11.

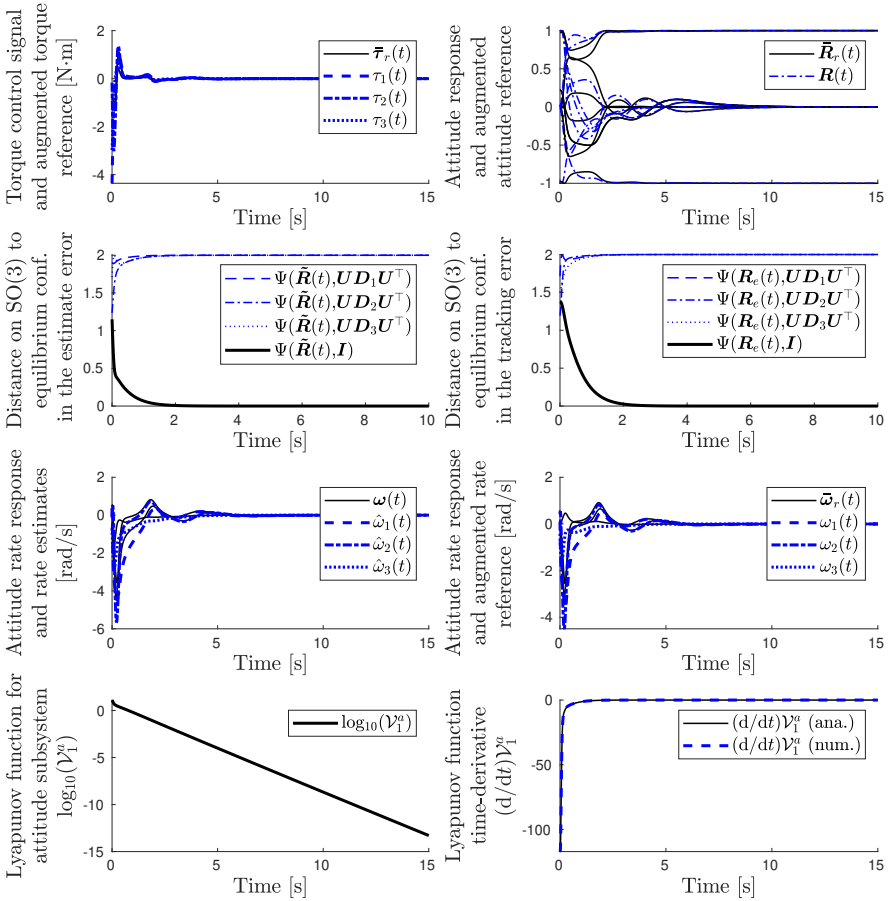

Figure 6.9 System response of the UAV dynamics Σ in (6.1) when controlled along Σ_r in (6.2) by the filtered output feedback solution in Theorem 6.2. *Signals associated with Σ_2^a* in the *stabilization* example, simulated *without measurement noise and with perfect knowledge of the inertia*. *Top, left:* Augmented torque trajectory, $\bar{\boldsymbol{\tau}}_r$, and computed control signals, $\boldsymbol{\tau}$. *Top, right:* Elements of the augmented reference attitude on $\bar{\boldsymbol{R}}_r \in \mathrm{SO}(3)$ and the controlled attitude on $\boldsymbol{R} \in \mathrm{SO}(3)$. *Center top:* Distance to configurations in $\mathcal{E}$ on SO(3) for estimate and tracking errors, $\tilde{\boldsymbol{R}}$ and $\boldsymbol{R}_e$, respectively. *Center bottom:* Estimate attitude rates, attitude rates, and reference attitude rates. *Bottom, left:* The Lyapunov function $\mathcal{V}_1^a$ in (5.11) decreasing in time in the 10-logarithm. *Bottom, right:* The time-derivative $(\mathrm{d}/\mathrm{d}t)\mathcal{V}_1^a$ evaluated numerically from $\mathcal{V}_1^a$ (blue) and analytically in the signals by (5.12) (black). The simulated system response is shown in the video chapter-6-simulations.mp4.

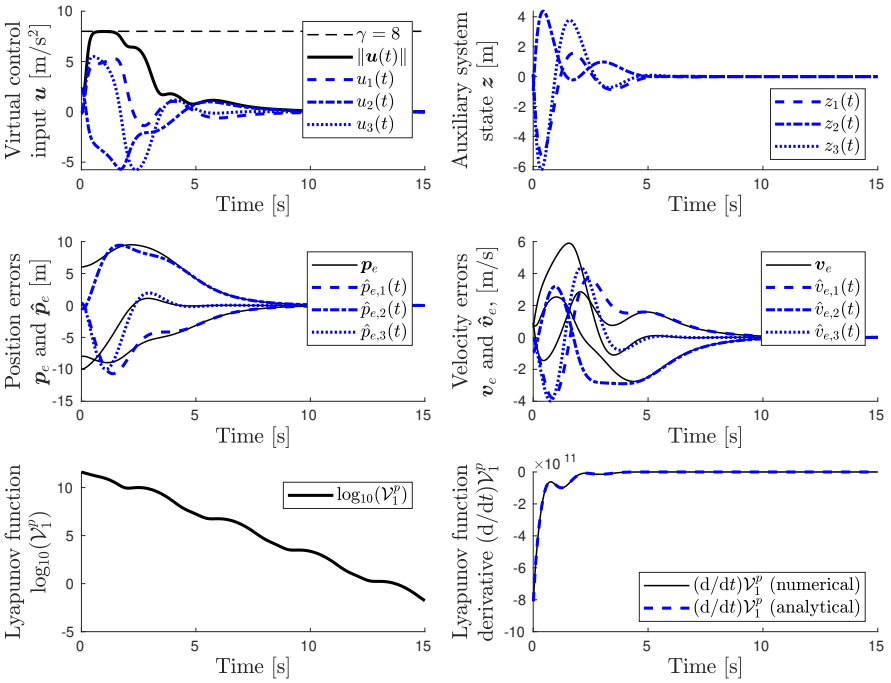

Figure 6.10 System response of the UAV dynamics Σ in (6.1) when controlled along Σ_r in (6.2) by the filtered output feedback solution in Theorem 6.2. *Signals associated with* Σ_1^p in the *stabilization* example, simulated *without measurement noise and with perfect knowledge of the inertia*. *Top, left:* The virtual control input $\boldsymbol{u}(t) \in \mathcal{B}_\gamma$ and its norm $\|\boldsymbol{u}(t)\|$. *Top, right:* Trajectory of the auxiliary system state $\boldsymbol{z}(t)$. *Center, left:* The positional tracking error $\boldsymbol{p}_e(t)$ (black) and the estimated tracking error $\hat{\boldsymbol{p}}_e(t)$ (blue). *Center, right:* The velocity tracking error $\boldsymbol{v}_e(t)$ (black) and the estimated tracking error $\hat{\boldsymbol{v}}_e(t)$ (blue). *Bottom, left:* The Lyapunov function $\mathcal{V}_1^p$ in (6.20) decreasing in time, decaying exponentially for small errors. *Bottom, right:* The time-derivative $(\mathrm{d}/\mathrm{d}t)\mathcal{V}_1^p$ evaluated numerically from $\mathcal{V}_1^p$ (black) and analytically in the signals of the system through in (6.21) (blue). The simulated system response is shown in the video chapter-6-simulations.mp4.

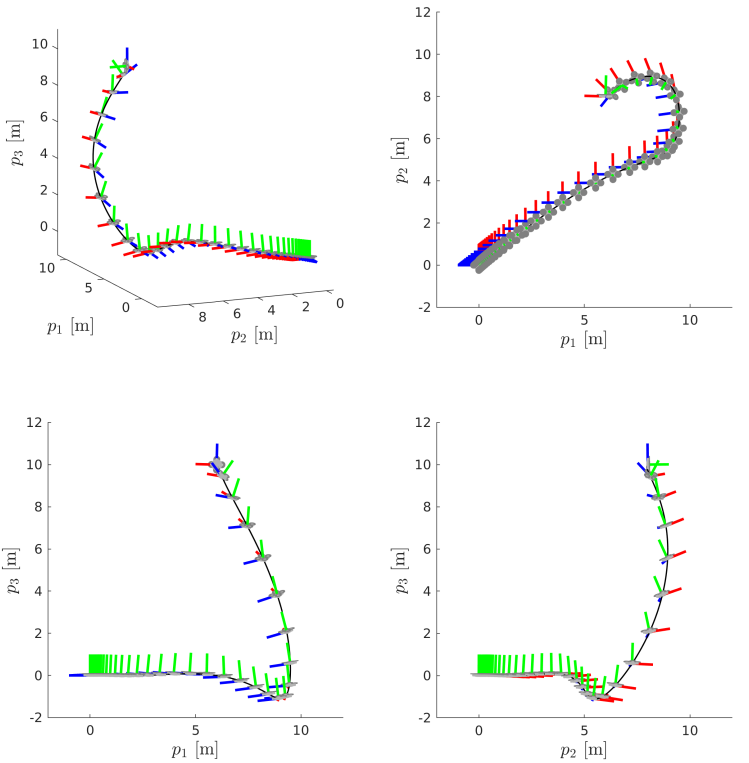

Figure 6.11 System response of the UAV dynamics Σ in (6.1) when controlled along Σ_r in (6.2) by the filtered output feedback solution in Theorem 6.2. *Configurations* in the *stabilization* example, simulated *without measurement noise and with perfect knowledge of the inertia*. The figures depict the same trajectory, showing it from different angles, with the positional trajectory (black), and the attitude illustrated in 50 configurations temporally equidistant over $t \in [0, 15]$ using the same color coding of the body basis vectors and illustration of the UAV as used in Figure 2.5 and Figure 2.6. *Top, left:* Trajectory in three-dimensional space. *Top, right:* Projection onto the-$\boldsymbol{e}_1\boldsymbol{e}_2$ plane. *Bottom, left:* Projection onto the $\boldsymbol{e}_1\boldsymbol{e}_3$-plane. *Bottom, right:* Projection onto the $\boldsymbol{e}_2\boldsymbol{e}_3$-plane. The simulated system response is shown in the video chapter-6-simulations.mp4.

Discussion From this simulation example, we start by noting that the attitude subsystem in Figure 6.9 behaves similar to the examples in Sec. 5.3, but that the augmented reference trajectory, $(\bar{\boldsymbol{R}}_r, \bar{\boldsymbol{\omega}}_r, \bar{\boldsymbol{\tau}}_r)$, now clearly differs from the constant reference, $(\boldsymbol{R}_r, \boldsymbol{\omega}_r, \boldsymbol{\tau}_r)$, as $\bar{\boldsymbol{\omega}}_r \neq \mathbf{0}$. While it is slightly difficult to discern in this simulation, the attitude rate estimates converge to the true attitude rates after which the attitude rates converge to the reference attitude rate trajectory. Furthermore, we note the usual linear decay of the Lyapunov function $\mathcal{V}_1^a$ in the logarithm in time, with the analytical expression of the Lyapunov function time-derivative evaluated in the solutions of the error dynamics corresponding perfectly to the numerically differentiated time-derivative when computed directly from $\mathcal{V}_1^a$. This indicates that the implementation is correct, and in particular that the augmented reference trajectory $(\bar{\boldsymbol{R}}_r, \bar{\boldsymbol{\omega}}_r, \bar{\boldsymbol{\tau}}_r)$ indeed satisfies the attitude dynamics.

When studying the errors associated with the translation subsystem in Figure 6.10, note that the virtual control input used to compute f is contained in a ball of radius γ. Since $f_r = mg = 1$, we have that $f(t) \in [f_r - m\gamma, f_r + m\gamma] = [0.2, 1.8]$ for all $t \geq t_\circ$, guaranteeing that the augmented reference trajectory is well defined (as the denominator in (6.32) is non-zero). Despite the substantial initial errors, the tracking errors in position and velocity converge to small values within 10 seconds, and asymptotically these errors converge to zero (down to expected numerical integration errors). Finally, when studying the Lyapunov function, it is clear that it approaches the origin rapidly (decreasing 10 orders of magnitude over 15 seconds). In this particular example, the Lyapunov function $\mathcal{V}_1^p$ does not exhibit peaking, but this phenomenon is observed in more extreme system initializations. However, even in the cases that exhibit peaking, the Lyapunov function $\mathcal{V}_1^p$ remains below the theoretical bound in (6.51) transiently, and all errors converge to the single stable equilibrium point corresponding to a zero tracking error.

The effects of the additive vanishing perturbation on the positional subsystem can be clearly seen in the bottom right subplot of Figure 6.10 in some simulations, which here may become positive transiently. The analytical time-derivative of $\mathcal{V}_1^p$ along the unperturbed system in $\Sigma_1^{p\prime}$ will not be the same as the time derivative of $\mathcal{V}_1^p$ along the perturbed system Σ_1^p. We stress that this is expected from the theoretical analysis and that even if $\mathcal{V}_1^p$ is increasing in the transient, it is bounded uniformly in time. As a sanity check, we show the function $\mathcal{V}_1^p$ along the perturbed system Σ_1^p in the signals of the system (blue) plotted of the numerically differentiated signal $\mathcal{V}_p^1$ in Figure 6.10, again indicating that the expressions in the proofs are correctly derived.

Given the definition of the initial errors as sampled from probability distributions, 1000 simulations were performed with similarly large initial errors. In all of these simulations, it was verified numerically that:

- All estimation and tracking errors in the closed-loop system converge to a small neighborhood of the origin within the simulation time;
- The virtual control input is saturated to $\mathcal{B}_\gamma$ at all times;
- The Lyapunov function $\mathcal{V}_1^a$ decreases strictly in time;
- The Lyapunov function $\mathcal{V}_1^p$ may peak, but decreases after a transient.

The example demonstrates the almost global stability properties of the closed-loop system defined by Theorem 6.2, showing an expected recovery and perfect stabilization from large initial errors. We stress that these are not only errors in the initial configuration with respect to the reference trajectory, but equally large errors are in the initial memory associated with the estimator. For a practitioner with experience of nonlinear Gaussian filtering in UAV applications, it should be highly remarkable that the system repeatably recovers from such an extreme initialization, as many of the nonlinear Gaussian filters are prone to diverge if the system initialization is poor. The example also demonstrates the theoretical properties of the control system, verifying the statements associated with Theorems 5.2, 6.1 and 6.2.

6.6.2 Stabilization with Noise and Parameter Errors

With the numerical results in the previous section verifying the proposed theory in an idealized scenario (without noise) with stabilization from large initial errors, we next assess the performance of the controller when introducing disturbances that may appear in practice. In particular, the following disturbances and parameter errors are introduced in the simulation:

- Gaussian noise, $\boldsymbol{p}_k^n \sim \mathcal{N}(\boldsymbol{0}, \sigma_p^2 \boldsymbol{I})$, sampled at 100 [Hz] and entering additively on the positional measurements, here with $\sigma_p = 0.1$;
- Gaussian noise, $\boldsymbol{\omega}_k^n \sim \mathcal{N}(\boldsymbol{0}, \sigma_\omega^2 \boldsymbol{I})$, entering additively on the gyroscopic measurements, with a noise density of 0.014 $[^\circ/\mathrm{s}/\sqrt{\mathrm{Hz}}]$ corresponding to the BMI088 gyroscope [Bosch Sensortec, 2020] used in the Crazyflie [Bitcraze, 2021c]. When sampled at a constant rate of 500 [Hz], this corresponds to a standard deviation in the noise of $\sigma_\omega = 0.0039$.
- Gaussian noise, $\boldsymbol{a}_k^n \sim \mathcal{N}(\boldsymbol{0}, \sigma_a^2 \boldsymbol{I})$, entering additively on the acceleration measurements, with a noise density of 230 $[\mu g/\sqrt{\mathrm{Hz}}]$ corresponding to the BMI088 accelerometer [Bosch Sensortec, 2020] used in the Crazyflie [Bitcraze, 2021c]. When sampled at a constant rate of 500 [Hz], this corresponds to a standard deviation in the noise of $\sigma_a = 0.0034$.
- Modeling errors in the system inertia, such that the controlled system is simulated with $\boldsymbol{J}_{sys} \triangleq 1.2\boldsymbol{J}$, whereas the controllers and estimators are implemented with an inertia of $\boldsymbol{J}$, here realized as in (6.55).

In the considered simulation setup, no noise is added to the magnetometer measurements and all noise terms are unbiased by assumption. Furthermore, no parametric errors are added in the mass and gravitational acceleration, as these are both presumed to be known very exactly. It should be noted that the noise on the positional states corresponds to the magnitude of the measurement noise when employing Ultra-Wideband (UWB) positioning [Mueller et al., 2015], and that these noise levels should be considered exaggerated in practical implementations with high-performance camera systems, GNSS positioning systems, or less conventional positioning systems such as the VIVE lighthouse system [Greiff et al., 2019a]. As such, this setup is representative of stabilization with realistic noise terms, albeit slightly exaggerated for the positional measurements. We emphasize that the control system only has access to measurements sampled from the associated measurement equations.

The simulation is run with the exact same realization as in Sec. 6.6.1 to make the results comparable, and the system response is shown in Figure 6.12 in the control signals and the key tracking errors. The measurements in the position and attitude rates are also depicted to give a sense of the noise levels.

Discussion In Figure 6.12, we observe minor effects on the errors of the attitude subsystem Σ_2^a in the initial transient. This is largely due to the fact that the reference trajectory $(\boldsymbol{p}_r, \boldsymbol{v}_r, \boldsymbol{R}_r, \boldsymbol{\omega}_r, f_r, \dot{f}_r, \ddot{f}_r, \boldsymbol{\tau}_r)$ is independent of the inertia in the case of stabilization. The inertia only appears in the computation of the augmented reference trajectory, $(\bar{\boldsymbol{R}}_r, \bar{\boldsymbol{\omega}}_r, \bar{\boldsymbol{\tau}}_r)$, and in the estimator update law (5.10c) of Theorem 5.2. All remaining terms including the inertia in the dynamic feed-forward of the FOF attitude controller are canceled out as $\boldsymbol{\omega}_r = 0$. Consequently, the effects of the inertia modeling error are barely visible in the initial transient when comparing the Lyapunov function $\mathcal{V}_1^a$ in Figure 6.9 (without noise) and Figure 6.12 (with noise).

In the same Lyapunov function, a slight degradation of performance in the attitude subsystem is visible, and the errors approach a noise floor at around $\mathcal{V}_a^1 \approx 10^{-5}$. These asymptotic errors are largely dependent on the magnitude of the measurement noise, specifically the positional noise, and less dependent on the inertia modeling errors. The effect of the positional measurement noise is seen in the Lyapunov function $\mathcal{V}_1^p$, which also reaches a noise floor. While the attitude rate deviates slightly from the reference, it closely follows the augmented reference trajectory (not plotted). Indeed, when studying the zoomed attitude rate subplot, we note that the tracking is very good in the ω_3-state, but slightly worse in the ω_1- and ω_2-states. The reason is that the augmented reference trajectory varies slightly along these dimensions when correcting for the positional errors induced by the positional measurement noise, whereas the corrective rotation $\boldsymbol{R}_d$ defined in (6.33) never induces a rotation about the $\boldsymbol{b}_3$-direction, its rotational axis is always orthogonal to $\boldsymbol{b}_3$. As such, the attitude rate errors seen in the bottom-center subplots are largely

induced by the positional errors. This is can also seen in that $\mathcal{V}_1^p$ (bottom left) approaches its noise floor slightly before $\mathcal{V}_1^a$ (bottom right).

This noise floor associated with $\mathcal{V}_1^p$ is seemingly large, with $\mathcal{V}_p^1 \approx 10^8$ asymptotically. However, due to its construction, this Lyapunov function should be comparatively large, and it is more insightful to study its change relative to the initial errors, which here decreases by several orders of magnitude in the initial transient. To get a sense of the asymptotic errors, these were zoomed in for the positional and attitude rate errors in the center and center-bottom subplots of Figure 6.12. The attitude rate errors are relatively large in comparison to the gyroscopic noise, due to the effects of the positional measurement noise (as discussed previously). However, the tracking errors in the position are significantly smaller than the standard deviation of the positional measurement noise, and this is in large part due to the filtering.

Finally, we observe that despite the substantial noise added to the measured signals, the control signals are not visibly noisy. When zooming in on the control signal torques (not shown), the measurement noise is seen, as it appears in these signals through $\ddot{\boldsymbol{u}}$ (see Example 6.4). However, the actuating force, f, is positive and smooth. Indeed f is C^1, as it is computed through the virtual control input $\boldsymbol{u}$ which is C^1 if the positional measurement noise is discontinuous (as explained in Sec. 6.3). This is one of the main reasons for considering the design of a *filtered output feedback*, and why the control signals are computed from the filter memory in the definition of Problem 6.2.

To conclude this simulation example and summarize the main points, it is clear that the proposed controller performs well in the face of adversarial disturbances that arise in practical implementations. The estimation and tracking errors asymptotically hit a noise floor, which in the case of stabilization is largely due to the positional measurement noise, and the asymptotic errors for realistic noise levels are comparatively small (relative to the measurement noise). As such, the controller not only works well in the idealized case for which it was designed, but also for the case where perturbations are added to the model parameters and noise introduced. This should come as no surprise, as a system with UAGAS and ULES properties is associated with generic robustness properties, as highlighted previously in Theorem 2.12.

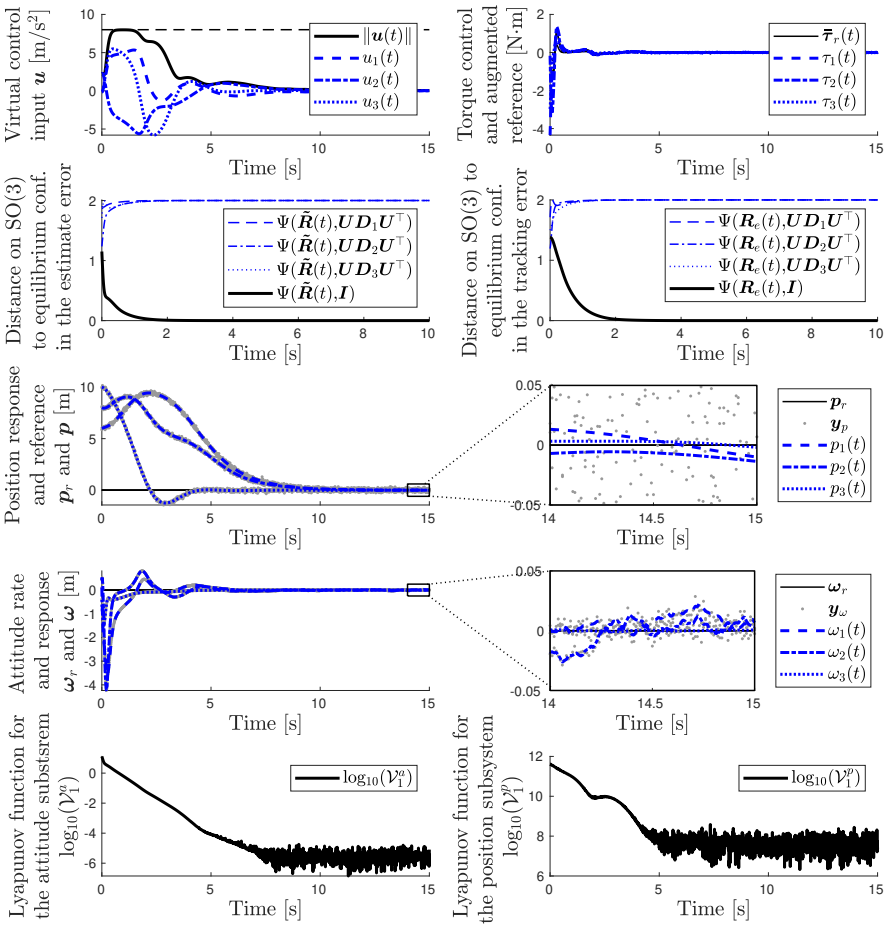

Figure 6.12 System response of the UAV dynamics Σ in (6.1) when controlled along Σ_r in (6.2) by the filtered output feedback solution in Theorem 6.2. *Control signals and key errors* for *stabilization* simulated *with measurement noise and parameter errors*. *Top, left:* The virtual control input $\boldsymbol{u}(t) \in \mathcal{B}_\gamma$ (blue) and its norm $\|\boldsymbol{u}(t)\|$ (black). *Top, right:* Augmented torque reference trajectory and control signal, $\boldsymbol{\tau}$. *Top center, left and right:* Distance to the configurations in $\mathcal{E}$ for estimation and tracking errors, $\tilde{\boldsymbol{R}}$ (left) and $\boldsymbol{R}_e$ (right), with respect to the augmented reference $\bar{\boldsymbol{R}}_r$. *Center, left and right:* Constant positional reference trajectory (black), here with sampled measurements $\boldsymbol{y}_p$ (gray), and the state of the controlled system (blue). *Bottom center, left and right:* Constant attitude rate reference trajectory (black), here with sampled measurements $\boldsymbol{y}_\omega$ (gray), and the state of the controlled system (blue). *Bottom, left:* The Lyapunov function $\mathcal{V}_1^a$ in (5.11). *Bottom, right:* The Lyapunov function $\mathcal{V}_1^p$ in (6.20). The simulated system response is shown in the video chapter-6-simulations.mp4.

6.6.3 Trajectory Tracking with Noise and Parameter Errors

In this final simulation example, the tracking performance of the controller is demonstrated using an example similar to that in [Lefeber et al., 2020]. However, here a slightly more realistic setup is considered, which is closer to what a large angle maneuver may look like in practice. Instead of performing a looping maneuver, we consider an example where the system is initialized with significant errors, although not as extreme as in the stabilization example. The system is the run with the measurement noise defined in Sec. 6.6.2, including positional, gyroscopic and accelerometer measurement noise, as well as poor model of the system's inertia. The system is controlled along a commanded flat output trajectory $\boldsymbol{\gamma}_c(t)$, defined with the Heaviside step function Θ as

$$\boldsymbol{\gamma}_c(t) = (5\Theta(t-5);\ 10\Theta(t-10);\ 5\sin(0.5t);\ (\pi/2)\sin(t)) \in \mathbb{F}_\Sigma. \tag{6.54}$$

This commanded flat output trajectory is discontinuous in time in the global p_1 position (east, γ_1) and the global p_2 position (north, γ_2), while the global p_3 position (up, γ_3) and the yaw $\psi(t)$ (yaw in Definition 2.20, γ_4) are both smooth. As such, the commands require smoothing in order to permit a flatness expansion to generate an associated reference trajectory. Following the approach in Sec. 2.2.5, the commanded trajectory is filtered through a system Σ_f in the form outlined in (2.25), with $m = 4$ and $q = 5$, and a speed defined by the pole location characterized by $c = 2$. This generates a flat output trajectory $\boldsymbol{\gamma}(t)$ in C^4 where the signals $\{\boldsymbol{\gamma}^{(i)}(t) | i = 0, ..., 4\}$ are known in the memory of the filter, Σ_f. This flat output trajectory is initialized with $\boldsymbol{\gamma}^{(i)}(t_\circ) = \mathbf{0}$ for all $i = 0, ..., 4$, and expanded into a reference trajectory $(\boldsymbol{p}_r, \boldsymbol{v}_r, \boldsymbol{R}_r, \boldsymbol{\omega}_r, \dot{\boldsymbol{\omega}}_r, f_r, \dot{f}_r, \ddot{f}_r, \boldsymbol{\tau}_r)$ using the flatness maps associated with Σ_r in (6.2) (see, e.g., [Greiff, 2017, Chapter 3.1]). This is precisely how the reference generation was implemented for the examples in Chapter 4.

Remark 6.7
Such an implementation represents a realistic approach for a practical implementation, as it permits the use of discontinuous commands through joystick control in the flat output space. But the pre-filtering can be omitted if the flat output trajectory is sufficiently smooth, and the flatness expansion can be omitted if a reference trajectory is computed by other means. □

The system is initialized with significant errors, although not as extreme as in the previous two subsections. Here, we let $\boldsymbol{p}(t_\circ) = (4;\ 4;\ 4)$ and take $\boldsymbol{\omega}(t_\circ), \boldsymbol{v}(t_\circ), \hat{\boldsymbol{v}}_e(t_\circ), \hat{\boldsymbol{p}}_e(t_\circ), \boldsymbol{z}(t_\circ), \hat{\boldsymbol{\omega}}(t_\circ) \sim \mathcal{U}([-0.5, 0.5]^3)$ with $\boldsymbol{R}(t_\circ) = \mathrm{Exp}_{\mathrm{SO}(3)}([\boldsymbol{n}]^\wedge_{\mathrm{SO}(3)})$, $\hat{\boldsymbol{R}}(t_\circ) = \mathrm{Exp}_{\mathrm{SO}(3)}([\hat{\boldsymbol{n}}]^\wedge_{\mathrm{SO}(3)})$ for $\boldsymbol{n}, \hat{\boldsymbol{n}} \sim \mathcal{U}([-0.5, 0.5]^3)$. The parameters are defined by a random dense inertia matrix $\boldsymbol{J} = \boldsymbol{J}^\top \succ \mathbf{0}$ satisfying $\lambda_m(\boldsymbol{J}) = 0.05$ and $\lambda_M(\boldsymbol{J}) = 0.1$, the gravitational acceleration is taken to be $g = 10$ [m/s^2], and the UAV mass is defined as $m = 0.1$ [kg]. The

simulation is again run from $t_\circ = 0$ over 15 [s]. In this example, the inertia matrix is dense (here rounded to three digits), as

$$\boldsymbol{J} = 0.01 \cdot \begin{bmatrix} 7.4 & 2.1 & 1.3 \\ 2.1 & 7.2 & 0.5 \\ 1.3 & 0.5 & 7.1 \end{bmatrix}. \tag{6.55}$$

The initial attitudes on SO(3) (here rounded to two digits), are

$$\boldsymbol{R}(t_\circ) = \begin{bmatrix} 0.85 & 0.47 & 0.23 \\ -0.48 & 0.87 & 0.03 \\ -0.19 & -0.13 & 0.97 \end{bmatrix}, \quad \hat{\boldsymbol{R}}(t_\circ) = \begin{bmatrix} 0.91 & -0.23 & -0.34 \\ 0.34 & 0.89 & 0.30 \\ 0.23 & -0.39 & 0.89 \end{bmatrix},$$

resulting in smaller initial attitude errors than in the previous examples, with

$$\Psi(\boldsymbol{R}_r(t_\circ), \boldsymbol{R}(t_\circ)) = 0.14, \tag{6.56a}$$

$$\Psi(\boldsymbol{R}_r(t_\circ), \hat{\boldsymbol{R}}(t_\circ)) = 0.15, \tag{6.56b}$$

$$\Psi(\boldsymbol{R}(t_\circ), \hat{\boldsymbol{R}}(t_\circ)) = 0.45. \tag{6.56c}$$

The controller is tuned in the exact same way as in the previous two simulation examples, the only exception being the saturation level, which is tuned down slightly to $\gamma = 2.5$ in order to show its effect on virtual control input $\boldsymbol{u}$. The numerical results are depicted in terms of the attitude errors corresponding to the positional subsystem in Figure 6.13, with the control signals and key responses in Figure 6.14, and an illustration of the configurations of the system in Figure 6.15.

Discussion In Figure 6.13, we note that the system exhibits very similar properties to the stabilization example. All errors converge to visibly small values as the auxiliary state starts to approach the origin, and the positional measurement noise is visible in the signal $\boldsymbol{p}_e$, as expected. As this noise enters directly in $\tilde{\boldsymbol{p}}$, which in turn enters the Lyapunov function $\mathcal{V}_p^a$ as a quadratic form scaled by a large parameter defined by (6.23), we should expect this Lyapunov function to hit a noise floor at a level similar to that in the noisy stabilization case in Sec. 6.6.2. This is clearly seen in the bottom left subplot of Figure 6.13. As the noise enters directly in the Lyapunov function, its numerical time-derivative cannot be evaluated numerically and hence omitted in the bottom right subplot. Notably, given the saturation level of $\gamma = 2.5$, the virtual control input is saturated in the transient, as seen in the top-left subplot of Figure 6.13. Consequently, the actuating force is confined to the interval, $f(t) \in [f_r(t) - m\gamma, f_r(t) + m\gamma]$ at all times as seen in Figure 6.14. However, despite saturating the virtual control, the force never reaches the boundary points of its associated interval. The reason for this is that $\boldsymbol{u}$ is not parallel with $\boldsymbol{e}_3$ in this particular simulation (see Equation 6.32).

In Figure 6.14, the actuating torques are relatively small. The measurement noise is visible when zooming in on these signals (this zoom is omitted here), but it is not detrimental to a real-time implementation. We note that the attitude errors quickly converge to the stable equilibrium, just as they did in the stabilization case, and that no errors are induced when performing the relatively large steps in p_1 and p_2. This is due to the augmented reference trajectory $(\bar{\boldsymbol{R}}_r, \bar{\boldsymbol{\omega}}_r, \bar{\boldsymbol{\tau}}_r)$ satisfying the attitude reference dynamics, for which the attitude subsystem is UAGAS and ULES. The two Lyapunov functions reach similar noise floors to what is observed in the stabilization example in Sec. 6.6.2, and as a consequence, we get similar performance in the position and attitude rate tracking as well.

Finally, the configuration response in (6.15) demonstrates how the UAV follows the commanded reference trajectory. The position tracking is best visible in the left-most subplots, and the attitude tracking is visible in the top right subplot, clearly indicating that the yaw follows the commanded reference trajectory defined in (6.54). We note that this system response looks very similar to how a UAV of the given mass and inertia behaves in practice, and stress that it can be run with even more extreme trajectories and initialization (as highlighted in [Lefeber et al., 2020]). The present example instead shows how the controlled system behaves when following aggressive reference trajectory subject to relatively large initial errors and realistic disturbances.

In conclusion, this simulation example demonstrates the tracking performance of the UAV dynamics Σ in (6.1) when in feedback with the FOF controller cascade in Theorem 6.2. The example is specifically designed to show how the control system may be implemented in practice, and how the differential flatness equations in [Greiff, 2017, Chapter 3.1] can be implemented with pre-filtering to expand a reference trajectory that the UAV subsequently can follow. In particular, when generating the reference trajectory in this manner, we observe a tracking performance that is extremely similar to the stabilization performance (c.f., the Lyapunov functions in Figure 6.12 and Figure 6.14). As such, the closed loop control system should be expected to perform equally well for tracking and stabilization applications when the measurements are corrupted by the unbiased Gaussian noise described in Sec. 6.6.2, and we recommend its use in practice.

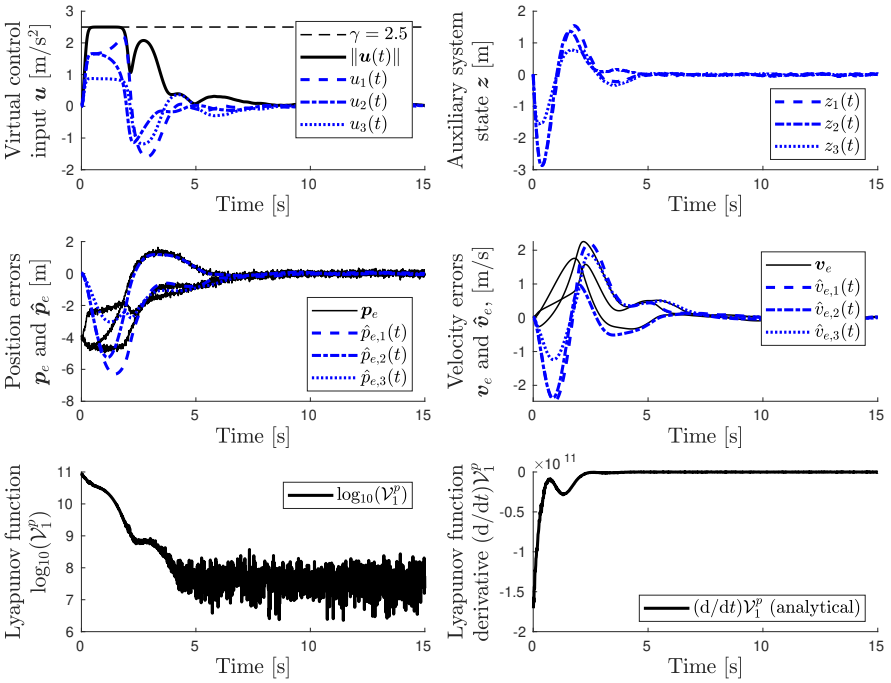

Figure 6.13 System response of the UAV dynamics Σ in (6.1) when controlled along Σ_r in (6.2) by the filtered output feedback solution in Theorem 6.2. *Signals associated with* Σ_1^p for *trajectory tracking* simulated *with measurement noise and parameter errors*. *Top, left:* The virtual control input $\boldsymbol{u}(t) \in \mathcal{B}_\gamma$ and its norm $\|\boldsymbol{u}(t)\|$. *Top, right:* Trajectory of the auxiliary system state $\boldsymbol{z}(t)$. *Center, left:* The positional tracking error $\boldsymbol{p}_e(t)$ (black) and the estimated tracking error $\hat{\boldsymbol{p}}_e(t)$ (blue). *Center, right:* The velocity tracking error $\boldsymbol{v}_e(t)$ (black) and the estimated tracking error $\hat{\boldsymbol{v}}_e(t)$ (blue). *Bottom, left:* The Lyapunov function $\mathcal{V}_1^p$ in (6.20) decreasing in time, decaying exponentially for small errors. *Bottom, right:* The time-derivative $(\mathrm{d}/\mathrm{d}t)\mathcal{V}_1^p$ evaluated analytically in the signals of the system using the expression in (6.21) (black). The simulated system response is shown in the video chapter-6-simulations.mp4.

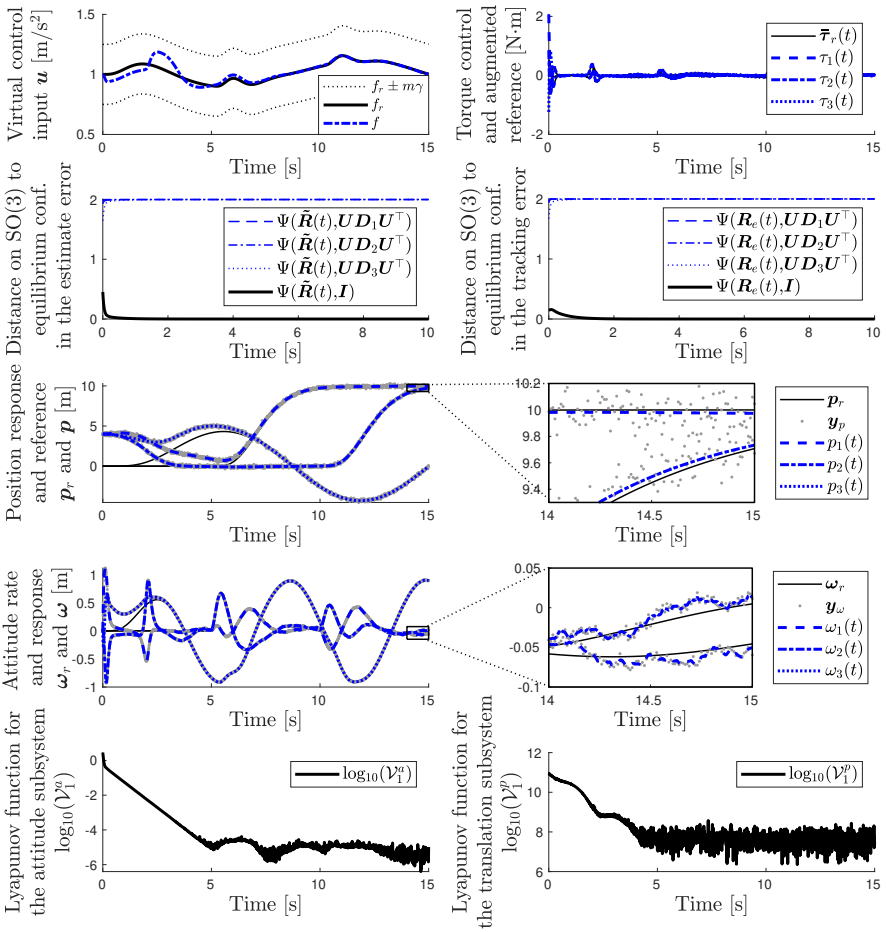

Figure 6.14 System response of the UAV dynamics Σ in (6.1) when controlled along Σ_r in (6.2) by the filtered output feedback solution in Theorem 6.2. *Control signals and key errors* for *trajectory tracking* simulated *with measurement noise and parameter errors*. *Top, left:* The reference force $f_r(t)$ (black) and the control signal $f(t)$ (blue). *Top, right:* Augmented torque trajectory and control signal, $\boldsymbol{\tau}$. *Top center, left and right:* Distance to the configurations in $\mathcal{E}$ for estimation and tracking errors, $\tilde{\boldsymbol{R}}$ (left) and $\boldsymbol{R}_e$ (right), with respect to the augmented reference $\bar{\boldsymbol{R}}_r$. *Center, left and right:* Constant positional reference trajectory (black), here with sampled measurements $\boldsymbol{y}_p$ (gray), and the state of the controlled system (blue). *Bottom center, left and right:* Constant attitude rate reference trajectory (black), here with sampled measurements $\boldsymbol{y}_\omega$ (gray), and the state of the controlled system (blue). *Bottom, left:* The Lyapunov function $\mathcal{V}_1^a$ in (5.11). *Bottom, right:* The Lyapunov function $\mathcal{V}_1^p$ in (6.20). The simulated system response is shown in the video chapter-6-simulations.mp4.

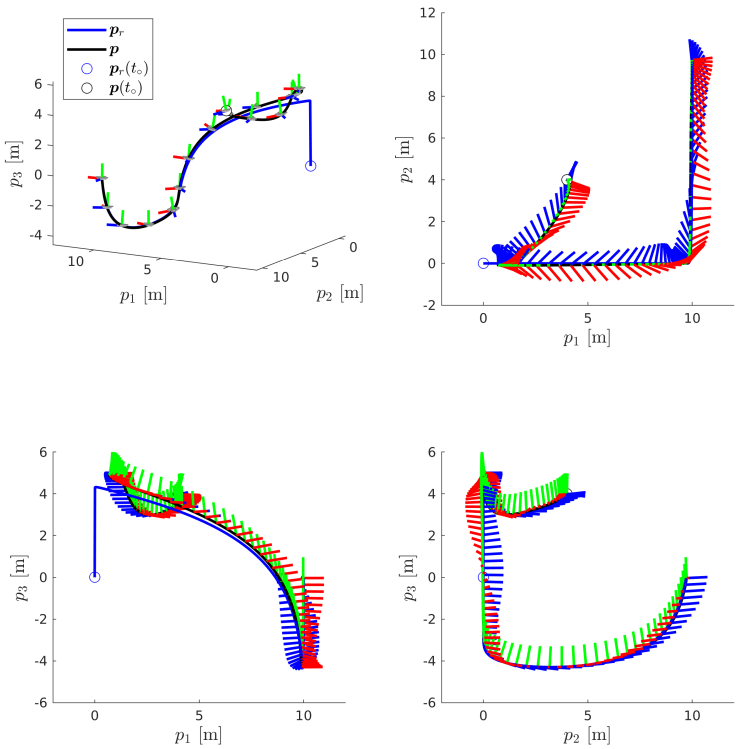

Figure 6.15 System response of the UAV dynamics Σ in (6.1) when controlled along Σ_r in (6.2) by the filtered output feedback solution in Theorem 6.2. *Configurations* in the *trajectory tracking* example, simulated *with measurement noise and parameter errors*. Illustration of the system configurations, with the positional reference trajectory (blue), the positional trajectory (black), and the system attitude illustrated temporally equidistant over $t \in [0, 15]$ using the same color coding of the body basis vectors and illustration of the UAV as used in Figure 2.5 and Figure 2.6. *Top, left:* Trajectory in three-dimensional space. *Top, right:* Projection onto the-$\boldsymbol{e}_1\boldsymbol{e}_2$ plane. *Bottom, left:* Projection onto the $\boldsymbol{e}_1\boldsymbol{e}_3$-plane. *Bottom, right:* Projection onto the $\boldsymbol{e}_2\boldsymbol{e}_3$-plane. The simulated system response is shown in the video chapter-6-simulations.mp4.

6.7 Summary

In this chapter, we have presented the filtered output feedback controller first published in [Lefeber et al., 2020, Proposition 3], which takes a diametrically different view of the UAV control system to conventional design methods, as illustrated in Figure 6.1. Instead of constructing a controller for the full UAV dynamics independently, and coupling this with a full or extended state estimator (the horizontal approach in Figure 6.1), we instead design a filtered output feedback controller for the attitude and position subsystems independently, before analyzing the resulting cascade (the vertical approach in Figure 6.1). This results in a solution to Problem 6.2 that yields *uniform almost global asymptotic* and *uniform local exponential* stability properties, in both the tracking and the estimation errors, granting the resulting closed-loop control system a measure of robustness in the sense of Theorem 2.12.

This is a powerful result, as it only assumes knowledge of the attitude through a set of directional measurements, the attitude rates in the body frame through gyroscopic measurements, and direct measurements of the UAV position in a global frame. These signals are readily available in most modern UAV applications, and can be made to encompass many additional sensors. For instance, UWB measurements [Mueller et al., 2015] or even the more recent VIVE Lighthouse positioning [Greiff et al., 2019a], can be converted to a direct position estimate without introducing memory. The controller can even handle monocular camera measurements, where the directional information can enter as a measurement on the attitude. As such, the FOF solution presented in this chapter has significant generality, and could be implemented for a wide variety of applications. However, the inclusion of pre-filtered estimates from a GNSS module should be considered with care, as such methods typically introduce additional dynamics in the positions.

It should be noted that the controller is extremely challenging to implement in practice. A typical approach to a UAV control system design often starts with the estimator, ensuring that it has been implemented correctly through rigorous testing, before introducing simple attitude control, and then progressing toward more elaborate methods of full state feedback, for instance those described in Chapters 3 and 4. In stark contrast, when implementing the cascaded FOF controller described in Theorem 6.2, one has to tune the FOF controller for the attitude subsystem first, and this has to be done in manual flight where the input commands are filtered to a sufficient degree of smoothness to be expanded into the signals of attitude reference subsystem. This is a difficult and potentially costly endeavor, and once it has been done, the entire control system needs to be re-tuned when connecting the cascade. In this case, we also require a complete reference trajectory, which typically needs to be computed by exploiting the property of differential flatness.

Furthermore, all of the developments in this chapter are done in continuous

time, and the update laws of the filter memory need to be discretized for the real-time implementation. This is made more difficult by the fact that parts of this memory evolves on SO(3). As such, to facilitate developments of this control system, a subset of the above results have been implemented in C with simulation options in Julia in the `AerialVehicleControl.jl` package [Greiff, 2020]. This implementation keeps an internal representation of the signal $\hat{\boldsymbol{R}}$ as a quaternion, and simulates this system using a first order CG method outlined in Sec. 2.3. While successful flights have been performed with the attitude FOF controller using the reference generation described in Sec. 2.2, the complete control system has only ever been successfully evaluated in simulation. Initial experiments implementing the controller were done in [Zeng et al., 2021], but in real-time, implementations of Theorem 6.2 have yet to yield tracking results comparable to the solutions in Chapter 4.

In this thesis, a simulation evaluation was provided in Sec. 6.6. Here, the focus was on illustrating the behavior of the system when initialized with large errors, to demonstrate its almost global stability properties and the local exponential decay of the error functions. This example was subsequently reused to show the performance of the controller subject to realistic measurement noise and parameter errors, corresponding to a high-performance IMU and positional information corresponding to a low cost UWB system. Finally, a similar simulation setup was used to demonstrate the tracking performance of the controller, when initialized with more realistic initial errors, and also including measurement noise and uncertainty in the inertia. Here, the UAV was controlled along an aggressive reference trajectory computed using the differential flatness maps associated with the UAV dynamics, after first filtering a set of discontinuous commands in the flat output space. This is representative of how the controller is intended to be used in practice, and shows that it can be considered for trajectory tracking applications.

In conclusion, we have presented a filtered output feedback solution for the UAV tracking control problem that is the first of its kind, taking a very different view of the UAV control system than what is customary. Instead of a disjoint design of the observer and controller, two filtered output feedback controllers are combined in a cascade, facilitating proofs of UAGAS and ULES. Based on the numerical results, we recommend that the presented control should be considered for applications requiring high degrees of maneuverability and almost global stability guarantees. However, it can also be considered for simpler applications, including safety-critical inspection and surveying missions, due to the favorable stability properties of the closed-loop system.

7

Summary of Part I

Several theoretical contributions were made in Part I of the thesis. In this summary, a subset of these are restated to give a comprehensive view of the developments and show how they relate to the larger body of UAV control literature. Each section describes the main results, and how these are generalized and used in subsequent chapters, as illustrated in Figure 7.1.

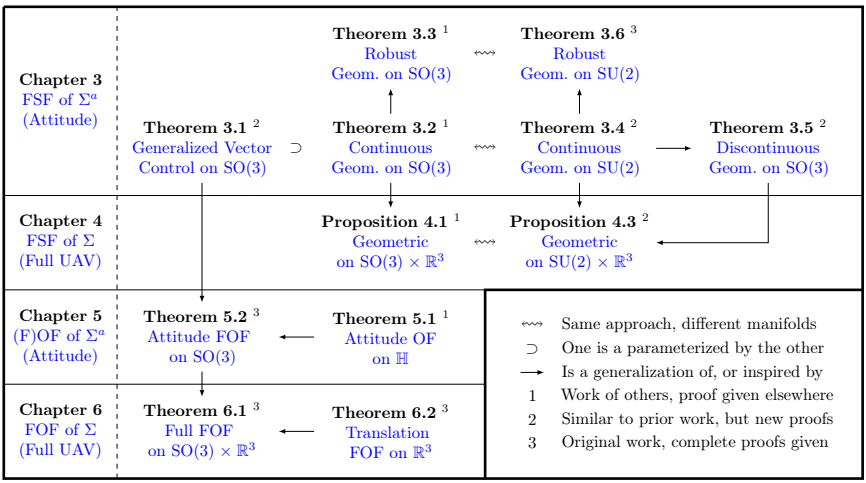

Figure 7.1 Summary and overview of key results in Part I of the thesis.

Chapter 3 One of the most important contributions in this chapter is the clarification of how several controllers for dynamical systems with rotational degrees of freedom are related. By working directly with elements of SU(2) and the Γ-distance in Definition 2.19, a clear link can be drawn between several attitude controllers on SU(2) and their counterparts on SO(3) that operate with the Ψ-distance in Definition 2.18. Of the latter controllers on SO(3), it

was also shown that several independently derived results are similar if not equivalent. For instance, the controller in Theorem 3.2 is characterized by Theorem 3.1, and analogous ideas can be traced back further (see, e.g., [Bullo and Murray, 1995, Theorem 4]). Importantly, due to the approach in the stability proofs for the controllers on SU(2), a robust feedback law was derived. The importance of clearly defining the stability properties of these controllers and clarifying how they relate should not be overlooked, as these results form the basis for the remaining theoretical developments in Part I of the thesis.

Chapter 4 In this chapter, it was demonstrated how the various attitude controllers can be used to define full state feedback controllers for the UAV dynamics. Due to the strong similarities between the geometric controllers on SO(3) and SU(2), their extensions to the full UAV dynamics are similar in the same sense. In particular, when working with the Ψ-distance on SO(3) the geometric controllers in [Lee et al., 2011] are found, and when working with the Γ-distance on SU(2), the controllers in [Brescianini and D'Andrea, 2018] are recovered. The performance of these controllers were discussed and illustrated both in simulation and in practice. In doing so, we highlighted three different problems of the considered full state feedback laws:

- There exist points at which the desired attitude reference is undefined;
- Computing this trajectory requires the second derivatives in the errors;
- Introducing an estimator with dynamics may result in instability.

While the controllers considered in this chapter work well in practice, these three problems remain, motivating the study of the *filtered output feedback* problem, representing a very different approach to the control system design.

Chapter 5 To facilitate a FOF solution for the full UAV dynamics, the attitude dynamics were first considered. Much like the FSF controllers for the full UAV dynamics, an attitude control result was used as a starting point, in this case Theorem 3.1. This approach to attitude control was chosen due to its UAGAS and ULES properties, and generalized by introducing an estimator operating with a 9-DOF IMU, devising a feedback so as not to use the measurements directly in the computation of the control signals. The resulting controller was presented in Theorem 5.2, yielding UAGAS and ULES properties of the error dynamics, and serving as a good starting point for the developments of a FOF with respect to the full UAV dynamics.

Chapter 6 In this chapter, the FOF solution for the attitude dynamics was combined with the FOF solution for the translation dynamics, designing an interconnection of the two systems by ideas similar to the geometric feedback laws for the full UAV dynamics in Chapter 4. However, in contrast to the FSF solutions, the FOF controller has the following properties:

- There exists no singularities in the computation of the desired attitude in the interconnection term, as the actuating force can be bound to a ball about the reference force f_r;
- The desired reference trajectory can be computed directly in the filter memory without the need for numerical differentiation;
- A joint stability proof is given for the tracking and estimation errors, showing UAGAS and ULES for the entire cascade.

While the resulting control system is difficult to implement and tailored for positional and IMU measurements, it provides rigorous stability guarantees for the entire closed-loop control system. This control system was studied in a set of simulation examples, introducing noise and parameter errors to emulate disturbances that can arise in practice. These numerical experiments verified the theoretical results, and constitute a strong argument for using the filtered output feedback controller in real-time applications.

Final Remarks In the first part of the thesis, several good solutions to the problem of attitude and UAV control are presented, both in the context of full state feedback laws, and the more exotic filtered output feedback laws. When considering UAV control in practice, it often suffices to use the solutions in Chapter 4. This is demonstrated by the agile and large-angle maneuvers in Sec. 4.4.1 and the example pertaining to supermarket inventorying in Sec. 4.4.2. However, if the application is safety critical, requiring rigorous joint stability proofs of both estimation and tracking errors, then we propose the solution in Chapter 5 for attitude control, and the solution in Chapter 6. These FOF control systems come with proofs of UAGAS and ULES for both estimator and tracking errors. This is made possible by taking a very different view of the control system, and effectively solves all of the problems identified for the FSF controllers in Chapter 4, but has the drawback of making the controller implementation more challenging. Regardless of the chosen control system, any practical implementation can benefit greatly from the code base in [Greiff, 2020]. This software implements many key results in Figure 7.1 in C code, offering simulation options through the computer language Julia. This includes all of the attitude controllers (including the filtered output feedback in Theorem 5.2) and various flatness maps.

Part II

Application Examples

8

Circumnavigation and Target Tracking

8.1 Introduction

The theory and algorithms developed in Part I of the thesis can be used in various ways. For example, applications can be envisioned where a UAV is to track a target with a circular motion, in order to maintain sight of the target at all times. Such problems are typically considered for fixed-wing UAVs, which need to maintain a non-zero velocity at all times to remain airborne. A tangible example is the circulating and tracking of a capsized boat during a search and rescue reconnaissance mission, where the UAV flies at a greater velocity than the drifting boat. For such missions, autonomous fixed-wing UAVs could be considered. However, the developments of this chapter are more general, and the presented results can be used to compute the velocity references for controlled quadrotor UAVs or even ground vehicles as well.

In this chapter, we present a circumnavigation and target tracking controller that is designed to suppress bounded disturbances on the control inputs by introducing integral action. Such problems can broadly be categorized into three cases based on available sensory information, with the agent knowing:

(i) its own position and relative distance and bearing angle to a target;

(ii) its own position and a relative distance to a target;

(iii) its own position and a bearing angle to a target.

In the works of [Marshall et al., 2006; Kim and Sugie, 2007; Ceccarelli et al., 2008] the target position is assumed to be known. Such approaches require significant sensory infrastructure: either communication between the target and agent, where the target communicates its own position, or a sensory setup as defined in (i). Even then, the target position is never known perfectly. Works assuming (ii), where controllers are developed with knowledge of a

relative distance to the target, are found in [Shames et al., 2011; Matveev et al., 2016; Milutinović et al., 2017]. But such sensing is typically active and realized by sonar, radar or LiDAR. Consequently, if the tracking agent wishes to remain undetected, the measurements assumed in (iii) are of special interest. The problem posed with (iii) has therefore seen significant attention with recent results in [Zhao and Zelazo, 2015; Deghat et al., 2015; Shao and Tian, 2018; Li et al., 2018; Zou et al., 2020]. It is often considered in a simplified setting, where it is assumed that the system can follow velocity references in the body-fixed frame. In this chapter, we consider circumnavigation and target tracking problem with bearing measurements, modeling the system as a single integrator in $\mathbb{R}^2$, where the controller computes velocity references for a controlled system, as summarized in Problem 8.1 and Figure 8.1.

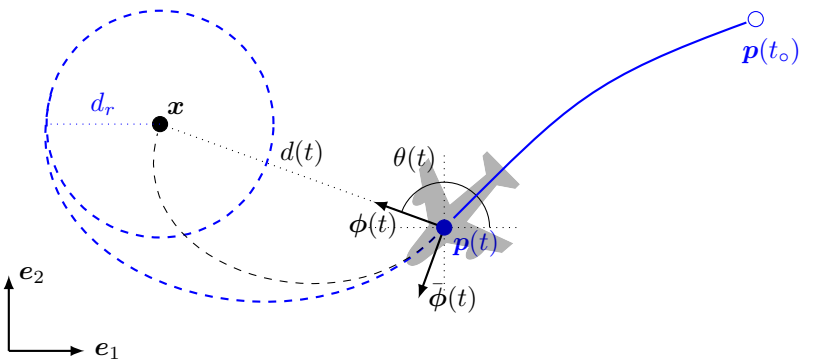

Figure 8.1 Geometry of the circumnavigation and target tracking problem.

Problem 8.1
Consider the geometry in Figure 8.1, where $\boldsymbol{x} \in \mathbb{R}^2$ is an unknown and stationary target position, that is, $\dot{\boldsymbol{x}} = \boldsymbol{0}$. Define the bearing direction to the target as $\boldsymbol{\phi}(t) = (\cos(\theta(t));\ \sin(\theta(t))) \in \mathbb{R}^2$ with an orthogonal bearing direction $\bar{\boldsymbol{\phi}}(t) = (-\sin(\theta(t));\ \cos(\theta(t))) \in \mathbb{R}^2$. Let $\dot{\boldsymbol{p}}(t) = \boldsymbol{u}(t)$ denote the simplified process dynamics, and take $\hat{\boldsymbol{x}}(t)$ to be the estimated position of the target. Find a feedback with integral action in (8.1b) and an estimator,

$$\boldsymbol{u}(t) = G(\boldsymbol{p}(t), \boldsymbol{\phi}(t), \hat{\boldsymbol{x}}(t), \boldsymbol{z}(t)), \qquad \boldsymbol{p}(t_\circ) = \boldsymbol{p}_\circ \in \mathbb{R}^2, \tag{8.1a}$$

$$\dot{\boldsymbol{z}}(t) = H_z(\boldsymbol{p}(t), \boldsymbol{\phi}(t), \hat{\boldsymbol{x}}(t)), \qquad \boldsymbol{z}(t_\circ) = \boldsymbol{z}_\circ \in \mathbb{R}^2, \tag{8.1b}$$

$$\dot{\hat{\boldsymbol{x}}}(t) = H_x(\boldsymbol{p}(t), \boldsymbol{\phi}(t), \hat{\boldsymbol{x}}(t)), \qquad \hat{\boldsymbol{x}}(t_\circ) = \hat{\boldsymbol{x}}_\circ \in \mathbb{R}^2, \tag{8.1c}$$

such that for any distance $d_r \in \mathbb{R}_{>0}$ and target velocity $\alpha_r \in \mathbb{R}_{>0}$, results in perfect tracking $d(t) = \|\boldsymbol{x} - \boldsymbol{p}(t)\| \to d_r$ and $\|\dot{\boldsymbol{p}}(t)\| \to \alpha_r$ as $t - t_\circ \to \infty$. □

Remark 8.1
When developing such controllers, we need to ensure that the tracking agent does not collide with the target in the initial transient, illustrated with the black dashed trajectory in Figure 8.1. In practice, when applying a solution to Problem 8.1 in $\mathbb{R}^3$ there will generally be no risk of physical collision, provided that target and UAV reside at different elevations. However, at any point in time where $\|\boldsymbol{x} - \boldsymbol{p}(t)\| \approx 0$, the bearing angle will become volatile. This should be avoided, as the bearing direction is used explicitly in (8.1a).□

Remark 8.2
In the case of the fixed-wing UAV, it is of great importance that its velocity remains bounded away from the origin. Indeed, it should never be less than some positive value, such that the UAV always remains airborne. This is less important in the context of the quadrotor UAVs and UGVs, but will remain a design requirement, as it facilitates arguments of persistent excitation (PE).□

A reasonable objection to this problem formulation is that few mechanical systems can be modeled as a single integrator. There exist actuation and modeling errors which appear in stationarity, and one may ask if it is an interesting problem to study. However, if we consider a quadrotor in closed-loop feedback with the control systems presented in the previous chapters, this system can be controlled along velocity references in $\mathbb{R}^2$. Consequently, a solution to Problem 8.1 can be used to compute the velocity references for a closed-loop system, and if we wish, the resulting cascade may even be analyzed using variants of Theorem 2.9. Indeed, any solution to Problem 8.1 can be considered for applications where the closed-loop system is capable of following velocity references in $\mathbb{R}^2$. This encompasses fixed-wing UAVs, quadrotor and multi-rotor UAVs, as well as UGVs. To highlight this generality, a differentially driven UGV will be used to demonstrate the theory in practice.

8.1.1 Chapter Motivation

Problem formulations assuming knowledge of the bearing direction are generally interesting, as such directions can be measured using passive methods, such as monocular camera systems (see e.g., [Jang et al., 2021]). Furthermore, the reason for considering a simple integrator is its generality, but this solution really only becomes interesting if (i) the resulting modeling errors can be dealt with, and (ii) there exists a controller for the system in question, be it an UAV or UGV, with the closed-loop system being UAGAS and ULES, such that the resulting cascade can be analyzed. As problem (ii) has been solved for the quadrotor UAV (see e.g., the solutions in Part I) and UGV systems (see e.g., [Lefeber, 2000]), there exist significant motivation to address the general circumnavigation problem outlined in Problem 8.1.

In this chapter, the solution proposed in [Greiff et al., 2021b] is presented. This solution extends the popular method in [Deghat et al., 2010] with

integral action, and characterizes the modeling and actuation errors under which the control system represents a solution to Problem 8.1. In light of Remark 8.2, the controller is constructed so as to ensure that the velocities of the system are non-zero at all times. Furthermore, in light of Remark 8.1, sufficient conditions ensuring collision avoidance in the transient phase of the error dynamics are given. Additionally, the controller is designed to ensure asymptotic convergence of the tracking errors if the adversarial disturbances are sufficiently small transiently, and asymptotically constant. The utility of the approach is illustrated with a real-time example using a UGV, but we emphasize that the intended application is a fixed-wing or quadrotor UAV.

8.1.2 Overview

The primary purpose of this chapter is to show that the controller works well in practice. To this end, a greater emphasis is put on explaining the control system used in the experiments, with more theoretical details given in [Greiff et al., 2021b]. To summarize the results, some additional mathematical preliminaries are given in Sec. 8.2. This is followed by a presentation of the two circumnavigation controllers before subsequently comparing them in simulation. The main components of the control system of the UGV are then detailed in Sec. 8.2, demonstrating the controller in practice in Sec. 8.4. Finally, the chapter is concluded with a summary in Sec. 8.5. To give an overview, the results and examples are summarized in Table 8.1.

Table 8.1 Overview of the results and examples of Chapter 8. Here, [1] indicates work of others, proofs given elsewhere; [2] indicates work tangential with others, but with independent proofs given; and [3] indicates new work.

Reference	Description
Thm. 8.1 [1]	Proportional circumnavigation output feedback controller, originally in [Deghat et al., 2010, Theorem 1].
Thm. 8.2 [3]	Proportional-integral circumnavigation output feedback controller, originally in [Greiff et al., 2021b, Theorem 3].
Example 8.1	Simulation example contrasting Thm. 8.1 versus Thm. 8.2 when adding asymptotically constant input disturbances
Sec. 8.4.3	Real-time example demonstrating Thm. 8.2 in practice with a small unmanned ground vehicle

8.2 Preliminaries

Throughout this chapter, $\boldsymbol{p} = (p_1;\ p_2) \in \mathbb{R}^2$ is taken to denote the tracking agent's position in a local east-north (EN) frame, omitting the usual up-direction and letting $\boldsymbol{p}(t) = p_1(t)\boldsymbol{e}_1 + p_2(t)\boldsymbol{e}_2$ for unit vectors $\boldsymbol{e}_i \in \mathbb{R}^2$ with the ith entry set to 1 (see Figure 8.1). The target's position is denoted $\boldsymbol{x} \in \mathbb{R}^2$, and the tracking agent's estimate of this position is denoted $\hat{\boldsymbol{x}} \in \mathbb{R}^2$. Let $\tilde{\boldsymbol{x}} \triangleq \hat{\boldsymbol{x}} - \boldsymbol{x}$ and take $d \triangleq \|\boldsymbol{x} - \boldsymbol{p}\|$ with $\hat{d} = \|\hat{\boldsymbol{x}} - \boldsymbol{p}\|$ denoting the true and estimated distance between the target and the tracking agent, respectively. Similarly, let $\Delta \triangleq d - d_r$, $\hat{\Delta} \triangleq \hat{d} - d_r$, and $\delta \triangleq d - \hat{d}$ denote differences between these various distances. Throughout this chapter, the velocity of the vehicle in the EN frame is denoted by $\dot{\boldsymbol{p}}$, and the velocity along the orthogonal bearing direction by $\alpha(t) \triangleq \dot{\boldsymbol{p}}(t) \cdot \bar{\boldsymbol{\phi}}(t)$. Furthermore, for a single-input single-output (SISO) linear time-invariant system without direct term,

$$\dot{\boldsymbol{\xi}} = \boldsymbol{A}\boldsymbol{\xi} + \boldsymbol{B}u \tag{8.2a}$$

$$y = \boldsymbol{C}\boldsymbol{\xi}, \tag{8.2b}$$

let $P(s) = \boldsymbol{C}(s\boldsymbol{I} - \boldsymbol{A})^{-1}\boldsymbol{B}$ denote its description in the Laplace domain, with impulse response $\mathcal{P}(t) = \boldsymbol{C}e^{\boldsymbol{A}(t-t_\circ)}\boldsymbol{B}$, and its system 1-norm given by

$$\|\mathcal{P}\|_1 = \int_{t_\circ}^{\infty} |\mathcal{P}(\sigma)| \mathrm{d}\sigma. \tag{8.3}$$

Note that if $u(t)$ denotes an input to the system in the time-domain, and its output is denoted $y(t)$, then $\|y\|_\infty \leq \|\mathcal{P}\|_1 \|u\|_\infty$, where for SISO systems

$$\|u\|_\infty \triangleq \sup_{t \geq t_\circ} |u(t)|. \tag{8.4}$$

This inequality will be used to derive conservative sufficient conditions for collision avoidance, which will be required in light of Remark 8.1.

8.3 Circumnavigation with Integral Action

Given these preliminaries, the elegant solution to Problem 8.1 originally presented in [Deghat et al., 2010, Theorem 1] is summarized below as follows.

Theorem 8.1—Proportional Circumnavigation Control
The controller-observer combination

$$\dot{\boldsymbol{p}}(t) = k_P \hat{\Delta}(t)\boldsymbol{\phi}(t) + \alpha_r \bar{\boldsymbol{\phi}}(t) \tag{8.5a}$$

$$\dot{\hat{\boldsymbol{x}}}(t) = k(\boldsymbol{I} - \boldsymbol{\phi}(t)\boldsymbol{\phi}(t)^\top)(\boldsymbol{p}(t) - \hat{\boldsymbol{x}}(t)) \tag{8.5b}$$

ensures global asymptotic convergence of the distance $d(t) = \|\boldsymbol{x} - \boldsymbol{p}(t)\| \to d_r$ and velocity $\|\dot{\boldsymbol{p}}(t)\| \to \alpha_r$ if $(k_P, k, d_r, \alpha_r) \in \mathbb{R}^4_{>0}$, and if $d(t) \neq 0,\ \forall t \geq t_\circ$. □

This result is appealing and has seen significant popularity due to two main reasons. Firstly, it offers an extremely simple implementation. Secondly, while the proof is concluded with PE arguments and comes without a joint Lyapunov function in the tracking and observer errors, the time derivative of a quadratic function in the observer errors is negative semi-definite. Consequently, in the case of the quadrotor UAV or UGV systems, it is safe to update the target position estimate at all times, even during a lack of persistent excitation. For instance, if the system is standing still before initializing the tracking controller, the estimates may still be updated continuously during this time. This would generally not be the case if the target position is estimated with a nonlinear Kalman filter, which may cause the variance of the estimate to diverge during such a lack of excitation (depending on the estimation model).

However, the feedback in Theorem 8.1 is essentially a proportional controller, and there is no feedback in the velocity along $\bar{\boldsymbol{\phi}}$. Consequently, any stationary load disturbance on the control inputs will cause stationary tracking errors. As mentioned previously, such disturbances are expected to appear in practice due to modeling errors. This problem can be mitigated by carefully introducing integral action in the distance and velocity tracking errors. With this idea, a slight extension of Theorem 8.1 is given in Theorem 8.2 below.

THEOREM 8.2—PROPORTIONAL-INTEGRAL CIRCUMNAVIGATION CONTROL
The controller-observer combination

$$\dot{\boldsymbol{p}}(t) = (u_{\boldsymbol{\phi}}(t) + \delta_{\boldsymbol{\phi}})\boldsymbol{\phi}(t) + (u_{\bar{\boldsymbol{\phi}}}(t) + \delta_{\bar{\boldsymbol{\phi}}})\bar{\boldsymbol{\phi}}(t) \tag{8.6a}$$

$$u_{\boldsymbol{\phi}}(t) = k_I z_1(t) + k_P \hat{\Delta}(t) \tag{8.6b}$$

$$u_{\bar{\boldsymbol{\phi}}}(t) = \alpha_r - c_1 \tanh(c_2 z_2(t)/c_1) \tag{8.6c}$$

$$\dot{z}_1(t) = \hat{\Delta}(t) \tag{8.6d}$$

$$\dot{z}_2(t) = \alpha - \alpha_r \tag{8.6e}$$

$$\dot{\hat{\boldsymbol{x}}}(t) = k(\boldsymbol{I} - \boldsymbol{\phi}(t)\boldsymbol{\phi}(t)^\top)(\boldsymbol{p}(t) - \hat{\boldsymbol{x}}(t)), \tag{8.6f}$$

ensures global asymptotic convergence of $d(t) = \|\boldsymbol{x} - \boldsymbol{p}(t)\| \to d_r$ and $\|\dot{\boldsymbol{p}}(t)\| \to \alpha_r$, if $(c_1, c_2, k, k_I, k_P, d_r, \alpha_r) \in \mathbb{R}^6_{>0}$ and $|\delta_{\bar{\boldsymbol{\phi}}}| < c_3 = \min(\alpha_r - c_1, c_1)$, where $(\delta_\phi, \delta_{\bar{\phi}})$ are bounded and asymptotically stationary, if $d(t) \neq 0$ for all $t \geq t_\circ$.□

Proof. The full proof is given in [Greiff et al., 2021b], and is here summarized briefly. The main idea is to consider the control in the directions $\boldsymbol{\phi}$ and $\bar{\boldsymbol{\phi}}$ separately. By analysis of the latter, using the ideas on smooth saturation functions in Chapter 6 with the hyperbolic tangent function in Example 6.1, it can be shown that $\alpha > 0$, $\forall t \geq t_\circ$. This ensures that a PE condition analogous to the one presented in [Deghat et al., 2010, Lemma 1] is met, ensuring exponential convergence of the estimation error $\tilde{\boldsymbol{x}}(t) = \hat{\boldsymbol{x}}(t) - \boldsymbol{x}$ to the origin, with an associated Lyapunov function $\mathcal{V} = \frac{1}{2}\|\tilde{\boldsymbol{x}}\|^2$. As such, there

exists a positive $m > 0$ expressed in $\|\tilde{\boldsymbol{x}}(t_\circ)\|$, and a constant $\beta > 0$, such that

$$\|\tilde{\boldsymbol{x}}\| \leq m e^{-\beta(t-t_\circ)}, \tag{8.7}$$

implying that the distance estimate error is bounded in the initial errors, as

$$|\delta(t)| = |d(t) - \hat{d}(t)| \leq \|\hat{\boldsymbol{x}}(t) - \boldsymbol{x}(t)\| = \|\tilde{\boldsymbol{x}}(t)\| \leq \gamma. \tag{8.8}$$

Furthermore, by (8.8), we note that

$$I_\delta(t) \triangleq \int_{t_\circ}^{t} \delta(\sigma) d\sigma \leq \int_{t_\circ}^{t} |\delta(\sigma)| d\sigma \leq \int_{t_\circ}^{t} \|\tilde{\boldsymbol{x}}(\sigma)\| d\sigma = \frac{m}{\beta}(1 - e^{-\beta(t-t_\circ)}) \leq \frac{m}{\beta}, \tag{8.9}$$

for all $t \geq t_\circ$. By writing out the dynamics of the true distance $\Delta(t)$, and using that $\boldsymbol{p}(t) - \boldsymbol{x} = -d(t)\boldsymbol{\phi}(t)$, $\boldsymbol{\phi}^\top \boldsymbol{\phi} = 1$, and $\boldsymbol{\phi}^\top \bar{\boldsymbol{\phi}} = 0$ by Figure 8.1,

$$\dot{\Delta} = \frac{\dot{\boldsymbol{p}}(t)^\top (\boldsymbol{p}(t) - \boldsymbol{x})}{d(t)} = -k_I I_\Delta(t) - k_P \Delta(t) + k_I I_\delta(t) + k_P \delta(t) - \delta_\phi, \tag{8.10}$$

where $I_\Delta(t) \triangleq \int_{t_\circ}^{t} \Delta(\sigma) \mathrm{d}\sigma$. By defining $u(t) \triangleq k_I I_\delta(t) + k_P \delta(t) - \delta_\phi$, and letting $\boldsymbol{\xi}(t) = (I_\Delta(t);\ \Delta(t))$ we note that (8.10) can be written in the form

$$\dot{\boldsymbol{\xi}}(t) = \underbrace{\begin{bmatrix} 0 & 1 \\ -k_I & -k_P \end{bmatrix}}_{\triangleq \boldsymbol{A}} \boldsymbol{\xi}(t) + \underbrace{\begin{bmatrix} 0 \\ 1 \end{bmatrix}}_{\triangleq \boldsymbol{B}} \underbrace{(k_I I_\delta(t) + k_P \delta(t) - \delta_\phi)}_{\triangleq u}. \tag{8.11}$$

Here, $|u(t)| \leq k_I m/b + k_P \gamma + c_3 \ \forall t \geq t_\circ$ by (8.8) and (8.9), and u converges to a stationary point by (8.7) if δ_ϕ is asymptotically stationary. As $\boldsymbol{A}$ in (8.11) is Hurwitz for all $(k_I, k_P) \in \mathbb{R}^2_{>0}$, $\Delta(t) \to 0 \Rightarrow d(t) \to d_r$ as $(t - t_\circ) \to \infty$. □

However, it is clear that this only holds when $d(t) \neq 0$ for all $t \geq t_\circ$. Otherwise, the distance error dynamics in (8.10) become ill defined. This is part of the reason for seeking a sufficient condition for the collision avoidance detailed in Remark 8.1. Such a condition can be given as follows.

Proposition 8.1—[Greiff et al., 2021b, Proposition 2]
Let $M = k_I(m/\beta) + k_P(\gamma + |\Delta(t_\circ)|) + c_3$, where γ is given in (8.8), m and β in (8.9) and $|\delta_\phi| < c_3$ denotes the upper bound of the disturbance. Let $\mathcal{G}$ denote the impulse response of the system $G(s) = s(s^2 + k_P s + k_I)^{-1}$. For a single integrator in closed-loop feedback with Theorem 8.2, if $M\|\mathcal{G}\|_1 < 2d_r$ then $d(t) > 0$ for all $t \geq t_o$. Furthermore, if the distance controller is tuned such that the system matrix $\boldsymbol{A}$ in (8.11) is critically damped, with $k_I = K^2$ and $k_P = 2K$ for some $K > 0$, then $M/(Ke) < d_r \Rightarrow d(t) > 0$ for all $t > t_\circ$.□

Remark 8.3
The choice of k_P, k_I to make (8.11) critically damped is motivated by attempting to keep $\|\mathcal{G}\|_1$ as small as possible, thereby permitting larger M while satisfying the condition in Proposition 8.1. Indeed, for any second order system $P(s) = s(s^2 + 2\xi\omega_n s + \omega_n^2)^{-1}$, $\xi = 1$ minimizes $\|\mathcal{P}\|_1$ for any $\omega_n > 0$.□

Remark 8.4
The condition for collision avoidance in Proposition 8.1 is reminiscent of that given in [Deghat et al., 2010, Lemma 1], which in this notation can be written $\gamma < d_r$. While the former is more restrictive, it is still quite insightful. If we seek to ensure collision avoidance when using the controller in Theorem 8.2, then we could (i) decrease the initial estimation error in (8.8) determining γ, (ii) increase the convergence rate of the observer in (8.8) by increasing k, (iii) reduce the upper bound on the load disturbances in the $\boldsymbol{\phi}$-direction, or (iv) decrease K in the distance controller provided $c_3 \ll (m/\beta)$ or increasing it if $c_3 \gg (m/\beta)$. However, we will always have a term $2K(\gamma + |\Delta(t_\circ)|)$ in M. Consequently, any guarantees for collision avoidance by Proposition 8.1 largely depend on the initial distance errors in (8.8). □

Remark 8.5
In practice, if the initial estimate error is large in relation to d_r, then it may be advantageous to disable the integral action initially, actuating the system with Theorem 8.1. When enough time has passed, and the estimate error $\|\tilde{\boldsymbol{x}}\|$ has become sufficiently small, such that collision avoidance can be ensured by Proposition 8.1, the controller in Theorem 8.2 may be switched on. □

An advantage with the control system for circumnavigation proposed in Theorem 8.2 is that it attenuates stationary tracking errors that can arise from non-perfect actuation. Consequently, while the theory assumes that the process can follow a desired velocity perfectly, deviations from this perfect actuation can typically be modeled as input disturbances. As long as these errors are sufficiently small and approximately constant in the body frame in stationarity, we should expect the integral states to converge to a nonzero value, and a vanishing tracking error in the distance and forward velocity.

Example 8.1
To illustrate and contrast the two theorems, and to highlight the practical utility of Theorem 8.2, an example is given with a fixed-wing UAV where two significant load disturbances are applied in the bearing- and orthogonal bearing directions, respectively. The UAV is controlled from a random initial location $\boldsymbol{p}(t_\circ) \sim \mathcal{U}([100, 200]^2)$ with a significant random initial target estimate error $\tilde{\boldsymbol{x}}(t_\circ) = \hat{\boldsymbol{x}}(t_\circ) - \boldsymbol{x} \sim \mathcal{U}([100, 200]^2)$, differing from the target position at $\boldsymbol{x} = \mathbf{0}$ by hundreds of meters. The tuning of the controller and observer is chosen as

$$k = 0.2, \quad \alpha_r = 15, \quad d_r = 100, \quad k_P = 1.5, \quad k_I = \frac{k_P^2}{4}, \quad c_1 = 10, \quad c_2 = 0.1.$$

This defines a circular target trajectory a distance $d_r = 100$ [m] from the initially unknown position of the target, which is to be traversed at a velocity of $\alpha_r = 15$ [m/s]. The controller is chosen to be critically damped in $\boldsymbol{\phi}$-direction, as motivated by Remark 8.3. Note that with the choice of $c_1 = 10$, we can guarantee that any load disturbance $|\delta_{\bar{\boldsymbol{\phi}}}| < \alpha_r - c_1 = 5$ ensures that $\alpha(t) > 0$ for all $t \geq t_\circ$. To illustrate the implications of introducing the integral action, the disturbances are defined with the Heaviside step function Θ, as

$$\delta_{\boldsymbol{\phi}}(t) = -20 + 40\Theta(t - 100), \qquad \delta_{\bar{\boldsymbol{\phi}}}(t) = 2 - 5\Theta(t - 200) \tag{8.12}$$

The system responses with Theorem 8.1 and Theorem 8.2, respectively, are shown in Figure 8.4, and clearly demonstrates the differences between the two feedback laws. With the applied disturbances, Theorem 8.1 yields stationary tracking errors, while the accumulation of errors in the integral states, $\boldsymbol{z}(t)$, result in the tracking error approaching zero when applying Theorem 8.2. Note that in neither case, the sufficient conditions for collision avoidance are satisfied. In practice the initial estimate error would be initialized using heuristics, such that the condition for collision avoidance $\gamma < d_r$ defined in [Deghat et al., 2010, Lemma 1] associated with Theorem 8.1 is satisfied. If so, the controller can be implemented as per Remark 8.5, switching on the integral states once the estimation errors have become sufficiently small. It is noteworthy that the closed-loop system here exhibits collision-free tracking despite the sufficient conditions for collision avoidance being violated. □

8.4 Experimental Results

To illustrate Theorem 8.2 in a more realistic setting, incorporating naturally arising noise, measurement outliers, unmodeled dynamics, and artifacts from the numerical discretization, a real-time example is given with an F1/10 UGV [O'Kelly et al., 2019] retrofitted with a u-blox GNSS receiver [Liu and Li, 2017] (see Figure 8.3). The car is differentially driven, and actuated by low-level Vedder's Electronic Speed Controller (VESC) developed in [Vedder, 2021], as wrapped in the PYVESC module [Bindle, 2021]. The two control signals that are used to interface with the system are here denoted by $c_v \in \mathbb{R}_{>0}$ [m/s], which relates to the velocity of the vehicle, v [m/s], and $c_\rho \in \mathbb{R}_{>0}$ [·], which relates to the car's steering angle, ρ [rad]. When thinking about the system, we consider it modeled as a unicycle actuated by a v and a rate ω [rad/s], driving the position $\boldsymbol{p} = (p_1;\, p_2)$ [m] and an attitude η [rad] through

$$\dot{p}_1 = \cos(\eta)v, \tag{8.13a}$$
$$\dot{p}_2 = \sin(\eta)v, \tag{8.13b}$$
$$\dot{\eta} = \omega. \tag{8.13c}$$

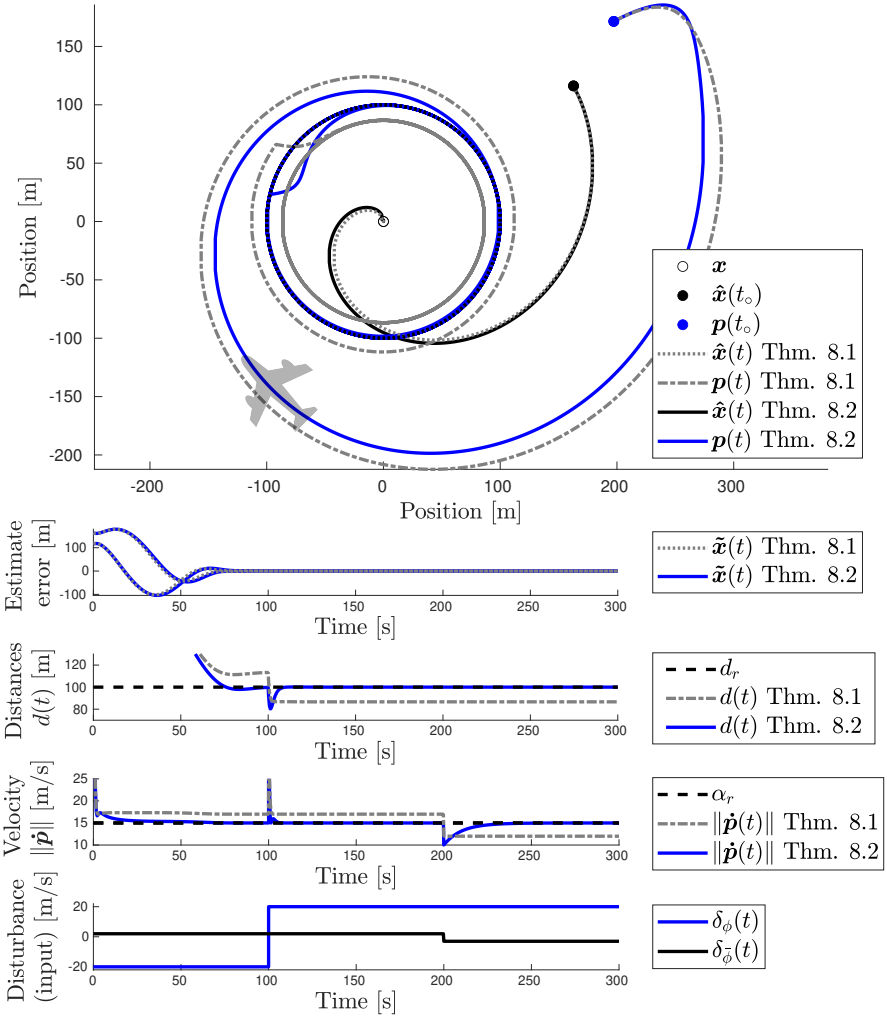

Figure 8.2 Example simulation of the circumnavigation and target tracking controllers in Theorem 8.1 (gray) and Theorem 8.2 (blue) for a fixed-wing UAV scenario. *Top:* Position of the UAV in relation to the target at the origin, with the target position estimate trajectories converging to the origin. *Top, center:* Target position estimate trajectories. *Center:* Distance reference (black dashed) and true distance to the target $d(t)$ when using Theorem 8.1 (gray) and Theorem 8.2 (blue). *Bottom, center:* Velocity reference (black dashed) and true velocity to the using Theorem 8.1 (gray) and Theorem 8.2 (blue). *Bottom:* Applied load disturbances. The system response with Theorem 8.1 is shown in the video chapter-8-circumnav.mp4.

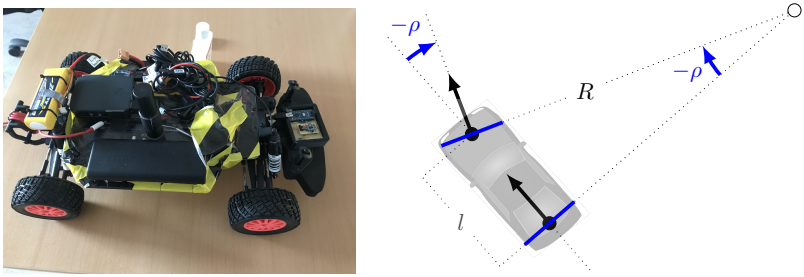

Figure 8.3 *Left:* Depiction of the car used in the experiments. *Right:* Illustration of the car geometry with steering angle ρ and turn radius R.

With knowledge of the vehicle length $l = 0.34$ [m], the relationship between car velocity, v, and commanded velocity, c_v, was determined to be $v \approx c_v$ [m/s] by a simple experiment. Similarly, the relationship between the car steering angle, ρ, and the commanded angle, c_ρ, was found to be linear, with

$$\rho \approx g(c_\rho) = ac_\rho + b, \tag{8.14}$$

with $a = -0.8667$ and $b = 0.4698$. From the geometry in Figure 8.3, the turn radius of the car is given by $R = l/\sin(\rho)$ and the turning rate with respect to the global reference frame is then given by

$$\omega = \frac{v}{R} = \frac{v}{l}\sin(\rho) = \frac{v}{l}\sin(g(c_\rho)), \tag{8.15}$$

relating the signals (c_v, c_ρ) to the unicycle inputs (v, ω).

8.4.1 Actuation

To actuate the car along the desired reference velocity $\boldsymbol{v}_r(t)$ expressed in the body-frame of the vehicle, we assume knowledge of the velocities of the UGV in the body frame in $\boldsymbol{v}(t)$, and construct an approximate attitude error by

$$\eta - \eta_r = \eta_e \approx \text{sign}(v_{1,r}v_2 - v_{2,r}v_1)\arccos\left(\frac{\boldsymbol{v}_r \cdot \boldsymbol{v}}{\|\boldsymbol{v}_r\|\|\boldsymbol{v}\|}\right). \tag{8.16}$$

Consider a feedback law in the control signals (c_v, c_ρ), as

$$c_v = \|\boldsymbol{v}_r\|, \qquad c_\rho = g^{-1}(-\eta_e/\|\boldsymbol{v}_r\|). \tag{8.17}$$

With this feedback, $\|\dot{\boldsymbol{p}}\| = \|\boldsymbol{v}_r\|(\cos^2(\eta) + \sin^2(\eta)) = \|\boldsymbol{v}_r\|$ at all times, and

$$\dot{\eta}_e = \dot{\eta} - \dot{\eta}_r = \omega - \omega_r = -\frac{\|\boldsymbol{v}_r\|}{l}\sin\left(\frac{\eta_e}{\|\boldsymbol{v}_r\|}\right) - \omega_r \approx -\frac{1}{l}\eta_e - \omega_r, \tag{8.18}$$

for small η_e. Here, the feedback is purposely designed to yield error dynamics that are locally exponentially stable when $\omega_r = 0$, with a decay rate characterized by l^{-1}, but where any sufficiently small non-zero ω_r results in bounded tracking errors in η_e. Furthermore, if ω_r is stationary, η_e converges to some stationary value, implying a constant attitude tracking error in the body frame of the vehicle. These are precisely the kinds of errors against which the closed-loop control system in Theorem 8.2 is designed to be robust.

Remark 8.6
More refined low-level control strategies are possible, which permit a cascade analysis. However, this lower-level velocity controller in (8.18) is specifically designed to demonstrate how the integral action in Theorem 8.2 can compensate for asymptotically stationary errors in modeling and actuation. Furthermore, we will employ nonlinear Gaussian filtering for the outlier rejection, and as such, no cascade analysis is undertaken for this chapter. □

8.4.2 State Estimation

As the car is modeled as a unicycle, and the relationships between (c_v, c_ρ) and (v, ω) are known, we consider a simple estimation model in the form

$$\dot{p}_1 = \cos(\eta)(v + \mathrm{d}\beta_1^1), \tag{8.19a}$$
$$\dot{p}_2 = \sin(\eta)(v + \mathrm{d}\beta_1^2), \tag{8.19b}$$
$$\dot{\eta} = \omega + \mathrm{d}\beta_2(t), \tag{8.19c}$$

where $\mathrm{d}\beta_i^j(t)$ denote colored Wiener processes, with $\mathrm{d}\beta_i^j(t_k) - \mathrm{d}\beta_i^j(t_{k-1}) \sim \mathcal{N}(0, h_k q_i)$, $q_i > 0$, and $t_k = t_\circ + \sum_{i=0}^{k} h_k$ with $h_k > 0$. Define the state vector $\bar{\boldsymbol{x}} \triangleq (p_1;\ p_2;\ \eta) \in \mathbb{R}^3$ and the control signal vector $\bar{\boldsymbol{u}} \triangleq (v\ ;\ \omega) \in \mathbb{R}^2$. The system in (8.19) is discretized using a zero-order hold assumption, as

$$\bar{\boldsymbol{x}}_{k+1} = \boldsymbol{f}(\bar{\boldsymbol{x}}_k, \bar{\boldsymbol{u}}_k) + \boldsymbol{q}_k, \qquad \boldsymbol{q}_k \sim \mathcal{N}(\boldsymbol{0}, \boldsymbol{Q}_k), \tag{8.20a}$$
$$\boldsymbol{y}_k = \boldsymbol{C}\bar{\boldsymbol{x}}_k + \boldsymbol{r}_k, \qquad \boldsymbol{r}_k \sim \mathcal{N}(\boldsymbol{0}, \boldsymbol{R}_k), \tag{8.20b}$$

where the noise is assumed to be independent and identically distributed,

$$\boldsymbol{f}(\bar{\boldsymbol{x}}_k, \bar{\boldsymbol{u}}_k) = \begin{bmatrix} p_{1,k} + h_k v_k \cos(\eta_k) \\ p_{2,k} + h_k v_k \sin(\eta_k) \\ \eta_k + h_k \omega_k \end{bmatrix}, \quad \boldsymbol{Q}_k \succ \boldsymbol{0}, \quad \boldsymbol{C} = \begin{bmatrix} 1 & 0 & 0 \\ 0 & 1 & 0 \end{bmatrix}, \quad \boldsymbol{R}_k = \sigma_p^2 \boldsymbol{I},$$

with the symmetric and positive definite process noise covariance given by

$$[\boldsymbol{Q}_k]_{11} = h_k q_1 + \tfrac{1}{3}(h_k^3 q_2 v_k^2 \sin^2(\eta_k)), \quad [\boldsymbol{Q}_k]_{12} = -\tfrac{1}{6}(h_k^3 q_2 v_k^2 \sin(2\eta_k)),$$
$$[\boldsymbol{Q}_k]_{13} = -\tfrac{1}{2}(h_k^2 q_2 v_k \sin(\eta_k)), \quad [\boldsymbol{Q}_k]_{22} = h_k q_1 + \tfrac{1}{3}(h_k^3 q_2 v_k^2 \cos(\eta_k)^2),$$
$$[\boldsymbol{Q}_k]_{23} = \tfrac{1}{2}(h_k^2 q_2 v_k \cos(\eta_k)), \quad [\boldsymbol{Q}_k]_{33} = h_k q_2.$$

In the filter implementation, the positional measurements for the circumnavigation controller are sampled at a uniform rate of 20 [Hz] from the filter prediction, and the measurements are included asynchronously and as soon as they arrive. If a measurement is zero (which is how outliers are represented in the GNSS module), or the expected filter measurement prediction error exceeds a threshold $\|\boldsymbol{y}_k - \boldsymbol{C}(\boldsymbol{f}(\hat{\bar{\boldsymbol{x}}}_{k-1}, \bar{\boldsymbol{u}}_{k-1}))\| > 100$ [m], the measurement $\boldsymbol{y}_k$ is discarded. The signals $\bar{\boldsymbol{u}}_k$ are computed from the applied controls (c_v, c_ρ) through the inverse kinematics. In this example, a simple Gaussian filter is used, here implemented with first-order moment approximations, resulting in a continuous-discrete EKF (see, e.g., [Axelsson and Gustafsson, 2014]).

8.4.3 Circumnavigation

In this circumnavigation experiment, the car is initialized with the actuation turned off, and the GNSS measurements are accumulated over a short amount of time to fix the EN coordinate frame. After the EN frame has been established, the EKF is initialized at a time $t_\circ = 0$, and permitted to converge over 10 [s]. It is slightly dangerous to have the EKF run for too long without movement, as the η-state is not observable in the GNSS measurements when the car is standing still. An advantage of estimating the angle η in the EKF is that this simplifies the experiments significantly, as they can be done with a known bearing direction to a virtual target. In this experiment, the target position $\boldsymbol{x}$ is randomized at a known location in the EN frame, and the bearing direction is computed and rotated into the body frame of the UGV using η from the filtering posterior. In different applications, such a direction in the body frame can be sensed by any of a multitude of sensors. As such, this example should not bee seen as an end application, but rather a validation that the ideas in Theorem 8.2 work as expected when run with realistic modeling errors, disturbances, and noises.

During the time $t \in [0, 10]$, the integral action in the controller is switched off, but the target position estimate is continuously updated, converging to a stationary point on a line connecting $\boldsymbol{x}$ and $\boldsymbol{p}_\circ$. As $(\mathrm{d}/\mathrm{d}t)\|\tilde{\boldsymbol{x}}(t)\|^2 \leq 0$ for all $t \geq t_\circ$, the target estimate error is expected to decrease to a stationary non-zero value due to the lack of persistent excitation when the car is standing still. At $t = 10$ [s], the actuation is promptly switched on, and the integral states are permitted to build up. After this point, the car converges to a near zero tracking error with respect to the desired motion (see Figure 8.4).

As $t > 10$ and increases, we note that the target estimate converges to a point close to the true target position. Indeed, the estimation error is approximately $\|\tilde{\boldsymbol{x}}\| \approx 10^{-2}$ [m] in stationarity, an error which can be attributed to the discretization of the estimator dynamics and noise in the system. We also observe that the car converges to the desired circular trajectory (here only the signals related to d_r are visualized). This despite the ω_r-term in (8.18)

being non-zero at all times, and the UGV system in feedback with the velocity controller in (8.17) being expected to yield stationary tracking errors when asymptotically $\omega_r \neq 0$. The reason for the visibly good trajectory tracking in the top-most subplot is found in the bottom-most subplot, where the integral state $z_1(t)$ related to $\Delta(t)$ converges to a non-zero value, effectively compensating for the input disturbance caused by the actuation errors.

This real-time example demonstrates the practical utility of introducing integral action in the circumnavigation controller in Theorem 8.1, as described in Theorem 8.2. It is clearly a valuable and feasible option for real-time implementations, and often necessary in order to achieve small tracking errors. We recommend its use in circumnavigation and target tracking problems for UAVs and UGVs implementing Theorem 8.1. The Python code used in the experiments as well as experiment logs are available in [Greiff, 2021].

8.5 Summary

In this chapter, a control system for circumnavigation is developed in Theorem 8.2, which solves the problem posed in Problem 8.1, and introduces integral action in the tracking errors. This solution imposes more restrictive sufficient conditions for collision avoidance than the related solution in Theorem 8.1. However, the proposed control system has the benefit of attenuating input disturbances in the body frame, provided that these are sufficiently small and asymptotically constant. This is clearly demonstrated with the fixed-wing UAV simulation in Example 8.1. Such load disturbances are often found in practice due to non-perfect actuation, as demonstrated in the real-time experiment with the differentially driven UGV in Sec. 8.4.

In the proposed solution, a feedback in the orthogonal bearing direction can only be introduced if the resulting velocities $\alpha(t)$ are bounded away from the origin at all times. To do this, the smooth saturation functions introduced in Chapter 6 are instrumental. These saturation functions can be used for a much wider variety of problems, not necessarily related to UAV control. Furthermore, the real-time example demonstrates the usefulness of bounding the system errors in time. In this particular case, it implies that the true target position is within a circle that shrinks in time. Thus, it is safe to update the target estimate even when the UGV stands still.

In conclusion, based on the promising demonstrations of the control system with the UGV, we propose the control system with integral action to be tested and evaluated for fixed-wing UAVs and boats in autonomous search and rescue missions. Such applications will introduce additional disturbances, and it is therefore interesting to investigate how a fixed-wing UAV in various wind conditions performs with the controllers in Theorem 8.1 and 8.2, respectively.

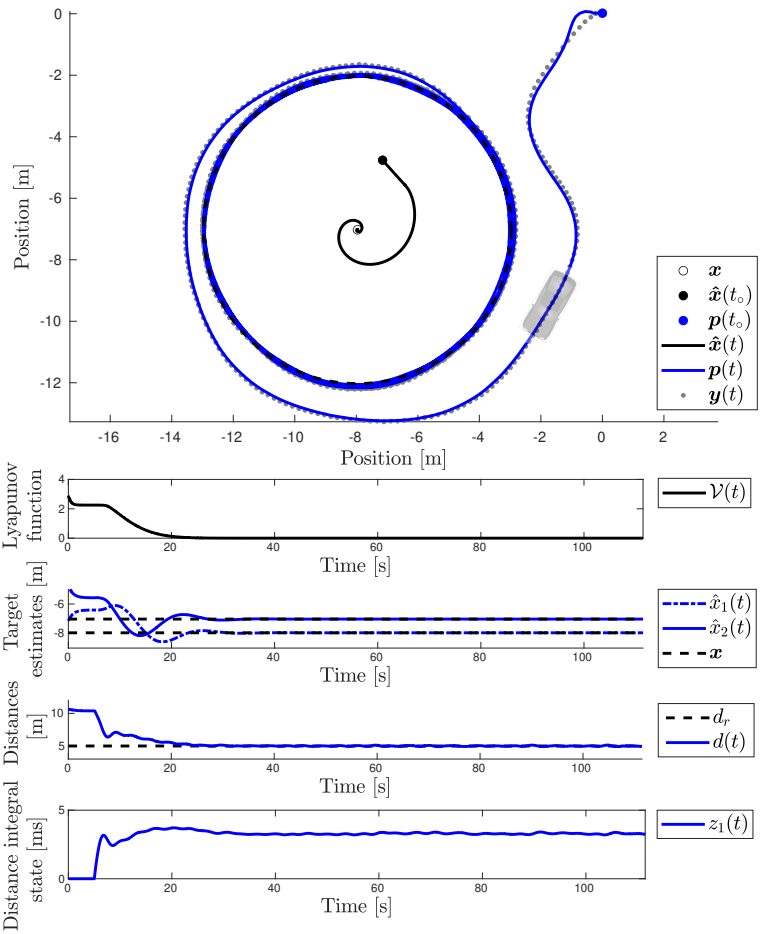

Figure 8.4 *Experimental results* when driving the UGV autonomously using the simple controller in (8.17) with the output feedback controller proposed in Theorem 8.2. *Top:* Two-dimensional position of the UGV, starting at the origin of the EN frame, with the target position estimate trajectories converging to the target position. The raw sampled GPS measurements are shown as gray dots. Lyapunov function $\mathcal{V} = \frac{1}{2}\|\tilde{\boldsymbol{x}}\|$ associated with the target estimation. *Center:* Target position estimate trajectories. *Bottom, center:* Distance reference d_r (black) and system response d (blue). *Bottom:* The integral state associated with the distance in the ϕ-direction. The experiment and system response is shown in the video chapter-8-circumnav.mp4.

9

Radiation Mapping

9.1 Introduction

A quadrotor UAV equipped with a good and robust control system is an incredibly useful tool that can find myriad applications in modern society. In particular, it can be used for short surveying missions and remote sensing, to collect data that are otherwise inaccessible for ground-based vehicles or human-operated sensors. An example is the measurement of radiation intensity at sites that are potentially hazardous to humans. Instead of walking with a sensor in a backpack through the terrain, it can be carried by a large UAV to quickly and efficiently survey the environment. In this chapter, we assume that such a UAV is controlled by a solution similar to those presented in Chapters 4 and 6, and proceed to consider the problem of mobile gamma spectroscopy (see Figure 9.1), inferring the parameters of a modeled radiation intensity function along a known surface from measurements taken by a UAV.

A popular approach for remote sensing and surveying with UAVs is to pose a joint estimation and path planning problem, planning the motion of the sensor to yield the most informative measurements [Hitz et al., 2017; Popović et al., 2020]. Such informative path planning (IPP) solutions typically rely on Gaussian Process (GP) regression or Kalman filtering, due to their favorable computational properties and the need for the algorithm to be run in real-time. An alternative approach is to consider a slightly more refined estimation model, incorporating known geometries, more complex measurement models, and non-Gaussian noise statistics. The estimation problem is then solved offline, increasing the computational resources afforded to the estimator.

As the measurements taken by the detector are Poisson distributed, it is natural to consider maximum-likelihood approaches with a Poisson likelihood. Such methods have been studied rigorously in the related field of gamma tomography, dating back to the early work in [Shepp and Vardi, 1982; Miller et al., 1985]. In any implementation, it is common to discretize the domain of the intensity function, here denoted as Ω, estimating an intensity per pixel or voxel (see left-most subplot in Figure 9.2). Such modeling assumptions naturally

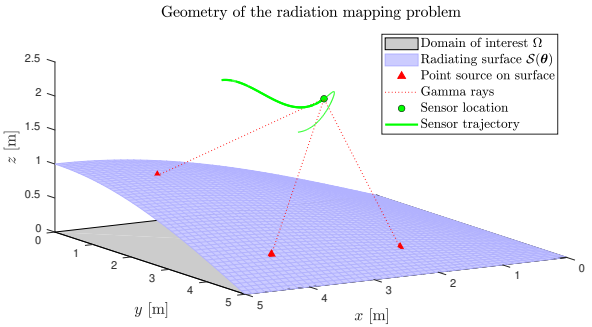

Figure 9.1 The geometry of the mobile radiation mapping problem.

carry over to the more recent algorithms designed specifically for gamma spectroscopy from UAVs. One such example is the Adaptively Reevaluated Bayesian Localization (ARBL) algorithm, presented in [Miller et al., 2015], which, for computational efficiency, approximates the measurement likelihood as being Gaussian. Another example is the work in [Joshi et al., 2017], where an intensity function is estimated using directional measurements, similarly discretizing the domain Ω and considering a finite set of point sources.

There are two potential problems with such approaches. Firstly, they generally introduce a large number of estimation variables. As such, if the sensor is flown along a trajectory, the resulting model may be able to predict the intensity measurements very well along this trajectory, but results may be poor when moving further away from the traveled path. If the resolution of the pixels is chosen too fine, the algorithm will tend to over-fit the data, often with a poor reconstruction of the underlying intensity function as a result. Secondly, the hyper-parameters of the estimation model, here the number of pixels, their size, and their location, are user-defined and fixed.

Both of these problems are addressed by the promising Additive Point Source Localization (APSL) algorithm in [Hellfeld et al., 2019; Vavrek et al., 2020], which closely resembles the approach in [Joshi et al., 2017] in its discrete form. However, in [Hellfeld et al., 2019], the APSL algorithm is also formulated in a continuous setting, in the sense that it not only estimates the intensity of the sources but also their spatial location and the cardinality of the set of point sources (see center subplot in Figure 9.2). This gives the estimation model significant flexibility, reducing the algorithm's propensity to overfit by minimizing a negative log-likelihood as well as the number of estimation variables with respect to a Bayesian Information Criterion (BIC). This is done in a maximum likelihood expectation-maximization algorithm (ML-EM) [Dempster et al., 1977] over the intensity of the point sources, combined with hyper-parameter optimization over their locations.

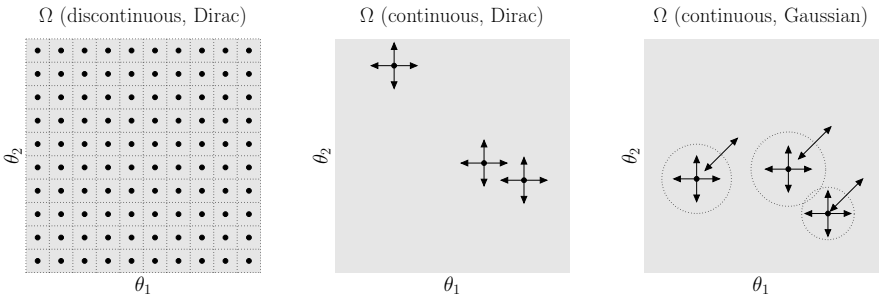

Figure 9.2 Illustration of a rectangular domain $\Omega \subset \mathbb{R}^2$. *Left*: Basis functions (Dirac) are fixed in the center of pixels, effectively discretizing Ω. *Center*: A much smaller number of basis functions (Dirac), here permitted to vary over Ω with two-degrees of freedom each. *Right*: A much smaller number of basis functions (Gaussian), where the kernel center is permitted to vary over Ω with an additional degree of freedom in its variance.

9.1.1 Chapter Motivation and Contributions

In the context of radiation mapping with mobile detectors, the computational complexity of the ML and ML-EM methods primarily depends on the number of observables (implicitly the coarseness of the discretization of the domain parameterizing the intensity function) and the number of measurements included. The continuous APSL enjoys a clear advantage over other candidate methods, typically requiring fewer estimation parameters if the intensity is well described by a small number of point sources. However, in many practical surveying applications, this assumption is no longer valid. For instance, if considering a meadow or roof that has been exposed to radioactive fallout, it is highly unlikely that the intensity function over this surface will be well described by a small number of point sources. In such scenarios, the original APSL requires modifications to facilitate estimation over a richer class of intensity functions. For this purpose, an extension of the APSL was proposed in [Greiff et al., 2021d]. The resulting generalized APSL (GAPSL) models the intensity function as a sum of weighted homogeneous Gaussian kernels and permits their width, weights, and location to vary, as well as the number of kernels entertained in the estimation model (see right-most subplot in Figure 9.2). In this extension, prior knowledge of the radiating surface geometry is included. In addition, the method addresses the problem of varying background intensity (highlighted in [Vavrek et al., 2020]).

9.1.2 Overview

In this chapter, we start by giving the necessary mathematical preliminaries specific to radiation mapping in Sec. 9.2. We then proceed to discuss the

modeling and its relation to prior work in Sec. 9.3. The GAPSL is then presented in Sec. 9.4, including a description of the ML-EM framework, the alternating optimization approach, and how it can be combined with model selection theory, here adapted to the case of Gaussian kernels. The algorithm is subsequently demonstrated in a simulation setup in Sec. 9.5 to show when and how it should be used, followed by an experimental verification in Sec. 9.6. The summary in Sec. 9.7 concludes the chapter, highlighting the utility of good UAV control and how it can solve problems in modern society.

9.2 Preliminaries

Throughout this chapter, take $\mathcal{P}(x|\lambda) = e^{-\lambda}\lambda^x/x!$ to denote a Poisson probability density function (PDF) with mean and variance λ, and support on the natural numbers $x \in \mathbb{N}_0$. Let $\mathcal{P}(\boldsymbol{x}|\boldsymbol{\lambda}) = \prod_{i=1}^{n} \mathcal{P}(x_i|\lambda_i)$ define a multivariate Poisson PDF. As in the previous chapters, let $\mathcal{N}(\boldsymbol{x}|\boldsymbol{\mu}, \boldsymbol{\Sigma})$ be a multivariate Gaussian PDF, with mean $\boldsymbol{\mu} \in \mathbb{R}^n$ and covariance $\boldsymbol{\Sigma} \in \mathbb{R}^{n\times n}$, and take $\mathrm{KL}(p\|q)$ to denote the Kullback-Leibler divergence of two PDFs, p and q, respectively (see, e.g., [Murphy, 2012]). In the following, we let $\circ$ and $\oslash$ denote element-wise multiplication and division, respectively. For future reference and to simplify the reading, the key variables particular to this chapter are summarized in Table 9.1, and will be defined in the forthcoming sections.

Notation	Description
$\Omega \subset \mathbb{R}^2$	Domain of interest
$\boldsymbol{\theta} \in \Omega$	Point on the domain Ω
$\mathcal{S} \ : \ \Omega \mapsto \mathbb{R}^3$	Known radiating surface geometry
$I \ : \ \Omega \mapsto \mathbb{R}_{\geq 0}$	Intensity moment function
$n \in \mathbb{N}$ $(n \gg 0)$	Number of measurements
$\boldsymbol{Y} \in \mathbb{N}_0^n$	Sampled measurements
$m \in \mathbb{N}$ $(m > 0)$	Number of kernels in model
$k_j \ : \ \Omega \mapsto \mathbb{R}$	Kernels approximating I
$\boldsymbol{\eta}_j \in D_{\eta,j}$	Hyper-parameters of k_j
$w_j \in \mathbb{R}_{>0}$	Weight associated with k_j
$\boldsymbol{S}_j = \{w_j, \boldsymbol{\eta}_j\}$	Solution associated with k_j
$\boldsymbol{\Xi} = \{\boldsymbol{\eta}_j\}_{j=1}^m$	Hyper-parameters of the model
$\boldsymbol{w} = (w_1;\ ...;\ w_m)$	Weights of model
$\boldsymbol{S} = \{\boldsymbol{S}_j\}_{j=1}^m$	Set of solutions

Table 9.1 Description of key parameters and variables. Depending on the considered kernel, $D_{\eta,j} = \mathbb{R}_{>0}$ or $D_{\eta,j} = \mathbb{R}_{>0} \times \Omega$ or $D_{\eta,j} = \Omega$.

9.3 Modeling and Relation to Prior Work

In the following, we consider a two-dimensional domain $\Omega \subseteq \mathbb{R}^2$, and let $\boldsymbol{\theta} \in \Omega$, which parameterizes a three-dimensional continuous surface $\mathcal{S} : \Omega \to \mathbb{R}^3$. This general modeling approach facilitates the estimation of intensity functions over silos, roofs of buildings, or lake sides. Consider a detector that resides at a point $\mathbf{p}^d \in \mathbb{R}^3$ with a rotation matrix given by $\boldsymbol{R}^d \in \mathrm{SO}(3)$, and a point source at $\boldsymbol{p}^s = \mathcal{S}(\boldsymbol{\theta}) \in \mathbb{R}^3$. The detector sensitivity is a function of its effective surface area, $A(\boldsymbol{p}^s, \boldsymbol{p}^d, \boldsymbol{R}^d)$, and the distance from the detector to the radiating point. The function A can be viewed as a calibration function, computed for specific detectors though a set of experiments in a lab environment, here omitted for brevity. Following [Tsoulfanidis, 1995, Chapter 8.2], we model the *solid-angle* for a point isotropic source and a detector with a circular aperture with radius R. Under the assumption that $R \ll \|\mathcal{S}(\boldsymbol{\theta}) - \boldsymbol{p}^d\|^2$, we let

$$v_s(\mathcal{S}(\boldsymbol{\theta}), \boldsymbol{p}^d, \boldsymbol{R}^d) \triangleq \frac{A(\mathcal{S}(\boldsymbol{\theta}), \boldsymbol{p}^d, \boldsymbol{R}^d)}{4\pi \|\mathcal{S}(\boldsymbol{\theta}) - \boldsymbol{p}^d\|^2}. \tag{9.1}$$

This function is an approximation of the fraction of radiated particles from a point source at any $\mathcal{S}(\boldsymbol{\theta})$ that are seen in the detector. If a specific point $\mathcal{S}(\boldsymbol{\theta}_s)$ radiates with $I(\boldsymbol{\theta}_s)$ [Bq], measured over t_i [s] , with the detector at $\boldsymbol{p}_i^d$ with an orientation $\boldsymbol{R}_i^d$, we should expect to see $I(\boldsymbol{\theta}_s) v_s(\mathcal{S}(\boldsymbol{\theta}_s), \boldsymbol{p}_i^d, \boldsymbol{R}_i^d) t_i$ events in the detector from this source. However, we may also parameterize this intensity function over larger portions of Ω. Consider an approximation of expected intensity by a sum of weighted basis functions, with

$$I(\boldsymbol{\theta}) = \sum_{j=1}^{m} w_j k_j(\boldsymbol{\theta}; \boldsymbol{\eta}_j). \tag{9.2}$$

Here, $\boldsymbol{\eta}_j$ denotes a set of free hyper-parameters associated with this basis function or kernel k_j. This could for instance be a point defined by a Dirac delta located at $\boldsymbol{\theta}_j \in \Omega$, as $k_j(\boldsymbol{\theta}) = \delta(\boldsymbol{\theta} - \boldsymbol{\theta}_j)$. If the location $\boldsymbol{\theta}_j \in \Omega$ is fixed, then $\boldsymbol{\eta}_j = \varnothing$, but if it is free and to be estimated, then $\boldsymbol{\eta}_j = \boldsymbol{\theta}_j$. This formulation also permits the use of a general Gaussian kernel

$$k_j(\boldsymbol{\theta}; \boldsymbol{\eta}_j) = \mathcal{N}(\boldsymbol{\theta} | \boldsymbol{\theta}_j, \sigma_j^2 \boldsymbol{I}_2). \tag{9.3}$$

Here, $\boldsymbol{\eta}_j = \varnothing$ if all parameters are fixed, but it can also take the form $\boldsymbol{\eta}_j = \boldsymbol{\theta}_j \in \Omega$ if the kernel centers are permitted to vary. It can also be defined by $\boldsymbol{\eta}_j = \sigma_j \in \mathbb{R}_{>0}$ if only the variance of the kernel function is to be estimated, or $\boldsymbol{\eta}_j = (\boldsymbol{\theta}_j, \sigma_j) \in \Omega \times \mathbb{R}_{>0}$ if both the kernel centers and the variances are permitted to vary. Let $\boldsymbol{S}_j = \{w_j, \boldsymbol{\eta}_j\}$ be the set of weight and free hyper-parameters, define a solution as $\boldsymbol{S} = \{\boldsymbol{S}_j\}_{j=1}^m$, and let $\boldsymbol{\Xi} = \{\boldsymbol{\eta}_1, ..., \boldsymbol{\eta}_m\}$ denote the set of all free hyper-parameters.

With the intensity moment function approximated as in (9.2), the measurements registered by the detector over a time-interval t_i [s] is modeled by

$$Y_i \sim \mathcal{P}\Big(y_i \Big| \int_\Omega t_i v_s(\mathcal{S}(\boldsymbol{\theta}), \boldsymbol{p}_i^d, \boldsymbol{R}_i^d) I(\boldsymbol{\theta}) \mathrm{d}\boldsymbol{\theta}\Big) \tag{9.4a}$$

$$= \mathcal{P}\Big(y_i \Big| \sum_{j=1}^m w_j t_i \int_\Omega v_s(\mathcal{S}(\boldsymbol{\theta}), \boldsymbol{p}_i^d, \boldsymbol{R}_i^d) k_j(\boldsymbol{\theta}; \boldsymbol{\eta}_j) \mathrm{d}\boldsymbol{\theta}\Big) \tag{9.4b}$$

$$= \mathcal{P}\Big(y_i \Big| \sum_{j=1}^m C_{ij}(\boldsymbol{\eta}_j) w_j\Big), \tag{9.4c}$$

with an expected intensity that is linear in the weights characterizing (9.2), and the contribution from each kernel k_j at each time t_i is defined by

$$C_{ij}(\boldsymbol{\eta}_j) = t_i \int_\Omega v_s(\mathcal{S}(\boldsymbol{\theta}), \boldsymbol{p}_i^d, \boldsymbol{R}_i^d) k_j(\boldsymbol{\theta}; \boldsymbol{\eta}_j) \mathrm{d}\boldsymbol{\theta}. \tag{9.5}$$

In the following, we let $\boldsymbol{C}(\boldsymbol{\Xi})$ denote a large matrix, where the entry in the i^{th} row and j^{th} column is given by the expression $C_{ij}(\boldsymbol{\eta}_j)$ in (9.5). When changing the cardinality of the solution set $\boldsymbol{S}$, the number of rows of $\boldsymbol{C}(\boldsymbol{\Xi})$ will remain constant, while the number of columns may vary as $\boldsymbol{S}$ changes.

9.3.1 Finite and Infinite Intensity Domains

An objection to the use of kernels other than the point-mass function is the need to compute the integral in (9.5) for each kernel and measurement when evaluating the measurement model. This is particularly problematic if the integration domain is finite, but simplifies significantly for infinite domains. In this case, we may apply the Gauss Hermite cubature in [Särkkä, 2013] or the spherical cubature rules in [Arasaratnam and Haykin, 2009]. For (9.5), letting $g_j(\boldsymbol{\theta}) \triangleq v_s(\mathcal{S}(\boldsymbol{\theta}), \boldsymbol{p}_i^d, \boldsymbol{R}_i^d)$ and $\bar{\boldsymbol{\theta}} = (\boldsymbol{\theta} - \boldsymbol{\theta}_j)/\sigma_j \in \mathbb{R}^2$,

$$C_{ij}(\boldsymbol{\eta}_j) = t_i \int_{\mathbb{R}^2} g_j(\boldsymbol{\theta}_j + \sigma_j \bar{\boldsymbol{\theta}}) \mathcal{N}(\bar{\boldsymbol{\theta}} | \mathbf{0}, \boldsymbol{I}) \mathrm{d}\bar{\boldsymbol{\theta}} \approx t_i \sum_{l=1}^M v^{(l)} g_j(\boldsymbol{\theta}_j + \sigma_j \boldsymbol{\xi}^{(l)}), \tag{9.6}$$

for a set of weights $v^{(l)} \in \mathbb{R}_{>0}$ and integration points $\boldsymbol{\xi}^{(l)} \in \mathbb{R}^2$. In the following, we consider the 3^{rd}-order spherical cubature in [Arasaratnam and Haykin, 2009], which when applied to (9.6) is characterized by $M = 4$, $v^{(l)} = 1/4$ for all $l \in \{1, 2, 3, 4\}$ and $(\boldsymbol{\xi}^{(1)}, ..., \boldsymbol{\xi}^{(4)}) = \sqrt{2}(\boldsymbol{I}, -\boldsymbol{I}) \in \mathbb{R}^{2\times 4}$. Compared to a single evaluation of (9.5), the Gaussian kernel then requires $M = 4$ evaluations, implying approximately a fourfold increase in the computational burden associated with evaluating the measurement model.

9.3.2 Measurement Model

The number of events measured in the scintillator crystal of the detector in time is well described by the Poisson process [Tsoulfanidis, 1995]. Here, we parameterize a Poisson process over Ω with the basis function approximation in (9.2), letting $\boldsymbol{w} = (w_1, ..., w_m)^\top \in \mathbb{R}^m$ and $\boldsymbol{t} = (t_1, ..., t_n)^\top \in \mathbb{R}^n_{>0}$. Following [Ebeigbe et al., 2020], we introduce a background rate b which is constant in time and affects all measurement equally. The measurements are modeled as being Poisson distributed, with

$$\boldsymbol{Y} \sim \mathcal{P}(\boldsymbol{y}|\boldsymbol{C}(\boldsymbol{\Xi})\boldsymbol{w} + b\boldsymbol{t}). \tag{9.7}$$

If the kernel is chosen as $k(\boldsymbol{\theta}) = \delta(\boldsymbol{\theta} - \boldsymbol{\theta}_j)$, and the parameters $\boldsymbol{\theta}_j$ are fixed to specific pixels, then a measurement model analogous to the one in [Ebeigbe et al., 2020] is obtained. If $\boldsymbol{\theta}_j$ is unknown and to be estimated, then we recover the continuous problem formulation in [Hellfeld et al., 2019]. However, by (9.6) the Gaussian kernels in (9.3) can also be considered, generating sparse estimation models for spatially continuous intensity statistics over Ω.

9.4 A Generalized Intensity Inference Algorithm

In this section, we start by presenting the ML-EM algorithm in the context of the measurement model in (9.7), followed by a discussion on model selection, and approaches to combining elements of the solution, $\boldsymbol{S}_i$, when this is deemed favorable with respect to an information criterion of interest.

9.4.1 The ML-EM Framework

The ML-EM framework dates back to the work in [Dempster et al., 1977], and is an iterative algorithm commonly used in parameter estimation problems (see, e.g., [Gibson and Ninness, 2005]). The method consists of an M-step and an E-step. Intuitively, the M-step computes the most likely estimates of a set of latent variables given a set of measurements, which is followed by the E-step, maximizing the expected log-likelihood over the estimation variables.

The development of an ML-EM algorithm for the Poisson distributed measurements was originally done for the related problem of gamma tomography in [Shepp and Vardi, 1982]. In the notation of this thesis, with $\boldsymbol{Y} \sim \mathcal{P}(\boldsymbol{y}|\boldsymbol{AZ}), \boldsymbol{Y} \in \mathbb{N}_0^n, \boldsymbol{A} \in \mathbb{R}^{n\times m}, \boldsymbol{Z} \in \mathbb{R}^m$, and $\boldsymbol{\lambda} = \boldsymbol{AZ}$, the negative log-likelihood of $\boldsymbol{Z}$ given $\boldsymbol{Y} \sim \mathcal{P}(\boldsymbol{y}|\boldsymbol{AZ})$ can be expressed in the form

$$\begin{aligned}
\bar{l}(\boldsymbol{Z}; \boldsymbol{Y}) &= -\log(\mathcal{P}(\boldsymbol{Y}|\boldsymbol{AZ})) && \text{(9.8a)}\\
&= \sum_{i=1}^{n} [\lambda_i - Y_i \log(\lambda_i) + \Gamma(Y_i + 1)] && \text{(9.8b)}\\
&= (\boldsymbol{AZ} - \boldsymbol{Y} \circ \log(\boldsymbol{AZ}) + \Gamma(\boldsymbol{Y} + \boldsymbol{1})) \cdot \boldsymbol{1}, && \text{(9.8c)}
\end{aligned}$$

where Γ here denotes the usual Gamma-function, applied element-wise. The ML-EM algorithm in [Shepp and Vardi, 1982], derived with respect to the likelihood in (9.8), reduces to a fixed-point iteration in the form

$$\hat{\boldsymbol{Z}}^{(q+1)} = (\hat{\boldsymbol{Z}}^{(q)} \oslash (\boldsymbol{A}^\top \mathbf{1}_n)) \circ (\boldsymbol{A}^\top (\boldsymbol{Y} \oslash (\boldsymbol{A}\hat{\boldsymbol{Z}}^{(q)})), \tag{9.9}$$

These iterations are easily generalized to the statistical measurement model in (9.7), where background radiation of intensity b is introduced, along with integration times for each sensor $\boldsymbol{t} \in \mathbb{R}^n_{>0}$. Here, the above ML-EM iterations can be applied with $\boldsymbol{A} = (\boldsymbol{C}(\boldsymbol{\Xi}), \boldsymbol{t}) \in \mathbb{R}^{n \times m+1}$ and observables $\boldsymbol{Z} = (\boldsymbol{w}^\top, b)^\top$, which then recovers a formulation analogous to that in [Hellfeld et al., 2019].

Remark 9.1
The negative log-likelihood in (9.8) is convex in $\boldsymbol{Z}$, and can be minimized by other methods than the ML-EM algorithm. Nonetheless, the ML-EM iterations in (9.9) are simple to implement, widely used, and have the property that the negative likelihood is non-increasing over the iterations, i.e., $\bar{l}(\hat{\boldsymbol{Z}}^{(q+1)}; \boldsymbol{Y}) \leq \bar{l}(\hat{\boldsymbol{Z}}^{(q)}; \boldsymbol{Y})$ for all $q > 0$ (see, e.g., [Dempster et al., 1977]). □

Furthermore, if all of the elements in $\boldsymbol{A}$ are positive, and $\boldsymbol{Z}^{(0)}$ is positive, then $\boldsymbol{Z}^{(q)}$ will remain positive for all iterations. As such, we can construct algorithms that change $\boldsymbol{A}$ as defined by $\boldsymbol{\Xi}$ and m, while simultaneously minimizing (9.8) through (9.9). Before doing so, we first demonstrate the general convergence properties of the ML-EM algorithm in Example 9.1.

Example 9.1
In this example, consider two simple problems characterized by $m = 3$ and $m = 100$, respectively. We let $\boldsymbol{Z} \sim \mathcal{U}([0, 10]^m)$, take $\boldsymbol{A} \sim \mathcal{U}([0, 10]^{n \times m})$, and sample $\boldsymbol{Y} \sim \mathcal{P}(\boldsymbol{y}|\boldsymbol{A}\boldsymbol{Z})$, with $n = 1000$. The ML-EM iterations in (9.9) are run to compute $\hat{\boldsymbol{Z}}$ from 10 different random initial $\hat{\boldsymbol{Z}}^{(0)} \sim \mathcal{U}([0, 10]^m)$ (here depicted in varying shades of blue), and the negative log-likelihood of the estimate relative to the true parameters is depicted as a function of time for each of these initializations (see Figure 9.3).

From this simple example, we make two observations. Firstly, for a small number of estimation variables ($m = 3$), the estimates converge to a point very close to the true parameters. This need not be the case when introducing a very large number of estimation variables in relation to the number of measurements, as seen in the bottom left subplot ($m = 100$), where the estimates vary significantly in $\hat{w}_2^{(*)}$ despite having very similar likelihood costs. Secondly, the number of iterations required to converge to a small cost generally increases with the number of estimation variables of the model.

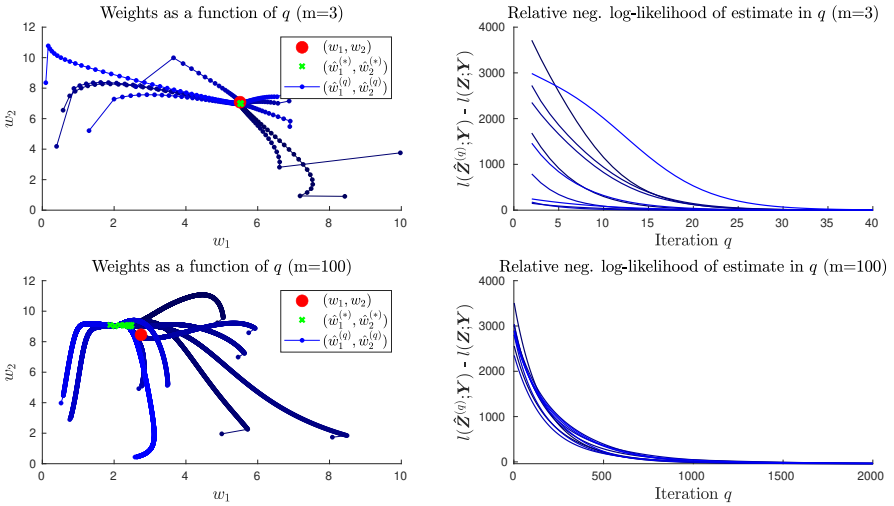

Figure 9.3 Example with ML-EM algorithm run on the two problems. *Left*: The first two elements of $\hat{\boldsymbol{Z}}^{(q)}$, here $(\hat{w}_1^{(q)}, \hat{w}_2^{(q)})$, as a function of the number of iterations, q, for the problems defined by $m = 3$ (top) and $m = 100$ (bottom). The true parameters $\boldsymbol{Z}$ (red) and the terminal estimates for the different initializations (green). *Right*: The relative negative log-likelihood of the estimate as a function of the number of iterations.

9.4.2 An Alternating Optimization Approach

From Example 9.1, it is clear that it can be advantageous to reduce the number of estimation variables in estimation model in (9.7), both with respect to the general convergence rates of the ML-EM algorithm and the accuracy its the estimates. This is one of the main reasons for refining the model characterized by $\boldsymbol{A}$ over the algorithm's execution, and one of the main motivations for constructing the sparse APSL algorithm in [Hellfeld et al., 2019]. Here, an ML-problem is solved by minimizing the negative log likelihood of a solution set $\boldsymbol{S}$ given measurements sampled from (9.7). In contrast to the ML-EM iterations, the APSL incorporates the weights as well as any free hyper-parameters defining the kernels approximating the intensity in (9.2). If $\mathcal{L}(\boldsymbol{S}; \boldsymbol{Y})$ denotes the likelihood of $\boldsymbol{S}$ given $\boldsymbol{Y}$, and $\boldsymbol{A}(\boldsymbol{\Xi}) = (\boldsymbol{C}(\boldsymbol{\Xi}), \boldsymbol{t}) \in \mathbb{R}^{n \times m+1}$ and $\boldsymbol{Z} = (\boldsymbol{w}^\top, b)^\top \in \mathbb{R}^{m+1}$, we can disregard the terms in the Γ-function, and let

$$-\log(\mathcal{L}(\boldsymbol{S}; \boldsymbol{Y})) \propto (\boldsymbol{A}(\boldsymbol{\Xi})\boldsymbol{Z} - \boldsymbol{Y} \circ \log(\boldsymbol{A}(\boldsymbol{\Xi})\boldsymbol{Z})) \cdot \mathbf{1} \triangleq l(\boldsymbol{S}; \boldsymbol{Y}),$$

permitting the ML-estimation problem to be written

$$\hat{\boldsymbol{S}} = \underset{\boldsymbol{S}}{\operatorname{argmin}}(l(\boldsymbol{S}; \boldsymbol{Y})), \tag{9.10}$$

The APSL solves (9.10) approximately by alternating

$$\hat{\boldsymbol{Z}}^{(q+1)} = \underset{\boldsymbol{Z},\boldsymbol{\Xi}=\hat{\boldsymbol{\Xi}}^{(q)}}{\operatorname{argmin}} \, l(\boldsymbol{S};\boldsymbol{Y}), \tag{9.11a}$$

$$\hat{\boldsymbol{\Xi}}^{(q+1)} = \underset{\boldsymbol{\Xi},\boldsymbol{Z}=\hat{\boldsymbol{Z}}^{(q+1)}}{\operatorname{argmin}} \, l(\boldsymbol{S};\boldsymbol{Y}). \tag{9.11b}$$

The first step is convex, as per Remark 9.1, and solved using the ML-EM iterations in (9.9). The second step is non-convex, solved by a constrained interior-point method. In the original APSL, the kernels are defined by the Dirac delta function in $\boldsymbol{k}_j(\boldsymbol{\theta};\boldsymbol{\eta}_j) = \delta(\boldsymbol{\theta}-\boldsymbol{\theta}_j)$ (and these are not constrained to a known surface). In contrast, the GAPSL proposed in [Greiff et al., 2021d] constrains the intensity function to $\mathcal{S}$, and employs the homogeneous Gaussian kernels in (9.3). For the APSL, the constraints $\boldsymbol{\theta}_j \in \Omega$ need to be enforced for all $j = 1, ..., m$ when solving (9.11b). In the GAPSL the additional constraints of $\sigma_j > 0$ are required if kernel j is Gaussian and σ_j is free.

Remark 9.2
When implementing the constrained optimization in (9.11b) with Gaussian kernels, it is advised to bound $0 < \sigma_j^- < \sigma_j < \sigma_j^+$ for some small σ_j^-. The former improves the numerical robustness of the CKF-integration, and the latter can be used to constrain $\boldsymbol{\theta}_j \in \Omega_j \subset \Omega$, such that $\boldsymbol{\theta}_j + \sqrt{2}\bar{\sigma}_j\boldsymbol{u} \in \Omega$ for all unit vectors $\|\boldsymbol{u}\| = 1$. In doing so, the evaluations in (9.6), given the considered CKF integration point set, are well defined at all times. □

9.4.3 Model Selection and Information Criteria

When alternating (9.11a) and (9.11b), it may be the case that the addition or removal of weighted basis functions can increase the likelihood of the estimate. For instance, if the data is well approximated by four point-sources, the cardinality of $\boldsymbol{S}$ should change to best reflect this in (9.10). Selecting the model that yields a good trade-off between a smaller number of parameters and maximizing likelihood amounts to a problem of model selection, which has been studied extensively (see, e.g., [Vrieze, 2012]). For this purpose, the Bayesian information criterion (BIC), the Akaike information criteria (AIC), or the second order AIC (AIC_c) could be considered. In the context of the problem in (9.10) with the model in (9.7), these information criteria are

$$\text{BIC}(\boldsymbol{S}) = -2\log(\mathcal{L}(\boldsymbol{S};\boldsymbol{Y})) + k\log(n), \tag{9.12a}$$

$$\text{AIC}(\boldsymbol{S}) = -2\log(\mathcal{L}(\boldsymbol{S};\boldsymbol{Y})) + 2k, \tag{9.12b}$$

$$\text{AIC}_c(\boldsymbol{S}) = -2\log(\mathcal{L}(\boldsymbol{S};\boldsymbol{Y})) + 2k(k+1)/(n-k-1), \tag{9.12c}$$

where n is the number of measurements and k is the number of estimation variables. For example, when using the discrete parameter space and a Dirac

kernel, $k = m+1$; if the continuous parameter space is used and $\boldsymbol{\theta}_j \in \Omega \subset \mathbb{R}^2$, then $k = 3m + 1$; and if we use the Gaussian kernel with free kernel centers $\boldsymbol{\theta}_j \in \Omega \subset \mathbb{R}^2$ and $\sigma_j \in \mathbb{R}_{>0}$, then $k = 4m+1$. The original APSL is developed with respect to the BIC [Hellfeld et al., 2019], but in [Anderson and Burnham, 2004], it is evident that the AIC is in many cases preferable, and that the AIC_c should be considered if $n/k \lesssim 40$, as will often be the case in the intended applications. In the following, we let IC be any information criteria in (9.12), but the experiments are done with the BIC to relate the GAPSL in [Greiff et al., 2021d] to the original APSL in [Hellfeld et al., 2019].

9.4.4 Extending, Fusing and Pruning

Consider a solution $\boldsymbol{S}$ with k parameters, and let this solution be augmented by adding or removing one weighted basis function yielding $\bar{\boldsymbol{S}}$ with $\bar{k}$ parameters. If $\text{IC}(\bar{\boldsymbol{S}}) < \text{IC}(\boldsymbol{S})$, then the new solution should be accepted in favor of the old. In the GAPSL, this solution augmentation is to be done in three different ways: by extending, pruning, and fusing solutions.

- `Extend()`: Randomize a new kernel and weight, and add to the solution. This is done on each GAPSL iteration, without reference to the IC.

- `Prune()`: Remove pairs of weights and kernels, $\boldsymbol{S}_j$, from the solution, $\boldsymbol{S}$, if doing so decreases the chosen IC.

- `Fuse()`: Fuse two elements of $\boldsymbol{S}$ if it decreases the chosen IC. If two kernels are located close to each other in Ω, then their contribution to the likelihood may potentially be well approximated by a single basis function at this location. The prune operation will not reduce the IC if the weights are sufficiently large, hence the need for the `Fuse()` operation, as outlined in Algorithm 2.

The only nontrivial aspect of these operations is the fusion of Gaussian kernels. Several approaches exist for related problems in sensor fusion, including covariance intersection (CI) and inverse covariance intersection (ICI) (see, e.g., [Chen et al., 2002; Hurley, 2002]). However, the problem is made more difficult in that we seek a single Gaussian kernel in the form (9.3) that best approximates two components of $\boldsymbol{S}$, making CI and ICI more difficult to apply. Instead, we consider a weighted sum of two kernels associated with $\boldsymbol{S}_i$ and $\boldsymbol{S}_j$, here denoted $q^{ij}(\boldsymbol{\theta}) = (w_i\mathcal{N}(\boldsymbol{\theta}|\boldsymbol{\theta}_i, \sigma_i^2\boldsymbol{I}) + w_j\mathcal{N}(\boldsymbol{\theta}|\boldsymbol{\theta}_j, \sigma_j^2\boldsymbol{I}))/(w_i + w_j)$ for $w_i >, w_j > 0$, and formulate a candidate kernel $p(\boldsymbol{\theta}) = \mathcal{N}(\boldsymbol{\theta}|\boldsymbol{\theta}_p, \sigma_p^2\boldsymbol{I})$. We then solve an optimization problem to find a pair $\boldsymbol{S}_i, \boldsymbol{S}_j \in \boldsymbol{S}$, such that

$$(i, j) = \underset{i\neq j}{\text{argmin}}\Big(\min_{\boldsymbol{\theta}_p, \sigma_p} \text{KL}(q^{ij}||p)\Big). \tag{9.13}$$

Solving this problem yields the homogeneous Gaussian kernel, $p(\boldsymbol{\theta})$, defined in $\{\boldsymbol{\theta}_p, \sigma_p\}$, which best approximates the mixture of two other Gaussian kernels, $q^{ij}(\boldsymbol{\theta})$, in its first two moments. The reason for considering this approach, is that the solution to the problem of minimizing the KL-cost in (9.13) over $\{\boldsymbol{\theta}_p, \sigma_p\}$ can be expressed in the parameters $\{w_i, \boldsymbol{\theta}_i, \sigma_i, w_j, \boldsymbol{\theta}_j, \sigma_j\}$.

$$w_p = w_i + w_j, \quad n_i = w_i/w_p, \quad n_j = w_j/w_p, \tag{9.14a}$$

$$\boldsymbol{\theta}_p = n_i\boldsymbol{\theta}_i + n_j\boldsymbol{\theta}_j, \tag{9.14b}$$

$$\sigma_p^2 = (n_i\sigma_i^2 + n_j\sigma_j^2) + \tfrac{1}{2}n_i n_j(n_i + n_j)\|\boldsymbol{\theta}_i - \boldsymbol{\theta}_j\|^2. \tag{9.14c}$$

This solution can be found using the conditional covariance formula (see Appendix D), and with it, the `Fuse()` operation is summarized in Algorithm 2.

Algorithm 2: Pseudo code of the `Fuse()` operation

```
Receive S;
Find candidates {S_i, S_j} ∈ S by (9.13);
S^(+) = {w_p, θ_p, σ_p} using (9.14);
S̄ = (S ∪ S^(+)) \ {S_i, S_j};
if IC(S̄) < IC(S) then
    S = S̄;
end
return S;
```

With these functions, the GAPSL is outlined in Algorithm 3. This algorithm is similar to the original APSL in [Hellfeld et al., 2019], but notably and significantly modified in (i) the evaluation of the measurement model, (ii) the formulation of the optimization problem, and (iii) the fusing operation, all to facilitate the inference of intensities parameterized by Gaussian kernels.

Remark 9.3
We emphasize that the APSL in this thesis differs slightly to the original APSL algorithm evaluated in [Hellfeld et al., 2019; Vavrek et al., 2020], as the algorithm is complex and implemented from scratch in Matlab based solely on a mathematical description in [Vavrek et al., 2020]. In addition, a different optimizer is used to solve (9.11b) over the hyper-parameters. Nonetheless, our APSL implementation generates results that are very similar to those in [Vavrek et al., 2020], as will be reported in the simulation examples. □

Algorithm 3: Pseudo code of the generalized APSL algorithm (GAPSL)

Receive geometries: $\Omega, \mathcal{S}$;
Receive data: $\{Y_i, t_i, \boldsymbol{p}_i^d, \boldsymbol{R}_i^d\}_{i=1}^n$;
Randomize: $\boldsymbol{S}^{(0)}$;
for $q = 1, ..., N_{\max}$ **do**
  $\bar{\boldsymbol{S}}^{(q-1)} \leftarrow \texttt{Extend}(\boldsymbol{S}^{(q-1)})$;
  Estimate $\hat{\boldsymbol{Z}}^{(q)}$ by solving (9.11a) with $\bar{\boldsymbol{S}}^{(q-1)}$;
  Estimate $\hat{\boldsymbol{\Xi}}^{(q)}$ by solving (9.11b) with $\bar{\boldsymbol{S}}^{(q-1)}$;
  Form $\bar{\boldsymbol{S}}^{(q)}$ from $\hat{\boldsymbol{Z}}^{(q)}$ and $\hat{\boldsymbol{\Xi}}^{(q)}$;
  $\boldsymbol{S}^{(q)} \leftarrow \texttt{Fuse}(\texttt{Prune}(\bar{\boldsymbol{S}}^{(q)}))$;
  if $\mathrm{IC}(\boldsymbol{S}^{(q)}) > \mathrm{IC}(\boldsymbol{S}^{(q-1)})$ **then**
    $\boldsymbol{S}^{(q)} \leftarrow \texttt{Fuse}(\texttt{Prune}(\boldsymbol{S}^{(q-1)}))$;
  end
end

9.5 Simulation Verification

To evaluate the generalized APSL, we give two examples with (i) the regular ML-EM iterations with a discrete parameter space, and the APSL with a continuous parameter space, both with (ii) the original version with Dirac kernels and (iii) the generalized version with Gaussian kernels. Specifically,

(i) The classical ML-EM algorithm with Dirac kernels, fixed at $N \times N$ pixels of length 0.1 [m]. Here, $\boldsymbol{\theta}_1 = (0.1, 0.1)$ and $\boldsymbol{\theta}_m = (0.1N, 0.1N)$ with $N = 50$. This corresponds to the left-most subplot in Figure 9.2.

(ii) The APSL with Dirac kernels, using the BIC in (9.12) for model selection, with the free hyper-parameters defined as $\boldsymbol{\eta}_j = \boldsymbol{\theta}_j \in \Omega$, which corresponds to the center subplot in Figure 9.2.´

(iii) The GAPSL with homogeneous Gaussian kernels, using the BIC in (9.12) for model selection, with the free hyper-parameters defined as $\boldsymbol{\eta}_j = \{\boldsymbol{\theta}_j, \sigma_j\}$. This corresponds to the right-most subplot in Figure 9.2.

To generate the synthetic data, we consider two different scenarios, in both cases with a surface characterized by $\mathcal{S}(\boldsymbol{\theta}) = (\theta_1, \theta_2, \sin(\pi\theta_1/10)\cos(\pi\theta_2/10))$ over a relatively small domain given by $\Omega = [0, 5]^2 \subset \mathbb{R}^2$. These are detailed separately below, with Scenario A corresponding to data generated from point sources, and Scenario B corresponding to data generated from a continuous intensity function parameterized in Gaussian kernels.

9.5.1 Scenario A

In this first scenario, we consider four point sources located at $\boldsymbol{\theta}_1^I = (1,1)$, $\boldsymbol{\theta}_2^I = (1,2)$, $\boldsymbol{\theta}_3^I = (4,4)$, $\boldsymbol{\theta}_4^I = (3,2)$, each radiating with an intensity of $w_1^I = 200$, $w_2^I = 300$, $w_3^I = 200$, $w_4^I = 400$ [Bq], respectively, such that the true intensity function used for sampling the Poisson distributed data is

$$I(\boldsymbol{\theta}) = \sum_{j=1}^{4} w_j^I \delta(\boldsymbol{\theta} - \boldsymbol{\theta}_j^I). \tag{9.15}$$

The integration time interval is taken to be $t_i = 1$ [s] for $i = 1, ..., n$, and a total of $n = 10^3$ measurements are sampled in a positional trajectory defined by a constant height of 1 [m] above the surface $\mathcal{S}$, such that $\boldsymbol{p}_i^d = \mathcal{S}(\boldsymbol{\theta}^d(t)) + (0,0,1)$, where $\boldsymbol{\theta}^d(t) = (2.5 + \sin(2\pi t/n), 2.5 + \cos(4\pi t/n))$ and $\boldsymbol{R}^d(t) = \boldsymbol{I}$. This corresponds to a 17 [min] long flight, which is roughly the length of a mission on a single set of batteries with the Matrice 600 Pro AV [DJI, 2021].

9.5.2 Scenario B

In the second scenario, the intensity function is parameterized using a set of Gaussian kernels in order to study the case where the intensity is not well approximated by point sources. For this purpose,

$$I(\boldsymbol{\theta}) = \sum_{j=1}^{4} w_j^I \mathcal{N}(\boldsymbol{\theta} | \boldsymbol{\theta}_j^I, (\sigma_j^I)^2 \boldsymbol{I}), \tag{9.16}$$

using the same four points $\boldsymbol{\theta}_j^I$ $j = 1, ..., 4$ as in the previous scenario, but now also characterized by the four standard deviations $\sigma_1^I = 1$, $\sigma_2^I = 1.2$, $\sigma_3^I = 1.5$ and $\sigma_4^I = 0.6$, resulting in a continuous intensity statistics over Ω.

9.5.3 Simulation Results and Discussion

The results from the Monte Carlo (MC) study are compared in the following statistics: the mean computational time; the number of parameters used in the model; the negative log-likelihood of the solution relative to the likelihood of the true model parameters given the sampled data $\Delta_l(\hat{\boldsymbol{S}}, \boldsymbol{S}) = l(\hat{\boldsymbol{S}}, \boldsymbol{Y}) - l(\boldsymbol{S}, \boldsymbol{Y})$; the BIC relative to the likelihood of the true model parameters $\Delta_{\text{BIC}}(\hat{\boldsymbol{S}}, \boldsymbol{S}) = \text{BIC}(\hat{\boldsymbol{S}}, \boldsymbol{Y}) - 2l(\boldsymbol{S}, \boldsymbol{Y})$; and the integrated difference of the estimated and true intensity function when integrated over Ω, $\Delta_I(\hat{\boldsymbol{S}}, \boldsymbol{S}) = \int_\Omega \|I(\boldsymbol{\theta}; \boldsymbol{S}) - I(\boldsymbol{\theta}; \hat{\boldsymbol{S}})\|^2 \mathrm{d}\boldsymbol{\theta}$. The results from 100 MC runs are summarized for Scenario A and B in Tables 9.2 and 9.3 respectively, and an example of the intensity reconstructions for (i), (ii) and (iii) in Scenario A is shown in Figure 9.4, and for Scenario B in Figure 9.5 and Figure 9.6.

Table 9.2 Scenario A, with point sources constituting the true intensity function. Average value and variance in parenthesis from $N_{mc} = 100$ runs.

Algorithm	Kernel	Form	Comp. time [s]	Num. param	$\Delta_l(\hat{\boldsymbol{S}}; \boldsymbol{S})$	$\Delta_{\text{BIC}}(\hat{\boldsymbol{S}}; \boldsymbol{S})$	$\Delta_I(\hat{\boldsymbol{S}}; \boldsymbol{S})$
(i) ML-EM	Dirac	Disc.	6.06 (0.15)	2500 (0)	-4.84 (3.08)	17259.7 (6.15)	21.62 (0.56)
(ii) APSL	Dirac	Cont.	11.14 (4.32)	12 (0)	-3.12 (1.81)	76.64 (3.61)	12.85 (8.22)
(iii) GAPSL	Gaussian	Cont.	54.82 (11.53)	17.6 (2.19)	36.04 (41.87)	193.66 (88.39)	15.03 (0.46)

Table 9.3 Scenario B, with point sources constituting the true intensity function. Average value and variance in parenthesis from $N_{mc} = 100$ runs.

Algorithm	Kernel	Form	Comp. time [s]	Num. param	$\Delta_l(\hat{\boldsymbol{S}}; \boldsymbol{S})$	$\Delta_{\text{BIC}}(\hat{\boldsymbol{S}}; \boldsymbol{S})$	$\Delta_I(\hat{\boldsymbol{S}}; \boldsymbol{S})$
(i) ML-EM	Dirac	Disc.	6.13 (0.09)	2500 (0)	-9.95 (4.02)	17249.48 (8.05)	8.37 (0.28)
(ii) APSL	Dirac	Cont.	17 (3.99)	16.2 (2.68)	23.94 (11.19)	159.78 (12.35)	13.52 (0.28)
(iii) GAPSL	Gaussian	Cont.	58.68 (16.32)	15.2 (1.79)	4.85 (5.8)	114.7 (14.84)	0.86 (0.38)

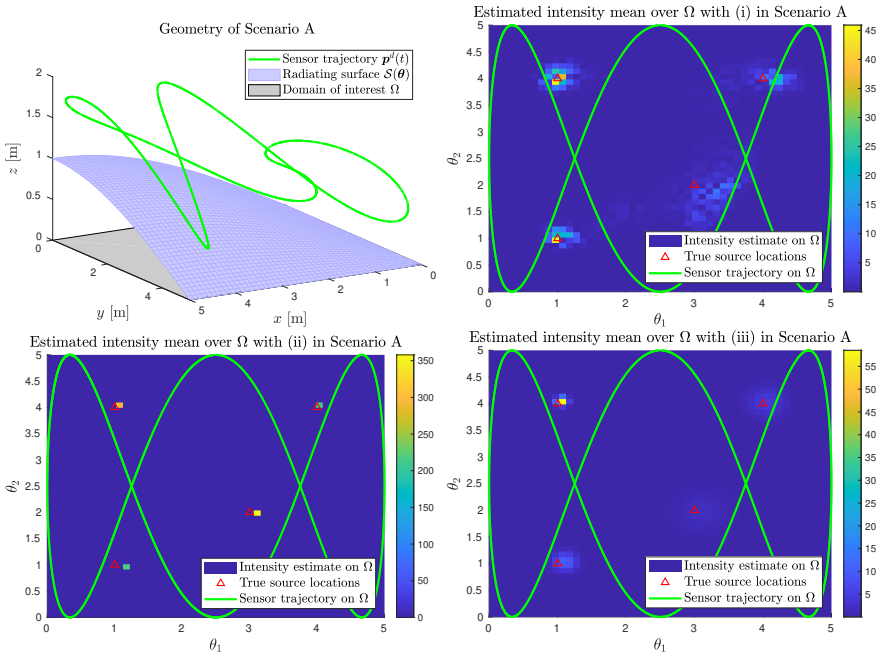

Figure 9.4 Depiction of the first MC run with Scenario A. *Top, left:* Problem geometry. *Top, right:* The estimated intensity $\hat{I}(\boldsymbol{\theta})$ with (i), discrete hyper-parameter space and Dirac kernel (ML-EM). *Bottom, left:* The estimated intensity $\hat{I}(\boldsymbol{\theta})$ with (ii), continuous hyper-parameter space and Dirac kernel (APSL). *Bottom, right:* The estimated intensity $\hat{I}(\boldsymbol{\theta})$ with (iii), continuous hyper-parameter space and Gaussian kernels (GAPSL).

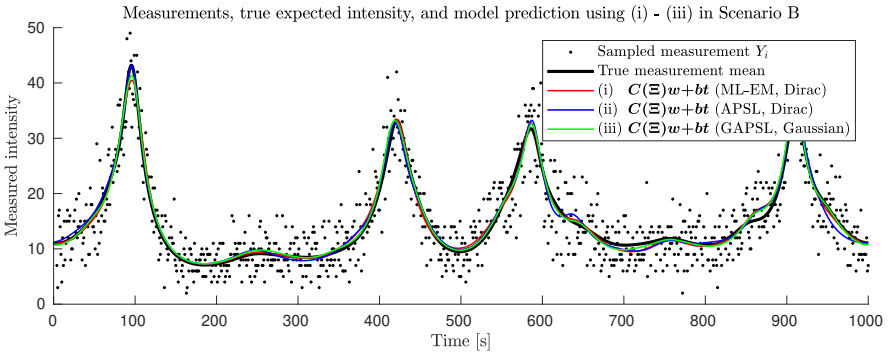

Figure 9.5 Depiction of the first MC run with Scenario B. True measurement mean, sampled measurements, and measurement mean prediction of the Poisson distributed models estimated by (i), (ii), and (iii).

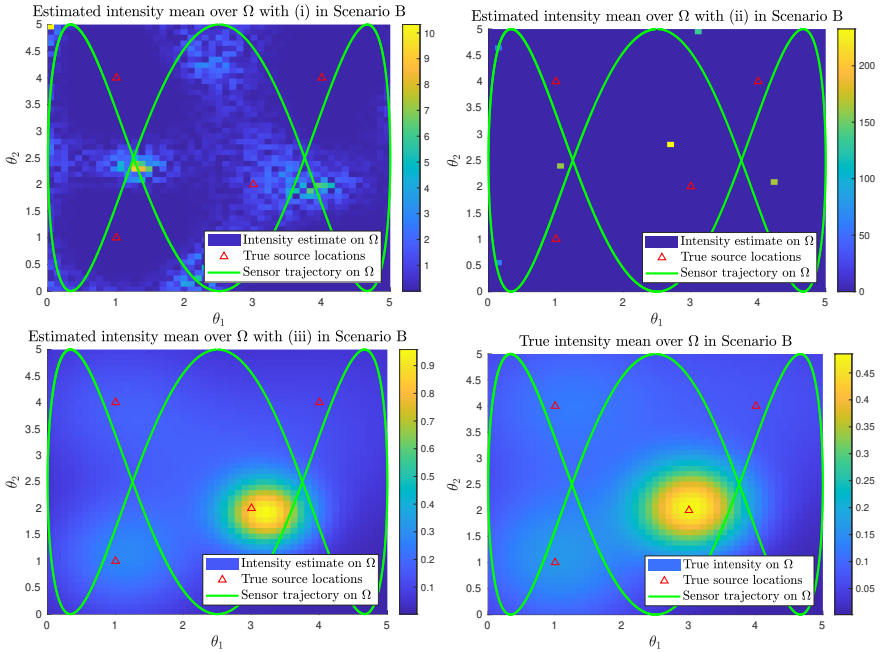

Figure 9.6 Depiction of the first MC run with Scenario B. *Top, left:* The estimated intensity mean $\hat{I}(\boldsymbol{\theta})$ with (i), discrete ML-EM and Dirac kernel. *Top, right:* The estimated intensity mean $\hat{I}(\boldsymbol{\theta})$ with (ii), continuous APSL and Dirac kernel. *Bottom, left:* The estimated intensity mean $\hat{I}(\boldsymbol{\theta})$ with (iii), continuous GAPSL and Gaussian kernel. *Bottom, right* Intensity used to generate the synthetic data.

One of the main contributions of the GAPSL in [Greiff et al., 2021d] is the introduction of Gaussian kernels in the APSL algorithm, which should result in approximately a factor of four slower execution time when compared to the original APSL with Dirac kernels, provided the assumption of infinite integration domains and subsequent application of the spherical cubature rule defined in Sec. 9.3.1. This difference in computational time is seen in the simulation study (see Tables 9.2-9.3), where the APSL with Gaussian kernels is almost exactly a factor four slower on average. The ML-EM algorithm is by far the fastest, but its computational speed depends greatly on the resolution of the grid and the set convergence criteria, as seen in Example 9.1. The problem of selecting the number of estimation parameters is dealt with automatically through evaluation of the solution with respect to the ICs in the APSL and GAPSL, resulting in a significantly fewer number of estimation parameters and the ML-EM iterations converging faster and more reliably.

In the simulation examples, the ML-EM formulation consistently finds a solution with a lower relative negative log-likelihood than the APSL and GAPSL algorithms. This can easily be misconstrued as a positive, but is here clearly indicative of over-fitting, as evident by the relative BIC in Tables 9.2-9.3, which far exceeds that in the APSL-algorithms. This is further illustrated in the integral of the intensity function construction error over Ω, where the discrete ML-EM algorithm is outperformed by both APSL and GAPSL in Scenario A, and by the GAPSL in Scenario B. In this measure, we note a significant variance in the APSL over the MC runs. The reason being that the integral is evaluated numerically, and that in some of the MC runs, the positional error in the point source estimates is large with respect to the small grid used in the evaluation of the considered measure. Note that despite the visibly poor reconstruction of the intensity function in Scenario B when using the ML-EM and APSL algorithms, the predicted mean intensity along the path of the sensor is near perfect (see Figure 9.5). This is a significant problem when considering practical applications, even for the APSL. The algorithms can yield deceptively low negative log-likelihoods close to the sensor trajectory and good reconstructions of the intensity to this trajectory. But generally, the models will not result in good predictions along other sensor trajectories, even when the model used to generate the data is perfectly known. This is seen visibly in the disparity of the reconstructions, comparing the reconstructions corresponding to the ML-EM algorithm and the APSL-algorithm in Scenario B, with the true intensity function in Figure 9.6.

When considering the reconstruction with the GAPSL, we should expect it to work well in Scenario A, as an intensity function described by a finite set of point sources can be approximated by a set of Gaussian kernels with small variance. The model should also be capable of generalizing well to Scenario B, as it can represent the true intensity function perfectly in this case.

For Scenario A, the GAPSL consistently finds the correct number of point

sources, as indicated by the number of parameters, and the kernel centers, $\boldsymbol{\theta}_j$, consistently converge to locations very close to the true point sources, $\boldsymbol{\theta}_j^I$, but the variance σ_j of the kernels does not always converge to a small value. When this happens, we observe a significant error in the likelihood as well, indicated by the large variance of the GAPSL in the relative likelihood measure. However, in the BIC, the GAPSL is still to be preferred over the ML-EM algorithm in Scenario A.

For Scenario B, we observe that the GAPSL-algorithm outperforms the ML-EM algorithm and the conventional APSL-algorithm in all performance metrics apart from the computational time. Importantly, we note that it will typically yield very good intensity reconstructions. This means that predictions of the measurement intensity as a function of the sensor position will be good when moving far away from the trajectory along which the intensity was measured. We note that the conventional methods do not yield good reconstructions for the specific scenario studied in Scenario B in this setup, and stress that the algorithms should be compared and evaluated on synthetic data which is representative of the experiment in which they are to be applied. If it is interesting to predict the intensity far away from the trajectory of the sensor, and the underlying intensity function is not well described by a small set of point sources, then one should be hesitant about relying on the reconstructions when using the ML-EM and conventional APSL algorithms. However, we stress that the original APSL is an excellent alternative if the data is well represented by a small number of point sources.

9.6 Experimental Results

To validate and demonstrate the performance of the GAPSL on real data, an experiment was set up much like Scenario A. Three point sources of ^{137}Cs, ^{133}Ba, and ^{60}Co with activities 135, 150, and 130 [MBq], respectively, were placed on a meadow by the Barsebäck nuclear power plant in a triangular formation, approximately 10 meters apart. A gamma-ray detector consisting of a 3" NaI(Tl) scintillator crystal coupled to a photomultiplier tube by Teledyne [Teledyne, 2021] and an Ortec Digibase [Ortec, 2021] was attached to a DJI Matrice 600 Pro UAV [DJI, 2021], as shown in Figure 9.7. The system was used to sample intensity data over $t_i \approx 2$ [s] integration intervals during a 17 [min] manual flight at various heights around the sources. The locations of the radioactive samples were measured in geodetic coordinates prior to the flight using the GPS receiver of the UAV, and this data set was also used to fit a three-dimensional plane to the ground as $\mathcal{S}(\boldsymbol{\theta}) = (0.033\theta_1, 0.014\theta_2, -0.800)$ in a local east-north-up (ENU) coordinate frame.

After the flight, the sampled GPS data was interpolated using a polyphase anti-aliasing filter, synchronized in time with the intensity, and re-sampled at

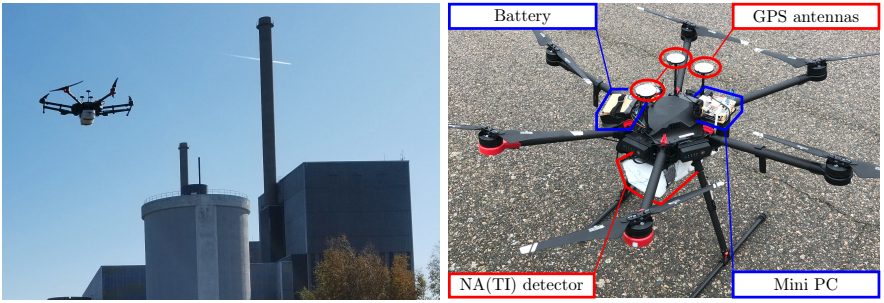

Figure 9.7 *Left*: Photo of the Matrice 600 pro UAV with detector package mounted underneath and the Barsebäck nuclear power plant in the background. *Right*: The Matrice 600 pro UAV with added components.

the center of the intensity measurement integration intervals. The domain of interest was defined by $\Omega = [-20, 20]^2$ [m^2], thus defining all required inputs to the generalized APSL in Algorithm 3. Three algorithms were tested, mirroring the simulation examples: (i) the ML-EM algorithm with a discretized hyperparameter space using 41 equidistant tiles of 1×1 [m^2] each direction on Ω, with a fixed Dirac kernel associated with each tile; (ii) the original APSL using Dirac kernels and a continuous parameter space; and (iii) the GAPSL with Gaussian kernels and a continuous parameter space.

The raw positional GPS data, as well as the re-sampled positional data and the intensity measurements, the intensity prediction along this positional trajectory of the sensor, and the resulting intensity function reconstruction over Ω are shown in Figure 9.8. In this case, the discrete grid in (i) results in a total of 1682 estimation parameters, while (ii) and (iii) converge to reconstructions with three kernel functions, with 10 and 13 parameters, respectively (as the variance in the Gaussian kernels is free). In (iii) the resulting solution approaches small variances in the kernel functions, with $\sigma_1^2 = 0.02$, $\sigma_2^2 = 0.06$, $\sigma_3^2 = 0.01$, as should be expected if the true underlying intensity is well described by point sources. Furthermore, the ML-EM approach in (i) seems to have over-fitted the data, as evident by the relatively large intensities estimated around $\boldsymbol{\theta} = (-20, -14)^\top$ where no radioactive materials were present. Despite this, the BIC of the solution in (i) is slightly smaller than that of (ii) and (iii) due to it better fitting the large peaks in the data, specifically around the sample indices $i = \{15, 100, 410\}$.

As the detector detects radiation from different isotopes with different efficiency, it is not possible to relate the estimated weights of the kernel functions to the known intensity of the point sources without extensive calibration of the detector in this experiment. However, we note that the weights associated with the kernels in the APSL and GAPSL were consistent,

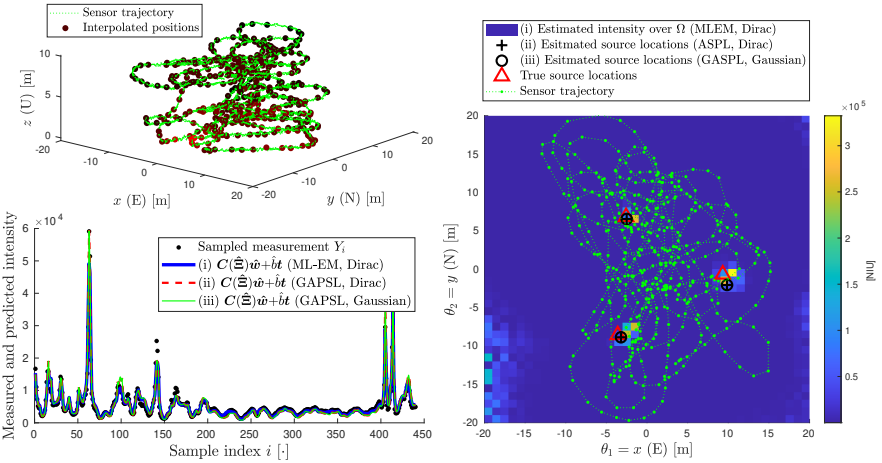

Figure 9.8 Data from experiments with a UAV and ground truth. *Top, left:* The measured sensor trajectory (green) and interpolated positions at which the intensity is sampled (with red indicating a higher intensity). *Bottom, left:* Sampled intensity, and predicted intensity when using (i) a the ML-EM algorithm with Dirac kernels (blue); (ii) the APSL with a continuous hyper-parameter space and Dirac kernels (red); and (iii) the GAPSL with continuous hyper-parameter space and Gaussian kernels (green). *Right:* True source locations inferred from separate GPS data (red); the estimated intensity with (i) discrete Dirac formulation shown in the surface plot; and the estimated locations of the kernels when using the continuous formulations are indicated with (ii) Dirac (black, plus), and (iii) Gaussian (black, circle). The normalized intensity units (NIU) simply refer to the intensity units of the sources with a nominal detector sensitivity in (9.1), and can be converted to [Bq] by an approximately linear transformation after detector calibration. The experiment setup and convergence of the GAPSL on the real data is demonstrated in the video chapter-9-radiation.mp4.

and that their kernel centers, $\boldsymbol{\theta}_j$, were estimated to near-identical locations (see Figure 9.8). Furthermore, the estimated models result in visibly good predictions of the intensity along the trajectory of the sensor. As such, this serves as a validation of the GAPSL against the APSL, and we should expect results similar to the ones generated for Scenario B when instead considering data that is not well described by point sources. However, such experiments are difficult to construct in practice, as it is nontrivial to safely construct experiments with continuous and known intensity functions over Ω.

9.7 Summary

In this chapter, we demonstrated one of many potential use-cases of UAVs equipped with good control systems: that of mobile radiation mapping. Specifically, we have discussed how the UAV can be used to detect the locations and intensities of radioactive sources. It was observed that many common approaches, such as the ML-EM algorithm with respect to a Poisson likelihood and discretized domain Ω, tend to include a very large number of estimation variables in relation to the number of measurements gathered during a typical UAV flight time. As such, these methods have a tendency to overfit the data. This is partly what warranted the development of the APSL in [Vavrek et al., 2020; Hellfeld et al., 2019], which yields a sparse reconstruction under the assumption that the intensity function is well represented by a small set of point sources. In this chapter, we presented the generalized APSL in [Greiff et al., 2021d], with the radioactive sources constrained to known surfaces in $\mathbb{R}^3$, and the intensity function being continuous over Ω. Furthermore, results from non-linear Gaussian filtering were used to yield an efficient implementation.

The method was developed and validated in a simulation environment, but also tested in an experimental setup where a detector was mounted on a large UAV and flown over a field. In these experiments, the background radiation was not known, but presumably negligible given the relatively strong radiating point sources. The APSL and GAPSL algorithms were both shown to converge to the three point sources in close vicinity of the true point sources, similar to the results in the simulation study of Scenario A. This was clearly replicated in Figure 9.8. It was also noted that the discrete ML-EM algorithm resulted in the lowest relative log-likelihood, but found significant radiation in a region which was not believed to be present. As such, the veracity of the extended Gaussian APSL algorithm is confirmed by the close proximity of its solution to that of the original APSL, and the true point source locations.

In conclusion, if the objective in the application is to predict the intensity measurements close to the trajectory of the sensor, then any of the three options can be implemented, as indicated by Figure 9.5 in the simulated scenario, and Figure 9.8 with the experimental data. However, if we seek to predict the measured intensity further away from the trajectory or draw any conclusions about the intensity function reconstruction, then the algorithm needs to be chosen with care. If it is a priori known that the intensity function over the domain Ω is well represented by a small set of point sources, we recommend the implementation of an APSL for the radiation reconstruction. However, the GAPSL can be used just as well, provided the hyper-parameters are initialized with very small variances. However, in applications where this cannot be assumed, we recommend the implementation of the GAPSL due to its great flexibility and good performance when the true intensity function is well approximated by a finite set of weighted Gaussian kernels.

10

Summary of Part II

Two applications are considered in Part II of the thesis: the first relates to circumnavigation, and the second to radiation mapping. In this summary, the ideas are restated and related to Part I, giving an overview of the developments.

Chapter 8 In this chapter, a result on target tracking is extended with integral action to deal with bounded load disturbances in the body frame of the vehicle, thereby attenuating disturbances that can arise in practice. The intention is to apply such controllers to compute a reference for an already closed-loop system, which is one of many ways that a reference system can be implemented. For instance, it is clear from the examples in Chapter 4 that the quadrotor UAV can be controlled to track smooth positional trajectory, and that the proposed methods work well even when the flat output trajectory is C^0. Computing a velocity reference using the controller in Theorem 8.2 can enable a UAV to perform circumnavigation tasks, safely inferring a target's position through bearing measurements and adjusting the reference trajectory accordingly. Apart from the possibility of using the control systems in previous sections together with the circumnavigation controller, we highlight that the ideas related to smooth saturation functions in Chapter 6 are instrumental in arriving at the result in Chapter 8 when introducing integral action.

While the intended applications primarily concern fixed-wing UAVs, the controller may also be used for circumnavigation with quadrotor UAVs and ground-based vehicles. As such, the theoretical results are demonstrated in practice using a small unmanned ground vehicle. The control system of the vehicle is designed heuristically using ideas analogous to the explicit vector control in Chapter 3 but disregarding any dynamic feed-forward terms, therefore giving rise to approximately constant asymptotic disturbances in the body frame. It is demonstrated that the controller attenuates these errors, achieving small asymptotic tracking errors with a non-zero integral state, thereby demonstrating the effects of the integral action. In Chapter 8, it is argued that no mechanical system behaves as a perfect single integrator. As such there will always be actuation errors in practice, which can be attenuated

by introducing integral action as described in Theorem 8.2. It is recommended to explore this controller further in practice for fixed-wing UAVs.

Chapter 9 This chapter considers scenarios where a UAV is to survey radiation in (i) potentially hazardous areas, or (ii) close to a facility such as a nuclear power plant. To carry the required sensory equipment, the UAV needs to have a significant load capacity, which in turn requires it to be large in size. Increasing the size of the UAV and flying it in environments such as (i) or (ii) makes it very important to guarantee that the control system is robust, as any malfunction may cause severe damage both to the UAV and its surroundings. This chapter explores how the gathered intensity data can be used to infer an intensity function over a known surface, such as a meadow in (i) or the wall of a nuclear power plant in (ii). As such, this chapter is primarily focused on estimation theory and not nonlinear control.

It is shown that the additive point-source localization algorithm (APSL) in [Hellfeld et al., 2019; Vavrek et al., 2020] can be extended with Gaussian kernels, and that results from nonlinear Gaussian filtering can be used to formulate a computationally tractable measurement model given certain assumptions on the integration domain. It is demonstrated that this generalized APSL (GAPSL) performs well when the radiation is not well described by a small number of point sources, which is likely to be the case in many practical scenarios. Importantly, it is also shown that the GAPSL is capable of representing a small number of point sources through the proposed hyper-parameter optimization. Importantly, this chapter also highlights the propensity of a standard voxelized ML-EM algorithm and the APSL to over-fit the data, especially when using omni-directional radiation sensors.

It is argued that the GAPSL should be considered when there is reason to suspect that the intensity is not well described by a small number of point sources, and that methods which introduce a large number of estimation variables should be used with care due to their propensity to over-fit.

Final Remarks In the second part of the thesis, it is demonstrated that the solutions presented to the various theoretical problems in Part I can facilitate applications that solve practical problems related to inspection and surveying. In particular, the reference dynamics in the FSF and FOF controller solutions can be replaced by the circumnavigation and target tracking controller, which then enables the system to track a target with an initially unknown position while simultaneously inferring the target's position using bearing measurements. It is also clear that robust control systems with rigorous uniform stability guarantees become important when considering applications such as the measuring of radiation intensity, where stakes are high with respect to the control system malfunctioning. For both of these applications, we recommend the use of the controllers in Chapter 4 and 6.

Bibliography

Abdessameud, A. and A. Tayebi (2010). "Global trajectory tracking control of VTOL-UAVs without linear velocity measurements". *Automatica* **46**:6, pp. 1053–1059. DOI: 10.1016/j.automatica.2010.03.010.

Abdolhosseini, M., Y. Zhang, and C. A. Rabbath (2013). "An efficient model predictive control scheme for an unmanned quadrotor helicopter". *Journal of Intelligent & Robotic Systems* **70**:1-4, pp. 27–38. DOI: 10.1007/s10846-012-9724-3.

Anderson, D. and K. Burnham (2004). *Model selection and multimodel inference : a practical information-theoretic approach*. 2nd ed. Springer-Verlag, NY, USA. ISBN: 0-387-95364-7.

Andrle, M. S. and J. L. Crassidis (2013). "Geometric integration of quaternions". *Journal of Guidance, Control, and Dynamics* **36**:6, pp. 1762–1767. DOI: 10.2514/1.58558.

Antsaklis, P. J. and A. N. Michel (2006). *Linear systems*. 2nd ed. Birkhauser Boston. ISBN: 3 978-0-8176-4434-5.

Arasaratnam, I. and S. Haykin (2009). "Cubature Kalman filters". *IEEE Transactions on Automatic Control* **54**:6, pp. 1254–1269. DOI: 10.1109/TAC.2009.2019800.

Atkinson, K. E. (1988). *An introduction to numerical analysis*. 2nd ed. John Wiley & Sons, Inc. ISBN: 0-471-62489-6.

Axelsson, P. and F. Gustafsson (2014). "Discrete-time solutions to the continuous-time differential Lyapunov equation with applications to Kalman filtering". *IEEE Transactions on Automatic Control* **60**:3, pp. 632–643. DOI: 10.1109/TAC.2014.2353112.

Bangura, M., M. Melega, R. Naldi, and R. Mahony (2016). "Aerodynamics of rotor blades for quadrotors". arXiv: 1601.00733 [physics.flu-dyn].

Bar-Itzhack, I. Y. (2000). "New method for extracting the quaternion from a rotation matrix". *Journal of Guidance, Control, and Dynamics* **23**:6, pp. 1085–1087. DOI: 10.2514/2.4654.

Barbălat, I. (1959). "Systemes d'équations différentielles d'oscillations non linéaires". *Rev. Math. Pures Appl* **4**:2, pp. 267–270.

Barnett, S. and C. Storey (1967). "Analysis and synthesis of stability matrices". *Journal of Differential Equations* **3**:3, pp. 414–422. DOI: 10.1016/0022-0396(67)90041-1.

Bernstein, D. S. and S. P. Bhat (1995). "Lyapunov stability, semistability, and asymptotic stability of matrix second-order systems". *Journal of Mechanical Design* **117**:B, pp. 145–153. ISSN: 1050-0472. DOI: 10.1115/1.2836448.

Bindle, L. (2021). *The PYVESC project*. Last accessed: 14/06-2021. URL: pyvesc.readthedocs.io/en/latest/.

Bitcraze (2021a). *Code reference for the master attitude controller in the Crazyflie*. Last accessed: 10-4-2021. URL: github.com/bitcraze/crazyflie-firmware/blob/master/src/modules/src/attitude_pid_controller.c.

Bitcraze (2021b). *Code reference for the master MEKF in the Crazyflie*. Last accessed: 10-4-2021. URL: github.com/bitcraze/crazyflie-firmware/blob/master/src/modules/src/kalman_core/kalman_core.c.

Bitcraze (2021c). *Product page of the Crazyflie 2.0*. Last accessed: 10-4-2021. URL: www.bitcraze.io/products/old-products/crazyflie-2-0.

Bitcraze (2021d). *Product page of the Loco positioning system (LPS)*. Last accessed: 10-4-2021. URL: www.bitcraze.io/documentation/system/positioning/loco-positioning-system.

Bloch, A. M., P. Krishnaprasad, J. E. Marsden, and T. S. Ratiu (1994). "Dissipation induced instabilities". In: *Annales de l'Institut Henri Poincare (C) Non Linear Analysis*. Vol. 11. 1. Elsevier, pp. 37–90. DOI: 10.1016/S0294-1449(16)30196-2.

Bosch Sensortec (2020). *BMI088: High-performance Inertial Measurement Unit (IMU)*. Last accessed: 2-12-2020. URL: www.bosch-sensortec.com.

Bouabdallah, S., A. Noth, and R. Siegwart (2004). "PID vs LQ control techniques applied to an indoor micro quadrotor". In: *2004 IEEE/RSJ International Conference on Intelligent Robots and Systems (IROS) IEEE Cat. No. 04CH37566*. Vol. 3. IEEE, pp. 2451–2456. DOI: 10.1109/IROS.2004.1389776.

Bouffard, P., A. Aswani, and C. Tomlin (2012). "Learning-based model predictive control on a quadrotor: onboard implementation and experimental results". In: *2012 IEEE International Conference on Robotics and Automation*. IEEE, pp. 279–284. DOI: 10.1109/ICRA.2012.6225035.

Brescianini, D. and R. D'Andrea (2018). "Tilt-prioritized quadrocopter attitude control". *IEEE Transactions on Control Systems Technology* **28**:2, pp. 376–387. DOI: 10.1109/TCST.2018.2873224.

Brescianini, D., M. Hehn, and R. D'Andrea (2013). *Nonlinear quadrocopter attitude control: Technical report*. Tech. rep. ETH Zurich. DOI: 10.3929/ethz-a-009970340.

Brouwer, L. (1909). "On continuous vector distributions on surfaces". *Proceedings 11*. Last accessed 05-05-2020. URL: www.dwc.knaw.nl/DL/publications/PU00013599.pdf.

Bullo, F. and R. M. Murray (1995). *Proportional derivative (PD) control on the Euclidean group*. Tech. rep. URL: www.resolver.caltech.edu/CaltechCDSTR:1995.CIT-CDS-95-010.

Butcher, J. C. (2016). *Numerical methods for ordinary differential equations*. 3rd ed. John Wiley & Sons, Chichester, West Sussex, United Kingdom. ISBN: 9781119121503.

Caccavale, F. and L. Villani (1999). "Output feedback control for attitude tracking". *Systems & Control Letters* **38**:2, pp. 91–98. DOI: 10.1016/S0167-6911(99)00050-X.

Ceccarelli, N., M. Di Marco, A. Garulli, and A. Giannitrapani (2008). "Collective circular motion of multi-vehicle systems". *Automatica* **44**:12, pp. 3025–3035. DOI: 10.1016/j.automatica.2008.04.024.

Chaturvedi, N. A., A. K. Sanyal, and N. H. McClamroch (2011). "Rigid-body attitude control". *IEEE Control Systems Magazine* **31**:3, pp. 30–51. DOI: 10.1109/MCS.2011.940459.

Chen, F., R. Jiang, K. Zhang, B. Jiang, and G. Tao (2016). "Robust backstepping sliding-mode control and observer-based fault estimation for a quadrotor UAV". *IEEE Transactions on Industrial Electronics* **63**:8, pp. 5044–5056. DOI: 10.1109/TIE.2016.2552151.

Chen, L., P. O. Arambel, and R. K. Mehra (2002). "Estimation under unknown correlation: covariance intersection revisited". *IEEE Transactions on Automatic Control* **47**:11, pp. 1879–1882. DOI: 10.1109/TAC.2002.804475.

Chetaev, N., M. Nadler, and A. Babister (1961). *The Stability of Motion*. 2nd ed. Pergamon Press, New York.

Cottle, R. W. (1974). "Manifestations of the Schur complement". *Linear Algebra and its Applications* **8**:3, pp. 189–211. DOI: 10.1016/0024-3795(74)90066-4.

Crouch, P. E. and R. Grossman (1993). "Numerical integration of ordinary differential equations on manifolds". *Journal of Nonlinear Science* **3**:1, pp. 1–33. DOI: 10.1007/BF02429858.

Cutler, M. and J. How (2012). "Actuator constrained trajectory generation and control for variable-pitch quadrotors". In: *AIAA Guidance, Navigation, and Control Conference*, p. 4777. DOI: 10.2514/6.2012-4777.

Das, A., F. Lewis, and K. Subbarao (2009). "Backstepping approach for controlling a quadrotor using lagrange form dynamics". *Journal of Intelligent and Robotic Systems* **56**:1, pp. 127–151. DOI: 10.1007/s10846-009-9331-0.

Deghat, M., I. Shames, B. D. O. Anderson, and C. Yu (2010). "Target localization and circumnavigation using bearing measurements in 2D". In: *49th IEEE Conference on Decision and Control (CDC)*. IEEE, pp. 334–339. DOI: 10.1109/CDC.2010.5717795.

Deghat, M., L. Xia, B. D. Anderson, and Y. Hong (2015). "Multi-target localization and circumnavigation by a single agent using bearing measurements". *International Journal of Robust and Nonlinear Control* **25**:14, pp. 2362–2374. DOI: 10.1002/rnc.3208.

Dempster, A. P., N. M. Laird, and D. B. Rubin (1977). "Maximum likelihood from incomplete data via the EM algorithm". *Journal of the Royal Statistical Society: Series B (Methodological)* **39**:1, pp. 1–22. DOI: 10.1111/j.2517-6161.1977.tb01600.x.

DJI (2021). *Product page of the DJI Matrice600 Pro*. Last accessed: 2-22-2021. URL: www.dji.com/matrice600-pro.

Ebeigbe, D., T. Berry, S. J. Schiff, and T. Sauer (2020). "Poisson Kalman filter for disease surveillance". *Physical Review Research* **2**:4, p. 043028. DOI: 10.1103/PhysRevResearch.2.043028.

Euston, M., P. Coote, R. Mahony, J. Kim, and T. Hamel (2008). "A complementary filter for attitude estimation of a fixed-wing UAV". In: *2008 IEEE/RSJ International Conference on Intelligent Robots and Systems*. IEEE, pp. 340–345. DOI: 10.1109/IROS.2008.4650766.

Ferrari-Trecate, G., F. A. Cuzzola, D. Mignone, and M. Morari (2001). "Analysis and control with performance of piecewise affine and hybrid systems". In: *Proceedings of the 2001 American Control Conference. (Cat. No. 01CH37148)*. Vol. 1. IEEE, pp. 200–205. DOI: 10.1109/ACC.2001.945542.

Fliess, M., J. Lévine, P. Martin, and P. Rouchon (1995). "Flatness and defect of non-linear systems: introductory theory and examples". *International Journal of Control* **61**:6, pp. 1327–1361. DOI: 10.1080/00207179508921959.

Fliess, M., J. Lévine, P. Martin, and P. Rouchon (1999). "A Lie-Bäcklund approach to equivalence and flatness of nonlinear systems". *IEEE Transactions on Automatic Control* **44**:5, pp. 922–937. DOI: 10.1109/9.763209.

Foehn, P. and D. Scaramuzza (2018). "Onboard state dependent LQR for agile quadrotors". In: *2018 IEEE International Conference on Robotics and Automation (ICRA)*. IEEE, pp. 6566–6572. DOI: 10.1109/ICRA.2018.8460885.

Forster, C., L. Carlone, F. Dellaert, and D. Scaramuzza (2017). "On-manifold preintegration for real-time visual–inertial odometry". *IEEE Transactions on Robotics* **33**:1, pp. 1–21. DOI: 10.1109/TRO.2016.2597321.

Fragopoulos, D. and M. Innocenti (2004). "Stability considerations in quaternion attitude control using discontinuous Lyapunov functions". *IEE Proceedings-Control Theory and Applications* **151**:3, pp. 253–258. DOI: 10.1049/ip-cta:20040311.

Fresk, E. and G. Nikolakopoulos (2013). "Full quaternion based attitude control for a quadrotor". In: *2013 European Control Conference (ECC)*. IEEE, pp. 3864–3869. DOI: 10.23919/ECC.2013.6669617.

Garcia, C. E., D. M. Prett, and M. Morari (1989). "Model predictive control: theory and practice—a survey". *Automatica* **25**:3, pp. 335–348. DOI: 10.1016/0005-1098(89)90002-2.

Garcia, R., F. Rubio, and M. Ortega (2012). "Robust PID control of the quadrotor helicopter". *IFAC Proceedings Volumes* **45**:3, pp. 229–234. DOI: 20120328-3-IT-3014.00039.

Gibson, S. and B. Ninness (2005). "Robust maximum-likelihood estimation of multivariable dynamic systems". *Automatica* **41**:10, pp. 1667–1682. DOI: 10.1016/j.automatica.2005.05.008.

Goodarzi, F., D. Lee, and T. Lee (2013). "Geometric nonlinear PID control of a quadrotor UAV on SE(3)", pp. 3845–3850. DOI: 10.23919/ECC.2013.6669644.

Grant, M. and S. Boyd (2014). *CVX: matlab software for disciplined convex programming, version 2.1*. Last accessed: 8-8-2021. URL: http://cvxr.com/cvx.

Greiff, M. and A. Robertsson (2018). "Incremental reference generation for nonsingular control on SE(3)". In: *2018 IEEE Conference on Control Technology and Applications (CCTA)*, pp. 132–137. DOI: 10.1109/CCTA.2018.8511419.

Greiff, M. (2017). *Modelling and control of the Crazyflie quadrotor for aggressive and autonomous flight by optical flow driven state estimation*. MA thesis. Lund University. ISBN: 0280-5316.

Greiff, M. (2018). "A time-warping transformation for time-optimal movement in differentially flat systems". In: *2018 Annual American Control Conference (ACC)*. IEEE, pp. 6723–6730. DOI: 10.23919/ACC.2018.8431230.

Greiff, M. (2020). *AerialVehicleControl.jl:, nonlinear and robust UAV control system synthesis*. Last accessed: 30/12-2020. DOI: https://doi.org/10.24433/CO.8469162.v1. URL: github.com/mgreiff/AerialVehicleControl.jl.

Greiff, M. (2021). *Circumnavigation-Control: a Python implementation of a target tracking controller*. Last accessed: 8-8-2021. CodeOcean. DOI: https://doi.org/10.24433/CO.1177566.v1. URL: github.com/mgreiff/circumnavigation-control/.

Greiff, M. and K. Berntorp (2018). "Evaluation of the discrete time feedback particle filter for IMU-driven systems configured on SE(2)". In: *2018 Annual American Control Conference (ACC)*. IEEE, pp. 5683–5689. DOI: 10.23919/ACC.2018.8431134.

Greiff, M. and K. Berntorp (2020). "Optimal measurement projections with adaptive mixture Kalman filtering for GNSS positioning". In: *2020 American Control Conference (ACC)*. IEEE, pp. 4435–4441. DOI: 10.23919/ACC45564.2020.9147675.

Greiff, M., K. Berntorp, S. Di Cairano, and K. Kim (2021a). "Mixed-integer linear regression Kalman filters for GNSS positioning". In: *IEEE Conference on Control Technology and Applications (CCTA)*. Article in press. San Diego, CA, USA.

Greiff, M., M. Deghat, Z. Sun, and A. Robertsson (2021b). "Target localization and circumnavigation with integral action in R^2". *IEEE Control Systems Letters* **6**, pp. 1250–1255. DOI: 10.1109/LCSYS.2021.3091633.

Greiff, M., P. Persson, Z. Sun, A. Robertsson, and K. Åström (2021c). "Quadrotor control on SU(2) x R3 with SLAM integration". Version 1. arXiv: 2110.01099 [eess.SY]. URL: arxiv.org/abs/2110.01099.

Greiff, M. and A. Robertsson (2017). "Optimisation-based motion planning with obstacles and priorities". *IFAC-PapersOnLine* **50**:1, pp. 11670–11676. DOI: 10.1016/j.ifacol.2017.08.1677.

Greiff, M., A. Robertsson, and K. Berntorp (2019a). "Performance bounds in positioning with the VIVE lighthouse system". In: *2019 22th International Conference on Information Fusion (FUSION)*. IEEE, pp. 1–8. ISBN: 978-1-7281-1840-6.

Greiff, M., A. Robertsson, and K. Berntorp (2020a). "Exploiting linear substructure in linear regression Kalman filters". In: *2020 59th IEEE Conference on Decision and Control (CDC)*. IEEE, pp. 2942–2948. DOI: 10.1109/CDC42340.2020.9304191.

Greiff, M., A. Robertsson, and K. Berntorp (2020b). "MSE-optimal measurement dimension reduction in Gaussian filtering". In: *2020 IEEE Conference on Control Technology and Applications (CCTA)*. IEEE, pp. 126–133. DOI: 10.1109/CCTA41146.2020.9206162.

Greiff, M., E. Rofors, A. Robertsson, R. Johansson, and R. Tyllström (2021d). "Gamma-ray imaging with spatially continuous intensity statistics". In: *2021 International Conference on Intelligent Robots and Systems (IROS)*. Article in press. IEEE.

Greiff, M., Z. Sun, and A. Robertsson (2021e). "Tuning and analysis of geometric tracking controllers on SO(3)". In: *2021 American Control Conference (ACC)*. IEEE, pp. 1674–1680. DOI: 10.23919/ACC50511.2021.9482745.

Greiff, M., Z. Sun, and A. Robertsson (2020c). "Coordination control of double-integrator systems with time-varying weighted inputs". *IFAC-PapersOnLine* **53**:2, pp. 2489–2494. DOI: 10.1016/j.ifacol.2020.12.202.

Greiff, M., Z. Sun, and A. Robertsson (2021f). "Attitude control on SU(2): stability, robustness, and similarities". *IEEE Control Systems Letters* **6**, pp. 73–78. DOI: 10.1109/LCSYS.2021.3049440.

Greiff, M., Z. Sun, A. Robertsson, and R. Johansson (2019b). "Temporal viability regulation for control affine systems with applications to mobile vehicle coordination under time-varying motion constraints". In: *2019 18th European Control Conference (ECC)*. IEEE, pp. 3571–3576. DOI: 10.23919/ECC.2019.8796018.

Hahn, W. (1967). *Stability of motion*. Vol. 138. Springer Verlag, Berlin, Germany. ISBN: 978-3-642-50085-5.

Hall, B. (2015). *Lie groups, Lie algebras, and representations: an elementary introduction*. Vol. 222. Springer International Publishing, Switzerland. ISBN: 978-3-319-13466-6. DOI: 0.1007/978-3-319-13467-3.

Hegrenæs, Ø., J. T. Gravdahl, and P. Tøndel (2005). "Spacecraft attitude control using explicit model predictive control". *Automatica* **41**:12, pp. 2107–2114. DOI: 10.1016/j.automatica.2005.06.015.

Hellfeld, D., T. H. Joshi, M. S. Bandstra, R. J. Cooper, B. J. Quiter, and K. Vetter (2019). "Gamma-ray point-source localization and sparse image reconstruction using Poisson likelihood". *IEEE Transactions on Nuclear Science* **66**:9, pp. 2088–2099. DOI: 10.1109/TNS.2019.2930294.

Higham, N. (1989). "Matrix nearness problems and applications". Last accessed: 08-08-2021, pp. 1–27. URL: citeseerx.ist.psu.edu/viewdoc/summary?doi=10.1.1.35.2899.

Hitz, G., E. Galceran, M.-È. Garneau, F. Pomerleau, and R. Siegwart (2017). "Adaptive continuous-space informative path planning for online environmental monitoring". *Journal of Field Robotics* **34**:8, pp. 1427–1449. DOI: 10.1002/rob.21722.

Hoffman, K. and R. A. Kunze (1971). *Linear Algebra*. 2nd ed. Prentice-Hall, Englewood Cliffs, New Jersey, USA. ISBN: 978-8-120-30270-9.

How, J. P., B. Behihke, A. Frank, D. Dale, and J. Vian (2008). "Real-time indoor autonomous vehicle test environment". *IEEE Control Systems Magazine* **28**:2, pp. 51–64. DOI: 10.1109/MCS.2007.914691.

Huang, M., B. Xian, C. Diao, K. Yang, and Y. Feng (2010). "Adaptive tracking control of underactuated quadrotor unmanned aerial vehicles via backstepping". In: *Proceedings of the 2010 American Control Conference*. IEEE, pp. 2076–2081. DOI: 10.1109/ACC.2010.5531424.

Hurley, M. B. (2002). "An information theoretic justification for covariance intersection and its generalization". In: *Proceedings of the Fifth International Conference on Information Fusion. FUSION 2002.* Vol. 1. IEEE, pp. 505–511. DOI: 10.1109/ICIF.2002.1021196.

Jackiewicz, Z., A. Marthinsen, and B. Owren (2000). "Construction of Runge–Kutta methods of Crouch–Grossman type of high order". *Advances in Computational Mathematics* **13**:4, pp. 405–415. DOI: 10.1023/A:1016645730465.

Jang, Y., C. Oh, Y. Lee, and H. J. Kim (2021). "Multirobot collaborative monocular SLAM utilizing rendezvous". *IEEE Transactions on Robotics*. Article in press. DOI: 10.1109/TRO.2021.3058502.

Johansson, M. and A. Rantzer (1997). "Computation of piecewise quadratic lyapunov functions for hybrid systems". In: *1997 European Control Conference (ECC)*. IEEE, pp. 2005–2010. DOI: 10.23919/ECC.1997.7082399.

Joshi, T. H., B. J. Quiter, J. S. Maltz, M. S. Bandstra, A. Haefner, N. Eikmeier, E. Wagner, T. Luke, R. Malchow, and K. McCall (2017). "Measurement of the energy-dependent angular response of the ARES detector system and application to aerial imaging". *IEEE Transactions on Nuclear Science* **64**:7, pp. 1754–1760. DOI: 10.1109/TNS.2017.2693988.

Kaufmann, E., A. Loquercio, R. Ranftl, M. Müller, V. Koltun, and D. Scaramuzza (2020). "Deep drone acrobatics". arXiv: 2006.05768 [cs.RO].

Khalil, H. (1996). *Nonlinear systems*. 2nd ed. Prentice hall Upper Saddle River, New Jersey, USA. ISBN: 978-0-132-28024-2.

Khalil, H. (2002). *Nonlinear systems*. 3rd ed. Prentice hall Upper Saddle River, New Jersey, USA. ISBN: 978-0-130-67389-3.

Kim, J., S. A. Gadsden, and S. A. Wilkerson (2019). "A comprehensive survey of control strategies for autonomous quadrotors". *Canadian Journal of Electrical and Computer Engineering* **43**:1, pp. 3–16. DOI: 10.1109/CJECE.2019.2920938.

Kim, T.-H. and T. Sugie (2007). "Cooperative control for target-capturing task based on a cyclic pursuit strategy". *Automatica* **43**:8, pp. 1426–1431. DOI: 10.1016/j.automatica.2007.01.018.

Lee, D., H. J. Kim, and S. Sastry (2009). "Feedback linearization vs. adaptive sliding mode control for a quadrotor helicopter". *International Journal of control, Automation and systems* **7**:3, pp. 419–428. DOI: 10.1007/s12555-009-0311-8.

Lee, T. (2008). *Computational geometric mechanics and control of rigid bodies*. PhD thesis. University of Michigan. ISBN: 978-0-549-81782-6.

Lee, T. (2015). "Global exponential attitude tracking controls on SO(3)". *IEEE Transactions on Automatic Control* **60**:10, pp. 2837–2842. DOI: 10.1109/TAC.2015.2407452.

Lee, T., M. Leok, and N. H. McClamroch (2010). "Geometric tracking control of a quadrotor UAV on SE(3)". In: *49th IEEE Conference on Decision and Control (CDC)*. IEEE, pp. 5420–5425. DOI: 10.1109/CDC.2010.5717652.

Lee, T., M. Leok, and N. H. McClamroch (2011). "Control of complex maneuvers for a quadrotor UAV using geometric methods on SE(3)". Version 4. arXiv: 1003.2005 [math.OC]. URL: arxiv.org/abs/1003.2005.

Lee, T., M. Leok, and N. H. McClamroch (2013). "Nonlinear robust tracking control of a quadrotor UAV on SE(3)". *Asian Journal of Control* **15**:2, pp. 391–408. DOI: 10.1002/asjc.567.

Lee, T., M. Leok, and N. H. McClamroch (2017). *Global formulations of Lagrangian and Hamiltonian dynamics on manifolds*. 1st ed. Springer. ISBN: 978-3-319-56951-2.

Lefeber, A. A. J. (2000). *Tracking control of nonlinear mechanical systems*. PhD thesis. ISBN: 90-365-1426-6.

Lefeber, E., S. van den Eijnden, and H. Nijmeijer (2017). "Almost global tracking control of a quadrotor UAV on SE(3)". In: *2017 IEEE 56th Annual Conference on Decision and Control (CDC)*. IEEE, pp. 1175–1180. DOI: 10.1109/CDC.2017.8263815.

Lefeber, E., M. Greiff, and A. Robertsson (2020). "Filtered output feedback tracking control of a quadrotor UAV". *IFAC-PapersOnLine* **53**:2, pp. 5764–5770. DOI: 10.1016/j.ifacol.2020.12.1609.

Lewis, A. D. and R. M. Murray (1997). "Configuration controllability of simple mechanical control systems". *SIAM Journal on Control and Optimization* **35**:3, pp. 766–790. DOI: 10.1137/S0363012995287155.

Li, R., Y. Shi, and Y. Song (2018). "Localization and circumnavigation of multiple agents along an unknown target based on bearing-only measurement: a three dimensional solution". *Automatica* **94**, pp. 18–25. DOI: 10.1016/j.automatica.2018.04.005.

Liu, T. and B. Li (2017). "Single-frequency BDS/GPS RTK with low-cost u-blox receivers". In: *2017 Forum on Cooperative Positioning and Service (CPGPS)*. IEEE, pp. 232–238. DOI: 10.1109/CPGPS.2017.8075131.

Loria, A. and E. Panteley (2005). *2 cascaded nonlinear time-varying systems: Analysis and design, in Advanced topics in control systems theory: Lecture Notes in Control and Information Science*. Vol. 311. Springer, London, pp. 23–64. DOI: 10.1007/11334774_2.

Loria, A., E. Panteley, D. Popovic, and A. R. Teel (2005). "A nested matrosov theorem and persistency of excitation for uniform convergence in stable nonautonomous systems". *IEEE Transactions on Automatic Control* **50**:2, pp. 183–198. DOI: 10.1109/TAC.2004.841939.

Loria, A., E. Panteley, and A. Teel (2000). "UGAS of nonlinear time-varying systems: a delta-persistency of excitation approach". In: *Proceedings of the 39th IEEE Conference on Decision and Control (Cat. No. 00CH37187)*. Vol. 4. IEEE, pp. 3489–3494. DOI: 10.1109/CDC.2000.912244.

Luukkonen, T. (2011). "Modelling and control of quadcopter". *Independent research project in applied mathematics, Espoo* **22**. Last accessed: 08-08-2021, p. 22. URL: https://www.mecharithm.com/wp-content/uploads/2020/11/quadrotor_dynamics.pdf.

Lyapunov, A. M. (1892). "Obschaya zadacha ob ustoicivosti dvizeniya (The general problem of the stability of motion)". *Kharkov Mathematical Society, Kharkov*.

Lyapunov, A. M. (1992). "The general problem of the stability of motion". *International Journal of Control* **55**:3, pp. 531–534. DOI: 10.1080/00207179208934253.

Mahony, R., T. Hamel, and J.-M. Pflimlin (2008). "Nonlinear complementary filters on the special orthogonal group". *IEEE Transactions on Automatic Control* **53**:5, pp. 1203–1218. DOI: 10.1109/TAC.2008.923738.

Mahony, R., V. Kumar, and P. Corke (2012). "Multirotor aerial vehicles: Modeling, estimation, and control of quadrotor". *IEEE Robotics and Automation Magazine* **19**:3, pp. 20–32. DOI: 10.1109/MRA.2012.2206474.

Manikonda, V., P. Arambel, M. Gopinathan, R. Mehra, and F. Hadaegh (1999). "A model predictive control-based approach for spacecraft formation keeping and attitude control". In: *Proceedings of the 1999 American Control Conference (Cat. No. 99CH36251)*. Vol. 6. IEEE, pp. 4258–4262. DOI: 10.1109/ACC.1999.786367.

Marshall, J. A., M. E. Broucke, and B. A. Francis (2006). "Pursuit formations of unicycles". *Automatica* **42**:1, pp. 3–12. DOI: 10.1016/j.automatica.2005.08.001.

Matrosov, V. (1962). "On the stability of motion". *Journal of Applied Mathematics and Mechanics* **26**:5, pp. 1337–1353. DOI: 10.1016/0021-8928(62)90010-2.

Matveev, A. S., A. A. Semakova, and A. V. Savkin (2016). "Range-only based circumnavigation of a group of moving targets by a non-holonomic mobile robot". *Automatica* **65**, pp. 76–89. DOI: 10.1016/j.automatica.2015.11.032.

Mayhew, C. G., R. G. Sanfelice, and A. R. Teel (2011a). "On quaternion-based attitude control and the unwinding phenomenon". In: *Proceedings of the 2011 American Control Conference*. IEEE, pp. 299–304. DOI: 10.1109/ACC.2011.5991127.

Mayhew, C. G., R. G. Sanfelice, and A. R. Teel (2011b). "Quaternion-based hybrid control for robust global attitude tracking". *IEEE Transactions on Automatic control* **56**:11, pp. 2555–2566. DOI: 10.1109/TAC.2011.2108490.

Mayhew, C. G., R. G. Sanfelice, and A. R. Teel (2012). "On path-lifting mechanisms and unwinding in quaternion-based attitude control". *IEEE Transactions on Automatic Control* **58**:5, pp. 1179–1191. DOI: 10.1109/TAC.2012.2235731.

Meckes, E. S. (2019). *The random matrix theory of the classical compact groups*. 1st ed. Vol. 218. Cambridge University Press. ISBN: 9781108303453.

Mellinger, D., N. Michael, and V. Kumar (2012). "Trajectory generation and control for precise aggressive maneuvers with quadrotors". *The International Journal of Robotics Research* **31**:5, pp. 664–674. DOI: 10.1177/0278364911434236.

Merheb, A.-R., H. Noura, and F. Bateman (2015). "Design of passive fault-tolerant controllers of a quadrotor based on sliding mode theory". *International Journal of Applied Mathematics and Computer Science* **25**:3. DOI: 10.1109/SysTol.2013.6693910.

Micaelli, A. (1993). *Trajectory tracking for unicycle-type and two-steering-wheels mobile robots*. Tech. rep. RR-2097, INRIA. inria-00074575. URL: hal.inria.fr/inria-00074575.

Miller, E. A., S. M. Robinson, K. K. Anderson, J. D. McCall, A. M. Prinke, J. B. Webster, and C. E. Seifert (2015). "Adaptively reevaluated bayesian localization (ARBL): a novel technique for radiological source localization". *Nuclear Instruments and Methods in Physics Research Section A: Accelerators, Spectrometers, Detectors and Associated Equipment* **784**, pp. 332–338. DOI: 10.1016/j.nima.2015.01.038.

Miller, M. I., D. L. Snyder, and T. R. Miller (1985). "Maximum-likelihood reconstruction for single-photon emission computed-tomography". *IEEE Transactions on Nuclear Science* **32**:1, pp. 769–778. DOI: 10.1109/TNS.1985.4336939.

Milutinović, D., D. Casbeer, Y. Cao, and D. Kingston (2017). "Coordinate frame free dubins vehicle circumnavigation using only range-based measurements". *International Journal of Robust and Nonlinear Control* **27**:16, pp. 2937–2960. DOI: 10.1002/rnc.3718.

Mishra, H., M. De Stefano, A. M. Giordano, R. Lampariello, and C. Ott (2020). "A geometric controller for fully-actuated robotic capture of a tumbling target". In: *2020 American Control Conference (ACC)*. IEEE, pp. 2150–2157. DOI: 10.23919/ACC45564.2020.9147294.

Mo, H. and G. Farid (2019). "Nonlinear and adaptive intelligent control techniques for quadrotor UAV–a survey". *Asian Journal of Control* **21**:2, pp. 989–1008. DOI: 10.1002/asjc.1758.

Mokhtari, A. and A. Benallegue (2004). "Dynamic feedback controller of Euler angles and wind parameters estimation for a quadrotor unmanned aerial vehicle". In: *IEEE International Conference on Robotics and Automation, 2004. Proceedings. ICRA'04. 2004.* Vol. 3. IEEE, pp. 2359–2366. DOI: 10.1109/ROBOT.2004.1307414.

Mortensen, R. E. (1968). "A globally stable linear attitude regulator". *International Journal of Control* **8**:3, pp. 297–302. DOI: 10.1080/00207176808905679.

Mueller, M. W., M. Hamer, and R. D'Andrea (2015). "Fusing ultra-wideband range measurements with accelerometers and rate gyroscopes for quadrocopter state estimation". In: *2015 IEEE International Conference on Robotics and Automation (ICRA)*. IEEE, pp. 1730–1736. DOI: 10.1109/ICRA.2015.7139421.

Mueller, M. W., M. Hehn, and R. D'Andrea (2016). "Covariance correction step for Kalman filtering with an attitude". *Journal of Guidance, Control, and Dynamics*, pp. 1–7. DOI: 10.2514/1.G000848.

Müller, P. C. and W. O. Schiehlen (1977). *Forced linear vibrations*. 1st ed. Vol. 172. Springer. ISBN: 978-3-211-81487-1. DOI: 10.1007/978-3-7091-4356-8.

Murphy, K. P. (2012). *Machine learning: a probabilistic perspective*. 1st ed. MIT press, Cambridge, MA, USA. ISBN: 978-0-262-01802-9.

Nieuwstadt, M. van, M. Rathinam, and R. M. Murray (1994). "Differential flatness and absolute equivalence". In: *Decision and Control, 1994., Proceedings of the 33rd IEEE Conference on*. Vol. 1. IEEE, pp. 326–332. DOI: 10.1109/CDC.1994.410908.

O'Kelly, M., V. Sukhil, H. Abbas, J. Harkins, C. Kao, Y. V. Pant, R. Mangharam, D. Agarwal, M. Behl, P. Burgio, and M. Bertogna (2019). "F1/10: an open-source autonomous cyber-physical platform". arXiv: 1901.08567 [cs.RO]. URL: arxiv.org/abs/1901.08567.

Ortec (2021). *Product page of the DigiBASE 14-pin PMT base with integrated bias supply, preamplifier, and MCA with digital signal processing*. Last accessed: 2/22-2021. URL: www.ortec-online.com/products/electronics/photomultiplier-tube-bases/digibase.

Panteley, E., A. Loría, and A. Teel (1999). "UGAS of NLTV systems: applications to adaptive control". *Technical Report 99-160, Lab. d'Automatique de Grenoble, UMR 5528, CNRS*.

Panteley, E. and A. Loria (1998). "On global uniform asymptotic stability of nonlinear time-varying systems in cascade". *Systems & Control Letters* **33**:2, pp. 131–138. DOI: 10.1016/S0167-6911(97)00119-9.

Parks, P. C. (1962). "A new proof of the Routh-Hurwitz stability criterion using the second method of Liapunov". In: *Mathematical Proceedings of the Cambridge Philosophical Society*. Vol. 58. 4. Cambridge University Press, pp. 694–702. DOI: 10.1017/S030500410004072X.

Persson, P. (2018). *Real-Time Monocular SLAM System Using an Inertial Measurement Unit to Estimate the Metric Scale and Gravity Direction*. MA thesis. Lund University. ISBN: 1404-6342.

PixHawk (2021). *Attitude controller in the PX4-autopilot*. Last accessed: 4/10-2021. URL: github.com/PX4/PX4-Autopilot/blob/master/src/modules/fw_att_control/ecl_roll_controller.cpp.

Popović, M., T. Vidal-Calleja, G. Hitz, J. J. Chung, I. Sa, R. Siegwart, and J. Nieto (2020). "An informative path planning framework for UAV-based terrain monitoring". *Autonomous Robots* **44**:6, pp. 889–911. DOI: 10.1007/s10514-020-09903-2.

Rathinam, M. and R. M. Murray (1998). "Configuration flatness of Lagrangian systems underactuated by one control". *SIAM Journal on Control and Optimization* **36**:1, pp. 164–179. DOI: 10.1137/S0363012996300987.

Rublee, E., V. Rabaud, K. Konolige, and G. Bradski (2011). "ORB: an efficient alternative to SIFT or SURF". In: *2011 International Conference on Computer Vision*, pp. 2564–2571. DOI: 10.1109/ICCV.2011.6126544.

Ryan, T. and H. J. Kim (2013). "LMI-based gain synthesis for simple robust quadrotor control". *IEEE Transactions on Automation Science and Engineering* **10**:4, pp. 1173–1178. DOI: 10.1109/TASE.2013.2259156.

Salcudean, S. (1991). "A globally convergent angular velocity observer for rigid body motion". *IEEE transactions on Automatic Control* **36**:12, pp. 1493–1497. DOI: 10.1109/9.106169.

Sanyal, A. and N. Chaturvedi (2008). "Almost global robust attitude tracking control of spacecraft in gravity". In: *AIAA Guidance, Navigation and Control Conference and Exhibit*, p. 6979. DOI: 10.2514/6.2008-6979.

Särkkä, S. (2013). *Bayesian filtering and smoothing*. Vol. 3. Cambridge University Press, University Printing House, United Kingdom. ISBN: 9781107030657.

Shames, I., S. Dasgupta, B. Fidan, and B. D. Anderson (2011). "Circumnavigation using distance measurements under slow drift". *IEEE Transactions on Automatic Control* **57**:4, pp. 889–903. DOI: 10.1109/TAC.2011.2173417.

Shao, J. and Y.-P. Tian (2018). "Multi-target localisation and circumnavigation by a multi-agent system with bearing measurements in 2D space". *International Journal of Systems Science* **49**:1, pp. 15–26. DOI: 10.1080/00207721.2017.1397803.

Shao, X., J. Liu, and H. Wang (2018). "Robust back-stepping output feedback trajectory tracking for quadrotors via extended state observer and sigmoid tracking differentiator". *Mechanical Systems and Signal Processing* **104**, pp. 631–647. DOI: 10.1016/j.ymssp.2017.11.034.

Shepp, L. A. and Y. Vardi (1982). "Maximum likelihood reconstruction for emission tomography". *IEEE Transactions on Medical Imaging* **1**:2, pp. 113–122. DOI: 10.1109/TMI.1982.4307558.

Slegers, N., J. Kyle, and M. Costello (2006). "Nonlinear model predictive control technique for unmanned air vehicles". *Journal of Guidance, Control, and Dynamics* **29**:5, pp. 1179–1188. DOI: 10.2514/1.21531.

Sola, J. (2017). "Quaternion kinematics for the error-state Kalman filter". Version 1. arXiv: 1711.02508 [cs.RO]. URL: arxiv.org/abs/1711.02508.

Sun, S., A. Romero, P. Foehn, E. Kaufmann, and D. Scaramuzza (2021). "A comparative study of nonlinear MPC and differential-flatness-based control for quadrotor agile flight". arXiv: 2109.01365 [cs.RO]. URL: arxiv.org/abs/2109.01365.

Sun, Z., M. Greiff, A. Robertsson, and R. Johansson (2019). "Feasible coordination of multiple homogeneous or heterogeneous mobile vehicles with various constraints". In: *2019 International Conference on Robotics and Automation (ICRA)*. IEEE, pp. 1008–1013. DOI: 10.1109/ICRA.2019.8793834.

Sveier, A., A. M. Sjøberg, and O. Egeland (2019). "Applied Runge–Kutta–Munthe-Kaas integration for the quaternion kinematics". *Journal of Guidance, Control, and Dynamics* **42**:12, pp. 2747–2754. DOI: 10.2514/1.G004578.

Tayebi, A. (2008). "Unit quaternion-based output feedback for the attitude tracking problem". *IEEE Transactions on Automatic Control* **53**:6, pp. 1516–1520. DOI: 10.1109/TAC.2008.927789.

Tayebi, A. and S. McGilvray (2006). "Attitude stabilization of a VTOL quadrotor aircraft". *IEEE Transactions on Control Systems Technology* **14**:3, pp. 562–571. DOI: 10.1109/TCST.2006.872519.

Teledyne (2021). *Teledyne Brown Engineering*. Last accessed: 2/22-2021. URL: www.tbe.com/lab/quality.

Toh, K.-C., M. J. Todd, and R. H. Tütüncü (1999). "SDPT3—a MATLAB software package for semidefinite programming, version 1.3". *Optimization Methods and Software* **11**:1-4, pp. 545–581. DOI: 10.1080/10556789908805762.

Tsiotras, P. (1995). "New control laws for the attitude stabilization of rigid bodies". In: *Automatic Control in Aerospace 1994 (Aerospace Control'94)*. Elsevier, pp. 321–326. DOI: 10.1016/B978-0-08-042238-1.50054-9.

Tsiotras, P. (1998). "Further passivity results for the attitude control problem". *IEEE Transactions on Automatic Control* **43**:11, pp. 1597–1600. DOI: 10.1109/9.728877.

Tsoulfanidis, N. (1995). *Measurement and detection of radiation*. 2nd ed. Taylor & Francis Inc, WA, USA. ISBN: 9781560323174.

Vavrek, J. R., D. Hellfeld, M. S. Bandstra, V. Negut, K. Meehan, W. J. Vanderlip, J. W. Cates, R. Pavlovsky, B. J. Quiter, R. J. Cooper, et al. (2020). "Reconstructing the position and intensity of multiple gamma-ray point sources with a sparse parametric algorithm". *IEEE Transactions on Nuclear Science* **67**:11, pp. 2421–2430. DOI: 10.1109/TNS.2020.3024735.

Vedder, B. (2021). *The VESC project*. Last accessed: 14/06-2021. URL: www.vesc-project.com.

Vrieze, S. I. (2012). "Model selection and psychological theory: a discussion of the differences between the Akaike information criterion (AIC) and the Bayesian information criterion (BIC)". *Psychological Methods* **17**:2, p. 228. DOI: 10.1037/a0027127.

Wie, B. and P. M. Barba (1985). "Quaternion feedback for spacecraft large angle maneuvers". *Journal of Guidance, Control, and Dynamics* **8**:3, pp. 360–365. DOI: doi.org/10.2514/3.19988.

Zeng, X., H. Nijmeijer, and A. Lefeber (2021). *Implementing Tracking Error Control for Quadrotor UAV*. MA thesis.

Zhao, S. and D. Zelazo (2015). "Bearing rigidity and almost global bearing-only formation stabilization". *IEEE Transactions on Automatic Control* **61**:5, pp. 1255–1268. DOI: 10.1109/TAC.2015.2459191.

Zou, Y. (2016). "Trajectory tracking controller for quadrotors without velocity and angular velocity measurements". *IET Control Theory & Applications* **11**:1, pp. 101–109. DOI: 10.1049/iet-cta.2016.0647.

Zou, Y., L. Wang, and Z. Meng (2020). "Distributed localization and circumnavigation algorithms for a multiagent system with persistent and intermittent bearing measurements". *IEEE Transactions on Control Systems Technology*. DOI: 10.1109/TCST.2020.3032395.

A

Preliminaries

A.1 Lie maps

For the considered matrix Lie groups, either SO(3) or SU(2), the exponential map $\mathrm{Exp}_G : \mathfrak{g} \to G$ is equivalent to the matrix exponential,

$$\mathrm{Exp}_G([\boldsymbol{\omega}]_G^\wedge) = \sum_{j=0}^{\infty} \frac{1}{j!}([\boldsymbol{\omega}]_G^\wedge)^j. \tag{A.1}$$

This power series reduces to simpler analytical expressions given in Definitions 2.9 and 2.10, here derived for SO(3) and SU(2) separately.

A.1.1 Exponential and Logarithmic Maps on SO(3)

Before defining the exponential map associated with SO(3), we recall the *hat*-map in Definition 2.12, and its relation to the screw operator $\boldsymbol{S} : \mathbb{R}^3 \to \mathfrak{so}(3)$ in Definition 2.8. For this skew-symmetric operator, we have that $\boldsymbol{S}(\boldsymbol{\omega})^\top = -\boldsymbol{S}(\boldsymbol{\omega})$ for any $\boldsymbol{\omega} \in \mathbb{R}^3$. Thus, for any unit vector $\boldsymbol{u} \in \mathbb{R}^3$,

$$\boldsymbol{S}(\boldsymbol{u})^2 = \boldsymbol{u}\boldsymbol{u}^\top - \boldsymbol{I}, \;\; \boldsymbol{S}(\boldsymbol{u})^n = -\boldsymbol{S}(\boldsymbol{u})^{n-2}, \;\; \boldsymbol{S}(\boldsymbol{\omega})^n = \theta^n \boldsymbol{S}(\boldsymbol{u})^n, \forall n > 1. \tag{A.2}$$

Now, as $[\boldsymbol{\omega}]_{\mathrm{SO}(3)}^\wedge = \boldsymbol{S}(\boldsymbol{\omega})$, if $\boldsymbol{\omega} = \theta\boldsymbol{u}$ with $\|\boldsymbol{u}\| = 1$ and $\theta \in \mathbb{R}$, we note that

$$([\boldsymbol{\omega}]_{\mathrm{SO}(3)}^\wedge)^{2n+1} = (-1)^n \theta^{2n+1} \boldsymbol{S}(\boldsymbol{u}), \quad ([\boldsymbol{\omega}]_{\mathrm{SO}(3)}^\wedge)^{2n+2} = (-1)^n \theta^{2n+2} \boldsymbol{S}(\boldsymbol{u})^2,$$

for all $n \geq 0$. Knowing this, the power-series in (A.1) simplifies as

$$\begin{aligned}
\boldsymbol{R} &= \sum_{n=0}^{\infty} \frac{1}{j!}([\boldsymbol{\omega}]_{\mathrm{SO}(3)}^\wedge)^j && \text{(A.3a)} \\
&= \boldsymbol{I} + \Big[\sum_{n=0}^{\infty} \frac{(-1)^n \theta^{2n+1}}{(2n+1)!}\Big] \boldsymbol{S}(\boldsymbol{u}) + \Big[1 - \sum_{n=0}^{\infty} \frac{(-1)^n \theta^{2n}}{(2n)!}\Big] \boldsymbol{S}(\boldsymbol{u})^2 && \text{(A.3b)} \\
&= \boldsymbol{I} + \sin(\theta)\boldsymbol{S}(\boldsymbol{u}) + (1 - \cos(\theta))\boldsymbol{S}(\boldsymbol{u})^2 && \text{(A.3c)} \\
&= \boldsymbol{I} + \mathrm{sinc}(\theta)[\boldsymbol{\omega}]_{\mathrm{SO}(3)}^\wedge + \frac{\mathrm{sinc}(\theta/2)^2}{2}([\boldsymbol{\omega}]_{\mathrm{SO}(3)}^\wedge)^2 \in \mathrm{SO}(3), && \text{(A.3d)}
\end{aligned}$$

which, it should be noted, is well defined for all $\theta \in \mathbb{R}$. Inversely,

$$\theta = \arccos\Big(\frac{\mathrm{Tr}(\boldsymbol{R}) - 1}{2}\Big), \qquad [\boldsymbol{\omega}]^{\wedge}_{\mathrm{SO}(3)} = \frac{1}{2\mathrm{sinc}(\theta)}(\boldsymbol{R} - \boldsymbol{R}^{\top}). \tag{A.4}$$

As such, the exponential map $\mathrm{Exp}_{\mathrm{SO}(3)} : \mathfrak{so}(3) \to \mathrm{SO}(3)$ is given by (A.3), and the inverse logarithmic map $\mathrm{Log}_{\mathrm{SO}(3)} : \mathrm{SO}(3) \to \mathfrak{so}(3)$ is given by (A.4).

A.1.2 Exponential and Logarithmic Maps on SU(2)

As for $\boldsymbol{X} \in \mathrm{SU}(2)$, if $\boldsymbol{\omega} = \theta\boldsymbol{u}$ with $\|\boldsymbol{u}\| = 1$, a very similar set of identities to (A.2) can be shown, here summarized as follows

$$([\boldsymbol{u}]^{\wedge}_{\mathrm{SU}(2)})^2 = -\boldsymbol{I}, \tag{A.5a}$$

$$([\boldsymbol{u}]^{\wedge}_{\mathrm{SU}(2)})^n = -([\boldsymbol{u}]^{\wedge}_{\mathrm{SU}(2)})^{n-2}, \tag{A.5b}$$

$$([\boldsymbol{\omega}]^{\wedge}_{\mathrm{SU}(2)})^n = \theta^n([\boldsymbol{u}]^{\wedge}_{\mathrm{SU}(2)})^n, \tag{A.5c}$$

for all $n > 1$. With these expressions, the exponential series in (A.1) becomes

$$\boldsymbol{X} = \sum_{j=0}^{\infty} \frac{1}{j!}([\boldsymbol{\omega}]^{\wedge}_{\mathrm{SU}(2)})^j \tag{A.6a}$$

$$= \Big[\sum_{n=0}^{\infty} \frac{(-1)^n\theta^{2n}}{(2n)!}\Big]\boldsymbol{I} + \Big[\sum_{j=0}^{\infty} \frac{(-1)^n\theta^{2n+1}}{(2n+1)!}\Big][\boldsymbol{u}]^{\wedge}_{\mathrm{SU}(2)} \tag{A.6b}$$

$$= \cos(\theta)\boldsymbol{I} + \mathrm{sinc}(\theta)[\boldsymbol{\omega}]^{\wedge}_{\mathrm{SU}(2)} \in \mathrm{SU}(2), \tag{A.6c}$$

and the inverse map follows directly from this expression, as

$$\theta = \arccos\Big(\frac{\mathrm{Tr}(\boldsymbol{X})}{2}\Big), \qquad [\boldsymbol{\omega}]^{\wedge}_{\mathrm{SU}(2)} = \frac{1}{\mathrm{sinc}(\theta)}(\boldsymbol{X} - \cos(\theta)\boldsymbol{I}). \tag{A.7}$$

As such, the exponential map $\mathrm{Exp}_{\mathrm{SU}(2)} : \mathfrak{su}(2) \to \mathrm{SU}(2)$ is given by (A.6), and the inverse logarithmic map $\mathrm{Log}_{\mathrm{SU}(2)} : \mathrm{SU}(2) \to \mathfrak{su}(2)$ is given by (A.7).

A.1.3 Projections to SO(3) and SU(2)

When considering real-time implementations, it may be necessary to compute attitudes from noisy measured directions. As such, we require a method of projecting a matrix $\boldsymbol{M} \in \mathbb{R}^{3\times3}$ to the nearest element of SO(3). This can be done by expressing an optimization problem in the Frobenius norm,

$$\boldsymbol{R} = \underset{\boldsymbol{R}\in\mathrm{SO}(3)}{\mathrm{argmin}} \|\boldsymbol{M} - \boldsymbol{R}\|_F \triangleq \mathrm{Proj}_{\mathrm{SO}(3)}(\boldsymbol{M}). \tag{A.8}$$

This is an orthogonal *matrix nearness problem* discussed in [Higham, 1989, Chapter 4], and here solved by taking an SVD $\boldsymbol{M} = \boldsymbol{U}\boldsymbol{\Sigma}\boldsymbol{V}^{\top}$, where

$$\boldsymbol{R} = \begin{cases} \boldsymbol{U}\boldsymbol{V}^{\top} & \text{if } \det(\boldsymbol{U}\boldsymbol{V}^{\top}) > 0 \\ \begin{bmatrix}[\boldsymbol{U}]_{:,1} & [\boldsymbol{U}]_{:,2} & -[\boldsymbol{U}]_{:,3}\end{bmatrix}\boldsymbol{V} & \text{if } \det(\boldsymbol{U}\boldsymbol{V}^{\top}) < 0 \end{cases}. \tag{A.9}$$

Similarly, if $\boldsymbol{M} \in \mathbb{C}^{2\times 2}$ and is to be projected to SU(2), we simply convert $\boldsymbol{M}$ to a quaternion $\boldsymbol{q}_{\boldsymbol{M}} \in \hat{\mathbb{H}}$ using the embedding in Definition 2.17, normalizing and converting this to an element $\boldsymbol{X} = E^{\mathbb{H}}_{\mathrm{SU}(2)}(\boldsymbol{q}_{\boldsymbol{M}}/\|\boldsymbol{q}_M\|) \in \mathrm{SU}(2)$.

A.1.4 Algebraic Properties of SO(3)

A set of algebraic properties relating to SO(3) can be summarized as follows:

$$\text{(i)} \quad \boldsymbol{R}_1^\top \boldsymbol{R}_2 \in \mathrm{SO}(3), \qquad \forall \boldsymbol{R}_1, \boldsymbol{R}_2 \in \mathrm{SO}(3), \tag{A.10a}$$

$$\text{(ii)} \quad [\boldsymbol{a}]^\wedge + [\boldsymbol{b}]^\wedge = [\boldsymbol{a}+\boldsymbol{b}]^\wedge \in \mathfrak{so}(3), \qquad \forall \boldsymbol{a}, \boldsymbol{b} \in \mathbb{R}^3, \tag{A.10b}$$

$$\text{(iii)} \quad [\alpha\boldsymbol{a}]^\wedge = \alpha[\boldsymbol{a}]^\wedge \in \mathfrak{so}(3), \qquad \forall \alpha \in \mathbb{R}, \boldsymbol{a} \in \mathbb{R}^3. \tag{A.10c}$$

From (A.10b) and (A.10c), the SO(3) *vee*-map is additive and homogeneous,

$$\text{(iv)} \quad [[\boldsymbol{a}]^\wedge + [\boldsymbol{b}]^\wedge]^\vee = [[\boldsymbol{a}+\boldsymbol{b}]^\wedge]^\vee = \boldsymbol{a}+\boldsymbol{b} \in \mathbb{R}^3, \quad \forall \boldsymbol{a}, \boldsymbol{b} \in \mathbb{R}^3, \tag{A.10d}$$

$$\text{(v)} \quad [\alpha[\boldsymbol{a}]^\wedge]^\vee = \alpha[[\boldsymbol{a}]^\wedge]^\vee = \alpha\boldsymbol{a} \in \mathbb{R}^3, \qquad \forall \alpha \in \mathbb{R}, \boldsymbol{a} \in \mathbb{R}^3. \tag{A.10e}$$

We also have that

$$\text{(vi)} \quad ([\boldsymbol{a}]^\wedge)^\top = -[\boldsymbol{a}]^\wedge \in \mathfrak{so}(3), \qquad \forall \boldsymbol{a} \in \mathbb{R}^3, \tag{A.10f}$$

$$\text{(vii)} \quad ([\boldsymbol{a}]^\wedge)^\top [\boldsymbol{a}]^\wedge = \|\boldsymbol{a}\|^2 \boldsymbol{I} - \boldsymbol{a}\boldsymbol{a}^\top, \qquad \forall \boldsymbol{a} \in \mathbb{R}^3. \tag{A.10g}$$

As the elements of the Lie algebra are skew-symmetric,

$$\text{(viii)} \quad \boldsymbol{b}^\top [\boldsymbol{a}]^\wedge \boldsymbol{b} = \boldsymbol{0} \in \mathbb{R}^3, \qquad \forall \boldsymbol{a}, \boldsymbol{b} \in \mathbb{R}^3, \tag{A.10h}$$

and as $[\boldsymbol{a}]^\wedge \boldsymbol{b} = \boldsymbol{a} \times \boldsymbol{b}$, we can reverse the order and use the Jacobi identity

$$\text{(ix)} \quad [\boldsymbol{a}]^\wedge \boldsymbol{b} = -[\boldsymbol{b}]^\wedge \boldsymbol{a} \in \mathbb{R}^3, \qquad \forall \boldsymbol{a}, \boldsymbol{b} \in \mathbb{R}^3, \tag{A.10i}$$

$$\text{(x)} \quad \boldsymbol{a}^\top [\boldsymbol{b}]^\wedge \boldsymbol{c} = \boldsymbol{c}^\top [\boldsymbol{a}]^\wedge \boldsymbol{b} = \boldsymbol{b}^\top [\boldsymbol{c}]^\wedge \boldsymbol{a} \in \mathbb{R}^3, \qquad \forall \boldsymbol{a}, \boldsymbol{b}, \boldsymbol{c} \in \mathbb{R}^3, \tag{A.10j}$$

It can also be verified that

$$\text{(xi)} \quad [[\boldsymbol{a}]^\wedge \boldsymbol{b}]^\wedge = \boldsymbol{b}\boldsymbol{a}^\top - \boldsymbol{a}\boldsymbol{b}^\top \in \mathfrak{so}(3), \qquad \forall \boldsymbol{a}, \boldsymbol{b} \in \mathbb{R}^3. \tag{A.10k}$$

A set of identities can be derived with respect to the trace operation, as

$$\text{(xii)} \ \mathrm{Tr}([\boldsymbol{a}]^\wedge \boldsymbol{M}) = -\boldsymbol{a}^\top [\boldsymbol{M} - \boldsymbol{M}^\top]^\vee, \qquad \forall \boldsymbol{a} \in \mathbb{R}^3, \boldsymbol{M} \in \mathbb{R}^{3\times 3}, \tag{A.10l}$$

$$\text{(xiii)} [\boldsymbol{a}]^\wedge \boldsymbol{M} + \boldsymbol{M}^\top [\boldsymbol{a}]^\wedge = [(\mathrm{Tr}(\boldsymbol{M})\boldsymbol{I} - \boldsymbol{M})\boldsymbol{a}]^\wedge, \forall \boldsymbol{a} \in \mathbb{R}^3, \boldsymbol{M} \in \mathbb{R}^{3\times 3}. \tag{A.10m}$$

Finally, we have

$$\text{(xiv)} \quad \boldsymbol{R}[\boldsymbol{a}]^\wedge = [\boldsymbol{R}\boldsymbol{a}]^\wedge \boldsymbol{R} \in \mathbb{R}^3, \qquad \forall \boldsymbol{a} \in \mathbb{R}^3, \boldsymbol{R} \in \mathrm{SO}(3), \tag{A.10n}$$

from which it also follows that

$$\text{(xv)} \quad \|\boldsymbol{R}[\boldsymbol{a}]^\wedge \boldsymbol{R}^\top\| = \|[\boldsymbol{R}\boldsymbol{a}]^\wedge\| = \|\boldsymbol{R}\boldsymbol{a}\| = \|\boldsymbol{a}\|, \quad \forall \boldsymbol{a} \in \mathbb{R}^3, \boldsymbol{R} \in \mathrm{SO}(3). \tag{A.10o}$$

A.1.5 Algebraic Properties of SU(2)

A set of algebraic properties relating to SU(2) can be summarized as follows:

$$\text{(i)} \quad \boldsymbol{X}_1^* \boldsymbol{X}_2 \in \mathrm{SU}(2), \qquad \forall \boldsymbol{X}_1, \boldsymbol{X}_2 \in \mathrm{SU}(2), \tag{A.11a}$$

$$\text{(ii)} \quad [\boldsymbol{a}]^\wedge + [\boldsymbol{b}]^\wedge = [\boldsymbol{a}+\boldsymbol{b}]^\wedge \in \mathfrak{su}(2), \qquad \forall \boldsymbol{a}, \boldsymbol{b} \in \mathbb{R}^3, \tag{A.11b}$$

$$\text{(iii)} \quad [\alpha \boldsymbol{a}]^\wedge = \alpha [\boldsymbol{a}]^\wedge, \qquad \forall \alpha \in \mathbb{R}, \boldsymbol{a} \in \mathbb{R}^3. \tag{A.11c}$$

From (A.11b) and (A.11c), it follows that

$$\text{(iv)} \quad [[\boldsymbol{a}]^\wedge + [\boldsymbol{b}]^\wedge]^\vee = [[\boldsymbol{a}+\boldsymbol{b}]^\wedge]^\vee = \boldsymbol{a}+\boldsymbol{b} \in \mathbb{R}^3, \qquad \forall \boldsymbol{a}, \boldsymbol{b} \in \mathbb{R}^3, \tag{A.11d}$$

$$\text{(v)} \quad [\alpha [\boldsymbol{a}]^\wedge]^\vee = \alpha [[\boldsymbol{a}]^\wedge]^\vee = \alpha \boldsymbol{a} \in \mathbb{R}^3, \qquad \forall \alpha \in \mathbb{R}, \boldsymbol{a} \in \mathbb{R}^3. \tag{A.11e}$$

By definition, the complex conjugate of elements of the lie algebra satisfies

$$\text{(vi)} \quad ([\boldsymbol{a}]^\wedge)^* = -[\boldsymbol{a}]^\wedge \in \mathfrak{su}(2), \qquad \forall \boldsymbol{a} \in \mathbb{R}^3, \tag{A.11f}$$

$$\text{(vii)} \quad ([\boldsymbol{a}]^\wedge)^* [\boldsymbol{a}]^\wedge = \|\boldsymbol{a}\|^2 \boldsymbol{I}, \qquad \forall \boldsymbol{a} \in \mathbb{R}^3. \tag{A.11g}$$

Similarly, by definition, an interesting trace identity can be derived as

$$\text{(viii)} \quad \mathrm{Tr}(\boldsymbol{X}[\boldsymbol{a}/2]^\wedge) = [\mathrm{Tr}(\boldsymbol{X})\boldsymbol{I}/2 - \boldsymbol{X}]^\vee \cdot \boldsymbol{a}, \quad \forall \boldsymbol{X} \in \mathrm{SU}(2), \boldsymbol{a} \in \mathbb{R}^3. \tag{A.11h}$$

With these basic identities, we can derive much more complicated expressions, such as the kinematics of elements of SU(2). If $\boldsymbol{X}(t) \in \mathrm{SU}(2) \Rightarrow \boldsymbol{X}(t)^* \boldsymbol{X}(t) = \boldsymbol{I}$, assume that $\frac{\mathrm{d}}{\mathrm{d}t}(\boldsymbol{X}(t)) = \boldsymbol{X}(t)\boldsymbol{A}(t)$ for some $\boldsymbol{A}(t) \in \mathbb{C}^{2\times 2}$, then

$$\frac{\mathrm{d}}{\mathrm{d}t}(\boldsymbol{X}(t)^* \boldsymbol{X}(t)) = \frac{\mathrm{d}}{\mathrm{d}t}\boldsymbol{I} \Rightarrow \dot{\boldsymbol{X}}(t)^* \boldsymbol{X}(t) + \boldsymbol{X}(t)^* \dot{\boldsymbol{X}}(t) = \boldsymbol{0} \Rightarrow \boldsymbol{A}(t)^* + \boldsymbol{A}(t) = \boldsymbol{0}.$$

Clearly, $\boldsymbol{A}(t) \in \mathfrak{su}(2)$ in Definition 2.10, and by Definition 2.17, it follows that

$$\text{(ix)} \quad \frac{\mathrm{d}}{\mathrm{d}t}(\boldsymbol{X}(t)) = \boldsymbol{X}(t)[\boldsymbol{\omega}(t)/2]^\wedge, \qquad \forall \boldsymbol{X}(t) \in \mathrm{SU}(2), \boldsymbol{\omega}(t) \in \mathbb{R}^3, \tag{A.11i}$$

where $\boldsymbol{\omega}$ denotes attitude rates in the body frame, as previously defined for SO(3). Finally, we can consider the time-derivative of the conjugate product $\boldsymbol{X}_1(t)^* \boldsymbol{X}_2(t) \in \mathrm{SU}(2)$. Dropping the time argument for notational simplicity, for all $\boldsymbol{X}_1, \boldsymbol{X}_2 \in \mathrm{SU}(2)$ evolving in time by $\frac{\mathrm{d}}{\mathrm{d}t}(\boldsymbol{X}_i) = \boldsymbol{X}_i[\boldsymbol{\omega}_i/2]^\wedge$,

$$\begin{aligned}
\frac{\mathrm{d}}{\mathrm{d}t}(\boldsymbol{X}_1^* \boldsymbol{X}_2) &= \dot{\boldsymbol{X}}_1^* \boldsymbol{X}_2 + \boldsymbol{X}_1^* \dot{\boldsymbol{X}}_2 \\
&= (\boldsymbol{X}_1[\boldsymbol{\omega}_1/2]^\wedge)^* \boldsymbol{X}_2 + \boldsymbol{X}_1^* (\boldsymbol{X}_2[\boldsymbol{\omega}_2/2]^\wedge) \\
&= -[\boldsymbol{\omega}_1/2]^\wedge \boldsymbol{X}_1^* \boldsymbol{X}_2 + \boldsymbol{X}_1^* \boldsymbol{X}_2 [\boldsymbol{\omega}_2/2]^\wedge \\
&= (\boldsymbol{X}_1^* \boldsymbol{X}_2)([\boldsymbol{\omega}_2/2]^\wedge - (\boldsymbol{X}_1^* \boldsymbol{X}_2)^* [\boldsymbol{\omega}_1/2]^\wedge (\boldsymbol{X}_1^* \boldsymbol{X}_2)) \\
&= (\boldsymbol{X}_1^* \boldsymbol{X}_2)([\boldsymbol{\omega}_2/2]^\wedge - [[(\boldsymbol{X}_1^* \boldsymbol{X}_2)^* [\boldsymbol{\omega}_1/2]^\wedge (\boldsymbol{X}_1^* \boldsymbol{X}_2)]^\vee]^\wedge) \\
&= (\boldsymbol{X}_1^* \boldsymbol{X}_2)[(\boldsymbol{\omega}_2 - [(\boldsymbol{X}_1^* \boldsymbol{X}_2)^* [\boldsymbol{\omega}_1]^\wedge (\boldsymbol{X}_1^* \boldsymbol{X}_2)]^\vee)/2]^\wedge
\end{aligned}$$

which can be summarized as

$$\text{(x)} \qquad \frac{\mathrm{d}}{\mathrm{d}t}(\boldsymbol{X}_1^*\boldsymbol{X}_2) = (\boldsymbol{X}_1^*\boldsymbol{X}_2)[(\boldsymbol{\omega}_2 - [(\boldsymbol{X}_1^*\boldsymbol{X}_2)^*[\boldsymbol{\omega}_1]^\wedge(\boldsymbol{X}_1^*\boldsymbol{X}_2)]^\vee)/2]^\wedge. \tag{A.11j}$$

A.1.6 Algebraic Properties of $\mathbb{H}$

For the quaternions, the two operations $[\cdot]_L$ and $[\cdot]_R$ represent left and right quaternion products, that is for any $\boldsymbol{p}, \boldsymbol{q} \in \mathbb{H}$, $\boldsymbol{p} \odot \boldsymbol{q} = [\boldsymbol{p}]_L\boldsymbol{q} = [\boldsymbol{q}]_R\boldsymbol{p} \in \mathbb{H}$. Now, by Definition 2.14, if we take $\Re(\boldsymbol{q}) = q_w$ and $\Re(\boldsymbol{q}) = \boldsymbol{q}_v$, then

$$[\boldsymbol{q}]_L = q_w\boldsymbol{I}_4 + \begin{bmatrix} 0 & -\boldsymbol{q}_v^\top \\ \boldsymbol{q}_v & \boldsymbol{S}(\boldsymbol{q}_v) \end{bmatrix}, \qquad [\boldsymbol{q}]_R = q_w\boldsymbol{I}_4 + \begin{bmatrix} 0 & -\boldsymbol{q}_v^\top \\ \boldsymbol{q}_v & -\boldsymbol{S}(\boldsymbol{q}_v) \end{bmatrix}. \tag{A.12}$$

A.2 Numerical Integration

While most of the simulation results presented in the thesis employ a fixed-order RK method available through Simulink in Matlab, the C-implementations of the controllers and numerical evaluation in Sec. 2.3 are done with respect to specific RK methods, characterized below as follows.

A.2.1 Butcher Tableau

The butcher tableau defines the properties of the RK method, and is commonly denoted by a matrix $\boldsymbol{A} \in \mathbb{R}^{s\times s}$ with elements a_{ij}, and two vectors $\boldsymbol{b} \in \mathbb{R}^s$ and $\boldsymbol{c} \in \mathbb{R}^s$, where s is an integer denoting the number of "stages" in the resulting method. We consider the following butcher tableau for the RK4 method,

$$\text{(RK4)} \qquad \boldsymbol{A} = \begin{bmatrix} 0 & 0 & 0 & 0 \\ \frac{1}{2} & 0 & 0 & 0 \\ 0 & \frac{1}{2} & 0 & 0 \\ 0 & 0 & 1 & 0 \end{bmatrix}, \qquad \boldsymbol{b} = \begin{bmatrix} 0 \\ \frac{1}{2} \\ \frac{1}{2} \\ 1 \end{bmatrix}, \qquad \boldsymbol{c} = \begin{bmatrix} \frac{1}{6} \\ \frac{1}{3} \\ \frac{1}{3} \\ \frac{1}{6} \end{bmatrix}, \tag{A.13}$$

Only one CG-method is considered, and this is the CG4, where the considered Butcher tableau was computed numerically using a least squares approach

in [Jackiewicz et al., 2000]. The tableau for the $s = 5$-stage algorithm is

$$
\begin{aligned}
a_{21} &= +0.8177227988124852 & a_{31} &= +0.3199876375476427 \\
a_{32} &= +0.0659864263556022 & a_{41} &= +0.9214417194464946 \\
a_{42} &= +0.4997857776773573 & a_{43} &= -1.0969984448371582 \\
a_{51} &= +0.3552358559023322 & a_{52} &= +0.2390958372307326 \\
a_{53} &= +1.3918565724203246 & a_{54} &= -1.1092979392113465 \\
b_1 &= +0.1370831520630755 & c_1 &= +0.0 \\
b_2 &= -0.0183698531564020 & c_2 &= +0.8177227988124852 \\
b_3 &= +0.7397813985370780 & c_3 &= +0.3859740639032449 \\
b_4 &= -0.1907142565505889 & c_4 &= +0.3242290522866937 \\
b_5 &= +0.3322195591068374 & c_5 &= +0.8768903263420429
\end{aligned}
$$

with the remaining entries in $\boldsymbol{A} \in \mathbb{R}^{s\times s}$ set to zero.

A.2.2 Quaternion Open-Loop Simulation Example

Consider the attitude dynamics in (2.16). Let $\boldsymbol{\omega}(t_\circ) = \boldsymbol{\omega}_\circ$ and $\boldsymbol{q}(t_\circ) = \boldsymbol{q}_\circ = \boldsymbol{q}_{\boldsymbol{I}}$, and take the inertia to be diagonal with $\boldsymbol{J} = \operatorname{diag}(J_T, J_T, J_3)$. If $\omega_n = \omega_{\circ,3}(J_T - J_3)/J_T$, $\omega_i = \|\boldsymbol{J}\boldsymbol{\omega}_\circ\|/J_T \in \mathbb{R}_{>0}$, $\boldsymbol{h}_\circ = \boldsymbol{J}\boldsymbol{\omega}_\circ/\|\boldsymbol{J}\boldsymbol{\omega}_\circ\| \in \mathbb{R}^3$, it can be verified that $\boldsymbol{x}(t) = (\boldsymbol{q}(t);\ \boldsymbol{\omega}(t)) \in \mathbb{H}\times\mathbb{R}^3$, given by

$$
\begin{aligned}
\omega_1(t) &= \omega_{\circ,1}\cos(\omega_n t) + \omega_{\circ,2}\sin(\omega_n t) && \text{(A.14a)}\\
\omega_2(t) &= \omega_{\circ,2}\cos(\omega_n t) - \omega_{\circ,1}\sin(\omega_n t) && \text{(A.14b)}\\
\omega_3(t) &= \omega_{\circ,3} && \text{(A.14c)}\\
y_1(t) &= \cos(a(t))\cos(b(t)) - h_{\circ,3}\sin(a(t))\sin(b(t)) && \text{(A.14d)}\\
y_2(t) &= h_{\circ,1}\cos(a(t))\sin(b(t)) + h_{\circ,2}\sin(a(t))\sin(b(t)) && \text{(A.14e)}\\
y_3(t) &= h_{\circ,2}\cos(a(t))\sin(b(t)) - h_{\circ,1}\sin(a(t))\sin(b(t)) && \text{(A.14f)}\\
y_4(t) &= h_{\circ,3}\cos(a(t))\sin(b(t)) + \sin(a(t))\cos(b(t)) && \text{(A.14g)}
\end{aligned}
$$

where $\boldsymbol{q}(t) = \boldsymbol{y}(t) \odot \boldsymbol{q}_\circ$, $a(t) = (1/2)\omega_n t$ and $b(t) = (1/2)\omega_i t$ is a solution to the dynamics in (2.16) when unforced, i.e., when letting $\boldsymbol{\tau} = \boldsymbol{0}$. It is with respect to this analytical solution that the integration schemes are evaluated.

A.3 Lyapunov Theory

In this appendix, we highlight useful results pertaining to linear Lyapunov theory that will be used to guide intuition in the various stability proofs.

Proof of Lemma 2.2. Let $\bar{\boldsymbol{A}}(t) = \bar{\boldsymbol{F}} + \bar{\boldsymbol{S}}(t) \in \mathbb{R}^{mn\times mn}$, where $\bar{\boldsymbol{F}} = \boldsymbol{F}\otimes\boldsymbol{I}_m$, and $\bar{\boldsymbol{S}}(t) = \boldsymbol{I}_n \otimes \boldsymbol{S}(t)$. Assume that $(\boldsymbol{P}, \boldsymbol{Q}(t))$ is a solution to the Lyapunov

equation with respect to $\boldsymbol{F} \in \mathbb{R}^{n\times n}$. As $\bar{\boldsymbol{F}} = \boldsymbol{F}\otimes \boldsymbol{I}_m$, there exist an orthogonal permutation matrix $\boldsymbol{T}$ such that

$$\bar{\boldsymbol{F}}_1 = \boldsymbol{T}\bar{\boldsymbol{F}}\boldsymbol{T}^\top = \boldsymbol{I}_m \otimes \boldsymbol{F} = \begin{bmatrix} \boldsymbol{F} & \boldsymbol{0} & \cdots & \boldsymbol{0} \\ \boldsymbol{0} & \boldsymbol{F} & \cdots & \boldsymbol{0} \\ \vdots & \vdots & \ddots & \vdots \\ \boldsymbol{0} & \boldsymbol{0} & \cdots & \boldsymbol{F} \end{bmatrix}. \tag{A.15}$$

Furthermore, as $(\boldsymbol{P}, \boldsymbol{Q}(t))$ solves the Lyapunov equation with respect to $\boldsymbol{F}$, it is clear that $(\bar{\boldsymbol{P}}_1, \bar{\boldsymbol{Q}}_1(t)) = (\boldsymbol{I}_m \otimes \boldsymbol{P}, \boldsymbol{I}_m \otimes \boldsymbol{Q}(t))$ is a solution with respect to $\bar{\boldsymbol{F}}_1$. It is then easy to verify that $(\bar{\boldsymbol{P}}, \bar{\boldsymbol{Q}}(t)) = (\boldsymbol{P} \otimes \boldsymbol{I}_m, \boldsymbol{Q}(t) \otimes \boldsymbol{I}_m)$ is a solution with respect to $\bar{\boldsymbol{F}}$. Finally, we note that $\bar{\boldsymbol{P}}$ and $\bar{\boldsymbol{S}}(t)$ commute, as

$$\bar{\boldsymbol{P}}\bar{\boldsymbol{S}}(t) = \begin{bmatrix} [\boldsymbol{P}]_{1,1}\boldsymbol{I}_m\boldsymbol{S}(t) & \vdots & [\boldsymbol{P}]_{1,n}\boldsymbol{I}_m\boldsymbol{S}(t) \\ \vdots & \ddots & \vdots \\ [\boldsymbol{P}]_{n,1}\boldsymbol{I}_m\boldsymbol{S}(t) & \vdots & [\boldsymbol{P}]_{n,n}\boldsymbol{I}_m\boldsymbol{S}(t) \end{bmatrix} = \bar{\boldsymbol{S}}(t)\bar{\boldsymbol{P}}.$$

Consequently,

$$\begin{aligned} \bar{\boldsymbol{A}}(t)^\top\bar{\boldsymbol{P}} + \bar{\boldsymbol{P}}\bar{\boldsymbol{A}}(t) &= (\bar{\boldsymbol{F}} + \bar{\boldsymbol{S}}(t))^\top\bar{\boldsymbol{P}} + \bar{\boldsymbol{P}}(\bar{\boldsymbol{F}} + \bar{\boldsymbol{S}}(t)) \\ &= \bar{\boldsymbol{F}}^\top\bar{\boldsymbol{P}} + \bar{\boldsymbol{P}}\bar{\boldsymbol{F}} + \bar{\boldsymbol{S}}(t)^\top\bar{\boldsymbol{P}} + \bar{\boldsymbol{S}}(t)\bar{\boldsymbol{P}} \\ &= \bar{\boldsymbol{Q}}(t) + (\bar{\boldsymbol{S}}(t) - \bar{\boldsymbol{S}}(t))\bar{\boldsymbol{P}} \\ &= \bar{\boldsymbol{Q}}(t), \end{aligned}$$

showing that $(\bar{\boldsymbol{P}}, \bar{\boldsymbol{Q}}(t))$ solves the Lyapunov equation with respect to $\bar{\boldsymbol{A}}(t)$.□

Proof of Lemma 2.3. Let $\boldsymbol{R}(t) \in \mathrm{SO}(3)$ evolving by $\dot{\boldsymbol{R}}(t) = \boldsymbol{R}(t)[\boldsymbol{\omega}(t)]^\wedge_{\mathrm{SO}(3)}$ for some $\boldsymbol{\omega}(t) \in \mathbb{R}^3$. If $\boldsymbol{z}(t) = \boldsymbol{R}(t)\boldsymbol{x}(t)$, then

$$\begin{aligned} \dot{\boldsymbol{z}}(t) &= \dot{\boldsymbol{R}}(t)\boldsymbol{x}(t) + \boldsymbol{R}(t)\dot{\boldsymbol{x}}(t) \\ &= \boldsymbol{R}(t)[\boldsymbol{\omega}(t)]^\wedge\boldsymbol{R}(t)^\top\boldsymbol{z}(t) + \boldsymbol{R}(t)\boldsymbol{A}(t)\boldsymbol{R}(t)^\top\boldsymbol{z}(t) \\ &= (\boldsymbol{R}(t)\boldsymbol{A}(t)\boldsymbol{R}(t)^\top + [\boldsymbol{R}(t)\boldsymbol{\omega}(t)]^\wedge_{\mathrm{SO}(3)})\boldsymbol{z}(t), \end{aligned} \tag{A.16}$$

where the last equality holds (A.10n), concluding the proof. □

Proof of Lemma 2.4. By assumption, there exists a time-varying solution $(\boldsymbol{P}, \boldsymbol{Q}(t))$ to the Lyapunov equation for $\boldsymbol{A}(t)$, implying that $\dot{\boldsymbol{P}}(t) = \boldsymbol{0}$, and

$$\boldsymbol{A}(t)^\top\boldsymbol{P} + \boldsymbol{P}\boldsymbol{A}(t) + \boldsymbol{Q}(t) = \boldsymbol{0}.$$

If $\boldsymbol{P}$ and $\boldsymbol{E}$ are both symmetric, positive definite and commute, then we can find a factorization $\boldsymbol{E} = \boldsymbol{E}^{1/2}\boldsymbol{E}^{1/2}$, where $\boldsymbol{E}^{-1/2}$ is symmetric and also commutes with $\boldsymbol{P}$. Insertion into the solution of the Lyapunov equation yields

$$\begin{aligned}
\boldsymbol{A}(t)^\top \boldsymbol{P} + \boldsymbol{P}\boldsymbol{A}(t) + \boldsymbol{Q}(t) = \boldsymbol{0} \Leftrightarrow \\
\boldsymbol{A}(t)^\top \boldsymbol{E}^{-\top}\boldsymbol{E}^\top \boldsymbol{P} + \boldsymbol{P}\boldsymbol{E}\boldsymbol{E}^{-1}\boldsymbol{A}(t) + \boldsymbol{Q}(t) = \boldsymbol{0} \Leftrightarrow \\
\bar{\boldsymbol{A}}(t)^\top \boldsymbol{E}^{1/2}\boldsymbol{P}\boldsymbol{E}^{1/2} + \boldsymbol{E}^{1/2}\boldsymbol{P}\boldsymbol{E}^{1/2}\boldsymbol{A}(t) + \boldsymbol{Q}(t) = \boldsymbol{0}.
\end{aligned}$$

Thus, the descriptor system in (2.41) characterized by $\bar{\boldsymbol{A}}(t) = \boldsymbol{E}^{-1}\boldsymbol{A}(t)$ satisfies the time-varying Lyapunov equation with a solution $(\boldsymbol{E}^{1/2}\boldsymbol{P}\boldsymbol{E}^{1/2}, \boldsymbol{Q}(t))$. As $\boldsymbol{E}^{1/2}$ is square and of full rank, and $\boldsymbol{P}$ is symmetric, the implications in stability stated in Lemma 2.4 follow directly from Theorem 2.1. □

B

Full State Feedback: Proofs

B.1 Theorem 3.1: Explicit vector FSF on SO(3)

Before giving the proof, we first recall a general Thompson-Tait-Chetaev stability theorem, dating back to [Chetaev et al., 1961], extended to the case of semidefinite damping in [Müller and Schiehlen, 1977], and concisely summarized by in [Bernstein and Bhat, 1995, Theorem 1] for the special case when the stiffness-matrix is singular, as restated below. This is rewritten into two short and convenient lemmas, followed by a third lemma showing an implication of an equation in the matrix $\boldsymbol{M}$. These lemmas are later used in the main proof of the explicit vector feedback law in Theorem 3.1.

Theorem B.1—[Bernstein and Bhat, 1995, Theorem 1]
For $\mathcal{M}, \mathcal{C}, \mathcal{G}, \mathcal{K} \in \mathbb{R}^{n\times n}$, with $\mathcal{M} \succ \mathbf{0}$, $\mathcal{C} \succeq \mathbf{0}$, $\mathcal{G} = -\mathcal{G}^\top$, and $\mathcal{K} = \mathcal{K}^\top \succeq \mathbf{0}$,

$$\mathcal{M}\ddot{\boldsymbol{q}} + (\mathcal{C}+\mathcal{G})\dot{\boldsymbol{q}} + \mathcal{K}\boldsymbol{q} = \mathbf{0}, \qquad \boldsymbol{q}(t_\circ) \in \mathbb{R}^n, \qquad \dot{\boldsymbol{q}}(t_\circ) \in \mathbb{R}^n, \tag{B.1}$$

at some initial time $t_\circ \in \mathbb{R}$, or equivalently stated

$$\dot{\boldsymbol{x}} = \boldsymbol{A}\boldsymbol{x}, \qquad \boldsymbol{x} \triangleq \begin{bmatrix}\boldsymbol{q}\\ \dot{\boldsymbol{q}}\end{bmatrix}, \qquad \boldsymbol{A} = \begin{bmatrix}\mathbf{0} & \boldsymbol{I}\\ -\mathcal{M}^{-1}\mathcal{K} & -\mathcal{M}^{-1}(\mathcal{C}+\mathcal{G})\end{bmatrix}, \tag{B.2}$$

is

(i) Stable, if and only if

$$\operatorname{rank}\begin{bmatrix}\mathcal{K} & \mathcal{G}\\ \mathbf{0} & \mathcal{K}\\ \mathbf{0} & \mathcal{C}\end{bmatrix} = \operatorname{rank}(\mathcal{K}) + n. \tag{B.3}$$

(ii) Semi-stable, that is $\lim_{(t-t_\circ)\to\infty} \boldsymbol{x}(t)$ exists for all initial conditions $\boldsymbol{x}(t_\circ)$, if and only if the system is stable, and

$$\operatorname{rank} \begin{bmatrix} \boldsymbol{C}_o \\ \boldsymbol{C}_o\boldsymbol{A}_o \\ \vdots \\ \boldsymbol{C}_o\boldsymbol{A}_o^{n-1} \end{bmatrix} = \operatorname{rank} \begin{bmatrix} \boldsymbol{C}_o \\ \boldsymbol{A}_o \end{bmatrix}, \tag{B.4}$$

where

$$\boldsymbol{A}_o \triangleq \begin{bmatrix} \boldsymbol{0} & \boldsymbol{I} \\ -\mathcal{M}^{-1}\mathcal{K} & -\mathcal{M}^{-1}\mathcal{G} \end{bmatrix}, \quad \boldsymbol{C}_o \triangleq \begin{bmatrix} \mathcal{C} & \boldsymbol{0} \end{bmatrix}. \tag{B.5}$$

(iii) Asymptotically stable, if and only if it is semi-stable and $\mathcal{K} \succ 0$. □

Lemma B.1
If $\mathcal{G} = \boldsymbol{0}$, the system in (B.1) is asymptotically stable if $\mathcal{C} \succ \boldsymbol{0}$, and $\mathcal{K} \succ \boldsymbol{0}$.□

Proof. The condition $\mathcal{C} \succ 0$ implies $\operatorname{rank}(\mathcal{C}) = n$ which implies semi-stability by Theorem B.1 (ii), asymptotic stability follows by (iii) as $\mathcal{K} \succ \boldsymbol{0}$. □

Lemma B.2
If $\mathcal{G} = \boldsymbol{0}$, the system in (B.1) is unstable if $\mathcal{C} \succ \boldsymbol{0}$ and the stiffness matrix $\mathcal{K}$ has at least one eigenvalue with negative real-part. □

Proof. This can be shown in many ways. One is to invoke Lyapunov's instability theorem, see e.g., [Bloch et al., 1994, Theorem 3.1]. □

Lemma B.3
Let $\boldsymbol{R} \in \mathrm{SO}(3)$, and take $\boldsymbol{0} \prec \boldsymbol{M} = \boldsymbol{M}^\top \in \mathbb{R}^{3\times 3}$ such that $\boldsymbol{M} = \boldsymbol{U}\boldsymbol{\Lambda}\boldsymbol{U}^\top$. If

$$\boldsymbol{R}^\top\boldsymbol{M} = \boldsymbol{M}\boldsymbol{R}, \tag{B.6}$$

then

$$\boldsymbol{R} \in \{\boldsymbol{I}\} \cup \{\boldsymbol{R} \in \mathrm{SO}(3) \mid \operatorname{Tr}(\boldsymbol{R}) = -1\}, \tag{B.7}$$

and if the eigenvalues of $\boldsymbol{M}$ are distinct, then

$$\boldsymbol{R} \in \{\boldsymbol{I}\} \cup \{\boldsymbol{U}\boldsymbol{D}_i\boldsymbol{U}^\top\}_{i=1}^3. \tag{B.8}$$

□

Proof. By the assumptions on $\boldsymbol{M}$, there exists a spectral decomposition $\boldsymbol{M} = \boldsymbol{U}\boldsymbol{\Lambda}\boldsymbol{U}^\top$ where $\boldsymbol{U}^\top\boldsymbol{U} = \boldsymbol{I}$. Following the proof in [Mahony et al., 2008, Theorem 5.1], denote the eigenvalues and vectors of $\boldsymbol{R}$ by $\boldsymbol{x}_i \in \mathbb{C}^3$, where

$$\boldsymbol{R}\boldsymbol{x}_i = \lambda_i\boldsymbol{x}_i \Rightarrow \boldsymbol{x}_i^*\boldsymbol{R}^\top = \lambda_i^*\boldsymbol{x}_i^*. \tag{B.9}$$

Then, (B.6) yields

$$\lambda_i^* \boldsymbol{x}_i^* \boldsymbol{M} \boldsymbol{x}_i = \boldsymbol{x}_i^* (\boldsymbol{R}^\top \boldsymbol{M}) \boldsymbol{x}_i = \boldsymbol{x}_i^* (\boldsymbol{M}\boldsymbol{R}) \boldsymbol{x}_i = \lambda_i \boldsymbol{x}_i^* \boldsymbol{M} \boldsymbol{x}_i \Rightarrow \lambda_i^* = \lambda_i, \quad \text{(B.10)}$$

for all $i \in \{1, 2, 3\}$ if $\boldsymbol{M} \succ \boldsymbol{0}$. Since the eigenvalues of $\boldsymbol{R} \in \mathrm{SO}(3)$ are given by

$$\mathrm{spec}(\boldsymbol{R}) = \{1, \cos(\theta) + i \sin(\theta), \cos(\theta) - i \sin(\theta)\},$$

it follows from (B.10) that $\mathrm{Tr}(\boldsymbol{R}) \in \{3, -1\}$ which in turn implies $\boldsymbol{R} = \boldsymbol{R}^\top$. This last implication can be seen by considering the parameterization of the rotation matrix in (2.5) in a unit quaternion (a, b, c, d), and the solution to

$$\begin{cases} 3a^2 - b^2 - c^2 - d^2 = \mathrm{Tr}(\boldsymbol{R}) \\ a^2 + b^2 + c^2 + d^2 = 1 \end{cases}, \quad \text{(B.11)}$$

which results in the non-symmetric part of $\boldsymbol{R}$ being zero. Now, consider the case where the eigenvalues are distinct, take $\bar{\boldsymbol{R}} = \boldsymbol{U}^\top \boldsymbol{R} \boldsymbol{U}$, then

$$\boldsymbol{R}^\top \boldsymbol{M} = \boldsymbol{M}\boldsymbol{R} \Rightarrow \bar{\boldsymbol{R}}^\top \boldsymbol{\Lambda} - \boldsymbol{\Lambda} \bar{\boldsymbol{R}}^\top = \boldsymbol{0} \Rightarrow (\lambda_j - \lambda_i)[\bar{\boldsymbol{R}}]_{ij} = 0.$$

Consequently, if all the eigenvalues are distinct, all off-diagonal elements of $\bar{\boldsymbol{R}}$ will necessarily be zero. Therefore, $\bar{\boldsymbol{R}} \in \{\boldsymbol{I}\} \cup \{\boldsymbol{D}_i\}_{i=1}^3 \Rightarrow \boldsymbol{R} \in \{\boldsymbol{I}\} \cup \{\boldsymbol{U}\boldsymbol{D}_i\boldsymbol{U}^\top\}_{i=1}^3$, yielding (B.8) and concluding the proof. □

Given these preliminaries, we can now give the proof of Theorem 3.1.

Proof of Theorem 3.1. Throughout this proof, for simplicity, the *hat*- and *vee*-maps of SO(3) in Definition 2.12 are abbreviated as $[\cdot]_{\mathrm{SO}(3)}^{\wedge} = [\cdot]^{\wedge}$ and $[\cdot]_{\mathrm{SO}(3)}^{\vee} = [\cdot]^{\vee}$, respectively. Plugging in the feedback law in (3.6), and taking the time-derivative of the errors $\boldsymbol{R}_e$ and $\boldsymbol{e}_\omega$, we obtain the error dynamics

$$\dot{\boldsymbol{R}}_e = \boldsymbol{R}_e \boldsymbol{S}(\boldsymbol{e}_\omega) \quad \text{(B.12a)}$$

$$\boldsymbol{J}\dot{\boldsymbol{e}}_\omega = -\boldsymbol{K}_\omega \boldsymbol{e}_\omega - \sum_{i=1}^{N} k_i \boldsymbol{S}(\boldsymbol{v}_i) \boldsymbol{R}_e^\top \boldsymbol{v}_i. \quad \text{(B.12b)}$$

Consider the Lyapunov function candidate

$$\mathcal{V} = \sum_{i=1}^{N} \frac{k_i}{2} \|\boldsymbol{R}_e \boldsymbol{v}_i - \boldsymbol{v}_i\|^2 + \frac{1}{2} \boldsymbol{e}_\omega^\top \boldsymbol{J} \boldsymbol{e}_\omega. \quad \text{(B.13)}$$

Differentiation of (B.13) along the solutions of the dynamics yields

$$\begin{aligned}\frac{\mathrm{d}\mathcal{V}}{\mathrm{d}t} &= \sum_{i=1}^{N} k_i(\boldsymbol{R}_e\boldsymbol{v}_i - \boldsymbol{v}_i)^\top \boldsymbol{R}_e\boldsymbol{S}(\boldsymbol{e}_\omega)\boldsymbol{v}_i + \boldsymbol{e}_\omega^\top \boldsymbol{J}\dot{\boldsymbol{e}}_\omega \\ &= \sum_{i=1}^{N} k_i(\boldsymbol{v}_i^\top \boldsymbol{S}(\boldsymbol{e}_\omega)\boldsymbol{v}_i - \boldsymbol{v}_i^\top \boldsymbol{R}_e\boldsymbol{S}(\boldsymbol{e}_\omega)\boldsymbol{v}_i) + \boldsymbol{e}_\omega^\top \boldsymbol{J}\dot{\boldsymbol{e}}_\omega \\ &= -\sum_{i=1}^{N} k_i\boldsymbol{v}_i^\top \boldsymbol{R}_e\boldsymbol{S}(\boldsymbol{v}_i)\boldsymbol{e}_\omega + \boldsymbol{e}_\omega^\top\Big[-\boldsymbol{K}_\omega\boldsymbol{e}_\omega - \sum_{i=1}^{N} k_i\boldsymbol{S}(\boldsymbol{v}_i)\boldsymbol{R}_e^\top\boldsymbol{v}_i\Big] \\ &= -\boldsymbol{e}_\omega^\top\boldsymbol{K}_\omega\boldsymbol{e}_\omega + \boldsymbol{e}_\omega^\top\Big[\sum_{i=1}^{N} k_i\boldsymbol{S}(\boldsymbol{v}_i)\boldsymbol{R}_e^\top\boldsymbol{v}_i - \sum_{i=1}^{N} k_i\boldsymbol{S}(\boldsymbol{v}_i)\boldsymbol{R}_e^\top\boldsymbol{v}_i\Big] \\ &= -\boldsymbol{e}_\omega^\top\boldsymbol{K}_\omega\boldsymbol{e}_\omega.\end{aligned}$$

Here, $\dot{\mathcal{V}}$ is negative definite in $\boldsymbol{e}_\omega$, implying that the Lyapunov function is bounded in $\mathcal{V}(t) \leq \mathcal{V}(t_\circ)$. Furthermore, we then have $\lambda_m(\boldsymbol{J})\|\boldsymbol{e}_\omega(t)\|^2 \leq \boldsymbol{e}_\omega(t)^\top\boldsymbol{J}\boldsymbol{e}_\omega(t) \leq 2\mathcal{V}(t_\circ)$, implying that $\dot{\mathcal{V}}$ is uniformly continuous, since

$$\frac{\mathrm{d}^2\mathcal{V}}{\mathrm{d}t^2} = -2\boldsymbol{e}_\omega\boldsymbol{K}_\omega\boldsymbol{J}^{-1}\Big[-\boldsymbol{K}_\omega\boldsymbol{e}_\omega - \sum_{i=1}^{N} k_i\boldsymbol{S}(\boldsymbol{v}_i)\boldsymbol{R}_e^\top\boldsymbol{v}_i\Big] \Rightarrow$$

$$\Big\|\frac{\mathrm{d}^2\mathcal{V}}{\mathrm{d}t^2}\Big\| \leq \frac{4\lambda_M(\boldsymbol{K}_\omega)^2}{\lambda_m(\boldsymbol{J})^2}\mathcal{V}(t_\circ) + \frac{2\sqrt{2}\lambda_M(\boldsymbol{K}_\omega)}{\lambda_m(\boldsymbol{J})^{3/2}}\sqrt{\mathcal{V}(t_\circ)}\Big(\sum_{i=1}^{N} k_i\Big), \quad \forall t \geq t_\circ.$$

Consequently, application of Lemma 2.5 (Barbălat) yields

$$\lim_{(t-t_\circ)\to\infty} \dot{\mathcal{V}}(t) = \boldsymbol{0} \Rightarrow \lim_{(t-t_\circ)\to\infty} \boldsymbol{e}_\omega(t) = \boldsymbol{0}. \tag{B.14}$$

Since $\boldsymbol{e}_\omega$ is bounded, the signal $f_0(t) = \sum_{i=1}^{N} k_i\boldsymbol{S}(\boldsymbol{v}_i)\boldsymbol{R}_e^\top\boldsymbol{v}_i$ is uniformly continuous in time. Thus, application of Lemma 2.6 to (B.12b) yields

$$\text{(B.14)} \Rightarrow \lim_{(t-t_\circ)\to\infty} \dot{\boldsymbol{e}}_\omega(t) = \lim_{(t-t_\circ)\to\infty} \sum_{i=1}^{N} k_i\boldsymbol{S}(\boldsymbol{v}_i)\boldsymbol{R}_e^\top\boldsymbol{v}_i = \boldsymbol{0}. \tag{B.15}$$

Finally, by invoking the identity in (A.10k), we have that

$$\sum_{i=1}^{N} k_i\boldsymbol{S}(\boldsymbol{v}_i)\boldsymbol{R}_e^\top\boldsymbol{v}_i = \Big[\sum_{i=1}^{N} k_i(\boldsymbol{R}_e^\top\boldsymbol{v}_i\boldsymbol{v}_i^\top - \boldsymbol{v}_i(\boldsymbol{R}_e^\top\boldsymbol{v}_i)^\top)\Big]^\vee = [\boldsymbol{R}_e^\top\boldsymbol{M} - \boldsymbol{M}^\top\boldsymbol{R}_e]^\vee,$$

with

$$\boldsymbol{M} \triangleq \sum_{i=1}^{N} k_i\boldsymbol{v}_i\boldsymbol{v}_i^\top \succ \boldsymbol{0}.$$

Consequently,

$$(\text{B.15}) \Rightarrow \lim_{(t-t_\circ)\to\infty} \boldsymbol{R}_e^\top \boldsymbol{M} - \boldsymbol{M}^\top \boldsymbol{R}_e = \boldsymbol{0} \Rightarrow \lim_{(t-t_\circ)\to\infty} \mathrm{Tr}(\boldsymbol{R}_e) \in \{-1, 3\},$$

where the last implication holds due to Lemma B.3. Therefore, all trajectories of the error dynamics tend towards a stationary point in the set $\mathcal{E} = \{(\boldsymbol{R}_e, \boldsymbol{e}_\omega) \in \mathrm{SO}(3) \times \mathbb{R}^3 \mid \mathrm{Tr}(\boldsymbol{R}_e) \in \{-1, 3\}, \boldsymbol{e}_\omega = \boldsymbol{0}\}$. Furthermore, if the eigenvalues of $\boldsymbol{M}$ are distinct, it follows by Lemma B.3 that the set $\mathcal{E}$ then consists of four disjoint points $\mathrm{SO}(3) \times \mathbb{R}^3$, namely $\{(\boldsymbol{U}\boldsymbol{D}_i\boldsymbol{U}^\top, \boldsymbol{0})\}_{i=1}^4$.

Local Linearizations To assess the nature of these equilibrium points, take a first order approximation of the rotation error about $(\boldsymbol{R}_\circ, \boldsymbol{e}_\omega) \in \mathcal{E}$, using the first two terms in the power series of $\mathrm{Exp}_{\mathrm{SO}(3)}$, as

$$\boldsymbol{R}_e(t) = \boldsymbol{R}_\circ(\boldsymbol{I} + [\boldsymbol{\epsilon}(t)]^\wedge) + o(\|\boldsymbol{\epsilon}(t)\|^2) \approx \boldsymbol{R}_\circ(\boldsymbol{I} + [\boldsymbol{\epsilon}(t)]^\wedge), \tag{B.16}$$

for small $\boldsymbol{\epsilon}(t) \in \mathbb{R}^3$. Then, the attitude error dynamics of the closed loop system in (B.12a), close to $(\boldsymbol{R}_e, \boldsymbol{e}_\omega) = (\boldsymbol{R}_\circ, \boldsymbol{0})$, can be written as

$$\begin{aligned}
\frac{\mathrm{d}}{\mathrm{d}t}(\boldsymbol{R}_\circ(\boldsymbol{I} + [\boldsymbol{\epsilon}]^\wedge)) &= \boldsymbol{R}_\circ((\boldsymbol{I} + [\boldsymbol{\epsilon}]^\wedge)[\boldsymbol{e}_\omega]^\wedge) \Leftrightarrow \\
\boldsymbol{R}_\circ\left[\frac{\mathrm{d}}{\mathrm{d}t}\boldsymbol{\epsilon}\right]^\wedge &= \boldsymbol{R}_\circ(\boldsymbol{I} + [\boldsymbol{\epsilon}]^\wedge)[\boldsymbol{e}_\omega]^\wedge \Leftrightarrow \\
\left[\frac{\mathrm{d}}{\mathrm{d}t}\boldsymbol{\epsilon}\right]^\wedge &= (\boldsymbol{I} + [\boldsymbol{\epsilon}]^\wedge)[\boldsymbol{e}_\omega]^\wedge \Leftrightarrow \\
\frac{\mathrm{d}\boldsymbol{\epsilon}}{\mathrm{d}t} &= \boldsymbol{e}_\omega + [[\boldsymbol{\epsilon}]^\wedge[\boldsymbol{e}_\omega]^\wedge]^\vee \triangleq f_1(\boldsymbol{\epsilon}, \boldsymbol{e}_\omega).
\end{aligned}$$

Given this local time-evolution of the perturbation, we find that

$$\left.\frac{\partial f_1(\boldsymbol{\epsilon}, \boldsymbol{e}_\omega)}{\partial \boldsymbol{\epsilon}}\right|_{(\boldsymbol{\epsilon}, \boldsymbol{e}_\omega)=\boldsymbol{0}} = \boldsymbol{0}, \quad \left.\frac{\partial f_1(\boldsymbol{\epsilon}, \boldsymbol{e}_\omega)}{\partial \boldsymbol{e}_\omega}\right|_{(\boldsymbol{\epsilon}, \boldsymbol{e}_\omega)=\boldsymbol{0}} = \boldsymbol{I}, \tag{B.17}$$

irrespective of the element $\boldsymbol{R}_\circ$. Consequently, in a neighborhood of $\boldsymbol{R}_\circ$, the attitude rate error represents the time-derivative of the perturbation. Consider the attitude rate error dynamics in (B.12b). Insertion of (B.64) yields

$$\begin{aligned}
\boldsymbol{J}\dot{\boldsymbol{e}}_\omega &= -\boldsymbol{K}_\omega \boldsymbol{e}_\omega - \sum_{i=1}^N k_i \boldsymbol{S}(\boldsymbol{v}_i)\boldsymbol{R}_e^\top \boldsymbol{v}_i && \text{(B.18a)} \\
&= -\boldsymbol{K}_\omega \boldsymbol{e}_\omega + [\boldsymbol{R}_e^\top \boldsymbol{M} - \boldsymbol{M}^\top \boldsymbol{R}_e]^\vee && \text{(B.18b)} \\
&= -\boldsymbol{K}_\omega \boldsymbol{e}_\omega + [(\boldsymbol{I} + [\boldsymbol{\epsilon}]^\wedge)^\top \boldsymbol{R}_\circ^\top \boldsymbol{M} - \boldsymbol{M}^\top \boldsymbol{R}_\circ(\boldsymbol{I} + [\boldsymbol{\epsilon}]^\wedge)]^\vee. && \text{(B.18c)}
\end{aligned}$$

Now, for any $(\boldsymbol{R}_\circ, \boldsymbol{e}_\omega) \in \mathcal{E}$, we have that $\mathrm{Tr}(\boldsymbol{R}_\circ) \in \{-1, 3\}$, which by Lemma B.3 implies that $\boldsymbol{R}_\circ = \boldsymbol{R}_\circ^\top$. Using this property, (B.18) becomes

$$\begin{aligned}\boldsymbol{J}\dot{\boldsymbol{e}}_\omega &= -\boldsymbol{K}_\omega \boldsymbol{e}_\omega + [-[\boldsymbol{\epsilon}]^\wedge \boldsymbol{R}_\circ^\top \boldsymbol{M} - \boldsymbol{M}^\top \boldsymbol{R}_\circ [\boldsymbol{\epsilon}]^\wedge]^\vee \\ &= -\boldsymbol{K}_\omega \boldsymbol{e}_\omega + (\boldsymbol{R}_\circ \boldsymbol{M} - \mathrm{Tr}(\boldsymbol{R}_\circ \boldsymbol{M})\boldsymbol{I})\boldsymbol{\epsilon} \\ &\triangleq f_2(\boldsymbol{\epsilon}, \boldsymbol{e}_\omega),\end{aligned}$$

where the second equality follows by the identity in (A.10m). Here, taking the Jacobian of f_2 at $(\boldsymbol{\epsilon}, \boldsymbol{e}_\omega) = \boldsymbol{0}$, we have that

$$\begin{aligned}\left.\frac{\partial f_2(\boldsymbol{\epsilon}, \boldsymbol{e}_\omega)}{\partial \boldsymbol{\epsilon}}\right|_{(\boldsymbol{\epsilon}, \boldsymbol{e}_\omega)=\boldsymbol{0}} &= (\boldsymbol{R}_\circ \boldsymbol{M} - \mathrm{Tr}(\boldsymbol{R}_\circ \boldsymbol{M})\boldsymbol{I}) &&\triangleq -\mathcal{K}, \\ \left.\frac{\partial f_2(\boldsymbol{\epsilon}, \boldsymbol{e}_\omega)}{\partial \boldsymbol{e}_\omega}\right|_{(\boldsymbol{\epsilon}, \boldsymbol{e}_\omega)=\boldsymbol{0}} &= -\boldsymbol{K}_\omega &&\triangleq -\mathcal{C}.\end{aligned}$$

Thus, with $\mathcal{M} = \mathcal{M}^\top = \boldsymbol{J} \succ 0$, $\mathcal{C} = \mathcal{C}^\top = \boldsymbol{K}_\omega \succ 0$, and in a neighborhood of a point $(\boldsymbol{R}_e, \boldsymbol{e}_\omega) \in \mathcal{E}$, the perturbation evolves by the second-order dynamics,

$$\mathcal{M}\ddot{\boldsymbol{\epsilon}} + \mathcal{C}\dot{\boldsymbol{\epsilon}} + \mathcal{K}\boldsymbol{\epsilon} = \boldsymbol{0}. \tag{B.19}$$

This result is reminiscent to that in [Chaturvedi et al., 2011] and [Mahony et al., 2008], but here in a different notation and for the tracking control errors. We proceed to analyze the resulting equilibrium points in two separate cases. First, when $\mathrm{spec}(\boldsymbol{M}) = \{\lambda_1, \lambda_2, \lambda_3\}$ is uniform (with $\lambda_1 = \lambda_2 = \lambda_3$), and second when the eigenvalues of $\boldsymbol{M}$ are distinct (with $\lambda_1 \neq \lambda_2 \neq \lambda_3 \neq \lambda_1$).

Uniform Spectrum Take $\boldsymbol{M}$ to have a uniform spectrum, such that $\boldsymbol{M} = \boldsymbol{U}\boldsymbol{\Lambda}\boldsymbol{U}^\top$, where then $\boldsymbol{\Lambda} = \lambda_\circ \boldsymbol{I}$ for some $\lambda_\circ > 0$. Consider the case where $\mathrm{Tr}(\boldsymbol{R}_\circ) = 3$, i.e. a rotational error of $\boldsymbol{R}_\circ = \boldsymbol{I}$. In this case, we obtain

$$\mathcal{K} = -(\boldsymbol{R}_\circ \boldsymbol{M} - \mathrm{Tr}(\boldsymbol{R}_\circ \boldsymbol{M})\boldsymbol{I}) = \lambda_\circ(3\boldsymbol{I} - \boldsymbol{I}) = 2\lambda_\circ \boldsymbol{I} \succ 0. \tag{B.20}$$

Consequently, as $\mathcal{C} \succ 0$ and $\mathcal{K} \succ \boldsymbol{0}$, the equilibrium point corresponding to a rotational error of $\boldsymbol{R}_\circ = \boldsymbol{I}$, the system (B.19) is locally asymptotically stable by Lemma B.1, and hence locally exponentially stable, as the system in (B.19) is linear and time-invariant.

Now, consider the case where $\mathrm{Tr}(\boldsymbol{R}_\circ) = -1$. This subset of SO(3) can be parameterized in all purely imaginary quaternions by (2.5), as is also evident by the geometry in Figure 2.3. Let $\boldsymbol{u} = (u_1;\ u_2;\ u_3) \in \mathbb{R}^3$, then

$$\begin{aligned}&\boldsymbol{R}_\circ \in \{\boldsymbol{R} \in \mathrm{SO}(3) | \mathrm{Tr}(\boldsymbol{R}) = -1\} \\ &= \left\{ \begin{bmatrix} +u_1^2 - u_2^2 - u_3^2 & 2u_1u_2 & 2u_1u_3 \\ 2u_1u_2 & -u_1^2 + u_2^2 - u_3^2 & 2u_2u_3 \\ 2u_1u_3 & 2u_2u_3 & -u_1^2 - u_2^2 + u_3^2 \end{bmatrix} \in \mathrm{SO}(3) \,\middle|\, \|\boldsymbol{u}\| = 1 \right\}\end{aligned} \tag{B.21}$$

The resulting stiffness matrix for any element in this subset of SO(3) is

$$\mathcal{K} = -\lambda_\circ(\boldsymbol{R}_\circ - \mathrm{Tr}(\boldsymbol{R}_\circ)\boldsymbol{I}) = -\lambda_\circ(\boldsymbol{R}_\circ + \boldsymbol{I}) = -\lambda_\circ(\boldsymbol{R}_\circ + \boldsymbol{I}\|\boldsymbol{u}\|^2) = -2\lambda_\circ \boldsymbol{u}\boldsymbol{u}^\top.$$

As $\boldsymbol{u}$ is a unit vector, we obtain a spectrum of the stiffness matrix as

$$\mathrm{spec}(\mathcal{K}) = \{-2\lambda_\circ, 0, 0\}. \tag{B.22}$$

Consequently, $\mathcal{C} \succ \boldsymbol{0}$ and $\mathcal{K} \preceq \boldsymbol{0}$, for any equilibrium point characterized by $(\boldsymbol{R}_\circ, \boldsymbol{0}) \in \mathcal{E}\backslash\{(\boldsymbol{I}, \boldsymbol{0})\}$. The local dynamics of perturbation (B.19) are unstable at these points by Lemma B.2.

Distinct Spectrum If we instead take $\boldsymbol{M}$ to have distinct eigenvalues, such that $\boldsymbol{M} = \boldsymbol{U}\boldsymbol{\Lambda}\boldsymbol{U}^\top$, with $\boldsymbol{\Lambda} = \mathrm{diag}(\lambda_1, \lambda_2, \lambda_3)$ and, without loss of generality let $\lambda_1 > \lambda_2 > \lambda_3 > 0$. Then we note that for any $\boldsymbol{D}_i \in \mathrm{SO}(3)$,

$$\boldsymbol{R}_\circ \boldsymbol{M} = \boldsymbol{U}\boldsymbol{D}_i\boldsymbol{U}^\top\boldsymbol{U}\boldsymbol{\Lambda}\boldsymbol{U}^\top = \boldsymbol{U}\boldsymbol{D}_i\boldsymbol{\Lambda}\boldsymbol{U}^\top, \tag{B.23}$$

and as the trace of a matrix is the sum of its eigenvalues,

$$\boldsymbol{U}^\top\mathcal{K}\boldsymbol{U} = -\boldsymbol{U}^\top(\boldsymbol{R}_\circ\boldsymbol{M} - \mathrm{Tr}(\boldsymbol{R}_\circ\boldsymbol{M})\boldsymbol{I})\boldsymbol{U} = \mathrm{Tr}(\boldsymbol{D}_i\boldsymbol{\Lambda})\boldsymbol{I} - \boldsymbol{D}_i\boldsymbol{\Lambda}. \tag{B.24}$$

We obtain the following stiffness matrices about the four equilibrium points

$$\begin{aligned}
(\boldsymbol{R}_\circ, \boldsymbol{e}_\omega) = (\boldsymbol{D}_1, \boldsymbol{0}) \quad &\Rightarrow \quad \mathrm{spec}(\mathcal{K}) = \{-\lambda_2 - \lambda_3, +\lambda_1 - \lambda_3, +\lambda_1 - \lambda_2\},\\
(\boldsymbol{R}_\circ, \boldsymbol{e}_\omega) = (\boldsymbol{D}_2, \boldsymbol{0}) \quad &\Rightarrow \quad \mathrm{spec}(\mathcal{K}) = \{+\lambda_2 - \lambda_3, -\lambda_1 - \lambda_3, +\lambda_2 - \lambda_3\},\\
(\boldsymbol{R}_\circ, \boldsymbol{e}_\omega) = (\boldsymbol{D}_3, \boldsymbol{0}) \quad &\Rightarrow \quad \mathrm{spec}(\mathcal{K}) = \{-\lambda_2 + \lambda_3, -\lambda_1 + \lambda_3, -\lambda_1 - \lambda_2\},\\
(\boldsymbol{R}_\circ, \boldsymbol{e}_\omega) = (\boldsymbol{D}_4, \boldsymbol{0}) \quad &\Rightarrow \quad \mathrm{spec}(\mathcal{K}) = \{+\lambda_2 + \lambda_3, +\lambda_1 + \lambda_3, +\lambda_1 + \lambda_2\}.
\end{aligned}$$

About $\boldsymbol{D}_4 = \boldsymbol{I}$, we have that $\mathcal{C} \succ \boldsymbol{0}$ and $\mathcal{K} \succ \boldsymbol{0}$, at the equilibrium point corresponding to a rotational error of $\boldsymbol{R}_\circ = \boldsymbol{I}$, the system (B.19) is locally asymptotically stable by Lemma B.1, hence locally exponentially stable.

About the remaining equilibrium points, the stiffness matrix has one negative eigenvalue in the case of $\boldsymbol{D}_1$, two negative eigenvalues in the case of $\boldsymbol{D}_2$ and three negative eigenvalues in the case of $\boldsymbol{D}_3$. Consequently, equilibrium points corresponding to these errors are all unstable by Lemma B.2. □

B.2 Remark 3.1: Equivalences of Controllers on SO(3)

Proof of Remark 3.1. Consider the cross-product term in (3.6), assume that $N = 3$, with $k_i = k_R/2$, $\forall i = \{1, 2, 3\}$, and take $(\boldsymbol{v}_1, \boldsymbol{v}_2, \boldsymbol{v}_3) = \boldsymbol{I}$. Then

$$
\begin{aligned}
\sum_{i=1}^{N} k_i \boldsymbol{S}(\boldsymbol{v}_i)\boldsymbol{R}_e^\top \boldsymbol{v}_i &= \Big[\big[\sum_{i=1}^{N} k_i \boldsymbol{S}(\boldsymbol{v}_i)\boldsymbol{R}_e^\top \boldsymbol{v}_i\big]^\wedge_{\mathrm{SO}(3)}\Big]^\vee_{\mathrm{SO}(3)} \\
&= \Big[\sum_{i=1}^{N} k_i (\boldsymbol{R}_e^\top \boldsymbol{v}_i \boldsymbol{v}_i^\top - \boldsymbol{v}_i (\boldsymbol{R}_e^\top \boldsymbol{v}_i)^\top)\Big]^\vee_{\mathrm{SO}(3)} \\
&= \Big[\sum_{i=1}^{N} k_i (\boldsymbol{R}_e^\top \boldsymbol{v}_i \boldsymbol{v}_i^\top - \boldsymbol{v}_i \boldsymbol{v}_i^\top \boldsymbol{R}_e)\Big]^\vee_{\mathrm{SO}(3)} \\
&= \frac{k_R}{2}\Big[\boldsymbol{R}_e^\top \sum_{i=1}^{N} (\boldsymbol{v}_i \boldsymbol{v}_i^\top) - \sum_{i=1}^{N} (\boldsymbol{v}_i \boldsymbol{v}_i)^\top \boldsymbol{R}_e)\Big]^\vee_{\mathrm{SO}(3)} \\
&= \frac{k_R}{2}\Big[\boldsymbol{R}_e^\top - \boldsymbol{R}_e\Big]^\vee_{\mathrm{SO}(3)} \\
&= \frac{k_R}{2}\Big[\boldsymbol{R}^\top \boldsymbol{R}_r - \boldsymbol{R}_r^\top \boldsymbol{R}\Big]^\vee_{\mathrm{SO}(3)} \\
&= -k_R \boldsymbol{e}_{\boldsymbol{R}},
\end{aligned}
$$

where the second equality follows by (A.10k). Here, $\boldsymbol{e}_{\boldsymbol{R}}$ is recognized as the attitude error of the geometric tracking control in (3.8a) of Theorem 3.2. In this setting, the controller in Theorem 3.1 and 3.2 are equivalent. □

B.3 Proposition 3.1: Ultimate Bound

Proof. Following [Lee et al., 2010], there exists a Lyapunov function

$$\mathcal{V} = k_R \Psi(\boldsymbol{R}_r, \boldsymbol{R}) + k_c \boldsymbol{e}_{\boldsymbol{R}} \cdot \boldsymbol{e}_{\boldsymbol{\omega}} + \frac{1}{2} \boldsymbol{e}_{\boldsymbol{\omega}} \cdot \boldsymbol{J} \boldsymbol{e}_{\boldsymbol{\omega}}, \tag{B.25}$$

such that, with

$$\boldsymbol{z} = \begin{bmatrix} \|\boldsymbol{e}_{\boldsymbol{R}}\| \\ \|\boldsymbol{e}_{\boldsymbol{\omega}}\| \end{bmatrix}, \qquad \boldsymbol{W} = \begin{bmatrix} \frac{k_c k_R}{\lambda_M(\boldsymbol{J})} & -\frac{k_c k_w}{2\lambda_m(\boldsymbol{J})} \\ -\frac{k_c k_w}{2\lambda_m(\boldsymbol{J})} & k_\omega - k_c \end{bmatrix}, \tag{B.26}$$

$$\boldsymbol{M}_1 = \frac{1}{2} \begin{bmatrix} k_R & -k_c \\ -k_c & \lambda_m(\boldsymbol{J}) \end{bmatrix}, \qquad \boldsymbol{M}_2 = \frac{1}{2} \begin{bmatrix} \frac{2k_R}{2-\phi} & k_c \\ k_c & \lambda_M(\boldsymbol{J}) \end{bmatrix}, \tag{B.27}$$

where $\phi \in [0, 2)$ and $\Psi(\boldsymbol{R}_r(t_\circ), \boldsymbol{R}(t_\circ)) \leq \phi < 2$. Differentiation of the Lyapunov function (B.25) along the solutions of the unperturbed system in (2.16),

$$\boldsymbol{z}^\top \boldsymbol{M}_1 \boldsymbol{z} \leq \mathcal{V} \leq \boldsymbol{z}^\top \boldsymbol{M}_2 \boldsymbol{z}, \qquad \dot{\mathcal{V}} \leq -\boldsymbol{z}^\top \boldsymbol{W} \boldsymbol{z}. \tag{B.28}$$

However, if we differentiate the very same Lyapunov function along the solutions of the perturbed system in (3.16), we instead obtain

$$\begin{aligned} \dot{\mathcal{V}} &\leq -\boldsymbol{z}^\top \boldsymbol{W} \boldsymbol{z} + \boldsymbol{e}_{\boldsymbol{\omega}} \cdot \boldsymbol{\Delta} + k_c \boldsymbol{e}_R \cdot \boldsymbol{J}^{-1} \boldsymbol{\Delta} \\ &\leq -\boldsymbol{z}^\top \boldsymbol{W} \boldsymbol{z} + z_2 \|\boldsymbol{\Delta}\| + k_c \lambda_M(\boldsymbol{J}^{-1}) z_1 \|\boldsymbol{\Delta}\| \\ &\leq -\boldsymbol{z}^\top \boldsymbol{W} \boldsymbol{z} + \|\boldsymbol{\Delta}\| \begin{bmatrix} k_c \lambda_M(\boldsymbol{J}^{-1}) & 1 \end{bmatrix}^\top \boldsymbol{z} \| \\ &\leq -\boldsymbol{z}^\top \boldsymbol{W} \boldsymbol{z} + \delta \|\boldsymbol{\Delta}\| \|\boldsymbol{z}\|, \end{aligned}$$

where

$$\delta \triangleq \sqrt{1 + k_c^2 \lambda_M(\boldsymbol{J}^{-1})^2}, \tag{B.29}$$

and subsequently, for any $0 < \theta < 1$,

$$\begin{aligned} \dot{\mathcal{V}} &\leq -\lambda_m(\boldsymbol{W})(1-\theta)\|\boldsymbol{z}\|^2 - \lambda_m(\boldsymbol{W})\theta\|\boldsymbol{z}\|^2 + \|\boldsymbol{z}\|\delta\|\boldsymbol{\Delta}\| \\ &\leq -\lambda_m(\boldsymbol{W})(1-\theta)\|\boldsymbol{z}\|^2 - \|\boldsymbol{z}\|(\lambda_m(\boldsymbol{W})\theta\|\boldsymbol{z}\| - \delta L). \end{aligned}$$

Finally, we arrive at,

$$\dot{\mathcal{V}} \leq -\lambda_m(\boldsymbol{W})(1-\theta)\|\boldsymbol{z}\|^2 \qquad \forall \|\boldsymbol{z}\| > \frac{\delta L}{\lambda_m(\boldsymbol{W})\theta} \triangleq \mu. \tag{B.30}$$

However, the above inequalities only hold if $\Psi(\boldsymbol{R}_r, \boldsymbol{R}) \leq \phi$ for all $t \geq t_\circ$. In the original stability proof, boundedness is shown by letting $k_c = 0$, and using the negative semi-definiteness of $\dot{\mathcal{V}}$ to find a sufficiently small domain for which $\Psi(\boldsymbol{R}_r, \boldsymbol{R}) \leq \phi$. However, this is not an option when including the disturbance,

as $k_c = 0 \Rightarrow \lambda_m(\boldsymbol{W}) = 0$ in (B.30). Instead, we utilize Remark 3.3. Assume that the parameters (k_R, k_c, k_ω) result in a feasible tuning, with a Lyapunov function in (B.25), bounded in the quadratic forms in (B.26). Then, any other cross term $0 < \bar{k}_c \leq k_c$ also represents a feasible tuning with a valid Lyapunov function, $\bar{\mathcal{V}}$, in the form (B.25), which is similarly bounded in positive definite matrices $\bar{\boldsymbol{M}}_1, \bar{\boldsymbol{M}}_2, \bar{\boldsymbol{W}}$. Using this insight, we can derive a sufficient condition for $\Psi(\boldsymbol{R}_r, \boldsymbol{R}) \leq \phi$ to hold at all times when $\boldsymbol{z} \in \mathcal{B}_r \subset \mathbb{R}^2$ of radius r. By defining $\bar{k}_c \triangleq k_c/2$,

$$\begin{aligned} k_R\Psi(\boldsymbol{R}_r(t), \boldsymbol{R}(t)) &\leq k_R\Psi(\boldsymbol{R}_r(t), \boldsymbol{R}(t)) + \frac{1}{2}\boldsymbol{e}_{\boldsymbol{\omega}}(t) \cdot \boldsymbol{J}\boldsymbol{e}_{\boldsymbol{\omega}}(t) \\ &= \bar{\mathcal{V}}(t) - \bar{k}_c \boldsymbol{e}_R(t) \cdot \boldsymbol{e}_{\boldsymbol{\omega}}(t) \\ &\leq \boldsymbol{z}(t)^\top \bar{\boldsymbol{M}}_2 \boldsymbol{z}(t) + \bar{k}_c z_1(t) z_2(t) \\ &= \boldsymbol{z}(t)^\top \boldsymbol{M}_2 \boldsymbol{z}(t) \\ &\leq \lambda_M(\boldsymbol{M}_2)\|\boldsymbol{z}(t)\|^2 \\ &\leq \frac{\lambda_M(\boldsymbol{M}_2)}{\lambda_m(\boldsymbol{M}_1)}\mathcal{V}(t). \end{aligned}$$

Consequently,

$$\frac{\lambda_M(\boldsymbol{M}_2)^2}{\lambda_m(\boldsymbol{M}_1)}\|\boldsymbol{z}(t_\circ)\|^2 \leq k_R\phi \Rightarrow \frac{\lambda_M(\boldsymbol{M}_2)}{\lambda_m(\boldsymbol{M}_1)}\mathcal{V}(t_\circ) \leq k_R\phi \Rightarrow \Psi(\boldsymbol{R}_r(t), \boldsymbol{R}(t)) \leq \phi$$

for all $t \geq t_\circ$. The inequalities in (B.30) hence hold for any $\boldsymbol{z} \in \mathcal{B}_r$ with

$$r \triangleq \sqrt{\phi k_R \lambda_m(\boldsymbol{M}_1)}/\lambda_M(\boldsymbol{M}_2). \tag{B.31}$$

These sets are illustrated for a feasible choice of parameters in Figure 3.4.

This permits an application of Theorem 2.13. We start by noting that $\mathcal{V}$ is continuously differentiable if $\boldsymbol{\Delta}(t)$ is continuous in time, and define the class-$\mathcal{K}$ functions $\alpha_1(r) \triangleq \lambda_m(\boldsymbol{M}_1)r^2$, $\alpha_2(r) \triangleq \lambda_M(\boldsymbol{M}_1)r^2$, and a positive constant $\mu \triangleq \delta L/(\theta\lambda_m(\boldsymbol{W}))$, then

$$\alpha_1(\|\boldsymbol{z}\|) \leq \boldsymbol{z}^\top \boldsymbol{M}_1 \boldsymbol{z} \leq \mathcal{V} \leq \boldsymbol{z}^\top \boldsymbol{M}_2 \boldsymbol{z} \leq \alpha_2(\|\boldsymbol{z}\|), \tag{B.32a}$$

and

$$\dot{\mathcal{V}} \leq -\lambda_m(\boldsymbol{W})(1-\theta)\|\boldsymbol{z}\|^2, \quad \forall \|\boldsymbol{z}\| \geq \mu > 0. \tag{B.32b}$$

Consequently, for any

$$\mu = \delta L/(\theta\lambda_m(\boldsymbol{W})) < (\alpha_2^{-1} \circ \alpha_1)(r) = \sqrt{\frac{\lambda_m(\boldsymbol{M}_1)}{\lambda_M(\boldsymbol{M}_2)}}r, \tag{B.33}$$

or equivalently in the bound of the disturbance L,

$$L < \frac{\theta\lambda_m(\boldsymbol{W})}{\delta}\sqrt{\frac{\lambda_m(\boldsymbol{M}_1)}{\lambda_M(\boldsymbol{M}_2)}}r = \frac{\theta\sqrt{\phi k_R}\lambda_m(\boldsymbol{W})\lambda_m(\boldsymbol{M}_1)}{\delta\lambda_M(\boldsymbol{M}_2)}, \tag{B.34}$$

and for sufficiently small initial errors,

$$\|\boldsymbol{z}(t_\circ)\| \leq (\alpha_2^{-1}\circ\alpha_1)(r) = \sqrt{\frac{\lambda_m(\boldsymbol{M}_1)}{\lambda_M(\boldsymbol{M}_2)}}r = \frac{\sqrt{\phi k_R}\lambda_m(\boldsymbol{M}_1)}{\lambda_M(\boldsymbol{M}_2)}, \tag{B.35}$$

the errors are ultimately bounded by

$$\|\boldsymbol{z}(t)\| \leq \beta(\|\boldsymbol{z}(t_\circ)\|, t-t_\circ), \qquad \forall t\in[t_\circ, t_\circ+T], \tag{B.36}$$
$$\|\boldsymbol{z}(t)\| \leq (\alpha_2\circ\alpha_1^{-1})(\mu) < r, \qquad \forall t \geq t_\circ+T, \tag{B.37}$$

where δ is given in (B.29) and r is given in (B.31). Finally, on $t_\circ \leq t \leq t_\circ+T$,

$$\dot{\mathcal{V}} \leq -\lambda_m(\boldsymbol{W})(1-\theta)\|\boldsymbol{z}\|^2 \leq -\frac{\lambda_m(\boldsymbol{W})}{\lambda_M(\boldsymbol{M}_2)}(1-\theta)\mathcal{V}, \tag{B.38}$$

concluding the proof. □

B.4 Theorem 3.4: Continuous Geometric FSF on SU(2)

Proof of Theorem 3.4. For simplicity, we here let $[\cdot]^\wedge = [\cdot]^\wedge_{\mathrm{SU}(2)}$ and $[\cdot]^\vee = [\cdot]^\vee_{\mathrm{SU}(2)}$ as defined in Definition 2.13. The ideas in this proof will closely follow that of [Lee et al., 2010], but all developments are done for elements $\boldsymbol{X}_r, \boldsymbol{X} \in \mathrm{SU}(2)$ using the distance $\Gamma(\boldsymbol{X}_r, \boldsymbol{X})$ and the identities in Appendix A.1.2. To start, consider an attitude error $\boldsymbol{X}_e = \boldsymbol{X}_r^*\boldsymbol{X} \in \mathrm{SU}(2)$, and note that Γ is positive for all $\boldsymbol{X}_e \in \mathrm{SU}(2)\backslash\{-\boldsymbol{I}\}$, and zero only when $\boldsymbol{X}_e = \boldsymbol{I}$. Consider the time derivative of this error, which by (A.11j) takes the form

$$\frac{\mathrm{d}}{\mathrm{d}t}(\boldsymbol{X}_r^*\boldsymbol{X}) = (\boldsymbol{X}_r^*\boldsymbol{X})[(\boldsymbol{\omega} - [(\boldsymbol{X}_r^*\boldsymbol{X})^*[\boldsymbol{\omega}_r]^\wedge(\boldsymbol{X}_r^*\boldsymbol{X})]^\vee)/2]^\wedge = (\boldsymbol{X}_r^*\boldsymbol{X})[\boldsymbol{e}_\omega/2]^\wedge, \tag{B.39}$$

where

$$\boldsymbol{e}_\omega \triangleq \boldsymbol{\omega} - [(\boldsymbol{X}_r^*\boldsymbol{X})^*[\boldsymbol{\omega}_r]^\wedge(\boldsymbol{X}_r^*\boldsymbol{X})]^\vee, \tag{B.40}$$

can be thought of as the difference between the attitude rate of the system, $\boldsymbol{\omega}$, and the attitude rate of the reference system, $\boldsymbol{\omega}_r$, when compared in the same tangent space $\mathrm{T}_{\boldsymbol{X}}\mathrm{SU}(2)$. Considering the attitude rate error in (B.40),

we proceed by expressing the time-derivative of Γ in this signal, as

$$\frac{\mathrm{d}}{\mathrm{d}t}\Gamma(\boldsymbol{X}_r, \boldsymbol{X}) = \frac{\mathrm{d}}{\mathrm{d}t}\frac{1}{2}\mathrm{Tr}(\boldsymbol{I} - \boldsymbol{X}_r^*\boldsymbol{X}) \tag{B.41a}$$

$$= -\frac{1}{2}\mathrm{Tr}\Big(\frac{\mathrm{d}}{\mathrm{d}t}(\boldsymbol{X}_r^*\boldsymbol{X})\Big) \tag{B.41b}$$

$$= -\frac{1}{2}\mathrm{Tr}\Big((\boldsymbol{X}_r^*\boldsymbol{X})[\boldsymbol{e}_{\boldsymbol{\omega}}/2]^\wedge\Big) \tag{B.41c}$$

$$= -\frac{1}{2}[\mathrm{Tr}(\boldsymbol{X}_r^*\boldsymbol{X})\boldsymbol{I}/2 - \boldsymbol{X}_r^*\boldsymbol{X}]^\vee \cdot \boldsymbol{e}_{\boldsymbol{\omega}} \tag{B.41d}$$

$$= \frac{1}{2}[\boldsymbol{X}_r^*\boldsymbol{X} - \mathrm{Tr}(\boldsymbol{X}_r^*\boldsymbol{X})\boldsymbol{I}/2]^\vee \cdot \boldsymbol{e}_{\boldsymbol{\omega}}, \tag{B.41e}$$

where the last equality follows from identity (A.11h). Consequently, if we choose to define an attitude error as

$$\boldsymbol{e}_{\boldsymbol{X}} \triangleq \frac{1}{2}[\boldsymbol{X}_r^*\boldsymbol{X} - \mathrm{Tr}(\boldsymbol{X}_r^*\boldsymbol{X})\boldsymbol{I}/2]^\vee, \tag{B.42}$$

the time-derivative of the attitude distance can be written concisely as

$$\frac{\mathrm{d}}{\mathrm{d}t}\Gamma(\boldsymbol{X}_r, \boldsymbol{X}) = \boldsymbol{e}_{\boldsymbol{X}} \cdot \boldsymbol{e}_{\boldsymbol{\omega}}. \tag{B.43}$$

Note that $\boldsymbol{e}_{\boldsymbol{X}} = \boldsymbol{0}$ if and only if $\boldsymbol{X}_r^*\boldsymbol{X} \in \{\boldsymbol{I}, -\boldsymbol{I}\}$, but $\boldsymbol{e}_{\boldsymbol{\omega}} = \boldsymbol{0}$ can hold for arbitrary $\boldsymbol{\omega}, \boldsymbol{\omega}_r \in \mathbb{R}^3$ of the same length if $\boldsymbol{X}_r^*\boldsymbol{X} \notin \{\boldsymbol{I}, -\boldsymbol{I}\}$. However, if we restrict the error dynamics to $\boldsymbol{X}_e \in \{\mathrm{SU}(2) | \Gamma(\boldsymbol{X}_r, \boldsymbol{X}) < 2\}$, then $\boldsymbol{e}_{\boldsymbol{X}} = \boldsymbol{0}$ if and only if $\boldsymbol{X}_r^*\boldsymbol{X} = \boldsymbol{I}$, and at the point $\boldsymbol{X}_r^*\boldsymbol{X} = \boldsymbol{I}$, $\boldsymbol{e}_{\boldsymbol{\omega}} = \boldsymbol{0} \Rightarrow \boldsymbol{\omega} = \boldsymbol{\omega}_r$. Consequently, if we consider the function

$$\mathcal{V}' = \Gamma(\boldsymbol{X}_r, \boldsymbol{X}) + \boldsymbol{e}_{\boldsymbol{\omega}} \cdot \boldsymbol{J}\boldsymbol{e}_{\boldsymbol{\omega}}, \tag{B.44}$$

we note that $\mathcal{V}' = 0 \Rightarrow \boldsymbol{X} = \boldsymbol{X}_r \Rightarrow \boldsymbol{\omega} = \boldsymbol{\omega}_r$ for all $\boldsymbol{X}_e \in \{\mathrm{SU}(2) | \Gamma(\boldsymbol{X}_r, \boldsymbol{X}) < 2\}$. Before defining the feedback law and writing out the error dynamics, note that if $\boldsymbol{u} \in \mathbb{R}^3$ is a unit vector such that $\boldsymbol{e}_{\boldsymbol{\omega}} = \|\boldsymbol{e}_{\boldsymbol{\omega}}\|\boldsymbol{u}$, then differentiating the attitude error along the solutions of (B.39) yields

$$\dot{\boldsymbol{e}}_{\boldsymbol{X}} = \frac{\mathrm{d}}{\mathrm{d}t}\frac{1}{2}[\boldsymbol{X}_r^*\boldsymbol{X} - \mathrm{Tr}(\boldsymbol{X}_r^*\boldsymbol{X})\boldsymbol{I}/2]^\vee \tag{B.45a}$$

$$= \frac{1}{2}\Big[\frac{\mathrm{d}}{\mathrm{d}t}(\boldsymbol{X}_r^*\boldsymbol{X}) - \mathrm{Tr}\Big(\frac{\mathrm{d}}{\mathrm{d}t}(\boldsymbol{X}_r^*\boldsymbol{X})\Big)\frac{\boldsymbol{I}}{2}\Big]^\vee \tag{B.45b}$$

$$= \frac{1}{2}\Big[(\boldsymbol{X}_r^*\boldsymbol{X})[\boldsymbol{e}_{\boldsymbol{\omega}}/2]^\wedge - \mathrm{Tr}\Big((\boldsymbol{X}_r^*\boldsymbol{X})[\boldsymbol{e}_{\boldsymbol{\omega}}/2]^\wedge\Big)\frac{\boldsymbol{I}}{2}\Big]^\vee \tag{B.45c}$$

$$= \frac{1}{2}\Big[(\boldsymbol{X}_r^*\boldsymbol{X})[(\|\boldsymbol{e}_{\boldsymbol{\omega}}\|/2)\boldsymbol{u}]^\wedge - \mathrm{Tr}\Big((\boldsymbol{X}_r^*\boldsymbol{X})[(\|\boldsymbol{e}_{\boldsymbol{\omega}}\|/2)\boldsymbol{u}]^\wedge\Big)\frac{\boldsymbol{I}}{2}\Big]^\vee \tag{B.45d}$$

$$= \frac{1}{2}\Big[(\|\boldsymbol{e}_{\boldsymbol{\omega}}\|/2)(\boldsymbol{X}_r^*\boldsymbol{X})[\boldsymbol{u}]^\wedge - \mathrm{Tr}\Big((\|\boldsymbol{e}_{\boldsymbol{\omega}}\|/2)(\boldsymbol{X}_r^*\boldsymbol{X})[\boldsymbol{u}]^\wedge\Big)\frac{\boldsymbol{I}}{2}\Big]^\vee \tag{B.45e}$$

$$= \frac{\|\boldsymbol{e}_{\boldsymbol{\omega}}\|}{4}\Big[(\boldsymbol{X}_r^*\boldsymbol{X})[\boldsymbol{u}]^\wedge - \mathrm{Tr}\Big((\boldsymbol{X}_r^*\boldsymbol{X})[\boldsymbol{u}]^\wedge\Big)\frac{\boldsymbol{I}}{2}\Big]^\vee, \tag{B.45f}$$

and by (A.11g), we have that $\tilde{\boldsymbol{X}} = (\boldsymbol{X}_r^* \boldsymbol{X})[\boldsymbol{u}]^\wedge \in \mathrm{SU}(2)$, as

$$\tilde{\boldsymbol{X}}^* \tilde{\boldsymbol{X}} = (\boldsymbol{X}_r^* \boldsymbol{X}[\boldsymbol{u}]^\wedge)^* (\boldsymbol{X}_r^* \boldsymbol{X})[\boldsymbol{u}]^\wedge = ([\boldsymbol{u}]^\wedge)^* [\boldsymbol{u}]^\wedge = (\boldsymbol{u}^\top \boldsymbol{u}) \boldsymbol{I} = \boldsymbol{I}, \tag{B.46}$$

if $\boldsymbol{u}$ is a unit vector satisfying $\boldsymbol{u}^\top \boldsymbol{u} = 1$. Thus the time-derivative of the attitude error is upper bounded in the attitude rate error as

$$\|\dot{\boldsymbol{e}}_{\boldsymbol{X}}\|^2 = \frac{1}{4^2} \|\boldsymbol{e}_{\boldsymbol{\omega}}\|^2 \Big(\Big[\tilde{\boldsymbol{X}} - \mathrm{Tr}(\tilde{\boldsymbol{X}}) \frac{\boldsymbol{I}}{2} \Big]^\vee \Big)^\top \Big[\tilde{\boldsymbol{X}} - \mathrm{Tr}(\tilde{\boldsymbol{X}}) \frac{\boldsymbol{I}}{2} \Big]^\vee \leq \frac{1}{4^2} \|\boldsymbol{e}_{\boldsymbol{\omega}}\|^2. \tag{B.47}$$

Differentiating the attitude rate error along the solutions of (2.16b), we have

$$\begin{aligned}
\frac{\mathrm{d}}{\mathrm{d}t}(\boldsymbol{J}\boldsymbol{e}_{\boldsymbol{\omega}}) =& \frac{\mathrm{d}}{\mathrm{d}t}[\boldsymbol{J}(\boldsymbol{\omega} - [\boldsymbol{X}_e^* [\boldsymbol{\omega}_r]^\wedge \boldsymbol{X}_e]^\vee)] \\
=& \boldsymbol{J}\dot{\boldsymbol{\omega}} - \boldsymbol{J} \frac{\mathrm{d}}{\mathrm{d}t}[\boldsymbol{X}_e^* [\boldsymbol{\omega}_r]^\wedge \boldsymbol{X}_e]^\vee)] \\
=& \boldsymbol{J}\dot{\boldsymbol{\omega}} - \boldsymbol{J}[(\boldsymbol{X}_e [\boldsymbol{e}_{\boldsymbol{\omega}}/2]^\wedge)^* [\boldsymbol{\omega}_r]^\wedge \boldsymbol{X}_e + \boldsymbol{X}_e^* [\dot{\boldsymbol{\omega}}_r]^\wedge \boldsymbol{X}_e + \boldsymbol{X}_e^* [\boldsymbol{\omega}_r]^\wedge (\boldsymbol{X}_e [\boldsymbol{e}_{\boldsymbol{\omega}}/2]^\wedge)]^\vee \\
=& \boldsymbol{J}\dot{\boldsymbol{\omega}} - \boldsymbol{J}[-[\boldsymbol{e}_{\boldsymbol{\omega}}/2]^\wedge \boldsymbol{X}_e^* [\boldsymbol{\omega}_r]^\wedge \boldsymbol{X}_e + \boldsymbol{X}_e^* [\dot{\boldsymbol{\omega}}_r]^\wedge \boldsymbol{X}_e + \boldsymbol{X}_e^* [\boldsymbol{\omega}_r]^\wedge \boldsymbol{X}_e [\boldsymbol{e}_{\boldsymbol{\omega}}/2]^\wedge]^\vee \\
=& -k_X \boldsymbol{e}_{\boldsymbol{X}} - k_\omega \boldsymbol{e}_{\boldsymbol{\omega}},
\end{aligned} \tag{B.48}$$

if the system is actuated with a feedback which cancels the cross product terms in the attitude rate dynamics in (2.16b) and introduces a negative feedback in the defined errors, that is, with

$$\begin{aligned}
\boldsymbol{\tau} =& -k_X \boldsymbol{e}_{\boldsymbol{X}} - k_\omega \boldsymbol{e}_{\boldsymbol{\omega}} - \boldsymbol{S}(\boldsymbol{J}\boldsymbol{\omega})\boldsymbol{\omega} \\
&+ \boldsymbol{J}[-[\boldsymbol{e}_{\boldsymbol{\omega}}/2]^\wedge \boldsymbol{X}_e^* [\boldsymbol{\omega}_r]^\wedge \boldsymbol{X}_e + \boldsymbol{X}_e^* [\dot{\boldsymbol{\omega}}_r]^\wedge \boldsymbol{X}_e + \boldsymbol{X}_e^* [\boldsymbol{\omega}_r]^\wedge \boldsymbol{X}_e [\boldsymbol{e}_{\boldsymbol{\omega}}/2]^\wedge]^\vee.
\end{aligned} \tag{B.49}$$

Having established the attitude error dynamics, consider the introduction of a cross-term in the Lyapunov function candidate, such that

$$\mathcal{V} = k_X \Gamma(\boldsymbol{X}_r, \boldsymbol{X}) + k_c \boldsymbol{e}_{\boldsymbol{\omega}} \cdot \boldsymbol{e}_{\boldsymbol{X}} + \frac{1}{2} \boldsymbol{e}_{\boldsymbol{\omega}} \cdot \boldsymbol{J}\boldsymbol{e}_{\boldsymbol{\omega}}. \tag{B.50}$$

It is not immediately obvious that this is a positive definite function in the errors, but since $4\|\boldsymbol{e}_{\boldsymbol{X}}\|^2 = \|\Im(E_{\mathbb{H}}^{\mathrm{SU}(2)}(\boldsymbol{X}_r^* \boldsymbol{X}))\|^2$, Remark 2.4 implies

$$2\|\boldsymbol{e}_{\boldsymbol{X}}\|^2 \leq \Gamma(\boldsymbol{X}_r, \boldsymbol{X}) \leq \frac{4}{(2-\phi)} \|\boldsymbol{e}_{\boldsymbol{X}}\|^2 \qquad \forall \Gamma(\boldsymbol{X}_r, \boldsymbol{X}) \leq \phi < 2. \tag{B.51}$$

Thus, if we let $\boldsymbol{z} = (z_1, z_2)^\top = (\|\boldsymbol{e}_{\boldsymbol{X}}\|, \|\boldsymbol{e}_{\boldsymbol{\omega}}\|)^\top$ and use the bound in (B.51),

$$\mathcal{V} \leq \frac{4k_X}{(2-\phi)} z_1^2 + k_c z_1 z_2 + \frac{\lambda_M(\boldsymbol{J})}{2} z_2^2 \triangleq \boldsymbol{z}^\top \boldsymbol{M}_2 \boldsymbol{z}, \tag{B.52}$$

and

$$\mathcal{V} \geq 2k_X z_1^2 - k_c z_1 z_2 + \frac{\lambda_m(\boldsymbol{J})}{2} z_2^2 \triangleq \boldsymbol{z}^\top \boldsymbol{M}_1 \boldsymbol{z}, \tag{B.53}$$

where

$$\boldsymbol{M}_1 \triangleq \frac{1}{2}\begin{bmatrix} 4k_X & -k_c \\ -k_c & \lambda_m(\boldsymbol{J}) \end{bmatrix}, \qquad \boldsymbol{M}_2 \triangleq \frac{1}{2}\begin{bmatrix} \frac{8k_X}{2-\phi} & k_c \\ k_c & \lambda_M(\boldsymbol{J}) \end{bmatrix}. \tag{B.54}$$

If we can find a set of controller parameters $k_X, k_c > 0$ such that $\boldsymbol{M}_1, \boldsymbol{M}_2$ are positive definite in $\boldsymbol{z}$, then it is clear that $\mathcal{V} = 0 \Rightarrow \boldsymbol{z} = \boldsymbol{0} \Rightarrow (\boldsymbol{e_X}, \boldsymbol{e_\omega}) = \boldsymbol{0} \Rightarrow \boldsymbol{X} = \boldsymbol{X}_r, \boldsymbol{\omega} = \boldsymbol{\omega}_r$ if $\Gamma(\boldsymbol{X}_r, \boldsymbol{X}) < \phi$. Furthermore, differentiating the Lyapunov function candidate in (B.50) along the dynamics in (2.16) with the feedback (B.49), that is, by plugging in (B.45) and (B.48), we note that

$$\begin{aligned}
\frac{\mathrm{d}\mathcal{V}}{\mathrm{d}t} &= + k_X \boldsymbol{e_X} \cdot \boldsymbol{e_\omega} + k_c \boldsymbol{e_\omega} \cdot \dot{\boldsymbol{e}}_{\boldsymbol{X}} + k_c \boldsymbol{e_X} \cdot \dot{\boldsymbol{e}}_{\boldsymbol{\omega}} + \boldsymbol{e_\omega} \cdot \boldsymbol{J} \dot{\boldsymbol{e}}_{\boldsymbol{\omega}} && \text{(B.55a)} \\
&= + k_X \boldsymbol{e_X} \cdot \boldsymbol{e_\omega} + k_c \boldsymbol{e_\omega} \cdot \dot{\boldsymbol{e}}_{\boldsymbol{X}} && \text{(B.55b)} \\
&\quad + k_c \boldsymbol{e_X} \cdot \boldsymbol{J}^{-1}(-k_X \boldsymbol{e_X} - k_\omega \boldsymbol{e_\omega}) + \boldsymbol{e_\omega} \cdot (-k_X \boldsymbol{e_X} - k_\omega \boldsymbol{e_\omega}) && \text{(B.55c)} \\
&= + k_c \boldsymbol{e_\omega} \cdot \dot{\boldsymbol{e}}_{\boldsymbol{X}} - k_X k_c \boldsymbol{e_X} \cdot \boldsymbol{J}^{-1} \boldsymbol{e_X} - k_\omega k_c \boldsymbol{e_X} \cdot \boldsymbol{J}^{-1} \boldsymbol{e_\omega} - k_\omega \boldsymbol{e_\omega} \cdot \boldsymbol{e_\omega} && \text{(B.55d)} \\
&= - (k_X k_c \boldsymbol{e_X} \cdot \boldsymbol{J}^{-1} \boldsymbol{e_X} + k_\omega k_c \boldsymbol{e_X} \cdot \boldsymbol{J}^{-1} \boldsymbol{e_\omega} + k_\omega \boldsymbol{e_\omega} \cdot \boldsymbol{e_\omega} - k_c \boldsymbol{e_\omega} \cdot \dot{\boldsymbol{e}}_{\boldsymbol{X}}) && \text{(B.55e)} \\
&\leq -\Big(\frac{k_X k_c}{\lambda_M(\boldsymbol{J})} z_1^2 - \frac{k_c k_\omega}{\lambda_m(\boldsymbol{J})} z_1 z_2 + k_\omega z_2^2 - \frac{k_c}{2} z_2^2 \Big) && \text{(B.55f)} \\
&= -\boldsymbol{z}^\top \boldsymbol{W} \boldsymbol{z}, && \text{(B.55g)}
\end{aligned}$$

where the inequality follows from the bound given in (B.47), and

$$\boldsymbol{W} \triangleq \begin{bmatrix} \frac{k_X k_c}{\lambda_M(\boldsymbol{J})} & -\frac{k_c k_\omega}{2\lambda_m(\boldsymbol{J})} \\ -\frac{k_c k_\omega}{2\lambda_m(\boldsymbol{J})} & k_\omega - \frac{k_c}{4} \end{bmatrix}. \tag{B.56}$$

Here we have arrived at matrices $\boldsymbol{M}_1, \boldsymbol{M}_2, \boldsymbol{W}$ that are similar to the ones arrived at in the stability proof of the geometric attitude control on SO(3), and the final thing to consider is under which conditions the attitude trajectories stay within the sub-level set of $\mathcal{L}_\phi = \{\boldsymbol{X}_r^* \boldsymbol{X} \in \mathrm{SU}(2) | \Gamma(\boldsymbol{X}_r, \boldsymbol{X}) \leq \phi < 2\}$. Clearly, if we pick controller gains such that $\boldsymbol{M}_1, \boldsymbol{M}_2, \boldsymbol{W} \succ 0$, then $\mathcal{V}$ is non-increasing, and

$$k_X \Gamma(\boldsymbol{X}_r(t), \boldsymbol{X}(t)) \leq \mathcal{V}(t) \leq \mathcal{V}(t_\circ) \leq \boldsymbol{z}(t_\circ) \boldsymbol{M}_2 \boldsymbol{z}(t_\circ) \leq k_X \phi, \tag{B.57}$$

implies that $\boldsymbol{X}_r(t)^* \boldsymbol{X}(t) \in \mathcal{L}_\phi \ \forall t \geq t_\circ$. Consequently, for any initial error on

$$D = \{\boldsymbol{z}(t_\circ) \in \mathbb{R}^2 | \boldsymbol{z}(t_\circ) \boldsymbol{M}_2 \boldsymbol{z}(t_\circ) \leq k_X \phi\}, \tag{B.58}$$

the trajectories of $\boldsymbol{X}_r(t)^* \boldsymbol{X}(t) \in \mathcal{L}_\phi$ for all $t \geq t_\circ$. By Theorem 2.4, we conclude uniform exponential stability of the origin $\boldsymbol{z} = \boldsymbol{0}$ on $\boldsymbol{z}(t_\circ) \in D$.

Application of Barbălat To show that the point $(\boldsymbol{X}_e, \boldsymbol{e}_{\boldsymbol{\omega}}) = (\boldsymbol{I}, \boldsymbol{0})$ is UAGAS, we start by considering the Lyapunov function candidate $\mathcal{V}' = \mathcal{V}|_{k_e=0}$ in (B.44). Differentiation along the solutions of the closed-loop dynamics yields

$$\frac{\mathrm{d}\mathcal{V}'}{\mathrm{d}t} = k_X \boldsymbol{e}_{\boldsymbol{X}} \cdot \boldsymbol{e}_{\boldsymbol{\omega}} + \boldsymbol{e}_{\boldsymbol{\omega}} \cdot (-k_X \boldsymbol{e}_{\boldsymbol{X}} - k_\omega \boldsymbol{e}_{\boldsymbol{\omega}}) = -k_\omega \|\boldsymbol{e}_{\boldsymbol{\omega}}\|^2, \tag{B.59}$$

$$\frac{\mathrm{d}^2\mathcal{V}'}{\mathrm{d}t^2} = -2k_\omega \boldsymbol{e}_{\boldsymbol{\omega}}^\top \dot{\boldsymbol{e}}_{\boldsymbol{\omega}} = 2k_\omega \boldsymbol{e}_{\boldsymbol{\omega}}^\top \boldsymbol{J}^{-1}(k_X \boldsymbol{e}_{\boldsymbol{X}} + k_\omega \boldsymbol{e}_{\boldsymbol{\omega}}). \tag{B.60}$$

As $\dot{\mathcal{V}}'$ is along the solutions of the error dynamics, $\mathcal{V}'$ is non-increasing, which implies that $\mathcal{V}'(t) \leq \mathcal{V}'(t_\circ)$ for all $t \geq t_\circ$, bounding the attitude rate error as

$$\lambda_m(\boldsymbol{J})\|\boldsymbol{e}_{\boldsymbol{\omega}}\|^2 \leq \boldsymbol{e}_{\boldsymbol{\omega}}^\top \boldsymbol{J} \boldsymbol{e}_{\boldsymbol{\omega}} \leq 2\mathcal{V}'(t_\circ) \Rightarrow \|\boldsymbol{e}_{\boldsymbol{\omega}}\| \leq \sqrt{2\mathcal{V}'(t_\circ)/\lambda_m(\boldsymbol{J})}. \tag{B.61}$$

Consequently, as $\|\boldsymbol{e}_{\boldsymbol{X}}\| \leq 1/2$ for all $\boldsymbol{X}_e \in \mathrm{SU}(2)$, we have that

$$\begin{aligned} \left\| \frac{\mathrm{d}^2\mathcal{V}'}{\mathrm{d}t^2} \right\| &\leq 2k_\omega \|\boldsymbol{e}_{\boldsymbol{\omega}}\| \lambda_M(\boldsymbol{J}^{-1})(k_X \|\boldsymbol{e}_{\boldsymbol{X}}\| + k_\omega \|\boldsymbol{e}_{\boldsymbol{\omega}}\|) \\ &\leq 2k_\omega \sqrt{2\mathcal{V}'(t_\circ)/\lambda_m(\boldsymbol{J})} \lambda_M(\boldsymbol{J}^{-1})(k_X/2 + k_\omega \sqrt{2\mathcal{V}'(t_\circ)/\lambda_m(\boldsymbol{J})}), \end{aligned} \tag{B.62}$$

is upper bounded in the initial errors. Hence, $\dot{\mathcal{V}}'$ is uniformly continuous, and application of Lemma 2.5 (Barbălat) yields

$$\lim_{(t-t_\circ)\to\infty} \dot{\mathcal{V}}'(t) = \boldsymbol{0} \Rightarrow \lim_{(t-t_\circ)\to\infty} \boldsymbol{e}_\omega(t) = \boldsymbol{0}. \tag{B.63}$$

Consider writing the closed-loop dynamics in (B.48) as

$$\dot{f}(t) = f_0(t) + \eta(t),$$

where

$$f(t) = \boldsymbol{J}\boldsymbol{e}_{\boldsymbol{\omega}}, \quad \eta(t) = -k_\omega \boldsymbol{e}_{\boldsymbol{\omega}}(t), \quad f_0(t) = -k_X \boldsymbol{e}_{\boldsymbol{X}}.$$

By (B.63), $f(t) \to \boldsymbol{0}$ and $\eta(t) \to \boldsymbol{0}$ as $t - t_\circ \to \infty$. Furthermore, by (B.47) and (B.61), $\|\dot{\boldsymbol{e}}_{\boldsymbol{X}}\| \leq (1/2)\|\boldsymbol{e}_{\boldsymbol{\omega}}\| \leq (1/2)\sqrt{2\mathcal{V}'(t_\circ)/\lambda_m(\boldsymbol{J})}$, implying that $f_0(t) = -k_X \boldsymbol{e}_{\boldsymbol{X}}$ is uniformly continuous. Application of Lemma 2.7 yields

$$\lim_{(t-t_\circ)\to\infty} \dot{f}(t) = \lim_{(t-t_\circ)\to\infty} f_0(t) = \boldsymbol{0} \Rightarrow \lim_{(t-t_\circ)\to\infty} \boldsymbol{X}_e(t) = \pm \boldsymbol{I}.$$

Consequently, all trajectories of the closed-loop system asymptotically converge to one of the points $(\boldsymbol{X}_e, \boldsymbol{e}_{\boldsymbol{\omega}}) = (\pm\boldsymbol{I}, \boldsymbol{0})$, and to assess the stability properties of these two equilibrium points, we perform local linearizations.

Local Linearizations Take a first order approximation of the attitude error around $\boldsymbol{X}_\circ \in \mathrm{SU}(2)$, as

$$\boldsymbol{X}_e(t) \approx \boldsymbol{X}_\circ(\boldsymbol{I} + [\boldsymbol{\epsilon}(t)/2]^\wedge), \tag{B.64}$$

with some small perturbation $\boldsymbol{\epsilon}(t) \in \mathbb{R}^3$. The attitude kinematics become

$$\begin{aligned}
\frac{\mathrm{d}}{\mathrm{d}t}(\boldsymbol{X}_\circ(\boldsymbol{I} + [\boldsymbol{\epsilon}(t)/2]^\wedge)) &= \boldsymbol{X}_\circ(\boldsymbol{I} + [\boldsymbol{\epsilon}(t)/2]^\wedge)[\boldsymbol{e}_\omega(t)/2]^\wedge \Leftrightarrow \\
\boldsymbol{X}_\circ\Big[\frac{1}{2}\frac{\mathrm{d}}{\mathrm{d}t}\boldsymbol{\epsilon}(t)\Big]^\wedge &= \boldsymbol{X}_\circ(\boldsymbol{I} + [\boldsymbol{\epsilon}(t)/2]^\wedge)[\boldsymbol{e}_\omega(t)/2]^\wedge \Leftrightarrow \\
\Big[\frac{\mathrm{d}}{\mathrm{d}t}\boldsymbol{\epsilon}(t)\Big]^\wedge &= (\boldsymbol{I} + [\boldsymbol{\epsilon}(t)/2]^\wedge)[\boldsymbol{e}_\omega(t)]^\wedge \Leftrightarrow \\
\frac{\mathrm{d}}{\mathrm{d}t}\boldsymbol{\epsilon}(t) &= \boldsymbol{e}_\omega(t) + [[\boldsymbol{\epsilon}(t)/2]^\wedge[\boldsymbol{e}_\omega(t)]^\wedge]^\vee \triangleq f_1(\boldsymbol{\epsilon}(t), \boldsymbol{e}_\omega(t)).
\end{aligned}$$

and a local linearization about $(\boldsymbol{\epsilon}, \boldsymbol{e}_{\boldsymbol{\omega}}) = (\boldsymbol{0}, \boldsymbol{0})$ yields

$$\frac{\partial f_1(\boldsymbol{\epsilon}, \boldsymbol{e}_\omega)}{\partial \boldsymbol{\epsilon}}\Big|_{(\boldsymbol{\epsilon}, \boldsymbol{e}_\omega)=(\boldsymbol{0},\boldsymbol{0})} = \boldsymbol{0}, \quad \frac{\partial f_1(\boldsymbol{\epsilon}, \boldsymbol{e}_\omega)}{\partial \boldsymbol{e}_\omega}\Big|_{(\boldsymbol{\epsilon}, \boldsymbol{e}_\omega)=(\boldsymbol{0},\boldsymbol{0})} = \boldsymbol{I}. \tag{B.65}$$

As such, close to the point $(\boldsymbol{\epsilon}, \boldsymbol{e}_\omega) = (\boldsymbol{0}, \boldsymbol{0})$, for any $\boldsymbol{X}_\circ \in \mathrm{SU}(2)$, the attitude rate error corresponds to the time-derivative of the perturbation $\boldsymbol{\epsilon}$. If we express the attitude error in terms of this perturbation, we obtain

$$\boldsymbol{e}_{\boldsymbol{X}} = \frac{1}{2}[\boldsymbol{X}_e - \mathrm{Tr}(\boldsymbol{X}_e)\boldsymbol{I}/2]^\vee = \frac{1}{2}[\boldsymbol{X}_\circ(\boldsymbol{I} + [\boldsymbol{\epsilon}(t)/2]^\wedge) - \mathrm{Tr}(\boldsymbol{X}_\circ(\boldsymbol{I} + [\boldsymbol{\epsilon}(t)/2]^\wedge))\boldsymbol{I}/2]^\vee,$$

and for $\boldsymbol{X}_\circ = \pm\boldsymbol{I}$, as $\mathrm{Tr}([\boldsymbol{\epsilon}(t)]^\wedge) = 0$, we obtain

$$\boldsymbol{e}_{\boldsymbol{X}}|_{\boldsymbol{X}_\circ = \pm\boldsymbol{I}} = \frac{1}{2}[\pm(\boldsymbol{I} + [\boldsymbol{\epsilon}(t)/2]^\wedge) - \mathrm{Tr}(\pm(\boldsymbol{I} + [\boldsymbol{\epsilon}(t)/2]^\wedge))\boldsymbol{I}/2]^\vee = \pm\frac{1}{4}\boldsymbol{\epsilon}(t). \tag{B.66}$$

Given this, the time-evolution of the attitude rate error expressed in the perturbation $\boldsymbol{\epsilon}$ close to $\boldsymbol{X}_\circ \in \{\boldsymbol{I}, -\boldsymbol{I}\}$. By (B.66), for $\boldsymbol{X}_\circ = \pm\boldsymbol{I}$, we obtain

$$\frac{\mathrm{d}}{\mathrm{d}t}(\boldsymbol{J}\boldsymbol{e}_{\boldsymbol{\omega}}) = -k_\omega \boldsymbol{e}_{\boldsymbol{\omega}} - k_X \boldsymbol{e}_{\boldsymbol{X}} = -k_\omega \boldsymbol{e}_{\boldsymbol{\omega}} \mp \frac{k_X}{4}\boldsymbol{\epsilon} \triangleq f_2(\boldsymbol{\epsilon}, \boldsymbol{e}_{\boldsymbol{\omega}}). \tag{B.67}$$

Here, taking the Jacobian of f_2 at $(\boldsymbol{\epsilon}, \boldsymbol{e}_\omega) = \boldsymbol{0}$, for $\boldsymbol{X}_\circ = \pm\boldsymbol{I}$, we have that

$$\frac{\partial f_2(\boldsymbol{\epsilon}, \boldsymbol{e}_\omega)}{\partial \boldsymbol{\epsilon}}\Big|_{(\boldsymbol{\epsilon}, \boldsymbol{e}_\omega)=\boldsymbol{0}} = \mp\frac{k_X}{4}\boldsymbol{I} \triangleq -\mathcal{K}, \quad \frac{\partial f_2(\boldsymbol{\epsilon}, \boldsymbol{e}_\omega)}{\partial \boldsymbol{e}_\omega}\Big|_{(\boldsymbol{\epsilon}, \boldsymbol{e}_\omega)=\boldsymbol{0}} = -k_{\boldsymbol{\omega}}\boldsymbol{I} \triangleq -\mathcal{C}.$$

Thus, as $\mathcal{M} = \mathcal{M}^\top = \boldsymbol{J} \succ \boldsymbol{0}$, $\mathcal{C} = \mathcal{C}^\top = k_\omega \boldsymbol{I} \succ \boldsymbol{0}$, and in a neighborhood of a point $(\boldsymbol{X}_e, \boldsymbol{e}_\omega) \in (\pm\boldsymbol{I}, \boldsymbol{0})$, the perturbation evolves locally by the dynamics,

$$\mathcal{M}\ddot{\boldsymbol{\epsilon}} + \mathcal{C}\dot{\boldsymbol{\epsilon}} + \mathcal{K}\boldsymbol{\epsilon} = \boldsymbol{0}. \tag{B.68}$$

Here, Lemma B.1 immediately yields that the point $(\boldsymbol{X}_e, \boldsymbol{e}_\omega) = (\boldsymbol{I}, \boldsymbol{0})$ is locally asymptotically stable, as it is semi-stable and in this case $\mathcal{K} = (k_X/4)\boldsymbol{I} \succ 0$. Additionally, the corresponding instability result in Lemma B.2 yields that the point $(\boldsymbol{X}_e, \boldsymbol{e}_\omega) = (-\boldsymbol{I}, \boldsymbol{0})$ is unstable, as in this case here $\mathcal{K} = -(k_X/4)\boldsymbol{I} \prec 0$. As such, the only stable equilibrium point is found in $(\boldsymbol{X}_e, \boldsymbol{e}_\omega) = (\boldsymbol{I}, \boldsymbol{0})$ and this point is UAGAS, as the only other equilibrium point is unstable. □

B.5 Proposition 3.2: Ultimate Bound

Proof of Proposition 3.2. The proof is analogous to the proof of Proposition 3.1 in Appendix B.3, but using the Lyapunov function B.50, and the associated matrices $\boldsymbol{M}_1, \boldsymbol{M}_2, \boldsymbol{W}$, given in (B.71) and (B.56). □

B.6 Theorem 3.5: Discontinuous Geometric FSF on SU(2)

Proof of Theorem 3.5. Consider two controllers operating on the domains $\mathrm{SU}(2)^+$ and $\mathrm{SU}(2)^-$ respectively. For the former, we can invoke Theorem 3.4 to show uniform exponential stability on $\mathrm{SU}(2)^+$, but the latter requires more thought. We start by noting that the time-derivative of $\bar{\Gamma}$ can be expressed,

$$\frac{\mathrm{d}}{\mathrm{d}t}\bar{\Gamma}(\boldsymbol{X}_r, \boldsymbol{X}) = -\frac{\mathrm{d}}{\mathrm{d}t}\Gamma(\boldsymbol{X}_r, \boldsymbol{X}) = -\frac{1}{2}[\boldsymbol{X}_r^*\boldsymbol{X} - \mathrm{Tr}(\boldsymbol{X}_r^*\boldsymbol{X})\boldsymbol{I}/2]^\vee \cdot \boldsymbol{e}_{\boldsymbol{\omega}} = \boldsymbol{e}_{\boldsymbol{X}}^- \cdot \boldsymbol{e}_{\boldsymbol{\omega}}$$

where $\boldsymbol{e}_{\boldsymbol{X}}^- = -\boldsymbol{e}_{\boldsymbol{X}}^+$. Here, the attitude rate error $\boldsymbol{e}_{\boldsymbol{\omega}}$ is exactly the same as that in the continuous control law. Furthermore, the attitude error time-derivative is upper bounded just as in (B.47), with

$$\|\dot{\boldsymbol{e}}_{\boldsymbol{X}}^\pm\| \leq \frac{1}{4}\|\boldsymbol{e}_{\boldsymbol{\omega}}\|. \tag{B.69}$$

Consider next the construction of two separate Lyapunov function candidates

$$\mathcal{V} = k_X\Gamma(\boldsymbol{X}_r, \boldsymbol{X}) + k_c\boldsymbol{e}_{\boldsymbol{\omega}} \cdot \boldsymbol{e}_{\boldsymbol{X}}^+ + \frac{1}{2}\boldsymbol{e}_{\boldsymbol{\omega}} \cdot \boldsymbol{J}\boldsymbol{e}_{\boldsymbol{\omega}} \quad \text{if} \quad \boldsymbol{X}_r^*\boldsymbol{X} \in \mathrm{SU}(2)^+, \tag{B.70a}$$

$$\bar{\mathcal{V}} = k_X\bar{\Gamma}(\boldsymbol{X}_r, \boldsymbol{X}) - k_c\boldsymbol{e}_{\boldsymbol{\omega}} \cdot \boldsymbol{e}_{\boldsymbol{X}}^- + \frac{1}{2}\boldsymbol{e}_{\boldsymbol{\omega}} \cdot \boldsymbol{J}\boldsymbol{e}_{\boldsymbol{\omega}} \quad \text{if} \quad \boldsymbol{X}_r^*\boldsymbol{X} \in \mathrm{SU}(2)^-. \tag{B.70b}$$

Here it is again not immediately clear that these are positive definite functions of the errors on their respective domains, but if defining $\boldsymbol{z}^\pm = (\|\boldsymbol{e}_{\boldsymbol{X}}^\pm\|, \|\boldsymbol{e}_{\boldsymbol{\omega}}\|)$, noting that $4\|\boldsymbol{e}_{\boldsymbol{X}}\|^2 = \|\Im(E_{\mathbb{H}}^{\mathrm{SU}(2)}(\boldsymbol{X}_r^*\boldsymbol{X}))\|^2$, these functions can be upper and lower-bounded on their respective domains by positive definite functions

$$c_1\|\boldsymbol{z}^\pm\|^2 \leq (\boldsymbol{z}^\pm)^\top\boldsymbol{M}_1\boldsymbol{z}^\pm \leq \mathcal{V} \leq (\boldsymbol{z}^\pm)^\top\boldsymbol{M}_2\boldsymbol{z}^\pm \leq c_2\|\boldsymbol{z}^\pm\|^2 \quad \forall \boldsymbol{X}_r^*\boldsymbol{X} \in \mathrm{SU}(2)^+,$$

$$c_1\|\boldsymbol{z}^\pm\|^2 \leq (\boldsymbol{z}^\pm)^\top\boldsymbol{M}_1\boldsymbol{z}^\pm \leq \bar{\mathcal{V}} \leq (\boldsymbol{z}^\pm)^\top\boldsymbol{M}_2\boldsymbol{z}^\pm \leq c_2\|\boldsymbol{z}^\pm\|^2 \quad \forall \boldsymbol{X}_r^*\boldsymbol{X} \in \mathrm{SU}(2)^-,$$

where $c_1 = \lambda_m(\boldsymbol{M}_1)$, $c_2 = \lambda_M(\boldsymbol{M}_2)$ for a $\phi = 1$, resulting in

$$\boldsymbol{M}_1 \triangleq \frac{1}{2}\begin{bmatrix} 4k_X & -k_c \\ -k_c & \lambda_m(\boldsymbol{J}) \end{bmatrix}, \qquad \boldsymbol{M}_2 \triangleq \frac{1}{2}\begin{bmatrix} 8k_X & k_c \\ k_c & \lambda_M(\boldsymbol{J}) \end{bmatrix}. \tag{B.71}$$

The existence of gains k_X, k_c, k_ω such that $\boldsymbol{M}_1, \boldsymbol{M}_2 \succ 0$ is guaranteed by Remark 3.6. Furthermore, consider any time $t_s \geq t_\circ$ where the attitude error traverses the line $\Gamma(\boldsymbol{X}_r, \boldsymbol{X}) = \bar{\Gamma}(\boldsymbol{X}_r, \boldsymbol{X}) = 1$. By defining $t_s^- < t_s < t_s^+$,

$$\lim_{t_s^- \to t_s} \mathcal{V}(t_s^-) = \lim_{t_s^+ \to t_s} \bar{\mathcal{V}}(t_s^+), \tag{B.72a}$$

$$\lim_{t_s^- \to t_s} \bar{\mathcal{V}}(t_s^-) = \lim_{t_s^+ \to t_s} \mathcal{V}(t_s^+), \tag{B.72b}$$

with equality between (B.72a) and (B.72b) over the time t_s if and only if $\boldsymbol{e}_{\boldsymbol{X}} \cdot \boldsymbol{e}_{\boldsymbol{\omega}} = \boldsymbol{0}$. However, as the sign in the attitude error is switched on the different sides of t_s, we can define a composite a Lyapunov function candidate

$$\mathcal{V}^{\pm} = \begin{cases} \mathcal{V} & \text{if} \quad \boldsymbol{X}_e \in \mathrm{SU}(2)^+ \\ \bar{\mathcal{V}} & \text{if} \quad \boldsymbol{X}_e \in \mathrm{SU}(2)^- \end{cases}, \tag{B.73}$$

which is then continuous over each switching time t_s by (B.70) and (B.72). Just is the proof of Theorem 3.4, differentiation of the Lyapunov functions along the solutions of the error dynamics and the invocation of (B.69) yields

$$\frac{\mathrm{d}\mathcal{V}}{\mathrm{d}t} \leq -(\boldsymbol{z}^{\pm})^\top \boldsymbol{W} \boldsymbol{z}^{\pm} \leq -c_3 \|\boldsymbol{z}^{\pm}\|^2 \qquad \forall \boldsymbol{X}_r^* \boldsymbol{X} \in \mathrm{SU}(2)^+, \tag{B.74}$$

$$\frac{\mathrm{d}\bar{\mathcal{V}}}{\mathrm{d}t} \leq -(\boldsymbol{z}^{\pm})^\top \boldsymbol{W} \boldsymbol{z}^{\pm} \leq -c_3 \|\boldsymbol{z}^{\pm}\|^2 \qquad \forall \boldsymbol{X}_r^* \boldsymbol{X} \in \mathrm{SU}(2)^-, \tag{B.75}$$

with $c_3 = \lambda_m(\boldsymbol{W})$ where

$$\boldsymbol{W} \triangleq \begin{bmatrix} \frac{k_X k_c}{\lambda_M(\boldsymbol{J})} & -\frac{k_c k_\omega}{2\lambda_m(J)} \\ -\frac{k_c k_\omega}{2\lambda_m(J)} & k_\omega - \frac{k_c}{4} \end{bmatrix}. \tag{B.76}$$

The existence of a constant $c_3 > 0$ again follows directly from Remark 3.6. In contrast to the continuous controller, we no longer need to restrict the attitude error trajectories to the sub-level sets of $\mathrm{SU}(2)^+$ or $\mathrm{SU}(2)^-$, as an escape from one implies entry into the other across the line $\Gamma(\boldsymbol{X}_r, \boldsymbol{X}) = \bar{\Gamma}(\boldsymbol{X}_r, \boldsymbol{X}) = 1$, over which the composite Lyapunov function candidate in (B.73) is continuous. However, $\mathcal{V}^{\pm}$ is no longer continuously differentiable in time (if any switching occurs), and we cannot use Theorem 2.3 as a consequence. Instead, the comparison lemma (see, e.g., [Khalil, 1996, Lemma 2.5]) is invoked on

$$(\mathrm{d}/\mathrm{d}t)\mathcal{V}^{\pm} \leq (\lambda_M(\boldsymbol{M}_2)/\lambda_M(\boldsymbol{W}))\mathcal{V}^{\pm}, \tag{B.77}$$

yielding global exponential stability of the origin $\boldsymbol{z}^{\pm} = \boldsymbol{0}$, for any $\boldsymbol{z}^{\pm}(t_\circ) \in \mathbb{R}^2_{\geq 0}$, and since $\boldsymbol{z}^{\pm} \to \boldsymbol{0} \Rightarrow (\boldsymbol{e}^{\pm}_{\boldsymbol{X}}, \boldsymbol{e}_{\boldsymbol{\omega}}) \to \boldsymbol{0} \Rightarrow (\pm\boldsymbol{X}, \boldsymbol{\omega}) \to (\boldsymbol{X}_r, \boldsymbol{\omega}_r) \Rightarrow (E^{\mathrm{SU}(2)}_{\mathrm{SO}(3)}(\pm\boldsymbol{X}), \boldsymbol{\omega}) \to (E^{\mathrm{SU}(2)}_{\mathrm{SO}(3)}(\boldsymbol{X}_r), \boldsymbol{\omega}_r)$, we have that convergence to this origin implies a zero tracking error on SO(3). □

B.7 Theorem 3.6: Robust Geometric FSF on SU(2)

Proof of Theorem 3.6. For notational simplicity, we denote the *hat*- and *vee*-maps associated with SU(2) in Definition 2.13 as $[\cdot]^{\wedge} = [\cdot]^{\wedge}_{\mathrm{SU}(2)}$ and $[\cdot]^{\vee} = [\cdot]^{\vee}_{\mathrm{SU}(2)}$, respectively. Consider the feedback law in Proposition 3.4. Following the proof in [Lee et al., 2013] for the robust controller on SO(3), we start by noting that with $\boldsymbol{e}_A$ defined as in (3.53c), we obtain

$$\boldsymbol{e}_A \cdot (\boldsymbol{\Delta} - \boldsymbol{\mu}_{\boldsymbol{X}}) \leq \|\boldsymbol{e}_A\| L - \frac{L^2 \|\boldsymbol{e}_A\|^2}{L\|\boldsymbol{e}_A\| + \epsilon_X} = \frac{L\|\boldsymbol{e}_A\|}{L\|\boldsymbol{e}_A\| + \epsilon_X} \epsilon_X \leq \epsilon_X.$$

Introducing the $\boldsymbol{\mu}_{\boldsymbol{X}}$-term (3.53b) when controlling the perturbed dynamics in (3.4), using the feedback law in (3.33) of Proposition 3.4 with the Lyapunov function in (B.50), the relationship in (B.51) still holds with the matrices in (3.31).The time-derivative of the Lyapunov function now becomes,

$$\begin{aligned}
\dot{\mathcal{V}} &= k_X \boldsymbol{e}_{\boldsymbol{X}} \cdot \boldsymbol{e}_{\boldsymbol{\omega}} + k_c \boldsymbol{e}_{\boldsymbol{\omega}} \cdot \dot{\boldsymbol{e}}_{\boldsymbol{X}} + k_c \boldsymbol{e}_{\boldsymbol{X}} \cdot \dot{\boldsymbol{e}}_{\boldsymbol{\omega}} + \boldsymbol{e}_{\boldsymbol{\omega}} \cdot \boldsymbol{J} \dot{\boldsymbol{e}}_{\boldsymbol{\omega}} \\
&\leq -\Big(\frac{k_X k_c}{\lambda_M(\boldsymbol{J})} z_1^2 - \frac{k_c k_\omega}{\lambda_m(\boldsymbol{J})} z_1 z_2 + k_\omega z_2^2 - \frac{k_c}{4} z_2^2 \Big) + (k_c \boldsymbol{J}^{-1} \boldsymbol{e}_{\boldsymbol{X}} + \boldsymbol{e}_{\boldsymbol{\omega}}) \cdot (\boldsymbol{\Delta} - \boldsymbol{\mu}_{\boldsymbol{X}}) \\
&= -\boldsymbol{z}^\top \boldsymbol{W} \boldsymbol{z} + \boldsymbol{e}_A \cdot (\boldsymbol{\Delta} - \boldsymbol{\mu}_{\boldsymbol{X}}) \\
&\leq -\boldsymbol{z}^\top \boldsymbol{W} \boldsymbol{z} + \epsilon_X,
\end{aligned} \tag{B.78}$$

and $\dot{\mathcal{V}} < 0$ whenever $\mathcal{V}$ is sufficiently large, specifically

$$\mathcal{V} > \frac{\lambda_M(\boldsymbol{M}_2)}{\lambda_m(\boldsymbol{W})} \epsilon_X = d_1 \Rightarrow \boldsymbol{z}^\top \boldsymbol{W} \boldsymbol{z} > \epsilon_X \Rightarrow \dot{\mathcal{V}} < 0. \tag{B.79}$$

If we consider the sub-level set of $\mathcal{V}$ characterized by $\mathcal{S}_1 = \{\boldsymbol{z} | \mathcal{V} < d_1\}$, and take a second sub-level set of $\mathcal{V}$ characterized by $\mathcal{S}_2 = \{\boldsymbol{z} | \mathcal{V} < d_2\}$, where

$$d_2 = \lambda_m(\boldsymbol{M}_1) \phi (2 - \phi),$$

then $\mathcal{S}_1 \subset \mathcal{S}_2 \subset D$ if $d_1 < d_2$, as $\mathcal{V}$ is increasing in $\boldsymbol{z}$ on D. A sufficient condition is found in

$$d_1 = \frac{\lambda_M(\boldsymbol{M}_2)}{\lambda_m(\boldsymbol{W})} \epsilon_X < \lambda_m(\boldsymbol{M}_1) \phi (2 - \phi) = d_2 \Leftrightarrow \epsilon_X < \frac{\lambda_m(\boldsymbol{W}) \lambda_m(\boldsymbol{M}_1)}{\lambda_M(\boldsymbol{M}_2)} \phi (2 - \phi).$$

Provided that $\boldsymbol{\Delta}(t)$ is continuous in time, The Lyapunov function $\mathcal{V}$ is continuously differentiable along the perturbed attitude system trajectories. Application of [Khalil, 1996, Theorem 5.1] yields that the solutions $\boldsymbol{z}(t)$ are uniformly ultimately bounded. Furthermore, a conservative estimate for the ultimate bound can be computed by [Khalil, 1996, Corollary 5.1], as

$$\lim_{t-t_o\to\infty} \|\boldsymbol{z}(t)\|^2 \leq \frac{\lambda_M(\boldsymbol{M}_2)}{\lambda_m(\boldsymbol{M}_1)\lambda_m(\boldsymbol{W})}\epsilon_X. \tag{B.80}$$

□

B.8 Proposition 4.3: Geometric FSF on $SU(2) \times \mathbb{R}^3$

Proof of Proposition 4.3. This proof is strikingly similar to the proof for the controller on $SO(3) \times \mathbb{R}^3$ in [Lee et al., 2010, Appendix D], and a sketch is given here with some key intermediary expressions. In the following, let

$$\boldsymbol{R} = E^{\mathrm{SU}(2)}_{\mathrm{SO}(3)}(\boldsymbol{X}) = E^{\mathbb{H}}_{\mathrm{SO}(3)}(\boldsymbol{q}), \quad \boldsymbol{R}_d = E^{\mathrm{SU}(2)}_{\mathrm{SO}(3)}(\boldsymbol{X}_d) = E^{\mathbb{H}}_{\mathrm{SO}(3)}(\boldsymbol{q}_d), \tag{B.81}$$

and consider errors defined as in Theorem 3.4 but with respect to the desired reference $(\boldsymbol{X}_d, \boldsymbol{\omega}_d, \dot{\boldsymbol{\omega}}_d) \in \mathrm{SU}(2) \times \mathbb{R}^3 \times \mathbb{R}^3$. Specifically, consider an error element $\boldsymbol{X}_e = \boldsymbol{X}_d^* \boldsymbol{X} \in \mathrm{SU}(2)$, in which the control errors are defined as

$$\boldsymbol{e}_{\boldsymbol{X}} = \frac{1}{2}[\boldsymbol{X}_e - \mathrm{Tr}(\boldsymbol{X}_e)\boldsymbol{I}/2]^{\vee}_{\mathrm{SU}(2)}, \quad \boldsymbol{e}_{\boldsymbol{\omega}} = \boldsymbol{\omega} - [\boldsymbol{X}_e^*[\boldsymbol{\omega}_d]^{\wedge}_{\mathrm{SU}(2)}\boldsymbol{X}_e]^{\vee}_{\mathrm{SU}(2)}, \tag{B.82}$$

and the translation errors defined as in the proposition statement, with

$$\boldsymbol{e}_{\boldsymbol{p}} = \boldsymbol{p} - \boldsymbol{p}_r, \qquad \boldsymbol{e}_{\boldsymbol{v}} = \boldsymbol{v} - \boldsymbol{v}_r. \tag{B.83}$$

In addition, consider errors related to the positional and attitude subsystems,

$$\boldsymbol{z}_p \triangleq (\|\boldsymbol{e}_{\boldsymbol{p}}\|;\ \|\boldsymbol{e}_{\boldsymbol{v}}\|) \in \mathbb{R}^2_{\geq 0}, \qquad \boldsymbol{z}_a \triangleq (\|\boldsymbol{e}_{\boldsymbol{X}}\|;\ \|\boldsymbol{e}_{\boldsymbol{\omega}}\|) \in \mathbb{R}^2_{\geq 0}, \tag{B.84}$$

respectively, as a combined error

$$\bar{\boldsymbol{z}} \triangleq (\boldsymbol{z}_p;\ \boldsymbol{z}_a) \in \mathbb{R}^4_{\geq 0}. \tag{B.85}$$

Define a Lyapunov function comprised of two parts, one relating the attitude subsystem, $\mathcal{V}_a$, and one relating to the translation subsystem, $\mathcal{V}_p$. The former is defined as in (B.50), and the latter is defined analogously, as

$$\mathcal{V}^a \triangleq k_X \Gamma(\boldsymbol{X}_d, \boldsymbol{X}) + c_a \boldsymbol{e}_{\boldsymbol{\omega}} \cdot \boldsymbol{e}_{\boldsymbol{X}} + \frac{1}{2}\boldsymbol{e}_{\boldsymbol{\omega}} \cdot \boldsymbol{J}\boldsymbol{e}_{\boldsymbol{\omega}}, \tag{B.86a}$$

$$\mathcal{V}^p \triangleq \frac{1}{2}k_p\|\boldsymbol{e}_{\boldsymbol{p}}\|^2 + c_p \boldsymbol{e}_{\boldsymbol{p}} \cdot \boldsymbol{e}_{\boldsymbol{v}} + \frac{1}{2}m\|\boldsymbol{e}_{\boldsymbol{v}}\|^2, \tag{B.86b}$$

respectively. Given that the attitude dynamics are actuated by Theorem 3.4, we can consider initial attitude errors on

$$(\boldsymbol{X}_e(t_\circ), \boldsymbol{e}_{\boldsymbol{\omega}}(t_\circ)) \in \{(\boldsymbol{X}_e, \boldsymbol{e}_{\boldsymbol{\omega}}) \in \mathcal{L}_\phi \times \mathbb{R}^3 \mid \mathcal{V}^a|_{c_a=0} \leq k_X \phi\}, \tag{B.87}$$

where

$$\mathcal{L}_\phi = \{\boldsymbol{X}_d^* \boldsymbol{X} \in \mathrm{SU}(2) \mid \Gamma(\boldsymbol{X}_d, \boldsymbol{X}) \leq \phi < 2\}. \tag{B.88}$$

With the result in Theorem 3.4, it follows that $\boldsymbol{X}_e(t) \in \mathcal{L}_\phi$ for all $t \geq t_\circ$ if $\mathcal{V}^a(t_\circ)|_{c_a=0} \leq k_X \phi$, and that the errors converge exponentially to $(\boldsymbol{X}_e, \boldsymbol{e}_{\boldsymbol{\omega}}) = (\boldsymbol{I}, \boldsymbol{0})$. As such, the main idea of the proof is to conduct the stability analysis on a domain $D = \{(\boldsymbol{e}_{\boldsymbol{p}}, \boldsymbol{e}_{\boldsymbol{v}}, \boldsymbol{X}_e, \boldsymbol{e}_{\boldsymbol{\omega}}) \in \mathbb{R}^3 \times \mathbb{R}^3 \times \mathcal{L}_\phi \times \mathbb{R}^3 \mid \|\boldsymbol{e}_{\boldsymbol{p}}\| \leq B_p\}$, and restrict the domain by making ϕ and B_p sufficiently small to guarantee that all solutions remain within D. To facilitate such an analysis, we first make a few preliminary geometric observations with respect to the vectors $\boldsymbol{b}_{d3} = \boldsymbol{R}_d \boldsymbol{e}_3$ and $\boldsymbol{b}_3 = \boldsymbol{R}\boldsymbol{e}_3$, and their cosine angle $\boldsymbol{b}_{d3} \cdot \boldsymbol{b}_3 = \cos(\theta)$:

- Firstly, note that for any $\phi < 1 - 1/\sqrt{2}$,

$$\Gamma(\boldsymbol{X}_d, \boldsymbol{X}) \leq \phi \Rightarrow 1 - \cos(\theta/2) < 1 - \frac{1}{\sqrt{2}} \Leftrightarrow \frac{1}{\sqrt{2}} < \cos(\theta/2) \Rightarrow \cos(\theta) > 0. \tag{B.89}$$

- Secondly, as $\sin^2(\theta) \leq 4\sin^2(\theta/2)$ for all $\cos(\theta) > 0$, we have that

$$\sin^2(\theta) \leq 2^2 \sin^2(\theta/2) = 2^4 \|\boldsymbol{e}_{\boldsymbol{X}}\|^2 \leq 2^3 \Gamma(\boldsymbol{X}_d, \boldsymbol{X}) \leq 2^3 \phi \triangleq \alpha^2, \tag{B.90}$$

  as $4\|\boldsymbol{e}_{\boldsymbol{X}}\|^2 = \|\Im(\boldsymbol{q}_d^* \odot \boldsymbol{q})\| = \frac{1}{4}\sin^2(\theta/2)$.

These geometric relationships are illustrated in Figure B.1, whereby

$$\Gamma(\boldsymbol{X}_d, \boldsymbol{X}) \leq \phi < 2^{-3} < 1 - 1/\sqrt{2} \Rightarrow \cos(\theta) > 0 \Rightarrow \begin{cases} \boldsymbol{b}_{d3} \cdot \boldsymbol{b}_3 > 0 \\ \alpha < 1 \end{cases}. \tag{B.91}$$

Therefore, consider performing the stability analysis on the domain characterized by D with $\phi = 2^{-3}$ with a Lyapunov function candidate $\mathcal{V} = \mathcal{V}^a + \mathcal{V}^p$.

Translation Error Dynamics The translation error dynamics are

$$m\dot{\boldsymbol{e}}_{\boldsymbol{v}} = m\ddot{\boldsymbol{p}} - m\ddot{\boldsymbol{p}}_r = -mg\boldsymbol{e}_3 + f\boldsymbol{R}\boldsymbol{e}_3 - m\ddot{\boldsymbol{p}}_r. \tag{B.92}$$

Note that $\boldsymbol{e}_3 \boldsymbol{R}_d^\top \boldsymbol{R}\boldsymbol{e}_3 = \boldsymbol{b}_{d3} \cdot \boldsymbol{b}_3 > 0$ if we can ensure that (B.89) holds. If so, the term $\frac{f}{\boldsymbol{e}_3 \boldsymbol{R}_d^\top \boldsymbol{R}\boldsymbol{e}_3} \boldsymbol{R}_d \boldsymbol{e}_3$ is well defined, and as such, (B.92) can be expressed

$$m\dot{\boldsymbol{e}}_{\boldsymbol{v}} = -mg\boldsymbol{e}_3 - m\ddot{\boldsymbol{p}}_r + \frac{f}{\boldsymbol{e}_3 \boldsymbol{R}_d^\top \boldsymbol{R}\boldsymbol{e}_3} \boldsymbol{R}_d \boldsymbol{e}_3 + \bar{\boldsymbol{f}}, \tag{B.93}$$

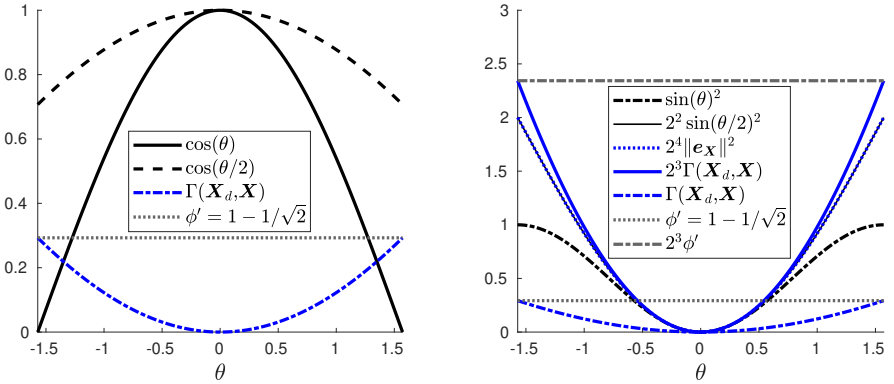

Figure B.1 Illustration of the geometric relationships that facilitate the stability proof. *Left:* Expressions relating to the cosine of the rotation angle θ. *Right:* Expressions relating to the squared sine of the rotation angle θ.

where

$$\bar{\boldsymbol{f}} = \frac{f}{\boldsymbol{e}_3 \boldsymbol{R}_d^\top \boldsymbol{R} \boldsymbol{e}_3} \boldsymbol{R}_d \boldsymbol{e}_3 \Big((\boldsymbol{e}_3 \boldsymbol{R}_d^\top \boldsymbol{R} \boldsymbol{e}_3) \boldsymbol{R} \boldsymbol{e}_3 - \boldsymbol{R}_d \boldsymbol{e}_3 \Big). \tag{B.94}$$

In addition, recalling the actuating force is computed by the desired force

$$\boldsymbol{f}_d = -k_p \boldsymbol{e}_{\boldsymbol{p}} - k_v \boldsymbol{e}_{\boldsymbol{v}} + mg\boldsymbol{e}_3 + m\ddot{\boldsymbol{p}}_r. \tag{B.95}$$

As $\boldsymbol{b}_{d3} = \boldsymbol{f}_d \|\boldsymbol{f}_d\|^{-1}$, we can express $\boldsymbol{f}_d = \|\boldsymbol{f}_d\| \boldsymbol{b}_{d3} = \|\boldsymbol{f}_d\| \boldsymbol{R}_d \boldsymbol{e}_3$, whereby

$$\frac{f}{\boldsymbol{e}_3 \boldsymbol{R}_d^\top \boldsymbol{R} \boldsymbol{e}_3} \boldsymbol{R}_d \boldsymbol{e}_3 = \frac{\boldsymbol{f}_d \cdot \boldsymbol{R} \boldsymbol{e}_3}{\boldsymbol{e}_3 \boldsymbol{R}_d^\top \boldsymbol{R} \boldsymbol{e}_3} \boldsymbol{R}_d \boldsymbol{e}_3 = \|\boldsymbol{f}_d\| \boldsymbol{R}_d \boldsymbol{e}_3 = \boldsymbol{f}_d. \tag{B.96}$$

Insertion of this expression in (B.93) yields

$$m\dot{\boldsymbol{e}}_{\boldsymbol{v}} = -mg\boldsymbol{e}_3 - m\ddot{\boldsymbol{p}}_r + \boldsymbol{f}_d + \bar{\boldsymbol{f}} = -k_p \boldsymbol{e}_{\boldsymbol{p}} - k_v \boldsymbol{e}_{\boldsymbol{v}} + \bar{\boldsymbol{f}}. \tag{B.97}$$

To proceed, we will bound $\bar{\boldsymbol{f}}$ in the control errors using the Assumptions (A1)–(A5), but first, we derive the expression for the time-derivative of the part of the Lyapunov function associated with the translation errors.

Translation Lyapunov Function Candidate Differentiation of the Lyapunov function associated with the translation dynamics yields

$$\dot{\mathcal{V}}^p = -(k_v - c_p)\|\boldsymbol{e}_{\boldsymbol{v}}\|^2 - \frac{c_p k_p}{m}\|\boldsymbol{e}_{\boldsymbol{p}}\|^2 - \frac{c_p k_v}{m}(\boldsymbol{e}_{\boldsymbol{p}} \cdot \boldsymbol{e}_{\boldsymbol{v}}) + \bar{\boldsymbol{f}} \cdot \Big(c_p m^{-1} \boldsymbol{e}_{\boldsymbol{p}} + \boldsymbol{e}_{\boldsymbol{v}} \Big). \tag{B.98}$$

Furthermore, by (B.96), we have that

$$\|\bar{\boldsymbol{f}}\| \leq \|\boldsymbol{f}_d\| \|(\boldsymbol{e}_3 \boldsymbol{R}_d^\top \boldsymbol{R} \boldsymbol{e}_3) \boldsymbol{R} \boldsymbol{e}_3 - \boldsymbol{R}_d \boldsymbol{e}_3\|, \tag{B.99}$$

where the second term is recognized as the sine angle of the smallest rotation angle between $\boldsymbol{b}_{d3}$ and $\boldsymbol{b}_3$, as pointed out in [Lee et al., 2010]. As such, we can utilize the fact that this rotation angle is bounded in the control errors on D, as per (B.89). By this simple observation, we obtain

$$\begin{aligned}
\|\bar{\boldsymbol{f}}\| &\leq \|\boldsymbol{f}_d\|\|(\boldsymbol{e}_3\boldsymbol{R}_d^\top\boldsymbol{R}\boldsymbol{e}_3)\boldsymbol{R}\boldsymbol{e}_3 - \boldsymbol{R}_d\boldsymbol{e}_3\| && \text{(B.100a)}\\
&\leq (k_p\|\boldsymbol{e_p}\| + k_v\|\boldsymbol{e_v}\| + B)\|(\boldsymbol{e}_3\boldsymbol{R}_d^\top\boldsymbol{R}\boldsymbol{e}_3)\boldsymbol{R}\boldsymbol{e}_3 - \boldsymbol{R}_d\boldsymbol{e}_3\| && \text{(B.100b)}\\
&\leq (k_p\|\boldsymbol{e_p}\| + k_v\|\boldsymbol{e_v}\| + B)4\|\boldsymbol{e_X}\| && \text{(B.100c)}\\
&\leq (k_p\|\boldsymbol{e_p}\| + k_v\|\boldsymbol{e_v}\| + B)\alpha, && \text{(B.100d)}
\end{aligned}$$

where the second inequality follows from Assumption (A3), and the third and fourth hold for all trajectories on D from the observations regarding the sine angle in (B.90). Insertion of this bound in (B.101) yields

$$\begin{aligned}
\dot{\mathcal{V}}^p =& -(k_v - c_p)\|\boldsymbol{e_v}\|^2 - \frac{c_p k_p}{m}\|\boldsymbol{e_p}\|^2 - \frac{c_p k_v}{m}(\boldsymbol{e_p}\cdot\boldsymbol{e_v}) + \bar{\boldsymbol{f}}\cdot\Big(\frac{c_p}{m}\boldsymbol{e_p} + \boldsymbol{e_v}\Big)\\
=& -(k_v(1-\alpha) - c_p)\|\boldsymbol{e_v}\|^2 - \frac{c_p k_p}{m}(1-\alpha)\|\boldsymbol{e_p}\|^2\\
&+ \frac{c_p k_v}{m}(1+\alpha)\|\boldsymbol{e_p}\|\|\boldsymbol{e_v}\|\\
&+ 4\|\boldsymbol{e_X}\|\Big(B\Big(\frac{c_p}{m}\|\boldsymbol{e_p}\| + \|\boldsymbol{e_v}\|\Big) + k_p\|\boldsymbol{e_p}\|\|\boldsymbol{e_v}\|\Big)\\
&\leq -\boldsymbol{z}_p^\top\boldsymbol{W}^{pp}\boldsymbol{z}_p + \boldsymbol{z}_p^\top\boldsymbol{W}^{pa}\boldsymbol{z}_a, && \text{(B.101)}
\end{aligned}$$

with $\boldsymbol{W}^{pp}$ and $\boldsymbol{W}^{pa}$ defined as in the proposition statement, in (4.20) and (4.21), respectively. In addition, we note that

$$\boldsymbol{z}_p^\top\boldsymbol{M}_1^{pp}\boldsymbol{z}_p \leq \mathcal{V}^p \leq \boldsymbol{z}_p^\top\boldsymbol{M}_2^{pp}\boldsymbol{z}_p, \tag{B.102}$$

for $\boldsymbol{M}_1^{pp}$ and $\boldsymbol{M}_2^{pp}$ defined as in (4.20) of the proposition.

Complete Lyapunov Function Candidate In addition to these definitions, take $\boldsymbol{M}_1^{aa}, \boldsymbol{M}_2^{aa}, \boldsymbol{W}^{aa}$, to be the matrices in (3.32) associated with the controller in Theorem 3.4, also given in (4.20). In addition, define the matrices

$$\bar{\boldsymbol{M}}_1 = \begin{bmatrix} \boldsymbol{M}_1^{pp} & \boldsymbol{0} \\ \star & \boldsymbol{M}_1^{aa} \end{bmatrix}, \quad \bar{\boldsymbol{M}}_2 = \begin{bmatrix} \boldsymbol{M}_2^{pp} & \boldsymbol{0} \\ \star & \boldsymbol{M}_2^{aa} \end{bmatrix}, \quad \bar{\boldsymbol{W}} = \begin{bmatrix} \boldsymbol{W}^{pp} & -\frac{1}{2}\boldsymbol{W}^{pa} \\ \star & \boldsymbol{W}^{aa} \end{bmatrix}.$$

When considering the combined Lyapunov function candidate $\mathcal{V} = \mathcal{V}^p + \mathcal{V}^a$,

$$\bar{\boldsymbol{z}}^\top\bar{\boldsymbol{M}}_1\bar{\boldsymbol{z}} \leq \mathcal{V} \leq \bar{\boldsymbol{z}}^\top\bar{\boldsymbol{M}}_2\bar{\boldsymbol{z}}. \tag{B.103}$$

Differentiating $\mathcal{V}$ along the solutions of the error dynamics on D yields

$$\dot{\mathcal{V}} = \dot{\mathcal{V}}^p + \dot{\mathcal{V}}^a \leq -\bar{\boldsymbol{z}}^\top\bar{\boldsymbol{W}}\bar{\boldsymbol{z}}. \tag{B.104}$$

By assumption (A5), we have that

$$\begin{aligned}
\dot{\mathcal{V}} &\leq -\bar{\boldsymbol{z}}^\top \bar{\boldsymbol{W}} \bar{\boldsymbol{z}} && \text{(B.105a)}\\
&\leq -\lambda_m(\boldsymbol{W}^{pp})\|\boldsymbol{z}_p\|^2 + \|\boldsymbol{W}^{pa}\|\|\boldsymbol{z}_p\|\|\boldsymbol{z}_a\| - \lambda_m(\boldsymbol{W}^{aa})\|\boldsymbol{z}_a\|^2 && \text{(B.105b)}\\
&\leq -\begin{bmatrix}\|\boldsymbol{z}_p\|\\ \|\boldsymbol{z}_a\|\end{bmatrix}\begin{bmatrix}\lambda_m(\boldsymbol{W}^{pp}) & -\frac{1}{2}\|\boldsymbol{W}^{pa}\|\\ \star & \lambda_m(\boldsymbol{W}^{aa})\end{bmatrix}\begin{bmatrix}\|\boldsymbol{z}_p\|\\ \|\boldsymbol{z}_a\|\end{bmatrix} && \text{(B.105c)}\\
&\leq -B_z(\|\boldsymbol{z}_p\|^2 + \|\boldsymbol{z}_a\|^2). && \text{(B.105d)}
\end{aligned}$$

Consequently, the Lyapunov function time-derivative is negative definite in $\bar{\boldsymbol{z}}$ along the solutions of the error dynamics on D. By (B.105), it follows that $\mathcal{V}$ is continuously differentiable on D, as the signals constituting $\ddot{\mathcal{V}}$ are bounded in the initial errors. As such, Theorem 2.5 yields that $\bar{\boldsymbol{z}} = \boldsymbol{0}$ is UES on D.□

C

Filtered Output Feedback: Proofs

C.1 Theorem 5.2: Explicit Vector FOF on SO(3)

We start by giving some preliminary results before stating the proof of Theorem 5.2. Here, Lemmas C.1 and C.2 concern quadratic functions of rotated vectors that appear in the proposed Lyapunov function candidate. This is followed by Lemma C.3, which details a specific set of solutions to the Lyapunov equation for a linear system that appears when investigating the local properties of the equilibrium points of the closed-loop system.

Lemma C.1
Consider the matrices in Definition 2.21, restated here as

$$\boldsymbol{D}_1 = \operatorname{diag}(1,-1,-1),\ \boldsymbol{D}_2 = \operatorname{diag}(-1,1,-1),\ \boldsymbol{D}_3 = \operatorname{diag}(-1,-1,1).$$

Let $\boldsymbol{v} = (v_1;\ v_2;\ v_3) \in \mathbb{R}^3$ and consider a function $f_i\ : \mathbb{R}^3 \to \mathbb{R}_{\geq 0}$ defined as

$$f_i(\boldsymbol{\epsilon}) = \|\operatorname{Exp}_{\mathrm{SO}(3)}([\boldsymbol{\epsilon}]^{\wedge}_{\mathrm{SO}(3)})\boldsymbol{D}_i\boldsymbol{v} - \boldsymbol{v}\|^2, \tag{C.1}$$

and let $\boldsymbol{e}_i$ denotes a unit vector with the ith element set to 1. If $\|\boldsymbol{v}\|^2 - v_i^2 \neq \boldsymbol{0}$, then $f_i(\theta \boldsymbol{e}_i)$ decreases with an increasing θ in a neighborhood of $\theta = 0$. □

Proof. Consider (A.3), and let $\boldsymbol{\epsilon} = \theta \boldsymbol{u}$ for some unit vector $\boldsymbol{u} \in \mathbb{R}^3$, and some small $\theta > 0$, such that

$$\boldsymbol{R}(\boldsymbol{\epsilon}) \triangleq \operatorname{Exp}_{\mathrm{SO}(3)}([\boldsymbol{\epsilon}]^{\wedge}_{\mathrm{SO}(3)}) = \boldsymbol{I} + \sin(\theta)[\boldsymbol{u}]^{\wedge}_{\mathrm{SO}(3)} + (1-\cos(\theta))([\boldsymbol{u}]^{\wedge}_{\mathrm{SO}(3)})^2 \in \mathrm{SO}(3),$$

then,

$$f_i(\boldsymbol{\epsilon}) = \boldsymbol{v}^\top(\boldsymbol{D}_i\boldsymbol{R}(\boldsymbol{\epsilon})^\top - \boldsymbol{I})(\boldsymbol{R}(\boldsymbol{\epsilon})\boldsymbol{D}_i - \boldsymbol{I})\boldsymbol{v} = \boldsymbol{v}^\top(2\boldsymbol{I} - \boldsymbol{D}_i\boldsymbol{R}(\boldsymbol{\epsilon})^\top - \boldsymbol{R}(\boldsymbol{\epsilon})\boldsymbol{D}_i)\boldsymbol{v},$$

If we instead express this function in θ and $\boldsymbol{e}_i$, we obtain a scalar function

$$\bar{f}_i(\theta) \triangleq f_i(\theta \boldsymbol{e}_i) = 2(\|\boldsymbol{v}\|^2 - v_i^2)(\cos(\theta) + 1), \tag{C.2}$$

where for small $\theta > 0$,

$$\frac{\mathrm{d}\bar{f}(\theta)}{\mathrm{d}\theta} = -2\sin(\theta)(\|\boldsymbol{v}\|^2 - v_i^2) < 0, \tag{C.3}$$

if $\|\boldsymbol{v}\|^2 - v_i^2 \neq 0$. As such, there exist (at least one) direction $\boldsymbol{e}_i$ associated with each element $\boldsymbol{D}_i$ in which the function in (C.1) is locally decreasing. □

This lemma will be useful in the forthcoming local Chetaev instability analysis, as it permits the construction of geodesics on SO(3) from a set of equilibrium points characterized by the diagonal matrices $\boldsymbol{D}_i$ in Definition 2.21, along which the quadratic function in (C.1) is locally decreasing. To make this clear, we will use the following version of the lemma.

Lemma C.2
Consider $\boldsymbol{D}_j \in \mathrm{SO}(3)$ be any element in Definition 2.21, take $N > 1$ gains $k_i > 0$ and equally many associated linearly independent directions $\boldsymbol{v}_i \in \mathbb{R}^3$. There exist an element $\tilde{\boldsymbol{R}}_j \in \mathrm{SO}(3)$ in the neighborhood of $\boldsymbol{I}$ for which

$$\sum_{i=1}^{N} k_i \|\tilde{\boldsymbol{R}}_j \boldsymbol{D}_j \boldsymbol{v}_i - \boldsymbol{v}_i\|^2 < \sum_{i=1}^{N} k_i \|\boldsymbol{D}_j \boldsymbol{v}_i - \boldsymbol{v}_i\|^2. \tag{C.4}$$

□

Proof. This follows from Lemma C.1. Let $\tilde{\boldsymbol{R}}_j = \mathrm{Exp}_{\mathrm{SO}(3)}([\theta \boldsymbol{e}_j]^{\wedge}_{\mathrm{SO}(3)})$, for a small $\theta > 0$. The left-hand side of (C.4) can be expressed in θ as using (C.2),

$$\sum_{i=1}^{N} k_i \|\tilde{\boldsymbol{R}}_j \boldsymbol{D}_j \boldsymbol{v}_i - \boldsymbol{v}_i\|^2 = \sum_{i=1}^{N} 2k_i(\|\boldsymbol{v}_i\|^2 - [\boldsymbol{v}_i]_j^2)(\cos(\theta)+1) = M(\cos(\theta)+1).$$

where $M = \sum_{i=1}^{N} 2k_i(\|\boldsymbol{v}_i\|^2 - [\boldsymbol{v}_i]_j^2) > 0$ by the assumption of k_i being positive and the directions $\boldsymbol{v}_i$ being linearly independent. As such, given an $\tilde{\boldsymbol{R}}_j$ constructed as above, for $\theta > 0$, derivative of $M(\cos(\theta) + 1)$ in θ is negative about $\theta = 0$. As such, there exist an element $\tilde{\boldsymbol{R}}_j$ arbitrarily close to the identity element of SO(3), for which the equality in (C.4) holds. □

A final preliminary result is stated before giving the main proof. This result shows that a matrix with a very particular structure is Hurwitz, and provides a parametric solution to the Lyapunov equation when imposing certain structure on the associated $\boldsymbol{Q}$ matrix. These results are later used in the main proof in the analysis of the local properties of the error dynamics.

LEMMA C.3
For any parameters $c > 0$ and $l > 0$, the matrix

$$\boldsymbol{D}(c,l) \triangleq \begin{bmatrix} 0 & 0 & 1 \\ cl & -2cl & 0 \\ -l & l & 0 \end{bmatrix}, \tag{C.5}$$

is Hurwitz, i.e., $\Re(\lambda) < 0$ for all $\lambda \in \operatorname{spec}(\boldsymbol{D}(c,l))$. □

Proof. This can be shown by the Routh-Hurwitz stability criterion (see, e.g., [Parks, 1962]). The characteristic polynomial of $\boldsymbol{D}(c,l)$ takes the form

$$p(\lambda) = \det(\lambda \boldsymbol{I} - \boldsymbol{D}(c,l)) = \lambda^3 + 2cl\lambda^2 + l\lambda + cl^2 = 0. \tag{C.6}$$

As the coefficients are positive, and $2cl \cdot l > cl^2$, the matrix is Hurwitz. □

REMARK C.1
For $\boldsymbol{D}(c,l)$ in (C.5), it is also possible to find structured solutions to

$$\boldsymbol{D}(c,l)^\top \boldsymbol{P}(c,l) + \boldsymbol{P}(c,l)\boldsymbol{D}(c,l) + \boldsymbol{Q}(c,l) = \boldsymbol{0}, \qquad \forall c,l > 0, \tag{C.7}$$

with a positive semi-definite $\boldsymbol{Q}(c,l)$. For instance, with $(c,l) \in \mathbb{R}^2_{>0}$,

$$\boldsymbol{P}(c,l) = \begin{bmatrix} l & -l & 0 \\ -l & 2l & 0 \\ 0 & 0 & 1 \end{bmatrix}, \qquad \boldsymbol{Q}(c,l) = \begin{bmatrix} 2 & -4 & 0 \\ -4 & 8 & 0 \\ 0 & 0 & 0 \end{bmatrix} cl^2, \tag{C.8}$$

solves the Lyapunov equation, where $\boldsymbol{Q}(c,l) = \boldsymbol{Q}(c,l)^\top \succeq \boldsymbol{0}$ with $\operatorname{spec}(\boldsymbol{Q}(c,l)) = \{0, 0, 10cl^2\}$ and $\boldsymbol{P}(c,l) = \boldsymbol{P}(c,l)^\top$ can be shown to positive definite by applying Sylvester's criterion (see, e.g., [Hoffman and Kunze, 1971, Theorem 6, page 328]) □

Proof of Theorem 5.2. In this proof, to simplify notation, the *hat*- and *vee*-maps of SO(3) are abbreviated as $[\cdot]^\wedge_{\mathrm{SO}(3)} = [\cdot]^\wedge = \boldsymbol{S}(\cdot)$ and $[\cdot]^\vee_{\mathrm{SO}(3)} = [\cdot]^\vee$, respectively (see Definition 2.12). To recapitulate, we are working with five different errors, which are notably differently defined to the attitude errors in Chapter 3. In the remainder of this proof, let

$$\boldsymbol{R}_e = \boldsymbol{R}_r\boldsymbol{R}^\top \in \mathrm{SO}(3), \qquad \tilde{\boldsymbol{R}} = \hat{\boldsymbol{R}}\boldsymbol{R}^\top \in \mathrm{SO}(3), \tag{C.9a}$$

$$\boldsymbol{\omega}_e = \boldsymbol{\omega}_r - \boldsymbol{\omega} \in \mathbb{R}^3, \qquad \tilde{\boldsymbol{\omega}} = \hat{\boldsymbol{\omega}} - \boldsymbol{\omega} \in \mathbb{R}^3, \tag{C.9b}$$

$$\hat{\boldsymbol{\omega}}_e = \boldsymbol{\omega}_r - \hat{\boldsymbol{\omega}} \in \mathbb{R}^3, \tag{C.9c}$$

where then

$$\hat{\boldsymbol{\omega}}_e = \boldsymbol{\omega}_r - \hat{\boldsymbol{\omega}} = \boldsymbol{\omega}_r - (\tilde{\boldsymbol{\omega}} + \boldsymbol{\omega}) = \boldsymbol{\omega}_e - \tilde{\boldsymbol{\omega}}. \tag{C.10}$$

The proof is structured as follows: we start by (i) deriving the error dynamics, then proceed with (ii) computing the time-derivative of a proposed Lyapunov function along the solutions of the error dynamics. We then (iii) show that the errors trajectories converge to an invariant set, and the resulting equilibrium points are found by variations of Barbălat's lemma. Then, (iv) uniform convergence is shown by a nested Matrosov theorem, after which (v) a Chetaev instability theorem is used to characterize the local properties of the equilibrium points, and finally (vi) the local properties of the single stable equilibrium point are investigated by means of a local linearization.

(i) Error Dynamics Taking the time-derivative of $\boldsymbol{R}_e, \boldsymbol{\omega}_e, \tilde{\boldsymbol{R}}_e, \tilde{\boldsymbol{\omega}}_e$, and plugging in the control law and estimator update in Theorem 5.2, we obtain

$$\begin{aligned}
\dot{\boldsymbol{R}}_e &\underset{(2.16a)}{=} \boldsymbol{R}_r\boldsymbol{S}(\boldsymbol{\omega}_r)\boldsymbol{R}^\top - \boldsymbol{R}_r\boldsymbol{S}(\boldsymbol{\omega})\boldsymbol{R}^\top \\
&\underset{(C.9a)}{=} (\boldsymbol{R}_r\boldsymbol{S}(\boldsymbol{\omega}_r)\boldsymbol{R}_r^\top - \boldsymbol{R}_r\boldsymbol{S}(\boldsymbol{\omega})\boldsymbol{R}_r^\top)\boldsymbol{R}_e \\
&\underset{(A.10n)}{=} [\boldsymbol{S}(\boldsymbol{R}_r\boldsymbol{\omega}_r) - \boldsymbol{S}(\boldsymbol{R}_r\boldsymbol{\omega})]\boldsymbol{R}_e \\
&\underset{(A.10b)}{=} [\boldsymbol{S}(\boldsymbol{R}_r\boldsymbol{\omega}_r - \boldsymbol{R}_r\boldsymbol{\omega})]\boldsymbol{R}_e \\
&\underset{(C.9b)}{=} \boldsymbol{S}(\boldsymbol{R}_r\boldsymbol{\omega}_e)\boldsymbol{R}_e.
\end{aligned} \tag{C.11a}$$

Here, we note that

$$\begin{aligned}
\boldsymbol{S}(\boldsymbol{J}\boldsymbol{\omega})\boldsymbol{\omega}_e + \boldsymbol{S}(\boldsymbol{J}\tilde{\boldsymbol{\omega}})\boldsymbol{\omega}_r &\underset{(C.9b)}{=} \boldsymbol{S}(\boldsymbol{J}\boldsymbol{\omega})(\boldsymbol{\omega}_r - \boldsymbol{\omega}) + \boldsymbol{S}(\boldsymbol{J}(\hat{\boldsymbol{\omega}} - \boldsymbol{\omega}))\boldsymbol{\omega}_r \\
&\underset{(A.10b)}{=} \boldsymbol{S}(\boldsymbol{J}\boldsymbol{\omega})\boldsymbol{\omega}_r - \boldsymbol{S}(\boldsymbol{J}\boldsymbol{\omega})\boldsymbol{\omega} + \boldsymbol{S}(\boldsymbol{J}\hat{\boldsymbol{\omega}})\boldsymbol{\omega}_r - \boldsymbol{S}(\boldsymbol{J}\boldsymbol{\omega})\boldsymbol{\omega}_r \\
&\underset{(C.9c)}{=} -\boldsymbol{S}(\boldsymbol{J}\boldsymbol{\omega})\boldsymbol{\omega} + \boldsymbol{S}(\boldsymbol{J}(\boldsymbol{\omega}_r - \hat{\boldsymbol{\omega}}_e))\boldsymbol{\omega}_r \\
&\underset{(A.10b)}{=} \boldsymbol{S}(\boldsymbol{J}\boldsymbol{\omega}_r)\boldsymbol{\omega}_r - \boldsymbol{S}(\boldsymbol{J}\boldsymbol{\omega})\boldsymbol{\omega} - \boldsymbol{S}(\boldsymbol{J}\hat{\boldsymbol{\omega}}_e)\boldsymbol{\omega}_r.
\end{aligned} \tag{C.11b}$$

Considering the dynamics in (2.16b), and the proposed feedback in (5.10a) the attitude tracking error dynamics can be expressed

$$\begin{aligned}
\boldsymbol{J}\dot{\boldsymbol{\omega}}_e &\underset{\text{(C.9b)}}{=} \boldsymbol{J}(\dot{\boldsymbol{\omega}}_r - \dot{\boldsymbol{\omega}}) \\
&\underset{\text{(2.16b)}}{=} \boldsymbol{S}(\boldsymbol{J}\boldsymbol{\omega}_r)\boldsymbol{\omega}_r + \boldsymbol{\tau}_r - [\boldsymbol{S}(\boldsymbol{J}\boldsymbol{\omega})\boldsymbol{\omega} + \boldsymbol{\tau}] \\
&\underset{\text{(5.10a)}}{=} \boldsymbol{S}(\boldsymbol{J}\boldsymbol{\omega}_r)\boldsymbol{\omega}_r - \Big[\boldsymbol{S}(\boldsymbol{J}\boldsymbol{\omega})\boldsymbol{\omega} + \boldsymbol{S}(\boldsymbol{J}\hat{\boldsymbol{\omega}}_e)\boldsymbol{\omega}_r + \boldsymbol{K}_\omega\hat{\boldsymbol{\omega}}_e + \sum_{i=1}^{N} k_i \boldsymbol{S}(\boldsymbol{R}_r^\top \boldsymbol{v}_i)\hat{\boldsymbol{R}}^\top \boldsymbol{v}_i\Big] \\
&\underset{\text{(C.11b)}}{=} \boldsymbol{S}(\boldsymbol{J}\boldsymbol{\omega})\boldsymbol{\omega}_e + \boldsymbol{S}(\boldsymbol{J}\tilde{\boldsymbol{\omega}})\boldsymbol{\omega}_r - \Big[\boldsymbol{K}_\omega\hat{\boldsymbol{\omega}}_e + \sum_{i=1}^{N} k_i \boldsymbol{S}(\boldsymbol{R}_r^\top \boldsymbol{v}_i)\hat{\boldsymbol{R}}^\top \boldsymbol{v}_i\Big] \\
&\underset{\text{(C.10)}}{=} \boldsymbol{S}(\boldsymbol{J}\boldsymbol{\omega})\boldsymbol{\omega}_e + \boldsymbol{S}(\boldsymbol{J}\tilde{\boldsymbol{\omega}})\boldsymbol{\omega}_r - \boldsymbol{K}_\omega(\boldsymbol{\omega}_e - \tilde{\boldsymbol{\omega}}) - \sum_{i=1}^{N} k_i \boldsymbol{S}(\boldsymbol{R}_r^\top \boldsymbol{v}_i)\hat{\boldsymbol{R}}^\top \boldsymbol{v}_i.
\end{aligned} \tag{C.11c}$$

The observer attitude error dynamics can similarly be expressed using the proposed estimator update in (5.10b), with an innovation term in (5.10d), and using the attitude kinematics on SO(3) in (2.16a), with the error dynamics

$$\begin{aligned}
\dot{\tilde{\boldsymbol{R}}} &\underset{\text{(C.9a)}}{=} \dot{\hat{\boldsymbol{R}}}\boldsymbol{R}^\top + \hat{\boldsymbol{R}}\dot{\boldsymbol{R}}^\top \\
&\underset{\text{(5.10b)}}{=} \hat{\boldsymbol{R}}\boldsymbol{S}(\boldsymbol{\omega} + \boldsymbol{\delta}_{\boldsymbol{R}})\boldsymbol{R}^\top - \hat{\boldsymbol{R}}\boldsymbol{S}(\boldsymbol{\omega})\boldsymbol{R}^\top \\
&\underset{\text{(A.10b)}}{=} \hat{\boldsymbol{R}}[\boldsymbol{S}(\boldsymbol{\omega}) + \boldsymbol{S}(\boldsymbol{\delta}_{\boldsymbol{R}})]\boldsymbol{R}^\top - \hat{\boldsymbol{R}}\boldsymbol{S}(\boldsymbol{\omega})\boldsymbol{R}^\top \\
&\underset{\text{(C.9a)}}{=} \hat{\boldsymbol{R}}\boldsymbol{S}(\boldsymbol{\delta}_{\boldsymbol{R}})\hat{\boldsymbol{R}}^\top\tilde{\boldsymbol{R}} \\
&\underset{\text{(A.10n)}}{=} \boldsymbol{S}(\hat{\boldsymbol{R}}\boldsymbol{\delta}_{\boldsymbol{R}})\tilde{\boldsymbol{R}},
\end{aligned} \tag{C.11d}$$

and the estimate attitude rate error simply becomes,

$$\boldsymbol{J}\dot{\tilde{\boldsymbol{\omega}}} \underset{\text{(C.9b)}}{=} \boldsymbol{J}(\dot{\hat{\boldsymbol{\omega}}} - \dot{\boldsymbol{\omega}}) \underset{\text{(5.10c)}}{=} \boldsymbol{\delta}_{\boldsymbol{\omega}}. \tag{C.11e}$$

(ii) Lyapunov Function Candidate Having established the error dynamics in equations (C.11), we next propose the Lyapunov function candidate

$$\mathcal{V}_1 = \sum_{i=1}^{N} \frac{k_i}{2}\|\boldsymbol{R}_e\tilde{\boldsymbol{R}}^\top \boldsymbol{v}_i - \boldsymbol{v}_i\|^2 + \frac{1}{2}\boldsymbol{\omega}_e^\top \boldsymbol{J}\boldsymbol{\omega}_e + \sum_{i=1}^{N} \frac{k_i}{2}\|\tilde{\boldsymbol{R}}\boldsymbol{v}_i - \boldsymbol{v}_i\|^2 + \frac{1}{2}\tilde{\boldsymbol{\omega}}^\top \boldsymbol{J}\tilde{\boldsymbol{\omega}}, \tag{C.12}$$

Differentiation of (C.12) along solutions of the error dynamics in (C.11) yields

$$\begin{aligned}\frac{\mathrm{d}\mathcal{V}_1}{\mathrm{d}t} =& + \sum_{i=1}^{N} k_i(\boldsymbol{R}_e\tilde{\boldsymbol{R}}^\top\boldsymbol{v}_i - \boldsymbol{v}_i)^\top \frac{\mathrm{d}}{\mathrm{d}t}(\boldsymbol{R}_e\tilde{\boldsymbol{R}}^\top\boldsymbol{v}_i)\\ &+ \boldsymbol{\omega}_e^\top\Big[\boldsymbol{S}(\boldsymbol{J}\boldsymbol{\omega})\boldsymbol{\omega}_e + \boldsymbol{S}(\boldsymbol{J}\tilde{\boldsymbol{\omega}})\boldsymbol{\omega}_r - \boldsymbol{K}_{\boldsymbol{\omega}}(\boldsymbol{\omega}_e - \tilde{\boldsymbol{\omega}}) - \sum_{i=1}^{N} k_i\boldsymbol{S}(\boldsymbol{R}_r^\top\boldsymbol{v}_i)\hat{\boldsymbol{R}}^\top\boldsymbol{v}_i\Big]\\ &+ \sum_{i=1}^{N} k_i(\tilde{\boldsymbol{R}}\boldsymbol{v}_i - \boldsymbol{v}_i)^\top \frac{\mathrm{d}}{\mathrm{d}t}(\tilde{\boldsymbol{R}}\boldsymbol{v}_i)\\ &+ \tilde{\boldsymbol{\omega}}^\top\boldsymbol{\delta}_{\boldsymbol{\omega}}. \end{aligned} \tag{C.13}$$

Noting that

$$\begin{aligned}\frac{\mathrm{d}}{\mathrm{d}t}(\boldsymbol{R}_e\tilde{\boldsymbol{R}}^\top) &= \dot{\boldsymbol{R}}_e\tilde{\boldsymbol{R}}^\top + \boldsymbol{R}_e\dot{\tilde{\boldsymbol{R}}}^\top\\ &\underset{\text{(C.11)}}{=} \boldsymbol{S}(\boldsymbol{R}_r\boldsymbol{\omega}_e)\boldsymbol{R}_e\tilde{\boldsymbol{R}}^\top + \boldsymbol{R}_e(\boldsymbol{S}(\hat{\boldsymbol{R}}\delta_{\boldsymbol{R}})\tilde{\boldsymbol{R}})^\top\\ &\underset{\text{(A.10f)}}{=} \boldsymbol{S}(\boldsymbol{R}_r\boldsymbol{\omega}_e)\boldsymbol{R}_e\tilde{\boldsymbol{R}}^\top - \boldsymbol{R}_e\tilde{\boldsymbol{R}}^\top\boldsymbol{S}(\hat{\boldsymbol{R}}\delta_{\boldsymbol{R}})\\ &\underset{\text{(A.10a)}}{=} \boldsymbol{S}(\boldsymbol{R}_r\boldsymbol{\omega}_e)\boldsymbol{R}_e\tilde{\boldsymbol{R}}^\top - \boldsymbol{R}_e\tilde{\boldsymbol{R}}^\top\boldsymbol{S}(\hat{\boldsymbol{R}}\delta_{\boldsymbol{R}})\Big(\boldsymbol{R}_e\tilde{\boldsymbol{R}}^\top\Big)^\top\boldsymbol{R}_e\tilde{\boldsymbol{R}}^\top\\ &\underset{\text{(A.10n)}}{=} \boldsymbol{S}(\boldsymbol{R}_r\boldsymbol{\omega}_e - \boldsymbol{R}_e\tilde{\boldsymbol{R}}^\top\hat{\boldsymbol{R}}\delta_{\boldsymbol{R}})\boldsymbol{R}_e\tilde{\boldsymbol{R}}^\top\\ &\underset{\text{(C.9a)}}{=} \boldsymbol{S}(\boldsymbol{R}_r\boldsymbol{\omega}_e - \boldsymbol{R}_r\boldsymbol{R}^\top\boldsymbol{R}\hat{\boldsymbol{R}}^\top\hat{\boldsymbol{R}}\delta_{\boldsymbol{R}})\boldsymbol{R}_e\tilde{\boldsymbol{R}}^\top\\ &\underset{\text{(A.10a)}}{=} \boldsymbol{S}(\boldsymbol{R}_r[\boldsymbol{\omega}_e - \boldsymbol{\delta}_{\boldsymbol{R}}])\boldsymbol{R}_e\tilde{\boldsymbol{R}}^\top, \end{aligned}$$

and inserting the tracking and observer attitude error dynamics yields

$$\begin{aligned}\frac{\mathrm{d}\mathcal{V}_1}{\mathrm{d}t} =& + \sum_{i=1}^{N} k_i(\boldsymbol{R}_e\tilde{\boldsymbol{R}}^\top\boldsymbol{v}_i - \boldsymbol{v}_i)^\top\boldsymbol{S}(\boldsymbol{R}_r[\boldsymbol{\omega}_e - \boldsymbol{\delta}_{\boldsymbol{R}}])\boldsymbol{R}_e\tilde{\boldsymbol{R}}^\top\boldsymbol{v}_i\\ &+ \boldsymbol{\omega}_e^\top\Big[\boldsymbol{S}(\boldsymbol{J}\boldsymbol{\omega})\boldsymbol{\omega}_e + \boldsymbol{S}(\boldsymbol{J}\tilde{\boldsymbol{\omega}})\boldsymbol{\omega}_r - \boldsymbol{K}_{\boldsymbol{\omega}}(\boldsymbol{\omega}_e - \tilde{\boldsymbol{\omega}}) - \sum_{i=1}^{N} k_i\boldsymbol{S}(\boldsymbol{R}_r^\top\boldsymbol{v}_i)\hat{\boldsymbol{R}}^\top\boldsymbol{v}_i\Big]\\ &+ \sum_{i=1}^{N} k_i(\tilde{\boldsymbol{R}}\boldsymbol{v}_i - \boldsymbol{v}_i)^\top\boldsymbol{S}(\hat{\boldsymbol{R}}\boldsymbol{\delta}_{\boldsymbol{R}})\tilde{\boldsymbol{R}}\boldsymbol{v}_i + \tilde{\boldsymbol{\omega}}^\top\boldsymbol{\delta}_{\boldsymbol{\omega}}. \end{aligned} \tag{C.14}$$

Canceling the quadratic forms in the skew-symmetric matrices, we obtain

$$\begin{aligned}\frac{\mathrm{d}\mathcal{V}_1}{\mathrm{d}t} =& -\sum_{i=1}^{N} k_i \boldsymbol{v}_i^\top \boldsymbol{S}(\boldsymbol{R}_r[\boldsymbol{\omega}_e - \boldsymbol{\delta}_{\boldsymbol{R}}])\boldsymbol{R}_e\tilde{\boldsymbol{R}}^\top \boldsymbol{v}_i \\ &+ \boldsymbol{\omega}_e^\top \Big[\boldsymbol{S}(\boldsymbol{J}\tilde{\boldsymbol{\omega}})\boldsymbol{\omega}_r - \boldsymbol{K}_{\boldsymbol{\omega}}(\boldsymbol{\omega}_e - \hat{\boldsymbol{\omega}}) - \sum_{i=1}^{N} k_i \boldsymbol{S}(\boldsymbol{R}_r^\top \boldsymbol{v}_i)\hat{\boldsymbol{R}}^\top \boldsymbol{v}_i\Big] \\ &- \sum_{i=1}^{N} k_i \boldsymbol{v}_i^\top \boldsymbol{S}(\hat{\boldsymbol{R}}\boldsymbol{\delta}_{\boldsymbol{R}})\tilde{\boldsymbol{R}}\boldsymbol{v}_i + \tilde{\boldsymbol{\omega}}^\top \boldsymbol{\delta}_{\boldsymbol{\omega}}. \end{aligned} \tag{C.15}$$

Here, we note that

$$\begin{aligned}\sum_{i=1}^{N} k_i \boldsymbol{v}_i^\top \boldsymbol{S}(\hat{\boldsymbol{R}}\boldsymbol{\delta}_{\boldsymbol{R}})\tilde{\boldsymbol{R}}\boldsymbol{v}_i &\underset{\text{(A.10n)}}{=} \sum_{i=1}^{N} k_i \boldsymbol{v}_i^\top \hat{\boldsymbol{R}}\boldsymbol{S}(\boldsymbol{\delta}_{\boldsymbol{R}})\hat{\boldsymbol{R}}^\top \tilde{\boldsymbol{R}}\boldsymbol{v}_i \\ &\underset{\text{(A.10i)}}{=} -\sum_{i=1}^{N} k_i \boldsymbol{\delta}_{\boldsymbol{R}}^\top \boldsymbol{S}(\hat{\boldsymbol{R}}^\top \boldsymbol{v}_i)\hat{\boldsymbol{R}}^\top \hat{\boldsymbol{R}}\boldsymbol{R}^\top \boldsymbol{v}_i \\ &\underset{\text{(A.10i)}}{=} \boldsymbol{\delta}_{\boldsymbol{R}}^\top \sum_{i=1}^{N} k_i \boldsymbol{S}(\boldsymbol{R}^\top \boldsymbol{v}_i)\hat{\boldsymbol{R}}^\top \boldsymbol{v}_i, \end{aligned} \tag{C.16a}$$

and, using the same set of identities, we obtain

$$\sum_{i=1}^{N} k_i \boldsymbol{v}_i^\top \boldsymbol{S}(\boldsymbol{R}_r[\boldsymbol{\omega}_e - \boldsymbol{\delta}_{\boldsymbol{R}}])\boldsymbol{R}_e\tilde{\boldsymbol{R}}^\top \boldsymbol{v}_i = [\boldsymbol{\omega}_e - \boldsymbol{\delta}_{\boldsymbol{R}}]^\top \sum_{i=1}^{N} k_i \boldsymbol{S}(\hat{\boldsymbol{R}}^\top \boldsymbol{v}_i)\boldsymbol{R}_r^\top \boldsymbol{v}_i. \tag{C.16b}$$

Using (C.16), the Lyapunov time-derivative in (C.15) simplifies to

$$\begin{aligned}\frac{\mathrm{d}\mathcal{V}_1}{\mathrm{d}t} =& -[\boldsymbol{\omega}_e - \boldsymbol{\delta}_{\boldsymbol{R}}]^\top \sum_{i=1}^{N} k_i \boldsymbol{S}(\hat{\boldsymbol{R}}^\top \boldsymbol{v}_i)\boldsymbol{R}_r^\top \boldsymbol{v}_i \\ &+ \boldsymbol{\omega}_e^\top \Big[\boldsymbol{S}(\boldsymbol{J}\tilde{\boldsymbol{\omega}})\boldsymbol{\omega}_r - \boldsymbol{K}_{\boldsymbol{\omega}}(\boldsymbol{\omega}_e - \tilde{\boldsymbol{\omega}}) - \sum_{i=1}^{N} k_i \boldsymbol{S}(\boldsymbol{R}_r^\top \boldsymbol{v}_i)\hat{\boldsymbol{R}}^\top \boldsymbol{v}_i\Big] \\ &- \boldsymbol{\delta}_{\boldsymbol{R}}^\top \sum_{i=1}^{N} k_i \boldsymbol{S}(\boldsymbol{R}^\top \boldsymbol{v}_i)\hat{\boldsymbol{R}}^\top \boldsymbol{v}_i + \tilde{\boldsymbol{\omega}}^\top \boldsymbol{\delta}_{\boldsymbol{\omega}}, \end{aligned} \tag{C.17}$$

whereby two of the terms in $\boldsymbol{\omega}_e$ terms cancel out, and we obtain

$$\begin{aligned}\frac{\mathrm{d}\mathcal{V}_1}{\mathrm{d}t} =& +\boldsymbol{\delta}_{\boldsymbol{R}}^\top \sum_{i=1}^{N} k_i \boldsymbol{S}(\hat{\boldsymbol{R}}^\top \boldsymbol{v}_i)(\boldsymbol{R}_r^\top \boldsymbol{v}_i + \boldsymbol{R}^\top \boldsymbol{v}_i) \\ &+ \boldsymbol{\omega}_e^\top \Big[\boldsymbol{S}(\boldsymbol{J}\tilde{\boldsymbol{\omega}})\boldsymbol{\omega}_r - \boldsymbol{K}_{\boldsymbol{\omega}}(\boldsymbol{\omega}_e - \tilde{\boldsymbol{\omega}})\Big] + \tilde{\boldsymbol{\omega}}^\top \boldsymbol{\delta}_{\boldsymbol{\omega}}. \end{aligned} \tag{C.18}$$

Here the second and third terms simplify using the symmetry of $\boldsymbol{J}$ and $\boldsymbol{K}_{\boldsymbol{\omega}}$,

$$\begin{aligned}
\boldsymbol{\omega}_e^\top \Big[\boldsymbol{S}(\boldsymbol{J}\tilde{\boldsymbol{\omega}})\boldsymbol{\omega}_r - \boldsymbol{K}_{\boldsymbol{\omega}}(\boldsymbol{\omega}_e - \tilde{\boldsymbol{\omega}})\Big] + \tilde{\boldsymbol{\omega}}^\top \boldsymbol{\delta}_{\boldsymbol{\omega}} & \\
= \; -\boldsymbol{\omega}_e^\top \boldsymbol{K}_{\boldsymbol{\omega}}\boldsymbol{\omega}_e + \boldsymbol{\omega}_e^\top \boldsymbol{S}(\boldsymbol{J}\tilde{\boldsymbol{\omega}})\boldsymbol{\omega}_r + \boldsymbol{\omega}_e^\top \boldsymbol{K}_{\boldsymbol{\omega}}\tilde{\boldsymbol{\omega}} + \tilde{\boldsymbol{\omega}}^\top \boldsymbol{\delta}_{\boldsymbol{\omega}} & \\
\underset{\text{(A.10j)}}{=} \; -\boldsymbol{\omega}_e^\top \boldsymbol{K}_{\boldsymbol{\omega}}\boldsymbol{\omega}_e + \boldsymbol{\omega}_r^\top \boldsymbol{S}(\boldsymbol{\omega}_e)\boldsymbol{J}\tilde{\boldsymbol{\omega}} + \boldsymbol{\omega}_e^\top \boldsymbol{K}_{\boldsymbol{\omega}}\tilde{\boldsymbol{\omega}} + \tilde{\boldsymbol{\omega}}^\top \boldsymbol{\delta}_{\boldsymbol{\omega}} & \\
= \; -\boldsymbol{\omega}_e^\top \boldsymbol{K}_{\boldsymbol{\omega}}\boldsymbol{\omega}_e + \tilde{\boldsymbol{\omega}}^\top \Big[\boldsymbol{J}\boldsymbol{S}(\boldsymbol{\omega}_r)\boldsymbol{\omega}_e + \boldsymbol{K}_{\boldsymbol{\omega}}\boldsymbol{\omega}_e + \boldsymbol{\delta}_{\boldsymbol{\omega}}\Big]. & \qquad \text{(C.19)}
\end{aligned}$$

Insertion of the estimator innovation terms in (5.10d) yields

$$\begin{aligned}
\frac{\mathrm{d}\mathcal{V}_1}{\mathrm{d}t} = & + \boldsymbol{\delta}_{\boldsymbol{R}}^\top \sum_{i=1}^{N} k_i \boldsymbol{S}(\hat{\boldsymbol{R}}^\top \boldsymbol{v}_i)(\boldsymbol{R}_r^\top \boldsymbol{v}_i + \boldsymbol{R}^\top \boldsymbol{v}_i) \qquad \text{(C.20)} \\
& - \boldsymbol{\omega}_e^\top \boldsymbol{K}_{\boldsymbol{\omega}}\boldsymbol{\omega}_e + \tilde{\boldsymbol{\omega}}^\top \Big[\boldsymbol{J}\boldsymbol{S}(\boldsymbol{\omega}_r)\boldsymbol{\omega}_e + \boldsymbol{K}_{\boldsymbol{\omega}}\boldsymbol{\omega}_e + \frac{1}{c_{\boldsymbol{\omega}}}\boldsymbol{\delta}_{\boldsymbol{\omega}}\Big] \\
= & - c_R \Big\| \sum_{i=1}^{N} k_i \boldsymbol{S}(\hat{\boldsymbol{R}}^\top \boldsymbol{v}_i)(\boldsymbol{R}_r^\top \boldsymbol{v}_i + \boldsymbol{R}^\top \boldsymbol{v}_i) \Big\|^2 - \boldsymbol{\omega}_e^\top \boldsymbol{K}_{\boldsymbol{\omega}}\boldsymbol{\omega}_e - \tilde{\boldsymbol{\omega}}^\top C_{\boldsymbol{\omega}}\tilde{\boldsymbol{\omega}}.
\end{aligned}$$

Here we arrive at a convenient expression of the Lyapunov function candidate time derivative, which is negative in the errors in time along the controlled system. To demonstrate that the above developments are sound, consider the plot of this time-derivative in Example 5.2, where it is shown that the analytical expression in (C.20) evaluated in the signals of the closed loop system is identical to a numerically differentiation of $\mathcal{V}$ in (C.12).

(iii) Application of Barbălat As the Lyapunov function time-derivative in (C.20) is negative semi-definite in the errors along the solutions of the error dynamics, the $\mathcal{V}_1$ is bounded by its initial value. Thus, for all $t \geq t_\circ$,

$$\begin{aligned}
\frac{\lambda_m(\boldsymbol{J})}{2}\|\boldsymbol{\omega}_e\|^2 \leq \frac{1}{2}\boldsymbol{\omega}_e^\top \boldsymbol{J}\boldsymbol{\omega}_e \leq \mathcal{V}_1(t_\circ) \Rightarrow \|\boldsymbol{\omega}_e\| \leq \sqrt{\frac{2\mathcal{V}_1(t_\circ)}{\lambda_m(\boldsymbol{J})}} \triangleq M_2, \qquad \text{(C.21)} \\
\frac{\lambda_m(\boldsymbol{J})}{2}\|\tilde{\boldsymbol{\omega}}\|^2 \leq \frac{1}{2}\tilde{\boldsymbol{\omega}}^\top \boldsymbol{J}\tilde{\boldsymbol{\omega}} \leq \mathcal{V}_1(t_\circ) \Rightarrow \|\tilde{\boldsymbol{\omega}}\| \leq \sqrt{\frac{2\mathcal{V}_1(t_\circ)}{\lambda_m(\boldsymbol{J})}} \triangleq M_2.
\end{aligned}$$

Consequently, by the assumption of a constant bounding $\sup_{t\geq t_\circ} \|\boldsymbol{\omega}_r(t)\| \leq M_1$, we have that the attitude rates are bounded in the initial errors as

$$\begin{aligned}
\sup_{t\geq t_\circ} \|\boldsymbol{\omega}\| = \sup_{t\geq t_\circ} \|\boldsymbol{\omega}_r - \boldsymbol{\omega}_e\| \leq \sup_{t\geq t_\circ} (\|\boldsymbol{\omega}_r\| + \|\boldsymbol{\omega}_e\|) \leq M_1 + M_2. \qquad \text{(C.22a)} \\
\sup_{t\geq t_\circ} \|\hat{\boldsymbol{\omega}}\| = \sup_{t\geq t_\circ} \|\tilde{\boldsymbol{\omega}} - \boldsymbol{\omega}\| \leq \sup_{t\geq t_\circ} (\|\tilde{\boldsymbol{\omega}}\| + \|\boldsymbol{\omega}\|) \leq M_1 + 2M_2.
\end{aligned}$$

As the error dynamics in (C.11) only contain elements of SO(3) and the attitude rates $\boldsymbol{\omega}, \boldsymbol{\omega}_r, \boldsymbol{\omega}_e, \tilde{\boldsymbol{\omega}}, \hat{\boldsymbol{\omega}}$ are all bounded by (C.21) and (C.22), there exists a conservative bound

$$\left\| \frac{\mathrm{d}^2 \mathcal{V}_1}{\mathrm{d}t^2} \right\| \leq B(M_1, M_2, \{k_i\}_{i=1}^N, \boldsymbol{K}_{\boldsymbol{\omega}}, \boldsymbol{C}_{\boldsymbol{\omega}}), \qquad \forall t \geq t_\circ.$$

Then, $\dot{\mathcal{V}}_1$ is uniformly continuous, application of Lemma 2.5 to (C.20) yields

$$\lim_{(t-t_\circ)\to\infty} \dot{\mathcal{V}}_1(t) = \mathbf{0} \Rightarrow \begin{cases} \lim\limits_{(t-t_\circ)\to\infty} \boldsymbol{\omega}_e = \mathbf{0} \\ \lim\limits_{(t-t_\circ)\to\infty} \tilde{\boldsymbol{\omega}} = \mathbf{0} \\ \lim\limits_{(t-t_\circ)\to\infty} \sum\limits_{i=1}^N k_i \boldsymbol{S}(\hat{\boldsymbol{R}}^\top \boldsymbol{v}_i)(\boldsymbol{R}_r^\top \boldsymbol{v}_i + \boldsymbol{R}^\top \boldsymbol{v}_i) = \mathbf{0} \end{cases}, \tag{C.23}$$

Next, consider the tracking attitude error dynamics in (C.11c) and let

$$\underbrace{\boldsymbol{J}\dot{\boldsymbol{\omega}}_e}_{\triangleq \dot{f}(t)} = \underbrace{\boldsymbol{S}(\boldsymbol{J}\boldsymbol{\omega})\boldsymbol{\omega}_e + \boldsymbol{S}(\boldsymbol{J}\tilde{\boldsymbol{\omega}})\boldsymbol{\omega}_r - \boldsymbol{K}_{\boldsymbol{\omega}}(\boldsymbol{\omega}_e - \tilde{\boldsymbol{\omega}})}_{\triangleq \eta(t)} \underbrace{- \sum_{i=1}^N k_i \boldsymbol{S}(\boldsymbol{R}_r^\top \boldsymbol{v}_i)\hat{\boldsymbol{R}}^\top \boldsymbol{v}_i}_{\triangleq f_0(t)}. \tag{C.24}$$

By (C.23), $f(t) = \boldsymbol{J}\boldsymbol{\omega}_e \to 0$ and $\eta(t) \to 0$ as $t - t_\circ \to \infty$. Furthermore, with the innovation term $\boldsymbol{\delta}_{\boldsymbol{R}}$ defined as in (5.10d), we have that

$$\|\boldsymbol{\delta}_{\boldsymbol{R}}\| \leq c_R \sum_{i=1}^N k_i \|S(\hat{\boldsymbol{R}}^\top \boldsymbol{v}_i)\|(\|\boldsymbol{R}_r^\top \boldsymbol{v}_i\| + \|\boldsymbol{R}^\top \boldsymbol{v}_i\|) = 2c_R \sum_{i=1}^N k_i, \tag{C.25}$$

the time derivative of f_0 is bounded in the initial errors, as

$$\begin{aligned}
\left\| \frac{\mathrm{d}f_0}{\mathrm{d}t} \right\| &= \left\| \frac{\mathrm{d}}{\mathrm{d}t} \sum_{i=1}^N k_i \boldsymbol{S}(\boldsymbol{R}_r^\top \boldsymbol{v}_i)\hat{\boldsymbol{R}}^\top \boldsymbol{v}_i \right\| \\
&= \left\| \sum_{i=1}^N k_i \Big(\boldsymbol{S}(\dot{\boldsymbol{R}}_r^\top \boldsymbol{v}_i)\hat{\boldsymbol{R}}^\top \boldsymbol{v}_i + \boldsymbol{S}(\boldsymbol{R}_r^\top \boldsymbol{v}_i)\dot{\hat{\boldsymbol{R}}}^\top \boldsymbol{v}_i \Big) \right\| \\
&= \left\| \sum_{i=1}^N k_i \Big(\boldsymbol{S}(\boldsymbol{\omega}_r)\boldsymbol{R}_r^\top \boldsymbol{v}_i \boldsymbol{S}(\hat{\boldsymbol{R}}^\top \boldsymbol{v}_i) - \boldsymbol{S}(\boldsymbol{R}_r^\top \boldsymbol{v}_i)\boldsymbol{S}(\boldsymbol{\omega} + \delta_{\boldsymbol{R}})\hat{\boldsymbol{R}}^\top \boldsymbol{v}_i \Big) \right\| \\
&\leq \sum_{i=1}^N k_i \Big(\|\boldsymbol{S}(\boldsymbol{\omega}_r)\|\|\boldsymbol{R}_r^\top \boldsymbol{v}_i\|\|\boldsymbol{S}(\hat{\boldsymbol{R}}^\top \boldsymbol{v}_i)\| + \|\boldsymbol{S}(\boldsymbol{R}_r^\top \boldsymbol{v}_i)\|\|\boldsymbol{S}(\boldsymbol{\omega} + \delta_{\boldsymbol{R}})\|\|\hat{\boldsymbol{R}}^\top \boldsymbol{v}_i\| \Big) \\
&= \sum_{i=1}^N k_i (\|\boldsymbol{\omega}_r\| + \|\boldsymbol{\omega} + \delta_{\boldsymbol{R}}\|) \\
&\leq \sum_{i=1}^N k_i \left(2M_1 + M_2 + 2c_R \sum_{i=1}^N k_i \right).
\end{aligned} \tag{C.26}$$

Thus, f_0 is uniformly continuous. Application of Lemma 2.7 to (C.24) yields

$$(\text{C.23}) \Rightarrow \lim_{(t-t_\circ)\to\infty} \boldsymbol{J}\dot{\boldsymbol{\omega}}_e(t) = \lim_{(t-t_\circ)\to\infty} \sum_{i=1}^{N} k_i \boldsymbol{S}(\boldsymbol{R}_r^\top \boldsymbol{v}_i)\hat{\boldsymbol{R}}^\top \boldsymbol{v}_i = \boldsymbol{0}. \quad \text{(C.27)}$$

combined with the third implication in (C.23), we conclude that the non-autonomous error dynamics converge to an invariant set characterized by

$$\mathcal{S} = \left\{ (\boldsymbol{R}_e, \tilde{\boldsymbol{R}}, \boldsymbol{\omega}_e, \tilde{\boldsymbol{\omega}}) \in \mathrm{SO}(3)^2 \times \mathbb{R}^6 \middle| \begin{array}{ll} \sum_{i=1}^N k_i \boldsymbol{S}(\boldsymbol{R}_r^\top \boldsymbol{v}_i)\hat{\boldsymbol{R}}^\top \boldsymbol{v}_i = \boldsymbol{0}, & \boldsymbol{\omega}_e = \boldsymbol{0} \\ \sum_{i=1}^N k_i \boldsymbol{S}(\boldsymbol{R}^\top \boldsymbol{v}_i)\hat{\boldsymbol{R}}^\top \boldsymbol{v}_i = \boldsymbol{0}, & \tilde{\boldsymbol{\omega}} = \boldsymbol{0} \end{array} \right\}. \quad \text{(C.28)}$$

Now, just as in the proof of Theorem 3.1 in Appendix B.1, for any $\boldsymbol{R} \in \mathrm{SO}(3)$,

$$\sum_{i=1}^{N} k_i \boldsymbol{S}(\boldsymbol{v}_i)\boldsymbol{R}^\top \boldsymbol{v}_i = \Big[\Big[\sum_{i=1}^{N} k_i \boldsymbol{S}(\boldsymbol{v}_i)\boldsymbol{R}^\top \boldsymbol{v}_i\Big]^\wedge\Big]^\vee = [\boldsymbol{R}^\top \boldsymbol{M} - \boldsymbol{M}^\top \boldsymbol{R}]^\vee,$$

with

$$\boldsymbol{M} = \sum_{i=1}^{N} k_i \boldsymbol{v}_i \boldsymbol{v}_i^\top \succ \boldsymbol{0},$$

which admits a spectral decomposition $\boldsymbol{M} = \boldsymbol{U}\boldsymbol{\Lambda}\boldsymbol{U}^\top$ with an orthogonal $\boldsymbol{U}$, as $\boldsymbol{M}$ is real and symmetric by the assumptions on $\{(k_i, \boldsymbol{v}_i)\}_{i=1}^N$. Then,

$$(\text{C.28}) \Rightarrow \begin{cases} \lim_{(t-t_\circ)\to\infty} (\hat{\boldsymbol{R}}\boldsymbol{R}_r^\top)^\top \boldsymbol{M} - \boldsymbol{M}^\top (\hat{\boldsymbol{R}}\boldsymbol{R}_r^\top) = \boldsymbol{0} \\ \lim_{(t-t_\circ)\to\infty} (\hat{\boldsymbol{R}}\boldsymbol{R}^\top)^\top \boldsymbol{M} - \boldsymbol{M}^\top (\hat{\boldsymbol{R}}\boldsymbol{R}^\top) = \boldsymbol{0} \end{cases} \quad \text{(C.29a)}$$

$$\Rightarrow \begin{cases} \lim_{(t-t_\circ)\to\infty} (\hat{\boldsymbol{R}}\boldsymbol{R}_r^\top) \in \{\boldsymbol{U}\boldsymbol{D}_l\boldsymbol{U}^\top\}_{l=1}^4 \\ \lim_{(t-t_\circ)\to\infty} \tilde{\boldsymbol{R}} \in \{\boldsymbol{U}\boldsymbol{D}_k\boldsymbol{U}^\top\}_{k=1}^4 \end{cases} \quad \text{(C.29b)}$$

$$\Rightarrow \begin{cases} \lim_{(t-t_\circ)\to\infty} (\tilde{\boldsymbol{R}}\boldsymbol{R}_e^\top) \in \{\boldsymbol{U}\boldsymbol{D}_l\boldsymbol{U}^\top\}_{l=1}^4 \\ \lim_{(t-t_\circ)\to\infty} \tilde{\boldsymbol{R}} \in \{\boldsymbol{U}\boldsymbol{D}_k\boldsymbol{U}^\top\}_{k=1}^4 \end{cases} \quad \text{(C.29c)}$$

$$\Rightarrow \begin{cases} \lim_{(t-t_\circ)\to\infty} \boldsymbol{R}_e \in \{\boldsymbol{U}\boldsymbol{D}_k\boldsymbol{D}_l\boldsymbol{U}^\top\}_{k=1,\, l=1}^{k=4,\, l=4} \\ \lim_{(t-t_\circ)\to\infty} \tilde{\boldsymbol{R}} \in \{\boldsymbol{U}\boldsymbol{D}_k\boldsymbol{U}^\top\}_{k=1}^4, \end{cases} \quad \text{(C.29d)}$$

where the second implication holds due to Lemma B.3, and the rest follows from the orthogonality of $\boldsymbol{U}$ and $\tilde{\boldsymbol{R}}$. Therefore, all trajectories of the error dynamics tend towards a set of 16 unique equilibrium points characterized by

$$\lim_{(t-t_\circ)\to\infty} (\boldsymbol{R}_e, \tilde{\boldsymbol{R}}, \boldsymbol{\omega}_e, \tilde{\boldsymbol{\omega}}) \in \{(\boldsymbol{U}\boldsymbol{D}_k\boldsymbol{D}_l\boldsymbol{U}^\top, \boldsymbol{U}\boldsymbol{D}_k\boldsymbol{U}^\top, \boldsymbol{0}, \boldsymbol{0})\}_{k=1,\, l=1}^{k=4,\, l=4} \triangleq \mathcal{E}. \quad \text{(C.30)}$$

(iv) Application of Matrosov As the error dynamics are non-autonomous, we need to prove that the convergence to the set of equilibrium points in (C.30) is uniform. To this end, let $\dot{\mathcal{V}}_1 \triangleq \mathcal{Y}_1$ and consider a function

$$\mathcal{V}_2 = \boldsymbol{\omega}_e^\top \sum_{i=1}^{N} k_i \boldsymbol{S}(\boldsymbol{R}_r^\top \boldsymbol{v}_i)\hat{\boldsymbol{R}}^\top \boldsymbol{v}_i. \tag{C.31}$$

Differentiation of $\mathcal{V}_2$ along the solutions of the error dynamics, combined with the bounds on the attitude rates following from the negative semi-definiteness of $\mathcal{V}_1$ summarized in (C.21) and assumed bound on $\boldsymbol{\omega}_r$, is upper bound by

$$\frac{\mathrm{d}\mathcal{V}_2}{\mathrm{d}t} \leq -\left\| \sum_{i=1}^{N} k_i \boldsymbol{S}(\boldsymbol{R}_r^\top \boldsymbol{v}_i)\hat{\boldsymbol{R}}^\top \boldsymbol{v}_i \right\|^2 + M_3 \left\| \begin{bmatrix} \boldsymbol{\omega}_e \\ \tilde{\boldsymbol{\omega}} \end{bmatrix} \right\| + M_4 \left\| \begin{bmatrix} \boldsymbol{\omega}_e \\ \tilde{\boldsymbol{\omega}} \end{bmatrix} \right\|^2 \triangleq \mathcal{Y}_2,$$

for some positive constants M_3 and M_4. Clearly, we have that $\mathcal{Y}_1 = \mathbf{0} \Rightarrow \mathcal{Y}_2 \leq \mathbf{0}$, and together, $\mathcal{Y}_1 = \mathbf{0}$ and $\mathcal{Y}_2 = \mathbf{0}$ imply that the tracking and estimate error trajectories converge to the invariant set $\mathcal{S}$ in (C.28). Consequently, the trajectories converge uniformly to $\mathcal{S}$ by Theorem 2.7, implying uniform convergence to the equilibrium points characterized by $\mathcal{E}$ in (C.30).

(v) Local Chetaev Instability Analysis To investigate the local stability properties of the equilibrium points in $\mathcal{E}$, we start by noting that

$$\dot{\mathcal{V}}_1(\boldsymbol{x}_\circ) = 0, \quad \forall \boldsymbol{x}_\circ \in \mathcal{E}, \tag{C.32a}$$

$$\dot{\mathcal{V}}_1(\boldsymbol{x}_\circ) < 0, \quad \forall \boldsymbol{x}_\circ \in \{\mathrm{SO}(3)^2 \times \mathbb{R}^6\} \backslash \mathcal{E}. \tag{C.32b}$$

However, if we consider the two quadratic sums in $\mathcal{V}_1$, knowing that $\boldsymbol{D}_k^2 = \boldsymbol{I}$,

$$\sum_{i=1}^{N} \frac{k_i}{2} \|\boldsymbol{U}\boldsymbol{D}_k\boldsymbol{D}_l\boldsymbol{U}^\top \boldsymbol{U}\boldsymbol{D}_k\boldsymbol{U}^\top \boldsymbol{v}_i - \boldsymbol{v}_i\| = \sum_{i=1}^{N} \frac{k_i}{2} \|\boldsymbol{U}(\boldsymbol{D}_l - \boldsymbol{I})\boldsymbol{U}^\top \boldsymbol{v}_i\| = 0,$$

if and only if $\boldsymbol{D}_l = \boldsymbol{I}$ (given that $\boldsymbol{v}_i$ are linearly independent), and similarly

$$\sum_{i=1}^{N} \frac{k_i}{2} \|\boldsymbol{U}(\boldsymbol{D}_k - \boldsymbol{I})\boldsymbol{U}^\top \boldsymbol{v}_i\| = 0,$$

if and only if $\boldsymbol{D}_k = \boldsymbol{I}$. Consequently, for any point on $\mathcal{E}$ we have that

$$\mathcal{V}_1(\boldsymbol{x}_\circ) > 0, \qquad \forall\, \boldsymbol{x}_\circ \in \mathcal{E}\backslash\{(\boldsymbol{I}, \boldsymbol{I}, \mathbf{0}, \mathbf{0})\} \subset \{\mathrm{SO}(3)^2 \times \mathbb{R}^6\}, \tag{C.33}$$

$$\mathcal{V}_1(\boldsymbol{x}_\circ) = 0, \qquad \text{if } \boldsymbol{x}_\circ = (\boldsymbol{I}, \boldsymbol{I}, \mathbf{0}, \mathbf{0}) \subset \{\mathrm{SO}(3)^2 \times \mathbb{R}^6\}. \tag{C.34}$$

Here, we note that by Lemma C.2, there exist points $\bar{\boldsymbol{x}}_\circ$ in the neighborhood of $\boldsymbol{x}_\circ \in \mathcal{E}\backslash\{(\boldsymbol{I}, \boldsymbol{I}, \mathbf{0}, \mathbf{0})\}$ for which $\mathcal{V}_1(\bar{\boldsymbol{x}}_\circ) < \mathcal{V}_1(\boldsymbol{x}_\circ)$, and by (C.32b),

$\mathcal{V}_1(\bar{\boldsymbol{x}}_\circ) < 0$ as $\bar{\boldsymbol{x}}_\circ \notin \mathcal{E}$. Consequently, the points characterized by the set (C.33) are locally unstable by Theorem 2.6 (Chetaev), and the point in (C.34) is asymptotically stable, as all solutions converge asymptotically to $\mathcal{E}$ by (C.30). As convergence to $\mathcal{E}$ is uniform, and locally unstable the equilibrium points in $\mathcal{E}\backslash(\boldsymbol{I},\boldsymbol{I},\boldsymbol{0},\boldsymbol{0})$ form a set of measure zero, we conclude that the point $(\boldsymbol{I},\boldsymbol{I},\boldsymbol{0},\boldsymbol{0})$ is UAGAS. Intuitively, the local error dynamics are non-autonomous, and all trajectories starting in the neighborhood of $(\boldsymbol{I},\boldsymbol{I},\boldsymbol{0},\boldsymbol{0})$ will converge uniformly and asymptotically to this point. For such an non-autonomous linear system, ULES the follows by the equivalence in Theorem 2.2. This can be shown more rigorously using the same linearization ideas as in the proof of Theorem 3.1 in Appendix B.1, by an explicit linearization of the dynamics about $(\boldsymbol{R}_e,\hat{\boldsymbol{R}},\boldsymbol{\omega}_e,\tilde{\boldsymbol{\omega}}) = (\boldsymbol{I},\boldsymbol{I},\boldsymbol{0},\boldsymbol{0})$ (this is done in brevity below). □

(vi) Local Linearization Consider an approach similar to the proof of Theorem 3.1. Assume that $\boldsymbol{R}_e$ and $\hat{\boldsymbol{R}}$ are close to elements $\boldsymbol{R}_\circ$ and $\tilde{\boldsymbol{R}}_o$ respectively, and that they are locally described by two small perturbations, $\boldsymbol{\epsilon}(t)$ and $\tilde{\boldsymbol{\epsilon}}(t)$, using the first two terms of the exponential series in (A.1), as

$$\boldsymbol{R}_e \approx \boldsymbol{R}_\circ(\boldsymbol{I}+\boldsymbol{S}(\boldsymbol{\epsilon})), \qquad \tilde{\boldsymbol{R}} \approx \tilde{\boldsymbol{R}}_\circ(\boldsymbol{I}+\boldsymbol{S}(\tilde{\boldsymbol{\epsilon}})). \tag{C.35}$$

For simplicity, we here consider the stable equilibrium at $\boldsymbol{R}_\circ = \boldsymbol{I}$ and $\tilde{\boldsymbol{R}}_\circ = \boldsymbol{I}$. With the first-order approximations in (C.35), the error dynamics in the perturbations (here omitting their exact expressions) becomes

$$\begin{aligned}
\dot{\boldsymbol{\epsilon}} &= \boldsymbol{f}_1(\boldsymbol{\epsilon},\tilde{\boldsymbol{\epsilon}},\boldsymbol{\omega}_e,\tilde{\boldsymbol{\omega}}),\\
\dot{\tilde{\boldsymbol{\epsilon}}} &= \boldsymbol{f}_2(\boldsymbol{\epsilon},\tilde{\boldsymbol{\epsilon}},\boldsymbol{\omega}_e,\tilde{\boldsymbol{\omega}}),\\
\boldsymbol{J}\dot{\boldsymbol{\omega}}_e &= \boldsymbol{f}_3(\boldsymbol{\epsilon},\tilde{\boldsymbol{\epsilon}},\boldsymbol{\omega}_e,\tilde{\boldsymbol{\omega}}),\\
\boldsymbol{J}\dot{\tilde{\boldsymbol{\omega}}} &= \boldsymbol{f}_4(\boldsymbol{\epsilon},\tilde{\boldsymbol{\epsilon}},\boldsymbol{\omega}_e,\tilde{\boldsymbol{\omega}}),
\end{aligned}$$

or more compactly with $\boldsymbol{X} \triangleq (\boldsymbol{\epsilon},\tilde{\boldsymbol{\epsilon}},\boldsymbol{\omega}_e,\tilde{\boldsymbol{\omega}})$ and $\boldsymbol{E} \triangleq \operatorname{diag}(\boldsymbol{I},\boldsymbol{I},\boldsymbol{J},\boldsymbol{J})$, as

$$\boldsymbol{E}\dot{\boldsymbol{X}} = \boldsymbol{f}(t,\boldsymbol{X}). \tag{C.36}$$

Taking the Jacobian of $\boldsymbol{f}$ with respect to $\boldsymbol{X}$ around $\boldsymbol{X}=\boldsymbol{0}$ yields

$$\begin{aligned}
\boldsymbol{A}(t) &\triangleq \frac{\partial f(t,\boldsymbol{X})}{\partial \boldsymbol{X}}\Big|_{\boldsymbol{X}=\boldsymbol{0}} \qquad\qquad (\text{C.37})\\
&= \begin{bmatrix}
\boldsymbol{0} & \boldsymbol{0} & \boldsymbol{R}_r(t) & \boldsymbol{0}\\
c_R\bar{\boldsymbol{M}} & -2c_R\bar{\boldsymbol{M}} & \boldsymbol{0} & \boldsymbol{0}\\
-\boldsymbol{R}_r(t)^\top\bar{\boldsymbol{M}} & \boldsymbol{R}_r(t)^\top\bar{\boldsymbol{M}} & \boldsymbol{S}(\boldsymbol{J}\boldsymbol{\omega}(t)) - \boldsymbol{K}_{\boldsymbol{\omega}} & +\boldsymbol{J}\boldsymbol{S}(\boldsymbol{\omega}_r(t)) + \boldsymbol{K}_{\boldsymbol{\omega}}\\
\boldsymbol{0} & \boldsymbol{0} & -\boldsymbol{J}\boldsymbol{S}(\boldsymbol{\omega}_r(t)) - \boldsymbol{K}_{\boldsymbol{\omega}} & -\boldsymbol{C}_{\boldsymbol{\omega}}
\end{bmatrix},
\end{aligned}$$

where $\bar{\boldsymbol{M}} \triangleq \big(\sum_{i=1}^N k_i\big)\boldsymbol{I} - \boldsymbol{M}$. Thus, about $(\boldsymbol{R}_\circ,\tilde{\boldsymbol{R}}_\circ) = (\boldsymbol{I},\boldsymbol{I})$, the perturbations and attitude rate errors evolve by time-varying descriptor dynamics

$$\boldsymbol{E}\dot{\boldsymbol{X}} = \boldsymbol{A}(t)\boldsymbol{X}. \tag{C.38}$$

As $\boldsymbol{E}$ is symmetric, positive definite and real, we can instead consider

$$\dot{\boldsymbol{X}} = \boldsymbol{A}(t)\boldsymbol{X}, \tag{C.39}$$

and find a solution to the Lyapunov equation with respect to $\boldsymbol{A}(t)$ in $(\boldsymbol{P}, \boldsymbol{Q}(t))$ such that $\boldsymbol{P}$ and $\boldsymbol{E}$ commute, permitting application of Lemma 2.4. The hunt for such a Lyapunov function becomes quite involved, and can be undertaken using Lemmas 2.1 and 2.3. By applying sequence of orthogonal transformations, the resulting system in the new coordinates can be partitioned in such a way that its stability can be analyzed using Lemma 2.1 where the non-autonomous part of the system matrix is Hurwitz if the matrix in $\boldsymbol{D}(c_R, l_i)$ studied in Lemma C.3 is Hurwitz with $l_i > 0$ being the eigenvalues of $\bar{\boldsymbol{M}}$. Taking such an approach, one arrives at a Lyapunov function candidate with

$$\boldsymbol{P} \triangleq \begin{bmatrix} \bar{\boldsymbol{M}} & -\bar{\boldsymbol{M}} & \boldsymbol{0} & \boldsymbol{0} \\ -\bar{\boldsymbol{M}} & 2\bar{\boldsymbol{M}} & \boldsymbol{0} & \boldsymbol{0} \\ \boldsymbol{0} & \boldsymbol{0} & \boldsymbol{I} & \boldsymbol{0} \\ \boldsymbol{0} & \boldsymbol{0} & \boldsymbol{0} & \boldsymbol{I} \end{bmatrix}, \tag{C.40}$$

where it can be verified that

$$\boldsymbol{A}(t)\boldsymbol{P} + \boldsymbol{P}\boldsymbol{A}(t) = -\begin{bmatrix} 2c_R\bar{\boldsymbol{M}}^2 & -4c_R\bar{\boldsymbol{M}}^2 & \boldsymbol{0} & \boldsymbol{0} \\ -4c_R\bar{\boldsymbol{M}}^2 & 8c_R\bar{\boldsymbol{M}}^2 & \boldsymbol{0} & \boldsymbol{0} \\ \boldsymbol{0} & \boldsymbol{0} & 2\boldsymbol{K}_{\boldsymbol{\omega}} & \boldsymbol{0} \\ \boldsymbol{0} & \boldsymbol{0} & \boldsymbol{0} & 2\boldsymbol{C}_{\boldsymbol{\omega}} \end{bmatrix} \triangleq -\boldsymbol{Q}, \tag{C.41}$$

where $\boldsymbol{P} \succ \boldsymbol{0}$ but $\boldsymbol{Q} \succeq \boldsymbol{0}$. Indeed, it can also be shown that

$$\operatorname{spec}(\boldsymbol{P}) = \{1, 1, 1\} \cup \left(\bigcup_{i=1}^{3} \operatorname{spec}(\boldsymbol{P}(c_R, l_i)) \right),$$

$$\operatorname{spec}(\boldsymbol{Q}) = \{0, 0, 0\} \cup \{10c_R l_1^2, 10c_R l_2^2, 10c_R l_3^2\} \cup \operatorname{spec}(2\boldsymbol{K}_{\boldsymbol{\omega}}) \cup \operatorname{spec}(2\boldsymbol{C}_{\boldsymbol{\omega}}),$$

with the matrix function $\boldsymbol{P}(c, l) \succ \boldsymbol{0}$ as defined in (C.8). As $\boldsymbol{P}$ and $\boldsymbol{E}$ commute, application of Lemma 2.4 then shows uniform stability of the origin of (C.36) by Theorem 2.1. Furthermore, analysis using Lemma 2.5 and subsequent signal chasing shows the expected asymptotic convergence to point $(\boldsymbol{\epsilon}, \tilde{\boldsymbol{\epsilon}}, \boldsymbol{\omega}_e, \tilde{\boldsymbol{\omega}}_e) = (\boldsymbol{0}, \boldsymbol{0}, \boldsymbol{0}, \boldsymbol{0})$, and this convergence can further be shown to be uniform by application of the Matrosov result in Theorem 2.7. Finally, as UAS and UES is a distinction without a difference for linear non-autonomous systems (see, e.g, Theorem 2.2), we conclude that the system in (2.4) is ULES.

C.2 Remark 6.3: Quadratic Bounds on $\mathcal{V}_\sigma$

Proof of Remark 6.3. To show that for any $\mathcal{V}_\sigma$ by Definition 6.2,

$$\frac{c_1}{2}\|\sigma(\boldsymbol{x})\|^2 \leq \mathcal{V}_\sigma(\boldsymbol{x}) \leq \frac{c_2}{2}\|\boldsymbol{x}\|^2, \qquad \forall \boldsymbol{x} \in \mathbb{R}^n, \tag{C.42}$$

simply let $x = \|\boldsymbol{x}\|$, and note that the statement (C.42) is equivalent to

$$f_1(x) = \int_0^x s(y)dy - (c_1/2)s(x)^2 \geq 0, \tag{C.43a}$$

$$f_2(x) = (c_2/2)x^2 - \int_0^x s(y)dy \geq 0, \tag{C.43b}$$

for all $x \geq 0$. For both of these functions, we have that $f_1(0) = f_2(0) = 0$, and

$$\frac{\mathrm{d}}{\mathrm{d}x} f_1(x) = s(x) - c_1 s(x)s'(x) \geq (1 - c_1 s'(0))s(x) \geq 0,$$
$$\frac{\mathrm{d}}{\mathrm{d}x} f_2(x) = c_2 x - s(x) \geq (c_2 - s'(0))x \geq 0,$$

if $0 < c_1 \leq s'(0)^{-1}$ and $s'(0) \leq c_2$. Under these sufficient conditions, f_1 and f_2 are increasing in $x \geq 0$ from $f_1(0) = f_2(0) = 0$, whereby (C.43) holds for all $x \geq 0$, implying (C.42) and concluding the proof. □

C.3 Remark 6.4: Time-derivative of $\mathcal{V}_\sigma$

Proof of Remark 6.4. Let $\boldsymbol{x}(t)$, and $(\mathrm{d}/\mathrm{d}t)\boldsymbol{x}(t) = \dot{\boldsymbol{x}}$. By the chain rule,

$$\frac{\mathrm{d}}{\mathrm{d}t}\mathcal{V}_\sigma(\boldsymbol{x}(t)) = s(\|\boldsymbol{x}\|)\frac{\mathrm{d}}{\mathrm{d}t}\sqrt{\boldsymbol{x}^\top \boldsymbol{x}} = s(\|\boldsymbol{x}\|)\frac{1}{2\sqrt{\boldsymbol{x}^\top \boldsymbol{x}}}(2\boldsymbol{x}^\top \dot{\boldsymbol{x}}) = \sigma(\boldsymbol{x})^\top \dot{\boldsymbol{x}}. \tag{C.44}$$

□

C.4 Proposition 6.1: Translation FSF

Proof of Proposition 6.1. By the assumptions of the proposition (reference trajectory feasibility and a smooth saturation function), there exist finite positive constants $\gamma_1 > 0$, $\gamma_2 > 0$ such that

$$\sup_{t \geq t_\circ} \|\boldsymbol{\omega}_r(t)\| \leq \gamma_1, \qquad \sup_{y \in \mathbb{R}_{\geq 0}} |s'(y)| \leq \gamma_2, \qquad \sup_{y \in \mathbb{R}_{\geq 0}} |s(y)y^{-1}| \leq \gamma_2. \tag{C.45}$$

These constants are required in showing that the Lyapunov function time-derivative is uniformly continuous. Furthermore, it is assumed that a vector-valued saturation function σ is constructed in accordance with Definition 6.1, where $s : \mathbb{R}_{\geq 0} \mapsto [0, \gamma]$ for some positive saturation level $\gamma > 0$. The proof follows the familiar structure of proposing a Lyapunov function candidate by which UGS can be shown, to which the lemma of Barbălat is applied to show GAS. The Matrosov theorem is subsequently used to show UGAS, and ULES follows by a local linearization. As usual, we do not write out the arguments of the Lyapunov function and time-varying signals.

Application of Barbălat Consider an error $\boldsymbol{e} \triangleq k_p \boldsymbol{p}_e + k_v \boldsymbol{v}_e \in \mathbb{R}^3$, and a Lyapunov function candidate

$$\mathcal{V}_1 = \frac{k_p}{2}\|\boldsymbol{v}_e\|^2 + \mathcal{V}_\sigma(\boldsymbol{e}). \tag{C.46}$$

Differentiating $\mathcal{V}_1$ along solutions of the error dynamics in (6.5) yields

$$\begin{aligned}
\dot{\mathcal{V}}_1 =& k_p \boldsymbol{v}_e^\top \dot{\boldsymbol{v}}_e + \dot{\boldsymbol{e}}^\top \sigma(\boldsymbol{e}) && \text{(C.47a)}\\
=& -k_p \boldsymbol{v}_e^\top \boldsymbol{S}(\boldsymbol{\omega}_r)\boldsymbol{v}_e - k_p \boldsymbol{v}_e^\top \sigma(\boldsymbol{e}) + k_p \boldsymbol{p}_e^\top \boldsymbol{S}(\boldsymbol{\omega}_r)\sigma(\boldsymbol{e}) && \text{(C.47b)}\\
&+ k_p \boldsymbol{v}_e^\top \sigma(\boldsymbol{e}) + k_v \boldsymbol{v}_e^\top \boldsymbol{S}(\boldsymbol{\omega}_r)\sigma(\boldsymbol{e}) - k_v \sigma(\boldsymbol{e})^\top \sigma(\boldsymbol{e}) && \text{(C.47c)}\\
=& \boldsymbol{e}^\top \boldsymbol{S}(\boldsymbol{\omega}_r)\sigma(\boldsymbol{e}) - k_v \sigma(\boldsymbol{e})^\top \sigma(\boldsymbol{e}) && \text{(C.47d)}\\
=& s(\|\boldsymbol{e}\|)\|\boldsymbol{e}\|^{-1} \boldsymbol{e}^\top \boldsymbol{S}(\boldsymbol{\omega}_r)\boldsymbol{e} - k_v \sigma(\boldsymbol{e})^\top \sigma(\boldsymbol{e}) &&\\
=& -k_v \sigma(\boldsymbol{e})^\top \sigma(\boldsymbol{e}) \leq 0, && \text{(C.47e)}
\end{aligned}$$

which is negative semi-definite in $\boldsymbol{p}_e$ and $\boldsymbol{v}_e$. As $\mathcal{V}_1$ is non-increasing in time,

$$\|\boldsymbol{v}_e\| \leq \sqrt{(2/k_p)\mathcal{V}_1(t_\circ)} \triangleq \bar{v}_e, \quad \forall t \geq t_\circ. \tag{C.48}$$

To proceed, let $x = \|\boldsymbol{e}\|$, and let $\boldsymbol{v}$ be a unit vector such that $\boldsymbol{e} = x\boldsymbol{v}$, then

$$\frac{\partial \sigma(\boldsymbol{e})}{\partial \boldsymbol{e}} = \Big(s'(x) - \frac{s(x)}{x}\Big)\boldsymbol{v}\boldsymbol{v}^\top + \frac{s(x)}{x}\boldsymbol{I}_3, \tag{C.49}$$

by application of the chain rule, and we note that

$$\lim_{x\to 0}\Big(s'(x) - \frac{s(x)}{x}\Big) = 0 \Rightarrow \lim_{x\to 0}\frac{\partial \sigma(\boldsymbol{e})}{\partial \boldsymbol{e}} = s'(0)\boldsymbol{I}_3. \tag{C.50}$$

Furthermore, if $a \triangleq s'(x) - s(x)x^{-1}$ and $b \triangleq s(x)x^{-1}$, then $\sup_{t\geq t_\circ}|a| \leq 2\gamma_2$ and $\sup_{t\geq t_\circ}|b| \leq \gamma_2$ by (C.66a). Consequently, (C.49) is bounded in γ_2, as

$$\Big(\frac{\partial \sigma(\boldsymbol{e})}{\partial \boldsymbol{e}}\Big)^\top \frac{\partial \sigma(\boldsymbol{e})}{\partial \boldsymbol{e}} \preceq (a^2 + 2ab)\boldsymbol{v}\boldsymbol{v}^\top + b^2\boldsymbol{I}_3 \preceq (|a| + |b|)^2\boldsymbol{I}_3,$$

whereby

$$\Big\|\frac{\partial \sigma(\boldsymbol{e})}{\partial \boldsymbol{e}}\Big\| = \sqrt{\lambda_M\Big(\Big(\frac{\partial \sigma(\boldsymbol{e})}{\partial \boldsymbol{e}}\Big)^\top \frac{\partial \sigma(\boldsymbol{e})}{\partial \boldsymbol{e}}\Big)} \leq |a| + |b| \leq 3\gamma_2, \quad \forall\, t \geq t_\circ.$$

Utilizing the expression in (C.49), we have that

$$\sigma(\boldsymbol{e})^\top \frac{\partial \sigma(\boldsymbol{e})}{\partial \boldsymbol{e}}\boldsymbol{S}(\boldsymbol{\omega}_r)\boldsymbol{e} = \frac{s(x)^2}{x^2}\boldsymbol{e}^\top \boldsymbol{S}(\boldsymbol{\omega}_r)\boldsymbol{e} = 0. \tag{C.51a}$$

Consequently, $\ddot{\mathcal{V}}_1$ is bounded in the initial errors in time, as

$$\|\ddot{\mathcal{V}}_1\| = 2k_v \left\| \sigma(\boldsymbol{e})^\top \frac{\mathrm{d}}{\mathrm{d}t}\sigma(\boldsymbol{e}) \right\| \tag{C.52a}$$

$$= 2k_v \left\| \sigma(\boldsymbol{e})^\top \frac{\partial \sigma(\boldsymbol{e})}{\partial \boldsymbol{e}} \dot{\boldsymbol{e}} \right\| \tag{C.52b}$$

$$= 2k_v \left\| \sigma(\boldsymbol{e})^\top \frac{\partial \sigma(\boldsymbol{e})}{\partial \boldsymbol{e}} (-\boldsymbol{S}(\boldsymbol{\omega}_r)\boldsymbol{e} + k_p \boldsymbol{v}_e - \sigma(\boldsymbol{e})) \right\| \tag{C.52c}$$

$$= 2k_v \left\| \sigma(\boldsymbol{e})^\top \frac{\partial \sigma(\boldsymbol{e})}{\partial \boldsymbol{e}} (k_\rho \boldsymbol{v}_e - \sigma(\boldsymbol{e})) \right\| \tag{C.52d}$$

$$\leq 6k_v \gamma\gamma_2 \|k_\rho \boldsymbol{v}_e - \sigma(\boldsymbol{e})\| \tag{C.52e}$$

$$\leq 6k_v \gamma\gamma_2 (k_\rho \bar{v}_e + \gamma). \tag{C.52f}$$

This implies that $\dot{\mathcal{V}}_1 \leq 0$ is uniformly continuous, and $\mathcal{V}_1 \geq 0$ is lower bounded, whereby application of Lemma 2.5 (Barbălat), yields

$$\lim_{t\to\infty} \dot{\mathcal{V}}_1 = 0 \Rightarrow \lim_{t\to\infty} \sigma(\boldsymbol{e}) = \boldsymbol{0} \Rightarrow \lim_{t\to\infty} \boldsymbol{e} = \boldsymbol{0}, \tag{C.53}$$

where the last implication follows by Definition 6.1. Furthermore, let

$$\underbrace{\dot{\boldsymbol{e}}}_{\triangleq \dot{f}(t)} = \underbrace{k_p \boldsymbol{v}_e}_{\triangleq f_0(t)} - \underbrace{\boldsymbol{S}(\boldsymbol{\omega}_r)\boldsymbol{e} - k_v \sigma(\boldsymbol{e})}_{\triangleq \eta(t)}. \tag{C.54}$$

As $\|\dot{\boldsymbol{v}}_e\| \leq \gamma_1 \bar{v}_e + \gamma$ is upper bounded by (C.66a) and (C.48), we have that $f_0(t)$ is uniformly continuous in time. We also note that $f(t) \to \boldsymbol{0}$ and $\eta(t) \to \boldsymbol{0}$ as $t \to \infty$ by (C.53). Consequently, Lemma 2.7 applied to (C.54) yields

$$\lim_{t\to\infty} \dot{\boldsymbol{e}}(t) = \lim_{t\to\infty} \boldsymbol{v}_e = \boldsymbol{0} \Rightarrow \lim_{t\to\infty} \boldsymbol{p}_e = \boldsymbol{0}, \tag{C.55}$$

where the last implication holds due to (C.53), showing that the origin $(\boldsymbol{p}_e, \boldsymbol{v}_e) = (\boldsymbol{0}, \boldsymbol{0})$ is GAS. Furthermore, as (i) $\mathcal{V}_1$ is continuously differentiable by (C.52), and (ii) this function is positive definite and radially unbounded in $(\boldsymbol{p}_e, \boldsymbol{v}_e)$ as per Remark 6.3, and (iii) $\dot{\mathcal{V}}_1$ is negative semi-definite in the same errors, Theorem 2.3 is invoked to show that $(\boldsymbol{p}_e, \boldsymbol{v}_e) = (\boldsymbol{0}, \boldsymbol{0})$ is UGS.

Intermediary Computation of an Error Bound Before showing UGAS, we derive a bound of the signal $(\mathrm{d}/\mathrm{d}t)(-\boldsymbol{e}^\top \dot{\boldsymbol{e}})$. As

$$\ddot{\boldsymbol{p}}_e = (-\boldsymbol{S}(\dot{\boldsymbol{\omega}}_r) + \boldsymbol{S}(\boldsymbol{\omega}_r)^2)\boldsymbol{p}_e - 2\boldsymbol{S}(\boldsymbol{\omega}_r)\boldsymbol{v}_e - \sigma(\boldsymbol{e}), \tag{C.56}$$

$$\ddot{\boldsymbol{v}}_e = (-\boldsymbol{S}(\dot{\boldsymbol{\omega}}_r) + \boldsymbol{S}(\boldsymbol{\omega}_r)^2)\boldsymbol{v}_e + S(\boldsymbol{\omega}_r)\sigma(\boldsymbol{e}) - \dot{\sigma}(\boldsymbol{e}),$$

$$\ddot{\boldsymbol{e}} = (-\boldsymbol{S}(\dot{\boldsymbol{\omega}}_r) + \boldsymbol{S}(\boldsymbol{\omega}_r)^2)\boldsymbol{e} - 2k_p \boldsymbol{S}(\boldsymbol{\omega}_r)\boldsymbol{v}_e + (k_v \boldsymbol{S}(\boldsymbol{\omega}_r) - k_p \boldsymbol{I})\sigma(\boldsymbol{e}) - k_v \dot{\sigma}(\boldsymbol{e}),$$

thus

$$\boldsymbol{e}^\top \ddot{\boldsymbol{e}} = \boldsymbol{e}^\top \boldsymbol{S}(\boldsymbol{\omega}_r)^2 \boldsymbol{e} - 2k_p \boldsymbol{e}^\top \boldsymbol{S}(\boldsymbol{\omega}_r)\boldsymbol{v}_e - k_p \boldsymbol{e}^\top \sigma(\boldsymbol{e}) - k_v \boldsymbol{e}^\top \dot{\sigma}(\boldsymbol{e}), \tag{C.57a}$$

and since

$$\begin{aligned}
\dot{\boldsymbol{e}}^\top \dot{\boldsymbol{e}} =& [k_p \boldsymbol{v}_e - \boldsymbol{S}(\boldsymbol{\omega}_r)\boldsymbol{e} - k_v \sigma(\boldsymbol{e})]^\top [k_p \boldsymbol{v}_e - \boldsymbol{S}(\boldsymbol{\omega}_r)\boldsymbol{e} - k_v \sigma(\boldsymbol{e})] && \text{(C.58a)}\\
=& + k_p^2 \boldsymbol{v}_e^\top \boldsymbol{v}_e - \boldsymbol{e}^\top \boldsymbol{S}(\boldsymbol{\omega}_r)^2 \boldsymbol{e} + k_v^2 \sigma(\boldsymbol{e})^\top \sigma(\boldsymbol{e}) && \text{(C.58b)}\\
& - 2k_p \boldsymbol{v}_e^\top \boldsymbol{S}(\boldsymbol{\omega}_r)\boldsymbol{e} - 2k_p k_v \boldsymbol{v}_e^\top \sigma(\boldsymbol{e}) && \text{(C.58c)}\\
& + 2k_v \sigma(\boldsymbol{e})^\top \boldsymbol{S}(\boldsymbol{\omega}_r)\boldsymbol{e} && \text{(C.58d)}\\
=& + k_p^2 \boldsymbol{v}_e^\top \boldsymbol{v}_e - \boldsymbol{e}^\top \boldsymbol{S}(\boldsymbol{\omega}_r)^2 \boldsymbol{e} + k_v^2 \sigma(\boldsymbol{e})^\top \sigma(\boldsymbol{e}) && \text{(C.58e)}\\
& - 2k_p \boldsymbol{v}_e^\top \boldsymbol{S}(\boldsymbol{\omega}_r)\boldsymbol{e} - 2k_p k_v \boldsymbol{v}_e^\top \sigma(\boldsymbol{e}), && \text{(C.58f)}
\end{aligned}$$

we get

$$\begin{aligned}
&\frac{\mathrm{d}}{\mathrm{d}t}(-\boldsymbol{e}^\top \dot{\boldsymbol{e}}) = && \text{(C.59)}\\
&= - k_p^2 \boldsymbol{v}_e^\top \boldsymbol{v}_e + \boldsymbol{e}^\top \boldsymbol{S}(\boldsymbol{\omega}_r)^2 \boldsymbol{e} + 2k_p \boldsymbol{v}_e^\top \boldsymbol{S}(\boldsymbol{\omega}_r)\boldsymbol{e} - k_v^2 \sigma(\boldsymbol{e})^\top \sigma(\boldsymbol{e}) + 2k_p k_v \boldsymbol{v}_e^\top \sigma(\boldsymbol{e})\\
&\qquad - \boldsymbol{e}^\top \boldsymbol{S}(\boldsymbol{\omega}_r)^2 \boldsymbol{e} + 2k_p \boldsymbol{e}^\top \boldsymbol{S}(\boldsymbol{\omega}_r)\boldsymbol{v}_e + k_p \boldsymbol{e}^\top \sigma(\boldsymbol{e}) + k_v \boldsymbol{e}^\top \dot{\sigma}(\boldsymbol{e})\\
&= - k_p^2 \boldsymbol{v}_e^\top \boldsymbol{v}_e - k_v^2 \sigma(\boldsymbol{e})^\top \sigma(\boldsymbol{e}) + 2k_p k_v \boldsymbol{v}_e^\top \sigma(\boldsymbol{e}) + k_p \boldsymbol{e}^\top \sigma(\boldsymbol{e}) + k_v \boldsymbol{e}^\top \dot{\sigma}(\boldsymbol{e})\\
&\leq - k_p^2 \boldsymbol{v}_e^\top \boldsymbol{v}_e + 2k_p k_v \bar{v}_e \gamma_2 \|\boldsymbol{e}\| + k_p \gamma_2 \|\boldsymbol{e}\|^2 + 3\gamma_2 k_v \|\boldsymbol{e}\| \|\dot{\boldsymbol{e}}\|\\
&\leq - k_p^2 \boldsymbol{v}_e^\top \boldsymbol{v}_e + 2k_p k_v \bar{v}_e \gamma_2 \|\boldsymbol{e}\| + k_p \gamma_2 \|\boldsymbol{e}\|^2 + 3\gamma_2 k_v \|\boldsymbol{e}\| (k_p \bar{v}_e + \gamma_1 \|\boldsymbol{e}\| + k_v \gamma_2 \|\boldsymbol{e}\|)\\
&= - k_p^2 \boldsymbol{v}_e^\top \boldsymbol{v}_e + (2k_p k_v \bar{v}_e \gamma_2 + k_p \bar{v}_e) \|\boldsymbol{e}\| + [k_p \gamma_2 + 3\gamma_2 k_v (\gamma_1 + k_v \gamma_2)] \|\boldsymbol{e}\|^2\\
&= - k_p^2 \boldsymbol{v}_e^\top \boldsymbol{v}_e + M_1 \|\boldsymbol{e}\|^1 + M_2 \|\boldsymbol{e}\|^2, && \text{(C.60)}
\end{aligned}$$

where $M_1 = (2k_p k_v \bar{v}_e \gamma_2 + k_p \bar{v}_e)$ and $M_2 = k_p \gamma_2 + 3\gamma_2 k_v (\gamma_1 + k_v \gamma_2)$.

Application of Matrosov To show that the convergence to the origin is uniform, consider a function

$$\dot{\mathcal{V}}_1 = -k_v \sigma(\boldsymbol{e})^\top \sigma(\boldsymbol{e}) \triangleq \mathcal{Y}_1(\boldsymbol{p}_e, \boldsymbol{v}_e), \tag{C.61}$$

then, condition (i) in Theorem 2.7 is satisfied, as $\mathcal{V}_1$ shows UGS. Furthermore, condition (ii) is met with respect to the functions $\{\mathcal{V}_1, \mathcal{Y}_1\}$ due to the equality in (C.61). Next, consider a function $\mathcal{V}_2 = -\boldsymbol{e}^\top \dot{\boldsymbol{e}}$. Differentiating this function along the solutions of the error dynamics as done in (C.60) yields

$$\dot{\mathcal{V}}_2 = - \dot{\boldsymbol{e}}^\top \dot{\boldsymbol{e}} - \boldsymbol{e}^\top \ddot{\boldsymbol{e}} \leq -k_p^2 \boldsymbol{v}_e^\top \boldsymbol{v}_e + B(\boldsymbol{e}) \triangleq \mathcal{Y}_2(\boldsymbol{p}_e, \boldsymbol{v}_e), \tag{C.62}$$

where

$$B(\boldsymbol{e}) = M_1 \|\boldsymbol{e}\|^1 + M_2 \|\boldsymbol{e}\|^2,$$

is a positive definite function in $\boldsymbol{e}$, where the constants M_1 and M_2 expressed in the initial errors, controller parameters, and signal bounds $\{k_p, k_v, \bar{v}_e, \gamma, \gamma_1, \gamma_2\}$. Thus, condition (ii) in Theorem 2.7 is satisfied with respect to $\{\mathcal{V}_2, \mathcal{Y}_2\}$. We also note that (iii) $\mathcal{Y}_1 = 0 \Rightarrow \boldsymbol{e} = \boldsymbol{0} \Rightarrow B(\boldsymbol{e}) = \boldsymbol{0} \Rightarrow \mathcal{Y}_2 = -k_p^2 \boldsymbol{v}_e^\top \boldsymbol{v}_e \leq 0$. Furthermore, it is clear that (iv) $\mathcal{Y}_1 = \mathcal{Y}_2 = 0 \Rightarrow (\boldsymbol{p}_e, \boldsymbol{v}_e) = (\boldsymbol{0}, \boldsymbol{0})$. Hence, the origin $(\boldsymbol{p}_e, \boldsymbol{v}_e) = (\boldsymbol{0}, \boldsymbol{0})$ is UGAS by Theorem 2.7.

Local Linearization To show that the origin is ULES, consider a simple linearization. Let $\boldsymbol{X} \triangleq (\boldsymbol{p}_e;\ \boldsymbol{v}_e)$, the closed-loop system can then be written in the form $\dot{\boldsymbol{X}} = \boldsymbol{f}(t, \boldsymbol{X})$. In a neighborhood of the origin, $\boldsymbol{X} = \boldsymbol{0}$, the errors evolve by a non-autonomous linear system

$$\dot{\boldsymbol{X}} = \boldsymbol{A}(t)\boldsymbol{X} + o(\|\boldsymbol{X}\|^2). \tag{C.63}$$

Using the expression for the Jacobian in (C.49) and the limit in (C.50),

$$\begin{aligned}
\frac{\partial \sigma(\boldsymbol{e})}{\partial \boldsymbol{p}_e}\Big|_{\boldsymbol{X}=\boldsymbol{0}} &= \frac{\partial \sigma(\boldsymbol{e})}{\partial \boldsymbol{e}}\frac{\partial \boldsymbol{e}}{\partial \boldsymbol{p}_e}\Big|_{\boldsymbol{X}=\boldsymbol{0}} = k_p s'(0)\boldsymbol{I} \triangleq a\boldsymbol{I}, \\
\frac{\partial \sigma(\boldsymbol{e})}{\partial \boldsymbol{v}_e}\Big|_{\boldsymbol{X}=\boldsymbol{0}} &= \frac{\partial \sigma(\boldsymbol{e})}{\partial \boldsymbol{e}}\frac{\partial \boldsymbol{e}}{\partial \boldsymbol{v}_e}\Big|_{\boldsymbol{X}=\boldsymbol{0}} = k_v s'(0)\boldsymbol{I} \triangleq b\boldsymbol{I},
\end{aligned}$$

where $a = k_p s'(0) > 0$, $k_v s'(0) > 0$, as $s'(0) > 0$ by definition. We then obtain

$$\begin{aligned}
\boldsymbol{A}(t) \triangleq \frac{\partial \boldsymbol{f}(t, \boldsymbol{X})}{\partial \boldsymbol{X}}\Big|_{\boldsymbol{X}=\boldsymbol{0}} &= \begin{bmatrix} -\boldsymbol{S}(\boldsymbol{\omega}_r) & \boldsymbol{I} \\ -k_p s'(0)\boldsymbol{I} & -\boldsymbol{S}(\boldsymbol{\omega}_r) - k_v s'(0)\boldsymbol{I} \end{bmatrix} \\
&= \begin{bmatrix} \boldsymbol{0} & \boldsymbol{I} \\ -a\boldsymbol{I} & -b\boldsymbol{I} \end{bmatrix} + \begin{bmatrix} -\boldsymbol{S}(\boldsymbol{\omega}_r) & \boldsymbol{0} \\ \boldsymbol{0} & -\boldsymbol{S}(\boldsymbol{\omega}_r) \end{bmatrix} \\
&= \underbrace{\boldsymbol{F} \otimes \boldsymbol{I}_3}_{\triangleq \bar{\boldsymbol{F}}} + \underbrace{\boldsymbol{I}_2 \otimes -\boldsymbol{S}(\boldsymbol{\omega}_r)}_{\triangleq \bar{\boldsymbol{S}}(t)},
\end{aligned}$$

where

$$\boldsymbol{F} = \begin{bmatrix} 0 & 1 \\ -a & -b \end{bmatrix} \in \mathbb{R}^{2\times 2}, \qquad \boldsymbol{S}(\boldsymbol{\omega}_r) = -\boldsymbol{S}(\boldsymbol{\omega}_r)^\top \in \mathbb{R}^{3\times 3}.$$

This is precisely the form of the system in Lemma 2.2. It is clear that $\boldsymbol{F}$ and implicitly $\bar{\boldsymbol{F}}$ is Hurwitz, and the Lyapunov equation $\bar{\boldsymbol{F}}^\top \bar{\boldsymbol{P}} + \bar{\boldsymbol{P}}\bar{\boldsymbol{F}} = -\bar{\boldsymbol{Q}}$ admits a block-structured symmetric solution for $\bar{\boldsymbol{Q}} = \boldsymbol{I}$,

$$\bar{\boldsymbol{P}} = \bar{\boldsymbol{P}}^\top = \begin{bmatrix} \frac{a^2+a+b^2}{ab} & -\frac{1}{2a} \\ \star & \frac{a+1}{2ab} \end{bmatrix} \otimes \boldsymbol{I}_3 \succ \boldsymbol{0}. \tag{C.64}$$

Given the solution in (C.64), we note that $\bar{\boldsymbol{S}}(t)\boldsymbol{P} = \boldsymbol{P}\bar{\boldsymbol{S}}(t)$, whereby

$$\bar{\boldsymbol{S}}(t)^\top \boldsymbol{P} + \boldsymbol{P}\bar{\boldsymbol{S}}(t) = -\bar{\boldsymbol{S}}(t)\boldsymbol{P} + \boldsymbol{P}\bar{\boldsymbol{S}}(t) = (\bar{\boldsymbol{S}}(t) - \bar{\boldsymbol{S}}(t))\boldsymbol{P} = \boldsymbol{0}, \tag{C.65}$$

and

$$\boldsymbol{A}(t)^\top \boldsymbol{P} + \boldsymbol{P}\boldsymbol{A}(t) = (\bar{\boldsymbol{F}} + \bar{\boldsymbol{S}}(t))^\top \boldsymbol{P} + \boldsymbol{P}(\bar{\boldsymbol{F}} + \bar{\boldsymbol{S}}(t)) = \bar{\boldsymbol{F}}^\top \boldsymbol{P} + \boldsymbol{P}\bar{\boldsymbol{F}} = -\boldsymbol{I}.$$

Thus, uniform local exponential stability of $\boldsymbol{X} = \boldsymbol{0}$ follows directly from Theorem 2.1, as $\boldsymbol{P}$ and $\boldsymbol{Q}$ are positive definite, symmetric and time-invariant. □

C.5 Theorem 6.1: Translation FOF

We start by recalling a preliminary result for Schur complements.

LEMMA C.4
For a symmetric matrix $\boldsymbol{M} = \boldsymbol{M}^\top$,

$$\boldsymbol{M} = \begin{bmatrix} \boldsymbol{A} & \boldsymbol{B} \\ \boldsymbol{B}^\top & \boldsymbol{C} \end{bmatrix} \succ \boldsymbol{0} \Leftrightarrow \boldsymbol{A} \succ \boldsymbol{0} \text{ and } \boldsymbol{C} - \boldsymbol{B}^\top \boldsymbol{A}^{-1} \boldsymbol{B} \succ \boldsymbol{0}. \qquad \square$$

Proof. See, e.g, the proof in [Cottle, 1974, Page 194]. $\square$

Proof of Theorem 6.1. By the assumptions in Theorem 6.1 (reference trajectory feasibility and a smooth saturation function), there exist finite positive constants $\gamma_1 > 0$, $\gamma_2 > 0$ such that

$$\sup_{t \geq t_\circ} \|\boldsymbol{\omega}_r(t)\| \leq \gamma_1, \qquad \sup_{y \in \mathbb{R}_{\geq 0}} |s'(y)| \leq \gamma_2, \qquad \sup_{y \in \mathbb{R}_{\geq 0}} |s(y) y^{-1}| \leq \gamma_2, \tag{C.66a}$$

where $s : \mathbb{R}_{\geq 0} \to [0, \gamma]$ is used in the construction the vector-valued saturation function σ in accordance with Definition 6.1. The proof follows the same structure as in the proof of Proposition 6.1. We start by stating the error dynamics, proceed to construct a Lyapunov function candidate by which UGS can be shown, to which the lemma of Barbălat is applied to show GAS. The Matrosov theorem is subsequently used to show UGAS, and ULES follows from a local linearization. For the clarity, we do not write out the arguments of the Lyapunov function nor the time argument of the signals of the system.

Errors and Error Dynamics In the following, consider the errors

$$\boldsymbol{p}_e = \boldsymbol{R}_r^\top (\boldsymbol{p}_r - \boldsymbol{p}), \qquad \boldsymbol{v}_e = \boldsymbol{v}_r - \boldsymbol{R}_r^\top \boldsymbol{R} \boldsymbol{v}, \tag{C.67a}$$

$$\tilde{\boldsymbol{p}}_e = \boldsymbol{p}_e - \hat{\boldsymbol{p}}_e, \qquad \tilde{\boldsymbol{v}}_e = \boldsymbol{v}_e - \hat{\boldsymbol{v}}_e, \tag{C.67b}$$

$$\tilde{\boldsymbol{z}} = \boldsymbol{z} - \tilde{\boldsymbol{p}}_e, \qquad \hat{\boldsymbol{e}} = k_p \hat{\boldsymbol{p}}_e + k_v \hat{\boldsymbol{v}}_e, \tag{C.67c}$$

Knowing time-evolution of the errors $\boldsymbol{p}_e$ and $\boldsymbol{v}_e$ from (6.5), insertion of the proposed estimator dynamics in (6.19b), (6.19c), and (6.19d) yields

$$\dot{\boldsymbol{p}}_e = -\boldsymbol{S}(\boldsymbol{\omega}_r) \boldsymbol{p}_e + \boldsymbol{v}_e, \tag{C.68a}$$

$$\dot{\boldsymbol{v}}_e = -\boldsymbol{S}(\boldsymbol{\omega}_r) \boldsymbol{v}_e + \boldsymbol{u}, \tag{C.68b}$$

$$\dot{\hat{\boldsymbol{e}}} = -\boldsymbol{S}(\boldsymbol{\omega}_r) \hat{\boldsymbol{e}} + k_p \hat{\boldsymbol{v}}_e + k_v \boldsymbol{u} + (k_p L_1 + k_v L_2) \boldsymbol{z} \tag{C.68c}$$

$$\dot{\tilde{\boldsymbol{p}}}_e = -\boldsymbol{S}(\boldsymbol{\omega}_r) \tilde{\boldsymbol{p}}_e + \tilde{\boldsymbol{v}}_e - L_1 \boldsymbol{z} \tag{C.68d}$$

$$\dot{\tilde{\boldsymbol{v}}}_e = -\boldsymbol{S}(\boldsymbol{\omega}_r) \tilde{\boldsymbol{v}}_e - L_2 \boldsymbol{z} \tag{C.68e}$$

$$\dot{\tilde{\boldsymbol{z}}} = -\boldsymbol{S}(\boldsymbol{\omega}_r) \tilde{\boldsymbol{z}} - L_3 \tilde{\boldsymbol{z}} + L_1 \tilde{\boldsymbol{p}}_e - \tilde{\boldsymbol{v}}_e. \tag{C.68f}$$

Application of Barbălat Consider the Lyapunov function candidate

$$\mathcal{V}_1 = \mathcal{V}_\sigma(\hat{\boldsymbol{e}}) + \frac{1}{2}k_p \boldsymbol{v}_e^\top \boldsymbol{v}_e + \frac{a}{2}(\tilde{\boldsymbol{p}}_e - b\tilde{\boldsymbol{v}}_e)^\top(\tilde{\boldsymbol{p}}_e - b\tilde{\boldsymbol{v}}_e) + \frac{ac}{2}\tilde{\boldsymbol{v}}_e^\top \tilde{\boldsymbol{v}}_e + \frac{a}{6}\tilde{\boldsymbol{z}}^\top \tilde{\boldsymbol{z}}. \tag{C.69}$$

This function is positive definite and radially unbounded in the errors $\hat{\boldsymbol{e}}$, $\boldsymbol{v}_e$, $\tilde{\boldsymbol{p}}_e$, $\tilde{\boldsymbol{v}}_e$ and $\tilde{\boldsymbol{z}}$. By a series of resulting implications, it can be shown that $\mathcal{V}_1 = 0 \Rightarrow \boldsymbol{p}_e = \boldsymbol{0}$, despite not explicitly appearing as an argument in $\mathcal{V}_1$. Consider a differentiation of this Lyapunov function candidate along the solutions of the error dynamics in (C.68). By defining $b = (2L_1)/(3L_2)$ and $c = (2L_1^2)/(9L_2^2) + 1/(L_2)$ and inserting the feedback in (6.19a), we obtain

$$\begin{aligned}
\dot{\mathcal{V}}_1 =& \sigma(\hat{\boldsymbol{e}})\dot{\hat{\boldsymbol{e}}} + k_p \boldsymbol{v}_e^\top \dot{\boldsymbol{v}}_e + a(\tilde{\boldsymbol{p}}_e - b\tilde{\boldsymbol{v}}_e)^\top(\dot{\tilde{\boldsymbol{p}}}_e - b\dot{\tilde{\boldsymbol{v}}}_e) + ac\tilde{\boldsymbol{v}}_e^\top \dot{\tilde{\boldsymbol{v}}}_e + \frac{a}{3}\tilde{\boldsymbol{z}}^\top \dot{\tilde{\boldsymbol{z}}}, \\
=& + \sigma(\hat{\boldsymbol{e}})^\top[k_p\hat{\boldsymbol{v}}_e + k_v\boldsymbol{u} + (k_pL_1 + k_vL_2)\boldsymbol{z}] && \text{(C.70a)} \\
& + k_p\boldsymbol{v}_e^\top \boldsymbol{u} && \text{(C.70b)} \\
& + a(\tilde{\boldsymbol{p}}_e - b\tilde{\boldsymbol{v}}_e)^\top[\tilde{\boldsymbol{v}}_e - L_1\boldsymbol{z} - b(-L_2\boldsymbol{z})] && \text{(C.70c)} \\
& - acL_2\tilde{\boldsymbol{v}}_e^\top \boldsymbol{z} && \text{(C.70d)} \\
& + \frac{a}{3}\tilde{\boldsymbol{z}}^\top[-L_3\tilde{\boldsymbol{z}} + L_1\tilde{\boldsymbol{p}}_e - \tilde{\boldsymbol{v}}_e] && \text{(C.70e)} \\
=& + \sigma(\hat{\boldsymbol{e}})^\top[-k_v\sigma(\hat{\boldsymbol{e}}) + (k_pL_1 + k_vL_2)(\tilde{\boldsymbol{z}} + \tilde{\boldsymbol{p}}_e)] && \text{(C.70f)} \\
& - a\Big[+ \frac{1}{3}L_1\tilde{\boldsymbol{p}}_e^\top \tilde{\boldsymbol{p}}_e + b\tilde{\boldsymbol{v}}_e^\top \tilde{\boldsymbol{v}}_e + \frac{4}{3}\tilde{\boldsymbol{z}}^\top \tilde{\boldsymbol{v}}_e + \frac{1}{3}L_3\tilde{\boldsymbol{z}}^\top \tilde{\boldsymbol{z}}\Big]. && \text{(C.70g)}
\end{aligned}$$

Equivalently, this expression for the Lyapunov function time-derivative can be written as a quadratic form in the signals $\boldsymbol{X} \triangleq (\sigma(\hat{\boldsymbol{e}});\ \tilde{\boldsymbol{p}}_e;\ \tilde{\boldsymbol{v}}_e;\ \tilde{\boldsymbol{z}})$, as

$$\dot{\mathcal{V}}_1 = -\boldsymbol{X}^\top \boldsymbol{M}\boldsymbol{X}, \tag{C.71}$$

where $\boldsymbol{M} \triangleq \bar{\boldsymbol{M}} \otimes \boldsymbol{I}_3$, and

$$\bar{\boldsymbol{M}} \triangleq \begin{bmatrix} +k_v & -\frac{k_pL_1+k_vL_2}{2} & +\frac{k_p}{2} & -\frac{k_pL_1+k_vL_2}{2} \\ -\frac{k_pL_1+k_vL_2}{2} & +\frac{aL_1}{3} & 0 & 0 \\ \frac{k_p}{2} & 0 & +\frac{2aL_1}{3L_2} & +\frac{2a}{3} \\ -\frac{k_pL_1+k_vL_2}{2} & 0 & +\frac{2a}{3} & +\frac{aL_3}{3} \end{bmatrix}. \tag{C.72}$$

The lower right block of $\bar{\boldsymbol{M}}$, specifically $[\bar{\boldsymbol{M}}]_{2:4,2:4} \in \mathbb{R}^{3\times 3}$ is recognized as being positive definite, and its eigenvalues can be made arbitrarily large by increasing the parameter a. Indeed, $\text{spec}([\bar{\boldsymbol{M}}]_{2:4,2:4}) = \{\lambda_1, \lambda_2, \lambda_3\}$, where

$$\lambda_1 = \frac{L_1}{3}a \tag{C.73a}$$

$$\lambda_2 = \frac{2L_1 - \sqrt{4L_1^2 - 4L_1L_2L_3 + L_2^2L_3^2 + 16L_2^2} + L_2L_3}{6L_2}a \tag{C.73b}$$

$$\lambda_3 = \frac{2L_1 + \sqrt{4L_1^2 - 4L_1L_2L_3 + L_2^2L_3^2 + 16L_2^2} + L_2L_3}{6L_2}a. \tag{C.73c}$$

From the Schur complement equivalence in Lemma C.4, $\boldsymbol{M} \succ \mathbf{0}$ if and only if

(i) $[\bar{\boldsymbol{M}}]_{1,1} \succ \mathbf{0}$, and

(ii) $[\bar{\boldsymbol{M}}]_{2:4,2:4} - [\bar{\boldsymbol{M}}]_{2:4,1}[\bar{\boldsymbol{M}}]_{1,1}^{-1}[\bar{\boldsymbol{M}}]_{1,2:4} \succ \mathbf{0}$.

Here, (i) holds by the assumptions on k_p, and a sufficient condition for (ii) can be found by examination of (C.73). Firstly, it can be verified that

$$\operatorname{spec}([\bar{\boldsymbol{M}}]_{2:4,1}[\bar{\boldsymbol{M}}]_{1,1}^{-1}[\bar{\boldsymbol{M}}]_{1,2:4}) = \left\{0, 0, \tfrac{(L_1k_p+L_2k_v)^2}{4k_v}\right\}.$$

Given that $k_p > 0, k_v > 0, L_1 > 0, L_2 > 0, L_3 > 0$, we must then have $[\bar{\boldsymbol{M}}]_{2:4,2:4} \succ \mathbf{0}$ for (ii) to hold. This can be guaranteed by letting

$$\begin{aligned}[\bar{\boldsymbol{M}}]_{2:4,2:4} \succ \mathbf{0} &\Leftrightarrow \lambda_2 > 0 \\ &\Leftrightarrow 4L_1^2 - 4L_1L_2L_3 + L_2^2L_3^2 + 16L_2^2 < (2L_1 + L_2L_3)^2 \\ &\Leftrightarrow 2L_2/L_1 < L_3.\end{aligned}$$

By imposing this constraint, a sufficient condition for (ii) to hold is found in

$$\tfrac{(L_1k_p+L_2k_v)^2}{4k_v} < \min(\lambda_1, \lambda_2),$$

or equivalently stated

$$a > \frac{(L_1k_p + L_2k_v)^2}{4k_v \min(\frac{L1}{3}, \frac{2L_1 - \sqrt{4L_1^2 - 4L_1L_2L_3 + L_2^2L_3^2 + 16L_2^2} + L_2L_3}{6L_2})} > 0. \tag{C.74}$$

To summarize, for any $L_3 > 2L_2/L_1$ and a satisfying the condition in (C.74),

$$\dot{\mathcal{V}}_1 = -\boldsymbol{X}^\top \boldsymbol{M} \boldsymbol{X} \leq 0, \tag{C.75}$$

and notably negative definite in $\boldsymbol{X}$. As such, the Lyapunov function candidate $\mathcal{V}_1$ is decreasing in time, and $\mathcal{V}_1(t) \leq \mathcal{V}_1(t_\circ)$ for all $t \geq t_\circ$. To proceed, consider a saturation function σ by Definition 6.1, the associated Lyapunov-like function in Definition 6.2 can be written

$$\mathcal{V}_\sigma(\boldsymbol{x}) = f_\sigma(\|\boldsymbol{x}\|) = \int_0^{\|\boldsymbol{x}\|} s(y)dy,$$

where $f_\sigma : \mathbb{R}_{\geq 0} \to \mathbb{R}_{\geq 0}$ is surjective by the constraints on s. Also, note that

$$\frac{a}{2}\begin{bmatrix}\tilde{\boldsymbol{p}}_e \\ \tilde{\boldsymbol{v}}_e\end{bmatrix} \underbrace{\begin{bmatrix}\boldsymbol{I} & -b\boldsymbol{I} \\ -b\boldsymbol{I} & (b^2+c)\boldsymbol{I}\end{bmatrix}}_{\triangleq \tilde{\boldsymbol{M}}} \begin{bmatrix}\tilde{\boldsymbol{p}}_e \\ \tilde{\boldsymbol{v}}_e\end{bmatrix} \leq \mathcal{V}(t) \leq \mathcal{V}(t_\circ), \qquad \forall t \geq t_\circ,$$

where $\tilde{\boldsymbol{M}} \succ \mathbf{0}$ for all $b > 0, c > 0$. As such, $\mathcal{V}_1$ being non-increasing implies

$$\|\hat{\boldsymbol{e}}\| \leq \gamma_{\hat{\boldsymbol{e}}}, \quad \|\boldsymbol{v}_e\| \leq \gamma_{\boldsymbol{v}_e}, \quad \|\tilde{\boldsymbol{p}}_e\| \leq \tilde{\gamma}, \quad \|\tilde{\boldsymbol{z}}\| \leq \gamma_{\tilde{\boldsymbol{z}}}, \quad \|\tilde{\boldsymbol{v}}_e\| \leq \tilde{\gamma}, \tag{C.76}$$

for all $t \geq t_\circ$, where

$$\gamma_{\hat{\boldsymbol{e}}} \triangleq f_\sigma^{-1}(\mathcal{V}_1(t_\circ)), \qquad \gamma_{\boldsymbol{v}_e} \triangleq \sqrt{\tfrac{2}{k_p}\mathcal{V}_1(t_\circ)},$$
$$\gamma_{\tilde{\boldsymbol{z}}} \triangleq \sqrt{\tfrac{6}{a}\mathcal{V}_1(t_\circ)}, \qquad \tilde{\gamma} \triangleq \sqrt{\tfrac{2}{a}\mathcal{V}(t_\circ)/\lambda_m(\tilde{\boldsymbol{M}})}.$$

Furthermore, as $\tilde{\boldsymbol{v}}_e$ and $\boldsymbol{v}_e$ are bounded in the initial errors, it follows that

$$\|\hat{\boldsymbol{v}}_e\| = \|\boldsymbol{v}_e - \tilde{\boldsymbol{v}}_e\| \leq \gamma_{\boldsymbol{v}_e} + \tilde{\gamma} \triangleq \gamma_{\hat{\boldsymbol{v}}_e}, \tag{C.77a}$$
$$\|\hat{\boldsymbol{p}}_e\| = \tfrac{1}{k_p}\|\hat{\boldsymbol{e}} - k_v\hat{\boldsymbol{v}}_e\| \leq \tfrac{1}{k_p}(\gamma_{\hat{\boldsymbol{e}}} + k_v\gamma_{\hat{\boldsymbol{v}}_e}) \triangleq \gamma_{\hat{\boldsymbol{p}}_e}, \tag{C.77b}$$
$$\|\boldsymbol{z}\| = \|\tilde{\boldsymbol{z}} + \tilde{\boldsymbol{p}}_e\| \leq \gamma_{\tilde{\boldsymbol{z}}} + \tilde{\gamma} \triangleq \gamma_{\boldsymbol{z}}. \tag{C.77c}$$

Thus, $\|\boldsymbol{X}\| \leq \sqrt{\gamma^2 + 2\tilde{\gamma}^2 + \gamma_{\tilde{\boldsymbol{z}}}}$ is bounded for all $t \geq t_\circ$. Furthermore, as all of the signals on the right-hand side of the error dynamics in (C.68) are bounded in the initial errors by (C.76) and (C.77), there exists a bound

$$\|\dot{\boldsymbol{X}}\| \leq B(\gamma_{\boldsymbol{\omega}_r}, \gamma_{\dot{\boldsymbol{\omega}}_r}, \gamma_{\hat{\boldsymbol{e}}}, \gamma_{\hat{\boldsymbol{v}}_e}, \gamma_{\boldsymbol{z}}, \tilde{\gamma}, \gamma_{\tilde{\boldsymbol{z}}}), \tag{C.78}$$

Consequently,

$$\ddot{\mathcal{V}}_1 = -2\boldsymbol{X}^\top \boldsymbol{M}\dot{\boldsymbol{X}} \leq 2\lambda_M(\boldsymbol{M})\|\boldsymbol{X}\|\|\dot{\boldsymbol{X}}\|, \tag{C.79}$$

is bounded in the initial errors, and $\dot{\mathcal{V}}_1 \leq 0$ is uniformly continuous. Application of the Lemma 2.5 (Barbălat) yields

$$\lim_{t\to\infty} \dot{\mathcal{V}}_1 = 0 \Rightarrow \lim_{t\to\infty} \boldsymbol{X} = \mathbf{0} \Rightarrow \begin{cases} \lim\limits_{t\to\infty} \hat{\boldsymbol{e}} = \mathbf{0} \\ \lim\limits_{t\to\infty} \tilde{\boldsymbol{p}}_e = \mathbf{0} \\ \lim\limits_{t\to\infty} \tilde{\boldsymbol{v}}_e = \mathbf{0} \\ \lim\limits_{t\to\infty} \tilde{\boldsymbol{z}} = \mathbf{0} \end{cases}, \tag{C.80}$$

To show that this implies the convergence of tracking errors $(\boldsymbol{p}_e, \boldsymbol{v}_e)$ to the origin, consider first the combined estimate error dynamics, and let

$$\underbrace{\dot{\hat{\boldsymbol{e}}}}_{\triangleq \dot{f}(t)} = + \underbrace{k_p\hat{\boldsymbol{v}}_e}_{\triangleq f_0(t)} \underbrace{- \boldsymbol{S}(\boldsymbol{\omega}_r)\hat{\boldsymbol{e}} - k_v\sigma(\hat{\boldsymbol{e}}) + (k_pL_1 + k_vL_2)(\tilde{\boldsymbol{z}} + \tilde{\boldsymbol{p}}_e)}_{\triangleq \eta(t)}. \tag{C.81}$$

As $\|\dot{\hat{\boldsymbol{v}}}_e\| \leq \gamma_{\boldsymbol{\omega}_r}\gamma_{\hat{\boldsymbol{v}}_e} + \gamma + L_2\gamma_{\boldsymbol{z}}$ is bounded in time in the initial errors, f_0 is uniformly continuous in time. Furthermore, $f(t) \to \mathbf{0}$ and $\eta(t) \to \mathbf{0}$ by (C.80) as $t \to \infty$. Consequently, Lemma 2.7 applied to (C.81) yields

$$\lim_{t\to\infty} \dot{\hat{\boldsymbol{e}}}(t) = \lim_{t\to\infty} k_p\hat{\boldsymbol{v}}_e = \mathbf{0} \Rightarrow \lim_{t\to\infty} \hat{\boldsymbol{p}}_e = \mathbf{0}, \tag{C.82}$$

where the last implication holds as $\hat{\boldsymbol{e}} = k_p \boldsymbol{p}_e + k_v \hat{\boldsymbol{v}}_e$. Combined with (C.80),

$$\begin{cases} \lim\limits_{t\to\infty} \hat{\boldsymbol{p}}_e = \boldsymbol{0} \\ \lim\limits_{t\to\infty} \tilde{\boldsymbol{p}}_e = \boldsymbol{0} \end{cases} \Rightarrow \lim_{t\to\infty} \boldsymbol{p}_e = \boldsymbol{0}, \quad \begin{cases} \lim\limits_{t\to\infty} \hat{\boldsymbol{v}}_e = \boldsymbol{0} \\ \lim\limits_{t\to\infty} \tilde{\boldsymbol{v}}_e = \boldsymbol{0} \end{cases} \Rightarrow \lim_{t\to\infty} \boldsymbol{v}_e = \boldsymbol{0}. \quad \text{(C.83)}$$

showing that the equilibrium point characterized by $(\boldsymbol{p}_e, \boldsymbol{v}_e, \tilde{\boldsymbol{v}}_e, \tilde{\boldsymbol{p}}_e, \tilde{\boldsymbol{z}}) = (\boldsymbol{0}, \boldsymbol{0}, \boldsymbol{0}, \boldsymbol{0}, \boldsymbol{0})$ is GAS. We also note that as $\mathcal{V}_1$ is continuously differentiable by (C.79), and a positive definite function in $(\hat{\boldsymbol{e}}, \boldsymbol{v}_e, \tilde{\boldsymbol{v}}_e, \tilde{\boldsymbol{p}}_e, \tilde{\boldsymbol{z}})$ with a negative semi-definite time-derivative in these signals, consequently $\mathcal{V}_1$ can be used to show UGS of the point $(\hat{\boldsymbol{e}}, \boldsymbol{v}_e, \tilde{\boldsymbol{v}}_e, \tilde{\boldsymbol{p}}_e, \tilde{\boldsymbol{z}}) = (\boldsymbol{0}, \boldsymbol{0}, \boldsymbol{0}, \boldsymbol{0}, \boldsymbol{0})$ by Theorem 2.3.

Application of Matrosov To show that the point $(\boldsymbol{p}_e, \boldsymbol{v}_e, \tilde{\boldsymbol{v}}_e, \tilde{\boldsymbol{p}}_e, \tilde{\boldsymbol{z}}) = (\boldsymbol{0}, \boldsymbol{0}, \boldsymbol{0}, \boldsymbol{0}, \boldsymbol{0})$ is UGAS, it suffices to show that convergence to the point $(\boldsymbol{v}_e, \hat{\boldsymbol{e}}, \tilde{\boldsymbol{p}}_e, \tilde{\boldsymbol{v}}_e, \tilde{\boldsymbol{z}}) = (\boldsymbol{0}, \boldsymbol{0}, \boldsymbol{0}, \boldsymbol{0}, \boldsymbol{0})$ is UGAS, as the latter implies the former. To start, let

$$\dot{\mathcal{V}}_1 = -\boldsymbol{X}^\top \boldsymbol{M} \boldsymbol{X} = \mathcal{Y}_1, \quad \text{(C.84)}$$

which satisfies conditions (i) and (ii) of Theorem 2.7 with respect to $\{\mathcal{V}_1, \mathcal{Y}_1\}$. Next, define $\mathcal{V}_2 \triangleq -\boldsymbol{v}_e^\top \hat{\boldsymbol{e}}$. Differentiating this function along the solutions of (C.68e) and (6.19d) yields

$$\begin{aligned}
\dot{\mathcal{V}}_2 =& -\boldsymbol{v}_e^\top \dot{\hat{\boldsymbol{e}}} - \hat{\boldsymbol{e}}^\top \dot{\boldsymbol{v}}_e \\
=& -\boldsymbol{v}_e^\top [-\boldsymbol{S}(\boldsymbol{\omega}_r)\hat{\boldsymbol{e}} + k_p \hat{\boldsymbol{v}}_e - k_v \sigma(\hat{\boldsymbol{e}}) + (k_p L_1 + k_v L_2)\boldsymbol{z}] \\
& - \hat{\boldsymbol{e}}^\top [-\boldsymbol{S}(\boldsymbol{\omega}_r)\boldsymbol{v}_e - \sigma(\hat{\boldsymbol{e}})] \\
=& -\boldsymbol{v}_e^\top [+k_p(\boldsymbol{v}_e - \tilde{\boldsymbol{v}}_e) - k_v \sigma(\hat{\boldsymbol{e}}) + (k_p L_1 + k_v L_2)(\tilde{\boldsymbol{z}} + \tilde{\boldsymbol{p}}_e)] \\
& - \hat{\boldsymbol{e}}^\top [-\sigma(\hat{\boldsymbol{e}})] \\
=& -k_p \boldsymbol{v}_e^\top \boldsymbol{v}_e + \boldsymbol{v}_e^\top [-k_p \tilde{\boldsymbol{v}}_e - k_v \sigma(\hat{\boldsymbol{e}}) + (k_p L_1 + k_v L_2)(\tilde{\boldsymbol{z}} + \tilde{\boldsymbol{p}}_e)] - \hat{\boldsymbol{e}}^\top [-\sigma(\hat{\boldsymbol{e}})] \\
\triangleq& \mathcal{Y}_2
\end{aligned}$$

Thus, condition (ii) in Theorem 2.7 is satisfied with respect to $\{\mathcal{V}_2, \mathcal{Y}_2\}$, and we note that (iii) $\mathcal{Y}_1 = 0 \Rightarrow \boldsymbol{X} = \boldsymbol{0} \Rightarrow \mathcal{Y}_2 = -k_p \boldsymbol{v}_e^\top \boldsymbol{v}_e \leq 0$. Furthermore, it is clear that (iv) $\mathcal{Y}_1 = \mathcal{Y}_2 = 0 \Rightarrow \boldsymbol{X} = \boldsymbol{0}$ and $\boldsymbol{v}_e = \boldsymbol{0}$. Hence, the origin $(\boldsymbol{v}_e, \hat{\boldsymbol{e}}, \tilde{\boldsymbol{v}}_e, \tilde{\boldsymbol{p}}_e, \tilde{\boldsymbol{z}}) = (\boldsymbol{0}, \boldsymbol{0}, \boldsymbol{0}, \boldsymbol{0}, \boldsymbol{0})$ is UGAS by Theorem 2.7. At this point

$$\begin{cases} \boldsymbol{v}_e = \boldsymbol{0} \\ \tilde{\boldsymbol{v}}_e = \boldsymbol{0} \end{cases} \Rightarrow \hat{\boldsymbol{v}}_e = \boldsymbol{0}, \quad \begin{cases} \hat{\boldsymbol{v}}_e = \boldsymbol{0} \\ \hat{\boldsymbol{e}} = \boldsymbol{0} \end{cases} \Rightarrow \hat{\boldsymbol{p}}_e = \boldsymbol{0}, \quad \begin{cases} \hat{\boldsymbol{p}}_e = \boldsymbol{0} \\ \tilde{\boldsymbol{p}}_e = \boldsymbol{0} \end{cases} \Rightarrow \boldsymbol{p}_e = \boldsymbol{0}$$

and we conclude that the point $(\boldsymbol{p}_e, \boldsymbol{v}_e, \tilde{\boldsymbol{v}}_e, \tilde{\boldsymbol{p}}_e, \tilde{\boldsymbol{z}}) = (\boldsymbol{0}, \boldsymbol{0}, \boldsymbol{0}, \boldsymbol{0}, \boldsymbol{0})$ is UGAS.

Local Linearization To show ULES, we once again consider a local linearization. This time, let $\boldsymbol{X} \triangleq (\boldsymbol{v}_e, \hat{\boldsymbol{e}}, \tilde{\boldsymbol{p}}_e, \tilde{\boldsymbol{v}}_e, \tilde{\boldsymbol{z}})$, the closed-loop system can then be written as a non-autonomous system on the form $\dot{\boldsymbol{X}} = \boldsymbol{f}(t, \boldsymbol{X})$. Close to the origin, $\boldsymbol{X} = \boldsymbol{0}$, the errors evolve by a non-autonomous linear system

$$\dot{\boldsymbol{X}} = \boldsymbol{A}(t)\boldsymbol{X} + o(\|\boldsymbol{X}\|^2). \tag{C.85}$$

Here, $\boldsymbol{A}(t)$ can be decomposed into two parts, a skew symmetric time-variant part, $\bar{\boldsymbol{S}}(t)$, and a time-invariant part, $\bar{\boldsymbol{F}}$, as

$$\boldsymbol{A}(t) = \bar{\boldsymbol{F}} + \bar{\boldsymbol{S}}(t) \in \mathbb{R}^{15\times 15}, \tag{C.86}$$

where

$$\bar{\boldsymbol{F}} = \boldsymbol{F} \otimes \boldsymbol{I}_3, \qquad \bar{\boldsymbol{S}}(t) = \boldsymbol{I}_5 \otimes (-\boldsymbol{S}(\boldsymbol{\omega}_r(t))), \tag{C.87}$$

and

$$\boldsymbol{F} = \begin{bmatrix} 0 & -s'(0) & 0 & 0 & 0 \\ k_p & -s'(0)k_v & L_1k_p + L_2k_v & -k_p & L_1k_p + L_2k_v \\ 0 & 0 & -L_1 & 1 & -L_1 \\ 0 & 0 & -L_2 & 0 & -L_2 \\ 0 & 0 & L_1 & -1 & -L_3 \end{bmatrix}. \tag{C.88}$$

While not immediately clear, we start by noting that $\boldsymbol{F}$ is Hurwitz for all $(k_p, k_v, s'(0), L_1, L_2, L_3) \in \mathbb{R}^6_{>0}$. This is perhaps easiest seen by considering its characteristic polynomial, which can be written in a factorized form as

$$\begin{aligned} p(\lambda) &= \det(\lambda \boldsymbol{I}_5 - \boldsymbol{F}) \\ &= (\lambda^2 + k_v s'(0)\lambda + k_p s'(0)) \times \\ &\quad (\lambda^3 + (L_1 + L_3)\lambda^2 + (L_1^2 + L_3L_1)\lambda + L_2L_1 + L_2L_3) \\ &= \underbrace{(\lambda^2 + b_1\lambda + b_2)}_{\triangleq p_b(\lambda)} \underbrace{(\lambda^3 + a_1\lambda^2 + a_2\lambda + a_3)}_{\triangleq p_a(\lambda)}, \end{aligned}$$

where

$$\begin{aligned} b_1 &= k_v s'(0), & b_2 &= k_p s'(0), \\ a_1 &= L_1 + L_3, & a_2 &= L_1^2 + L_3L_1, & a_3 &= L_2L_1 + L_2L_3. \end{aligned}$$

By the assumptions on s', k_p, k_v, we have that $b_1, b_2 > 0$, which is sufficient to conclude that the roots of the characteristic polynomial $p_b(\lambda)$ reside in the open left half plane by the Routh-Hurwitz stability criterion (see, e.g., [Parks, 1962]). Similarly, by the same stability criterion, the solutions to $p_a(\lambda) = 0$ reside in the open left half plane if $a_1 > 0, a_2 > 0, a_3 > 0$ and $a_1a_2 > a_3$.

The first condition holds trivially given the assumptions that the parameters $\{L_i\}_{i=1}^3$ are positive, and second condition can be written

$$a_1 a_2 > a_3 \Leftrightarrow (L_1 + L_3)(L_1^2 + L_3 L_1) > (L_2 L_1 + L_2 L_3) \tag{C.89a}$$
$$\Leftrightarrow L_1(L_1 + L_3)^2 > L_2(L_1 + L_3) \tag{C.89b}$$
$$\Leftrightarrow L_3 > L_2/L_1 - L_1. \tag{C.89c}$$

Given the Theorem's assumption that $L_3 > 2L_2/L_1$, we have that $a_1 a_2 > a_3$, all of the solutions to $p_a(\lambda) = 0$ reside in the open left half plane, and $\boldsymbol{F}$ is Hurwitz. As such, there exists a solution $(\boldsymbol{P}, \boldsymbol{Q})$ to the Lyapunov equation

$$\boldsymbol{F}^\top \boldsymbol{P} + \boldsymbol{P}\boldsymbol{F} = -\boldsymbol{Q}, \tag{C.90}$$

for some positive definite symmetric $\boldsymbol{P} = \boldsymbol{P}^\top \succ \boldsymbol{0}$ and $\boldsymbol{Q} = \boldsymbol{Q}^\top \succ \boldsymbol{0}$. Furthermore, $\bar{\boldsymbol{P}} = \boldsymbol{P} \otimes \boldsymbol{I}_3$ and $\bar{\boldsymbol{Q}} = \boldsymbol{Q} \otimes \boldsymbol{I}_3$ then solve the Lyapunov equation

$$\bar{\boldsymbol{F}}^\top \bar{\boldsymbol{P}} + \bar{\boldsymbol{P}}\bar{\boldsymbol{F}} = -\bar{\boldsymbol{Q}}. \tag{C.91}$$

The solution $\bar{\boldsymbol{P}}$ has a three-by-three block structure by its definition through the Kronecker product, and similar to the local linearization in the proof of Theorem 6.1 (see Appendix C.4), $\bar{\boldsymbol{S}}(t)$ commutes with $\bar{\boldsymbol{P}}$. As a consequence,

$$\bar{\boldsymbol{S}}(t)^\top \bar{\boldsymbol{P}} + \bar{\boldsymbol{P}}\bar{\boldsymbol{S}}(t) = (\bar{\boldsymbol{S}}(t)^\top + \bar{\boldsymbol{S}}(t))\bar{\boldsymbol{P}} = \boldsymbol{0}. \tag{C.92}$$

Using this fact, $\bar{\boldsymbol{P}}$ also solves the Lyapunov equation $\boldsymbol{A}(t)$ in (C.85), as

$$\boldsymbol{A}(t)^\top \bar{\boldsymbol{P}} + \bar{\boldsymbol{P}}\boldsymbol{A}(t) = (\bar{\boldsymbol{F}} + \bar{\boldsymbol{S}}(t))^\top \bar{\boldsymbol{P}} + \bar{\boldsymbol{P}}(\bar{\boldsymbol{F}} + \bar{\boldsymbol{S}}(t)) = \bar{\boldsymbol{F}}^\top \bar{\boldsymbol{P}} + \bar{\boldsymbol{P}}\bar{\boldsymbol{F}} = -\bar{\boldsymbol{Q}}.$$

Thus, ULES of $\boldsymbol{X} = \boldsymbol{0}$ follows directly from Theorem 2.1, as $\bar{\boldsymbol{P}}$ and $\bar{\boldsymbol{Q}}$ are positive definite, symmetric and time-invariant, concluding the proof. □

C.6 Theorem 6.2: Cascade Analysis

Before stating the proof, we note that the two nonlinear ODEs

$$\dot{x}(t) = 2\delta_1 \sqrt{x(t)}, \qquad x(t_\circ) = x_\circ > 0, \qquad \delta_1 > 0, \tag{C.93a}$$
$$\dot{y}(t) = 2\delta_2 \sqrt{y(t)} e^{-\delta_3 (t - t_\circ)}, \qquad y(t_\circ) = y_\circ > 0, \qquad \delta_2, \delta_3 > 0, \tag{C.93b}$$

can be solved analytically, with the particular solutions

$$x(t) = \phi_A(t; t_\circ, x_\circ) = (\delta_1 (t - t_\circ) + \sqrt{x_\circ})^2, \tag{C.94a}$$
$$y(t) = \phi_B(t; t_\circ, y_\circ) = \frac{1}{\delta_3^2} e^{-2\delta_3 t} (\delta_2 (e^{\delta_3 t_\circ} - e^{\delta_3 t}) + \sqrt{y_\circ} \delta_3 e^{\delta_3 t})^2, \tag{C.94b}$$

where notably, the limit

$$\lim_{t\to\infty} \phi_B(t; t_\circ, y_\circ) = \frac{(\delta_2 + \sqrt{y_\circ}\delta_3)^2}{\delta_3^2}, \tag{C.95}$$

exists and is finite for any $y_\circ, \delta_2, \delta_3 > 0$. With these preliminaries, the proof will be developed with respect to the solutions defined in ϕ_A and ϕ_B.

Lemma C.5
For any saturation function σ by Definition 6.1, and any two vectors $\boldsymbol{v}_1, \boldsymbol{v}_2$ with associated positive constants $c_1, c_2 > 0$, there exist $c_4, c_3 > 0$, such that

$$\|c_1\boldsymbol{v}_1 + c_2\sigma(\boldsymbol{v}_2)\|^2 \leq c_3(\|\boldsymbol{v}_1\|^2 + c_4\mathcal{V}_\sigma(\boldsymbol{v}_2)). \tag{C.96}$$

Specifically, this holds for sufficiently large $c_3 \geq c_1^2 + c_2^2$ and $c_4 > 2s'(0)$. □

Proof. To start, we note that

$$\|c_1\boldsymbol{v}_1 + c_2\sigma(\boldsymbol{v}_2)\|^2 \leq c_3(\|\boldsymbol{v}_1\|^2 + \|\sigma(\boldsymbol{v}_2)\|^2), \tag{C.97}$$

if

$$\boldsymbol{A} = \begin{bmatrix} (c_3 - c_1^2)\boldsymbol{I} & -c_1c_2\boldsymbol{I} \\ -c_1c_2\boldsymbol{I} & (c_3 - c_2^2)\boldsymbol{I} \end{bmatrix} \succeq \boldsymbol{0}. \tag{C.98}$$

Here, a sufficient condition for $\boldsymbol{A} \succeq \boldsymbol{0}$ can be found by taking c_3 sufficiently large, with $c_3 \geq c_1^2 + c_2^2$. Furthermore, by Remark 6.3, for any $c_4 > 2s'(0)$,

$$\|\sigma(\boldsymbol{v}_2)\|^2 \leq c_4\mathcal{V}_\sigma(\boldsymbol{v}_2). \tag{C.99}$$

Combining (C.97) and (C.99), we obtain the sought expression

$$\|c_1\boldsymbol{v}_1 + c_2\sigma(\boldsymbol{v}_2)\|^2 \leq c_3(\|\boldsymbol{v}_1\|^2 + c_4\mathcal{V}_\sigma(\boldsymbol{v}_2)). \tag{C.100}$$

□

Proof of Theorem 6.2. In this proof, we consider the system

$$\Sigma_1 : \ \dot{\boldsymbol{X}}_1 = \boldsymbol{f}_1(t, \boldsymbol{X}_1) + \boldsymbol{g}(t, \boldsymbol{X}_1, \boldsymbol{X}_2)\boldsymbol{X}_2 \tag{C.101a}$$

$$\Sigma_2 : \ \dot{\boldsymbol{X}}_2 = \boldsymbol{f}_2(t, \boldsymbol{X}_2) \tag{C.101b}$$

with Σ_1 defined in (6.47), where $\boldsymbol{f}_1(t, \boldsymbol{X}_1)$ describes to the error dynamics of the closed-loop translation subsystem without the interconnection; the interconnection term $\boldsymbol{g}(t, \boldsymbol{X}_1, \boldsymbol{X}_2)\boldsymbol{X}_2$ is given in (6.48); and the system Σ_2 corresponds to the error dynamics of the attitude subsystem. Let

$$\Sigma_1' : \ \dot{\boldsymbol{X}}_1 = \boldsymbol{f}_1(t, \boldsymbol{X}_1), \tag{C.102}$$

denote the dynamics of the translation FOF subsystem when not interconnected with the attitude FOF subsystem. To start, consider the Lyapunov function associated with the translation FOF subsystem in (C.69), as

$$\mathcal{V} = \mathcal{V}_\sigma(\hat{\boldsymbol{e}}) + \frac{1}{2}k_p \boldsymbol{v}_e^\top \boldsymbol{v}_e + \frac{a}{2}(\tilde{\boldsymbol{p}}_e - b\tilde{\boldsymbol{v}}_e)^\top(\tilde{\boldsymbol{p}}_e - b\tilde{\boldsymbol{v}}_e) + \frac{ac}{2}\tilde{\boldsymbol{v}}_e^\top \tilde{\boldsymbol{v}}_e + \frac{a}{6}\tilde{\boldsymbol{z}}^\top \tilde{\boldsymbol{z}}. \quad \text{(C.103)}$$

When differentiated along Σ_1', we recall that $\dot{\mathcal{V}} \leq 0$ is negative semi-definite in the errors. When instead differentiating this function along Σ_1, we obtain

$$\begin{aligned}
\dot{\mathcal{V}} &\leq -[k_p \boldsymbol{v}_e + k_v \sigma(\hat{\boldsymbol{e}})]^\top \frac{\|f_r \boldsymbol{e}_3 - m\boldsymbol{u}\|}{m} \boldsymbol{R}_r^\top (\boldsymbol{R}_e - \boldsymbol{I}) \boldsymbol{R} \boldsymbol{e}_3 && \text{(C.104a)} \\
&\leq \|k_p \boldsymbol{v}_e + k_v \sigma(\hat{\boldsymbol{e}})\| \frac{\|f_r \boldsymbol{e}_3 - m\boldsymbol{u}\|}{m} \|\boldsymbol{R}_e - \boldsymbol{I}\| && \text{(C.104b)} \\
&\leq \sqrt{c_3(\|\boldsymbol{v}_e\|^2 + c_4 \mathcal{V}_\sigma(\hat{\boldsymbol{e}}))} \frac{\|f_r \boldsymbol{e}_3 - m\boldsymbol{u}\|}{m} \|\boldsymbol{R}_e - \boldsymbol{I}\|, && \text{(C.104c)}
\end{aligned}$$

where the last inequality follows by Lemma C.5, and holds for sufficiently large $c_3 \geq k_p^2 + k_v^2$ and $c_4 > 2s'(0)$. Furthermore, as

$$c_3(\|\boldsymbol{v}_e\|^2 + c_4 \mathcal{V}_\sigma(\hat{\boldsymbol{e}})) = c_3 c_4 \Big(\frac{1}{c_4} \|\boldsymbol{v}_e\|^2 + \mathcal{V}_\sigma(\hat{\boldsymbol{e}}) \Big) \leq c_3 c_4 \mathcal{V}, \quad \text{(C.105)}$$

for any $1/c_4 \leq k_p/2 \Leftrightarrow 2/k_p \leq c_4$. Thus, the bound in (C.104) can be written

$$\dot{\mathcal{V}}(t) \leq \delta_1 \sqrt{\mathcal{V}} \|\boldsymbol{R}_e - \boldsymbol{I}\|, \qquad \forall\, t \geq t_\circ, \quad \text{(C.106)}$$

for any

$$\delta_1 \geq \sqrt{2(k_p^2 + k_v^2) \max\{s'(0), 1/k_p\}} \Big(\frac{f_r^+ + m\gamma}{m} \Big). \quad \text{(C.107)}$$

The second subsystem is UAGAS, and when considering trajectories on its almost global domain of asymptotic attraction, there exists a finite time $T \geq t_\circ$ at which point the errors, $\boldsymbol{X}_2$, approach a neighborhood of the origin. In this neighborhood, the only stable equilibrium is at $\boldsymbol{R}_e = \boldsymbol{I}$ which implies that $\boldsymbol{R}_e \to \boldsymbol{I}$ exponentially after a time $t > T$, with some positive decay rate of $\delta_2 > 0$. And as $\|\boldsymbol{R}_e - \boldsymbol{I}\| \leq 2$ for all $\boldsymbol{R}_e \in \mathrm{SO}(3)$, we have that $\|\boldsymbol{R}_e - \boldsymbol{I}\| \leq 2$ for $t_\circ \leq t \leq T$ and $\|\boldsymbol{R}_e - \boldsymbol{I}\| \leq 2e^{-\delta_2(t-T)}$ for $t \geq T$. As such, we can express a conservative bound of the Lyapunov function associated with the translation subsystem along the solutions of the interconnected system in Σ_1 as

$$\dot{\mathcal{V}}(t) \leq \begin{cases} 2\delta_1 \sqrt{\mathcal{V}} & \forall\, t \in [t_\circ, T] \\ 2\delta_1 \sqrt{\mathcal{V}} e^{-\delta_2(t-T)} & \forall\, t > T \end{cases}, \quad \text{(C.108)}$$

whereby the comparison lemma (see, e.g., [Khalil, 1996, Lemma 2.5]) is applied to express this upper bound in the solutions ϕ_A and ϕ_B in (C.94), as

$$\mathcal{V}(t) \leq \begin{cases} \phi_A(t; t_\circ, \mathcal{V}(t_\circ)), & \forall\, t_\circ \leq t \leq T \\ \phi_B(t; T, \phi_A(T; t_\circ, \mathcal{V}(t_\circ))), & \forall\, t > T \end{cases}. \tag{C.109}$$

This upper bound is finite in time as T is finite, where then (i) the bound converges to a finite limit as shown in (C.95), and (ii) it attains a maximum

$$\mathcal{V}(t) \leq B(\mathcal{V}(t_\circ), t_\circ, T, \delta_1, \delta_2), \qquad \forall\, t \geq t_\circ, \tag{C.110}$$

where

$$\begin{aligned} &B(\mathcal{V}(t_\circ), t_\circ, T, \delta_1, \delta_2) = \\ &\quad = \max\left\{ \left(\delta_1(T - t_\circ) + \sqrt{\mathcal{V}(t_\circ)}\right)^2, \left(\delta_1(\delta_2^{-1} - (T - t_\circ)) - \sqrt{\mathcal{V}(t_\circ)}\right)^2 \right\}. \end{aligned} \tag{C.111}$$

This is illustrated in two cases, one where the first expression dominates the second, in which case the maximum is attained at T, and the other where the exponential decay rate is much smaller, where the second expression dominates the first, in which case the maximum of this bound is found in the limit (see Figure C.1). Regardless of the system initialization, the bound $B(\mathcal{V}(t_\circ), t_\circ, T, \delta_1, \delta_2)$ is finite. As the arguments within the quadratic functions are linear in $t_\circ$, the bound attaining a maximum at the endpoints where $t_\circ = 0$ or $t_\circ = T$. Irrespective of the initial time, we have that

$$\begin{aligned} \mathcal{V} &\leq B(\mathcal{V}(t_\circ), t_\circ, T, \delta_1, \delta_2) \\ &\leq \max\left\{ \left(\delta_1 T + \sqrt{\mathcal{V}(t_\circ)}\right)^2, \left(\delta_1(\delta_2^{-1} - T) - \sqrt{\mathcal{V}(t_\circ)}\right)^2, \left(\delta_1 \delta_2^{-1} - \sqrt{\mathcal{V}(t_\circ)}\right)^2 \right\} \\ &\triangleq \bar{B}(\mathcal{V}(t_\circ), T, \delta_1, \delta_2) \end{aligned} \tag{C.112}$$

As such, the solutions to the interconnected system, Σ_1, are uniformly bounded for all times in the initial errors $\boldsymbol{X}_1(t_\circ)$ and all $\boldsymbol{X}_2(t_\circ)$ on the domain of asymptotic attraction of Σ_2^a. Furthermore, as Σ_2 is UAGAS its solutions are uniformly bounded. A such, ULES and UGAS of the resulting cascade follows by Theorem 2.11 when considered on the almost global region of attraction of Σ_2^a, and we conclude that the resulting cascade is ULES and UAGAS. □

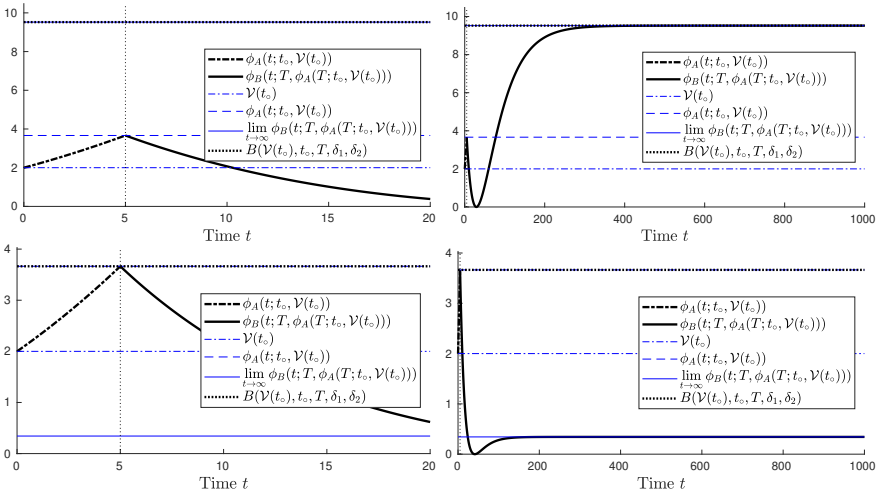

Figure C.1 Example demonstrating the solutions ϕ_A and ϕ_B in relation to the bound $B(\mathcal{V}(t_\circ), t_\circ, T, \delta_1, \delta_2)$ when the decay rate is varied. For this example, $\mathcal{V}(t_\circ) = 2$, $t_\circ = 0$, $T = 5$, $\delta_1 = 0.1$. In the top plots, $\delta_2 = 0.2/(T - t_\circ)^{-1}$ and in the bottom plots, $\delta_2 = 0.1/(T - t_\circ)^{-1}$.

D

Radiation Mapping

D.1 Fusion of Gaussian Kernels

In this appendix, we consider the problem of fusing two components of the solution, $\boldsymbol{S}$, required to implement the `Fuse()` function in the GAPSL for Gaussian kernels. Specifically, the problem is to combine two weighted Gaussian kernels $w_1\mathcal{N}(\boldsymbol{\theta}|\boldsymbol{\theta}_1, \sigma_1^2\boldsymbol{I}_2)$ and $w_2\mathcal{N}(\boldsymbol{\theta}|\boldsymbol{\theta}_2, \sigma_2^2\boldsymbol{I}_2)$, into to a single kernel, $w_p\mathcal{N}(\boldsymbol{\theta}|\boldsymbol{\theta}_p, \sigma_p^2\boldsymbol{I}_2)$, which also is homogeneous. Consider a weighted sum of the two kernels by a variable $n_i = w_i/(w_1 + w_2)$, as

$$q(\boldsymbol{\theta}) = \sum_{i=1}^{2} n_i\mathcal{N}(\boldsymbol{\theta}|\boldsymbol{\theta}_i, \sigma_i^2\boldsymbol{I}_2). \tag{D.1}$$

If we were to take $w_q = w_1 + w_2$, then

$$\int w_q q(\theta)d\boldsymbol{\theta} = \int w_1\mathcal{N}(\boldsymbol{\theta}|\boldsymbol{\theta}_1, \sigma_1^2\boldsymbol{I}_2) + w_2\mathcal{N}(\boldsymbol{\theta}|\boldsymbol{\theta}_1, \sigma_1^2\boldsymbol{I}_2)d\boldsymbol{\theta}. \tag{D.2}$$

However, unless the kernel centers θ_1 and θ_2 coincide, we need to approximate this function by a single Gaussian kernel. A feasible approach is to compute the first two moments of $q(\boldsymbol{\theta})$ by the conditional covariance formula, which can be expressed as

$$\begin{aligned} \boldsymbol{\theta}_q =& n_1\boldsymbol{\theta}_1 + n_2\boldsymbol{\theta}_2 \\ \boldsymbol{\Sigma}_q =& (n_1\sigma_1^2 + n_1\sigma_2^2)\boldsymbol{I} + n_1n_2(n_1 + n_2)(\boldsymbol{\theta}_1 - \boldsymbol{\theta}_2)(\boldsymbol{\theta}_1 - \boldsymbol{\theta}_2)^\top. \end{aligned} \tag{D.3}$$

This expression may contain cross-covariance in $\boldsymbol{\Sigma}_q$, but we seek a homogeneous Gaussian density $p(\boldsymbol{\theta}) = \mathcal{N}(\boldsymbol{\theta}|\boldsymbol{\theta}_p, \sigma_p^2\boldsymbol{I}_2)$ that best approximates $q(\boldsymbol{\theta})$. This problem can be posed as minimizing KL-divergence from p to q, as

$$\{\boldsymbol{\theta}_p, \sigma_p\} = \underset{\boldsymbol{\theta}_p, \sigma_p}{\operatorname{argmin}} \left(\mathrm{KL}(p||q)\right). \tag{D.4}$$

As the KL-divergence of multivariate Gaussian distributions takes the form

$$\mathrm{KL}(q||p) = \frac{1}{2}\Big(\log \frac{|\boldsymbol{\Sigma}_p|}{|\boldsymbol{\Sigma}_q|} - 2 + \mathrm{Tr}(\boldsymbol{\Sigma}_p^{-1}\boldsymbol{\Sigma}_q) + (\boldsymbol{\theta}_q - \boldsymbol{\theta}_p)^\top \boldsymbol{\Sigma}_p^{-1}(\boldsymbol{\theta}_q - \boldsymbol{\theta}_p)\Big),$$

we can zero the quadratic term by $\boldsymbol{\theta}_p = \boldsymbol{\theta}_q$. Consider the equivalent problem

$$\sigma_p = \underset{\sigma_p}{\mathrm{argmin}}\ (\mathrm{KL}(p||q)) \quad \text{with} \quad \boldsymbol{\theta}_p = \boldsymbol{\theta}_q. \tag{D.5}$$

Now, let $x = \sqrt{\det(\boldsymbol{\Sigma}_p)} = \sigma_p^2$. Then

$$2\mathrm{KL}(q||p)\Big|_{\theta_p=\theta_q} = \log(x^2) - \log(|\boldsymbol{\Sigma}_q|) - 2 + \mathrm{Tr}(\boldsymbol{\Sigma}_q)/x. \tag{D.6}$$

Then,

$$\frac{\mathrm{d}}{\mathrm{d}x}\Big(2\mathrm{KL}(q||p)\Big|_{\theta_p=\theta_q}\Big) = \frac{2x - \mathrm{Tr}(\boldsymbol{\Sigma}_q)}{x^2} = 0, \tag{D.7}$$

when $x = \mathrm{Tr}(\boldsymbol{\Sigma}_q)/2 \Rightarrow \sigma_p = \sqrt{\mathrm{Tr}(\boldsymbol{\Sigma}_q)/2}$, is a minimizer of (D.5) as the function in (D.6) is convex on $x > 0$. Expressed in (D.3), we obtain

$$\begin{aligned} w_p &= w_1 + w_2 \\ \boldsymbol{\theta}_p &= n_1\boldsymbol{\theta}_1 + n_2\boldsymbol{\theta}_2, \\ \sigma_p^2 &= (n_1\sigma_1^2 + n_2\sigma_2^2), + \tfrac{1}{2}n_1n_2(n_1+n_2)\|\boldsymbol{\theta}_1 - \boldsymbol{\theta}_2\|^2, \end{aligned} \tag{D.8}$$

which are the equations used in the `Fuse()` operation of the GAPSL.

Printed by Media-Tryck, Lund 2021 NORDIC SWAN ECOLABEL 3041 0903

Department of Automatic Control
P.O. Box 118, 221 00 Lund, Sweden
www.control.lth.se

PhD Thesis TFRT-1131
ISBN 978-91-8039-047-7
ISSN 0280–5316